Multi-scale analysis of freezing process in mining applications: From equilibrium to non-equilibrium

MINGHAN XU
Doctor of Philosophy

Department of Mining and Materials Engineering
Faculty of Engineering
McGill University
Montreal, Quebec, Canada

August 15, 2024

A thesis submitted to McGill University in partial
fulfillment of the requirements of the degree of
Doctor of Philosophy

To my partner, parents, and grandparents:

I am grateful for how you have shaped me into the person I am today.

Abstract

The mining sector is crucial to Canada's economy but faces challenges in transitioning to sustainable practices amid increasing global energy demands and climate change. Dependency on fossil fuels contributes to carbon emissions, while rising temperatures in northern regions accelerate permafrost degradation, threatening critical infrastructure and mining operations. Addressing these challenges requires innovative solutions and a deeper understanding of physical phenomena in cold climates that are unique to Canada, such as solid-liquid phase changes, to ensure the industry's long-term sustainability.

This dissertation focuses on advancing our fundamental knowledge of solidification, including both equilibrium and non-equilibrium processes, at multiple temporal and spatial scales through theoretical and experimental analyses. It begins with a state-of-the-art review of freezing processes, outlining recent progress from fundamental, methodological, and applied perspectives. The thesis then addresses macro-scale equilibrium solidification by developing novel analytical solutions to two-phase Stefan problems via singular perturbation and asymptotic analysis, which are both accurate and computationally efficient. These solutions facilitate the thermal estimation of phase change materials (PCMs) for cold thermal energy storage, as well as artificial ground freezing (AGF) for stabilizing ore deposits and protecting permafrost.

The thesis advances to the study of multi-stage and multi-scale non-equilibrium solidification, characterized by innovative laboratory experiments and unified mathematical models. Specifically, it examines the five-stage solidification of pure substances and mixtures, including stochastic heterogeneous nucleation, non-linear crystal growth, and coupled heat and mass transport with freeze-point depression. The multi-scale analysis captures temporal and spatial phenomena using novel experimental and mathematical frameworks. Non-equilibrium solidification significantly enhances the development of PCMs for cold thermal energy storage, as well as spray freezing (SF) for heating, cooling, and decontaminating wastewater in mines.

The combination of equilibrium and non-equilibrium solidification, investigated through theoretical and experimental frameworks, contributes to our fundamental understanding of complex phase-change processes. The developed analytical solution to two-phase Stefan problems significantly reduces the computational time for equilibrium processes compared to numerical methods. The novel multi-stage and multi-scale frameworks for both pure substances and mixtures accurately characterize non-equilibrium behaviors (e.g., heterogeneous nucleation and non-linear crystal growth) that are otherwise difficult to obtain via conventional approaches.

From an applied perspective, the freezing process (both at equilibrium and non-equilibrium) is a key influential factor in the thermal estimation and design of AGF, PCMs, and SF. The developed frameworks delineate practical parameters such as total freezing time, interface movement, thermal storage capacity, freeze concentration, ice quality, and ice production. Accurate analysis of freezing phenomena is of great importance in the innovation, development, and integration of these cutting-edge clean technology solutions, tailored specifically to the unique landscapes and environments of Canadian mines in today's global energy transition and climate crisis.

Abrégé

Le secteur minier est essentiel à l'économie du Canada, mais il doit relever des défis pour passer à des pratiques durables dans un contexte d'augmentation de la demande mondiale d'énergie et de changement climatique. La dépendance à l'égard des combustibles fossiles contribue aux émissions de carbone, tandis que la hausse des températures dans les régions septentrionales accélère la dégradation du pergélisol, menaçant les infrastructures essentielles et les opérations minières. Pour relever ces défis, il faut des solutions innovantes et une meilleure compréhension des phénomènes physiques dans les climats froids qui sont uniques au Canada, tels que les changements de phase solide-liquide, afin d'assurer la durabilité à long terme de l'industrie.

Cette thèse se concentre sur l'avancement de nos connaissances fondamentales de la solidification, y compris les processus d'équilibre et de non-équilibre, à de multiples échelles temporelles et spatiales par le biais d'analyses théoriques et expérimentales. Elle commence par une revue de l'état de l'art des processus de congélation, soulignant les progrès récents d'un point de vue fondamental, méthodologique et appliqué. La thèse aborde ensuite la solidification à l'équilibre à grande échelle en développant de nouvelles solutions analytiques aux problèmes de Stefan à deux phases par perturbation singulière et analyse asymptotique, qui sont à la fois précises et efficaces sur le plan informatique. Ces solutions facilitent l'estimation thermique des matériaux à changement de phase (MCP) pour le stockage de l'énergie thermique froide, ainsi que la congélation artificielle du sol (AGF) pour la stabilisation des gisements de minerais et la protection du pergélisol.

La thèse porte sur l'étude de la solidification non-équilibrée en plusieurs étapes et à

plusieurs échelles, caractérisée par des expériences de laboratoire innovantes et des modèles mathématiques unifiés. Plus précisément, elle examine la solidification en cinq étapes de substances pures et de mélanges, y compris la nucléation hétérogène stochastique, la croissance cristalline non linéaire et le transport couplé de chaleur et de masse avec la dépression du point de congélation. L'analyse multi-échelle saisit les phénomènes temporels et spatiaux à l'aide de nouveaux cadres expérimentaux et mathématiques. La solidification hors équilibre améliore considérablement le développement des MCP pour le stockage de l'énergie thermique froide, ainsi que la congélation par pulvérisation (SF) pour le chauffage, le refroidissement et la décontamination des eaux usées dans les mines.

La combinaison de la solidification à l'équilibre et de la solidification hors équilibre, étudiée dans des cadres théoriques et expérimentaux, contribue à notre compréhension fondamentale des processus complexes de changement de phase. La solution analytique développée pour les problèmes de Stefan à deux phases réduit considérablement le temps de calcul pour les processus d'équilibre par rapport aux méthodes numériques. Les nouveaux cadres multi-étapes et multi-échelles pour les substances pures et les mélanges caractérisent avec précision les comportements hors équilibre (par exemple, la nucléation hétérogène et la croissance cristalline non linéaire) qui sont autrement difficiles à obtenir par des approches conventionnelles.

D'un point de vue appliqué, le processus de congélation (à l'équilibre et hors équilibre) est un facteur d'influence clé dans l'estimation thermique et la conception des AGF, MCP et SF. Les cadres développés délimitent des paramètres pratiques tels que la durée totale de congélation, le mouvement de l'interface, la capacité de stockage thermique, la concentration de gel, la qualité de la glace et la production de glace. L'analyse précise des phénomènes de congélation est d'une grande importance pour l'innovation, le développement et l'intégration de ces solutions technologiques propres de pointe, adaptées spécifiquement aux paysages et environnements uniques des mines canadiennes dans le cadre de la transition énergétique mondiale et de la crise climatique d'aujourd'hui.

Contribution of Authors

In accordance with the guidelines on manuscript-based (article-based) thesis preparation provided by the Office of Graduate and Postdoctoral Studies (GPS) at McGill University, an overview of my contributions and those of my co-authors is provided as follows.

I, **Minghan Xu**, am the first author of all the chapters presented in this dissertation. My primary contributions to the research presented in this dissertation are listed below. I took the lead in

- conceptualizing the problem;
- developing the mathematical framework;
- deriving the governing equations and analytical/semi-analytical solutions by hand and using software (Wolfram Mathematica);
- writing the code for computational methods, data analysis, and visualization (in MATLAB);
- validating and verifying the experimental and simulation results;
- conducting formal analysis and data curation; and
- writing the original drafts, coordinating the reviews from other team members, responding to reviewers during the peer-review process, and editing the manuscripts.

This dissertation consists of six peer-reviewed journal publications from Chapters 3 to 6. In addition to my primary authorship, Prof. Agus Sasmito is the corresponding author, and Dr. Saad Akhtar is one of the co-authors in all the chapters. Their contributions are specified as follows:

- **Prof. Agus P. Sasmito** (McGill University) is my Ph.D. thesis supervisor, providing significant guidance by: (i) advising me throughout the research process; (ii) giving useful and timely insights when encountering obstacles; (iii) supervising and administering the research project; (iv) training my skills in communicating and collaborating with academic and industrial stakeholders; and (v) assisting with the review and editing of all dissertation chapters.

- **Dr. Saad Akhtar** (National Renewable Energy Laboratory) is my Ph.D. mentor, offering generous support by: (i) sharing his knowledge and research expertise with me; (ii) sparking my research interests and motivating me to advance existing knowledge in the field; and (iii) assisting with the review and editing of Chapters 3 to 8.

For the other coauthors, their contributions are explicitly stated chapter by chapter as follows:

- In Chapter 3, Dr. Ahmad F. Zueter established the initial code of the numerical algorithm for verification; Mr. Victor Auger provided meaningful insights for the derivation of the perturbation solution; Prof. Mahmoud A. Alzoubi offered guidance on the thermal analysis of artificial ground freezing and transport phenomena in porous media, significantly helping me conceptualize and solve the research problem.

- In Chapter 4, Dr. Ahmad F. Zueter established the initial code of the numerical algorithm for verification; Prof. Mahmoud A. Alzoubi offered important guidance on the thermal analysis of phase change materials and data visualization; Prof. Laxmi Sushama acted as a co-supervisor of this research project and funded the project through the Trottier Institute for Sustainability in Engineering and Design (TISED) at McGill University.

- In Chapter 5, Mr. Mohammaderfan Mohit assisted me in analyzing the mathematical problem and visualizing the data; Dr. Ahmad F. Zueter established the initial code of the numerical algorithm for verification.

- In Chapter 6, Prof. Yuguo Gao acted as a co-supervisor of this research project, leading the design and execution of the laboratory experiments; Mr. Fu Fang performed the experimental testing and collected the data; Ms. Benitta A. Chaedir assisted me in conducting a thorough literature review and analyzing the experimental and simulation data.

- In Chapter 7, Mr. Mohammaderfan Mohit provided meaningful insights into analyzing the mathematical problem and presenting the results.

- In Chapter 8, international collaboration with SCREEEN Holdings Co., Ltd., and Kyoto Institute of Technology (KIT) in Japan was involved: Dr. Yosuke Hanawa led the design and execution of the laboratory experiments at SCREEN and collected the experimental data; Prof. Atsushi Sakuma acted as a co-supervisor of this research project at KIT, coordinating with SCREEN and McGill on the data analysis and visualization; Mr. Jianliang Zhang performed image analysis from the raw experimental data, significantly contributing to the analysis and validation parts of this research. Mr. Junichi Yoshida, Masakazu Sanada, and Yuta Sasaki are executives of SCREEN on the development of sublimation drying for semiconductor devices. They took an important management role and oversaw the research project, which will help in the development of intellectual property among the three parties.

It is also noted that all of them have taken roles in reviewing and editing the manuscript during the publishing process.

Acknowledgements

This dissertation owes its existence to the invaluable support and guidance of my thesis supervisor, mentor, and collaborators. First and foremost, I express my deepest gratitude to Prof. Agus P. Sasmito, my doctoral thesis supervisor. Prof. Sasmito, your guidance, patience, dedication, empathy, and generosity have been beyond measure. I am profoundly grateful for the wealth of knowledge and skills I have gained under your training.

I extend heartfelt thanks to Dr. Saad Akhtar, my Ph.D. mentor. You have one of the most beautiful minds that I have ever seen, and I could not be where I am in research without you. To my other mentor, Prof. Mahmoud A. Alzoubi, your advice, collaboration, and companionship have made this arduous journey easy for me, filled with joy and happiness. Additionally, I appreciate the significant contributions to various chapters of this dissertation from my colleagues, Dr. Ahmad F. Zueter, Mr. Victor Auger, Ms. Benitta A. Chaedir, and Mr. Mohammaderfan Mohit.

Furthermore, I am grateful for the fruitful collaboration with Prof. Laxmi Sushama (Civil Engineering Department, McGill University, Canada), Prof. Yuguo Gao and his team (North China University of Water Resources and Electric Power, China), Dr. Yosuke Hanawa and his team (SCREEEN Holdings Co., Ltd., Japan), and Prof. Atsushi Sakuma and his team (Kyoto Institute of Technology, Japan), which have broadened the scope and impact of my research.

As I mark a decade of academic pursuit at McGill University, including both bachelor's and doctoral studies, I am extremely fortunate to have crossed paths with exceptional individuals. Since the inception of my Ph.D. journey in 2019, I extend my gratitude to the members of Prof. Sasmito's Research Group (in chronological order): Prof. Amiri, Matthew, Putra, Ika, Azlan, Rasyid, Erlei, Jiyuan, Adel, Fatemeh, Khalil, Mohammad, Saad (Tareen), Hamidreza, Kim, Ivana, Prof. Wijayanta, Prof. Zhao, Yunzhuo, and Galih. It is my privilege to meet and know you all. Your camaraderie and support have been invaluable.

I also acknowledge the financial support provided by several graduate scholarships, including the McGill Engineering Doctoral Award (MEDA), Fonds de recherche du Québec - Nature et technologies (FRQNT) Doctoral and Master's Scholarships, Mitacs Accelerate International Award, and the Vanier Canada Graduate Scholarship (Vanier CGS) from the Natural Sciences and Engineering Research Council of Canada (NSERC). These scholarships have not only eased the financial burden but also fueled my research pursuits with freedom and purpose.

Above all, I owe an immense debt of gratitude to my family. To my partner (Dorsa), my parents, and my grandparents, your unwavering support, sacrifices, and love have been the keystone of my journey. Thank you for believing in me and nurturing my dreams.

Contents

List of Figures

List of Tables

Part I

Introduction and Literature Review

Chapter 1

Introduction

Contents

1.1 Background

The mining sector is vital for our economy and a leader in the world, contributing $156 billion to Canada's Gross Domestic Product (GDP) and providing up to 22% of total merchandise exports [4]. With increasing demand to produce minerals and metals for the global energy transition, the mining industry is encountering technical, economic, and environmental issues that need to be addressed to guarantee the sustainable growth of this cornerstone of our economy in today's changing climate and global energy transition.

One key challenge is that the industry is heavily dependent on fossil fuels for operations (e.g., fleets), power supply, energy storage, and heating and cooling. While Canada has one of the world's cleanest electricity grids, carbon dependency remains intensive in mines that are not connected to the electric grid or natural gas pipelines, and renewable alternatives are still expensive. Additionally, heating demand is particularly high in mines located in cold-climate regions, like Canada, and the cooling requirement is also significant for deep mines. This could take up to half of the total energy costs [1]. The most common practice for air heating and cooling in mines is burning propane or natural gas or using diesel engines, yet this results in a considerable amount of carbon emissions.

Another contemporary issue in the mining industry is related to the climate crisis. As we look towards the future, it becomes evident that economic and regulatory factors will necessitate the adoption of advanced and sustainable mining practices, particularly in the pristine landscapes of Canada's northern regions. Northern Canada, where mining makes up a substantial portion of the economy, is now faced with the consequences of a changing climate. The average temperature in this remote expanse has been rising at an alarming rate, nearly three times faster than the global average, presenting a stark challenge in the form of permafrost degradation. Permafrost, the frozen ground that underlies nearly half of Canadian land, is currently at risk of thawing, unleashing a cascade of threats to the built environment and infrastructure, including the crucial mining operations that are the lifeblood of these northern communities [2, 3, 5].

The unique environment in Canada under today's energy and climate crisis is hinged on our fundamental understanding of the physical process of phase transitions in cold climates. Specifically, it includes the phase change between liquid and solid (i.e., freezing and melting). These phase transitions usually take place in pure substances (e.g., water/ice), mixtures (e.g., aqueous solution), and porous media (e.g., ground, permafrost); their transport phenomena vary with spatial and temporal scales. Consequently, it is of utmost importance to foster the development of the phase-change physics in different types of substances at multiple scales.

1.2 Objectives

The overarching objective of this doctoral dissertation is to advance our fundamental understanding of solidification and its applications in mine operations and energy systems under the Canadian context. The applications include: (i) phase change materials (PCMs) for cold thermal energy storage in northern mines; (ii) artificial ground freezing (AGF) for stabilizing intricate uranium ore deposits and thawing permafrost; and (iii) spray freezing (SF) technology to produce ice stopes for mine heating/cooling and decontaminate mine wastewater. Canadian mines that have adopted or will soon utilize these technologies are the Giant Mine (Northwest Territories), Cigar Lake Mine (Saskatchewan), Frood-Stobie Mine (Ontario), and LaRonde Mine (Québec). To achieve the main objective, the following two sub-objectives can be specified:

1. Develop a fast-to-compute and mathematically rigorous analytical model for equilibrium solidification in pure substances and porous media at the macro-scale, which can provide a rule-of-thumb estimation of the freezing processes in PCMs and AGF for cold thermal energy storage and ground support; and
2. Characterize and predict the non-equilibrium solidification in pure substances and mixtures through experimental and mathematical frameworks that involve multi-stage and multi-scale phenomena, which can be utilized in PCMs and SF for cold thermal energy storage and mine heating, cooling, and wastewater pre-treatment.

1.3 Thesis organization

This doctoral dissertation is structured into four parts with nine chapters, as shown in Fig. 1.1.

- Part I introduces the background, objectives, and outline of this thesis in Chapter 1. It also conducts a comprehensive literature review on the freezing process from the fundamental, methodological, and applied aspects in Chapter 2.
- Part II focuses on the equilibrium solidification at the macro-scale through the so-called Stefan problem. Chapter 3 employs the singular perturbation method to characterize

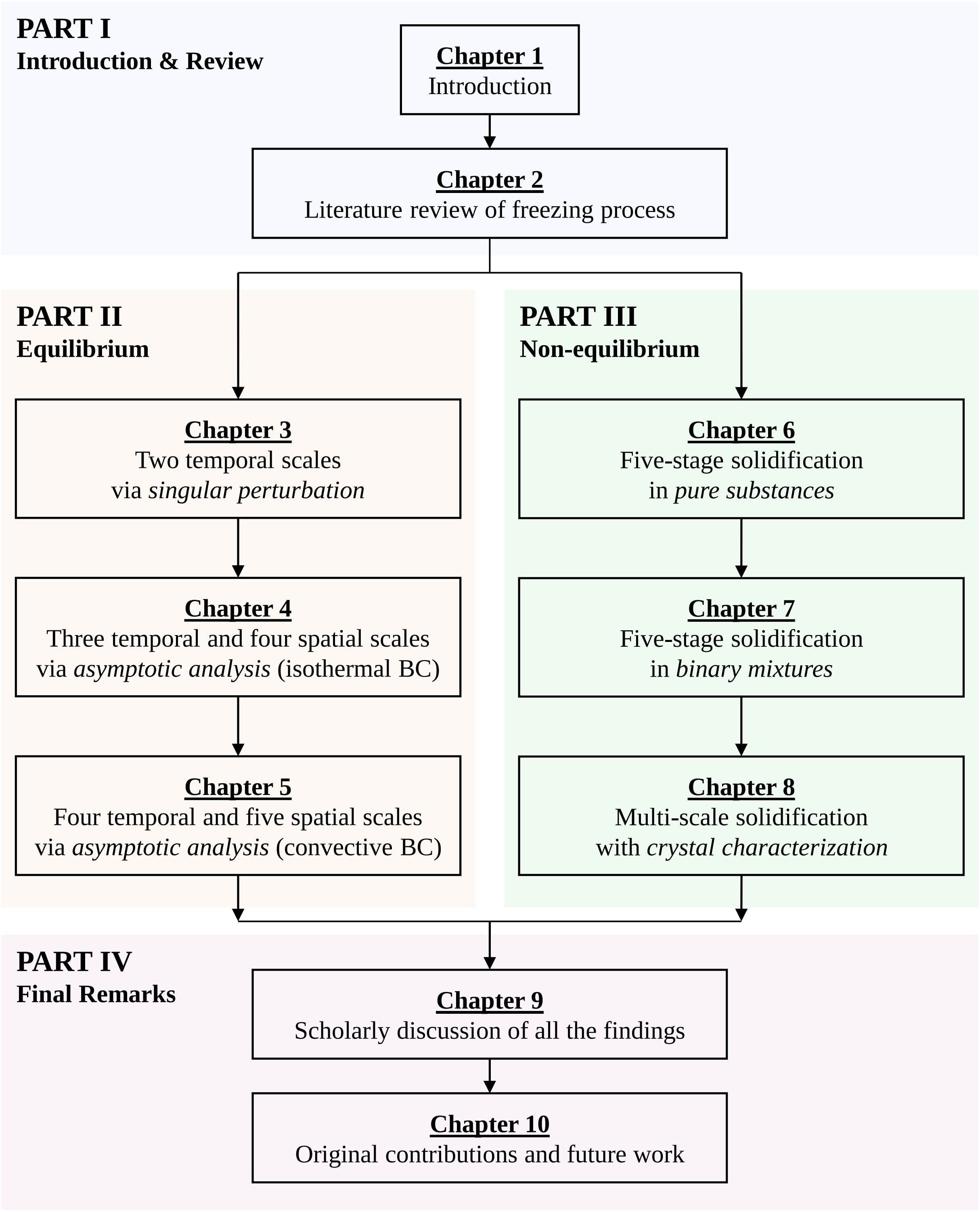

Figure 1.1: A diagram for the roadmap of this doctoral dissertation.

two temporal scales and its application to AGF in porous media. Chapter 4 utilizes the asymptotic analysis and solves a two-phase Stefan problem with multiple spatio-temporal scales (i.e., three temporal and four spatial scales). Chapter 5 incorporates a similar asymptotic analysis yet to a more general Stefan problem subject to a realistic convective boundary, where four temporal and five spatial scales are studied.

- Part III investigates the non-equilibrium solidification through experimental and mathematical approaches. Chapter 6 establishes an experimental system and a unified mathematical model on the non-equilibrium five-stage solidification of PCM for cold thermal energy storage. Chapter 7 extends the five-stage solidification framework into the non-equilibrium freezing of binary mixtures, which facilitates the development of SF for mine heating, cooling, and wastewater decontamination. Chapter 8 conducts multi-scale analysis of PCM through experimental and hybrid analytical-numerical approaches, where the growth and morphology of crystals are thoroughly characterized.
- Part IV provides general discussion and key conclusions of this thesis along with potential directions of future work in Chapter 9.

Bibliography

[1] S. Akhtar, A. Madiseh, and A. Sasmito. Numerical investigation of a novel phase-change renewable energy system for underground mine heating and cooling. *Refrigeration Science and Technology*, 2018, 2018.

[2] J. D. Ford, N. Couture, T. Bell, and D. G. Clark. Climate change and Canada's north coast: Research trends, progress, and future directions. *Environmental Reviews*, 26(1):82–92, 2018.

[3] A. G. Lewkowicz and R. G. Way. Extremes of summer climate trigger thousands of thermokarst landslides in a high arctic environment. *Nature communications*, 10(1):1329, 2019.

[4] Mining Association of Canada. The Canadian mining story: Economic impacts

and drivers for the global energy transition. `https://mining.ca/flippingbooks/mac-report-2023`, 2023.

[5] T. J. Porter, S. W. Schoenemann, L. J. Davies, E. J. Steig, S. Bandara, and D. G. Froese. Recent summer warming in northwestern Canada exceeds the holocene thermal maximum. *Nature communications*, 10(1):1631, 2019.

Chapter 2

A state-of-the-art review of freezing process: Fundamentals, methodology, and applications

Contents

2.1 Introduction

Freezing, the transformation of a liquid into a solid state, represents one of the fundamental phase transitions ubiquitous on Earth. Typically instigated by a decrease in temperature or cooling, this phase transition requires surpassing the fusion point of the material, thereby initiating the phase change from a liquid to a solid state. While appearing ostensibly straightforward, freezing exhibits distinctive fundamental characteristics such as latent heat release, supercooling degree, crystal growth, and interfacial dynamics, among others. Moreover, when the material is impure, such as in solutions or colloids, the freezing process introduces an additional layer of complexity, manifesting in phenomena like freezing-point depression and solute segregation. The scholarly discourse surrounding the topic of "freezing" has witnessed remarkable growth since the mid-20th century, as evidenced by a notable surge in publications, exemplified in Fig. 2.1. This burgeoning interest demonstrates the growing significance of freezing within the academic community, indicative of its multifaceted nature and pervasive relevance.

Beyond its fundamental complexity, the burgeoning field of freezing has spurred the development of innovative methodologies and diverse applications aimed at both predicting and harnessing this process. In the 19th century, J. Stefan pioneered a mathematical formulation to analyze the temperature distribution and motion of the solid-liquid interface during water solidification, thereby formulating what is now known as the Stefan problem [6]. This mathematical problem, characterized by partial differential equations and a moving boundary condition, has captivated applied mathematicians owing to its intriguing nonlinearity. Concurrently, various other methodologies, including the enthalpy method, level-set method, and phase field method, have been extensively explored in the realms of applied mathematics and computation, enriching our understanding of the freezing phenomenon. Fundamental studies on the freezing process have been comprehensively summarized in several classic texts [73, 78, 115, 113].

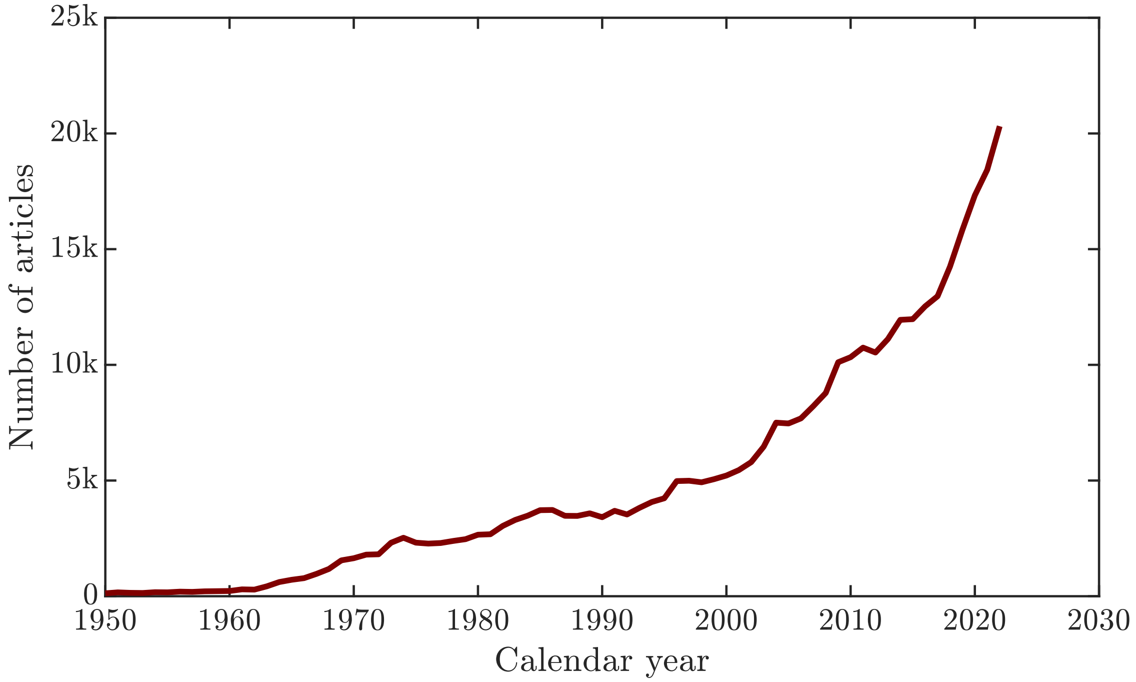

Figure 2.1: Number of published articles over time in the Scopus database from 1950 to 2022. The keywords in the search are “(freez*) OR (solidify*) OR (solidification)”.

Freezing finds extensive applications across diverse natural and engineering domains, as depicted in Fig. 2.2. From atmospheric occurrences such as snow [105] and freezing rain [62] to geological phenomena like permafrost [11], the ramifications of freezing are far-reaching. With the exacerbation of climate change and the escalation of extreme weather events, the prevalence of freezing phenomena is expected to intensify, which needs a deeper understanding of its implications in both atmospheric and subsurface environments. Additionally, the distinctive attributes of freezing, including the conversion of fluidic substances into stable solids and the liberation of latent heat, have been exploited across a spectrum of engineering applications. These applications span from the storage of cold thermal energy using phase change materials [144] to mine heating systems [2] and the preservation of agricultural and pharmaceutical products through spray freezing [81], revealing the versatile utility of freezing processes.

Given the progressive evolution and burgeoning interest surrounding freezing phenomena, it is imperative to conduct a comprehensive review of existing literature and provide critical

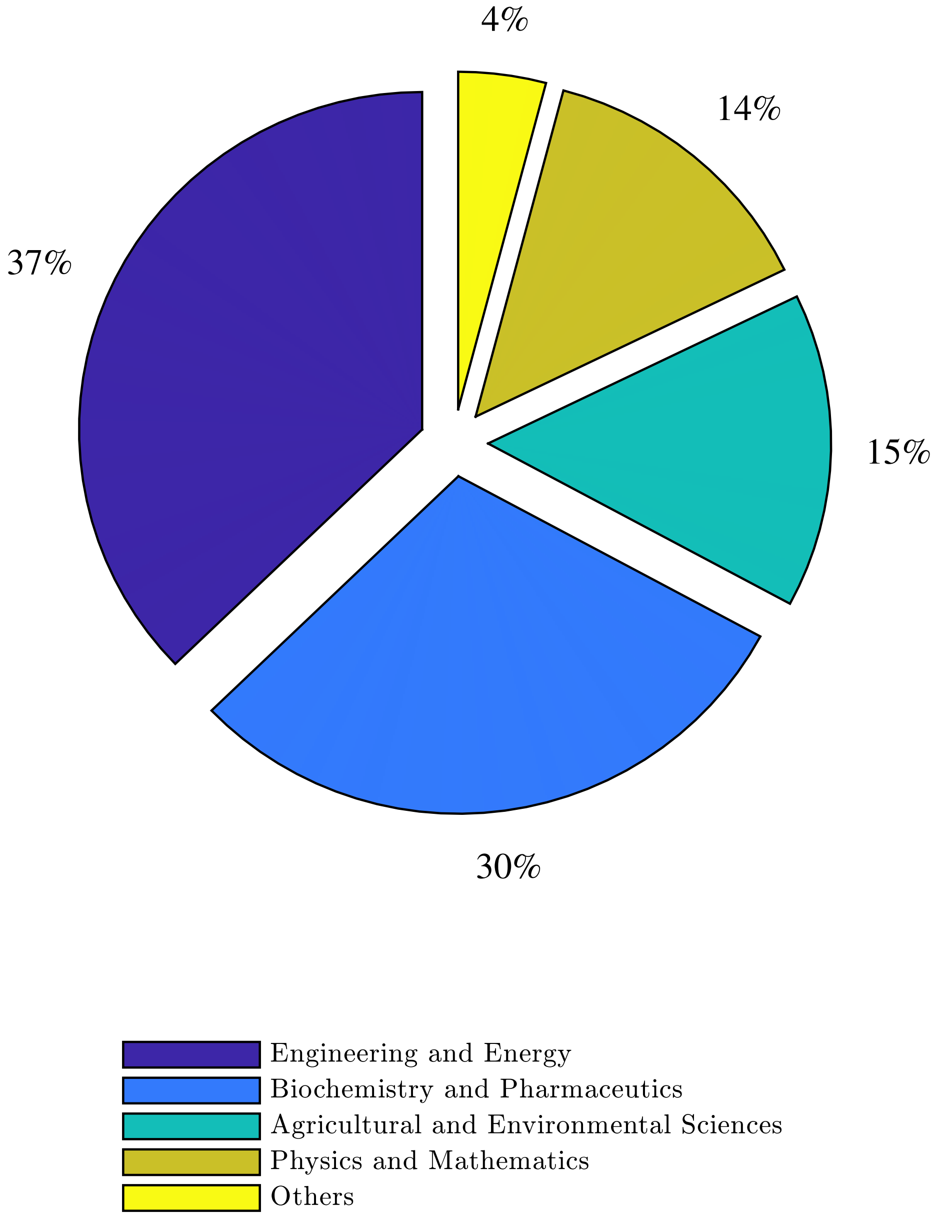

Figure 2.2: Published articles categorized based on the main subjects from 1950 to 2022 with the same criteria as Fig. 2.1.

insights for future research endeavors. The overarching objectives of this review are outlined as follows:

1. To comprehensively summarize key fundamental knowledge, methodologies, and applications pertaining to the freezing process.

2. To critically analyze and compare various understandings and approaches to freezing,

offering nuanced insights for both emerging and established scholars.

3. To delineate future research directions aimed at advancing the field of freezing while addressing contemporary challenges such as climate change and the energy crisis.

This review embarks on a systematic exploration, commencing with an elucidation of fundamental aspects of the freezing process, with particular emphasis on the key physical phenomena observed in both pure substances and mixtures. Subsequently, an overview of diverse methodologies spanning experimental, theoretical, and computational approaches is presented, accompanied by a nuanced discussion of their respective advantages and limitations. Furthermore, notable freezing-related applications across natural and engineering domains are summarized, highlighting the significance and implications of freezing phenomena within each context. Finally, the review culminates with a synthesis of major achievements and advancements across fundamental, methodological, and applied dimensions of the freezing process, while concurrently charting potential future research trajectories in each realm.

2.2 Fundamental aspect

2.2.1 Freezing in pure substances

When considering the freezing process in pure substances (e.g., solutions or metals without any impurity), it can be either stable or unstable [84], which is also referred to as the mechanisms without or with crystallization. Most pure liquids freeze by crystallization that is unstable. This mainly implies that the liquid is firstly supercooled or undercooled below its freezing point, resulting in a thermodynamically unstable (or metastable) state. In this case, there are five distinct solidification stages: (i) supercooling of liquid, (ii) nucleation, (iii) recalescence or crystal growth, (iv) equilibrium freezing, and (v) subcooling of solid. The five stages occur in the freezing of pure substances. However, some of the stages will be changed or combined when freezing non-pure substances, including binary mixture and porous media. The non-pure systems will be discussed thoroughly in the subsequent sub-section.

The stable process does not involve crystallization. The liquid cools till its freezing point and starts to form a solid portion right afterward. As a result, there are only three solidification stages: (i) pre-cooling of liquid, (ii) equilibrium freezing, and (iii) subcooling of solid. The nucleation and recalescence stages in the unstable freezing process do not occur here. That is, the effects of thermodynamics and kinetics are absent in the stable process. An alternative way to distinguish between the stable and unstable processes can be the ambient or surrounding temperature that prompts the solidification. If the surrounding temperature is lower or much lower than the supercooling temperature, unstable freezing will likely occur. Otherwise, the stable freezing process will happen. This finding was implicitly shown in Sebastiao et al.'s experimental data [164] along with Hindmarsh et al.'s results [75] on the solidification of pure water and sucrose aqueous droplets. A conceptual diagram for the freezing curves of the stable and unstable processes is schematically shown in Fig. 2.3.

Stable or equilibrium process

The stable process is often referred to as the equilibrium process or macro-scale solidification due to the absence of nucleation and recalescence happening at micro- and meso-scales. The first stage is pre-cooling, where the liquid's temperature drops down to the freezing point by sensible heat without any formation of the solid phase. Once the temperature goes below its fusion, the solid phase starts to form and both phases coexist within the domain, known as the (equilibrium) freezing stage. During equilibrium freezing, a large amount of latent heat is released due to the phase transition that is substantially higher than the sensible heat. Depending on the material properties (e.g., specific heat) and operating temperatures, the effect of sensible heat can even be neglected when predicting the freezing process [198]. A moving interface also occurs between the solid and liquid phases, in which the latent and sensible heats are the driving mechanisms. Lastly, the subcooling stage takes place after no

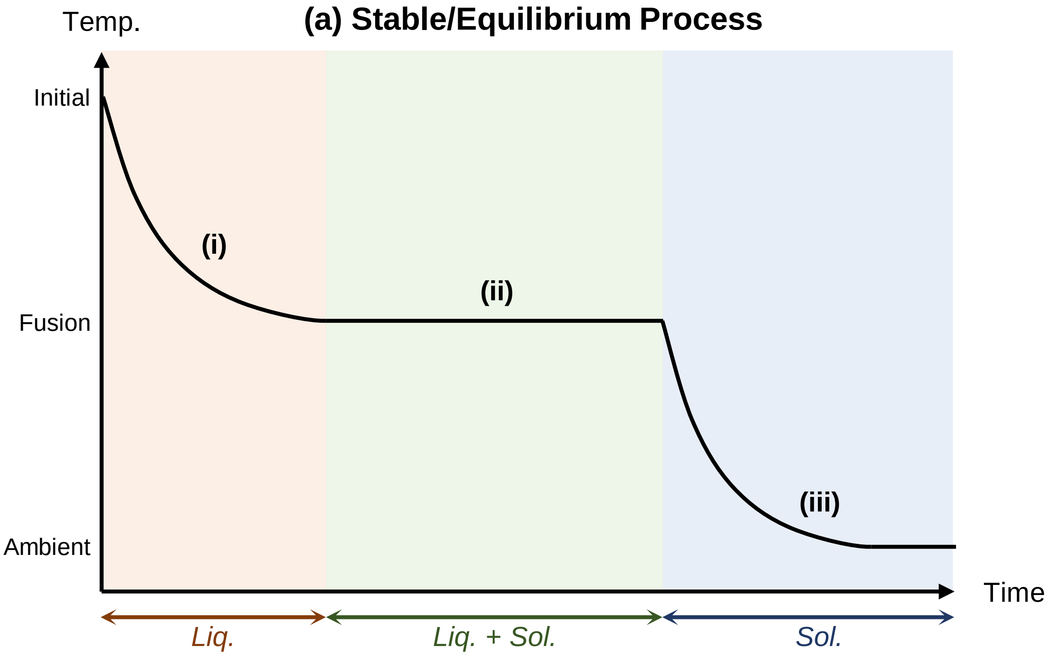

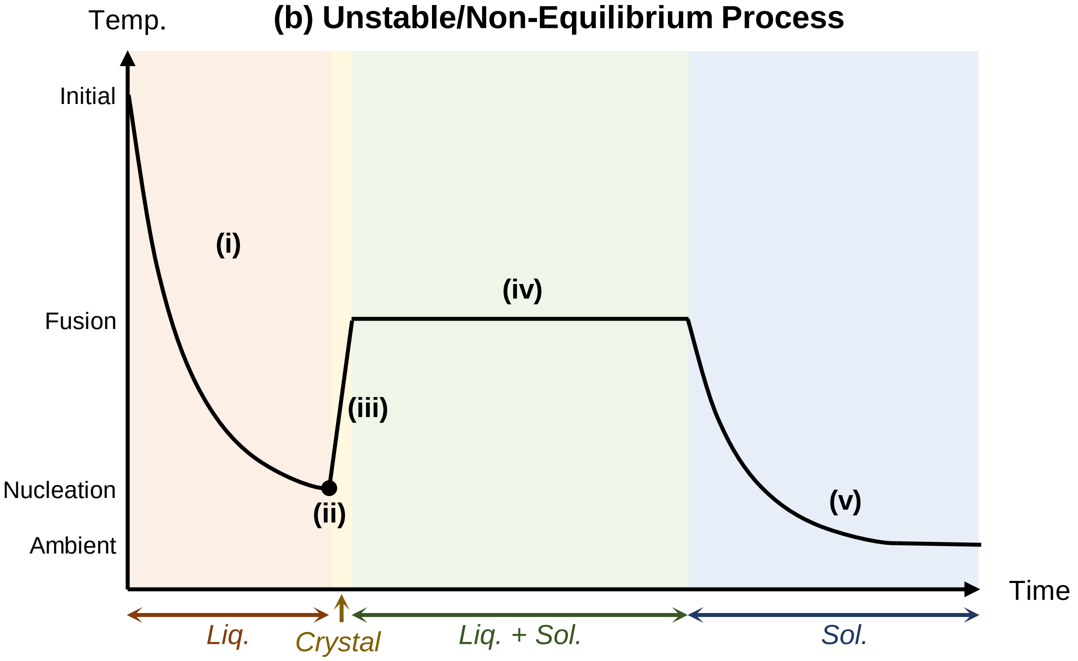

Figure 2.3: Conceptual diagram of the stable/equilibrium and unstable/non-equilibrium processes in terms of the temperature over time graphs (or freezing curves). The abbreviations “sol.” and “liq.” denote the solid and liquid phases, respectively. Roman numerals represent the solidification stages: in (a), (i) pre-cooling of liquid, (ii) equilibrium freezing, and (iii) subcooling of solid; in (b), (i) supercooling of liquid, (ii) nucleation, (iii) recalescence, (iv) equilibrium freezing, and (v) subcooling of solid.

liquid remains in the domain. The solid's temperature subcools by sensible heat and then reaches an equilibrium point that is often the ambient temperature.

Unstable or non-equilibrium process

Unstable or non-equilibrium freezing happens due to the material and its thermal condition. There are two main categories of solids based on their crystal structures, namely amorphous and crystalline solids. Most solids are crystalline, implying that their particles (atoms, molecules, or ions) arrange themselves in a repetitive lattice structure that extends over substantial distances in atomic terms. In this context, atoms can be analogous to spheres with diameters ranging from 2 to 6 Angstroms (1 Angstrom = 10^{-10} meters) [6]. The formation of a crystal might necessitate the movement of atoms into the solid lattice structure. Consequently, it is possible that the material's temperature is reduced without the solid formation taking place. The liquid at a temperature that is below its fusion is called supercooled liquid, which is considered to be thermodynamics metastable.

When looking into the nucleation stage after supercooling, the creation of a small nucleus happens by surpassing Gibbs free energy, constituting a spontaneous and stochastic nucleation phenomenon occurring at a microscopic level. There are two types of nucleation – homogeneous and heterogeneous nucleation. Homogeneous nucleation means the spontaneous formation and growth of small nuclei in the new phase, while the new phase is prompted by a foreign agent (e.g., a particle or a surface) in heterogeneous nucleation [85]. The theoretical examination of nucleation traces its origins to the 1920s with Max Volmer, a German physical chemist, who delved into the undercooling phenomenon observed in liquids [189]. Volmer elucidated an energy barrier that a new phase must overcome for its creation within the bulk phase. This new phase or nucleus holds less stability compared to the bulk phase due to surface tension. Later, classical nucleation theory (CNT) was developed, consisting of a cluster of nucleating particles and the bulk liquid; the kinetic process of the nucleating particles is governed by the macroscopic principles [48]. By incorporating the ef-

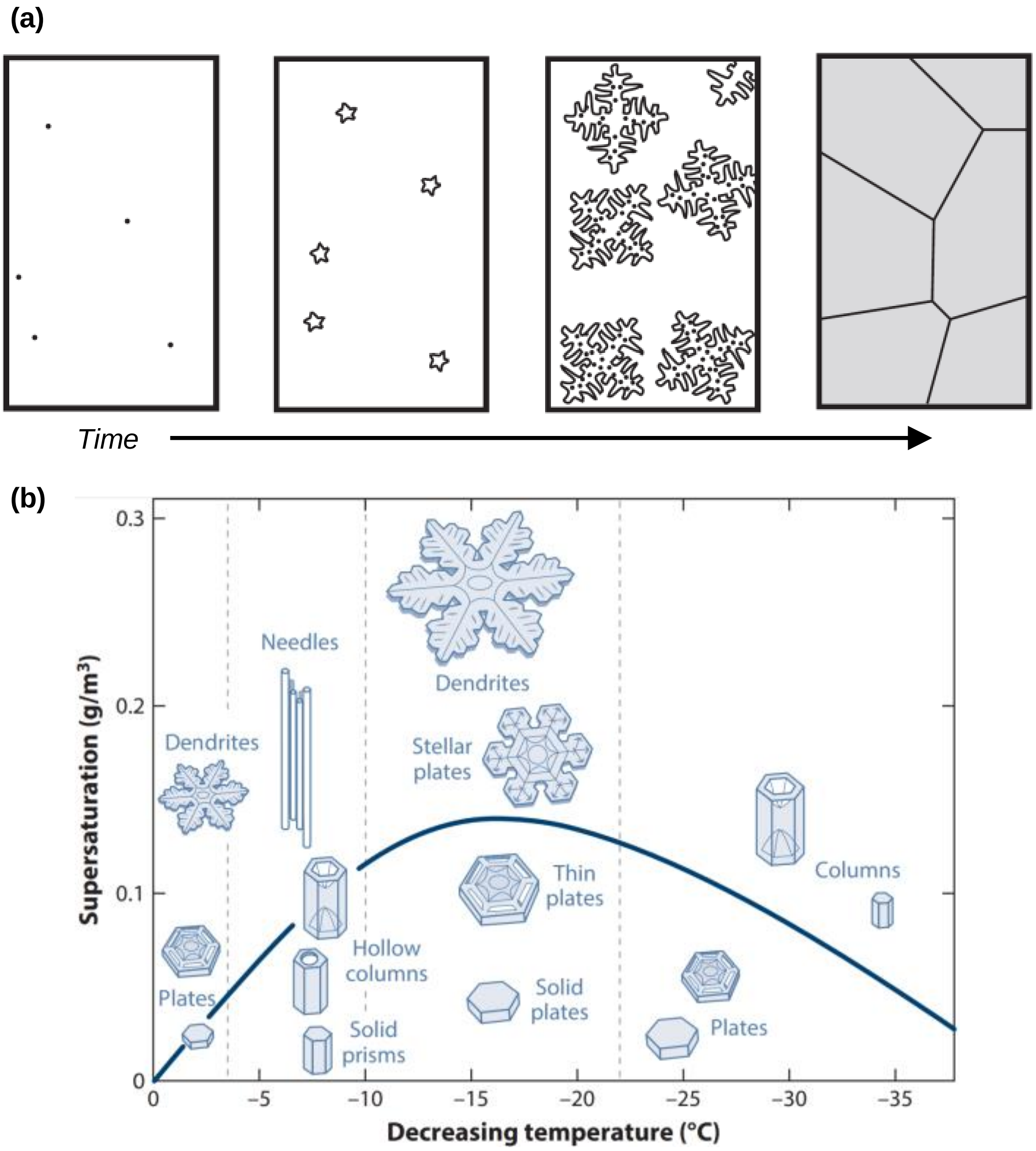

Figure 2.4: (a) Conceptual diagrams of crystal growth: Nuclei; small dendrites begin to develop from the nuclei; dendrites continue to develop; and grain boundaries without any dendrites (reprinted from [146]), and (b) Morphology diagram of snow crystals as a function of temperature and water vapor supersaturation (reprinted from [105]).

fect of impurity or foreign agents on the probability of nuclei formation, both homogeneous and heterogeneous nucleation can be predicted through the CNT.

The temperature quickly returns to the freezing point after nucleation. The stage from the nucleation temperature to the freezing point is referred to as crystal growth or recalescence. A crystalline interface is formed, which is non-linear and non-equilibrium [100]. The growth rate of this interface can be mainly influenced by three factors: thermal (or diffusive), kinetic, and surface curvature (or Gibbs-Thompson) effects [85, 3]. A conceptual diagram for the time evolution of crystal growth during the solidification of a pure substance, specifically metal, is illustrated in Fig. 2.4. As can be seen, the nuclei define the origin of dendritic growth, and the morphology changes over time. It is noted that the crystal morphology can have a variety of shapes, including plates, needles, columns, and prisms, which are not limited to dendrites [104, 139].

The solid phase starts to form right after the temperature returns to the freezing point, where both solid and liquid phases coexist in the domain, known as equilibrium freezing. The transport phenomena at this stage are the same as the above-mentioned second stage during the stable process. A solid-liquid interface also exists that can be either sharp or diffusive; both sensible and latent heats are released at this stage. Once all the domain becomes solid, the subcooling stage occurs identical to the one in the stable freezing process mentioned in Section 2.2.1.

2.2.2 Freezing in mixtures

The most significant difference between freezing in mixtures and pure substances arises from the inclusion of solutes, altering the stages and dynamics of solidification. As depicted conceptually in Fig. 2.5, freezing in mixtures (comprising binary or multi-component systems) also involves five solidification stages, each with distinct attributes. Fundamentally, three key aspects differentiate these processes: the degree of supercooling (or nucleation temperature), freezing point, and equilibrium freezing stage. Firstly, in mixtures, the degree of supercooling is relatively smaller compared to pure materials, resulting in a higher nucleation temperature. This discrepancy occurs due to solute addition, acting as an impurity in the supercooled liquid, thus stimulating the nucleation mechanism. Secondly, the freezing point of mixtures is reduced compared to their corresponding pure substances, a phenomenon termed freezing-point depression (FPD). Lastly, the depressed freezing temperature leads to a declining trend in the equilibrium freezing stage, illustrating the influence of solute concentration during the phase transition. This curvature reflects how the solute concentration impacts the freezing process.

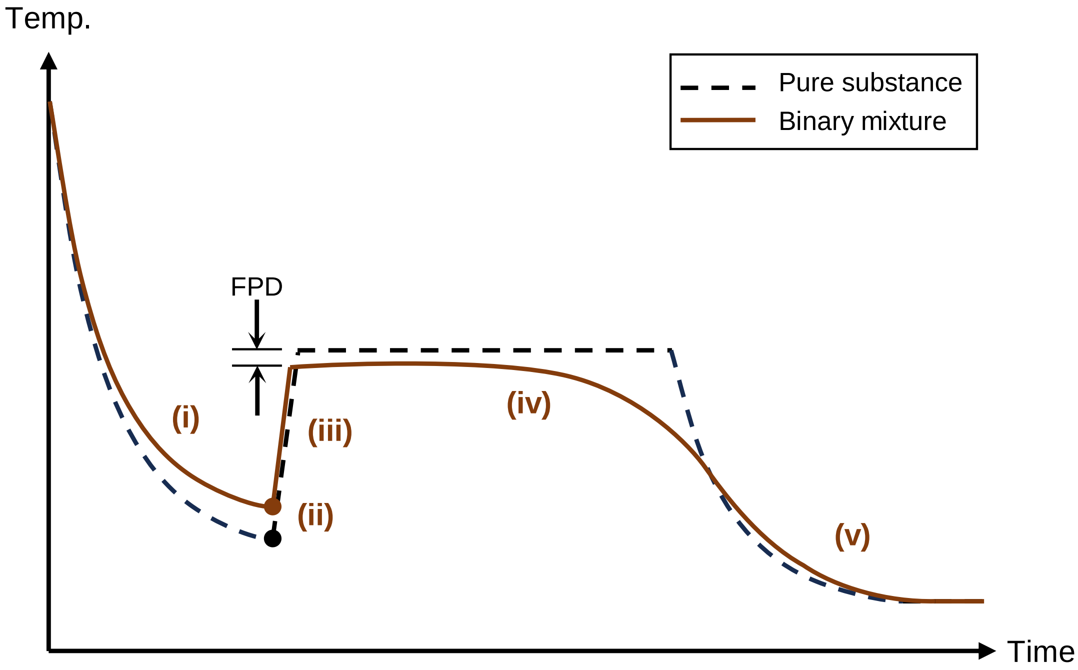

Figure 2.5: Conceptual diagram of solidification of pure substances and binary mixtures in terms of the temperature over time graphs (or freezing curves). Roman numerals represent the solidification stages (modified from [74]).

Solute segregation

When binary or multi-component systems reach equilibrium, one phase usually has a different composition compared to the others. At true equilibrium, there are no composition differences within each phase, meaning their composition is consistent and matches the correct temperature. It is nevertheless rare to achieve such balance in practice because the true equilibrium requires an extremely long-time duration even after the solid is formed. As a result, the segregation process of solutes is commonly investigated during phase change. Solute segregation can contribute to the formation of non-equilibrium new phases and non-uniform concentration within the pre-existing phase, which in turn facilitates materials exhibiting non-uniform thermo-physical and mechanical properties [13].

Segregation can be directly predicted by making assumptions, such as the existence of true equilibrium (namely Lever Rule) and uniform local composition of solid (namely Scheil equation) [63]. However, the basic phenomenon is the mass diffusion of solutes during freezing, where solute concentration varies in the solid and liquid phase changes over time and space. It is noted that solutes may not always be solvable in the solid phase. For instance, in the case of freezing sucrose aqueous solution, sucrose is not soluble in ice. This implies that the solute will be trapped in the liquid phase, as the solid propagates during freezing. Moreover, segregation is an influential factor for many freezing phenomena, including constitutional supercooling, heterogeneous nucleation, and crystallization or crystal growth rate.

Freezing-point depression

When a nonvolatile solute, one that does not readily vaporize, is dissolved in water or other solvents, it consistently lowers or depresses the freezing point of the solvent [33]. This occurrence is known as freezing-point depression (FPD). For instance, while the freezing point of water is 0°C, the addition of sugar or salt causes the freezing point to drop below 0°C. The degree of FPD is influenced by the solute type and concentration. During the equilibrium freezing stage, as the concentration in the liquid phase changes over time, the FPD also alters, resulting in a downward trend in the temperature profile, as illustrated in Fig. 2.5. This represents a significant difference between solidification in pure substances and binary mixtures. Figure 2.6 shows four examples of solutes, including sucrose, salt, glucose, and hydrogen chloride, and their corresponding FPD at different concentrations.

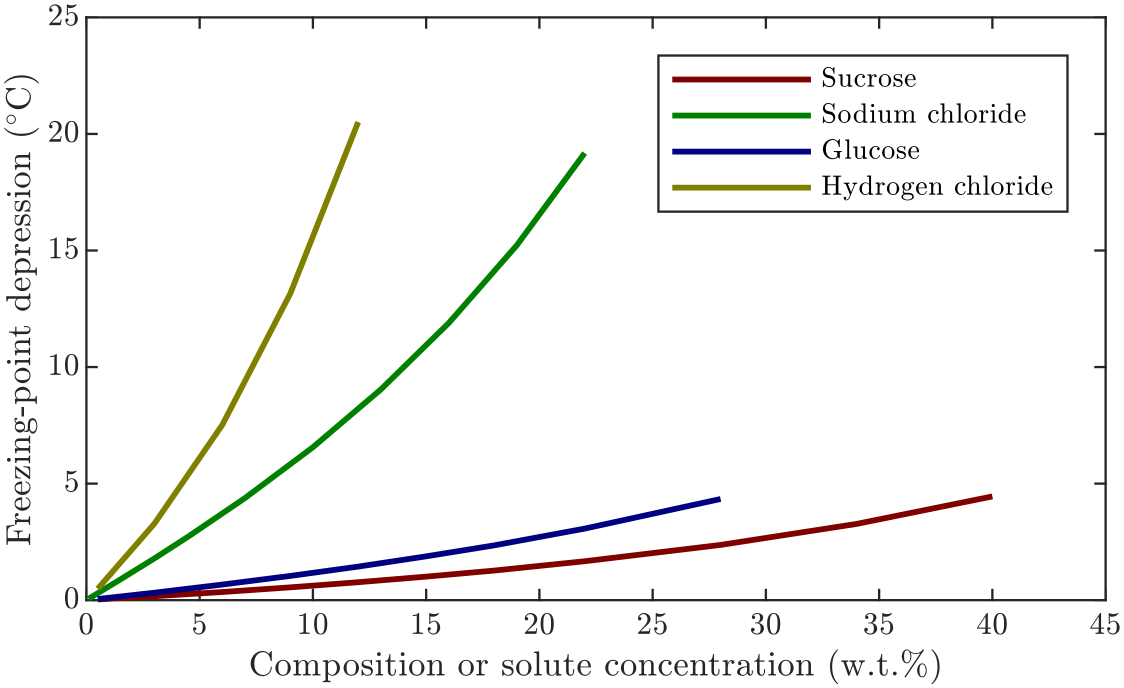

Figure 2.6: A graph of freezing-point depression over composition concentration for four solutes: sucrose $C_{12}H_{22}O_{11}$, sodium chloride or salt NaCl, α-D-glucose $C_6H_{12}O_6$, and hydrogen chloride HCl (data extracted from [106]).

Water activity in aqueous systems

Both temperature changes and the addition of a solute disrupt the water structure, modifying the nature and extent of hydrogen bonding [101]. Introducing solutes generally diminishes mass transfer from aqueous liquid or solid phases by reducing the equilibrium vapor pressure. This phenomenon of water interaction with solutes is commonly referred to as water activity [50]. In the freezing process, water activity holds significance in assessing convective mass transfer interactions with the surroundings. For instance, when an aqueous solution freezes in ambient air, water activity measures the impact of evaporation and sublimation.

2.3 Methodological aspect

2.3.1 Experimental methods

Experimental setup at a laboratory scale for solidification usually includes three main components: cooling equipment, measuring instruments, and data acquisition. Firstly, cooling equipment is essential for all solidification experiments to initiate the freezing process by lowering the temperature. The equipment typically includes thermoelectric cooling devices (e.g., Peltier [118]) or chillers (e.g., water-ethylene glycol bath, liquid nitrogen bath [77]), which are employed to cool down the temperature of the substrate plate or air in contact with the sample that needs to be solidified.

Measuring instruments are required to accurately quantify the temperature, nucleus, crystal growth, morphology, and so on. The most common instrument for temperature measurement is thermocouples. Standard calibration of thermocouples is mandatory before testing by identifying the device's error margin, and the accuracy of thermocouples varies significantly with their type (e.g., T-type, K-type) and material. Further correction or calibration was also conducted to consider effects like thermal inertia induced by the thermocouple [119]. Thermal cameras are also used in some experiments where the spatial variation of temperature is of great interest. The thermal cameras are generally not as accurate as thermocouples, but they preserve the sample without making any contact that could influence solidification, e.g., to prompt heterogeneous nucleation [76]. In cases where the characterization of nucleation and crystal evolution are important, high-speed cameras with sufficient lighting are used for optical measurements [145]. It is noted that image data captured by high-speed cameras may still demand significant processing, especially at meso- and micro-scale levels. As regards data acquisition systems, data loggers and computers are the standards for recording measurements and facilitating further analysis and visualization.

Experimental designs for solidification can be categorized based on the geometry or con-

Table 2.1: A list of works on experimental studies based on geometry since 2000.

Category			**Ref.**
Cartesian	enclosed	cavity	[79, 194, 95, 67, 31, 68, 22, 129, 111, 159]
		film	[161]
	channel		[177, 190, 136]
Cylindrical	inward		[137, 14, 152, 61, 59]
	outward	vertical	[108, 107]
		horizontal	[112, 65, 109]
		inclined	[175]
		finned	[82, 88]
Spherical	suspended		[77, 74, 90, 119, 207, 205]
	sessile		[191, 39, 86, 118, 202, 206, 208, 87, 145, 46, 37, 38, 47]
	encapsulated		[34, 36, 35, 180, 210, 184]

figuration of the samples: rectangular, cylindrical, and spherical geometries. The rectangular configuration is a frequently investigated geometry, commonly explored within a fully or partially enclosed cavity or channel featuring inlet and outlet flows. The solidification of metallic alloys is often assessed within a rectangular cavity that enforces thermal gradients from two opposing ends. Investigations may extend to include the influence of natural and forced convection [194, 68, 159]. In the context of the freezing process in a flow channel, this simulation mirrors various engineering applications, including metallic systems [177], direct reactor auxiliary cooling systems [190], and crystallizers for desalination [136]. While these typical rectangular setups can examine solidification with natural and forced convection concerning temperatures, they may fall short in the examination of crystal growth and morphology. Recent studies addressing this limitation have reduced the liquid volume, transforming it into a thin film [161, 200]. This not only stabilizes heat transfer but also facilitates the visualization of interfacial motion at different scales, particularly during the recalescence stage.

Solidification occurring within cylindrical or hollow geometries may exhibit either inward or outward directions. Inward solidification is often conducted within a tube vertically placed into a cold water bath [137, 14, 152, 61, 59]. Challenges in such experiments may arise from the impact of natural convection from the top and bottom, as well as mechanical vibrations from the water bath or chiller. Outward solidification in a hollow cylinder can occur in various orientations, including vertical [108, 107], horizontal [112, 65, 109], and inclined [175]. Some studies also introduce fins in the hollow cylinder to enhance thermal performance [82, 88].

Experiments employing a spherical geometry represent a common approach due to their simplicity and thermal stability, resulting in less disturbance from other machinery and easier control and stabilization of the surrounding or substrate. Generally, three methods are employed for droplet placement: suspending a droplet by a thermocouple, placing it sessile on a cold surface, and encapsulating it in a spherical shell. Freezing a suspended droplet offers advantages such as maintaining an overall spherical shape, visualizing the solidification process (especially crystal growth through high-speed cameras [77, 74]), and studying volume expansion during freezing. However, this method has limitations in examining different droplet volumes and nucleation sites due to the influence of the thermocouple. Meng and Zhang [119] recently attempted to control the nucleation site by hanging the droplet through a copper ring.

Considerable research has been dedicated to freezing sessile droplets. By placing a droplet on a flat [39, 86, 202, 208, 87, 46, 37, 38], patterned [206, 145], or inclined [191, 47] cold plate, researchers can study the entire freezing process at various spatiotemporal scales, volume expansion, wettability, and surface roughness. While the hemispherical shape of the droplet may not always be practical for certain applications, such as cloud development and spray freezing, it is particularly effective for aircraft icing and anti-/de-icing technologies, as the experimental setup considers the effects of surfaces. In addition to freezing suspended and sessile droplets, pure substances and mixtures in their liquid state can be encapsulated in a spherical capsule or shell and exposed to cold media [34, 36, 35, 180, 210, 184], allowing for well-controlled volume and uniformity of surface conditions (either in temperature or heat flux).

2.3.2 Theoretical and computational methods

Macro-scale models

The macro-scale model overlooks the impacts of supercooling, nucleation, and crystal growth, focusing instead on transport phenomena at a macroscopic level. Typically, the macro-scale models fall into two primary categories: explicit and implicit methods. The explicit method, also referred to as the front-tracking method, explicitly monitors the movement of the solid-liquid boundary during the freezing process. This boundary movement is determined through an energy balance that accounts for both sensible and latent heat.

$$\underbrace{\rho L v}_{\text{latent heat}} = \underbrace{\Big[\vec{q}\cdot\vec{n}\Big]_{\text{solid}}^{\text{liquid}}}_{\text{sensible heat}}, \tag{2.1}$$

where $\rho, L, v, \vec{q}, \vec{n}$ are the mass density, latent heat, interface velocity, and heat flux at the interface, respectively. By utilizing the solid-liquid moving boundary alongside the heat equation in the solid and liquid phases, one can establish a partial differential equation problem involving a moving boundary, often termed the Stefan problem. Exact solutions to the Stefan problem are attainable in some semi-infinite domains under specific combinations of boundary conditions, yet they are limited. Approximate solutions are of great interest, which can be derived by assuming either a polynomial approximation (known as the heat-balance integral method) or an asymptotic expansion (referred to as the perturbation method or asymptotic analysis).

The heat-balance integral method (HBIM) involves three primary steps: (i) Introduction of a heat penetration depth, beyond which temperatures are disregarded. (ii) Assumption of an approximate polynomial expression for temperature, allowing determination of unknown coefficients based on the heat penetration depth through application of boundary conditions. (iii) Integration of the partial differential equation (PDE) over the heat penetration depth, reducing it to an ordinary differential equation (ODE) often solvable analytically. Initially proposed by Goodman [64], the HBIM has undergone modifications and improvements in contemporary literature, such as the refined integral method and combined integral method. Caldwell and Kwan [26] provided a concise review of Stefan problems that incorporated HBIM. Subsequently, Mitchell and Myers [124] conducted a comprehensive review specifically focusing on HBIM's application in solving one-dimensional Stefan problems under various boundary conditions. The research conducted on HBIM for Stefan problems post-2020 is summarized in Table 2.2, highlighting the current advancements in this field.

Another widely utilized and efficient approximate technique is the perturbation method, also referred to as asymptotic analysis or the method of asymptotics. The concepts of asymptotics trace their origins back to the eighteenth and nineteenth centuries, offering both a mathematically formal and heuristic approach for approximating differential and integral equations in cases where exact solutions are not available [132]. Within the scope of the Stefan problem, this method capitalizes on the substantial latent heat released or absorbed during phase transitions, often significantly outweighing sensible heat. Mathematically, the Stefan number (Ste), the ratio of sensible to latent heat, is assumed to be small and much less than unity. Consequently, an asymptotic solution is formulated in the form of a perturbation series, with the Stefan number acting as the small perturbation parameter. For example, the dimensionless temperature θ is represented as an asymptotic expansion:

$$\theta \sim \theta_0 + \mathrm{Ste}\theta_1 + \mathrm{Ste}^2\theta_2 + \mathrm{Ste}^3\theta_3 + ..., \tag{2.2}$$

where θ_0, θ_1, θ_2, and θ_3 represent the zeroth, first, second, and third orders of θ, respectively. Following the asymptotic assumption, the Stefan problem can be solved order by order, breaking down the unsolvable problem into subproblems at each order of the asymptotic expansion that are readily solvable. In the zeroth or leading order, particularly, the time derivative(s) in the governing equation are omitted, resulting in a quasi-steady-state approximation of the Stefan problem. Prof. James M. Hill comprehensively presented perturbation

Table 2.2: A list of works on solving Stefan problems for solid-liquid phase change via integral and asymptotic methods since 2000.

Category				**Ref. on integral methods**	**Ref. on asymptotic methods**
1D	1-phase	Cartesian	classic formulation	[127, 133]	
			time-dependent boundary	[158, 141, 20, 21]	[25, 135, 148]
			varying property	[21, 40, 94]	[27]
			non-classical formulation		[91, 204, 71]
		Cylindrical		[156, 42]	[25, 135]
		Spherical		[156, 28, 29, 170]	[72, 25, 135, 176]
	2-phase	Cartesian	classical formulation	[155, 201, 134]	[123]
			time-dependent boundary	[122]	[138, 138, 149]
			varying property		[97]
			non-classical formulation	[123]	[23]
		Cylindrical		[155]	
		Spherical		[155]	[70, 151, 4, 192]
2D				[171, 41]	[172, 203, 121, 89, 128]
3D				[116]	[117]

solutions for one-dimensional one-phase Stefan problems in his book [73]. Recent advancements in asymptotic methods applied to various types of Stefan problems are cataloged in Table 2.2.

Numerical schemes, particularly those founded on the Stefan problem and similar explicit methodologies, necessitate an accurate tracing of the solid-liquid moving boundary. Despite advancements [52, 154], this requirement for numerical front tracking inherently demands finer time steps and spatial meshes to ensure precision. This renders a substantial need for computational power and time in most existing numerical schemes. Consequently, implicit methods, which do not explicitly trace the moving interface, have garnered significant attention in recent decades. These implicit schemes are also referred to as diffusive methods since the resulting interface is not a sharp surface but rather a diffusive one with certain widths. Among these schemes, commonly implemented in macro-scale models, are the apparent heat capacity, enthalpy, volume-of-fluid, and level set methods.

The apparent heat capacity method involves an implicit representation of the phase change interface by solving a single heat equation for both phases using effective thermophysical properties. This approach incorporates the abrupt changes between phases by employing effective thermal conductivity while introducing a new term termed the "apparent heat capacity" to account for the latent heat of fusion during freezing. Mathematically, the general expression of the apparent heat capacity $c_{p,\mathrm{app}}$ is the sum of the equivalent heat capacity c_{eq} and latent heat distribution $c_L(T)$ [126, 174, 12]:

$$c_{p,\mathrm{app}} = c_{\mathrm{eq}} + c_L(T) = \frac{1}{\rho}\left[\phi_{\mathrm{hcm}}\rho_{\mathrm{s}}c_{p,\mathrm{s}} + (1-\phi)\rho_{\mathrm{l}}c_{p,\mathrm{l}}\right] + L\frac{\mathrm{d}\phi}{\mathrm{d}T}, \tag{2.3}$$

where ϕ_{hcm} is the solid fraction. On the other hand, the enthalpy method (also known as the enthalpy-porosity method) transforms the governing heat transfer equations into a unified energy conservation equation in terms of enthalpy H:

$$\frac{\partial H}{\partial t} = \nabla \cdot (k\nabla T), \tag{2.4}$$

where H is expressed as:

$$H = (1 - \phi_{\mathrm{em}}) \int_{T_{\mathrm{solidus}}}^{T} \rho c_{p,\mathrm{s}} \mathrm{d}T + \phi_{\mathrm{em}} \int_{T_{\mathrm{liquidus}}}^{T} \rho c_{p,\mathrm{l}} \mathrm{d}T + \phi_{\mathrm{em}} \rho L. \tag{2.5}$$

The enthalpy method was initially established by Voller and his co-workers [187, 188]. The presence of liquidus and solidus temperatures (i.e., T_{liquidus} and T_{solidus}) defines a mushy zone between the liquid and solid phases, resulting in an implicit algorithm that predicts interface motion alongside temperature distributions.

The traditional level set method (LSM) constructs a level set function ϕ_{lsm} that denotes the signed distance function from the interface. In this representation, ϕ_{lsm} is positive in the liquid phase and negative in the solid phase, which is mathematically described as:

$$\phi_{\mathrm{lsm}} = \begin{cases} +d, & \text{in the liquid phase} \\ 0, & \text{at the interface} \\ -d, & \text{in the solid phase} \end{cases} \tag{2.6}$$

where d is the distance from the solid-liquid interface. The objective of LSM is to appropriately advance ϕ_{lsm} with the speed v at the interface, thereby implicitly storing the new front position in ϕ_{lsm} and updating field variables (e.g., temperature T) accordingly [43]. Similarly, the volume-of-fluid (VOF) approach also employs a scalar function ϕ_{vof}, often termed the fraction function, to differentiate between the phases and interface. This function can be expressed as:

$$\phi_{\mathrm{vof}} = \begin{cases} 0, & \text{in the liquid phase} \\ (0,1), & \text{at the interfacial cells} \\ 1, & \text{in the solid phase} \end{cases} \tag{2.7}$$

It is noted that the scalar function can also be used in the level set method, which is called the conservative LSM [142, 143]. A transport equation is then introduced as:

$$\frac{\partial \phi_{\text{vof}}}{\partial t} + \vec{u} \cdot \nabla \phi_{\text{vof}} = 0 \tag{2.8}$$

Despite the fact that the VOF method has been widely employed for predicting interfacial flows using fixed grids [160], it is commonly coupled with interfacial reconstruction techniques for solidification problems, e.g., the piecewise linear interface calculation [114]. In addition to the previously discussed implicit schemes, the phase field method (PFM) provides another means to implicitly address interfacial dynamics. However, it is worth mentioning that the PFM incorporates considerations of free energy density and non-equilibrium thermodynamics [19, 58]. This method is frequently applied in situations involving unstable freezing processes, specifically in the context of crystal growth, which will be further detailed in the following section.

Nucleation models

Nucleation, based on a probabilistic event of the formation of the critical nucleus, is highly stochastic. In most cases, direct observation of the critical nucleus is feasible in experiments, and gathering detailed information about its size or structure is challenging [163]. Although many multi-stage works in the literature take the nucleation temperature as a priori [44, 77, 74, 49, 181], it is of paramount importance to estimate the nucleation temperature and time for accurate predictions of freezing processes. Primarily, there are two modeling approaches for predicting nucleation: thermodynamic and kinetic methods [45]. The thermodynamic approach assesses nucleation conditions, specifically overcoming the free-energy barrier, employing the classical nucleation theory (CNT). In contrast, the kinetic approach delves into cluster dynamics and explores particle/molecule interactions based on conservation laws. While the CNT and cluster dynamics can be interconnected and yield similar results, the vast majority of multi-stage and multi-scale solidification models in the literature opt for the CNT under the thermodynamic approach due to its simplicity.

The CNT, whether applied to homogeneous or heterogeneous nucleation, begins by estimating the nucleation rate. Subsequently, it establishes the nucleation time and temperature based on specific criteria. The nucleation rate is mathematically represented by an Arrhenius equation, comprising a prefactor and an exponential factor:

$$J(T) = J_0 \exp\Big[-J_1(T)\Big] = J_0 \exp\Big[-\frac{\Delta G^*}{k_\mathrm{B}T}\Big] \tag{2.9}$$

In cases where experimental data is available (e.g., nucleation time and temperature), one can directly correlate the prefactor and exponential factor and develop an empirical equation for a specific material [75, 164]. This method is effective and practical, albeit lacking a physical foundation. Alternatively, a physics-based approach involves expanding the terms in the equation. Thus, the prefactor can be expressed as [183, 178]:

$$J_0 = nZf = n \underbrace{\frac{\sqrt{2\sigma/(\pi k_\mathrm{B}T)}}{3i^{*2/3}}}_{\substack{\text{homogeneous}\\ \text{part of } Z}} \underbrace{\sqrt{\frac{4}{2+\zeta_\mathrm{het}}}}_{\substack{\text{heterogeneous}\\ \text{part of } Z}} \underbrace{Ai^{*2/3}n^{4/3}D}_{f} \tag{2.10}$$

and the free-energy barrier with the critical nucleus is written as [131]:

$$\Delta G^* = \frac{16\pi\sigma v_\mathrm{mol}}{3(k_\mathrm{B}T\ln S)^2} \tag{2.11}$$

Once the nucleation rate over temperature or time is known, the determination of the occurrence of nucleation—referred to as the nucleation criterion—becomes imperative. Within existing literature, two prevalent forms of the nucleation criterion have been employed. Assessing the cumulative probability P_n is more broadly applicable based on the cooling rate β, which is expressed as [166, 167]:

$$P_\mathrm{n} = 1 - \exp\Big[-\frac{1}{\beta}\int_{\widetilde{T}=T_\mathrm{f}}^{T} J(\widetilde{T})\mathrm{d}\widetilde{T}\Big] \tag{2.12}$$

When the cooling rate is not extremely high, theoretical studies also suggest that the number of critical nuclei should be 1 [178]. In this case, quantifying the count of critical nuclei is more practical to implement; that is,

$$N_V = \int_{\widetilde{t}=0}^{t} (V_0 - V^*) J(\widetilde{t}) \mathrm{d}\widetilde{t} \tag{2.13}$$

While CNT is capable of predicting the supercooling degree or nucleation temperature, the Arrhenius equation cannot demonstrate the nucleation site(s), i.e., spatial variation of J caused by the microstructure inhomogeneities is missing. One solution to address this issue is the use of the phase field method (PFM). PFM describes phases through continuum fields, and spatiotemporal evolution is driven by differential equations, such as the Allen-Cahn equation (without solute diffusion) and Cahn-Hilliard equation (with solute diffusion) [19]. It is primarily used for crystal growth, which will be discussed later in this subsection, but it can incorporate CNT to consider phase inhomogeneities and some works have been done in the fields of binary alloys [169, 195, 168].

Recalescence models

The growth rate, morphology, and spacing of crystals heavily depend on the behavior of the tip region [56]. Both temperature and concentration fields can influence the diffusion process at the tip, making the undercooling temperature and shape of the tip particularly significant. Papapetrou [80] proposed a parabolic dendrite tip representing a steady-state shape. Subsequently, Ivantsov [83] mathematically proved Papapetrou's theory using a complex Stefan problem with an isothermal interface (i.e., $T_\mathrm{i} \equiv T_\mathrm{f}$). This verification produced a valid steady-state solution, demonstrating the thermal effect of the undercooling temperature $\Delta T = T_\mathrm{f} - T_\mathrm{nuc}$. Ivantsov's solution is commonly known as the Ivantsov function $\mathrm{Iv}(\mathrm{Pe})$:

$$\mathrm{Iv}(\mathrm{Pe_t}) = \mathrm{Pe_t} \exp(\mathrm{Pe_t}) \mathrm{Ei}(\mathrm{Pe_t}) \tag{2.14}$$

where the thermal Peclet number is $\mathrm{Pe_t} = vR/(2\alpha)$ In addition to the thermal field, kinetics, surface curvature, and composition can also impact undercooling. The general expression of the total undercooling, applicable to both pure substances and mixtures, is as follows:

$$\Delta T = \Delta T_\mathrm{t} + \Delta T_\mathrm{k} + \Delta T_\sigma + \Delta T_\mathrm{c} \tag{2.15}$$

While the thermal undercooling is calculated by the Ivantsov function, i.e., $\Delta T_\mathrm{t} = \mathrm{Iv}(\mathrm{Pe})L/c_p$, the kinetic undercooling is the temperature difference between the fusion and interfacial temperatures, i.e., $\Delta T_\mathrm{k} = T_\mathrm{f} - T_\mathrm{i}$. This can be analyzed based on the assumption of linear attachment kinetics given by v/μ, where μ is the kinetic undercooling parameter [130]. The linear assumption might not be universally applicable to all substances, as evidenced by studies using molecular dynamics (MD) simulations on materials like Lennard-Jones liquids [24] and silicon [66]. These simulations have revealed inconsistencies in the interfacial velocity. A more precise representation for kinetic undercooling, known as the Wilson-Frenkel model, is present in the current literature. This model aligns well with the temperature-dependent interfacial velocities identified through MD simulations [157]. The Wilson-Frenkel model is written as [85, 193]:

$$v = \frac{6d_0 D(T_\mathrm{i})}{2\alpha\sigma^*\sigma_\mathrm{k}}\left[\exp\left(-\frac{L_\mathrm{mol}/N_\mathrm{A}}{k_\mathrm{B}T_\mathrm{f}}\right) - \exp\left(-\frac{L_\mathrm{mol}/N_\mathrm{A}}{k_\mathrm{B}T_\mathrm{i}}\right)\right]. \tag{2.16}$$

With the total undercooling expression in Eq. (2.15), v and T_i can be numerically found based on the two algebraic equations. Regarding undercooling caused by surface curvature, the normal fusion point along a curved interface is depressed compared to that on a planar surface, meaning that the undercooling diminishes for flat interfaces. Owing to the Gibbs-Thomson effect, it can be mathematically represented as [130]:

$$\Delta T_\sigma = \frac{1}{R}\frac{\sigma_\mathrm{sl}}{\Delta S} \tag{2.17}$$

where ΔS is the entropy of fusion per unit volume. The tip radius R can be further elucidated using the Mullins-Sekerka instability length [3]. Lastly, constitutional undercooling arises from the gradient in solute concentration affected by the initial solute composition c_0, solute partition coefficient k, and equilibrium liquidus slope m [179, 76]. Its mathematical representation is as follows:

$$\Delta T_{\mathrm{c}} = (T_{\mathrm{i}} - T_{\infty}) - m(c_{\mathrm{i}} - c_0) = mc_0 \frac{(k-1)\mathrm{Iv}(\mathrm{Pe}_{\mathrm{c}})}{1-(k-1)\mathrm{Iv}(\mathrm{Pe}_{\mathrm{c}})} \tag{2.18}$$

where Pe_{c} is the compositional Peclet number given by $vR/(2D)$. In the literature, the thermal undercooling is often called the LMK model established by Langer and Muller-Krumbhaar [100, 99]. The complete undercooling formulation with solutes is known as the LKT model analyzed by Lipton, Kurtz and Trivedi [179].

While employing the total undercooling for calculating crystal growth velocity proves effective, it lacks the ability to provide spatial insight into dendritic growth during the recalescence stage. Modeling approaches (explicit and implicit schemes) designed for macro-scale freezing can be adapted for crystal growth by adjusting the interface to simulate th evolution of the dendritic tip. Jaafar et al. [84] conducted a comprehensive review of numerical simulations concerning dendritic growth during solidification. The phase field method (PFM) stands out as the most popular numerical framework. PFM utilizes a scalar order parameter or phase field variable, ϕ_{pfm} to represent the crystal, supercooled liquid, and interfacial transition, in a similar fashion as the VOF's fraction function in Eq. (2.7). This order parameter enables the formulation of a free energy function expressed as:

$$F = \int_V \left[f(\phi_{\mathrm{pfm}}, c, T) + \frac{\varepsilon_\phi^2}{2} |\nabla \phi_{\mathrm{pfm}}|^2 + \frac{\varepsilon_c^2}{2} |\nabla c|^2 \right] \mathrm{d}V \tag{2.19}$$

Here, $f(\phi_{\mathrm{pfm}}, c, T)$ is the free energy density, while ε_ϕ^2 and ε_c^2 are the gradient energy coefficients related to the interface and solute. The effects of anisotropy and supercooling degree can also be incorporated into these gradient energy coefficients. There are two primary formulations of PFM based on the presence of solutes [19]:

$$\frac{\partial \phi_{\mathrm{pfm}}}{\partial t} = -M_{\phi}\left[\frac{\partial f}{\partial \phi_{\mathrm{pfm}}} - \varepsilon_{\phi}^{2}\nabla^{2}\phi_{\mathrm{pfm}}\right] \tag{2.20}$$

$$\frac{\partial c}{\partial t} = \nabla \cdot \left[M_{c}c(1-c)\nabla\left(\frac{\partial f}{\partial c} - \varepsilon_{c}^{2}\nabla^{2}c\right)\right] \tag{2.21}$$

where M_ϕ and M_c represents the mobilities for ε_ϕ^2 and ε_c^2. It is noted that Eq. (2.20) and Eq. (2.21) are known as the Allen-Cahn and Cahn-Hilliard equations, respectively. The computation of PFM is rather straightforward compared with other models, as it neither tracks the nonlinear interface explicitly nor requires a fine approximation of mesh elements. Back in 1990s, Kobayashi developed finite-difference schemes to numerically solve the phase field equations in 2D [92] and 3D [93]. A systematic guideline for programming PFM was recently provided in Biner's book [17].

Multi-stage and multi-scale models

While multi-stage models can effectively simulate three-stage stable freezing processes employing macro-scale methods, they are more commonly associated with five-stage unstable freezing, which includes supercooling, nucleation, and crystal growth at multiple scales. The two sensible heat stages, i.e., liquid supercooling and solid subcooling, can be modeled through the heat equation or energy balance without accounting for the significant release of latent heat. Furthermore, explicit or implicit schemes within macro-scale models can simulate the equilibrium freezing stage and predict the interfacial motion. However, special attention is needed for accurately modeling the nucleation and recalescence stages at the micro- and meso-scales, respectively.

Several notable contributions on the multi-stage and multi-scale solidification models were summarized in Table 2.3. Hindmarsh et al. [77] pioneered a multi-stage model for freezing water droplets, establishing a numerical model based on heat balance and the Stefan con-

Table 2.3: A list of works on multi-stage and multi-scale solidification frameworks since 2000.

Ref.	Problem	Framework	Solver	Accuracy
Hindmarsh et al. [77]	Inward solidification of a suspended water droplet	Multi-stage via heat balance and 0D crystal growth	Numerical	All five stages were validated against experiments.
Hindmarsh et al. [74]	Inward solidification of a suspended sucrose droplet	Multi-stage via heat balance and Scheil equation	Numerical	Equilibrium freezing and solid subcooling stages were validated against experiments.
Dehghani-Sanij et al. [49]	Inward solidification of a saline droplet	Multi-stage via heat balance with Stefan condition and empirical freezing point	Hybrid analytical-numerical	All stages were validated against exiting experiments [77].
Meng and Zhang [119]	Inward solidification of a suspended water droplet (attached with a copper ring)	Multi-stage via 3D enthalpy method and CNT-based heterogeneous nucleation	Numerical	All five stages were validated against experiments at different operating conditions.
Sebastiao et al. [164]	Inward solidification of a sucrose droplet	Multi-stage via 0D heat balance model and FPD	Numerical	All five stages were validated against experiments at different concentrations [74].
Carvalho et al. [32]	Inward solidification of a pure droplet	Multi-stage via 1D heat equation with Stefan condition and 0D crystal growth	Hybrid analytical-numerical	All five stages were validated against existing experiment [77].
Van der Sman et al. [181]	Solidification of a slab with sucrose solution	Multi-scale via 2D heat equation and PFM for recalescence	Numerical	2D crystal morphology was verified with theoretical data.
Akhtar et al. [3]	Inward solidification of a suspended water droplet	Multi-stage via 1D heat equation with Stefan condition, CNT-based heterogeneous nucleation, and 1D crystal growth	Semi-analytical	All five stages were validated against existing experiments at different operating conditions [77, 119].
Meng and Zhang [120]	Inward solidification of a micro-sized water droplet	Multi-stage via 3D enthalpy method and CNT-based heterogeneous nucleation	Numerical	Effect of single and double nucleation sites was explored.

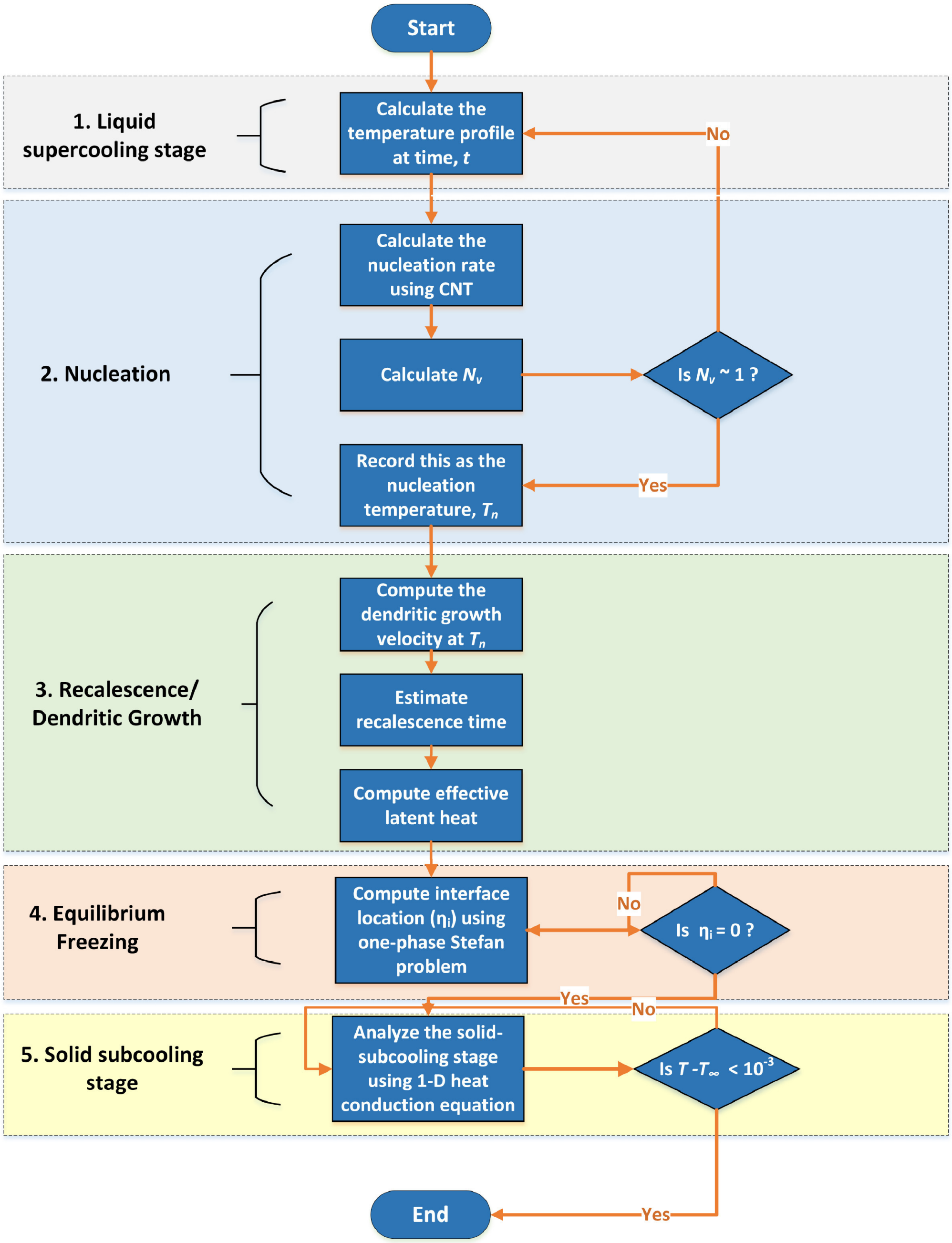

Figure 2.7: Flowchart of a semi-analytical, five-stage solidification framework for droplet freezing (reprinted from [3]).

dition. They validated their predictions against experimental data, capturing four distinct solidification stages. Later, their model was extended to simulate sucrose droplets, accounting for freezing-point depression via the Scheil equation, which was in good agreement with experimental results across different concentrations [74]. Meng and Zhang [119] presented a 3D numerical simulation for droplet solidification using the enthalpy method, considering heterogeneous nucleation based on CNT. Their model was validated against experiments under various operating conditions, and an extension for freezing micro-sized droplets was explored, studying the effects of single and double nucleation sites [120].

Akhtar et al. [3] developed a semi-analytical, five-stage solidification model incorporating heterogeneous nucleation, interface kinetics, and surface curvature effects. They utilized exact solutions to 1D heat equations and perturbation solutions to one-phase Stefan problems. Validation against multiple experiments was conducted, followed by gradient-based optimization of the Arrhenius-type equation and modified Wilson-Frenkel model for recalescence [5]. The computation of Akhtar et al.'s multi-stage framework is shown in Fig. 2.7. Much less time has been spent on comprehensive multi-scale solidification frameworks in the literature. Van der Sman [181] developed a numerical framework encompassing both macroscopic and mesoscopic scales, utilizing the PFM (specifically the Cahn-Hilliard equation) to simulate solidification. They incorporated scale separation and cellular automaton rules to address solute trapping for freezing sucrose solutions, which showed close agreements with the theoretical finger profile to the dendritic tip.

2.4 Applied aspect

2.4.1 Applications to natural sciences

Atmospheric icing

Freezing occurs naturally in the atmosphere due to temperature differences across the fusion point. This phenomenon, collectively termed atmospheric icing, has been extensively studied in the literature.

- Frost accumulates when moist air contacts a cold surface below the water triple point and air dew point. Experimental setups like direct-flow and circulation-flow air tunnels face challenges in accurately controlling air temperature and humidity [173]. The literature details theoretical models and empirical correlations, particularly for flat surfaces, summarized by Leoni [102].

- Snow and freezing rain are also types of atmospheric icing. Snow, whether dry or wet, comprises ice/snow crystals falling in symmetrical patterns, influencing various environmental and meteorological aspects [104]. Freezing rain occurs when the snow melts into rain in an above-freezing layer of air, then turns into supercooled freezing rain upon descending into sub-freezing temperatures [15].
- In-cloud icing, which includes soft and hard rimes as well as glaze [147], happens when an unheated substance is exposed to supercooled water droplets at temperatures below freezing. It is prevalent in elevated mountainous regions, lasting for days or even weeks, often accompanied by strong winds [140]. The ice accumulation can lead to instabilities and damage to infrastructure, such as power networks [55], wind turbines [98], and aircraft [30].

Permafrost

Approximately a quarter of the Northern Hemisphere and around 17% of the Earth's exposed land surface is covered by permafrost, frozen ground that maintains temperatures at or below 0°C for a minimum of two consecutive years [18]. Within permafrost regions, the upper layer, known as the active layer, undergoes seasonal thawing in summer and refreezing in winter, ranging from several decimetres to over a meter in depth [53]. Figure 2.8 provides an illustrative schematic depicting seasonal temperature profiles within permafrost areas. The expansion of the active layer due to climate warming significantly impacts the carbon and nutrient cycles within permafrost soils. This can lead to the permafrost carbon feedback, potentially releasing greenhouse gases upon permafrost thawing, thus exacerbating global warming [162, 182].

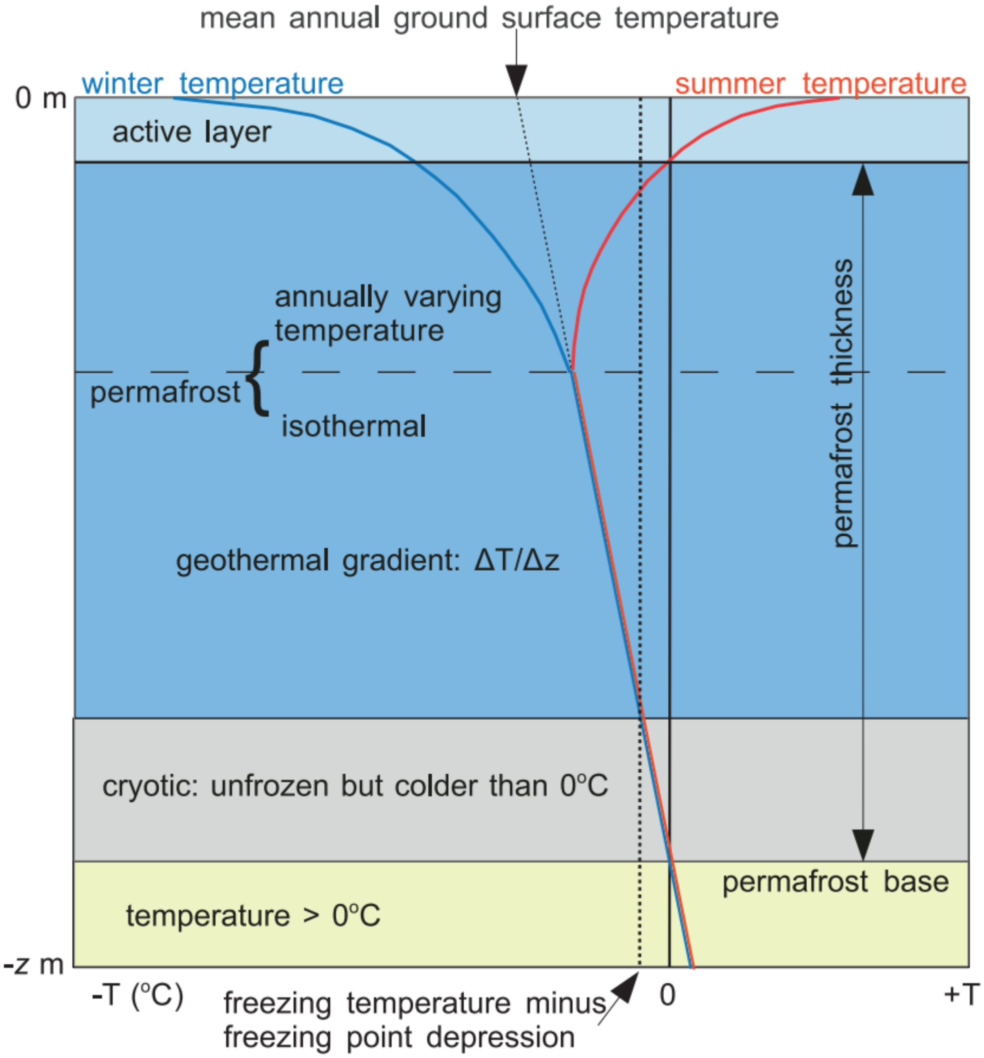

Figure 2.8: Conceptual diagram of vertical temperature profiles in permafrost, including both summer and winter seasons (reprinted from [182]).

While a widely used simple model predicts active layer thickness using a solution derived from a 1D Stefan problem [96], accurate forecasts require a fundamental understanding of the interactions between various physical processes: freeze-thaw cycles, fluid flow, structural changes, and carbon emissions within porous media. Current research within the literature extensively employs multi-physics models in porous media, such as thermo-hydro-mechanical (THM) models [51, 69]. These frameworks also play a critical role in developing thermal energy systems designed to prevent permafrost from thawing under today's changing climate, notably artificial ground freezing, discussed further in subsequent subsections.

2.4.2 Applications to engineering

Phase change materials

Phase change materials (PCMs) undergo the solid-liquid phase transition, a.k.a., the freeze-melt cycle, within a specific temperature range. When transitioning from liquid to solid, PCMs release a significant amount of latent heat to the surroundings and reorganize into a solid form. Conversely, during the melting process, they absorb energy from their surroundings and loosen the atomic bounds for liquid [57]. These materials can be classified into three main categories: organic PCMs (e.g., paraffins and fatty acids), inorganic PCMs (e.g., salt hydrates and metallic), and eutectic PCMs (e.g., mixtures of organic and/or inorganic PCMs) [153].

Over the past decades, PCMs have shown promise in latent thermal energy storage (LTES). In comparison to the commonly used sensible thermal energy storage using materials like water or rock beds, LTES are not heavy and bulky in size, offering higher energy storage density within a smaller temperature interval. Despite great advantages, there are practical hurdles arise when applying LTES using PCMs, such as low thermal conductivity, density/volume changes, segregation, and supercooling during phase transition [54]. Consequently, understanding and simulating the intricate multiphysics and multiscale behaviors of solid-liquid phase changes, including solidification, becomes imperative.

Spray freezing

Spray freezing involves the atomization of water into a sub-zero air environment, leading to the solidification of liquid water into ice. This process finds applications in various domains, including food [81] and pharmaceutical [165] drying, seawater desalination [110], mine waste water decontamination [16], mine heating [2, 125], and ice slurry production [60]. For instance, Figure 2.9 depicts a schematic illustrating the role of a droplet in the spray freezing process. The substantial release of latent heat during solidification warms the incoming

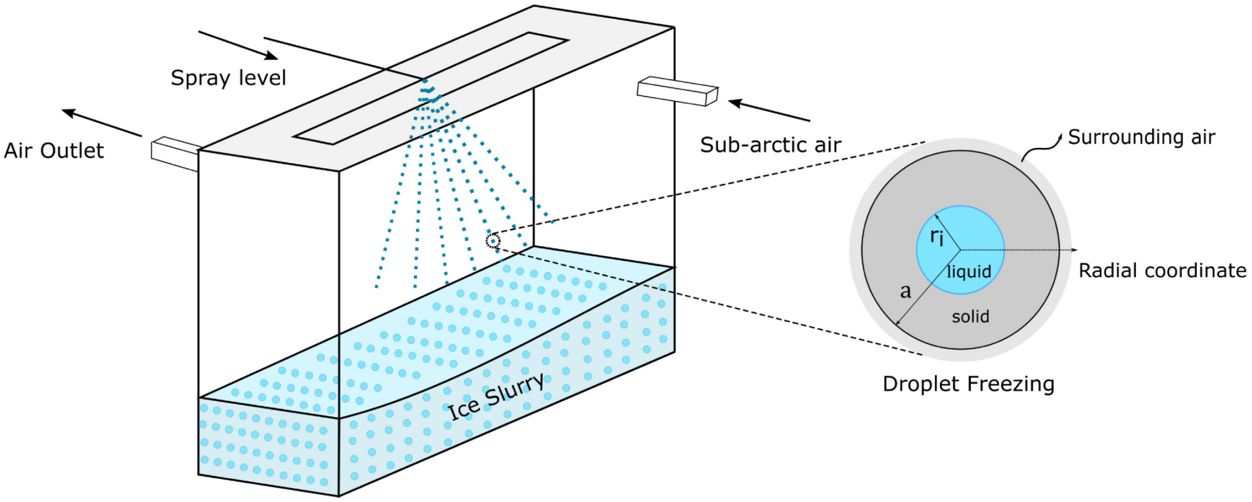

Figure 2.9: Conceptual diagram of a droplet during the spray freezing process (reprinted from [4]).

sub-arctic air, resulting in warmer outlet air suitable for mine heating. In regions with cold climates and a need for heating, spray freezing proves to be an effective, economical, and sustainable solution.

To enhance and optimize spray freezing technology, a comprehensive understanding of droplet solidification in both pure substances and mixtures is crucial [1]. Existing literature predominantly focuses on experimental studies involving the freezing of suspended droplets [77, 76, 119], capturing the five-stage freezing process [49, 3]. Furthermore, multi-stage models for droplet solidification have been developed for various solutions (e.g., pure water and aqueous solution [197]), while assuming a perfect spherical shape without volume expansion.

Artificial ground freezing

Artificial ground freezing (AGF) is a geotechnical support method used to create a frozen area around freezing pipes. This process enhances and stabilizes the ground structure while restricting groundwater flow. It can prevent shaft sinking [209], groundwater seepage [196], hazardous wastes [9], soil contamination [103], and permafrost thawing [7]. Generally, AGF operates by cooling the ground below the groundwater's freezing point via freezing pipes, which, compared to other geotechnical methods, offers versatility across project scales and

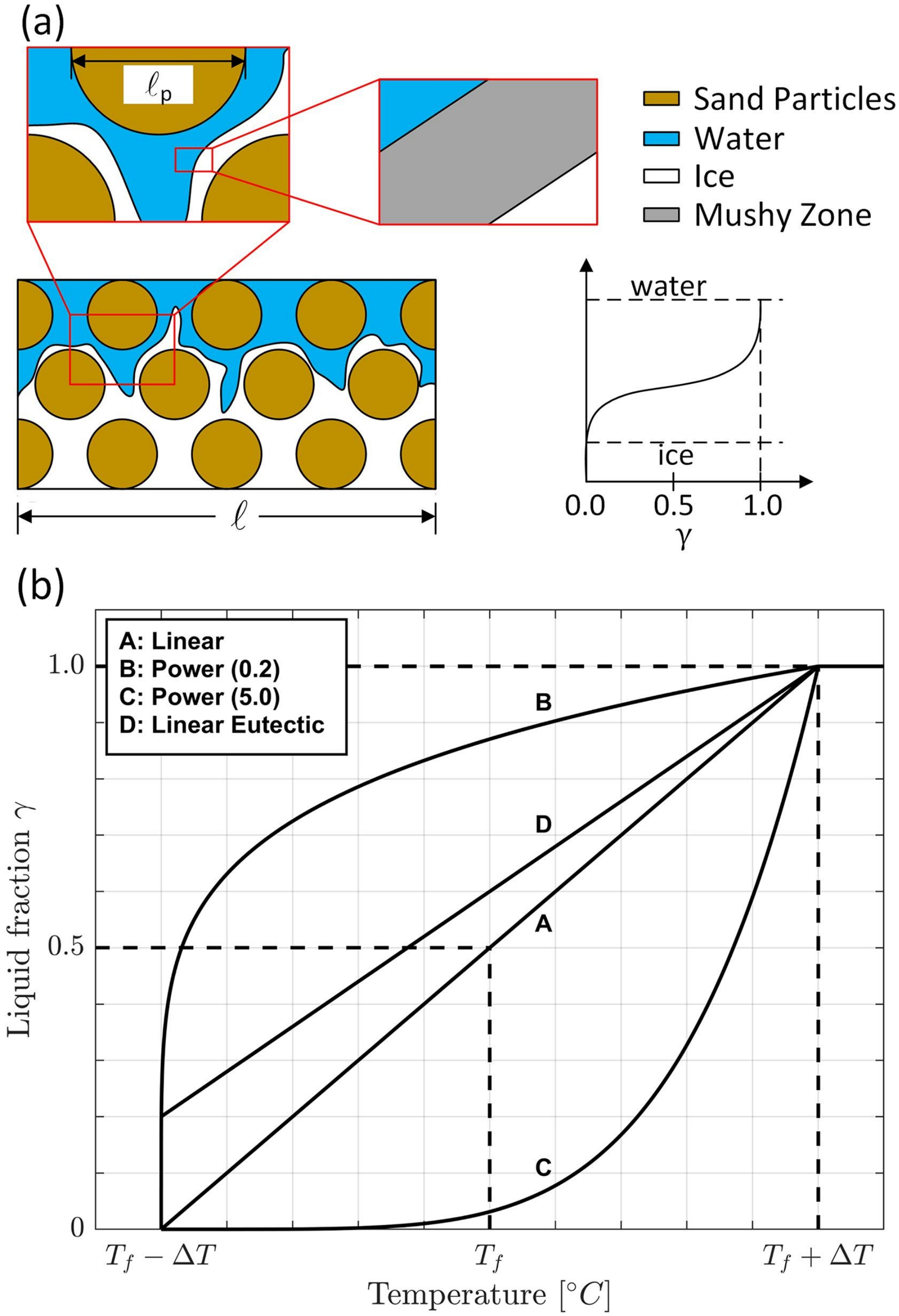

Figure 2.10: Conceptual diagram of a representative elementary volume during the AGF process: (a) contains sand particles, water, ice, and a mushy zone for the solid-liquid interface; (b) shows different forms of liquid fractions for the mushy zone (reprinted from [10]).

ground types. Meanwhile, it does not introduce any hazardous substances to the environment [10].

The AGF process exhibits complex transport phenomena across multiple and interactive physical fields, including heat transfer, hydraulic flow, structural changes, and species diffusion. The primary focus lies on understanding freezing in porous media. Figure 2.10 demonstrates a representative volume during AGF involving sand particles, water, ice, and a mushy zone representing the solid-liquid interface, along with various liquid fractions within the mushy zone. While most experiments in the literature consisted of an insulated tank filled with soil and freezing pipes installed in the center [186, 8, 211], modeling freezing in porous media often assumed local thermal equilibrium and volume-averaged thermophysical properties [150, 185, 8, 199].

2.5 Conclusion

In this review, we presented an in-depth examination of the contemporary advancements in the freezing process, including fundamental physical phenomena, experimental and mathematical methodologies, and diverse applications in both natural sciences and engineering domains. Despite its ostensibly simple nature as a phase transition from liquid to solid, freezing unveils complex transport phenomena with substantial implications in various scientific and engineering contexts, making it a focal point of current research endeavors in the past decades. Some major contributions to the freezing process and directions of future work are summarized in the following subsections.

2.5.1 Fundamentals

The fundamental understanding of freezing on both pure substances and mixtures has been expounded upon, elucidating stable and unstable processes, solidification stages at macro-, meso-, and micro-scales, and the influence of impurities or solutes on freezing dynamics. Key concepts such as supercooling degree, nucleation mechanisms, crystal growth velocity, undercooling at the dendritic tip, freeze-point depression (FPD), water activity, and solute segregation have been investigated in the literature.

Recent research has concentrated on unfolding meso- and micro-scale phenomena during unstable freezing, specifically focusing on crystal growth, nucleation, and temperature/concentration changes in pure solutions and mixtures. While advancements in these phenomena have primarily centered around temperature/freezing curves and solute concentrations over time, multi-scale analyses with spatiotemporal effects, despite the establishment of theories like Classical Nucleation Theory (CNT), remain recondite. Addressing temporal and spatial effects, such as the location and number of nucleation sites and crystal morphology, and their impact on temperature and concentration fields, necessitates further exploration.

2.5.2 Methodology

Laboratory experiments, theoretical analyses, and computational frameworks have been instrumental in characterizing and predicting the freezing process. Despite the extensive efforts in experimental setups of varying geometries, each design is inherently limited in capturing specific aspects of freezing dynamics. The choice of methodology, therefore, requires careful consideration aligned with the research purpose.

Mathematical frameworks such as the Stefan problem, apparent heat capacity method, enthalpy method, level set Method (LSM), volume-of-fluid (VOF), and phase field method (PFM) have been developed for tracking the solid-liquid interface, offering macro-scale predictions, mostly on iterative implicit models facilitate estimations. Computationally efficient models are still in great demand, particularly in cylindrical geometries. Additionally, nucleation and crystal growth present daunting challenges, with CNT being fundamental but entailing advancements to address stochastic, temporally, and spatially dependent events. Non-uniform crystal morphology with a non-linear growth rate also requires further exploration.

2.5.3 Applications

The applications of freezing extend across atmospheric phenomena, from frosting to in-cloud icing and from snow to freezing rain, influencing climatic conditions and atmospheric or underground events. With the increasing global temperatures and heightened possibilities of extreme weather events, integrating the freezing process into regional climate models is recommended for enhanced resolution and forecasting capabilities.

Beyond natural sciences, freezing plays a pivotal role in the energy sector through the engineering of novel materials and thermal systems such as phase change materials (PCMs), spray freezing, and artificial ground freezing (AGF). PCMs and spray freezing technologies leverage latent heat release for effective energy storage and heating systems, while AGF employs ground freezing for hydraulic sealing in geotechnical support. All these engineering applications have shown their effectiveness and utilities in mining and civil projects. The utilization of cold energy in northern regions, where cold temperatures are abundant and renewable, holds particular promise for promoting sustainability. However, the technologies related to cold energy are nascent without sufficient pilot projects to prove the concept, which grants numerous opportunities for future research and industrial development in the energy sector.

Bibliography

[1] S. Akhtar, M. Xu, M. Mohit, and A. P. Sasmito. A comprehensive review of modeling water solidification for droplet freezing applications. *Renewable and Sustainable Energy Reviews*, 188:113768, 2023.

[2] S. Akhtar, M. Xu, and A. Sasmito. Spray freezing for mine heating a statistical perspective. In *Mine Ventilation*, pages 357–365. CRC Press, 2021.

[3] S. Akhtar, M. Xu, and A. P. Sasmito. Development and validation of a semi-analytical framework for droplet freezing with heterogeneous nucleation and non-linear interface kinetics. *International Journal of Heat and Mass Transfer*, 166:120734, 2021.

[4] S. Akhtar, M. Xu, and A. P. Sasmito. Development and validation of an asymptotic solution for a two-phase stefan problem in a droplet subjected to convective boundary condition. *International Journal of Thermal Sciences*, 164:106923, 2021.

[5] S. Akhtar, M. Xu, and A. P. Sasmito. A novel crystal growth model with nonlinear interface kinetics and curvature effects: Sensitivity analysis and optimization. *Crystal Growth & Design*, 21(6):3251–3265, 2021.

[6] V. Alexiades. *Mathematical modeling of melting and freezing processes.* Routledge, 2018.

[7] M. Alzoubi, S. A. Ghoreishi-Madiseh, A. P. Sasmito, N. Kunz, and A. Guimaraes. Renewable energy-based artificial ground freezing as an adaptation solution for sustainability of permafrost in post-climate change conditions. In *IOP Conference Series: Earth and Environmental Science*, volume 268, page 012128. IOP Publishing, 2019.

[8] M. A. Alzoubi, A. Nie-Rouquette, and A. P. Sasmito. Conjugate heat transfer in artificial ground freezing using enthalpy-porosity method: Experiments and model validation. *International Journal of Heat and Mass Transfer*, 126:740–752, 2018.

[9] M. A. Alzoubi, S. Poncet, and A. P. Sasmito. Hybrid artificial ground freezing as a sustainable solution for containing hazardous-waste in critical environmental projects. *Cold Regions Science and Technology*, 192:103401, 2021.

[10] M. A. Alzoubi, M. Xu, F. P. Hassani, S. Poncet, and A. P. Sasmito. Artificial ground freezing: A review of thermal and hydraulic aspects. *Tunnelling and Underground Space Technology*, 104:103534, 2020.

[11] O. B. Andersland and B. Ladanyi. *Frozen ground engineering.* John Wiley & Sons, 2003.

[12] S. Arena, E. Casti, J. Gasia, L. F. Cabeza, and G. Cau. Numerical simulation of a finned-tube lhtes system: influence of the mushy zone constant on the phase change behaviour. *Energy Procedia*, 126:517–524, 2017.

[13] T. Battle. Mathematical modelling of solute segregation in solidifying materials. *International Materials Reviews*, 37(1):249–270, 1992.

[14] N. Beaupere, U. Soupremanien, and L. Zalewski. Experimental measurements of the residual solidification duration of a supercooled sodium acetate trihydrate. *International Journal of Thermal Sciences*, 158:106544, 2020.

[15] B. C. Bernstein, T. P. Ratvasky, D. R. Miller, and F. McDonough. Freezing rain as an in-flight icing hazard. Technical report, 2000.

[16] K. W. Biggar, R. Donahue, D. Sego, M. Johnson, and S. Birch. Spray freezing decontamination of tailings water at the colomac mine. *Cold Regions Science and Technology*, 42(2):106–119, 2005.

[17] S. B. Biner et al. *Programming phase-field modeling.* Springer, 2017.

[18] B. K. Biskaborn, S. L. Smith, J. Noetzli, H. Matthes, G. Vieira, D. A. Streletskiy, P. Schoeneich, V. E. Romanovsky, A. G. Lewkowicz, A. Abramov, et al. Permafrost is warming at a global scale. *Nature Communications*, 10(1):264, 2019.

[19] W. J. Boettinger, J. A. Warren, C. Beckermann, and A. Karma. Phase-field simulation of solidification. *Annual Review of Materials Research*, 32(1):163–194, 2002.

[20] J. Bollati, J. Semitiel, and D. A. Tarzia. Heat balance integral methods applied to the one-phase Stefan problem with a convective boundary condition at the fixed face. *Applied Mathematics and Computation*, 331:1–19, 2018.

[21] J. Bollati and D. A. Tarzia. Approximate solutions to one-phase stefan-like problems with space-dependent latent heat. *European Journal of Applied Mathematics*, 32(2):337–369, 2021.

[22] R. Boussaa, L. Hachani, O. Budenkova, V. Botton, D. Henry, K. Zaidat, H. B. Hadid, and Y. Fautrelle. Macrosegregations in sn-3 wt% pb alloy solidification: Experimental and 3d numerical simulation investigations. *International Journal of Heat and Mass Transfer*, 100:680–690, 2016.

[23] F. Brosa Planella, C. P. Please, and R. A. Van Gorder. Extended Stefan problem for solidification of binary alloys in a finite planar domain. *SIAM Journal on Applied Mathematics*, 79(3):876–913, 2019.

[24] J. Broughton, G. Gilmer, and K. A. Jackson. Crystallization rates of a lennard-jones liquid. *Physical Review Letters*, 49(20):1496, 1982.

[25] J. Caldwell and Y. Kwan. On the perturbation method for the Stefan problem with time-dependent boundary conditions. *International Journal of Heat and Mass Transfer*, 46(8):1497–1501, 2003.

[26] J. Caldwell and Y.-Y. Kwan. A brief review of several numerical methods for one-dimensional Stefan problems. *Thermal Science*, 13(2):61–72, 2009.

[27] M. Calvo-Schwarzwälder. Non-local effects and size-dependent properties in Stefan problems with Newton cooling. *Applied Mathematical Modelling*, 76:513–525, 2019.

[28] E. Canzian, F. Santiago, A. B. Lopes, and A. Barañano. Spherical solidification: An application of the integral methods. *International Journal of Thermal Sciences*, 177:107575, 2022.

[29] E. Canzian, F. Santiago, A. B. Lopes, M. Barbosa, and A. Barañano. On the application of the double integral method with quadratic temperature profile for spherical solidification of lead and tin metals. *Applied Thermal Engineering*, 219:119528, 2023.

[30] Y. Cao, W. Tan, and Z. Wu. Aircraft icing: An ongoing threat to aviation safety. *Aerospace Science and Technology*, 75:353–385, 2018.

[31] T. Carozzani, C.-A. Gandin, H. Digonnet, M. Bellet, K. Zaidat, and Y. Fautrelle. Direct simulation of a solidification benchmark experiment. *Metallurgical and Materials Transactions A*, 44:873–887, 2013.

[32] I. S. Carvalho, R. M. Cotta, C. P. Naveira-Cotta, and M. K. Tiwari. Hybrid integral transform analysis of supercooled droplets solidification. *Proceedings of the Royal Society A*, 477(2248):20200874, 2021.

[33] A. S. Casparian and G. Sirokman. *Applied Chemistry for Environmental Engineering.* Momentum Press, 2016.

[34] C. Chan and F. Tan. Solidification inside a sphere—an experimental study. *International Communications in Heat and Mass Transfer*, 33(3):335–341, 2006.

[35] P. Chandrasekaran, M. Cheralathan, and R. Velraj. Effect of fill volume on solidification characteristics of di (deionized) water in a spherical capsule–an experimental study. *Energy*, 90:508–515, 2015.

[36] P. Chandrasekaran, M. Cheralathan, and R. Velraj. Influence of the size of spherical capsule on solidification characteristics of DI (deionized water) water for a cool thermal energy storage system–an experimental study. *Energy*, 90:807–813, 2015.

[37] S. Chang, H. Qi, S. Zhou, and Y. Yang. Experimental study on freezing characteristics of water droplets on cold surfaces. *International Journal of Heat and Mass Transfer*, 194:123108, 2022.

[38] S. Chang, H. Qi, S. Zhou, and Y. Yang. Experimental and numerical study on freezing process of water droplets under surfaces with different wettability. *Applied Thermal Engineering*, 219:119516, 2023.

[39] G. Chaudhary and R. Li. Freezing of water droplets on solid surfaces: An experimental and numerical study. *Experimental Thermal and Fluid Science*, 57:86–93, 2014.

[40] V. Chaurasiya, R. Kumar Chaudhary, A. Wakif, and J. Singh. A one-phase stefan problem with size-dependent thermal conductivity and moving phase change material under the most generalized boundary condition. *Waves in Random and Complex Media*, pages 1–29, 2022.

[41] V. Chaurasiya, S. Upadhyay, K. N. Rai, and J. Singh. A new look in heat balance integral method to a two-dimensional stefan problem with convection. *Numerical Heat Transfer, Part A: Applications*, 82(9):529–542, 2022.

[42] V. Chaurasiya, A. Wakif, N. A. Shah, and J. Singh. A study on cylindrical moving boundary problem with variable thermal conductivity and convection under the most realistic boundary conditions. *International Communications in Heat and Mass Transfer*, 138:106312, 2022.

[43] S. Chen, B. Merriman, S. Osher, and P. Smereka. A simple level set method for solving stefan problems. *Journal of Computational Physics*, 135(1):8–29, 1997.

[44] X. D. Chen and P. Chen. Freezing of aqueous solution in a simple apparatus designed for measuring freezing point. *Food Research International*, 29(8):723–729, 1996.

[45] E. Clouet. Modeling of nucleation processes. *arXiv preprint arXiv:1001.4131*, 2010.

[46] Q. Dang, M. Song, C. Dang, T. Zhan, and L. Zhang. Experimental study on solidification characteristics of sessile urine droplets on a horizontal cold plate surface under natural convection. *Langmuir*, 38(25):7846–7857, 2022.

[47] Q. Dang, M. Song, X. Zhang, L. Zhang, K. Shao, and J. Shen. Experimental study about solidification processes of sessile deformed water droplets on the biaxial inclined cold plate surface under natural convection. *Applied Thermal Engineering*, 236:121883, 2024.

[48] S. P. Das. *Statistical physics of liquids at freezing and beyond*. Cambridge University Press, 2011.

[49] A. Dehghani-Sanij, S. MacLachlan, G. Naterer, Y. Muzychka, R. Haynes, and V. Enjilela. Multistage cooling and freezing of a saline spherical water droplet. *International Journal of Thermal Sciences*, 147:106095, 2020.

[50] A. Delgado and D.-W. Sun. Heat and mass transfer models for predicting freezing processes–a review. *Journal of Food Engineering*, 47(3):157–174, 2001.

[51] X. Deng, S. Pan, Z. Wang, K. Ke, and J. Zhang. Application of the Darcy-Stefan model to investigate the thawing subsidence around the wellbore in the permafrost region. *Applied Thermal Engineering*, 156:392–401, 2019.

[52] A. Ditkowski and Y. Harness. High-order embedded finite difference schemes for initial boundary value problems on time dependent irregular domains. *Journal of Scientific Computing*, 39:394–440, 2009.

[53] W. Dobinski. Permafrost. *Earth-Science Reviews*, 108(3-4):158–169, 2011.

[54] M. M. Farid, A. M. Khudhair, S. A. K. Razack, and S. Al-Hallaj. A review on phase change energy storage: materials and applications. *Energy Conversion and Management*, 45(9-10):1597–1615, 2004.

[55] M. Farzaneh. *Atmospheric icing of power networks*. Springer Science & Business Media, 2008.

[56] D. Fisher, M. Rappaz, and W. Kurz. Fundamentals of solidification. *Fundamentals of Solidification*, pages 1–353, 2023.

[57] A. S. Fleischer. *Thermal energy storage using phase change materials: fundamentals and applications*. Springer, 2015.

[58] A. Galfré, X. Huang, F. Couenne, and C. Cogné. The phase field method—from fundamentals to practical applications in crystal growth. *Journal of Crystal Growth*, page 127334, 2023.

[59] Y. Gao, J. Luo, F. Fang, M. Xu, M. Mohit, T. Shamim, and A. P. Sasmito. On the stability of nanofluid ice slurry produced via impinging stream method under thermal and phase-change cycles. *Case Studies in Thermal Engineering*, 52:103725, 2023.

[60] Y. Gao, Y. Ning, C. Wu, M. Xu, S. Akhtar, A. S. Mujumdar, and A. P. Sasmito. Experimental investigation of producing ice slurry with water using opposed-nozzle impinging jet method. *Applied Thermal Engineering*, 219:119568, 2023.

[61] Y. Gao, Y. Ren, M. Xu, J. Liu, A. S. Mujumdar, and A. P. Sasmito. Influence of thermal cycling on stability and thermal conductivity of nanofluid ice slurry. *International Journal of Thermal Sciences*, 185:108113, 2023.

[62] T. S. Glickman. *Glossary of meteorology.* American Meteorological Soc., 2000.

[63] T. Gong, Y. Chen, S. Li, Y. Cao, D. Li, X.-Q. Chen, G. Reinhart, and H. Nguyen-Thi. Revisiting dynamics and models of microsegregation during polycrystalline solidification of binary alloy. *Journal of Materials Science & Technology*, 74:155–167, 2021.

[64] T. R. Goodman. The heat balance integral and its application to problems involving change of phase. *ASME Journal of Heat Transfer*, 80:335, 1958.

[65] M. Gortych, Z. Lipnicki, and B. Weigand. An experimental and theoretical study of the solidification process of phase change materials in a horizontal annular enclosure. *Applied Thermal Engineering*, 161:114140, 2019.

[66] M. H. Grabow, G. H. Gilmer, and A. F. Bakker. Molecular dynamics studies of silicon solidification and melting. *MRS Online Proceedings Library*, 141:349–354, 1988.

[67] L. Hachani, B. Saadi, X. D. Wang, A. Nouri, K. Zaidat, A. Belgacem-Bouzida, L. Ayouni-Derouiche, G. Raimondi, and Y. Fautrelle. Experimental analysis of the solidification of Sn–3 wt.% Pb alloy under natural convection. *International Journal of Heat and Mass Transfer*, 55(7-8):1986–1996, 2012.

[68] L. Hachani, K. Zaidat, and Y. Fautrelle. Experimental study of the solidification of Sn–10 wt.% Pb alloy under different forced convection in benchmark experiment. *International Journal of Heat and Mass Transfer*, 85:438–454, 2015.

[69] J. Hao, P. Jia, T. Wu, W. Li, J. Chen, X. Yang, X. Wu, G. Hu, K. Cui, and M. Zhang. Numerical analysis of the impacts of rainfall on permafrost-related slope stability on the qinghai–tibet plateau. *Journal of Hydrology: Regional Studies*, 47:101439, 2023.

[70] M. G. Hennessy, M. Calvo-Schwarzwälder, and T. G. Myers. Modelling ultra-fast nanoparticle melting with the Maxwell-Cattaneo equation. *Applied Mathematical Modelling*, 69:201–222, 2019.

[71] M. G. Hennessy, M. C. Schwarzwälder, and T. G. Myers. Asymptotic analysis of the guyer–krumhansl–stefan model for nanoscale solidification. *Applied Mathematical Modelling*, 61:1–17, 2018.

[72] L. A. Herraiz, M. A. Herrero, and J. J. Velázquez. A note on the dissolution of spherical crystals. *Proceedings of the Royal Society of Edinburgh Section A: Mathematics*, 131(2):371–389, 2001.

[73] J. M. Hill. *One-dimensional Stefan problems: An introduction*. Longman Scientific & Technical, 1987.

[74] J. Hindmarsh, A. Russell, and X. Chen. Experimental and numerical analysis of the temperature transition of a freezing food solution droplet. *Chemical Engineering Science*, 59(12):2503–2515, 2004.

[75] J. Hindmarsh, A. Russell, and X. Chen. Observation of the surface and volume nucleation phenomena in undercooled sucrose solution droplets. *The Journal of Physical Chemistry C*, 111(16):5977–5981, 2007.

[76] J. Hindmarsh, A. Russell, and X. D. Chen. Measuring dendritic growth in undercooled sucrose solution droplets. *Journal of Crystal Growth*, 285(1-2):236–248, 2005.

[77] J. P. Hindmarsh, A. B. Russell, and X. D. Chen. Experimental and numerical analysis of the temperature transition of a suspended freezing water droplet. *International Journal of Heat and Mass Transfer*, 46(7):1199–1213, 2003.

[78] P. V. Hobbs. *Ice physics*. OUP Oxford, 2010.

[79] F. Hong and H.-H. Qiu. Experimental study on rapid solidification process using a novel ultrasound technique. *Experimental Thermal and Fluid Science*, 30(1):17–26, 2005.

[80] J. Hunt and K. Jackson. Binary eutectic solidification. *Transactions of the Metallurgical Society of AIME*, 236(6):843, 1966.

[81] S. P. Ishwarya, C. Anandharamakrishnan, and A. G. Stapley. Spray-freeze-drying: A novel process for the drying of foods and bioproducts. *Trends in Food Science & Technology*, 41(2):161–181, 2015.

[82] K. Ismail, C. Alves, and M. Modesto. Numerical and experimental study on the solidification of pcm around a vertical axially finned isothermal cylinder. *Applied Thermal Engineering*, 21(1):53–77, 2001.

[83] G. Ivantsov. Temperature field around a spherical, cylindrical, and needle-shaped crystal, growing in a pre-cooled melt. *Temperature Field Around a Spherical*, 58:567–569, 1985.

[84] M. A. Jaafar, D. R. Rousse, S. Gibout, and J.-P. Bédécarrats. A review of dendritic growth during solidification: Mathematical modeling and numerical simulations. *Renewable and Sustainable Energy Reviews*, 74:1064–1079, 2017.

[85] K. A. Jackson. *Kinetic processes: Crystal growth, diffusion, and phase transitions in materials*. John Wiley & Sons, 2010.

[86] Z. Jin, H. Zhang, and Z. Yang. Experimental investigation of the impact and freezing processes of a water droplet on an ice surface. *International Journal of Heat and Mass Transfer*, 109:716–724, 2017.

[87] L. Karlsson, H. Lycksam, A.-L. Ljung, P. Gren, and T. S. Lundström. Experimental study of the internal flow in freezing water droplets on a cold surface. *Experiments in Fluids*, 60:1–10, 2019.

[88] A. Khalifa, L. Tan, A. Date, and A. Akbarzadeh. A numerical and experimental study of solidification around axially finned heat pipes for high temperature latent heat thermal energy storage units. *Applied Thermal Engineering*, 70(1):609–619, 2014.

[89] L. Khatra and H. El Qarnia. Semianalytical solution for pcm solidification during the discharging of a planar thermal energy accumulator. *International Journal of Energy Research*, 43(13):7573–7582, 2019.

[90] H. Kiani, Z. Zhang, and D.-W. Sun. Experimental analysis and modeling of ultrasound assisted freezing of potato spheres. *Ultrasonics Sonochemistry*, 26:321–331, 2015.

[91] J. King and D. Riley. Asymptotic solutions to the stefan problem with a constant heat source at the moving boundary. *Proceedings of the Royal Society of London. Series A: Mathematical, Physical and Engineering Sciences*, 456(1997):1163–1174, 2000.

[92] R. Kobayashi. Modeling and numerical simulations of dendritic crystal growth. *Physica D: Nonlinear Phenomena*, 63(3-4):410–423, 1993.

[93] R. Kobayashi. A numerical approach to three-dimensional dendritic solidification. *Experimental Mathematics*, 3(1):59–81, 1994.

[94] A. Kumar, Rajeev, and J. Gómez-Aguilar. A numerical solution of a non-classical stefan problem with space-dependent thermal conductivity, variable latent heat and robin boundary condition. *Journal of Thermal Analysis and Calorimetry*, 147(24):14649–14657, 2022.

[95] A. Kumar, M. J. Walker, S. Sundarraj, and P. Dutta. Grain floatation during equiaxed solidification of an al-cu alloy in a side-cooled cavity: Part i—experimental studies. *Metallurgical and Materials Transactions B*, 42:825–836, 2011.

[96] B. L. Kurylyk. Discussion of 'a simple thaw-freeze algorithm for a multi-layered soil using the Stefan equation' by Xie and Gough (2013). *Permafrost and Periglacial Processes*, 26(2):200–206, 2015.

[97] J. Kyselica, P. Guba, and M. Chudjak. Recalescence dynamics and solidification of a supercooled melt in a finite domain. *International Journal of Heat and Mass Transfer*, 159:120048, 2020.

[98] F. Lamraoui, G. Fortin, R. Benoit, J. Perron, and C. Masson. Atmospheric icing impact on wind turbine production. *Cold Regions Science and Technology*, 100:36–49, 2014.

[99] J. Langer and H. Müller-Krumbhaar. Theory of dendritic growth—i. elements of a stability analysis. *Acta Metallurgica*, 26(11):1681–1687, 1978.

[100] J. Langer, R. Sekerka, and T. Fujioka. Evidence for a universal law of dendritic growth rates. *Journal of Crystal Growth*, 44(4):414–418, 1978.

[101] M. Le Maguer. Mechanics and influence of water binding on water activity. In *Water Activity*, pages 1–25. Routledge, 2017.

[102] A. Léoni, M. Mondot, F. Durier, R. Revellin, and P. Haberschill. State-of-the-art review of frost deposition on flat surfaces. *International Journal of Refrigeration*, 68:198–217, 2016.

[103] G.-y. Li, J. Zhang, Z.-w. Zhou, F. Wang, D. Chen, Y.-p. Cao, and G. Wu. A novel freezing point determination method for oil–contaminated soils based on electrical resistance measurement and its influencing factors. *Science of the Total Environment*, 721:137821, 2020.

[104] K. G. Libbrecht. The physics of snow crystals. *Reports on Progress in Physics*, 68(4):855, 2005.

[105] K. G. Libbrecht. Physical dynamics of ice crystal growth. *Annual Review of Materials Research*, 47:271–295, 2017.

[106] D. R. Lide. *CRC handbook of chemistry and physics*, volume 85. CRC press, 2004.

[107] Z. Lipnicki, D. Sasse, and B. Weigand. Experimental and analytical investigation of the solidification around cooled cylinders subjected to free convection. *International Journal of Heat and Mass Transfer*, 78:321–329, 2014.

[108] Z. Lipnicki and B. Weigand. An experimental and theoretical study of solidification in a free-convection flow inside a vertical annular enclosure. *International Journal of Heat and Mass Transfer*, 55(4):655–664, 2012.

[109] Z. Lipnicki, B. Weigand, T. Małolepszy, and P. Grabas. An experimental and analytical study of solidification around an array of horizontal cylinders subjected to free convection flow. *International Journal of Thermal Sciences*, 173:107378, 2022.

[110] Y. Liu, T. Ming, Y. Wu, R. de Richter, Y. Fang, and N. Zhou. Desalination of seawater by spray freezing in a natural draft tower. *Desalination*, 496:114700, 2020.

[111] Z. Liu, F. Lou, X. Qi, Q. Wang, B. Zhao, J. Yan, and Y. Shen. Experimental study on cold storage phase-change materials and quick-freezing plate in household refrigerators. *Journal of Food Process Engineering*, 42(7):e13279, 2019.

[112] Z. Liu, X. Sun, and C. Ma. Experimental study of the characteristics of solidification of stearic acid in an annulus and its thermal conductivity enhancement. *Energy Conversion and Management*, 46(6):971–984, 2005.

[113] G. S. H. Lock. *Latent heat transfer: an introduction to fundamentals.* Oxford University Press, 1994.

[114] J. López, P. Gómez, and J. Hernández. A volume of fluid approach for crystal growth simulation. *Journal of Computational Physics*, 229(19):6663–6672, 2010.

[115] V. J. Lunardini. *Heat transfer in cold climates*. Van Nostrand Reinhold Co, 1981.

[116] M. M. MacDevette and T. G. Myers. Contact melting of a three-dimensional phase change material on a flat substrate. *International Journal of Heat and Mass Transfer*, 55(23-24):6798–6807, 2012.

[117] S. W. Mccue, J. R. King, and D. S. Riley. The extinction problem for three-dimensional inward solidification. *Journal of Engineering Mathematics*, 52:389–409, 2005.

[118] B. McDonald, P. Patel, and B. Zhao. Droplet freezing and ice adhesion strength measurement on super-cooled hydrophobic surfaces. *The Journal of Adhesion*, 93(5):375–388, 2017.

[119] Z. Meng and P. Zhang. Dynamic propagation of ice-water phase front in a supercooled water droplet. *International Journal of Heat and Mass Transfer*, 152:119468, 2020.

[120] Z. Meng and P. Zhang. Freezing dynamics of supercooled micro-sized water droplets. *International Journal of Heat and Mass Transfer*, 193:122955, 2022.

[121] S. Mitchell and M. Vynnycky. Verified reduction of a model for a continuous casting process. *Applied Mathematical Modelling*, 48:476–490, 2017.

[122] S. L. Mitchell. Applying the combined integral method to two-phase stefan problems with delayed onset of phase change. *Journal of Computational and Applied Mathematics*, 281:58–73, 2015.

[123] S. L. Mitchell and T. G. Myers. Approximate solution methods for one-dimensional solidification from an incoming fluid. *Applied Mathematics and Computation*, 202(1):311–326, 2008.

[124] S. L. Mitchell and T. G. Myers. Application of standard and refined heat balance integral methods to one-dimensional Stefan problems. *SIAM Review*, 52(1):57–86, 2010.

[125] M. Mohit, S. Akhtar, M. Xu, and A. Sasmito. Incorporating droplet dynamics to improve the reduced-order model of spray freezing for mine heating applications. In *Underground Ventilation*, pages 569–577. CRC Press, 2023.

[126] N. O. Moraga and C. H. Salinas. Numerical model for heat and fluid flow in food freezing. *Numerical Heat Transfer: Part A: Applications*, 35(5):495–517, 1999.

[127] F. Mosally, A. S. Wood, and A. Al-Fhaid. An exponential heat balance integral method. *Applied Mathematics and Computation*, 130(1):87–100, 2002.

[128] A. Mostafavi, M. Parhizi, and A. Jain. Theoretical modeling and optimization of fin-based enhancement of heat transfer into a phase change material. *International Journal of Heat and Mass Transfer*, 145:118698, 2019.

[129] S. Motahar, A. A. Alemrajabi, and R. Khodabandeh. Experimental study on solidification process of a phase change material containing tio2 nanoparticles for thermal energy storage. *Energy Conversion and Management*, 138:162–170, 2017.

[130] A. M. Mullis. A free boundary model for shape preserving dendritic growth at high undercooling. *Journal of Applied Physics*, 80(7):4129–4136, 1996.

[131] B. J. Murray, S. Broadley, T. Wilson, J. Atkinson, and R. Wills. Heterogeneous freezing of water droplets containing kaolinite particles. *Atmospheric Chemistry and Physics*, 11(9):4191–4207, 2011.

[132] J. D. Murray. *Asymptotic analysis*, volume 48. Springer Science & Business Media, 2012.

[133] T. Myers. Optimal exponent heat balance and refined integral methods applied to Stefan problems. *International Journal of Heat and Mass Transfer*, 53(5-6):1119–1127, 2010.

[134] T. Myers and S. L. Mitchell. Application of the combined integral method to stefan problems. *Applied Mathematical Modelling*, 35(9):4281–4294, 2011.

[135] C. Naaktgeboren. The zero-phase stefan problem. *International Journal of Heat and Mass Transfer*, 50(23-24):4614–4622, 2007.

[136] A. Najim and S. Krishnan. Experimental study on progressive freeze-concentration based desalination employing a rectangular channel crystallizer. *Environmental Science: Water Research & Technology*, 9(3):850–860, 2023.

[137] R. Nigo, Y. M. J. Chew, N. Houghton, W. Paterson, and D. Wilson. Experimental studies of freezing fouling of model food fat solutions using a novel spinning disc apparatus. *Energy & fuels*, 23(12):6131–6145, 2009.

[138] C. Nikolopoulos. A model for melting of a pure material during modulated temperature differential scanning calorimetry. *SIAM Journal on Applied Mathematics*, 62(4):1176–1196, 2002.

[139] T. Nishinaga. *Handbook of crystal growth: Fundamentals*. Elsevier, 2014.

[140] B. E. K. Nygaard, J. E. Kristjánsson, and L. Makkonen. Prediction of in-cloud icing conditions at ground level using the wrf model. *Journal of Applied Meteorology and Climatology*, 50(12):2445–2459, 2011.

[141] M. Olguin, M. Medina, M. C. Sanziel, and D. A. Tarzia. Behavior of the solution of a stefan problem by changing thermal coefficients of the substance. *Applied Mathematics and Computation*, 190(1):765–780, 2007.

[142] E. Olsson and G. Kreiss. A conservative level set method for two phase flow. *Journal of Computational Physics*, 210(1):225–246, 2005.

[143] E. Olsson, G. Kreiss, and S. Zahedi. A conservative level set method for two phase flow ii. *Journal of Computational Physics*, 225(1):785–807, 2007.

[144] E. Oró, A. De Gracia, A. Castell, M. M. Farid, and L. F. Cabeza. Review on phase change materials (PCMs) for cold thermal energy storage applications. *Applied Energy*, 99:513–533, 2012.

[145] Y. Pan, K. Shi, X. Duan, and G. F. Naterer. Experimental investigation of water droplet impact and freezing on micropatterned stainless steel surfaces with varying wettabilities. *International Journal of Heat and Mass Transfer*, 129:953–964, 2019.

[146] P. Papon, J. Leblond, and P. H. Meijer. The physics of phase transitions: Concepts and applications. 2006.

[147] O. Parent and A. Ilinca. Anti-icing and de-icing techniques for wind turbines: Critical review. *Cold Regions Science and Technology*, 65(1):88–96, 2011.

[148] M. Parhizi and A. Jain. Solution of the phase change stefan problem with time-dependent heat flux using perturbation method. *Journal of Heat Transfer*, 141(2):024503, 2019.

[149] M. Parhizi and A. Jain. Theoretical modeling of a phase change heat transfer problem with a pre-melted or pre-solidified region. *International Journal of Heat and Mass Transfer*, 136:635–643, 2019.

[150] E. Pimentel, S. Papakonstantinou, and G. Anagnostou. Numerical interpretation of temperature distributions from three ground freezing applications in urban tunnelling. *Tunnelling and Underground Space Technology*, 28:57–69, 2012.

[151] F. B. Planella, C. P. Please, and R. A. Van Gorder. Extended Stefan problem for the solidification of binary alloys in a sphere. *European Journal of Applied Mathematics*, 32(2):242–279, 2021.

[152] K. Raj, P. Vellaichamy, V. Ramalingam, et al. Development of novel correlations towards the freezing time estimation of phase change material inside a cylindrical capsule involving thickness and its thermal conductivity for thermal storage applications–an experimental and parametric studies. *Journal of Energy Storage*, 72:108629, 2023.

[153] M. K. Rathod and J. Banerjee. Thermal stability of phase change materials used in latent heat energy storage systems: A review. *Renewable and Sustainable Energy Reviews*, 18:246–258, 2013.

[154] S. Ray, A. K. Suthar, and S. Saha. An exponentially accurate spectral reconstruction technique for the single-phase one-dimensional stefan problem with constant coefficients. *International Journal of Heat and Mass Transfer*, 158:119841, 2020.

[155] H.-S. Ren. Application of the heat-balance integral to an inverse stefan problem. *International Journal of Thermal Sciences*, 46(2):118–127, 2007.

[156] H. Ribera, T. G. Myers, and M. M. MacDevette. Optimising the heat balance integral method in spherical and cylindrical Stefan problems. *Applied Mathematics and Computation*, 354:216–231, 2019.

[157] D. Rozmanov and P. G. Kusalik. Temperature dependence of crystal growth of hexagonal ice (i h). *Physical Chemistry Chemical Physics*, 13(34):15501–15511, 2011.

[158] N. Sadoun, E.-K. Si-Ahmed, and P. Colinet. On the refined integral method for the one-phase stefan problem with time-dependent boundary conditions. *Applied Mathematical Modelling*, 30(6):531–544, 2006.

[159] I. Sari, L. Hachani, A. Kharicha, Y. Fautrelle, B. Pichat, and K. Zaidat. 3d numerical simulation and experimental investigation of pure tin solidification under natural and forced convection. *International Journal of Thermal Sciences*, 164:106900, 2021.

[160] R. Scardovelli and S. Zaleski. Direct numerical simulation of free-surface and interfacial flow. *Annual Review of Fluid Mechanics*, 31(1):567–603, 1999.

[161] M. Schremb, J. M. Campbell, H. K. Christenson, and C. Tropea. Ice layer spreading along a solid substrate during solidification of supercooled water: Experiments and modeling. *Langmuir*, 33(19):4870–4877, 2017.

[162] E. A. Schuur, A. D. McGuire, C. Schädel, G. Grosse, J. W. Harden, D. J. Hayes, G. Hugelius, C. D. Koven, P. Kuhry, D. M. Lawrence, et al. Climate change and the permafrost carbon feedback. *Nature*, 520(7546):171–179, 2015.

[163] R. P. Sear. Nucleation: Theory and applications to protein solutions and colloidal suspensions. *Journal of Physics: Condensed Matter*, 19(3):033101, 2007.

[164] I. B. Sebastião, B. Bhatnagar, and S. Tchessalov. A kinetic model for spray-freezing of pharmaceuticals. *Journal of Pharmaceutical Sciences*, 110(5):2047–2062, 2021.

[165] I. B. Sebastião, B. Bhatnagar, S. Tchessalov, S. Ohtake, M. Plitzko, B. Luy, and A. Alexeenko. Bulk dynamic spray freeze-drying part 2: model-based parametric study for spray-freezing process characterization. *Journal of Pharmaceutical Sciences*, 108(6):2075–2085, 2019.

[166] R. Shaw, A. Kostinski, and M. L. Larsen. Towards quantifying droplet clustering in clouds. *Quarterly Journal of the Royal Meteorological Society: A journal of the atmospheric sciences, applied meteorology and physical oceanography*, 128(582):1043–1057, 2002.

[167] R. A. Shaw, A. J. Durant, and Y. Mi. Heterogeneous surface crystallization observed in undercooled water. *The Journal of Physical Chemistry B*, 109(20):9865–9868, 2005.

[168] C. Shen, J. Simmons, and Y. Wang. Effect of elastic interaction on nucleation: Ii. implementation of strain energy of nucleus formation in the phase field method. *Acta Materialia*, 55(4):1457–1466, 2007.

[169] J. Simmons, C. Shen, and Y. Wang. Phase field modeling of simultaneous nucleation and growth by explicitly incorporating nucleation events. *Scripta Materialia*, 43(10):935–942, 2000.

[170] T. Singla, B. Kumar, and S. Sharma. Numerical study of the melting process of spherical phase change material with variable thermal conductivity. *Indian Journal of Physics*, pages 1–9, 2023.

[171] J. W. Sitison and D. A. Edwards. The heat balance integral method for cylindrical extruders. *Journal of Engineering Mathematics*, 122:1–16, 2020.

[172] W. R. Smith. Models for solidification and splashing in laser percussion drilling. *SIAM Journal on Applied Mathematics*, 62(6):1899–1923, 2002.

[173] M. Song and C. Dang. Review on the measurement and calculation of frost characteristics. *International Journal of Heat and Mass Transfer*, 124:586–614, 2018.

[174] D. M. Stefanescu. *Science and engineering of casting solidification.* Springer, 2015.

[175] K. Szilder. Theoretical and experimental study of ice accretion due to freezing rain on an inclined cylinder. *Cold Regions Science and Technology*, 150:25–34, 2018.

[176] S. Tabakova, F. Feuillebois, and S. Radev. Freezing of a supercooled spherical droplet with mixed boundary conditions. *Proceedings of the Royal Society A: Mathematical, Physical and Engineering Sciences*, 466(2116):1117–1134, 2010.

[177] F. Tan. An experimental study on channels formation during solidification of aqueous ammonium chloride. *Applied Thermal Engineering*, 25(14-15):2169–2192, 2005.

[178] K. K. Tanaka and Y. Kimura. Theoretical analysis of crystallization by homogeneous nucleation of water droplets. *Physical Chemistry Chemical Physics*, 21(5):2410–2418, 2019.

[179] R. Trivedi and W. Kurz. Dendritic growth. *International Materials Reviews*, 39(2):49–74, 1994.

[180] J. J. Vadasz, J. P. Meyer, S. Govender, and G. Ziskind. Experimental study of vibration effects on heat transfer during solidification of paraffin in a spherical shell. *Experimental Heat Transfer*, 29(3):285–298, 2016.

[181] R. van der Sman. Multiscale simulations of directional ice crystal growth in sugar solutions. *Food Structure*, 30:100214, 2021.

[182] J. Van Huissteden. *Thawing Permafrost*, volume 1143. Springer, 2020.

[183] H. Vehkamäki, A. Määttänen, A. Lauri, I. Napari, and M. Kulmala. The heterogeneous zeldovich factor. *Atmospheric Chemistry and Physics*, 7(2):309–313, 2007.

[184] M. P. Vikram, V. Kumaresan, S. Christopher, and R. Velraj. Experimental studies on solidification and subcooling characteristics of water-based phase change material (pcm) in a spherical encapsulation for cool thermal energy storage applications. *International Journal of Refrigeration*, 100:454–462, 2019.

[185] M. Vitel, A. Rouabhi, M. Tijani, and F. Guérin. Modeling heat transfer between a freeze pipe and the surrounding ground during artificial ground freezing activities. *Computers and Geotechnics*, 63:99–111, 2015.

[186] M. Vitel, A. Rouabhi, M. Tijani, and F. Guérin. Thermo-hydraulic modeling of artificial ground freezing: Application to an underground mine in fractured sandstone. *Computers and Geotechnics*, 75:80–92, 2016.

[187] V. Voller and M. Cross. Accurate solutions of moving boundary problems using the enthalpy method. *International Journal of Heat and Mass Transfer*, 24(3):545–556, 1981.

[188] V. R. Voller, M. Cross, and N. Markatos. An enthalpy method for convection/diffusion phase change. *International Journal for Numerical Methods in Engineering*, 24(1):271–284, 1987.

[189] M. Volmer and A. Weber. Keimbildung in übersättigten gebilden. *Zeitschrift für physikalische Chemie*, 119(1):277–301, 1926.

[190] V. Voulgaropoulos, N. Le Brun, A. Charogiannis, and C. N. Markides. Transient freezing of water between two parallel plates: A combined experimental and modelling study. *International Journal of Heat and Mass Transfer*, 153:119596, 2020.

[191] G.-X. Wang and E. Matthys. Experimental determination of the interfacial heat transfer during cooling and solidification of molten metal droplets impacting on a metallic substrate: effect of roughness and superheat. *International Journal of Heat and Mass Transfer*, 45(25):4967–4981, 2002.

[192] S. Wang, C. Wang, J. Wang, S. Jiang, T. Zhang, and Z. Ma. An analytical solution for a phase change nano-capsule cooled by forced convection. *International Journal of Heat and Mass Transfer*, 212:124267, 2023.

[193] T. Wang, Y. Lu, L. Ai, Y. Zhou, and M. Chen. Dendritic growth model involving interface kinetics for supercooled water. *Langmuir*, 35(15):5162–5167, 2019.

[194] X. Wang and Y. Fautrelle. An investigation of the influence of natural convection on tin solidification using a quasi two-dimensional experimental benchmark. *International Journal of Heat and Mass Transfer*, 52(23-24):5624–5633, 2009.

[195] Y. Wen, J. Simmons, C. Shen, C. Woodward, and Y. Wang. Phase-field modeling of bimodal particle size distributions during continuous cooling. *Acta Materialia*, 51(4):1123–1132, 2003.

[196] T. Wu, X. Zhou, L. Zhang, X. Zhang, X. He, and Y. Xu. Theory and technology of real-time temperature field monitoring of vertical shaft frozen wall under high-velocity groundwater conditions. *Cold Regions Science and Technology*, 189:103337, 2021.

[197] M. Xu, S. Akhtar, M. Mohit, and A. P. Sasmito. Development of a multi-stage model for freezing of a suspended binary solution droplet. *International Journal of Heat and Mass Transfer*, 221:125115, 2024.

[198] M. Xu, S. Akhtar, A. F. Zueter, M. A. Alzoubi, L. Sushama, and A. P. Sasmito. Asymptotic analysis of a two-phase Stefan problem in annulus: Application to outward solidification in phase change materials. *Applied Mathematics and Computation*, 408:126343, 2021.

[199] M. Xu, S. Akhtar, A. F. Zueter, V. Auger, M. A. Alzoubi, and A. P. Sasmito. Development of analytical solution for a two-phase Stefan problem in artificial ground freezing using singular perturbation theory. *Journal of Heat Transfer*, 142(12):122401, 2020.

[200] M. Xu, Y. Hanawa, S. Akhtar, A. Sakuma, J. Zhang, J. Yoshida, M. Sanada, Y. Sasaki, and A. P. Sasmito. Multi-scale analysis for solidification of phase change materials (PCMs): Experiments and modeling. *International Journal of Heat and Mass Transfer*, 212:124182, 2023.

[201] B. Yang, X. Fu, W. Yang, N. Sun, S. Hu, Y. Lu, and M.-B. Yang. Prediction of heat conduction with phase-change effects during cooling stage of injection molding of high-density polyethylene: approximate integral approach. *Journal of Macromolecular Science, Part B*, 49(4):734–749, 2010.

[202] Y. Yao, C. Li, Z. Tao, R. Yang, and H. Zhang. Experimental and numerical study on the impact and freezing process of a water droplet on a cold surface. *Applied Thermal Engineering*, 137:83–92, 2018.

[203] F. Yigit. Approximate analytical and numerical solutions for a two-dimensional stefan problem. *Applied Mathematics and Computation*, 202(2):857–869, 2008.

[204] Z.-T. Yu, L.-W. Fan, Y.-C. Hu, and K.-F. Cen. Perturbation solution to heat conduction in melting or solidification with heat generation. *Heat and Mass Transfer*, 46:479–483, 2010.

[205] H. Zhang, K. El Kadi, M. I. H. Ali, and I. Janajreh. Cryo-powered desalination: Experimental investigations on brine droplets freezing in a natural convection environment. *Desalination*, 567:116974, 2023.

[206] H. Zhang, Z. Jin, M. Jiao, and Z. Yang. Experimental investigation of the impact and freezing processes of a water droplet on different cold concave surfaces. *International Journal of Thermal Sciences*, 132:498–508, 2018.

[207] H. Zhang, S. Savvopoulos, H. Hatzikirou, and I. Janajreh. Experimental and mathematically validated studies of pure water droplet freezing under natural free convection. *Desalination*, 555:116512, 2023.

[208] X. Zhang, X. Liu, X. Wu, and J. Min. Simulation and experiment on supercooled sessile water droplet freezing with special attention to supercooling and volume expansion effects. *International Journal of Heat and Mass Transfer*, 127:975–985, 2018.

[209] M. Zhelnin, A. Kostina, A. Prokhorov, O. Plekhov, M. Semin, and L. Levin. Coupled thermo-hydro-mechanical modeling of frost heave and water migration during artificial freezing of soils for mineshaft sinking. *Journal of Rock Mechanics and Geotechnical Engineering*, 14(2):537–559, 2022.

[210] Z.-Q. Zhu, M.-J. Liu, N. Hu, Y.-K. Huang, L.-W. Fan, Z.-T. Yu, and J. Ge. Inward solidification heat transfer of nano-enhanced phase change materials in a spherical capsule: an experimental study. *Journal of Heat Transfer*, 140(2):022301, 2018.

[211] A. Zueter, A. Nie-Rouquette, M. A. Alzoubi, and A. P. Sasmito. Thermal and hydraulic analysis of selective artificial ground freezing using air insulation: Experiment and modeling. *Computers and Geotechnics*, 120:103416, 2020.

Part II

Macro-scale Equilibrium Solidification

Chapter 3

Development of analytical solution for a two-phase Stefan problem in artificial ground freezing using singular perturbation theory

Contents

Preface (Bridging Text)

Artificial ground freezing (AGF) is a geotechnical support method that has been widely utilized due to its reliability and compatibility with a broad range of ground types. In mining engineering, AGF can be applied to stabilize ore deposits, protect underground infrastructure, seal hazardous waste, and prevent permafrost from thawing. In Canada, AGF has been implemented in the Cigar Lake Mine, a large high-grade underground uranium mine in Saskatchewan.

The process of AGF involves complex transport phenomena that are fundamentally related to macro-scale solidification in porous media. The literature is rife with numerical modeling of AGF; the two commonly used methods are the apparent heat capacity and enthalpy methods. The two-phase Stefan problem is one of the few analytical methods for macro-scale solidification, which implicitly tracks the solid-liquid moving boundary during phase transition. However, the analytical solutions are limited for two-phase Stefan problems, particularly in cylindrical coordinates, but they can rapidly estimate the non-linear moving interface and temperature profile.

In this chapter, we developed an analytical solution for understanding macro-scale equilibrium solidification in porous media, providing insights into estimating the freezing front and ground temperature in AGF. By employing the singular perturbation method, a two-phase Stefan problem within an annulus was solved; two temporal scales were constructively separated. Additionally, the method of volume averages was utilized to characterize the effective thermophysical properties of the porous media.

The outcome of this chapter provided a rule-of-thumb thermal prediction of AGF without any requirements for computational power and software expertise, which in turn facilitated the industrial design and optimization of AGF in mines. Meanwhile, from a fundamental aspect, this research contributed a singular perturbation solution to two-phase Stefan problems in cylindrical coordinates. The findings and discussions in this chapter were published in the peer-reviewed journal article mentioned below.

M. Xu, S. Akhtar, A. F. Zueter, V. Auger, M. A. Alzoubi, and A. P. Sasmito. Development of analytical solution for a two-phase Stefan problem in artificial ground freezing using singular perturbation theory. *Journal of Heat Transfer*, 142(12):122401, 2020.

Abstract

Artificial ground freezing (AGF) has historically been used to stabilize underground structure. Numerical methods generally require high computational power to be applicable in practice. Therefore, it is of interest to develop accurate and reliable analytical frameworks for minimizing computational cost. This paper proposes a singular perturbation solution for a two-phase Stefan problem that describes outward solidification in AGF. Specifically, the singular perturbation method separates two distinct temporal scales to capture the subcooling and freezing stages in the ground. The ground was considered as a porous medium with volume-averaged thermophysical properties. Further, Stefan number was assumed to be small, and effects of a few site-dependent parameters were investigated. The analytical solution was verified by numerical results and found to have similar conclusions yet with much lesser computational cost.

Keywords: artificial ground freezing, Stefan-like problems, singular perturbation, porous media, outward solidification

3.1 Introduction

Artificial ground freezing (AGF) is a construction technique in underground mines and tunnelling projects to provide temporary support for underground structures through freezing saturated soil, making it less susceptible to water seepage [35, 5]. There has been growing interest in exploring the complex phenomena in AGF by using either experiments or mathematical modeling over the past decades. Recently, many researchers have conducted laboratory-scale experiments [25, 4] and validated numerical models [2, 3, 34, 45, 33]. These experimental and numerical frameworks can be time-consuming and computationally expensive. Consequently, applying experimental and numerical methods cannot offer rapid assessment and rule-of-thumb decision making in AGF. Analytical models, on the other hand, are complicated to establish due to the nonlinear moving boundary that describes phase change. However, corresponding solutions are straightforward to compute after comprehensive mathematical formulations.

Many analytical approaches of freezing problems are taken by assuming that the solid phase is initially at the fusion temperature, namely one-phase Stefan problems. The problems with semi-infinite domains often exist similarity solutions [11, 1] and those with finite domains can be approximated by perturbation series [18, 26] and heat balance integral method [17, 40, 10, 27]. Over the past decades, there had also been considerable analytical frameworks in two-phase Stefan problems, where the domain does not start at the fusion temperature. Singular perturbation theory uses two or more asymptotic expansions to capture the initial condition of two-phase problems [31]. According to this theory, many problems were solved by assuming small Stefan numbers in rectangular [38, 8], inward spherical [22] and inward cylindrical solidification [19, 21]. Moreover, Kummer's function (also known as confluent hypergeometric function) were applied on semi-infinite domains with variable latent heat in two-phase problems [43, 6] extended from one-phase solutions [37, 36, 44]. Apart from the aforementioned fully analytical frameworks, alternative approaches are to partially utilize numerical schemes on the nonlinear moving interface [12, 29] or to build multiple thermal layers coupled with iterations [24]. In addition, analytical solutions on these Stefan problems have also been vastly applied in other engineering fields, such as solidification of binary alloys [16, 8], thermal management of lithium-ion batteries [23, 42], heaters for additive manufacturing [13], nanoparticles [41, 15] and tissue engineering [28, 30].

To date, very few studies have been published in the literature that developed analytical solutions to a two-phase Stefan problem of porous media in finite annular domains. Jiji and Weinbaum's work [19] applied singular perturbation theory for the inward solidification process on a set of boundary-fixing equations. However, some of these boundary-fixing formulations were complicated such that less information was extracted in the final solution. It is therefore vital to refine this work and extend it to porous media that practically facilitates thermal design and operations of AGF.

This paper proposes an asymptotic solution for a two-phase Stefan problem that models outward solidification process in porous media over a finite annular region using singular perturbation theory. The singular perturbation theory incorporates two distinct temporal scales with physical scaling analysis, which in turn describe both subcooling and freezing stages during phase change. Specifically, the initial (i.e., not at the fusion temperature) and quasi-steady state behaviors were captured in the asymptotic solution by assuming small Stefan number. Since the ground in AGF is considered as porous media, this assumption of small Stefan number naturally appears. Consequently, thermophysical properties of the ground can be obtained by the method of volume averaging. Furthermore, a numerical model based on the enthalpy method in porous media is also conducted to verify the presented analytical solution.

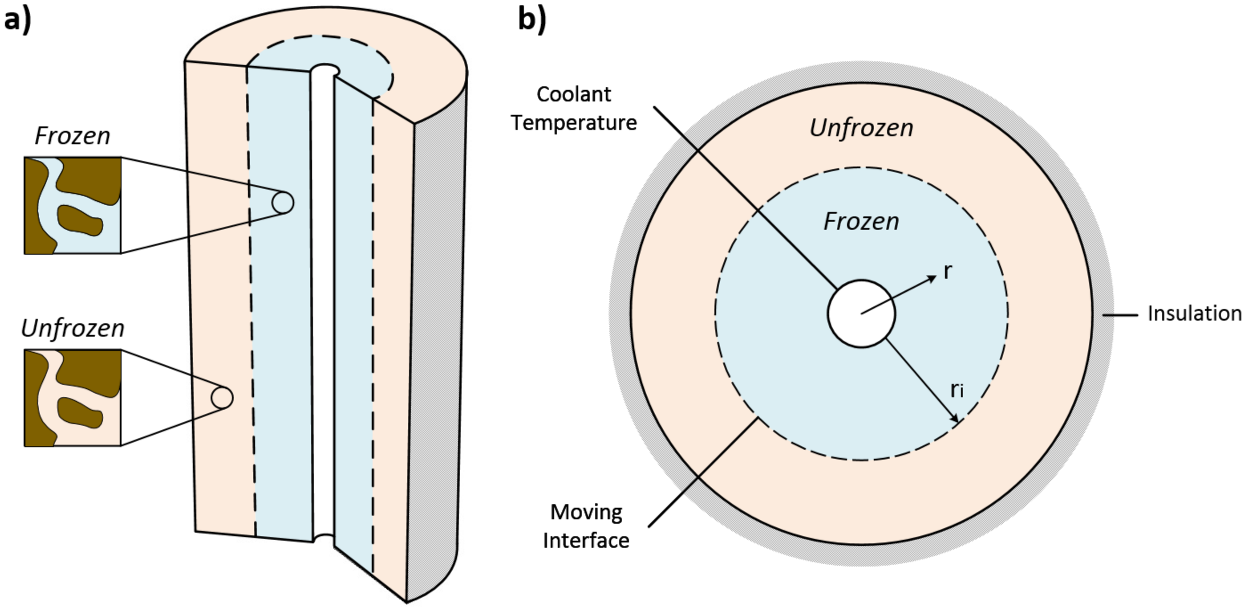

Figure 3.1: Schematic diagram: a) A three-dimensional view of AGF system with magnified frozen and unfrozen ground, and b) A cross-sectional view of AGF system. Additionally, three materials are shown in the magnified view of frozen and unfrozen ground: sand particles in brown, water in peach fade, and ice in blue.

3.2 Analytical modeling

In this section, a new analytical framework of a two-phase Stefan problem was developed in the concept of AGF. The two-phase Stefan problem was firstly formulated. Corresponding thermophysical properties were then calculated based on the method of volume averaging in porous media. Lastly, singular perturbation theory was applied in two temporal scales to forge an asymptotic solution to the problem.

3.2.1 Formulation

The outward freezing problem considered is schematically shown in Figure 3.1. The ground body (i.e., the annular space) is initially filled with unfrozen ground and starts at a uniform temperature T_{init}, which is higher than the fusion temperature T_f. Consequently, the unfrozen ground is at liquid state in the beginning. A freeze pipe located at the inner surface $r = b$ is suddenly activated at time $t = 0$. The coolant temperature T_b is then maintained for time $t > 0$. Therefore, the unfrozen ground starts to solidify from $r = b$, and a frozen ground (i.e., at solid state) is now involved in the domain. An axially symmetric interface that separates the unfrozen and frozen grounds moves in the positive r direction and stays at the fusion temperature T_f. This formulation can also be described as a classical two-phase Stefan problem, where the system ends once the moving interface reaches the outer radius $r_i = a$ in finite domains. Physically, the classical two-phase Stefan problem interprets subcooling and freezing stages during phase change.

For the purpose of mathematical simplification, the following assumptions are made: i) The thermophysical properties in each phase are uniform and remain constant; ii) There is no energy generation as the heat conducts; iii) Volumetric change due to changes in density is negligible; and iv) Natural convection in the unfrozen phase is also negligible because of low Rayleigh number and Darcy number in porous media.

The heat conduction equations for the frozen and unfrozen phases are

$$\begin{aligned} \frac{\partial T_s}{\partial t} &= \alpha_s\left(\frac{\partial^2 T_s}{\partial r^2} + \frac{1}{r}\frac{\partial T_s}{\partial r}\right),\ b < r < r_i(t),\ t > 0; \\ \frac{\partial T_\ell}{\partial t} &= \alpha_\ell\left(\frac{\partial^2 T_\ell}{\partial r^2} + \frac{1}{r}\frac{\partial T_\ell}{\partial r}\right),\ r_i(t) < r < a,\ 0 \le t < t_c, \end{aligned} \tag{3.1}$$

where T, α, r, and t are the temperature [K], thermal diffusivity [m^2/s], radial coordinate [m], and time [s], respectively. a and b are the outer and inner radii [m]. The subscripts s and ℓ represent the frozen ground (solid phase) and unfrozen ground (liquid phase). t_c is the critical time when the ground completes freezing [s], also referred as the total freezing time of the ground. Further, the moving boundary interface is described based on the energy balance from the frozen and unfrozen control volumes. In this energy balance, both sensible and latent heat are considered. This condition at the moving boundary interface, also known as the Stefan condition, is

$$k_s\frac{\partial T_s}{\partial r}\bigg|_{r=r_i(t)} - k_\ell\frac{\partial T_\ell}{\partial r}\bigg|_{r=r_i(t)} = \rho_s L\frac{\mathrm{d}r_i}{\mathrm{d}t},\ 0 \le t < t_c, \tag{3.2}$$

where k, ρ, L, and r_i are the thermal conductivity [W/(m·K)], mass density [kg/m^3], latent heat of fusion [J/kg], and solid-liquid interface location [m], respectively. The boundary conditions are

$$\begin{aligned} T_s(r = b, t) &= T_b, \\ T_s(r = r_i(t), t) &= T_f, \\ T_\ell(r = r_i(t), t) &= T_f, \\ \left.\frac{\partial T_\ell}{\partial r}\right|_{r=a} &= 0, \end{aligned} \tag{3.3}$$

where T_b and T_f are the coolant temperature [K] and fusion temperature [K], respectively. The insulated (or no-flux) boundary condition is applied at the outer radius, because the dimension of freeze pipe is substantially small compared with the outer dimension affected in the field of AGF, which can be assumed as boundary independent. Same assumption has also been used in laboratory-scale experiments, where the working tank filled with soil was adequately insulated at the wall [4, 45]. Moreover, the temporal conditions are

$$\begin{aligned} r_i(t = 0) &= b, \\ T_\ell(r, t = 0) &= T_{\text{init}}, \\ r_i(t = t_c) &= a, \end{aligned} \tag{3.4}$$

where T_{init} is the initial temperature [K]. The last equation in Eqn. (3.4) can be seen as a terminal condition for the freezing stage.

3.2.2 Method of volume averaging

Apart from the freezing physics, the ground in AGF is also considered as a porous medium at the macroscopic scale. Specifically, the porous ground consists of sand particles and voids filled with either ice or water. It is therefore necessary to define two types of voids as the frozen and unfrozen phases. In this subsection, thermophysical properties of the frozen and unfrozen are calculated based on the method of volume averaging [39].

The aforementioned frozen and unfrozen phases satisfy the criteria of local thermal equilibrium, as shown in [4, 45]. This local thermal equilibrium implies that the local temperature difference between the phases are negligible compared with the one at the pore level [20]. Consequently, the method of local volume averaging can be applied to the thermophysical properties. The effective mass density, ρ_e [kg/m^3], thermal conductivity, k_e [W/(m·K)], and volumetric heat capacity, $(\rho c_p)_e$ [J/(K·m^3)], are obtained by the local volume averaging method

$$\begin{aligned} \rho_e &= \epsilon \rho_{\text{void}} + (1-\epsilon)\rho_{\text{sand}}, \\ k_e &= \epsilon k_{\text{void}} + (1-\epsilon) k_{\text{sand}}, \\ (\rho c_p)_e &= \epsilon (\rho c_p)_{\text{void}} + (1-\epsilon)(\rho c_p)_{\text{sand}}, \end{aligned} \tag{3.5}$$

where the subscripts void and sand are the corresponding properties of void and sand particles, respectively. ϵ represents the porosity of the ground. In this case, the void can be changed by either ice or water for frozen or unfrozen phase. The effective specific heat, $c_{p,e}$ [J/(kg·K)], is then calculated by

$$c_{p,e} = \frac{(\rho c_p)_e}{\rho_e}. \tag{3.6}$$

Moreover, the effective latent heat of fusion is volume-averaged by multiplying the porosity [20]. Table 3.1 shows numerical values of thermophysical properties in plain media (i.e., sand, ice, water) and volume averaged properties in porous media (i.e., frozen, unfrozen), taken the fact that the porosity is 40%. These thermophysical properties include thermal conductivity, mass density, and specific heat. Note that the effective latent heat of fusion is 133600 [J/kg] in this scenario.

Table 3.1: Thermophysical properties of pure and porous media (e.g., sand, ice, water, porous frozen phase and porous unfrozen phase) when the porosity is 40% for porous media [4]. Specifically, the thermophysical properties including thermal conductivity, k [W/(m·K)], mass density, ρ [kg/m^3], and specific heat, c_p [J/(kg·K)]. Additionally, the effective latent heat of fusion is 133600 [J/kg].

	Pure Media			**Porous Media**	
	Sand	Ice	Water	Frozen	Unfrozen
k	3.73	2.30	0.579	3.16	2.47
ρ	2634	918.9	999.7	1948	1980
c_p	946	2000	4200	1145	1603

3.2.3 Singular perturbation analysis

An asymptotic solution of the freezing process is established in the subsection. To begin with the asymptotic analysis, general scalings and dimensionless numbers are firstly introduced. The scalings of thermophysical properties and geometry are defined as

$$\alpha = \frac{\alpha_s}{\alpha_\ell}, \qquad k = \frac{k_s}{k_\ell}, \qquad c_p = \frac{c_{p,s}}{c_{p,\ell}}, \qquad \rho = \frac{\rho_s}{\rho_\ell}, \qquad \beta = \frac{b}{a}. \tag{3.7}$$

The dimensionless spaces and temperatures are

$$\xi = \frac{r}{a}, \qquad \xi_i = \frac{r_i}{a}, \qquad \theta_s = \frac{T_s - T_f}{T_{\text{init}} - T_f}, \qquad \theta_\ell = \frac{T_\ell - T_f}{T_{\text{init}} - T_f}, \tag{3.8}$$

where a is also referred as the characteristic length and $(T_{\text{init}} - T_f)$ is the liquid-based temperature scaling that has been consistently used in this paper. Further, the dimensionless numbers are defined as

$$\text{Fo}_\ell = \frac{\alpha_\ell t}{a^2}, \qquad \text{Ste}_\ell = \frac{c_{p,\ell}(T_{\text{init}} - T_f)}{L}, \tag{3.9}$$

where c_p is the specific heat at constant pressure [J/(kg·K)]. Fo_ℓ and Ste_ℓ are the Fourier and Stefan numbers. In this paper, we scaled the Fourier and Stefan numbers by the unfrozen phase to characterize subcooling and freezing stages in AGF.

The exact solution to this problem is nearly impossible. However, singular perturbation method can be applied to find an approximate analytical solution. This solution can also be referred to as an asymptotic or singularly perturbed solution. There are two distinct scales implemented in this problem and they are related to the nature of subcooling and freezing stages in the AGF. Mathematically, this two-phase Stefan problem is decoupled into two temporal scales by asymptotic analysis. The first scale (i.e., subcooling stage) aims to capture the initial state, where the entire domain is at unfrozen phase with a uniform temperature above fusion. The temperature profile for the unfrozen phase is then found at the leading order. Following the initial scale, a quasi-steady scale (i.e., freezing stage) can be introduced by assuming that the Stefan number approaches zero, and thus the initial conditions will be abandoned. The problem is then reduced to a one-phase Stefan problem, where the interface location and frozen phase solution can be obtained.

Inner solution (subcooling stage)

To capture the subcooling behaviour and initial condition of the unfrozen phase, the dimensionless time at the initial scale is

$$t_\ell = \mathrm{Fo}_\ell. \tag{3.10}$$

Re-scaling the interface variable, we get:

$$\xi_i = \beta + \mathrm{Ste}_\ell^{\frac{1}{2}} \widetilde{\xi_i}, \tag{3.11}$$

where $\widetilde{\xi_i}$ is the newly scaled variable of the dimensionless interface motion. The power of the Stefan number in this scaling is $\frac{1}{2}$, which relates to the exact solution of classical Stefan problems with semi-infinite domains. The mathematical stability of this type of scaling has been proved by Brosa Planella et al [7] and has applied in the Cartesian [8] and spherical coordinates [22, 9]. With the re-scaled interface the spatial domain of frozen phase becomes

$$\beta < \xi < \left(\beta + \mathrm{Ste}_{\ell}^{\frac{1}{2}}\widetilde{\xi}_i\right) \tag{3.12}$$

and the frozen phase vanishes at the leading order. The unfrozen phase, on the other hand, exists at the leading order (i.e., $\beta < \xi < 1$) and the problem reduces to a transient heat conduction problem:

$$\frac{\partial \theta_{\ell,0}}{\partial t_{\ell}} = \left(\frac{\partial^2 \theta_{\ell,0}}{\partial \xi^2} + \frac{1}{\xi}\frac{\partial \theta_{\ell,0}}{\partial \xi}\right), \ \beta < \xi < 1, \tag{3.13}$$

subject to the fixed boundary condition

$$\theta_{\ell,0}(\beta, t_{\ell}) = 0, \qquad \left.\frac{\partial \theta_{\ell,0}}{\partial \xi}\right|_{\xi=1} = 0, \qquad \theta_{\ell,0}(\xi, 0) = 1. \tag{3.14}$$

It is worthy to mention that the moving boundary will not appear at the leading order, because only one phase exists. Since both boundary conditions are homogeneous, the method of separation of variables can be applied directly. We find the exact solution

$$\theta_{\ell,0} = \sum_{n=1}^{\infty} C_n \left[J_0(\lambda_n \xi) Y_0(\lambda_n \beta) - J_0(\lambda_n \beta) Y_0(\lambda_n \xi)\right] \exp(-\lambda_n^2 t_{\ell}), \tag{3.15}$$

where J_n and Y_n are the Bessel functions of the first and second kinds of order n, and in this case order 0 ($n = 0$). The eigenvalues λ_n are obtained by the transcendental equation

$$J_1(\lambda_n) Y_0(\lambda_n \beta) - J_0(\lambda_n \beta) Y_1(\lambda_n) = 0, \ n = 1, 2, 3, ... \tag{3.16}$$

and corresponding coefficients C_n are found by substituting the initial condition and applying orthogonality

$$C_n = \frac{\int_{\xi=\beta}^{1} \xi[J_0(\lambda_n\xi)Y_0(\lambda_n\beta) - J_0(\lambda_n\beta)Y_0(\lambda_n\xi)]\mathrm{d}\xi}{\int_{\xi=\beta}^{1} \xi[J_0(\lambda_n\xi)Y_0(\lambda_n\beta) - J_0(\lambda_n\beta)Y_0(\lambda_n\xi)]^2\mathrm{d}\xi}. \tag{3.17}$$

The unfrozen temperature θ_ℓ is approximated by its leading order as seen in Eqn. (3.15) from the inner expansion. The next order will not be solvable due to the complexity of this solution at the leading order. As a result, this temporal scale for the inner expansion only yields a fairly short-time solution, which implies that the evolution of moving interface cannot be captured. Another time scale is therefore required and will be presented in the following outer solution at the freezing stage.

Outer solution (freezing stage)

Following the subcooling stage, the ground starts to freeze. Recall that the ground is assumed to be porous media, which leads to an intrinsically small Stefan number. The time scale can then be assumed at quasi-steady state, where the Stefan number is less than unity

$$\tau_\ell = \mathrm{Ste}_\ell \mathrm{Fo}_\ell. \tag{3.18}$$

The dimensionless temperatures are the same as ones at the initial scale, i.e., θ_s and θ_ℓ. As a result, the heat conduction equations and the Stefan condition are written as

$$\begin{aligned} \alpha\left(\frac{\partial^2\theta_s}{\partial\xi^2} + \frac{1}{\xi}\frac{\partial\theta_s}{\partial\xi}\right) &= \mathrm{Ste}_\ell\frac{\partial\theta_s}{\partial\tau_\ell}, \\ \frac{\partial^2\theta_\ell}{\partial\xi^2} + \frac{1}{\xi}\frac{\partial\theta_\ell}{\partial\xi} &= \mathrm{Ste}_\ell\frac{\partial\theta_\ell}{\partial\tau_\ell}, \\ \frac{k}{\alpha}\frac{\partial\theta_s}{\partial\xi}\bigg|_{\xi=\xi_i} - \frac{\partial\theta_\ell}{\partial\xi}\bigg|_{\xi=\xi_i} &= \rho\frac{\mathrm{d}\xi_i}{\mathrm{d}\tau_\ell}. \end{aligned} \tag{3.19}$$

The problem at its leading order becomes

$$\begin{aligned}\alpha\left(\frac{\partial^2\theta_{s,0}}{\partial\xi^2}+\frac{1}{\xi}\frac{\partial\theta_{s,0}}{\partial\xi}\right)&=0,\\ \frac{\partial^2\theta_{\ell,0}}{\partial\xi^2}+\frac{1}{\xi}\frac{\partial\theta_{\ell,0}}{\partial\xi}&=0,\\ \frac{k}{\alpha}\frac{\partial\theta_{s,0}}{\partial\xi}\bigg|_{\xi=\xi_{i,0}}-\frac{\partial\theta_{\ell,0}}{\partial\xi}\bigg|_{\xi=\xi_{i,0}}&=\rho\frac{\mathrm{d}\xi_{i,0}}{\mathrm{d}\tau_\ell},\end{aligned}\tag{3.20}$$

subject to the dimensionless boundary conditions

$$\begin{aligned}&\theta_{s,0}(\beta,\tau_\ell)=\theta_b,\quad \theta_{s,0}(\xi_{i,0},\tau_\ell)=0,\\ &\theta_{\ell,0}(\xi_{i,0},\tau_\ell)=0,\quad \frac{\partial\theta_{\ell,0}}{\partial\xi}\bigg|_{\xi=1}=0.\end{aligned}\tag{3.21}$$

Thus, the temperature profiles can be readily obtained from these boundary conditions

$$\theta_{s,0}=\theta_b+\theta_b\frac{\ln\xi/\beta}{\ln\beta/\xi_{i,0}},\ \ \theta_{\ell,0}=0.\tag{3.22}$$

Since the unfrozen phase solution is zero, the problem reduces to a one-phase Stefan problem. Further, the interface motion can be implicitly calculated by substituting the temperature solution into the interface equation. After integrating from 0 to τ_ℓ, we find

$$\tau_\ell=\frac{\rho\alpha}{4k\theta_b}\left(\xi_{i,0}^2-\beta^2+2\xi_{i,0}^2\ln\frac{\beta}{\xi_{i,0}}\right).\tag{3.23}$$

The total freezing time can then be obtained by setting $\xi_i=1=\xi_{i,0}$

$$\tau_\ell(\xi_{i,0}=1)=\frac{\rho\alpha}{4k\theta_b}\left(1-\beta^2+2\ln\beta\right).\tag{3.24}$$

Consequently, the interface motion ξ_i and frozen temperature θ_s are obtained in this outer solution.

3.2.4 Computation of analytical solution

To compute temperature profile of the ground (i.e., consisting both frozen and unfrozen phases), the eigenvalues λ_n and corresponding coefficients C_n in Eqn. (3.15) are firstly obtained. Particularly, a FOR loop can be used by guessing λ_n with a fine precision (e.g., 10^{-4}). If any neighboring guess value changes its sign, it will be recorded as an eigenvalue. The number of terms of eigenvalues n depends, but it must be checked if computing N number of terms where $N > n$ still gives the same unfrozen phase solution. In this case, 50 eigenvalues were used and it had been confirmed that the solution remained the same when 100 eigenvalues were computed. On the other hand, the undetermined coefficients are solved by numerical quadrature with a relative tolerance of 10^{-14}. Since the eigenvalues and their coefficients depend on β only, they can be stored for future use, rather than computing them for each scenario (e.g., Locations I, II, III, IV in Section 3.4).

The frozen phase solution is then solved by Eqn. (3.22) from the outer expansion. In AGF, the temperature profile over time at a fixed location is often desired to examine the energy consumption, temperature distribution or other practical analysis. Consequently, the interface solution can be utilized to determine whether the unfrozen or frozen temperature is used. The interface solution given by Eqn. (3.23) is in an implicit form, where time is a function of interface location. Since the range of dimensionless interface location is between β and 1, corresponding time from this range can be computed. For each time step, the temperature is calculated from the unfrozen phase if the examined location is smaller than interface (i.e., the ground is not frozen yet). Otherwise, the frozen phase temperature will be used.

3.3 Numerical modeling

A numerical model that discretizes and solves the energy equation has been developed to verify the accuracy of the analytical solution. Energy flow within the computational domain in the cylindrical coordinates is governed by heat conduction

$$\frac{\partial H}{\partial t} = \frac{1}{r}\frac{\partial}{\partial r}\left(k\frac{\partial T}{\partial r}\right), \tag{3.25}$$

where H is the enthalpy [J/m^3]. The enthalpy represents the total energy of fluid, which can be linearized by the following function [14]:

$$H = \begin{cases} \rho_s c_{p,s}(T - T_{\text{solidus}}) & , \ T < T_{\text{solidus}} \\ \overline{\rho c_p}(T - T_{\text{solidus}}) + \gamma \rho_\ell L & , \ T_{\text{solidus}} \leq T \leq T_{\text{liquidus}} \\ \rho_\ell c_{p,\ell}(T - T_{\text{liquidus}}) + \overline{\rho c_p}\Delta T_{\text{mushy}} + \rho_\ell L & , \ T > T_{\text{liquidus}}, \end{cases} \tag{3.26}$$

where T_{solidus} and T_{liquidus} are the solidus and liquidus temperatures [K], respectively. ΔT_{mushy} is defined as the temperature difference of the mushy zone, i.e., $\Delta T_{\text{mushy}} = T_{\text{liquidus}} - T_{\text{solidus}}$. $\overline{\rho c_p}$ is the average properties for the product of mass density and specific heat defined as $(\rho_s c_{p,s} + \rho_\ell c_{p,\ell})/2$. γ is the liquid fraction which can be obtained from a piecewise function based on the liquidus and solidus temperatures

$$\gamma = \begin{cases} 0 & , \ T < T_{\text{solidus}}; \\ \frac{T - T_{\text{solidus}}}{\Delta T_{\text{mushy}}} & , \ T_{\text{solidus}} \leq T \leq T_{\text{liquidus}}; \\ 1 & , \ T > T_{\text{liquidus}}. \end{cases} \tag{3.27}$$

Further, the initial and boundary conditions are consistent with the analytical model in Section 3.2.1. Volume-averaged thermophysical properties for frozen and unfrozen phases are also used as shown in Section 3.2.2.

The temporal and spatial terms of the energy equation, presented in Eqn. (3.25), has been discretized using first and second order schemes, respectively. The discretized point form equation can be written as

$$d_i(H_i^j - H_i^{\text{old}}) = c_{i-1}T_{i-1}^j + c_iT_i^j + c_{i+1}T_{i+1}^j, \tag{3.28}$$

where the subscript i and superscript j represent the i-th node and the j-th iteration. The symbols c and d are the coefficients of discretized equation. A robust and efficient linearized enthalpy algorithm, developed by Swaminathan and Voller [32], is adapted to solve for the temperature field. The main idea behind this algorithm is to linearize the energy equation by using a truncated Taylor series to express H_i^j as a function of T_i^j as

$$H_i^j = H_i^{j-1} + \left(\frac{\partial H}{\partial T}\right)_i^{j-1}(T_i^j - T_i^{j-1}), \tag{3.29}$$

where $\partial H/\partial T$ is the slope of Eqn. (3.26) calculated using the second-order accurate finite-difference method. The linearized system of equation can now be obtained by substituting the enthalpy expression in Eqn. (3.29) into Eqn. (3.26) as

$$d_i\left[H_i^{j-1} + \left(\frac{\partial H}{\partial T}\right)_i^{j-1}(T_i^j - T_i^{j-1}) - H_i^{\text{old}}\right] = c_{i-1}T_{i-1}^j + c_iT_i^j + c_{i+1}T_{i+1}^j, \tag{3.30}$$

where the terms T_i^{j-1} and H_i^{j-1} are known from the previous iteration level. According to the above equations, the iterative scheme is given as follows:

1. In the first iteration, the enthalpy and temperature fields are assumed to be equal to the enthalpy and temperature fields of the previous time step;
2. $\partial H/\partial T$ and corresponding coefficients in Eqn. (3.30) are evaluated;
3. The temperature field in Eqn. (3.30) is solved implicitly using the LU decomposition method;
4. The enthalpy field is updated according to Eqn. (3.26); and

5. Repeat Steps 2-4 until convergence is achieved. The convergence criterion is met when the maximum difference of the temperature fields of two successive iterations drop to below 10^{-5} [°C]. This implies that the temperature field is consistent with the enthalpy fields.

This numerical scheme has been firstly verified with a commercial solver, ANSYS Fluent 2019R3, which has been validated against a laboratory-scale experiment. Further details on this laboratory-scale experiment can be found in the paper [45].

3.4 Model verification

As mentioned in the previous section, a numerical model was built via MATLAB software program to verify the newly developed analytical model. This numerical model implemented the linearized enthalpy algorithm to solve the energy equation. Since the enthalpy method considered the freezing interface as a mushy zone, the mushy-zone width (i.e., the temperature difference ΔT_{mushy}) was minimized to facilitate the verification of the analytical framework based on a sharp interface. In other words, as the mushy-zone width is greatly minimized, the mushy zone in the enthalpy method acts as a sharp interface in the Stefan problem. In addition, the volume averaged properties were taken as input in both numerical and analytical model to represent the porous ground.

Figure 3.2 shows temperature profiles to compare the numerical results with analytical solution at a laboratory scale that has been used in [45]. To ensure this verification, transient temperature distribution at four equally spaced locations throughout the domain are shown in subplot. At this laboratory scale, the spatial dimensions are chosen to be 21.126 [inch]-diameter ground with 1.25 [inch]-diameter freezing pipe, i.e., $a = 0.2683$ [m] and $b = 0.0159$ [m]. Further, ground temperature is initially set to be 20 [°C], while the coolant temperature remains at -20 [°C]. Thermophysical properties are volume averaged by 40% porosity as listed in Table 3.1.

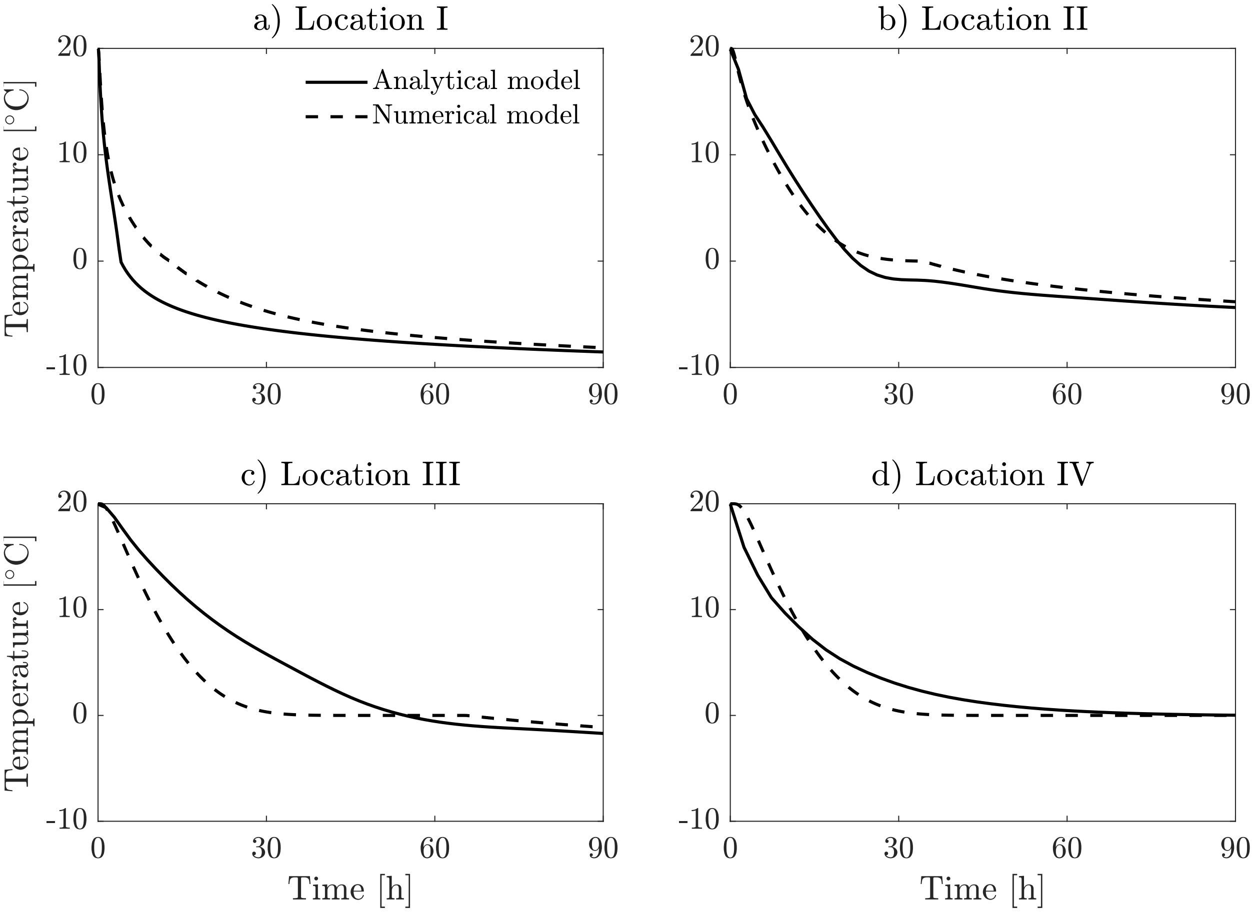

Figure 3.2: Comparisons of numerical model versus presented analytical model in terms of temperature profiles at four equally spaced locations: a) Location I is the first quarter over the domain, i.e., $r = b+0.25(a-b)$; b) Location II is the second quarter, i.e., $r = b+0.5(a-b)$; c) Location III is the third quarter, i.e., $r = b + 0.75(a - b)$; and d) Location IV is the outer surface, i.e., $r = a$.

It is rather clear that the analytical solution captures the initial ground temperature and has a strong agreement with the numerical model at a longer time scale. This longer time scale is fairly essential in practical applications to estimate the thickness and temperature of frozen body. In other words, this verification indicates that both subcooling and freezing stages can be predicted over the entire domain in the presented analytical model with much lesser computational cost. The analytical temperature profiles at the freezing stage are generally underestimated. This is mainly because the small Stefan number assumption used in the singular perturbation method leads to a quasi-steady approximation, which slightly overestimates the solid-liquid interface. This overestimation of the interface reflects a lower

Table 3.2: Design parameters for effects of coolant temperature and ground porosity.

Coolant Temperature	Ground Porosity
-10 [°C]	20%
-20 [°C]	40%
-30 [°C]	100%

temperature profile after the fusion temperature, which in turn gives an overall error of 11.03% on average. In typical civil/mining application of AGF, the growth of frozen body is usually around 2 [m] in thickness from the freeze pipe (i.e., $r_i = 2$ [m]). This indicates that Locations I and II are in the range of interest at a laboratory scale, which has a much lesser average error of 5.56% and such error is more than sufficient for the practical application of AGF.

3.5 Results and discussion

Followed by the verification of analytical model, a few practical parameters were investigated in the concept of AGF. These parameters were often site-dependent and essential to the thermal design and operation of AGF. For a more practical demonstration, a field-scale dimension is used and consequently the freezing time will be much longer than the one in previous section, where a laboratory scale was examined for verification purposes.

3.5.1 Effect of coolant temperature

Coolant temperature is an imposed boundary contributed to the outward freezing process in AGF. Therefore, it is essential to investigate this parameter in different values corresponded to practical scenarios. As explained previously, the mathematical formulations of the coolant temperature, T_b, is the inner boundary condition. In AGF, the coolant temperature often varies from -10 to -30 [°C] depending on specific sites while the ground temperature can be assumed to be 10 [°C] on average in Canada. Consequently, three cases were examined based on the ranges: i) $T_b = -10$ [°C], ii) $T_b = -20$ [°C], and iii) $T_b = -30$ [°C], as $T_{\text{init}} = 10$ [°C].

Figure 3.3 shows temperature distributions for three coolant temperatures; field-scale dimensions of AGF are used. The freezing pipe diameter is 0.127 [m] (equivalent to 5 [inch]) and outer diameter is 100 [m], i.e., $b = 0.0635$ [m] and $a = 5$ [m]. This 0.127-meter-diameter pipe can be set up of brine freezing pipes and the 100-meter-diameter outer boundary can be reasonably assumed to have no heat flux. Additionally, the temperature profile is recorded at a distance of 1 meter away from the pipe center. As can be observed in the figure, the initial ground temperature is well captured in the presented analytical model, in particular the inner solution. This initial temperature is often referred as unfrozen state above the fusion temperature in AGF applications. Since the inner expansion sketches the time scale to satisfy the initial condition, the unfrozen temperature profile can be characterized. Therefore, this developed analytical solution serves classical two-phase Stefan problems, rather than one-phase problems where no unfrozen or liquid state exists.

As for the frozen temperature distributions, it can be seen from Figure 3.3 that a quasi-steady temperature is reached after 600 days in all cases of coolant temperatures. According to the variation on temperature intervals, the quasi-steady temperature is found to be higher when the coolant temperature increases. That is, the quasi-steady temperature for $T_b = -10$ [°C] is higher than the ones for $T_b = -20$ [°C] and $T_b = -30$ [°C]. The temperature interval can also be a good indicator of the energy required to freeze the ground, also called freezing demand. It is therefore concluded that as the quasi-steady temperature increases, the coolant temperature also rises, which leads to a lower freezing demand and less energy consumption and cost.

3.5.2 Effect of ground porosity

Another study is to explore the effect of ground porosity in AGF since ground porosity is a site-dependent parameter. The ground in AGF is intrinsically porous and the pore size lies within a fairly large range. Such large range of porosity can be determined by soil texture,

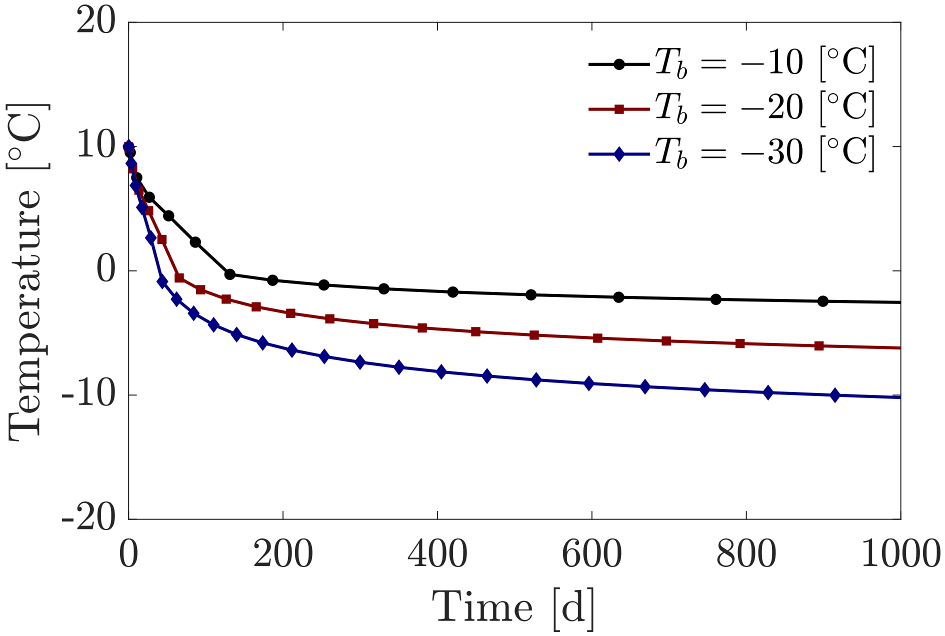

Figure 3.3: Comparisons of three different coolant temperatures: $T_b = -10$ [°C] in black, $T_b = -20$ [°C] in red, and $T_b = -30$ [°C] in blue.

like the percentages of sand or silt or clay. In the context of analytical modeling, volume-averaging method is applied by assuming local thermal equilibrium in the porous structure. That is, the local temperature difference between the frozen and unfrozen phases is negligible compared with the difference at the pore level. Specifically, the thermophysical properties are recalculated from ground porosity as mentioned in Section 3.2.2. This ground porosity in AGF lies from 20% to 40% in practice.

Figure 3.4 illustrates the effect of porosities and corresponding temperature distributions are plotted. Particularly, three ground porosities were used in the analytical model: $\varepsilon = 20\%$, $\varepsilon = 40\%$ and $\varepsilon = 100\%$. Spatial dimensions and the point of evaluation are based on a typical field scale consistent with the previous subsection. The initial ground temperature and coolant temperatures are set to be 20 [°C] and -20 [°C], respectively. It is rather clear to see that the temperature profile has a positive proportionality to the ground porosity, which means that the overall temperature increases with porosity. This is because the thermal diffusivity of unfrozen phase reduces from 1.09×10^{-6} to 1.38×10^{-7} [m^2/s] when the porosity increases. Recall that the thermal diffusivity measures the rate of heat transfer and bundles

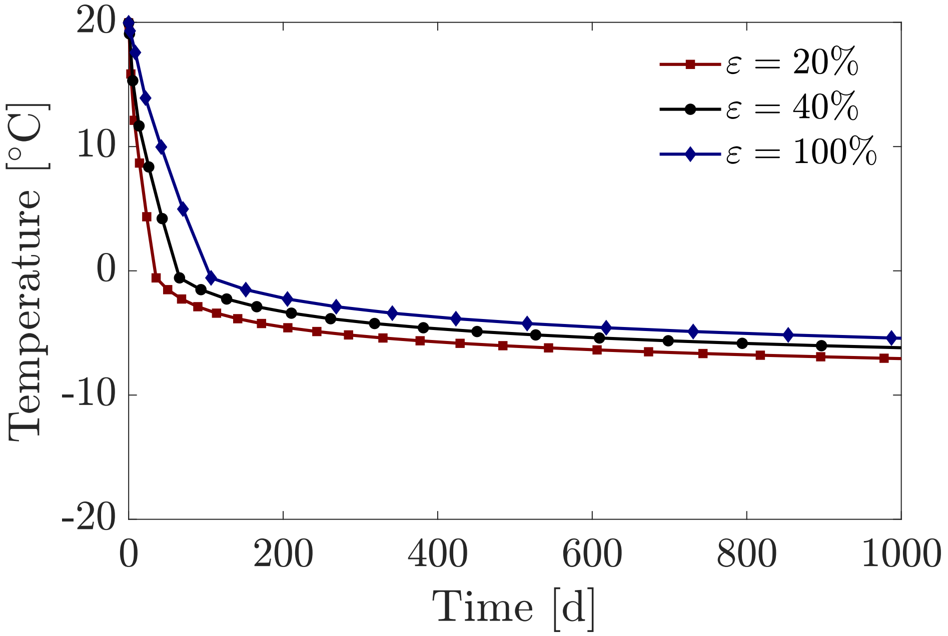

Figure 3.4: Comparisons of three different ground porosities: $\varepsilon = 20\%$ in red, $\varepsilon = 40\%$ in black, and $\varepsilon = 100\%$ in blue.

the mass density, specific heat and thermal conductivity since all of them have changed after volume averaging. Consequently, it can be explained that the heat conducts faster in the high-porosity ground than low-porosity ground. It is also worthwhile to mention that the temperature profile becomes more parabolic as the ground porosity decreases. In other words, the temperature profile at a low ground porosity offers similar behaviour to the one without latent heat or phase change. This parabolic behaviour implies that the latent heat of fusion has been proportionally reduced by the porosity and a very low value of latent heat gives fairly similar results to heat conduction only. That is, the phase change phenomenon is not conspicuous.

3.6 Conclusions

A singular perturbation solution for a two-phase Stefan problem was developed in the context of examining thermal performance of AGF. This problem described an outward solidification process through porous media in a finite annular space. Physical scaling parameters and volume averaging method were also used. Small Stefan number, which naturally appears in porous media, was assumed to serve the singular perturbation analysis. Singular perturbation theory was applied to split this two-phase Stefan problem into two distinct temporal scales: a transient heat conduction for the unfrozen phase and a one-phase Stefan problem to obtain the frozen phase and interface solutions. This analytical solution agrees fairly well with the numerical results in terms of the temperature profile for both phases yet with much lesser computational cost.

Nomenclature

Letters

a	Outer radius [m]
b	Inner radius [m]
c_p	Specific heat [J/(kg·K)]
Fo	Fourier number
H	Enthalpy [J/m^3]
k	Thermal conductivity [W/(m·K)]
L	Latent heat of fusion [J/kg]
r	Radial coordinate [m]
r_i	Interface location [m]
Ste	Stefan number
T	Temperature [K]
T_b	Coolant temperature [K]
T_f	Fusion temperature [K]
T_{init}	Initial temperature [K]
ΔT_{mushy}	Mushy-zone temperature difference [K]
t	Time [s]
t_c	Critical freezing time [s]

Greek symbols

α	Thermal diffusivity [m^2/s]
β	Ratio of inner over outer radii
γ	Liquid fraction
ε	Porosity
θ	Dimensionless temperature
λ	Eigenvalues
ξ	Dimensionless radial coordinate
ξ_i	Dimensionless interface location
ρ	Mass density [kg/m^3]
τ	Dimensionless time

Superscripts and subscripts

$\bar{\ }$	Average value of frozen and unfrozen phases
$\tilde{\ }$	Newly scaled variable
$_e$	Effective (volume-averaged) property
$_\ell$	Unfrozen phase
$_{\text{liquidus}}$	Liquidus state
$_{\text{mushy}}$	Mushy zone
$_s$	Frozen phase
$_{\text{sand}}$	Sand particle

solidus	Solidus state
void	Void space

Bibliography

[1] V. Alexiades. *Mathematical modeling of melting and freezing processes.* CRC Press, 1992.

[2] M. A. Alzoubi, A. Madiseh, F. P. Hassani, and A. P. Sasmito. Heat transfer analysis in artificial ground freezing under high seepage: Validation and heatlines visualization. *International Journal of Thermal Sciences*, 139:232–245, 2019.

[3] M. A. Alzoubi, A. Nie-Rouquette, S. A. Ghoreishi-Madiseh, F. P. Hassani, and A. P. Sasmito. On the concept of the freezing-on-demand (FoD) in artificial ground freezing for long-term applications. *International Journal of Heat and Mass Transfer*, 143:118557, 2019.

[4] M. A. Alzoubi, A. Nie-Rouquette, and A. P. Sasmito. Conjugate heat transfer in artificial ground freezing using enthalpy-porosity method: Experiments and model validation. *International Journal of Heat and Mass Transfer*, 126:740–752, 2018.

[5] M. A. Alzoubi, A. Zueter, A. Nie-Rouquette, and A. P. Sasmito. Freezing on demand: A new concept for mine safety and energy savings in wet underground mines. *International Journal of Mining Science and Technology*, 29(4):621–627, 2019.

[6] J. Bollati and D. A. Tarzia. Exact solution for a two-phase Stefan problem with variable latent heat and a convective boundary condition at the fixed face. *Zeitschrift für Angewandte Mathematik und Physik*, 69(2):38, 2018.

[7] F. Brosa Planella, C. P. Please, and R. A. Van Gorder. Instability in the self-similar motion of a planar solidification front. *IMA Journal of Applied Mathematics*, 83(1):106–130, 2018.

[8] F. Brosa Planella, C. P. Please, and R. A. Van Gorder. Extended Stefan problem for solidification of binary alloys in a finite planar domain. *SIAM Journal on Applied Mathematics*, 79(3):876–913, 2019.

[9] F. Brosa Planella, C. P. Please, and R. A. Van Gorder. Extended Stefan problem for the solidification of binary alloys in a sphere. *European Journal of Applied Mathematics*, page 1–38, 2020.

[10] J. Caldwell and Y. Kwan. On the perturbation method for the Stefan problem with time-dependent boundary conditions. *International Journal of Heat and Mass Transfer*, 46(8):1497–1501, 2003.

[11] H. S. Carslaw and J. C. Jaeger. Conduction of heat in solids. *Oxford: Clarendon Press, 1959, 2nd ed.*, 1959.

[12] D. S. de Oliveira and F. B. Ribeiro. Heat conduction equation solution in the presence of a change of state in a bounded axisymmetric cylindrical domain. *ASME Journal of Heat Transfer*, 133(6), 2011.

[13] D. A. Edwards and M. E. Mackay. Postextrusion heating in three-dimensional printing. *ASME Journal of Heat Transfer*, 142(5), 2020.

[14] M. Faden, A. König-Haagen, and D. Brüggemann. An optimum enthalpy approach for melting and solidification with volume change. *Energies*, 12(5):868, 2019.

[15] L. Fan and J. Khodadadi. A theoretical and experimental investigation of unidirectional freezing of nanoparticle-enhanced phase change materials. *ASME Journal of Heat Transfer*, 134(9), 2012.

[16] D. L. Feltham and J. Garside. Analytical and numerical solutions describing the inward solidification of a binary melt. *Chemical Engineering Science*, 56(7):2357–2370, 2001.

[17] T. R. Goodman. The heat balance integral and its application to problems involving change of phase. *ASME Journal of Heat Transfer*, 80:335, 1958.

[18] J. M. Hill. *One-dimensional Stefan problems: An introduction.* Longman Scientific & Technical, 1987.

[19] L. M. Jiji and S. Weinbaum. Perturbation solutions for melting or freezing in annular regions initially not at the fusion temperature. *International Journal of Heat and Mass Transfer*, 21(5):581–592, 1978.

[20] M. Kaviany. *Principles of heat transfer in porous media.* Springer Science & Business Media, 2012.

[21] A. Kucera and J. M. Hill. On inward solidifying cylinders and spheres initially not at their fusion temperature. *International Journal of Non-linear Mechanics*, 21(1):73–82, 1986.

[22] S. W. McCue, B. Wu, and J. M. Hill. Classical two-phase Stefan problem for spheres. *Proceedings of the Royal Society A: Mathematical, Physical and Engineering Sciences*, 464(2096):2055–2076, 2008.

[23] M. Parhizi and A. Jain. Analytical modeling and optimization of phase change thermal management of a Li-ion battery pack. *Applied Thermal Engineering*, 148:229–237, 2019.

[24] M. Parhizi and A. Jain. Solution of the phase change stefan problem with time-dependent heat flux using perturbation method. *Journal of Heat Transfer*, 141(2):024503, 2019.

[25] E. Pimentel, A. Sres, and G. Anagnostou. Large-scale laboratory tests on artificial ground freezing under seepage-flow conditions. *Geotechnique*, 62(3):227, 2012.

[26] M. Prud'Homme, T. H. Nguyen, and D. L. Nguyen. A heat transfer analysis for solidification of slabs, cylinders, and spheres. *ASME Journal of Heat Transfer*, 111(3):699–705, 1989.

[27] H. Ribera, T. G. Myers, and M. M. MacDevette. Optimising the heat balance integral method in spherical and cylindrical Stefan problems. *Applied Mathematics and Computation*, 354:216–231, 2019.

[28] B. Rubinsky and A. Shitzer. Analysis of a Stefan-like problem in a biological tissue around a cryosurgical probe. *ASME Journal of Heat Transfer*, 98(3):514–519, 1976.

[29] H. Shabgard, W. Zhu, and A. Faghri. Integral solution of two-region solid–liquid phase change in annular geometries and application to phase change materials–air heat exchangers. *Energies*, 12(23):4474, 2019.

[30] A. Shitzer. Cryosurgery: Analysis and experimentation of cryoprobes in phase changing media. *ASME Journal of Heat Transfer*, 133(1):011005, 2011.

[31] D. R. Smith. *Singular-perturbation theory: An introduction with applications.* Cambridge University Press, 1985.

[32] C. Swaminathan and V. R. Voller. A general enthalpy method for modeling solidification processes. *Metallurgical Transactions B*, 23(5):651–664, 1992.

[33] H. Tounsi, A. Rouabhi, and E. Jahangir. Thermo-hydro-mechanical modeling of artificial ground freezing taking into account the salinity of the saturating fluid. *Computers and Geotechnics*, 119:103382, 2020.

[34] H. Tounsi, A. Rouabhi, M. Tijani, and F. Guérin. Thermo-hydro-mechanical modeling of artificial ground freezing: application in mining engineering. *Rock Mechanics and Rock Engineering*, 52(10):3889–3907, 2019.

[35] M. Vitel, A. Rouabhi, M. Tijani, and F. Guérin. Thermo-hydraulic modeling of artificial ground freezing: Application to an underground mine in fractured sandstone. *Computers and Geotechnics*, 75:80–92, 2016.

[36] V. R. Voller. An exact solution of a limit case Stefan problem governed by a fractional diffusion equation. *International Journal of Heat and Mass Transfer*, 53(23-24):5622–5625, 2010.

[37] V. R. Voller, J. B. Swenson, and C. Paola. An analytical solution for a Stefan problem with variable latent heat. *International Journal of Heat and Mass Transfer*, 47(24):5387–5390, 2004.

[38] S. Weinbaum and L. Jiji. Singular perturbation theory for melting or freezing in finite domains initially not at the fusion temperature. *Journal of Applied Mechanics*, 44(1):25–30, 1977.

[39] S. Whitaker. Flow in porous media I: A theoretical derivation of Darcy's law. *Transport in Porous Media*, 1(1):3–25, 1986.

[40] A. S. Wood. A new look at the heat balance integral method. *Applied Mathematical Modelling*, 25(10):815–824, 2001.

[41] B. Wu, S. W. McCue, P. Tillman, and J. M. Hill. Single phase limit for melting nanoparticles. *Applied Mathematical Modelling*, 33(5):2349–2367, 2009.

[42] M. Ye, G. Hu, F. Guo, W. Huang, Z. Wang, X. Zhao, and Y. Li. A novel semi-analytical solution for calculating the temperature distribution of the lithium-ion batteries during nail penetration based on Green's function method. *Applied Thermal Engineering*, page 115129, 2020.

[43] Y. Zhou, X.-Y. Shi, and G.-Q. Zhou. Exact solution for a two-phase Stefan problem with power-type latent heat. *Journal of Engineering Mathematics*, 110(1):1–13, 2018.

[44] Y. Zhou, Y.-J. Wang, and W.-K. Bu. Exact solution for a Stefan problem with latent heat a power function of position. *International Journal of Heat and Mass Transfer*, 69:451–454, 2014.

[45] A. Zueter, A. Nie-Rouquette, M. A. Alzoubi, and A. P. Sasmito. Thermal and hydraulic analysis of selective artificial ground freezing using air insulation: Experiment and modeling. *Computers and Geotechnics*, 120:103416, 2020.

Chapter 4

Asymptotic analysis of a two-phase Stefan problem in annulus: Application to outward solidification in phase change materials

Contents

Preface (Bridging Text)

Conventional artificial ground freezing (AGF) circulates a heat transfer fluid as a refrigerant, such as brine, in a closed loop, which requires a mechanical refrigeration plant to cool down the fluid. The refrigeration plant is often energy-intensive and associated with a large amount of carbon footprints. A more environmentally friendly alternative is to utilize passive heat exchangers like thermosiphons and transfer heat between the cold air above the surface and the ground. In Canada, thermosiphons have been implemented in the Giant Mine, a gold mine located in the Northwest Territories, for remediation purposes.

A major drawback of thermosiphons is their diminishing efficiency during warm seasons when the air is not cold enough, especially when there is relatively low wind speed. As a result, thermal energy storage units, such as phase change materials (PCMs), are in high demand to store cold energy during winter and supply it to thermosiphons in summer without using mechanical plants that could harm the environment. PCMs are particularly effective and inexpensive in northern climates, where abundant cold energy can be extracted during the winter.

In the previous chapter, a singular perturbation solution was derived for a two-phase Stefan problem in a hollow cylinder, capturing phenomena across two temporal scales and a two-stage freezing process. The solution successfully and efficiently predicts the cooling of liquid and equilibrium freezing for macro-scale solidification in porous media, which is particularly applicable to AGF. It is noted that macro-scale solidification possesses a third stage that describes the cooling of solids. The third stage may not be of special interest in AGF, as the total freezing time, i.e., the end of equilibrium freezing, is sufficient in practice. However, it is important to predict the entire freezing cycle or charging cycle for PCM energy storage, which fundamentally involves multiple temporal and spatial scales.

In this chapter, we investigated the development of analytical solutions to two-phase Stefan problems by utilizing systematic asymptotic analysis, aiming to simulate all three solidification stages and enhance spatiotemporal resolution for the application of cold thermal energy storage with phase change materials (PCMs). A thorough scaling analysis was conducted to characterize three temporal and four spatial scales and subsequently solve them. Furthermore, an application to outward solidification in PCMs was highlighted by examining the impact of geometric ratios, thermophysical properties, and Stefan numbers. The insights and discussions presented in this chapter were published in the peer-reviewed journal article listed below.

M. Xu, S. Akhtar, A. F. Zueter, M. A. Alzoubi, L. Sushama, and A. P. Sasmito. Asymptotic analysis of a two-phase Stefan problem in annulus: Application to outward solidification in phase change materials. *Applied Mathematics and Computation*, 408:126343, 2021.

Abstract

Stefan problems provide one of the most fundamental frameworks to capture phase change processes. The problem in cylindrical coordinates can model outward solidification, which ensures the thermal design and operation associated with phase change materials (PCMs). However, this moving boundary problem is highly nonlinear in most circumstances. Exact solutions are restricted to certain domains and boundary conditions. It is therefore vital to develop approximate analytical solutions based on physically tangible assumptions, e.g., a small Stefan number. A great amount of work has been done in one-phase Stefan problems, where the initial state is at its fusion temperature, yet very few literature has considered two-phase problems particularly in cylindrical coordinates. This paper conducts an asymptotic analysis for a two-phase Stefan problem for outward solidification in a hollow cylinder, consisting of three temporal and four spatial scales. The results are compared with the enthalpy method that simulates a mushy region between two phases by numerical iterations, rather than a sharp interface in Stefan problems. After studying both mathematical models, the role of mushy-zone thickness in the enthalpy method is also unveiled. Moreover, a wide range of geometric ratios, thermophysical properties and Stefan numbers are selected from the literature to explore their effects on the developed model with regards to interface motion and temperature profile. It can be concluded that the asymptotic solution is capable of tracking the moving interface and evaluating the transient temperature for various geometric ratios and thermophysical properties in PCMs. The accuracy of this solution is found to be affected by Stefan number only, and the computational cost is much less compared with the enthalpy method and other numerical schemes.

Keywords: Phase change, two-phase Stefan problems, outward solidification, analytical solution, asymptotic analysis, phase change material (PCM)

4.1 Introduction

Outward solidification in a long hollow cylinder or an annular geometry have various applications in ground freezing [6, 67, 8], permafrost stabilization by thermosyphons [65, 24, 64], and phase change materials (PCMs) in thermal and cold energy storage [4, 44, 52]. It is therefore essential to explore mathematical models to describe such phase change process. There has been a great amount of mathematical frameworks for phase change in the literature, such as Stefan problems [28, 25], enthalpy method [56, 57], volume of fluid method [35, 60], level set method [45, 34], and phase field method [49, 17]. A recent review of all these models can be found in [29]. Stefan problems are among the only formulation that can be treated analytically, whereas other frameworks are mostly solved by numerical iterations associated with relatively high computational time and power. Stefan problems are considered as a front-tracking formulation that models the solid-liquid interface by an energy balance equation, also known as Stefan condition. Since the Stefan condition has high nonlinearity, exact solutions are limited to semi-infinite domains subjected to particular boundary conditions [15, 26], which gives the driving force to develop approximate analytical solutions.

One of the approximate analytical methods for solving Stefan problems is the heat balance integral method (HBIM). The main thrust of this method is to introduce an approximate function (often a polynomial) as the temperature profile and integrate the governing partial differential equation over a suitable interval. As a result, the partial differential equation is reduced to an ordinary differential equation which may often be solved analytically. The HBIM was firstly developed by Goodman [23] and then summarized in many texts [28, 25, 15]. Many modifications of the HBIM have also been studied extensively in the modern literature to improve its accuracy of approximation, such as the refined integral method (RIM) [41, 9, 50] and combined integral method (CIM) [39, 42]. Mitchell and Myers [40] made a comprehensive comparison between the standard HBIM and RIM for solving one-dimensional Stefan problems subjected to different boundary conditions.

Another approximate analytical method is the use of asymptotic analysis to obtain an asymptotic or perturbation solution. In asymptotic analysis, a small perturbation parameter (often the Stefan number defined by the ratio of sensible heat over latent heat) is used to expand into a power series, namely a perturbation series solution or an asymptotic solution. The vast majority of studies have been focused on one-phase Stefan problems, where the initial temperature is assumed to be at fusion temperature. Pedroso and Domoto [47] introduced a perturbation solution to a one-phase Stefan problem for inward spherical solidification. Later, perturbations solutions for other coordinates and solidification directions [51, 53] as well as convective and radiative boundary conditions [46, 55] were also studied. A systematic derivation and review of these perturbation solutions in one-dimensional one-phase Stefan problems can be found in Hill's text [28]; a few two-dimensional Stefan problems have also been investigated through asymptotic analysis in spite of their geometrical complexity [58, 36]. Meanwhile, the framework of asymptotic analysis has recently been extended to a number of Stefan problems with non-Fourier heat conduction [21, 13, 27, 14].

Much less time has been spent on two-phase Stefan problems, where the initial temperature is not at fusion temperature. In modern literature, the two-phase Stefan problems are often further categorized into classical and extended two-phase Stefan problems. The classical two-phase Stefan problem relaxes the assumption of initial fusion temperature in one-phase problems, and thus the liquid phase has to be considered. On the other hand, extended two-phase problems incorporate constitutional supercooling, which in return consists of heat and mass transport phenomena. This framework is particularly applicable for solidification of binary alloys. For the classical two-phase Stefan problems, Weinbaum and Jiji [59] applied the singular perturbation theory (specifically, two temporal scales) along with the boundary-fixing technique in a finite slab. Same analytical approach has been used for inward spherical solidification [1] as well as inward [30] and outward [62, 63] cylindrical solidification. McCue et al. [37] established four temporal scales and defined the asymptotic limits of both small time and slow thermal diffusion around a small Stefan number. In contrast, a large Lewis number (defined by the ratio of thermal diffusivity over mass diffusivity) is usually assumed in extended two-phase Stefan problems. Feltham and Garside [19] developed asymptotic and numerical solutions to an extended Stefan problem after using the boundary-fixing technique for inward solidification of a binary melt. Brosa Planella et al. [10] recently introduced four temporal and ten spatial scales in their asymptotic analysis for an extended Stefan problem in a finite planar geometry, and then further studied the same problem in the spherical coordinates [11]. The moving boundary in Stefan problems had also been modified by incorporating the Gibbs-Thomson relation to study the phase change behaviors of nanoparticles [38, 61, 22, 20]. While the asymptotic solutions are revealed, some numerical schemes on Stefan problems have been explored in recent literature [32, 33]. Further, approximation of modified error function is also proved to be effective in Stefan problems with temperature-dependent thermal conductivity [16].

A recent work by Khalid et al. [31] applied the separation of variables and eigenfunction expansion method to solve a two-phase Stefan problem in cylindrical domains. Nonetheless, the method of eigenfunction expansion used in their analysis could yield imaginary eigenvalues; specific heat was assumed to be the same in solid and liquid phases; and the results were verified at a relatively low time resolution. Asymptotic solutions, on the other hand, are more reliable in terms of producing real and stable series solutions to Stefan problems. Another solution to such cylindrical two-phase Stefan problem was lately established from our previous work by using singular perturbation theory for artificial ground freezing [63]. This framework expanded two leading-order perturbation series around a small Stefan number from two distinct temporal scales, thus characterizing the subcooling and freezing stages of solidification. However, spatial variables were not scaled and the third temporal regime was not well captured because of its methodology. These deficiencies omitted a few physical aspects of solidification: i) thermal contribution of solid phase during subcooling; ii) sensible heat at equilibrium freezing; and iii) cooling stage after the domain is completed frozen.

To date, asymptotic analysis with multiple spatial and temporal scales have been developed in the Cartesian [10] and spherical [37, 11] domains, yet none of such asymptotic analysis has been conducted in the cylindrical coordinates. As a result, the aim of this study is to develop an accurate asymptotic solution to a two-phase Stefan problem based on multiple scales, particularly four spatial and three temporal scales, with phase-dependent thermophysical properties (e.g., thermal conductivity, specific heat, and thermal diffusivity). Comparisons between the presented solution and numerical results by enthalpy method are made: i) to verify the asymptotic solution; and ii) to investigate the role of mushy zone thicknesses regarding the interface motion, temperature profile, and total freezing time. Moreover, a broad range of geometric ratios and thermophysical properties in PCMs are chosen to explore their effects and ensure the accuracy of asymptotic solutions against numerical data.

The outline of this paper is as follows. In Section 4.2, we formulate a two-phase Stefan problem which models outward solidification for PCMs in cylindrical coordinates. Then, the problem is solved by asymptotic analysis in Section 4.3, where three temporal (regimes) and four spatial (layers) scales are considered. In Section 4.4, the enthalpy method is applied to solve the phase change problem numerically by introducing a mushy region between two phases. Section 4.5 verifies the developed asymptotic solution against the numerical results. In Section 4.6, effects of geometry, thermophysical properties and Stefan numbers in the asymptotic solution are then investigated along with corresponding numerical results. Lastly, the main findings of this study are summarized in Section 4.7.

4.2 Mathematical model

4.2.1 Formulation

In this mathematical framework, a few assumptions will be made: i) The solidification process is assumed to occur at the macroscale level, i.e., nucleation and recalescence are not present; ii) Thermophysical properties in each phase are uniform and remain constant; iii) Mass densities are prescribed to be equal in both phases implying that volume changes are negligible. This is justified since the inner and outer radial surfaces are mostly fixed by walls in PCM applications; iv) Effect of natural convection is ignored, because the Richardson number is much less than 1 for most freezing problems; v) The solid-liquid interface is modeled as a sharp line, rather than a mushy zone; and vi) The amount of sensible heat contributed during phase change is much smaller than the one of latent heat, and thus the Stefan number is less than unity.

Consider an annular domain or a long hollow cylinder with inner radius b and outer radius a, as schematically shown in Figure 4.1. The domain is initially at the liquid state of a PCM, and thus the initial temperature T_{init} is higher than the fusion temperature T_f. A constant temperature $T_b < T_f$ on the inner surface $r = b$ is prescribed for time $t \geq 0$. Consequently, the liquid-state PCM starts to solidify from $r = b$ and a solid phase will appear in the domain. An axially symmetric interface, which separates the liquid and solid phases, moves in the positive r-direction and stays at the fusion temperature T_f. Thus far, this analysis can be described as a classical two-phase Stefan problem in the cylindrical coordinates, where

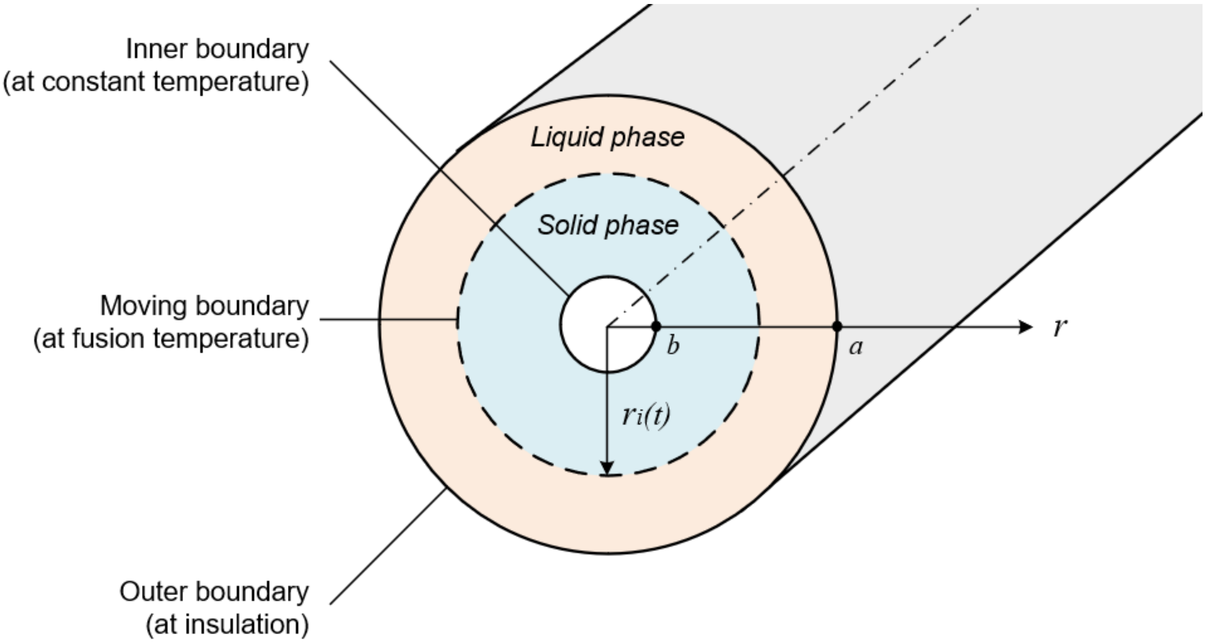

Figure 4.1: Schematic diagram of outward solidification in a PCM, consisting of solid and liquid phases separated by a moving boundary. The solid phase is in light blue, whereas the liquid phase is in light red.

the solidification terminates once the moving interface reaches the outer radius $r_i = a$ in a finite domain.

From a physical point of view, the classical two-phase Stefan problem interprets the subcooling and freezing stages in solidification. However, a third stage, so-called cooling (or solid subcooling), starts right after the interface vanishes, i.e., only the solid phase exists at this stage. As a result, an extension of the classical Stefan formulation needs to be considered, with respect to a new set of boundary and time conditions to capture the cooling stage.

In this paper, a Stefan problem in the cylindrical coordinates is studied to describe multistage cooling and freezing for outward solidification at macroscale. The following heat conduction equations for solid and liquid phases are used as the governing equations of this problem:

$$\frac{\partial T_s}{\partial t} = \alpha_s\left(\frac{\partial^2 T_s}{\partial r^2} + \frac{1}{r}\frac{\partial T_s}{\partial r}\right),\ b < r < r_i(t),\ t > 0; \tag{4.1}$$

$$\frac{\partial T_\ell}{\partial t} = \alpha_\ell\left(\frac{\partial^2 T_\ell}{\partial r^2} + \frac{1}{r}\frac{\partial T_\ell}{\partial r}\right),\ r_i(t) < r < a,\ 0 \le t < t_c, \tag{4.2}$$

where T, α, r, and t are the temperature [K], thermal diffusivity [m^2/s], radial coordinate [m], and time [s], respectively. a and b are the outer and inner radii [m]. The subscripts s and ℓ represent the solid and liquid phases. Additionally, t_c is the critical time when the entire annular domain is solidified [s].

Recall that Stefan problems are categorized as a front-tracking formulation, which involve calculation of the moving front from an energy balance between solid and liquid control volumes. Both sensible and latent heats are taken into account. This expression of the moving front is also known as the Stefan condition:

$$k_s\frac{\partial T_s}{\partial r}\bigg|_{r=r_i(t)} - k_\ell\frac{\partial T_\ell}{\partial r}\bigg|_{r=r_i(t)} = \rho L\frac{\mathrm{d}r_i}{\mathrm{d}t},\ 0 \le t \le t_c, \tag{4.3}$$

where k, ρ, L, and r_i are the thermal conductivity [W/(m·K)], mass density [kg/m^3], latent heat of fusion [J/kg], and solid-liquid interface location [m], respectively. Apart from the moving boundary condition, the fixed boundary conditions are defined as:

$$\begin{aligned} T_s(r=b,t) &= T_b, \\ T_s(r=r_i(t),t) &= T_f, \\ T_\ell(r=r_i(t),t) &= T_f, \\ \frac{\partial T_\ell}{\partial r}\bigg|_{r=a} &= 0, \end{aligned} \tag{4.4}$$

where T_b and T_f are the prescribed temperature [K] at the inner surface and fusion temper-

Table 4.1: Non-dimensional scaling parameters and variables.

Type	Scaling	Expression
Geometry/coordinate	β	b/a
	ξ	r/a
	ξ_i	r_i/a
Thermophysical property	$\widetilde{\alpha}$	α_s/α_ℓ
	$\widetilde{k}$	k_s/k_ℓ
	$\widetilde{c}_p$	$c_{p,s}/c_{p,\ell}$
Temperature	θ_s	$(T_s - T_f)/(T_f - T_b)$
	θ_ℓ	$(T_\ell - T_f)/(T_f - T_b)$
	θ_{init}	$(T_{\text{init}} - T_f)/(T_f - T_b)$
Dimensionless number	Fo	$\alpha_s t/a^2$
	Ste	$c_{p,s}(T_f - T_b)/L$

ature [K]. Lastly, the time conditions are given by:

$$
\begin{aligned}
r_i(t=0) &= b, \\
T_\ell(r, t=0) &= T_{\text{init}}, \\
r_i(t=t_c) &= a, \\
T_s(r, t=t_c) &= f(r).
\end{aligned}
\tag{4.5}
$$

where T_{init} is the initial temperature [K]. $f(r)$ is the temperature distribution [K] at the total freezing time t_c, which provides the initial condition of the cooling stage after freezing. The last time conditions in Eqn. (4.5) are not usually considered in classical Stefan problems; however, they are important constraints that mathematically capture the transition from freezing to solid cooling stage. As for the cooling stage, the formulation will be reduced into a linear finite-extent heat conduction problem from $t_c < t < \infty$.

4.2.2 Scaling analysis

The presented dimensional problem can be non-dimensionalized prior to asymptotic analysis. The scaling parameters and variables are listed and categorized in Table 4.1. Particularly, the geometry and radial coordinates are scaled by the outer radius a such that the entire domain is non-dimensionlized from β to 1. The outer radius is also considered as a characteristic length. The thermophysical properties are scaled as the ratio of solid over liquid phase. Further, the dimensionless temperatures in both phases are defined as:

$$\theta_s = \frac{T_s - T_f}{T_f - T_b}, \qquad \theta_\ell = \frac{T_\ell - T_f}{T_f - T_b}, \qquad \text{and} \qquad \theta_{\text{init}} = \frac{T_{\text{init}} - T_f}{T_f - T_b}. \tag{4.6}$$

All temperature variables are scaled by the solid-based temperature interval, and thus the imposed constant temperature at the inner radius T_b is non-dimensionalized into -1. Here we introduce two dimensionless numbers: Fourier number (Fo) and Stefan number (Ste). The Fourier number is the ratio of thermally diffusive transport rate over heat storage rate, whereas the Stefan number is the ratio of sensible heat over latent heat. It is worthwhile to mention that some research apply the inverse ratio as Stefan number; however, to neglect the contribution of sensible heat by the asymptotic of Ste $\to 0$ makes more physical sense in this work due to its application in PCMs. The dimensionless time will be defined in the following section by either the Fourier number or the combination of Fourier and Stefan numbers to capture different temporal scales. In this study, these two dimensionless numbers are consistent with the temperature scaling which uses the solid-based temperature interval. Before conducting the asymptotic analysis, the dimensional model without any additional spatial and temporal scalings can be expressed as:

$$\frac{\partial \theta_s}{\partial \tau} = \frac{\partial^2 \theta_s}{\partial \xi^2} + \frac{1}{\xi}\frac{\partial \theta_s}{\partial \xi}, \ \beta < \xi < \xi_i; \tag{4.7}$$

$$\frac{\partial \theta_\ell}{\partial \tau} = \frac{1}{\widetilde{\alpha}}\left(\frac{\partial^2 \theta_\ell}{\partial \xi^2} + \frac{1}{\xi}\frac{\partial \theta_\ell}{\partial \xi}\right), \ \xi_i < \xi < 1, \tag{4.8}$$

subject to the moving boundary condition

$$\left.\frac{\partial \theta_s}{\partial \xi}\right|_{\xi=\xi_i} - \frac{1}{\widetilde{k}}\left.\frac{\partial \theta_\ell}{\partial \xi}\right|_{\xi=\xi_i} = \frac{1}{\text{Ste}}\frac{\mathrm{d}\xi_i}{\mathrm{d}\tau}, \tag{4.9}$$

Table 4.2: Summary of asymptotic analysis based on each stage of solidification. Note that the tilde notion (∼) is used when a new scaling variable is introduced.

Stage	Regime	Layer	Variable		
			τ	ξ	ξ_i
Subcooling	I	A	Fo	ξ	$\beta + \mathrm{Ste}^{\frac{1}{2}}\widetilde{\xi}_i$
		B	Fo	$\beta + \mathrm{Ste}^{\frac{1}{2}}\widetilde{\xi}$	$\beta + \mathrm{Ste}^{\frac{1}{2}}\widetilde{\xi}_i$
Freezing	II	C	$\mathrm{Ste}^{-1}\widetilde{\tau}$	ξ	ξ_i
Cooling	III	D	$\tau_c + \widetilde{\tau}$	ξ	–

and fixed boundary conditions

$$\theta_s(\beta,\tau) = -1, \qquad \theta_s(\xi_i,\tau) = 0, \qquad \theta_\ell(\xi_i,\tau) = 0, \qquad \left.\frac{\partial\theta_\ell}{\partial\xi}\right|_{\xi=1} = 0, \tag{4.10}$$

along with the time conditions

$$\theta_\ell(\xi,0) = \theta_{\mathrm{init}}, \qquad \xi_i(0) = \beta, \qquad \xi_i(\tau_c) = 1, \qquad \theta_s(\xi,\tau_c) = f(\xi). \tag{4.11}$$

4.3 Asymptotic analysis

The exact solution to this Stefan problem is not known and difficult to be obtained due to its high nonlinearity of the moving boundary. Consequently, asymptotic analysis can be applied to find an approximate analytical solution, as conceptually illustrated in Fig. 4.2. According to freezing physics, macroscale solidification happens in three stages: subcooling, freezing and cooling. These stages can reflect three distinct temporal scales implemented in the asymptotic analysis, namely Regime I, Regime II and Regime III. Further, one or more spatial scales called "layers" can also be presented in each regime. The terminology of regimes and layers for temporal and spatial scales have been previously introduced in Stefan-like problems by Brosa Planella et al. [10, 11]. In this paper, we will also use "regime" and "layer" as temporal and spatial scales.

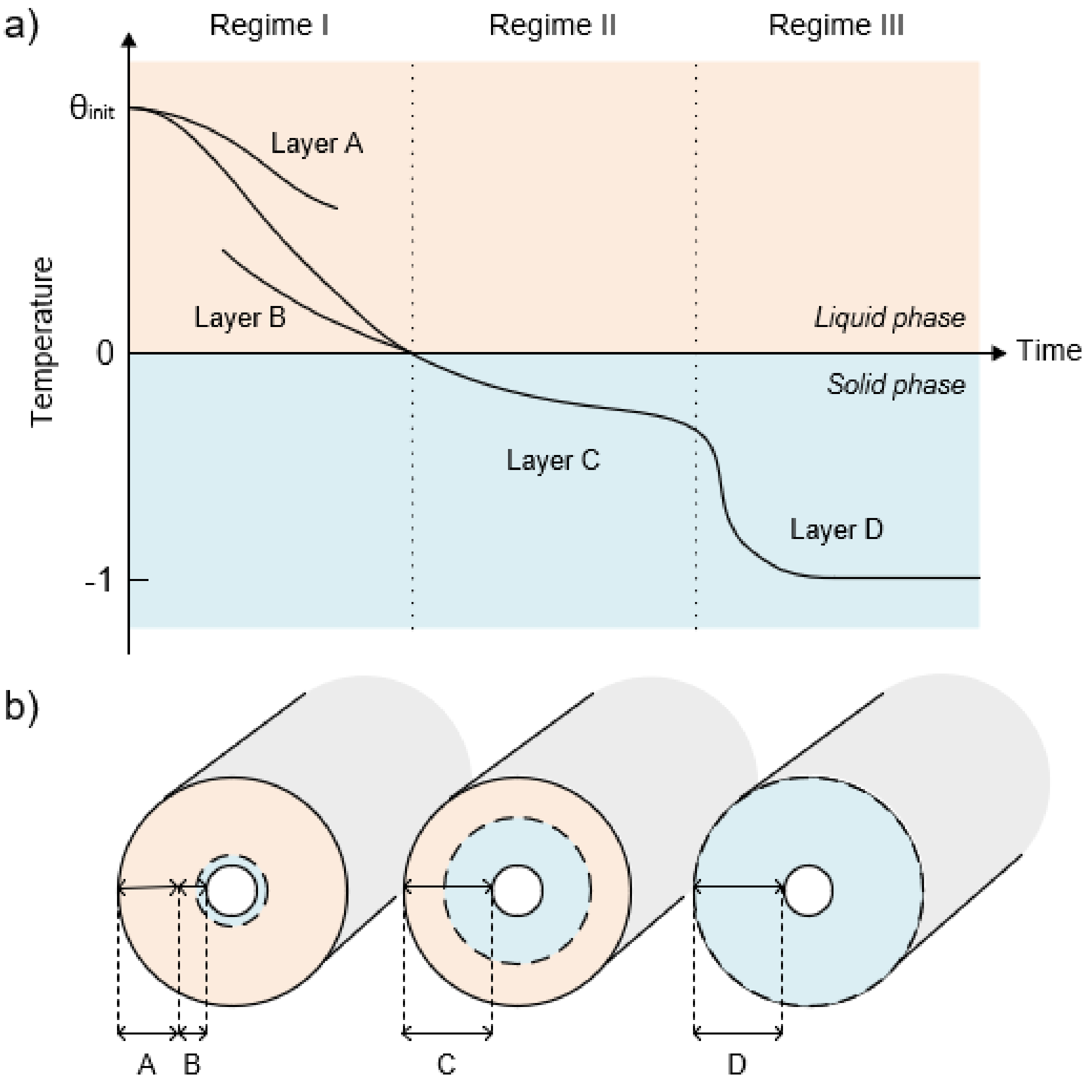

Figure 4.2: Conceptual diagram of asymptotic analysis: a) Temperature profile of outward solidification with three regimes and four layers; and b) Corresponding schematic diagram in each regime with layers.

As can be seen in Table 5.3, Regime I is the first temporal scale that aims to capture the subcooling stage of solidification. This temporal scale is a small-time expansion, which characterizes the initial state of the simulated domain and satisfies the initial condition $T_\ell(r, t = 0) = T_{\text{init}}$. In this regime, two spatial scales are also specified in reference to the moving boundary, namely Layer A (an outer layer far from the moving boundary) and Layer B (an inner layer near the moving boundary). Both layers will be evaluated asymptotically and then matched at the leading and first orders. Following by the subcooling stage, a freezing stage is described in Regime II. Regime II is at quasi-steady state, where the temporal scale is stretched by the Stefan number. This problem will be reduced to a one-phase Stefan problem, since the temperature in the liquid phase is at its fusion temperature. Interface motion and solid-phase temperature profile can be obtained. Lastly, the solid-liquid interface stops at the outer surface (i.e., the liquid phase vanishes) and a conduction scale is then performed in the solid phase. Consequently, the moving boundary condition of the solid phase will become an insulated boundary condition. Note that the dimensionless time to complete freezing is denoted as $\tau_c = \alpha_s t_c / a^2$.

4.3.1 Regime I

In this regime, two spatial layers are firstly found and the undetermined variables are then found by the method of matched asymptotic expansions. This treatment has been previously used for inward solidification of a sphere by McCue et al. [37]. However, there are two main differences between McCue et al.'s work and this study: i) An outward solidification problem in cylindrical coordinates (specifically, an annular region) is considered in this study, whereas McCue et al. [37] studied inward solidification in spherical coordinates. The difference in freezing direction and coordinates will lead to the variation in spatial scalings and asymptotic solutions between the two works; and ii) The definitions of Stefan number and non-dimensionalized scalings for thermophysical properties are inversed between two analyses. Thus, the asymptotic limit taken in the matching part is zero in this study, rather than infinity in McCue et al.'s work.

Layer A

Layer A represents an outer region which is far away from the moving boundary by rescaling the interface variable as:

$$\xi_i = \beta + \mathrm{Ste}^{\frac{1}{2}} \widetilde{\xi}_i. \tag{4.12}$$

The solid and liquid temperatures are assumed to have the following asymptotic expansions:

$$\theta_s(\xi, \tau; \mathrm{Ste}) \sim \theta_{s,0} + \mathrm{Ste}^{\frac{1}{2}} \theta_{s,1} + O(\mathrm{Ste}); \tag{4.13}$$

$$\theta_\ell(\xi, \tau; \mathrm{Ste}) \sim \theta_{\ell,0} + \mathrm{Ste}^{\frac{1}{2}} \theta_{\ell,1} + O(\mathrm{Ste}). \tag{4.14}$$

At the leading order, the solid phase vanishes and the problem reduces to transient heat conduction in a finite domain:

$$\begin{aligned} \frac{1}{\widetilde{\alpha}}\left(\frac{\partial^2 \theta_{\ell,0}}{\partial \xi^2} + \frac{1}{\xi}\frac{\partial \theta_{\ell,0}}{\partial \xi}\right) &= \frac{\partial \theta_{\ell,0}}{\partial \tau},\ \beta < \xi < 1, \\ \theta_{\ell,0}(\beta, \tau) &= 0, \\ \left.\frac{\partial \theta_{\ell,0}}{\partial \xi}\right|_{\xi=1} &= 0, \\ \theta_{\ell,0}(\beta, 0) &= \theta_{\mathrm{init}}. \end{aligned} \tag{4.15}$$

The exact solution for $\theta_{\ell,0}$ can be found by separation of variables:

$$\theta_{\ell,0} = \sum_{n=1}^{\infty} C_n \Big[J_0(\lambda_n \xi) Y_0(\lambda_n \beta) - J_0(\lambda_n \beta) Y_0(\lambda_n \xi) \Big] \exp(-\frac{\lambda_n^2}{\widetilde{\alpha}} \tau), \tag{4.16}$$

where the eigenvalues λ_n can be determined term by term in the following transcendental equation:

$$J_1(\lambda_n) Y_0(\lambda_n \beta) - J_0(\lambda_n \beta) Y_1(\lambda_n) = 0,\ n = 1, 2, 3, ... \tag{4.17}$$

and the corresponding coefficients are given by:

$$C_n = \frac{\int_{\xi=\beta}^{1} \theta_{\text{init}}\xi[J_0(\lambda_n\xi)Y_0(\lambda_n\beta) - J_0(\lambda_n\beta)Y_0(\lambda_n\xi)]\mathrm{d}\xi}{\int_{\xi=\beta}^{1} \xi[J_0(\lambda_n\xi)Y_0(\lambda_n\beta) - J_0(\lambda_n\beta)Y_0(\lambda_n\xi)]^2\mathrm{d}\xi}. \tag{4.18}$$

Layer B

Layer B is an inner region near the moving boundary and can be characterized by rescaling the radial coordinate and interface variable as:

$$\xi = \beta + \mathrm{Ste}^{\frac{1}{2}}\widetilde{\xi} \qquad \text{and} \qquad \xi_i = \beta + \mathrm{Ste}^{\frac{1}{2}}\widetilde{\xi}_i. \tag{4.19}$$

Therefore, the heat conduction equations for both phases become:

$$\beta\mathrm{Ste}\frac{\partial\widetilde{\theta}_s}{\partial\tau} + \mathrm{Ste}^{\frac{3}{2}}\widetilde{\xi}\frac{\partial\widetilde{\theta}_s}{\partial\tau} = \beta\frac{\partial^2\widetilde{\theta}_s}{\partial\widetilde{\xi}^2} + \mathrm{Ste}^{\frac{1}{2}}\widetilde{\xi}\frac{\partial^2\widetilde{\theta}_s}{\partial\widetilde{\xi}^2} + \mathrm{Ste}^{\frac{1}{2}}\frac{\partial\widetilde{\theta}_s}{\partial\widetilde{\xi}},\ 0 < \widetilde{\xi} < \widetilde{\xi}_i; \tag{4.20}$$

$$\beta\mathrm{Ste}\frac{\partial\widetilde{\theta}_\ell}{\partial\tau} + \mathrm{Ste}^{\frac{3}{2}}\widetilde{\xi}\frac{\partial\widetilde{\theta}_\ell}{\partial\tau} = \frac{1}{\widetilde{\alpha}}\beta\frac{\partial^2\widetilde{\theta}_\ell}{\partial\widetilde{\xi}^2} + \frac{1}{\widetilde{\alpha}}\mathrm{Ste}^{\frac{1}{2}}\widetilde{\xi}\frac{\partial^2\widetilde{\theta}_\ell}{\partial\widetilde{\xi}^2} + \frac{1}{\widetilde{\alpha}}\mathrm{Ste}^{\frac{1}{2}}\frac{\partial\widetilde{\theta}_\ell}{\partial\widetilde{\xi}},\ \widetilde{\xi} > \widetilde{\xi}_i, \tag{4.21}$$

where $\widetilde{\theta}_s$ and $\widetilde{\theta}_\ell$ are the newly scaled temperatures in this layer. These temperatures along with the interface are assumed to be in the following asymptotic forms:

$$\widetilde{\theta}_s(\widetilde{\xi},\tau;\mathrm{Ste}) \sim \widetilde{\theta}_{s,0} + \mathrm{Ste}^{\frac{1}{2}}\widetilde{\theta}_{s,1} + O(\mathrm{Ste}); \tag{4.22}$$

$$\widetilde{\theta}_\ell(\widetilde{\xi},\tau;\mathrm{Ste}) \sim \widetilde{\theta}_{\ell,0} + \mathrm{Ste}^{\frac{1}{2}}\widetilde{\theta}_{\ell,1} + O(\mathrm{Ste}); \tag{4.23}$$

$$\widetilde{\xi}_i(\tau;\mathrm{Ste}) \sim \widetilde{\xi}_{i,0} + \mathrm{Ste}^{\frac{1}{2}}\widetilde{\xi}_{i,1} + O(\mathrm{Ste}). \tag{4.24}$$

At the leading order, the heat equations are

$$\frac{\partial^2\widetilde{\theta}_{s,0}}{\partial\widetilde{\xi}^2} = 0,\ 0 < \widetilde{\xi} < \widetilde{\xi}_{i,0}, \qquad \widetilde{\theta}_{s,0}(\beta,\tau) = -1, \qquad \widetilde{\theta}_{s,0}(\widetilde{\xi}_{i,0},\tau) = 0; \tag{4.25}$$

$$\frac{\partial^2\widetilde{\theta}_{\ell,0}}{\partial\widetilde{\xi}^2} = 0,\ \widetilde{\xi} > \widetilde{\xi}_{i,0}, \qquad \widetilde{\theta}_{\ell,0}(\widetilde{\xi}_{i,0},\tau) = 0, \qquad \widetilde{\theta}_{\ell,0}(\infty,\tau) \sim \widetilde{a}_0(\tau)\widetilde{\xi}, \tag{4.26}$$

where $\widetilde{a}_0(\tau)$ is a matching variable to unify Layer A (outer solution) with Layer B (inner solution). The solutions of $\widetilde{\theta}_{s,0}$ and $\widetilde{\theta}_{\ell,0}$ are found to be

$$\widetilde{\theta}_{s,0} = -1 + \frac{\widetilde{\xi}}{\widetilde{\xi}_{i,0}} \qquad \text{and} \qquad \widetilde{\theta}_{\ell,0} = \widetilde{a}_0(\tau)(\widetilde{\xi} - \widetilde{\xi}_{i,0}). \tag{4.27}$$

At the first order, the heat equations become:

$$\beta \frac{\partial^2 \widetilde{\theta}_{s,1}}{\partial \widetilde{\xi}^2} + \widetilde{\xi} \frac{\partial^2 \widetilde{\theta}_{s,0}}{\partial \widetilde{\xi}^2} + \frac{\partial \widetilde{\theta}_{s,0}}{\partial \widetilde{\xi}} = 0, \tag{4.28}$$

$$\left.\frac{\partial \widetilde{\theta}_{s,0}}{\partial \widetilde{\xi}}\right|_{\widetilde{\xi}=\widetilde{\xi}_{i,0}} \widetilde{\xi}_{i,1} + \widetilde{\theta}_{s,1}(\widetilde{\xi}_{i,0}, \tau) = 0, \tag{4.29}$$

$$\widetilde{\theta}_{s,1}(0, \tau) = 0; \tag{4.30}$$

$$\beta \frac{\partial^2 \widetilde{\theta}_{\ell,1}}{\partial \widetilde{\xi}^2} + \widetilde{\xi} \frac{\partial^2 \widetilde{\theta}_{\ell,0}}{\partial \widetilde{\xi}^2} + \frac{\partial \widetilde{\theta}_{\ell,0}}{\partial \widetilde{\xi}} = 0, \tag{4.31}$$

$$\left.\frac{\partial \widetilde{\theta}_{\ell,0}}{\partial \widetilde{\xi}}\right|_{\widetilde{\xi}=\widetilde{\xi}_{i,0}} \widetilde{\xi}_{i,1} + \widetilde{\theta}_{\ell,1}(\widetilde{\xi}_{i,0}, \tau) = 0, \tag{4.32}$$

$$\widetilde{\theta}_{\ell,1}(\infty, \tau) \sim \widetilde{a}_0(\tau) \widetilde{\xi}^2 + \widetilde{a}_1(\tau) \widetilde{\xi}, \tag{4.33}$$

where $\widetilde{a}_1(\tau)$ is also a matching variable which will be found in the subsequent matching section. Similar to the leading order, solutions of $\widetilde{\theta}_{s,1}$ and $\widetilde{\theta}_{\ell,1}$ can be found as:

$$\widetilde{\theta}_{s,1} = -\frac{1}{2\beta \widetilde{\xi}_{i,0}} \widetilde{\xi}^2 + \left(\frac{1}{2\beta} - \frac{\widetilde{\xi}_{i,1}}{\widetilde{\xi}_{i,0}^2}\right) \widetilde{\xi}, \tag{4.34}$$

$$\widetilde{\theta}_{\ell,1} = \widetilde{a}_0(\tau) \Bigg(-\frac{1}{2\beta} \widetilde{\xi}^2 + \frac{1}{2\beta} \widetilde{\xi}_{i,0}^{\,2} - \widetilde{\xi}_{i,1} \Bigg) + \widetilde{a}_1(\tau) \Bigg(\widetilde{\xi} - \widetilde{\xi}_{i,0} \Bigg). \tag{4.35}$$

The method of matched asymptotic expansions

As can be seen in Sections 4.3.1 and 4.3.1, the variables $\widetilde{a}_0(\tau)$ and $\widetilde{a}_1(\tau)$ in the liquid temperature have not been defined yet. These variables will be determined by applying the method of matched asymptotic expansions in this section. Specifically, the outer region (Layer A) solution is firstly written in terms of the inner region (Layer B) variables $(\widetilde{\xi}, \tau)$. A limit is then taken as Ste → 0 to obtain an asymptote as $\widetilde{\xi} \to \infty$, which subsequently matches the outer region with the inner one.

At the leading order, the outer region solution can be rewritten in terms of the inner variables $(\widetilde{\xi}, \tau)$ as follows:

$$\begin{aligned}\theta_{\ell,0}(\widetilde{\xi}, \tau) = \sum_{n=1}^{\infty} C_n \Bigg\{ & J_0\left[\lambda_n(\beta + \mathrm{Ste}^{\frac{1}{2}}\widetilde{\xi})\right] Y_0(\lambda_n\beta) \\ & - J_0(\lambda_n\beta) Y_0\left[\lambda_n(\beta + \mathrm{Ste}^{\frac{1}{2}}\widetilde{\xi})\right]\Bigg\} \exp(-\frac{\lambda_n^2}{\widetilde{\alpha}}\tau),\end{aligned} \tag{4.36}$$

The leading-order matching solution $\overline{\theta}_{\ell,0}(\widetilde{\xi}, \tau)$ can then be found by taking the limit as Ste → 0:

$$\begin{aligned}\overline{\theta}_{\ell,0}(\widetilde{\xi}, \tau) &= \lim_{\mathrm{Ste}\to 0} \theta_{\ell,0}(\widetilde{\xi}, \tau) \\ &= \sum_{n=1}^{\infty} C_n \left[J_0(\lambda_n\beta) Y_0(\lambda_n\beta) - J_0(\lambda_n\beta) Y_0(\lambda_n\beta)\right] \exp(-\frac{\lambda_n^2}{\widetilde{\alpha}}\tau) = 0.\end{aligned} \tag{4.37}$$

Similarly, the first-order matching solution $\theta_{\ell,1}(\widetilde{\xi}, \tau)$ is found by rewriting the variables $(\widetilde{\xi}, \tau)$ and taking the limit as Ste → 0:

$$\begin{aligned}\overline{\theta}_{\ell,1}(\widetilde{\xi}, \tau) = \lim_{\mathrm{Ste}\to 0} \mathrm{Ste}^{-\frac{1}{2}} \sum_{n=1}^{\infty} C_n \Bigg\{ & J_0\left[\lambda_n(\beta + \mathrm{Ste}^{\frac{1}{2}}\widetilde{\xi})\right] Y_0(\lambda_n\beta) \\ & - J_0(\lambda_n\beta) Y_0\left[\lambda_n(\beta + \mathrm{Ste}^{\frac{1}{2}}\widetilde{\xi})\right]\Bigg\} \exp(-\frac{\lambda_n^2}{\widetilde{\alpha}}\tau).\end{aligned} \tag{4.38}$$

This limit has an indeterminate form by direct substitution, and thus the L'Hôpital's rule can be applied. We find the first-order matching solution $\theta_{\ell,1}$ as:

$$\overline{\theta}_{\ell,1}(\widetilde{\xi}, \tau) = \sum_{n=1}^{\infty} C_n \lambda_n \widetilde{\xi} \left[J_0(\lambda_n\beta) Y_1(\lambda_n\beta) - J_1(\lambda_n\beta) Y_0(\lambda_n\beta)\right] \exp(-\frac{\lambda_n^2}{\widetilde{\alpha}}\tau). \tag{4.39}$$

Since the liquid-phase solution in the inner region (Layer B) was assumed to be in the form of:

$$\widetilde{\theta}_{\ell,0} \sim \widetilde{a}_0(\tau)\widetilde{\xi}, \qquad\qquad \widetilde{\theta}_{\ell,1} \sim \widetilde{a}_0(\tau)\widetilde{\xi}^2 + \widetilde{a}_1(\tau)\widetilde{\xi}, \tag{4.40}$$

the undetermined variables $\widetilde{a}_0$ and $\widetilde{a}_1$ can be readily found by matching:

$$\widetilde{a}_0(\tau) = 0, \tag{4.41}$$

$$\widetilde{a}_1(\tau) = \sum_{n=1}^{\infty} C_n\lambda_n \Big[J_0(\lambda_n\beta)Y_1(\lambda_n\beta) - J_1(\lambda_n\beta)Y_0(\lambda_n\beta)\Big] \exp(-\frac{\lambda_n^2}{\widetilde{\alpha}}\tau). \tag{4.42}$$

As a result, the liquid-phase solution at the leading and first orders in the inner region (Layer B) can be written as:

$$\widetilde{\theta}_{\ell,0} = 0, \qquad\qquad \widetilde{\theta}_{\ell,1} = \Big(\widetilde{\xi} - \widetilde{\xi}_{i,0}\Big) \sum_{n=1}^{\infty} D_n \exp(-\frac{\lambda_n^2}{\widetilde{\alpha}}\tau), \tag{4.43}$$

where D_n is defined for simplification as follows:

$$D_n = C_n\lambda_n \Big[J_0(\lambda_n\beta)Y_1(\lambda_n\beta) - J_1(\lambda_n\beta)Y_0(\lambda_n\beta)\Big]. \tag{4.44}$$

The interface solution in Layer B can be therefore solved at the leading and first orders:

$$\frac{\partial\widetilde{\theta}_{s,0}}{\partial\widetilde{\xi}}\bigg|_{\widetilde{\xi}=\widetilde{\xi}_{i,0}} - \frac{1}{\widetilde{k}}\frac{\partial\widetilde{\theta}_{\ell,0}}{\partial\widetilde{\xi}}\bigg|_{\widetilde{\xi}=\widetilde{\xi}_{i,0}} = \frac{\mathrm{d}\widetilde{\xi}_{i,0}}{\mathrm{d}\tau}, \qquad\qquad \widetilde{\xi}_{i,0}(0) = 0; \tag{4.45}$$

$$\frac{\partial\widetilde{\theta}_{s,1}}{\partial\widetilde{\xi}}\bigg|_{\widetilde{\xi}=\widetilde{\xi}_{i,0}} - \frac{1}{\widetilde{k}}\frac{\partial\widetilde{\theta}_{\ell,1}}{\partial\widetilde{\xi}}\bigg|_{\widetilde{\xi}=\widetilde{\xi}_{i,0}} = \frac{\mathrm{d}\widetilde{\xi}_{i,1}}{\mathrm{d}\tau}, \qquad\qquad \widetilde{\xi}_{i,1}(0) = 0. \tag{4.46}$$

Substituting the solid and liquid temperature solutions at the leading and first orders, we find the interface motion as:

$$\widetilde{\xi}_{i,0} = \sqrt{2\tau}, \qquad \widetilde{\xi}_{i,1} = -\frac{\tau}{3\beta} + \frac{1}{\widetilde{k}}\sum_{n=1}^{\infty} D_n \left[\frac{\widetilde{\alpha}e^{-\lambda_n^2\tau/\widetilde{\alpha}}}{\lambda_n^2} - \frac{\widetilde{\alpha}^{\frac{3}{2}}\pi^{\frac{1}{2}}\mathrm{erf}(\widetilde{\alpha}^{\frac{1}{2}}\lambda_n\tau^{\frac{1}{2}})}{2\lambda_n^3\tau^{\frac{1}{2}}}\right]. \tag{4.47}$$

4.3.2 Regime II

Following the subcooling stage in Regime I, Regime II aims to characterize the freezing stage of solidification by introducing a new temporal scale. At this scale, the liquid phase is found to remain at the fusion temperature, and thus the two-phase Stefan problem reduces to a one-phase problem. Recently, this reduced one-phase Stefan problem has directly been considered as the equilibrium freezing stage, while modeling each solidification stage separately [2]. For mathematical simplification, the transformed one-phase problem is firstly rewritten such that (ξ, ξ_i) are the independent variables and $(\widetilde{\theta}_s, \widetilde{\tau})$ are the dependent variables. Then, asymptotic solutions of dimensionless solid temperature and time are found at leading and first orders.

This temporal scale is also referred as a quasi-steady state or quasi-analytical solution or quasi-stationary approximation for Stefan-like problems [28, 3, 25]. In two-phase Stefan problems, the perturbation series solution of this scale is often viewed as an "outer solution", which has been previously studied by applying singular perturbation theory in Cartesian [59], spherical [1] and cylindrical [30, 62] coordinates. The singular perturbation method often incorporates boundary-fixing technique to immobilize the moving boundary, and the initial condition of liquid phase is abandoned. Some works have been done without giving up the initial condition by using the method of composite asymptotic expansions in Cartesian [43] and spherical [37] coordinates. Due to the general form of composite asymptotic expansions, the obtained liquid-phase solution is expected to contribute exponentially small terms to the interface motion, as proved in [37]. Once again, the two-phase Stefan problem will be reduced to a one-phase case. As a result, we directly reduce the problem into a one-phase Stefan problem based on the fixed boundary conditions in this study.

Layer C

Rescaling the temporal variable $\widetilde{\tau} = \mathrm{Ste}\tau$, the heat equations for both phases become:

$$\mathrm{Ste}\frac{\partial\widetilde{\theta}_s}{\partial\widetilde{\tau}} = \frac{\partial^2\widetilde{\theta}_s}{\partial\xi^2} + \frac{1}{\xi}\frac{\partial\widetilde{\theta}_s}{\partial\xi}, \qquad \mathrm{Ste}\frac{\partial\widetilde{\theta}_\ell}{\partial\widetilde{\tau}} = \frac{1}{\widetilde{\alpha}}\left(\frac{\partial^2\widetilde{\theta}_\ell}{\partial\xi^2} + \frac{1}{\xi}\frac{\partial\widetilde{\theta}_\ell}{\partial\xi}\right), \tag{4.48}$$

subject to the moving boundary condition

$$\left.\frac{\partial\widetilde{\theta}_s}{\partial\xi}\right|_{\xi=\xi_i} - \frac{1}{\widetilde{k}}\left.\frac{\partial\widetilde{\theta}_\ell}{\partial\xi}\right|_{\xi=\xi_i} = \frac{\mathrm{d}\xi_i}{\mathrm{d}\widetilde{\tau}}, \tag{4.49}$$

and fixed boundary conditions

$$\widetilde{\theta}_s(\xi=\beta,\widetilde{\tau}) = -1, \qquad \widetilde{\theta}_s(\xi=\xi_i,\widetilde{\tau}) = 0, \qquad \widetilde{\theta}_\ell(\xi=\xi_i,\widetilde{\tau}) = 0, \qquad \left.\frac{\partial\widetilde{\theta}_\ell}{\partial\xi}\right|_{\xi=1} = 0. \tag{4.50}$$

It is rather clear that the liquid phase temperature subjected to fixed boundary conditions is found to be 0 at any order of asymptotic expansions. This is because the condition of initial temperature is abandoned and the two boundary conditions give the solution of 0 (i.e., the fusion temperature). The two-phase Stefan problem therefore reduces to a one-phase problem. Further, the dimensionless time $\widetilde{\tau}$ can be expressed as a function of the dimensionless interface ξ_i. This re-formulation will significantly simplify the solution procedure, since it is lengthy to find an explicit form of the interface solution. After re-formulating the equations, the problem becomes:

$$\frac{\partial^2\widetilde{\theta}_s}{\partial\xi^2} + \frac{1}{\xi}\frac{\partial\widetilde{\theta}_s}{\partial\xi} = \mathrm{Ste}\frac{\partial\widetilde{\theta}_s}{\partial\widetilde{\xi}_i}\left(\left.\frac{\partial\widetilde{\theta}_s}{\partial\xi}\right|_{\xi=\xi_i}\right), \qquad \frac{\mathrm{d}\widetilde{\tau}}{\mathrm{d}\xi_i}\left(\left.\frac{\partial\widetilde{\theta}_s}{\partial\xi}\right|_{\xi=\xi_i}\right) = 1, \tag{4.51}$$

subject to boundary and initial conditions

$$\widetilde{\theta}_s(\xi=\beta,\widetilde{\tau}) = -1, \qquad \widetilde{\theta}_s(\xi=\xi_i,\widetilde{\tau}) = 0, \qquad \widetilde{\tau}(\xi_i=\beta) = 0. \tag{4.52}$$

Then, we approach the asymptotic solutions to be in the form of:

$$\widetilde{\theta}_s(\xi, \xi_i; \mathrm{Ste}) \sim \widetilde{\theta}_{s,0} + \mathrm{Ste}\widetilde{\theta}_{s,1} + O(\mathrm{Ste}^2); \tag{4.53}$$

$$\widetilde{\tau}(\xi_i; \mathrm{Ste}) \sim \widetilde{\tau}_0 + \mathrm{Ste}\widetilde{\tau}_1 + O(\mathrm{Ste}^2). \tag{4.54}$$

At the leading order, the heat equation and moving boundary are

$$\frac{\partial^2 \widetilde{\theta}_{s,0}}{\partial \xi^2} + \frac{1}{\xi}\frac{\partial \widetilde{\theta}_{s,0}}{\partial \xi} = 0, \qquad \frac{\mathrm{d}\widetilde{\tau}_0}{\mathrm{d}\xi_i}\left(\frac{\partial \widetilde{\theta}_{s,0}}{\partial \xi}\bigg|_{\xi=\xi_i}\right) = 1, \tag{4.55}$$

subject to the following boundary and initial conditions

$$\widetilde{\theta}_{s,0}(\xi = \beta) = -1, \qquad \widetilde{\theta}_{s,0}(\xi = \xi_i) = 0, \qquad \widetilde{\tau}_0(\xi_i = \beta) = 0. \tag{4.56}$$

Therefore, we find the dimensionless solid temperature and time as follows:

$$\widetilde{\theta}_{s,0} = \frac{\ln \xi_i - \ln \xi}{\ln \beta - \ln \xi_i}, \qquad \widetilde{\tau}_0 = \frac{1}{4}\left(\beta^2 - \xi_i^2 + 2\xi_i^2 \ln \frac{\xi_i}{\beta}\right). \tag{4.57}$$

Similar to the leading order, the first-order problem becomes:

$$\frac{\partial^2 \widetilde{\theta}_{s,1}}{\partial \xi^2} + \frac{1}{\xi}\frac{\partial \widetilde{\theta}_{s,1}}{\partial \xi} = \frac{\partial \widetilde{\theta}_{s,0}}{\partial \xi_i}\left(\frac{\partial \widetilde{\theta}_{s,0}}{\partial \xi}\bigg|_{\xi=\xi_i}\right), \quad \frac{\mathrm{d}\widetilde{\tau}_0}{\mathrm{d}\xi_i}\left(\frac{\partial \widetilde{\theta}_{s,1}}{\partial \xi}\bigg|_{\xi=\xi_i}\right) + \frac{\mathrm{d}\widetilde{\tau}_1}{\mathrm{d}\xi_i}\left(\frac{\partial \widetilde{\theta}_{s,0}}{\partial \xi}\bigg|_{\xi=\xi_i}\right) = 0, \tag{4.58}$$

subject to the boundary and initial conditions

$$\widetilde{\theta}_{s,1}(\xi = \beta) = 0, \qquad \widetilde{\theta}_{s,1}(\xi = \xi_i) = 0, \qquad \widetilde{\tau}_1(\xi_i = \beta) = 0. \tag{4.59}$$

Thus, the first-order solutions are found to be

$$\widetilde{\theta}_{s,1} = \frac{(\xi_i^2 - \xi^2)(\ln\beta - \ln\xi - \ln\xi_i + 1)\ln\beta}{4\xi_i^4(\ln\beta - \ln\xi_i)^4} \tag{4.60}$$

$$+ \frac{(\xi^2 - \beta^2)\ln\xi_i + [\beta^2 - \xi_i^2 + (\xi_i^2 - \xi^2)\ln\xi_i]\ln\xi}{4\xi_i^4(\ln\beta - \ln\xi_i)^4}, \tag{4.61}$$

$$\widetilde{\tau}_1 = \frac{1}{4}\left(\beta^2 + \xi_i^2 + \frac{\beta^2 - \xi_i^2}{\ln\xi_i - \ln\beta}\right). \tag{4.62}$$

The interface motion in this regime gives the time evolution of moving boundary except its initial state, because ln(0) in the $\widetilde{\tau}$ expression is undefined. This implies that the interface breaks down as time approaches 0, which is the reason why the interface has been studied in the first temporal scale by satisfying the initial condition.

It is also of interest to obtain a final expression of total freezing time τ_c in an explicit form. Here, the total freezing time is calculated by setting the interface to its terminal value (i.e., $\xi_i = 1$), and thus

$$\tau_c \sim \frac{1}{4\mathrm{Ste}}\left(\beta^2 - 1 + 2\ln\frac{1}{\beta}\right) + \frac{1}{4}\left(\beta^2 + 1 + \frac{1 - \beta^2}{\ln\beta}\right). \tag{4.63}$$

There could be an additional term for a second-phase correction by solving the liquid phase problem in this regime, as demonstrated in the spherical coordinates [37]. However, it is inevitable for the additional term to be exponentially small because of the method of composite expansions in the liquid phase problem. Due to its lengthy calculation, a detailed proof of liquid phase contribution to moving interface has been presented in 4.7, which quantitatively identifies the term. For practical purposes of PCMs in this study, it is therefore safe to omit the exponentially small second-phase correction.

4.3.3 Regime III

Regime III is the last temporal scale to capture the cooling stage of solidification and only one spatial scale (Layer D) exists. This regime starts as the moving boundary stops at the outer surface, and thus a new temporal scale can be found by a linear shift with regards to the total freezing time τ_c. Both liquid phase and interface vanish in this regime, and exact solution of the solid phase can be found by using the method of superposition and separation of variables.

Layer D

Applying a new temporal scale $\widetilde{\tau} = \tau - \tau_c$, the two-phase Stefan-like problem reduces to a finite-extent heat conduction problem for the solid phase only:

$$\begin{aligned}
\frac{\partial^2 \widetilde{\theta}_s}{\partial \xi^2} + \frac{1}{\xi}\frac{\partial \widetilde{\theta}_s}{\partial \xi} &= \frac{\partial \widetilde{\theta}_s}{\partial \widetilde{\tau}}, \\
\widetilde{\theta}_s(\xi = \beta, \widetilde{\tau}) &= -1, \\
\left.\frac{\partial \widetilde{\theta}_s}{\partial \xi}\right|_{\xi=1} &= 0, \\
\widetilde{\theta}_s(\xi, \widetilde{\tau} = 0) &= f(\xi).
\end{aligned} \tag{4.64}$$

Even though the heat equation is a homogeneous partial differential equation, the boundary conditions are not both homogeneous. Therefore, the method of superposition is required prior to separation of variables. After a linear shift of temperature to remove the non-homogeneity, the exact solution is expressed as:

$$\widetilde{\theta}_s = -1 + \sum_{n=1}^{\infty} \widetilde{C}_n \left[J_0(\widetilde{\lambda}_n \xi) Y_0(\widetilde{\lambda}_n \beta) - J_0(\widetilde{\lambda}_n \beta) Y_0(\widetilde{\lambda}_n \xi) \right] \exp(-\widetilde{\lambda}_n^2 \widetilde{\tau}), \tag{4.65}$$

where the eigenvalues can be determined term by term based on the two boundary conditions by solving the following transcendental equation:

$$J_1(\widetilde{\lambda}_n) Y_0(\widetilde{\lambda}_n \beta) = J_0(\widetilde{\lambda}_n \beta) Y_1(\widetilde{\lambda}_n), \tag{4.66}$$

and the corresponding coefficients can be found by the initial condition:

$$\widetilde{C}_n = \frac{\int_\beta^1 \left[f(\xi)+1\right]\xi\left[J_0(\widetilde{\lambda}_n\xi)Y_0(\widetilde{\lambda}_n\beta) - J_0(\widetilde{\lambda}_n\beta)Y_0(\widetilde{\lambda}_n\xi)\right]\mathrm{d}\xi}{\int_\beta^1 \xi\left[J_0(\widetilde{\lambda}_n\xi)Y_0(\widetilde{\lambda}_n\beta) - J_0(\widetilde{\lambda}_n\beta)Y_0(\widetilde{\lambda}_n\xi)\right]^2\mathrm{d}\xi}. \tag{4.67}$$

4.4 Numerical analysis

There has been a variety of numerical methods developed to model solidification, as mentioned in Section 4.1. Among all, the enthalpy method is a versatile and computationally efficient framework, even for higher dimensions with irregular topology [29, 54]. In this section, a general implicit source-based enthalpy method is used to model a mushy region between two phases, rather than a sharp-interface in the Stefan-like problem. This enthalpy method will further facilitate the verification against the developed asymptotic solution in Section 4.3.

4.4.1 Enthalpy method

The enthalpy method considers a heat conduction equation in terms of enthalpy as the governing equation [54]:

$$\frac{\partial H}{\partial t} = \frac{1}{r}\frac{\partial}{\partial r}\left(k\frac{\partial T}{\partial r}\right), \tag{4.68}$$

where H is the enthalpy that represents the total thermal energy of fluid. The enthalpy is primarily calculated by integrating heat capacity with respect to temperature [54] but it can also be linearized by the following function [18]:

$$H = \begin{cases} \rho c_{p,s}(T - T_{\text{solidus}}) & , \ T < T_{\text{solidus}} \\ \rho\overline{c_p}(T - T_{\text{solidus}}) + \gamma\rho L & , \ T_{\text{solidus}} \leq T \leq T_{\text{liquidus}} \\ \rho c_{p,\ell}(T - T_{\text{liquidus}}) + \rho\overline{c_p}\Delta T_{\text{mushy}} + \rho L & , \ T > T_{\text{liquidus}} \end{cases} \tag{4.69}$$

where T_{solidus} and T_{liquidus} are the solidus and liquidus temperatures [K], respectively. ΔT_{mushy} is defined as the temperature difference of the mushy zone, i.e., $\Delta T_{\text{mushy}} = T_{\text{liquidus}} - T_{\text{solidus}}$. $\overline{c_p}$ is the average specific heat in the mushy zone defined as $(c_{p,s} + c_{p,\ell})/2$. It is worthwhile to mention that this linearization of enthalpy assumes a relatively small mushy zone, where the change in latent heat is much larger than the change in sensible heat. Since the verification against the analytical model also requires such small mushy region, the linearization is a valid assumption in this study. Meanwhile, the liquid fraction, γ, is also assumed to change linearly with temperature in the mushy zone:

$$\gamma = \begin{cases} 0 & , \ T < T_{\text{solidus}} \\ \frac{T - T_{\text{solidus}}}{\Delta T_{\text{mushy}}} & , \ T_{\text{solidus}} \leq T \leq T_{\text{liquidus}} \\ 1 & , \ T > T_{\text{liquidus}} \end{cases} \tag{4.70}$$

The boundary conditions and initial conditions are

$$T(r = b, t) = T_b, \qquad \left.\frac{\partial T}{\partial r}\right|_{r=a} = 0, \qquad T(r, t = 0) = T_{\text{init}}. \tag{4.71}$$

4.4.2 Discretization scheme

The governing equation expressed in Eqn. (4.68) can be firstly discretized term by term. The unsteady term (left hand side of the equation) is discretized by a first-order scheme, while the diffusive term (right hand side of the equation) is done by a second-order scheme. The transformed discretized equation is written as:

$$d_i(H_i - H_i^{\text{old}}) = c_{i-1}T_{i-1} + c_i T_i + c_{i+1}T_{i+1}, \tag{4.72}$$

where the subscript i represents the i-th node and the notation “old” means the previous time step. The symbols c and d are the coefficients of discretized equation.

Applying a first-order Taylor series approximation, the enthalpy H_i^j can be obtained:

$$H_i^j = H_i^{j-1} + \left.\frac{\partial H}{\partial T}\right|_i^{j-1} (T_i^j - T_i^{j-1}), \tag{4.73}$$

where the j-th iteration is denoted by the superscript j. The enthalpy equation can then be linearized by substituting Eqn. (4.73) in Eqn. (4.72) as follows:

$$d_i \left[H_i^{j-1} + \left.\frac{\partial H}{\partial T}\right|_i^{j-1} (T_i^j - T_i^{j-1}) - H_i^{\text{old}} \right] = c_{i-1} T_{i-1}^j + c_i T_i^j + c_{i+1} T_{i+1}^j. \tag{4.74}$$

Figure 4.3 demonstrates the numerical solution algorithm of the enthalpy method. This algorithm begins with the initialization of enthalpy and temperature. Then, the enthalpy and temperature are iterated by solving the linearized enthalpy equation shown in Eqn. (4.74) until convergence. The convergence criteria signifying the tolerance between the current and previous iterations, is set to be well below 10^{-5} [K] in temperature. If the given convergence condition is not met, then another iteration of solving the linearized enthalpy equation will be required. Once the solution is converged, the next time step will be started. The algorithm ends when the convergent solutions to all the prescribed time steps are obtained. In addition, a mesh independence study is conducted in 4.7 on five different numbers of mesh elements for selecting the optimal mesh count, thus setting a reference for the subsequent model comparisons on computational cost.

4.5 Model verification

As mentioned in Section 4.1, the solid-liquid interface can be either simulated by a sharp line or a mushy zone, where the mushy-zone model is usually solved by numerical schemes (e.g., enthalpy method). To verify the presented analytical model governed by the sharp interface, the enthalpy method was utilized based on various mushy-zone thicknesses (i.e., $\Delta T_{\text{mushy}} = T_{\text{liquidus}} - T_{\text{solidus}}$). It is expected that the enthalpy method approaches sharp

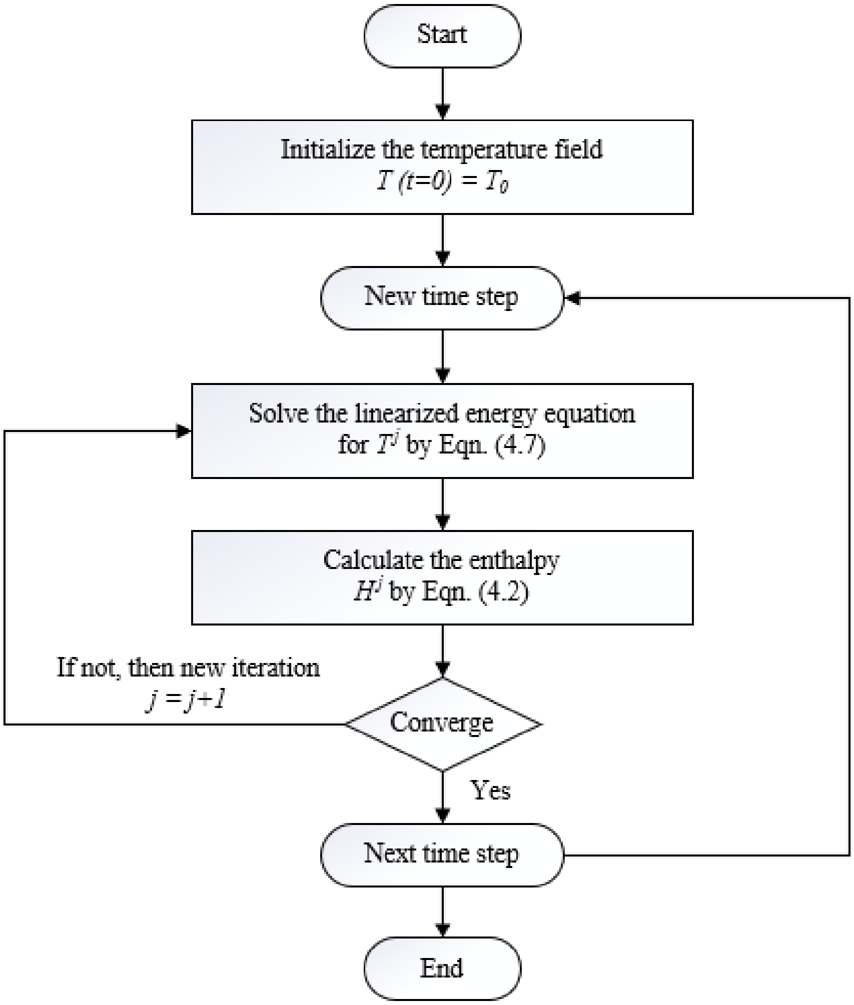

Figure 4.3: Numerical algorithm for the enthalpy method. Convergence criterion is prescribed as 10^{-5} [K] in temperature between two neighboring iterations.

interface model as the mushy-zone thickness decreases. Here the mushy-zone thickness is a numerical parameter of a fixed temperature interval for defining the piecewise function of enthalpy as shown in Eqn. (4.69) and it relies on the liquidus and solidus temperatures. The physical mushy-zone thickness in units of length between the solid and liquid phases, nonetheless, depends on other parameters and often requires experimental observations which will not be discussed in this work. In this section, the analytical model was compared and verified by the enthalpy method. Both interface motion and temperature profiles at various locations were plotted and discussed in details.

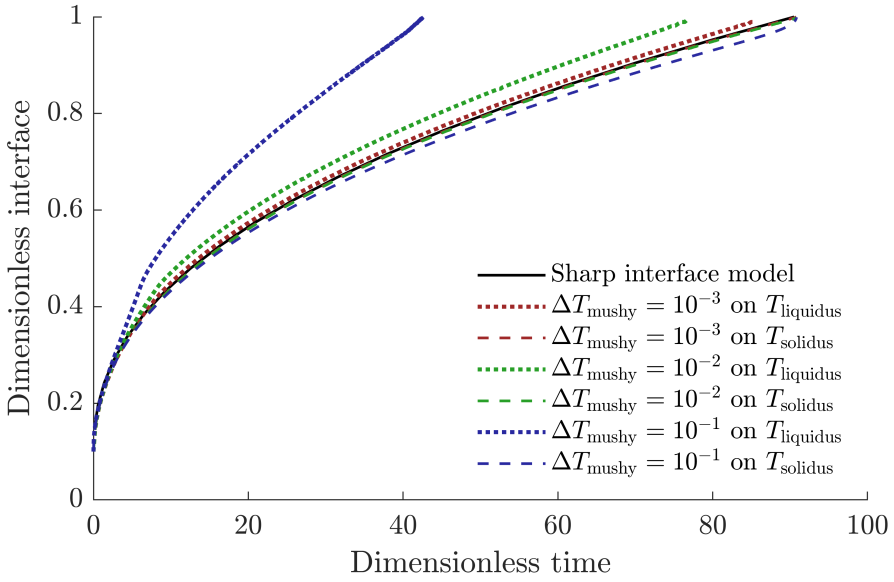

Figure 4.4: Comparisons between the sharp-interface (analytical) and mushy-region (numerical) models with different mushy-zone thicknesses in terms of interface motion for the case: $\widetilde{k} = \widetilde{c}_p = 1.0,\ \beta = 0.1,\ \theta_{\text{init}} = 1,\ \text{Ste} = 0.01$. The analytical solution is given by the solid line, while numerical results at liquid and solid temperatures are given by the dotted and dashed lines.

Figure 4.4 compares the analytical model with numerical results in terms of interface motion. Dimensionless interface location over dimensionless time was plotted based on the analytical solution and numerical model with three mushy-zone thicknesses. Specifically, the mushy-zone thicknesses were considered as 0.001, 0.010, and 0.100 [K]; the interface locations at both liquidus and solidus temperatures were recorded for each thickness. According to these numerical models with different mushy-zone thicknesses, a few notable results can be observed. First, the mushy-zone thickness has a direct impact on the difference between the interface at the liquidus temperature and the one at the solidus temperature. The decrease in mushy-zone thickness minimizes difference between the two interfaces, which results in the tendency to a nearly sharp interface model (e.g., $\Delta T_{\text{mushy}} = 0.001$ [K]). This observation facilitates verification to the analytical model, where a perfectly sharp interface is assumed. Secondly, the total freezing time at the solidus temperature is roughly the same among different mushy-zone thicknesses. In other words, the interfaces of three thicknesses

Table 4.3: Total freezing time in the analytical and three numerical results calculated based on different temperature references. Deviations among these results are also listed.

	Total freezing time, $\bar{\alpha} t_c / a^2$			Deviation	
ΔT_{mushy}	Analytical (t_c)	T_{liquidus} ($t_{c,1}$)	T_{solidus} ($t_{c,2}$)	$\frac{t_{c,1}-t_{c,2}}{t_{c,2}}$	$\frac{t_c-t_{c,2}}{t_{c,2}}$
10^{-3} [K]	90.52	86.00	90.80	-5.29%	-0.31%
10^{-2} [K]	90.52	76.60	90.80	-15.64%	-0.31%
10^{-1} [K]	90.52	39.20	90.80	-56.83%	-0.31%

terminate at similar times when $r_i = a$. The interface motion at the solidus temperature can therefore be a reasonable indicator to determine the total freezing time. The liquid temperature, however, offers different freezing times for each mushy region. This finding can be practical in many engineering applications on PCMs concerned with the total freezing or melting time.

Additionally, many researchers have been focusing on the end-behavior of interface motion in Stefan problems by introducing a fairly short temporal scale in the asymptotic analysis [51, 37, 10, 11]. Based on our comparisons, the curved end-behavior is seemingly caused by the thickness of mushy zone, rather than other physical phenomena. For instance, the end-behavior can be observed at $\Delta T_{\text{mushy}} = 0.100$ [K], but it is barely seen at $\Delta T_{\text{mushy}} = 0.001, 0.010$ [K]. It is also worthy to note that the total freezing time remains the same with or without such end-behavior. As a result, the end-behavior can be safely ignored in sharp-interface models from a physical standpoint.

The total freezing times of the asymptotic solution and three mushy-zone results are expressed in a dimensionless form (i.e., $\bar{\alpha} t_c / a^2$) listed in Table 4.3. Particularly, the numerical values of total freezing times are calculated as the times when interfaces arrives the outer surface; that is, $\xi_i = 1$. The deviation between the liquidus and solidus temperatures is firstly examined. Then, the total freezing time for solidus temperature is set as a reference to calculate the deviation between the asymptotic and numerical solutions. As can be seen, this deviation between liquidus and solidus temperatures enlarges greatly from -5.29% to

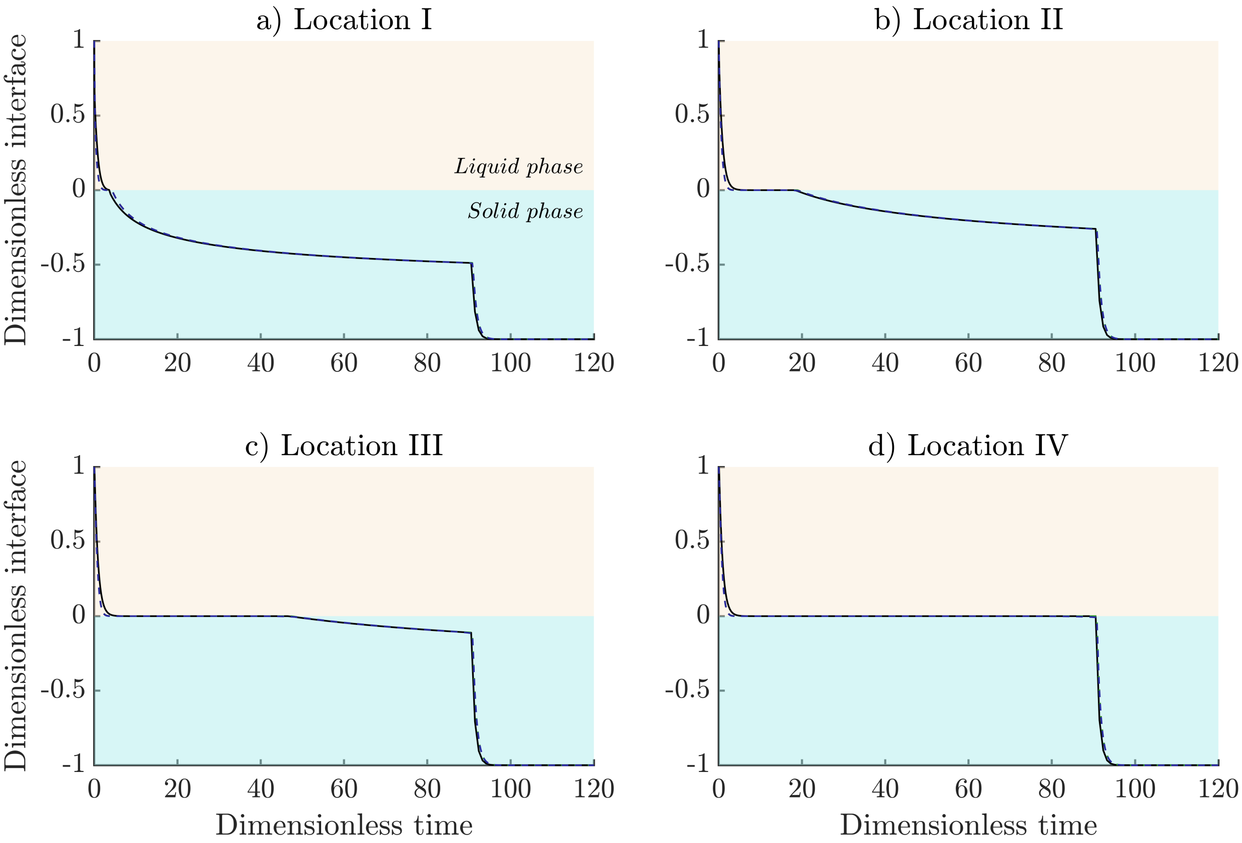

Figure 4.5: Comparisons between the sharp-interface (analytical) and mushy-region (numerical) models with different mushy-zone thicknesses in terms of temperature profile. The temperature profile is recorded at four locations: a) 25%, b) 50%, c) 75%, and d) 100% of the entire domain away from inner boundary. The analytical solution is given by the solid line, while numerical solution is given by the dashed lines.

−56.83%, while the thickness of mushy zones increases. However, the discrepancy remains the same at 0.31% between asymptotic and numerical (for solidus temperature) solutions in all mushy-zone thicknesses.

Figure 4.5 shows dimensionless temperature profile for the same comparison as in Figure 4.4. To verify the temperature profiles, four locations were chosen equally over the domain: a) 25%, b) 50%, c) 75%, and d) 100% of the domain away from the inner cylinder. As can be seen in Fig. 4.5, temperature distributions on three thicknesses of mushy zone were almost the same and overlapped with each other. This is because the interfaces on solidus temperature move in similar speeds as explained in Fig. 4.4. Recall that the solidus

Table 4.4: Comparisons between analytical and numerical solutions in regard to the computational time of total freezing time, interface motion, and temperature profile.

	Computational time	
	Analytical [minute : second]	Numerical [minute : second]
Total freezing time	instantaneously	01 : 39.78
Interface motion	00 : 00.69	01 : 39.78
Temperature profile	00 : 01.65	01 : 39.78

temperature is more crucial for interface tracking in freezing problems since the latent heat is fully contributed at this temperature. It can be concluded that mushy-zone thickness does not have much influence on the temperature when other parameters are fixed. Overall, the presented analytical solution has a strong agreement with numerical results in terms of temperature distributions, especially at the freezing stage.

With regards to computational cost, the numerical algorithm implemented in MATLAB (R2020a) computer programming language takes approximately 1 minute and a half for computing the total freezing time, interface motion, and temperature profile. The workstation has 2 cores, 4 logical processors, and 8GB of RAM; the optimal number of mesh elements is used as chosen in Section 4.7. Under the same computing environment, the analytical model takes well below 2 seconds for temperature and less than 1 second for the interface. This is because an explicit form of total freezing time has been obtained in the asymptotic analysis that can be computed instantaneously. Specific values of these computational times are recorded to compare the analytical and numerical models in Table 4.4, which illustrates the advantage of the analytical framework further. Moreover, the numerical time will increase along with number of mesh elements and time steps. Numerical instability will also occur as the thickness of mushy zone decreases. However, the only influential factor for analytical computation is the number of eigenvalues; in this case, the first five terms of eigenvalues guarantee convergence. Thus, it can be concluded that the computational time of analytical solution is less than 3% of the numerical algorithm.

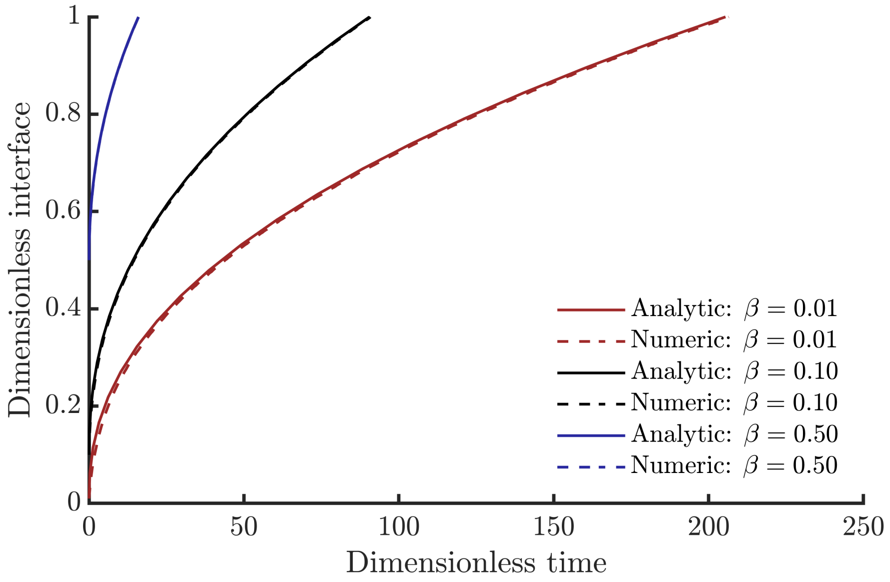

Figure 4.6: Dimensionless interface location over dimensionless time at three different geometric ratios: $\beta = 0.01, 0.10, 0.50$ in red, black and blue lines, respectively. The analytical solution is given by the solid lines, while numerical solution is given by the dashed lines.

4.6 Results and discussion

4.6.1 Effect of geometry

The moving boundary interface location over time at three different spatial dimensions is shown in Fig. 4.6. That is, three geometric ratios of inner radius over outer radius are taken into account (i.e., $\beta = 0.01, 0.10, 0.50$). These spatial dimensions are particularly chosen for typical engineering applications of artificial ground freezing [7, 5, 66] and thermal/cold energy storage systems [44]. As can be seen in Fig. 4.6, all analytical solutions agree very well with numerical results and the geometry is insensitive to the accuracy of analytical solution. The geometric ratio represents the relative size of inner boundary compared with the outer boundary. This ratio is found to have a negative influence on the moving interface. Therefore, it takes shorter time to freeze/melt the domain for a larger geometric ratio.

Figure 4.7 provides the dimensionless temperature profile at four evenly distributed points for the analytical and numerical solutions under the selected spatial dimensions. As explained

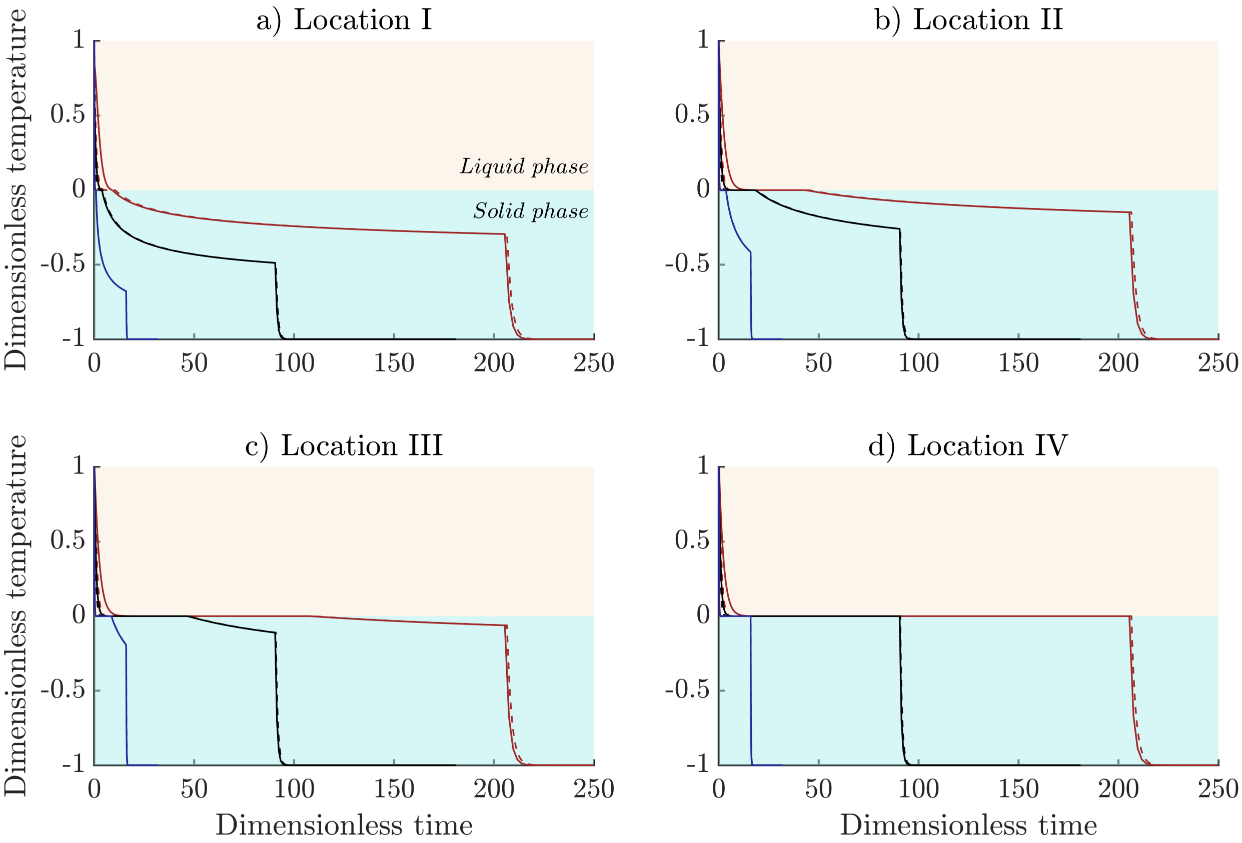

Figure 4.7: Dimensionless temperature profile at three different geometric ratios: $\beta = 0.01, 0.10, 0.50$ in red, black and blue lines, respectively. The temperature profile is recorded at four locations: a) 25%, b) 50%, c) 75%, and d) 100% of the entire domain away from inner boundary. The analytical solution is given by the solid lines, while numerical solution is given by the dashed lines.

by Fig. 4.5, the analytical results of temperature profile is consistent numerical solutions at all locations. It can be summarized that the accuracy of our asymptotic solution affects neither the interface motion nor temperature distributions. The temperature experiences a temporal delay as the geometric ratio decreases. This effect is particularly intensive during the freezing and cooling stages which leads to a longer total freezing time as illustrated in Fig. 4.6.

Table 4.5: Ratios of thermophysical properties in typical PCMs: organic, inorganic salts hydrates, and eutectic compounds [12, 48]. $L_{\mathrm{H_2O}}$ is the latent heat of fusion for pure water.

	$\widetilde{k} = k_s/k_\ell$	$\widetilde{c}_p = c_{p,s}/c_{p,\ell}$	$\widetilde{\rho} = \rho_s/\rho_\ell$	$L/L_{\mathrm{H_2O}}$
Organic	$1.09 - 2.21$	$0.56 - 1.50$	$1.05 - 1.18$	$0.47 - 1.15$
Inorganic	$1.21 - 2.62$	$0.48 - 0.83$	$1.06 - 1.13$	$0.37 - 1.00$
Eutectic Compound	$0.92 - 2.22$	$0.62 - 1.24$	$0.95 - 0.98$	$0.25 - 1.11$
Overall	$0.92 - 2.62$	$0.48 - 1.50$	$0.95 - 1.18$	$0.25 - 1.15$

4.6.2 Effect of phase-dependent thermophysical properties

Thermophysical properties of phase change materials (PCMs) have been studied extensively and experimental measurements of these properties are thoroughly documented in the literature. According to the reviews [12, 48], the ratios of solid phase over liquid phase in terms of thermal conductivity, specific heat, and mass density are calculated and categorized by organic, inorganic salt hydrate, and eutectic compounds PCMs, as listed in Table 4.5. These ranges of property ratios will be the guideline for making a realistic modeling in the subsequent analysis. It is worthwhile to notice that the ratio of mass density varies within a rather small range in PCMs (from 0.95 to 1.18). The effect of density change can be studied by a dual moving boundary problem [22, 3], which would incorporate the motion of the free surface due to density difference in the phases. However, this effect cannot be incorporated in the current setup since the radial surfaces in the annular PCMs (e.g., freeze pipes, heat exchangers) are immobilized by the bounding walls. The density difference would cause mechanical stresses in the frozen phase, but it is beyond the scope of our investigation. Further, the ratio of latent heat of fusion is divided by the latent heat for pure water ($L_{\mathrm{H_2O}}$) as a reference. The effect of latent heat along with the temperature difference will be studied in Section 4.6.3 because this will be one of the most influential parameters on the Stefan number.

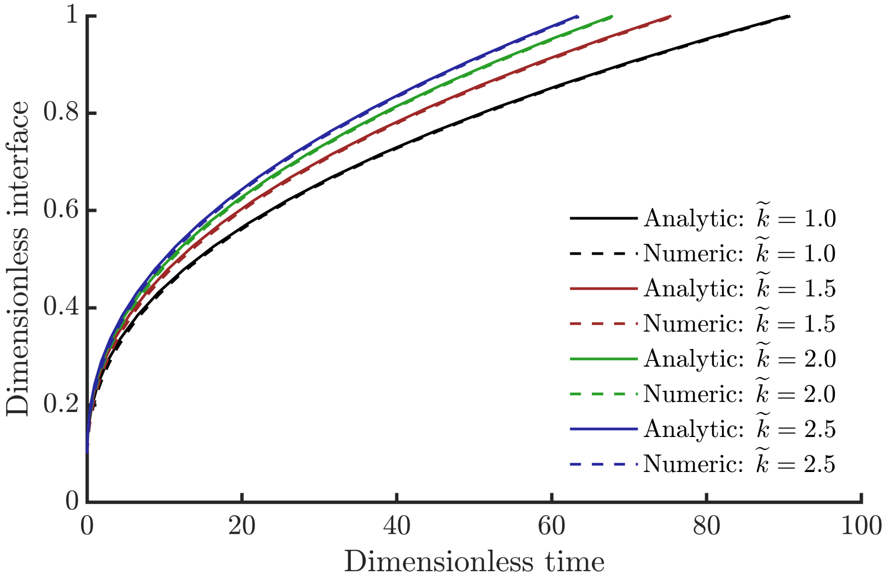

Figure 4.8: Dimensionless interface location over dimensionless time at four different thermal conductivity ratios: $\widetilde{k} = 1.0, 1.5, 2.0, 2.5$ in black, red, green and blue lines, respectively. The analytical solution is given by the solid lines, while numerical solution is given by the dashed lines.

Thermal conductivity

As can be seen in Table 4.5, the ratio of thermal conductivity of solid over liquid phase varies from 0.92 to 2.62 for most PCMs. Therefore, four ratios of thermal conductivity can be chosen within this calculated range (i.e., $\widetilde{k} = k_s/k_\ell = 1.0, 1.5, 2.0, 2.5$) to investigate the effect of thermal conductivity. Since the mass density and specific heat are sometimes assumed to be the same in both phases, similar ratio range has also been used for thermal diffusivity, which is the thermal conductivity divided by mass density and specific heat. However, in this study, the thermal conductivity and specific heat are phase-dependent and analyzed separately to extract more insights.

Figures 4.8 & 4.9 are the non-dimensionalized interface location and temperature profile for these ratios of thermal conductivity, respectively. Thermal conductivity gives a quantitative measure of a material's ability to conduct heat. The ratio of thermal conductivity of solid over liquid phase is therefore an implication of how fast the solidification process

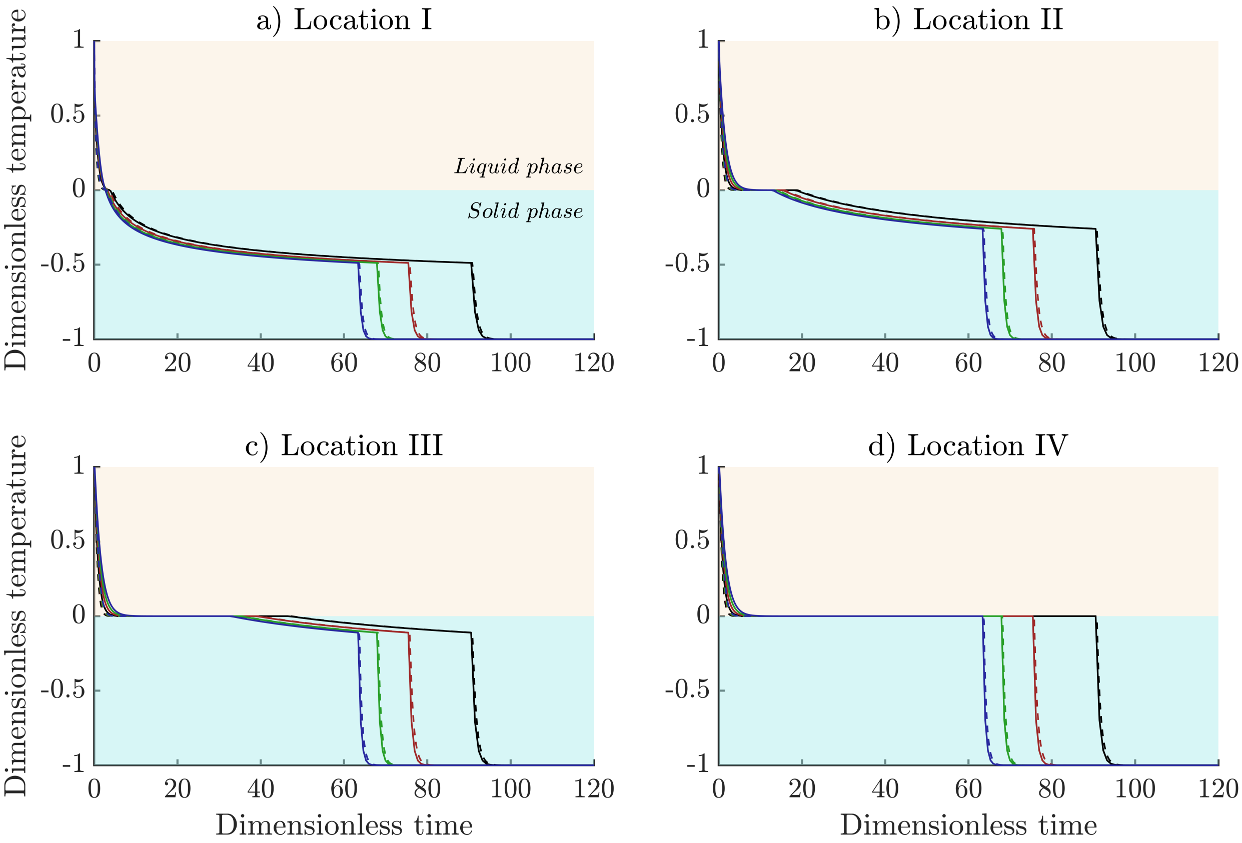

Figure 4.9: Dimensionless temperature profile at three different thermal conductivity ratios: $\widetilde{k} = 1.0, 1.5, 2.0, 2.5$ in black, red, green and blue lines, respectively. The temperature profile is recorded at four locations: a) 25%, b) 50%, c) 75%, and d) 100% of the entire domain away from inner boundary. The analytical solution is given by the solid lines, while numerical solution is given by the dashed lines.

occurs, i.e., the interface speed. The interface moves faster at a higher ratio of thermal conductivity, and consequently the temperature decays more rapidly as shown in Fig. 4.9. For example, when the ratio of thermal conductivity is doubled from $\widetilde{k} = 1$ to $\widetilde{k} = 2$, the interface and temperature are reduced by roughly 20%. It is worthy to mention that the agreement between the analytical and numerical results still holds under different thermal conductivities.

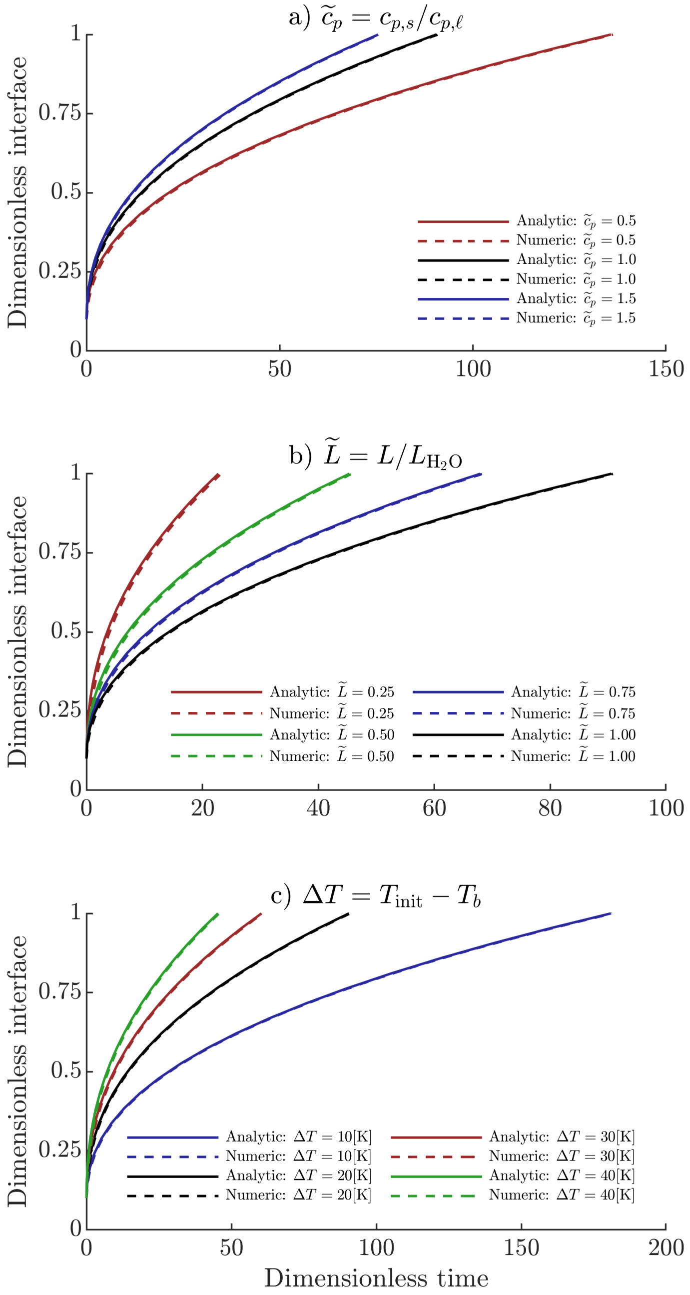

Figure 4.10: Dimensionless interface location over dimensionless time at various a) specific heat ratios ($\widetilde{c}_p$), b) latent heat of fusion ratios ($\widetilde{L}$), and c) temperature intervals (ΔT). Solid lines are analytical solutions and dashed lines are numerical results.

Specific heat

Figure 4.10a demonstrates dimensionless interface location over dimensionless time at various ratios of specific heat. As can be seen in Fig. 4.10a, three ratios of specific heat (i.e., $\widetilde{c_p} = c_{p,s}/c_{p,\ell} = 0.5, 1.0, 1.5$) are selected from a variety of PCMs listed in Table 4.5. Recall that the specific heat (capacity) is defined by the amount of heat required for a unit mass to increase one unit in temperature. If a material has a higher specific heat, then the material is more capable to raise its temperature per unit mass. In the context of solidification, the solid phase is dominant for the interface motion; a higher specific heat in the solid implies a faster interface motion (i.e., a shorter total freezing time). This expectation is consistent with the results in Figure 4.10a, since the ratio of specific heat is proportional to the solid specific heat.

4.6.3 Effect of Stefan numbers

Stefan number is a ratio of sensible heat over latent heat, i.e., $\mathrm{Ste} = \overline{c_p}\Delta T/L$. Consequently, all of the three parameters (averaged specific heat, total temperature interval and latent heat of fusion) need to be considered. It is expected that the discrepancy between analytical and numerical solutions may not be identical because the Stefan number governing the accuracy of the analytical solution varies. Since the difference between two solutions could not be apparent in the interface plots, a quantitative analysis on their deviations will be shown in the end.

First, the ratio of latent heat of a PCM over pure water (i.e., $L/L_{\mathrm{H_2O}}$) is studied as seen in Fig. 4.10b, and a series of values is examined within the range between 0.25 and 1.00 while maintaining the other parameters. The discrepancy between two solutions is fairly minimal, despite the fact that the Stefan number has been dropped from 0.08 to 0.02 as $\widetilde{L}$ rises. Secondly, several values of total temperature interval (i.e., $\Delta T = T_{\mathrm{init}} - T_b$) are investigated from 10 to 40 [K], as depicted in Fig. 4.10c. Since it takes more time for a lower

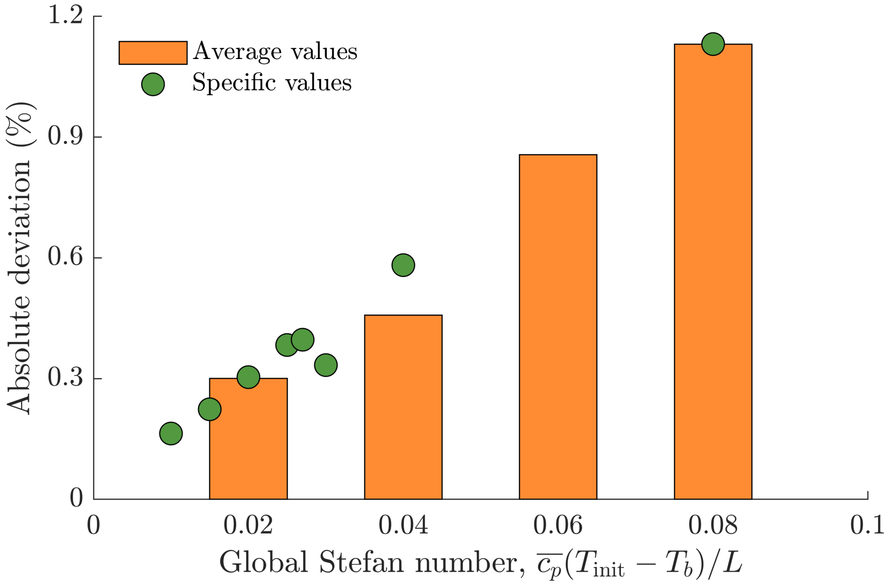

Figure 4.11: A graph of absolute deviation of the asymptotic solution in total freezing time over global Stefan number. This deviation is defined as $|(t_c - t_{c,2})/t_{c,2}| \times 100\%$, where $t_{c,2}$ is the total freezing time at solidus temperature.

temperature differential to freeze the domain, it is expected that the total freezing time decreases with the temperature interval. The developed asymptotic solution still agrees very well with numerical results in these temperature intervals.

Lastly, all the aforementioned data on specific heat, latent heat and total temperature interval are bundled together as a global Stefan number, $\overline{c_p}(T_{\text{init}} - T_b)/L$. This global Stefan number considers the average specific heat (i.e., $\overline{c_p} = (c_{p,s} + c_{p,\ell})/2$) and total temperature interval between two phases. A plot of absolute deviation of asymptotic solution in total freezing time over global Stefan number is shown in Fig. 4.11. Despite the fact that specific heat, temperature interval, and latent heat can all influence the precision of asymptotic solution, the global Stefan number is an overall indicator of solution's accuracy. As the global Stefan number increases, the deviation of asymptotic solution also increases, which could return a less accurate solution. It is found that the accuracy varies linearly (e.g., from 0.2% to 1.2%) for the Stefan number below 0.1, as illustrated in Fig. 4.11. The dominance of Stefan number to asymptotic solution is inevitable due to the truncation of asymptotic expansions in the analysis. However, for applications of PCMs, the small Stefan number approximation is intrinsic and offers a quite accurate solution (less than 1.2% deviation from numerical results).

4.7 Conclusion

An asymptotic solution to a two-phase Stefan problem in a hollow cylinder was developed to model outward solidification in phase change materials (PCMs). The approximate analytical solution was verified against numerical results by enthalpy method, and different mushy-zone thicknesses were investigated to reveal the differences between two mathematical frameworks of phase change (i.e., Stefan problems and enthalpy method). Further, a range of geometries, thermophysical properties and Stefan numbers were explored based on the PCMs measured in the literature. It can be therefore concluded that:

1) The asymptotic solution yielded by four spatial and three temporal scales (a.k.a., four layers and three regimes) can characterize the subcooling, freezing and cooling stages during solidification. This framework provides a guideline for solving other variations of Stefan problems by reflecting on the physical phenomenon;

2) The developed solution to Stefan problem modeled the same temperature profile (yet not interface motion) while comparing different mushy-zone thicknesses by enthalpy method. These comparisons between the Stefan problem and enthalpy method could have a significant impact on choosing a phase change model for the purpose of verification and validation;

3) The accuracy of the presented asymptotic solution is solely affected by the Stefan number due to its asymptotic limit. That is, the accuracy is not sensitive to geometry or thermal conductivity. As a result, this study offers an accurate and reliable asymptotic solution, particularly in the applications of PCMs; and

4) The presented model greatly reduces the computational time in enthalpy method, and the deviations between the asymptotic solution and numerical results are acceptable within the field of PCMs studied in the literature.

This study focused on the asymptotic analysis of a one-dimensional two-phase Stefan problem in a hollow cylinder subjected to a Dirichlet boundary condition. Higher dimensions, complex geometries and other boundaries (e.g., Neumann, Robin) could be investigated by conducting a similar asymptotic analysis in the future. Other recommendations for future studies include: modifying the parabolic heat equations into hyperbolic ones for non-Fourier heat conduction; adding mass diffusion equations to form an extended Stefan problem; and redefining the moving boundary to incorporate nonequilibrium interface kinetics.

Appendix A. Proof of liquid phase contribution to moving interface in Regime II Layer C

The liquid phase problem is

$$\mathrm{Ste}\frac{\partial\widetilde{\theta}_\ell}{\partial\widetilde{\tau}} = \frac{1}{\widetilde{\alpha}}\left(\frac{\partial^2\widetilde{\theta}_\ell}{\partial\xi^2} + \frac{1}{\xi}\frac{\partial\widetilde{\theta}_\ell}{\partial\xi}\right),\ \xi_i(\widetilde{\tau}) < \xi < 1, \tag{4.75}$$

$$\widetilde{\theta}_\ell(\xi_i(\widetilde{\tau}),\widetilde{\tau}) = 0, \tag{4.76}$$

$$\left.\frac{\partial\widetilde{\theta}_\ell}{\partial\xi}\right|_{\xi=1} = 0, \tag{4.77}$$

$$\widetilde{\theta}_\ell(\xi,0) = \theta_{\mathrm{init}}. \tag{4.78}$$

This problem was firstly solved by the method of composite asymptotic expansions in the Cartesian coordinates by Nayfeh [43], and similar method has also been applied to a sphere [37]. Here, we will closely follow the analytical procedure documented in [43].

Applying the method of composite expansions, we assume that $\widetilde{\theta}_\ell$ has a uniformly valid asymptotic expansion of the form

$$\widetilde{\theta}_\ell(\xi,\widetilde{\tau};\mathrm{Ste}) = \sum_{n=0}^{\infty}\mathrm{Ste}^n f_n(\xi,\widetilde{\tau}) + \exp\left[-\frac{g(\widetilde{\tau})}{\mathrm{Ste}}\right]\sum_{n=0}^{\infty}\mathrm{Ste}^n h_n(\xi,\widetilde{\tau}), \tag{4.79}$$

where the special function $\exp[-g(\widetilde{\tau})/\mathrm{Ste}]$ along with $g(\widetilde{\tau}) \to \widetilde{\tau}$ as $\widetilde{\tau} \to 0$ characterizes the initial behavior. This treatment is required, because the time derivative is multiplied by the perturbation parameter which cannot satisfy the initial condition.

For $n = 0$:

$$\begin{aligned}\mathrm{Ste}\left\{\frac{\partial f_0}{\partial\widetilde{\tau}} - \frac{g'(\widetilde{\tau})}{\mathrm{Ste}}\exp\left[-\frac{g(\widetilde{\tau})}{\mathrm{Ste}}\right]h_0 + \exp\left[-\frac{g(\widetilde{\tau})}{\mathrm{Ste}}\right]\frac{\partial h_0}{\partial\widetilde{\tau}}\right\} &= \\ \alpha\left\{\frac{\partial^2 f_0}{\partial\xi^2} + \exp\left[-\frac{g(\widetilde{\tau})}{\mathrm{Ste}}\right]\frac{\partial^2 h_0}{\partial\xi^2} + \frac{1}{\xi}\frac{\partial f_0}{\partial\xi} + \frac{1}{\xi}\exp\left[-\frac{g(\widetilde{\tau})}{\mathrm{Ste}}\right]\frac{\partial h_0}{\partial\xi}\right\}&.\end{aligned}$$

Equating the coefficients of Ste^0 and $\mathrm{Ste}^0\exp[-g(\widetilde{\tau})/\mathrm{Ste}]$, we have

$$\frac{\partial^2 f_0}{\partial\xi^2} + \frac{1}{\xi}\frac{\partial f_0}{\partial\xi} = 0 \tag{4.80}$$

$$\frac{\partial^2 h_0}{\partial\xi^2} + \frac{1}{\xi}\frac{\partial h_0}{\partial\xi} + \widetilde{\alpha}g'(\widetilde{\tau})h_0 = 0 \tag{4.81}$$

subject to

$$f_0(\xi_i(\widetilde{\tau}),\widetilde{\tau}) = 0, \qquad \left.\frac{\partial f_0}{\partial\xi}\right|_{\xi=1} = 0, \qquad h_0(\xi_i(\widetilde{\tau}),\widetilde{\tau}) = 0, \qquad \left.\frac{\partial h_0}{\partial\xi}\right|_{\xi=1} = 0. \tag{4.82}$$

and

$$f_0(\xi,0) + h_0(\xi,0) = \theta_{\mathrm{init}}. \tag{4.83}$$

Firstly, the solution to f_0 is $f_0 = 0$. Then, the equation for h_0 has a nontrivial solution if and only if g' is one of the eigenvalues

$$g'_k = \frac{1}{\widetilde{\alpha}}\left[\frac{k\pi}{\xi_i(\widetilde{\tau})}\right]^2,\ k = 1, 2, 3, ... \tag{4.84}$$

Substituting these eigenvalues, we find

$$h_0 = a_0(\widetilde{\tau})\chi_k(\xi, \widetilde{\tau}), \tag{4.85}$$

where the eigenfunction, χ_k, can be found by

$$\chi_k = C_k\left[J_0(k\pi)Y_0\left(\frac{k\pi\xi}{\xi_i}\right) - J_0\left(\frac{k\pi\xi}{\xi_i}\right)Y_0(k\pi)\right], \tag{4.86}$$

and ξ_i is determined by the following transcendental equation

$$J_1\left(\frac{k\pi}{\xi_i}\right)Y_0(k\pi) - J_0(k\pi)Y_1\left(\frac{k\pi}{\xi_i}\right) = 0,\ \text{for } \xi_i \neq 0. \tag{4.87}$$

Note that the undetermined variable, $a_0(\widetilde{\tau})$, will be proved to be a constant after analyzing the equation for h_1 by orthogonality. Similar to the analysis in Nayfeh [43], this constant will be merged into the coefficient C_k in χ_k. Substituting the solutions of f_0 and h_0 into $\widetilde{\theta}_\ell$, we can write the leading order solution for the eigenvalue term $k = 1$:

$$\begin{aligned}\widetilde{\theta}_\ell(\xi, \widetilde{\tau}; \mathrm{Ste}) \sim &\sum_{k=0}^{\infty} C_k\left[J_0(k\pi)Y_0\left(\frac{k\pi\xi}{\xi_i}\right) - J_0\left(\frac{k\pi\xi}{\xi_i}\right)Y_0(k\pi)\right]\exp\left[-\frac{k^2\pi^2}{\widetilde{\alpha}\mathrm{Ste}}\int_0^{\widetilde{\tau}}\frac{1}{\xi_i(\zeta)^2}\mathrm{d}\zeta\right]\\ &+ O(\mathrm{Ste}),\end{aligned}$$

where ξ_i is determined by the following transcendental equation (4.87) and C_k is given by applying the initial condition

$$C_k = \frac{\int_{\xi=0}^{\xi_i} \xi \theta_{\mathrm{init}} \left[J_0(k\pi) Y_0\left(\frac{k\pi\xi}{\xi_i}\right) - J_0\left(\frac{k\pi\xi}{\xi_i}\right) Y_0(k\pi) \right] \mathrm{d}\xi}{\int_{\xi=0}^{\xi_i} \xi \left[J_0(k\pi) Y_0\left(\frac{k\pi\xi}{\xi_i}\right) - J_0\left(\frac{k\pi\xi}{\xi_i}\right) Y_0(k\pi) \right]^2 \mathrm{d}\xi}. \tag{4.88}$$

Its derivative at the interface becomes

$$\begin{aligned} \frac{\partial \widetilde{\theta}_\ell}{\partial \xi}\bigg|_{\xi=\xi_i} &\sim \sum_{k=0}^{\infty} C_k \frac{k\pi}{\xi_i} \Big[J_1(k\pi) Y_0(k\pi) - J_0(k\pi) Y_1(k\pi) \Big] \exp\left[-\frac{k^2\pi^2}{\widetilde{\alpha}\mathrm{Ste}} \int_0^{\widetilde{\tau}} \frac{1}{\xi_i(\zeta)^2} \mathrm{d}\zeta \right] \\ &\sim \sum_{k=0}^{\infty} \frac{2C_k}{\pi \xi_i} \exp\left[-\frac{k^2\pi^2}{\widetilde{\alpha}\mathrm{Ste}} \int_0^{\widetilde{\tau}} \frac{1}{\xi_i(\zeta)^2} \mathrm{d}\zeta \right]. \end{aligned}$$

As can be seen, the liquid phase is now proved to have an exponentially small contribution to the interface motion as Ste → 0. Same conclusions have been drawn in the Cartesian [43] and spherical [37] coordinates.

Appendix B. Mesh independence study

Five different numbers of mesh elements (N_{node}) are studied under same scenario (as shown in Figure 4.4) and computational environment. The objectives of this mesh independence study are: i) to select the optimal number of nodes; and ii) to use the optimal mesh as a reference to compare the computational time against analytical solution. Figure 4.12 demonstrates the dimensionless interface motion measured on the solidus and liquidus temperatures among five mesh counts. It is quite evident that the fourth and fifth mesh counts (i.e., $N_{\mathrm{node}} = 6 \times 10^2,\ 1 \times 10^3$) yield similar results, which implies that the number of mesh elements is no longer dependent when $N_{\mathrm{node}} > 6 \times 10^2$. The fourth mesh count is therefore chosen for the model verification and parametric studies.

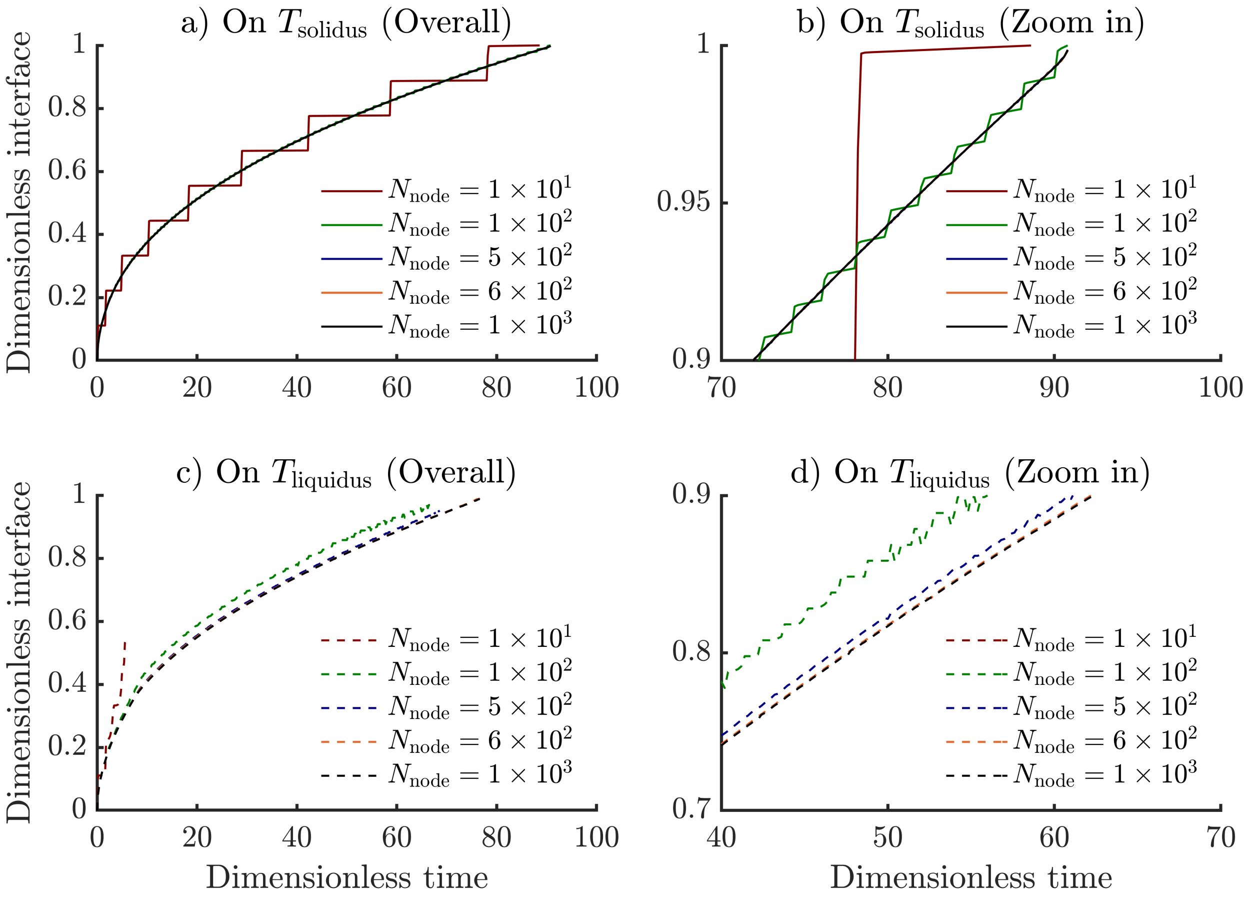

Figure 4.12: Comparisons among various node numbers in regard to interface motion monitored on the solidus and liquidus temperatures for the case: $\widetilde{k} = \widetilde{c}_p = 1.0,\ \beta = 0.1,\ \theta_{\text{init}} = 1,\ \text{Ste} = 0.01,\ \Delta T_{\text{mushy}} = 10^{-2}$ [K]. Solid lines are for interfaces on solidus temperature and dashed lines are for the ones on liquidus temperature.

Bibliography

[1] S. Akhtar, M. Xu, and A. Sasmito. Verification and validation of droplet freezing for convective boundary condition using matched asymptotic perturbation method and computational fluid dynamics. In *ASME International Mechanical Engineering Congress and Exposition*, volume 59452, page V008T09A053. American Society of Mechanical Engineers, 2019.

[2] S. Akhtar, M. Xu, and A. P. Sasmito. Development and validation of a semi-analytical framework for droplet freezing with heterogeneous nucleation and non-linear interface kinetics. *International Journal of Heat and Mass Transfer*, 166:120734, 2021.

[3] V. Alexiades. *Mathematical modeling of melting and freezing processes.* CRC Press, 1992.

[4] H. M. Ali, M. M. Janjua, U. Sajjad, W.-M. Yan, et al. A critical review on heat transfer augmentation of phase change materials embedded with porous materials/foams. *International Journal of Heat and Mass Transfer*, 135:649–673, 2019.

[5] M. A. Alzoubi, A. Madiseh, F. P. Hassani, and A. P. Sasmito. Heat transfer analysis in artificial ground freezing under high seepage: Validation and heatlines visualization. *International Journal of Thermal Sciences*, 139:232–245, 2019.

[6] M. A. Alzoubi, A. Nie-Rouquette, S. A. Ghoreishi-Madiseh, F. P. Hassani, and A. P. Sasmito. On the concept of the freezing-on-demand (FoD) in artificial ground freezing for long-term applications. *International Journal of Heat and Mass Transfer*, 143:118557, 2019.

[7] M. A. Alzoubi, A. Nie-Rouquette, and A. P. Sasmito. Conjugate heat transfer in artificial ground freezing using enthalpy-porosity method: Experiments and model validation. *International Journal of Heat and Mass Transfer*, 126:740–752, 2018.

[8] M. A. Alzoubi, M. Xu, F. P. Hassani, S. Poncet, and A. P. Sasmito. Artificial ground freezing: A review of thermal and hydraulic aspects. *Tunnelling and Underground Space Technology*, 104:103534, 2020.

[9] J. Bollati, J. Semitiel, and D. A. Tarzia. Heat balance integral methods applied to the one-phase Stefan problem with a convective boundary condition at the fixed face. *Applied Mathematics and Computation*, 331:1–19, 2018.

[10] F. Brosa Planella, C. P. Please, and R. A. Van Gorder. Extended Stefan problem for solidification of binary alloys in a finite planar domain. *SIAM Journal on Applied Mathematics*, 79(3):876–913, 2019.

[11] F. Brosa Planella, C. P. Please, and R. A. Van Gorder. Extended Stefan problem for the solidification of binary alloys in a sphere. *European Journal of Applied Mathematics*, page 1–38, 2020.

[12] L. F. Cabeza, A. Castell, C. Barreneche, A. De Gracia, and A. I. Fernández. Materials used as PCM in thermal energy storage in buildings: A review. *Renewable and Sustainable Energy Reviews*, 15(3):1675–1695, 2011.

[13] M. Calvo-Schwarzwälder. Non-local effects and size-dependent properties in Stefan problems with Newton cooling. *Applied Mathematical Modelling*, 76:513–525, 2019.

[14] M. Calvo-Schwarzwälder, T. G. Myers, and M. G. Hennessy. The one-dimensional Stefan problem with non-Fourier heat conduction. *International Journal of Thermal Sciences*, 150:106210, 2020.

[15] H. S. Carslaw and J. C. Jaeger. *Conduction of heat in solids*. Clarendon press, 1992.

[16] A. N. Ceretani, N. N. Salva, and D. A. Tarzia. Approximation of the modified error function. *Applied Mathematics and Computation*, 337:607–617, 2018.

[17] P. Ding and Z. Liu. Accelerating phase-field modeling of solidification with a parallel adaptive computational domain approach. *International Communications in Heat and Mass Transfer*, 111:104452, 2020.

[18] M. Faden, A. König-Haagen, and D. Brüggemann. An optimum enthalpy approach for melting and solidification with volume change. *Energies*, 12(5):868, 2019.

[19] D. L. Feltham and J. Garside. Analytical and numerical solutions describing the inward solidification of a binary melt. *Chemical Engineering Science*, 56(7):2357–2370, 2001.

[20] B. Florio and T. Myers. The melting and solidification of nanowires. *Journal of Nanoparticle Research*, 18(6):168, 2016.

[21] F. Font. A one-phase Stefan problem with size-dependent thermal conductivity. *Applied Mathematical Modelling*, 63:172–178, 2018.

[22] F. Font, T. Myers, and S. Mitchell. A mathematical model for nanoparticle melting with density change. *Microfluidics and Nanofluidics*, 18(2):233–243, 2015.

[23] T. R. Goodman. The heat balance integral and its application to problems involving change of phase. *ASME Journal of Heat Transfer*, 80:335, 1958.

[24] L. Guo, Z. Zhang, X. Wang, Q. Yu, Y. You, C. Yuan, Y. Xie, and T. Gou. Stability analysis of transmission tower foundations in permafrost equipped with thermosiphons and vegetation cover on the Qinghai-Tibet Plateau. *International Journal of Heat and Mass Transfer*, 121:367–376, 2018.

[25] S. C. Gupta. *The classical Stefan problem: Basic concepts, modelling and analysis with quasi-analytical solutions and methods*, volume 45. Elsevier, 2017.

[26] D. W. Hahn and M. N. Özisik. *Heat conduction.* John Wiley & Sons, 2012.

[27] M. G. Hennessy, M. Calvo-Schwarzwälder, and T. G. Myers. Modelling ultra-fast nanoparticle melting with the Maxwell-Cattaneo equation. *Applied Mathematical Modelling*, 69:201–222, 2019.

[28] J. M. Hill. *One-dimensional Stefan problems: An introduction.* Longman Scientific & Technical, 1987.

[29] M. A. Jaafar, D. R. Rousse, S. Gibout, and J.-P. Bédécarrats. A review of dendritic growth during solidification: Mathematical modeling and numerical simulations. *Renewable and Sustainable Energy Reviews*, 74:1064–1079, 2017.

[30] L. M. Jiji and S. Weinbaum. Perturbation solutions for melting or freezing in annular regions initially not at the fusion temperature. *International Journal of Heat and Mass Transfer*, 21(5):581–592, 1978.

[31] M. Z. Khalid, M. Zubair, and M. Ali. An analytical method for the solution of two phase Stefan problem in cylindrical geometry. *Applied Mathematics and Computation*, 342:295–308, 2019.

[32] A. Kumar. A Stefan problem with moving phase change material, variable thermal conductivity and periodic boundary condition. *Applied Mathematics and Computation*, 386:125490, 2020.

[33] J. Kyselica, P. Guba, and M. Chudjak. Recalescence dynamics and solidification of a supercooled melt in a finite domain. *International Journal of Heat and Mass Transfer*, 159:120048, 2020.

[34] J. Lee and G. Son. A sharp-interface level-set method for compressible bubble growth with phase change. *International Communications in Heat and Mass Transfer*, 86:1–11, 2017.

[35] J. López, P. Gómez, and J. Hernández. A volume of fluid approach for crystal growth simulation. *Journal of Computational Physics*, 229(19):6663–6672, 2010.

[36] S. W. McCue, J. R. King, and D. S. Riley. Extinction behaviour for two–dimensional inward-solidification problems. *Proceedings of the Royal Society of London. Series A: Mathematical, Physical and Engineering Sciences*, 459(2032):977–999, 2003.

[37] S. W. McCue, B. Wu, and J. M. Hill. Classical two-phase Stefan problem for spheres. *Proceedings of the Royal Society A: Mathematical, Physical and Engineering Sciences*, 464(2096):2055–2076, 2008.

[38] S. W. McCue, B. Wu, and J. M. Hill. Micro/nanoparticle melting with spherical symmetry and surface tension. *IMA Journal of Applied Mathematics*, 74(3):439–457, 2009.

[39] S. L. Mitchell and T. Myers. Improving the accuracy of heat balance integral methods applied to thermal problems with time dependent boundary conditions. *International Journal of Heat and Mass Transfer*, 53(17-18):3540–3551, 2010.

[40] S. L. Mitchell and T. G. Myers. Application of standard and refined heat balance integral methods to one-dimensional Stefan problems. *SIAM Review*, 52(1):57–86, 2010.

[41] T. Myers. Optimal exponent heat balance and refined integral methods applied to Stefan problems. *International Journal of Heat and Mass Transfer*, 53(5-6):1119–1127, 2010.

[42] T. Myers and S. L. Mitchell. Application of the combined integral method to stefan problems. *Applied Mathematical Modelling*, 35(9):4281–4294, 2011.

[43] A. H. Nayfeh. *Perturbation methods*. John Wiley & Sons, 2008.

[44] H. Nazir, M. Batool, F. J. B. Osorio, M. Isaza-Ruiz, X. Xu, K. Vignarooban, P. Phelan, A. M. Kannan, et al. Recent developments in phase change materials for energy storage applications: A review. *International Journal of Heat and Mass Transfer*, 129:491–523, 2019.

[45] S. Osher and J. A. Sethian. Fronts propagating with curvature-dependent speed: Algorithms based on Hamilton-Jacobi formulations. *Journal of Computational Physics*, 79(1):12–49, 1988.

[46] M. Parang, D. Crocker, and B. Haynes. Perturbation solution for spherical and cylindrical solidification by combined convective and radiative cooling. *International Journal of Heat and Fluid Flow*, 11(2):142–148, 1990.

[47] R. Pedroso and G. Domoto. Perturbation solutions for spherical solidification of saturated liquids. *ASME Journal of Heat Transfer*, 95(1):42–46, 02 1973.

[48] J. Pereira da Cunha and P. Eames. Thermal energy storage for low and medium temperature applications using phase change materials - A review. *Applied Energy*, 177:227–238, 2016.

[49] N. Provatas and K. Elder. *Phase-field methods in materials science and engineering.* John Wiley & Sons, 2011.

[50] H. Ribera, T. G. Myers, and M. M. MacDevette. Optimising the heat balance integral method in spherical and cylindrical Stefan problems. *Applied Mathematics and Computation*, 354:216–231, 2019.

[51] D. Riley, F. Smith, and G. Poots. The inward solidification of spheres and circular cylinders. *International Journal of Heat and Mass Transfer*, 17(12):1507–1516, 1974.

[52] M. Sheikholeslami and O. Mahian. Enhancement of PCM solidification using inorganic nanoparticles and an external magnetic field with application in energy storage systems. *Journal of Cleaner Production*, 215:963–977, 2019.

[53] A. Soward. A unified approach to Stefan's problem for spheres and cylinders. *Proceedings of the Royal Society of London. A. Mathematical and Physical Sciences*, 373(1752):131–147, 1980.

[54] C. Swaminathan and V. R. Voller. A general enthalpy method for modeling solidification processes. *Metallurgical Transactions B*, 23(5):651–664, 1992.

[55] S. Tabakova, F. Feuillebois, and S. Radev. Freezing of a supercooled spherical droplet with mixed boundary conditions. *Proceedings of the Royal Society A: Mathematical, Physical and Engineering Sciences*, 466(2116):1117–1134, 2010.

[56] V. Voller and M. Cross. Accurate solutions of moving boundary problems using the enthalpy method. *International Journal of Heat and Mass Transfer*, 24(3):545–556, 1981.

[57] V. Voller and M. Cross. An explicit numerical method to track a moving phase change front. *International Journal of Heat and Mass Transfer*, 26(1):147–150, 1983.

[58] A. Wallman, J. King, and D. Riley. Asymptotic and numerical solutions for the two-dimensional solidification of a liquid half-space. *Proceedings of the Royal Society of London. Series A: Mathematical, Physical and Engineering Sciences*, 453(1962):1397–1410, 1997.

[59] S. Weinbaum and L. M. Jiji. Singular perturbation theory for melting or freezing in finite domains initially not at the fusion temperature. *Journal of Applied Mechanics, Transactions ASME*, 44(1):25–30, 1977.

[60] J. A. Wilson, M. Haghshenas, and R. Kumar. Phase-change mechanism for evaporation in porous media using volume of fluid: Implicit formulation of interfacial temperature. *International Communications in Heat and Mass Transfer*, 103:90–99, 2019.

[61] B. Wu, S. W. McCue, P. Tillman, and J. M. Hill. Single phase limit for melting nanoparticles. *Applied Mathematical Modelling*, 33(5):2349–2367, 2009.

[62] M. Xu, S. Akhtar, M. A. Alzoubi, and A. P. Sasmito. Singular perturbation solution for a two-phase Stefan problem in outward solidification. In *ASME International Mechanical Engineering Congress and Exposition*, volume 59452, page V008T09A050. American Society of Mechanical Engineers, 2019.

[63] M. Xu, S. Akhtar, A. F. Zueter, V. Auger, M. A. Alzoubi, and A. P. Sasmito. Development of analytical solution for a two-phase Stefan problem in artificial ground freezing using singular perturbation theory. *Journal of Heat Transfer*, 142(12):122401, 2020.

[64] Z. Yan, M. Zhang, Y. Lai, W. Pei, T. Luo, F. Yu, and S. Yang. Countermeasures combined with thermosyphons against the thermal instability of high-grade highways in permafrost regions. *International Journal of Heat and Mass Transfer*, 153:119047, 2020.

[65] M. Zhang, W. Pei, Y. Lai, F. Niu, and S. Li. Numerical study of the thermal characteristics of a shallow tunnel section with a two-phase closed thermosyphon group in a permafrost region under climate warming. *International Journal of Heat and Mass Transfer*, 104:952–963, 2017.

[66] J. Zhou, W. Zhao, and Y. Tang. Practical prediction method on frost heave of soft clay in artificial ground freezing with field experiment. *Tunnelling and Underground Space Technology*, 107:103647, 2021.

[67] A. Zueter, A. Nie-Rouquette, M. A. Alzoubi, and A. P. Sasmito. Thermal and hydraulic analysis of selective artificial ground freezing using air insulation: Experiment and modeling. *Computers and Geotechnics*, 120:103416, 2020.

Chapter 5

Asymptotic analysis of a two-phase Stefan problem in an annulus with the convective boundary

Contents

Preface (Bridging Text)

In Chapter 4, phase change materials (PCMs) were modeled with a fast-to-compute and easy-to-implement analytical solution, which facilitated the thermal estimation of cold thermal energy storage with thermosiphons for mining in the North. Specifically, an asymptotic solution to a two-phase Stefan problem was derived, encompassing multiple spatial and temporal scales, which extended the spatiotemporal resolution of the singular perturbation theory in the previous chapter.

Nevertheless, a major assumption in the problem formulation is that the solid-liquid interface will move instantaneously with time, rendering a relatively ideal isothermal condition. A more realistic scenario in practice would be a convective one that depends on the thermal and flow conditions of the heat transfer fluid, as well as its response to climatic conditions, such as wind speed, which could significantly affect energy storage. In this case, the interface would not be assumed or required to move instantly; instead, the pre-cooling time should depend on the heat transfer fluid and climatic conditions.

In this chapter, a Robin or convective boundary for the two-phase Stefan problem was explored. This introduced significant complexity to the mathematical problem and asymptotic analysis, as the interface did not move instantaneously with time. Through systematic asymptotic analysis, four temporal and five spatial scales were identified and resolved. Furthermore, the impact of Biot and Stefan numbers was investigated, which fundamentally govern the solidification process.

The outcome of this study, from the applied aspect, characterized the effect of climatic conditions, including wind velocity and air temperature, through the convective heat transfer at the PCM's surface (which was fundamentally quantified as the Biot number). This provided a realistic and computationally efficient estimation of PCM energy storage in terms of charging time, temperature profile, and interface motion. The insights and discussions presented in this chapter were published in the peer-reviewed journal article listed below.

M. Xu, S. Akhtar, M. Mohit, A. F. Zueter, and A. P. Sasmito. Asymptotic analysis of a two-phase Stefan problem in an annulus with the convective boundary. *International Journal of Thermal Sciences*, 196:108744, 2024.

Abstract

The Stefan problem (whether in its classical form or not) has assumed that the interface moves instantaneously with time as a prescribed initial condition. This assumption is valid in the problems subjected to an isothermal boundary. Yet, it may not represent the physics for a convective boundary since a certain amount of time is needed to cool or melt the convective surface to its fusion depending on the heat transfer coefficient (or Biot number in a dimensionless way). In this study, we formulate a two-phase Stefan problem in an annulus for outward solidification subjected to a convective or Robin boundary condition while not assuming that the interface moves right away at time $t = 0$. A comprehensive asymptotic analysis is performed by expanding around a small Stefan number; four spatial and five temporal scales are characterized based on the Stefan problems involving a convective surface. The method of property averaging is also employed at the scale where the equilibrium freezing occurs. The developed asymptotic solution is verified with numerical data generated by the enthalpy method at various Biot and Stefan numbers. The results demonstrate the significance of abandoning the initial assumption (i.e., the interface does not move immediately with time), especially towards small Biot numbers. Further, it is found that the presented asymptotic solution considerably extends the valid range of the Stefan number when compared with the conventional asymptotic technique.

Keywords: Stefan problem, Robin boundary condition, asymptotic analysis, solidification, phase change heat transfer

5.1 Introduction

A fundamental understanding of phase change heat transfer between solid and liquid states (also referred to as melting and freezing) can facilitate many applications. These applications include but are not limited to thawing and degradation of permafrost soils [35, 13, 39], melting process in polymer and metal 3D printing [26, 24, 16, 25], droplet and spray freezing [3, 2, 12], freeze-drying technology of biological materials [38, 11, 14], artificial ground freezing for stabilization [55, 61, 4], continuous casting of binary alloys [48, 49], and (cold) thermal energy storage systems using phase change materials (PCM) [37, 29, 56]. There are a variety of mathematical modeling approaches, such as the front-tracking method, enthalpy method, heat capacity method, level set method, and phase field method. The front-tracking method, in particular, has been historically studied since the establishment of the so-called *Stefan problem* by G. Lamé and B.P. Clapeyron in 1831 [28], but it still perplexes mathematicians and natural scientists. The problem introduces an energy balance of sensible and latent heat at the interface between the two phases, namely the Stefan condition. The general form of this Stefan condition can be expressed as

$$\underbrace{\rho L v}_{\text{latent heat}} = \underbrace{\Big[\vec{q}\cdot\vec{n}\Big]_{\text{solid}}^{\text{liquid}}}_{\text{sensible heat}}, \tag{5.1}$$

where $\rho, L, v, \vec{q}, \vec{n}$ are the mass density, latent heat, interface velocity, heat flux, and normal vector, respectively. However, the Stefan condition can also have an alternative form that takes into account the Gibbs-Thomson effect, implying that the freezing or equilibrium temperature at the curved surface is higher than that at the planar surface [52, 15, 18].

Some Stefan problems possess self-similar solutions that are exact. By introducing a single similarity variable such as $x/t^{\frac{1}{2}}$, the spatial and temporal independent variables (i.e., x and t, respectively) are merged, thus obtaining an exact solution. However, self-similar solutions only apply to idealized situations, restricting the domain, coordinate(s), and boundary conditions into specific combinations. Most of these self-similar solutions can be found in the texts [20, 19] and references thereinafter. New development of self-similar solutions includes: power-type latent heat problems with Kummer functions [60, 5, 59, 6, 58], fractional Stefan problems for extreme diffusion behaviors [45, 27, 36], and problems with non-linear diffusivities or thermal conductivities [7, 44, 10].

When the exact solution cannot be found or does not exist, approximate analytical or semi-analytical methods are largely employed. The perturbation method, also referred to as asymptotic analysis, is the primary approximate technique for solving the Stefan problems, which often uses the intrinsically small Stefan number (i.e., $\mathrm{Ste} \ll 1$) as the asymptotic limit to assume an asymptotic expansion. The complex Stefan problem with the partial differential equation (PDE) and the non-linear moving boundary is then broken down into several ordinary differential equations (ODEs) that are comparatively easy to solve. Hill's book [20] summarized perturbation solutions to one-dimensional one-phase classical Stefan problems with Dirichlet and Robin boundaries that are time-independent. Recent development emphasizes perturbation solutions to the problems with a time-dependent temperature [9] or heat flux [33, 22], thus taking into account the periodic charging-discharging behavior in energy storage. When the second phase is not assumed to be at its fusion/melting point, the Stefan problem becomes a two-phase one, making the Stefan condition for the moving interface more non-linear than before. Weinbaum and Jiji applied the singular perturbation method along with the boundary-fixing technique to a finite planar domain and captured the subcooling behavior by introducing a shorter temporal scale (a.k.a., inner solution), while the unstretched scale (a.k.a., outer solution) reduced to a one-phase problem [51]. Similar methodologies were also used to solve inward [23] and outward solidification [53] in an annular domain, and inward solidification in spheres [1, 3]. Recently, Wang et al. [50] developed an asymptotic solution for the solidification of nano-capsules, incorporating the Gibbs-Thomson effect and a convective term during phase change. It is noted that all the studies mentioned above considered two temporal scales.

McCue et al. [30] analyzed four temporal scales along with small-time and slow (thermal) diffusion limits for inward solidification in spheres. Xu et al. [54] performed an asymptotic analysis of a two-phase Stefan problem in a hollow cylinder, characterizing three distinct temporal and four spatial scales. The classical two-phase Stefan problems can also be coupled with mass diffusion equations for both phases, namely extended Stefan problems [19]. These problems were recently studied by asymptotic analysis for modeling the solidification of binary alloys in finite planar [8], and spherical domains [34]. Nevertheless, it is worthwhile mentioning that the asymptotic solutions to these two-phase problems are mostly subjected to a constant temperature boundary.

Most studies on analytical solutions to two-phase Stefan problems focus on formulating a Dirichlet or first-type boundary condition with a constant temperature. The consideration of realistic boundaries based on Newton's law of cooling, also known as the convective, mixed, or third-type boundary condition, is still missing. Tarzia and Turner studied the pre-cooling time for a heat flux condition or a convective boundary in the one-dimensional Cartesian [42] and spherical [43] coordinates. A time-dependent convective boundary condition in a one-dimensional semi-infinite domain was investigated in [41]. Nevertheless, the convective boundary in the cylindrical coordinates has profound practical applications, such as the outward freezing of a circular pipe. As a consequence, the asymptotic solution to a two-phase Stefan problem in an annulus with a convective boundary condition can be in great demand.

Another research gap is on the approach to finding the moving interface for two-phase Stefan problems in asymptotic analysis. To our knowledge, most solutions of interface motion for two-phase problems in the literature have been primarily obtained by reducing them into one-phase problems. Though some effort was made to match the start and end behaviors with the one-phase interface, the overall evolution of the interface is still dominated by one phase. Hence, it lacks information of the second phase when both phases exist and can vastly overestimate the interface motion as the Stefan number increases. In this study, we perform an asymptotic analysis for a two-phase Stefan problem subjected to a convective boundary in an annulus for outward solidification. The analysis consists of four distinct temporal scales (called *regimes*) and five spatial scales (called *layers*) and includes regular and matched asymptotic expansions based on a small Stefan number limit as well as the method of property averaging for larger Stefan numbers. The developed solution applies to small Stefan numbers and all Biot numbers. Further, the result of interface motion also takes account of both phases during freezing owing to the property averaging.

The paper is structured as follows. Section 5.2 begins with the mathematical formulation of the Stefan problem (including governing equations, boundary conditions, and time conditions) along with assumptions. The problem is then nondimensionalized, and key dimensionless numbers (such as Stefan and Biot) are introduced. Section 5.3 demonstrates the asymptotic analysis performed to solve the Stefan problem. Every regime and layer are solved mathematically with physical insights. A well-established numerical scheme is briefly presented in Section 5.4 to be used to verify the presented analytical solution in the following section. Section 5.5 shows the effect of Stefan and Biot numbers on the asymptotic solution with the numerical results. Section 5.6 concludes this work's main findings and importance and summarizes some potential future research directions for Stefan problems.

5.2 Mathematical modeling

We consider a commonly used annulus PCM with a realistic convective boundary at the inner surface due to a heat transfer fluid (HTF) or refrigerant operating inside. On the other hand, an insulated outer surface is prescribed, as schematically illustrated in Fig. 5.1(a). The PCM is initially at its liquid state, i.e., at a constant temperature higher than its fusion, but the colder HTF makes the PCM freeze as time passes. Figure 5.1(b) shows the freezing stages in chronological order. Here, the key assumptions are listed as follows:

1) Heat conduction prevails over other modes of heat transfer and physical fields within

the PCM which is the domain of the problem.

2) The freezing process of this PCM is considered to happen in a one-dimensional cylindrical coordinate and at the macro-scale. That is, there are no meso- and micro-scale phenomena (such as the crystal growth and nucleation [2, 56] as well as microstructures [21]).

3) The effect of density change is negligible for the solid and liquid phases. The change in density causes an increase or decrease in volume, which then turns into a dual-moving boundary problem [17].

5.2.1 Formulation

In this problem, the heat conduction equation for the solid phase is expressed as

$$\frac{1}{\alpha_{\mathrm{s}}}\frac{\partial T_{\mathrm{s}}}{\partial t} = \frac{\partial^2 T_{\mathrm{s}}}{\partial r^2} + \frac{1}{r}\frac{\partial T_{\mathrm{s}}}{\partial r}, \qquad b < r < r_{\mathrm{i}}(t), \qquad t_0 < t < \infty, \tag{5.2}$$

and the one for the liquid phase is given by

$$\frac{1}{\alpha_{\mathrm{l}}}\frac{\partial T_{\mathrm{l}}}{\partial t} = \frac{\partial^2 T_{\mathrm{l}}}{\partial r^2} + \frac{1}{r}\frac{\partial T_{\mathrm{l}}}{\partial r}, \qquad r_{\mathrm{i}}(t) < r < a, \qquad 0 < t < t_{\mathrm{c}}, \tag{5.3}$$

where $T(r,t)$ is the temperature depending on the radial coordinate r and time t, and $r_{\mathrm{i}}(t)$ is the time-dependent solid-liquid moving interface location. The parameters a, b, α are the outer radius, inner radius, and thermal diffusivity (determined by dividing the thermal conductivity by the mass density and specific heat, i.e., $k/(\rho c_p)$), respectively. The subscripts s and l stand for the solid and liquid phases. It is also noted that the time interval for each phase varies: the solid starts at t_0 (when the interface starts to move) and continues to exist, while the liquid begins at $t = 0$ and ends at t_{c} (when the whole domain is solidified).

There are two fixed boundary conditions located at the inner and outer surfaces. The inner surface is subjected to a convective boundary based on *Newton's law of cooling*

$$-k\frac{\partial T}{\partial r}\bigg|_{r=b} = h\Big[T_\infty - T(r=b,t)\Big], \tag{5.4}$$

and the outer surface is thermally insulated given by

$$\frac{\partial T}{\partial r}\bigg|_{r=a} = 0, \tag{5.5}$$

where h is the convective heat transfer coefficient and T_∞ is the surrounding temperature, presumably lower than the material's fusion point T_f. It is noted that the convective (Robin) boundary is the most realistic condition among others. However, if a constant temperature (Dirichlet) [54] or heat flux (Neumann) [31, 32] boundary is needed, the heat transfer coefficient can be adjusted to a very high or low value. Moreover, the moving boundary conditions are

$$k_\mathrm{s}\frac{\partial T_\mathrm{s}}{\partial r}\bigg|_{r=r_\mathrm{i}(t)} - k_\mathrm{l}\frac{\partial T_\mathrm{l}}{\partial r}\bigg|_{r=r_\mathrm{i}(t)} = \rho L\frac{\mathrm{d}r_\mathrm{i}}{\mathrm{d}t}, \qquad r = r_\mathrm{i}(t), \qquad t_0 < t < t_\mathrm{c}, \tag{5.6}$$

and

$$T_\mathrm{s}(r=r_\mathrm{i}(t),t) = T_\mathrm{l}(r=r_\mathrm{i}(t),t) = T_\mathrm{f}, \qquad r = r_\mathrm{i}(t), \qquad t_0 < t < t_\mathrm{c}. \tag{5.7}$$

The first moving boundary condition in Eq. (5.6) in particular represents the energy balance at $r_\mathrm{i}(t)$ in which the release of latent heat is caused by the difference in heat fluxes from two phases; the second condition in Eq. (5.7) indicates that the interface is at the material's fusion temperature. As for the time conditions, the material is initially in its liquid state with a uniform initial temperature that is above the fusion temperature

$$T_\mathrm{l}(r,t=0) = T_\mathrm{init}, \qquad b < r < a,\ t=0, \tag{5.8}$$

while the solid-liquid interface moves from the inner to outer surface, implying an outward

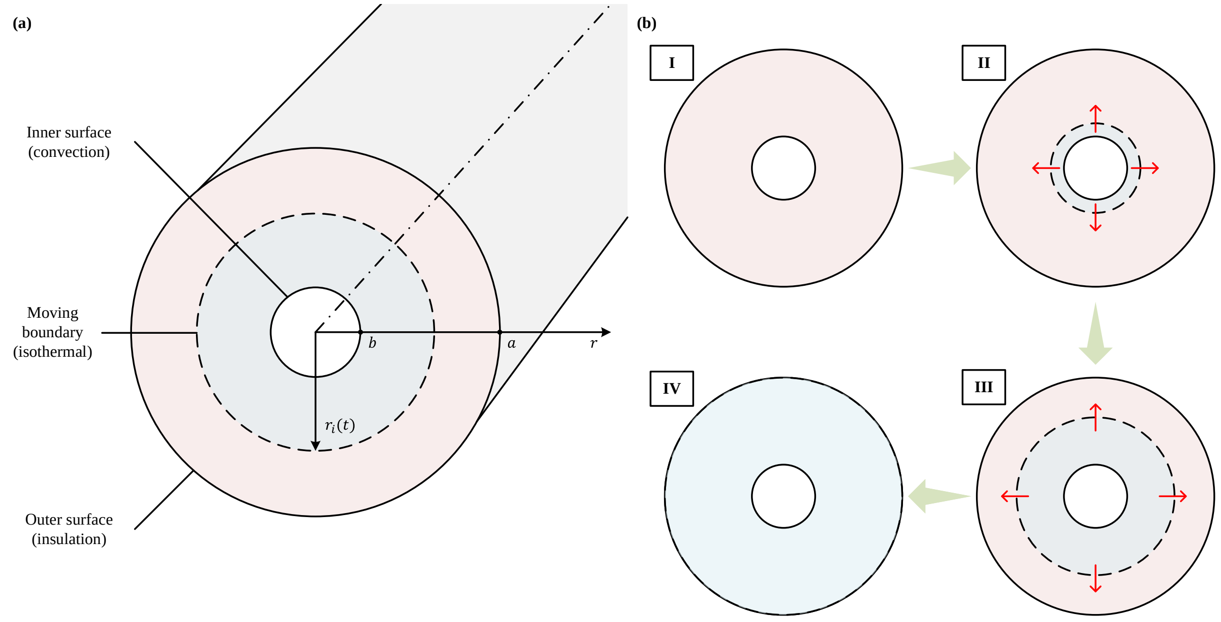

Figure 5.1: Schematic diagram of computational geometry along with the coordinate and boundary conditions, as shown in (a); Characterization of the interface motion over time into four stages/regimes (denoted by I, II, III, IV) demonstrated in (b).

solidification during the time interval $[t_0, t_\mathrm{c}]$

$$r_\mathrm{i}(t = t_0) = b, \qquad r_\mathrm{i}(t = t_\mathrm{c}) = a. \tag{5.9}$$

5.2.2 Nondimensionalization

Table 5.1 introduces a list of scalings (including geometry, temperature, and time) used in the nondimensionalization. Mainly, the geometric scaling consists of the ratio of inner to outer radii β, dimensionless radial coordinate ξ, and dimensionless interface location ξ_i. Since each of these is calculated by dividing the outer radius a, the interval for ξ and ξ_i is given by $[\beta, 1]$. As for the temperature, the difference in reference temperature ΔT is defined by the fusion and surrounding temperature $T_\mathrm{f} - T_\infty$, and thus this difference is used to calculate the temperature in both phases as well as the initial temperature, i.e., θ_s, θ_l, and θ_init. Lastly, the dimensionless time is calculated through $\alpha_\mathrm{s} t/a^2$.

Table 5.1: List of geometric, temperature and time scalings used in the nondimensionalization.

Type	Name	Expression
Geometric	β	b/a
	ξ	r/a
	ξ_{i}	r_{i}/a
Temperature	ΔT	$T_{\mathrm{f}} - T_{\infty}$
	θ_{s}	$(T_{\mathrm{s}} - T_{\mathrm{f}})/\Delta T$
	θ_{l}	$(T_{\mathrm{l}} - T_{\mathrm{f}})/\Delta T$
	θ_{init}	$(T_{\mathrm{init}} - T_{\mathrm{f}})/\Delta T$
Time	τ	$\alpha_{\mathrm{s}} t/a^2$

As a consequence of the scalings, some dimensionless thermophysical properties and dimensionless numbers can be introduced listed in Table 5.2. Three scaling parameters of thermophysical property (e.g., $\widetilde{\alpha}, \widetilde{k}, \widetilde{c}_p$) are determined by the ratio of solid to liquid phases. There are also two dimensionless numbers in this mathematical model:

$$\mathrm{Bi} = \frac{ha}{k_{\mathrm{s}}}, \qquad \mathrm{Ste} = \frac{c_{p,\mathrm{s}}\Delta T}{L}. \tag{5.10}$$

The convective heat transfer from the surface of the body to its interior is quantified by the Biot number (Bi), while the proportion of sensible to latent heat during a phase change is considered in the Stefan number (Ste). It is noted that the two dimensionless numbers and the dimensionless time are evaluated primarily by the solid phase, as it is the more dominant phase in terms of solidification.

The dimensional mathematical model (5.2)–(5.9) is therefore nondimensionalized as fol-

Table 5.2: List of dimensionless parameters involved in the nondimensionalization.

Type	Name	Expression
Thermophysical property	$\widetilde{\alpha}$	$\alpha_\mathrm{s}/\alpha_\mathrm{l}$
	$\widetilde{k}$	$k_\mathrm{s}/k_\mathrm{l}$
	$\widetilde{c}_p$	$c_{p,\mathrm{s}}/c_{p,\mathrm{l}}$
Dimensionless number	Bi	ha/k_s
	Ste	$c_{p,\mathrm{s}}\Delta T/L$

lows:

$$\frac{\partial \theta_\mathrm{s}}{\partial \tau} = \frac{\partial^2 \theta_\mathrm{s}}{\partial \xi^2} + \frac{1}{\xi}\frac{\partial \theta_\mathrm{s}}{\partial \xi}, \qquad \beta < \xi < \xi_\mathrm{i}(\tau), \qquad \tau_0 < \tau < \infty, \tag{5.11}$$

$$\frac{\partial \theta_\mathrm{l}}{\partial \tau} = \frac{1}{\widetilde{\alpha}}\left(\frac{\partial^2 \theta_\mathrm{l}}{\partial \xi^2} + \frac{1}{\xi}\frac{\partial \theta_\mathrm{l}}{\partial \xi}\right), \qquad \xi_\mathrm{i}(\tau) < \xi < 1, \qquad 0 < \tau < \tau_\mathrm{c}, \tag{5.12}$$

$$-\left.\frac{\partial \theta}{\partial \xi}\right|_{\xi=\beta} = \mathrm{Bi}\left[-1 - \theta(\xi=\beta,\tau)\right], \tag{5.13}$$

$$\left.\frac{\partial \theta}{\partial \xi}\right|_{\xi=1} = 0, \tag{5.14}$$

$$\left.\frac{\partial \theta_\mathrm{s}}{\partial \xi}\right|_{\xi=\xi_\mathrm{i}(\tau)} - \frac{1}{\widetilde{k}}\left.\frac{\partial \theta_\mathrm{l}}{\partial \xi}\right|_{\xi=\xi_\mathrm{i}(\tau)} = \frac{1}{\mathrm{Ste}}\frac{\mathrm{d}\xi_\mathrm{i}}{\mathrm{d}\tau}, \qquad \xi = \xi_\mathrm{i}(\tau), \qquad \tau_0 < \tau < \tau_\mathrm{c}, \tag{5.15}$$

$$\theta_\mathrm{s}(\xi=\xi_\mathrm{i}(\tau),\tau) = \theta_\mathrm{l}(\xi=\xi_\mathrm{i}(\tau),\tau) = 0, \qquad \xi = \xi_\mathrm{i}(\tau), \qquad \tau_0 < \tau < \tau_\mathrm{c}, \tag{5.16}$$

$$\theta_\mathrm{l}(\xi,\tau=0) = \theta_\mathrm{init}, \qquad \xi_\mathrm{i}(\tau=\tau_0) = \beta, \qquad \xi_\mathrm{i}(\tau=\tau_\mathrm{c}) = 1. \tag{5.17}$$

5.3 Asymptotic analysis

This section presents a solution to the two-phase Stefan problem using the asymptotic method by expanding around a small Stefan number. The Stefan number is defined as the product of two terms, namely, the ratio of the specific heat to the latent heat, c_p/L, and the temperature gradient, ΔT. The former is a material property, while the latter is an operational variable. The small Stefan number assumption, required for the asymptotic analysis, is often valid in engineering applications of phase change materials. The asymptotic

Table 5.3: Summary of scalings used in the asymptotic analysis categorized by the regimes and layers. Note that the tilde notion ($\sim$) is used when introducing a new scaling variable.

Regime	Layer	Variable			Temperature	
		τ	ξ	$\xi_\mathrm{i}(\tau)$	$\theta_\mathrm{s}(\xi,\tau)$	$\theta_\mathrm{l}(\xi,\tau)$
I	A	τ	ξ	β	–	$\theta_\mathrm{l}(\beta,\tau)$
II	B	$\widetilde{\tau}+\tau_0$	ξ	$\beta+\mathrm{Ste}^{\frac{1}{2}}\widetilde{\xi}_\mathrm{i}$	–	$\theta_{\mathrm{l},0}$
	C	$\widetilde{\tau}+\tau_0$	$\beta+\mathrm{Ste}^{\frac{1}{2}}\widetilde{\xi}$	$\beta+\mathrm{Ste}^{\frac{1}{2}}\widetilde{\xi}_\mathrm{i}$	–	$\theta_{\mathrm{l},0}+\mathrm{Ste}^{\frac{1}{2}}\theta_{\mathrm{l},1}$
III	D	$(\mathrm{Ste}^{-1}\widetilde{\tau}+\tau_0)_\mathrm{avg}$	ξ	ξ_i	$\theta_{\mathrm{s},0}+\mathrm{Ste}^{\frac{1}{2}}\theta_{\mathrm{s},1}$	–
IV	E	$\widetilde{\tau}+\tau_\mathrm{c}$	ξ	1	θ_s	–

analysis comprises four temporal and five spatial scales referred to as *regimes* and *layers*, respectively. Figure 5.2 is a conceptual diagram of the asymptotic analysis concerning temperature profile and solid-liquid interface motion, while Table 5.3 summarizes each regime and layer used in the asymptotic analysis. In summary, the established regimes correspond to four solidification stages subjected to a convective boundary: (i) a pre-cooling stage when the interface does not move yet; (ii) a cooling stage in which the interface begins to move and a slight piece of solid is formed, but most of the domain is still dominated by the liquid; (iii) a freezing stage when both phases co-exist in the domain; and (iv) a sub-cooling stage in which the entire domain is solid and the heat only conducts through the sensible heat. It is worth mentioning that the first stage is unique to problems with a non-isothermal boundary (e.g., a heat flux [31, 32] or convective boundary here), since the solid-liquid interface does not move instantaneously. In the subsequent sub-sections, every regime and layer will be explained in detail from physical and mathematical perspectives.

5.3.1 Regime I

Regime I includes a single spatial layer, namely *Layer A*; at this spatial-temporal scale, the solid phase is not formed since the inner surface has not cooled down to the fusion temperature by the convective boundary. The scaling for *Regime I Layer A* therefore forces

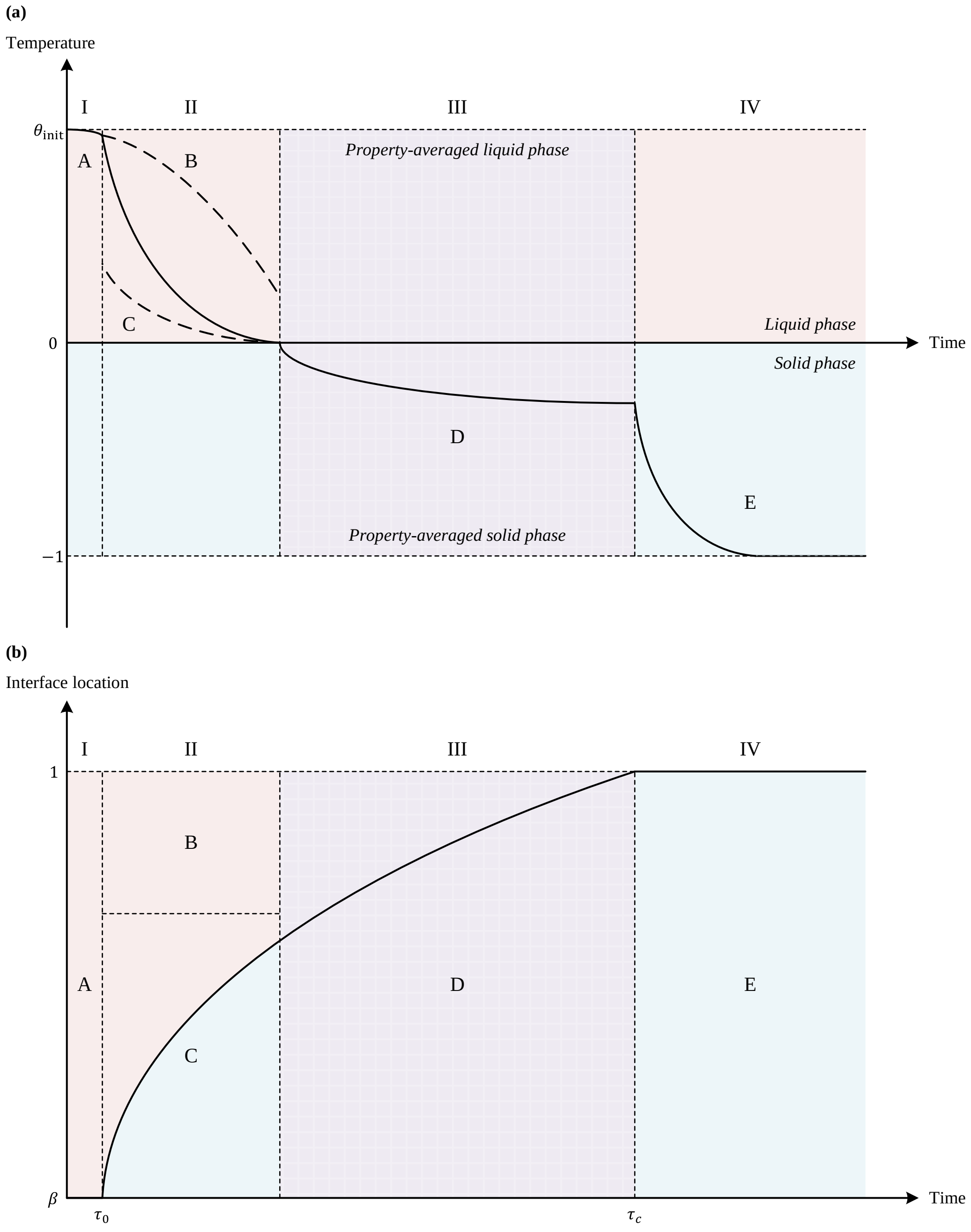

Figure 5.2: Conceptual diagram of the regimes (denoted by I, II, III, IV) and layers (denoted by A, B, C, D, E) in the asymptotic analysis: (a) Temperature θ over time τ taken at the domain's midpoint; and (b) Solid-liquid interface location ξ_{i} over time τ. Note that the proportion of every regime and layer could depend on the prescribed parameters, such as Bi, Ste, $\widetilde{k}$, α, and θ_{init}.

the moving boundary to be at the inner surface

$$\xi_{\mathrm{i}} = \beta, \tag{5.18}$$

and the time is then restricted between 0 and τ_0 owing to the absence of a solid. The re-scaled problem turns into finite-extent transient heat conduction in a hollow cylinder subjected to a convective boundary

$$\begin{aligned}
\frac{\partial \theta_{\mathrm{l}}}{\partial \tau} &= \frac{1}{\widetilde{\alpha}}\left(\frac{\partial^2 \theta_{\mathrm{l}}}{\partial \xi^2} + \frac{1}{\xi}\frac{\partial \theta_{\mathrm{l}}}{\partial \xi}\right), \qquad \beta < \xi < 1, \qquad 0 < \tau < \tau_0,\\
-\frac{1}{\widetilde{k}}\frac{\partial \theta_{\mathrm{l}}}{\partial \xi}\bigg|_{\xi=\beta} &= \mathrm{Bi}\bigg[-1 - \theta_{\mathrm{l}}(\xi = \beta, \tau)\bigg],\\
\frac{\partial \theta_{\mathrm{l}}}{\partial \xi}\bigg|_{\xi=1} &= 0,\\
\theta_{\mathrm{l}}(\xi, \tau = 0) &= \theta_{\mathrm{init}}.
\end{aligned} \tag{5.19}$$

Since the problem is separable, an exact solution can be found using the method of separation of variables. The exact solution to a general form of the above-mentioned problem with the convective-insulated boundaries is derived in Appendix A. 1. Here, we directly write down the final solution as follows

$$\begin{aligned}
\theta_{\mathrm{l}}(\xi, \tau) &= -1 - \sum_{\mathrm{n}=1}^{\infty} c_{\mathrm{n}} R_{\mathrm{n}}(\lambda_{\mathrm{n}}, \xi) \exp\left(-\frac{1}{\widetilde{\alpha}}\lambda_{\mathrm{n}}^2 \tau\right),\\
R_{\mathrm{n}}(\lambda_{\mathrm{n}}, \xi) &= -J_0(\lambda_{\mathrm{n}}\xi)\bigg[\mathrm{Bi}Y_0(\lambda_{\mathrm{n}}\beta) + \frac{1}{\widetilde{k}}\lambda_{\mathrm{n}} Y_1(\lambda_{\mathrm{n}}\beta)\bigg] + Y_0(\lambda_{\mathrm{n}}\xi)\bigg[\mathrm{Bi}J_0(\lambda_{\mathrm{n}}\beta) + \frac{1}{\widetilde{k}}\lambda_{\mathrm{n}} J_1(\lambda_{\mathrm{n}}\beta)\bigg],\\
-J_1(\lambda_{\mathrm{n}})&\bigg[\mathrm{Bi}Y_0(\lambda_{\mathrm{n}}\beta) + \frac{1}{\widetilde{k}}\lambda_{\mathrm{n}} Y_1(\lambda_{\mathrm{n}}\beta)\bigg] + Y_1(\lambda_{\mathrm{n}})\bigg[\mathrm{Bi}J_0(\lambda_{\mathrm{n}}\beta) + \frac{1}{\widetilde{k}}\lambda_{\mathrm{n}} J_1(\lambda_{\mathrm{n}}\beta)\bigg] = 0,\\
c_{\mathrm{n}} &= \left\{\bigg[-1 - \theta_{\mathrm{init}}\bigg]\int_{\widetilde{\xi}=\beta}^{1} \widetilde{\xi} R_{\mathrm{n}}(\lambda_{\mathrm{n}}, \widetilde{\xi}) \mathrm{d}\widetilde{\xi}\right\} \bigg/ \left\{\int_{\widetilde{\xi}=\beta}^{1} \widetilde{\xi} R_{\mathrm{n}}^2(\lambda_{\mathrm{n}}, \widetilde{\xi}) \mathrm{d}\widetilde{\xi}\right\},
\end{aligned} \tag{5.20}$$

where λ_{n} and c_{n} are the eigenvalues and corresponding eigencoefficients, respectively. J_{n} and Y_{n} represent the Bessel functions of order n of the first and second kinds, respectively.

It is noted that this spatial-temporal scale is decoupled with the adjacent *Regime II Layer B* in terms of: (i) the temperature for $\theta(\xi \neq \beta, \tau > \tau_0)$, and (ii) the interface location for $\xi_{\mathrm{i}}(\tau > \tau_0)$. However, it offers information on τ_0 (the time when the interface starts to move), $\theta_{\mathrm{l}}(\xi, 0 \leq \tau \leq \tau_0)$ (the liquid temperature before the interface moves), and $\xi_{\mathrm{i}}(0 \leq \tau \leq \tau_0) = \beta$ (the static period of the interface before it moves).

5.3.2 Regime II

The solid develops from the inner surface of the annulus when the solid-liquid interface begins to move. *Regime II* is the time scale during which most of the domain is still liquid, and only a tiny piece of it is solid. Though the inclusion of both phases with a non-linear interface makes this scale particularly complicated, the spatial domain can be broken down into two layers called *Layer B* and *Layer C* as described below.

Layer B

Firstly, *Layer B* is an outer layer far away from the moving boundary after $\tau > \tau_0$, which can also be seen as a boundary layer at the outer surface right after the interface moves. From a physical perspective, this layer considers the liquid phase that occupies the bulk of the domain since the solid only begins to develop at the inner surface. To capture this, we re-scale the following dimensionless variables

$$\tau = \widetilde{\tau} + \tau_0, \qquad \xi_{\mathrm{i}} = \beta + \mathrm{Ste}^{\frac{1}{2}}\widetilde{\xi}_{\mathrm{i}}. \tag{5.21}$$

Then, we can expand θ_{l} as

$$\begin{aligned} \theta_{\mathrm{l}} &\sim \theta_{\mathrm{l},0} + \mathrm{Ste}\theta_{\mathrm{l},1} + \mathcal{O}(\mathrm{Ste}^2), \\ \theta_{\mathrm{s}} &\sim \theta_{\mathrm{s},0} + \mathrm{Ste}\theta_{\mathrm{s},1} + \mathcal{O}(\mathrm{Ste}^2), \\ \xi_{\mathrm{i}} &\sim \xi_{\mathrm{i},0} + \mathrm{Ste}\xi_{\mathrm{i},1} + \mathcal{O}(\mathrm{Ste}^2). \end{aligned} \tag{5.22}$$

At the leading order $\mathcal{O}(1)$, the solid phase is eliminated. The Stefan condition is also removed due to $\mathrm{Ste}^{\frac{1}{2}}$ in ξ_{i}, thus leaving $\theta_{\mathrm{l},0}(\xi=\beta,\widetilde{\tau})=0$ as the inner surface boundary. The problem is then reduced to heat conduction in the liquid phase only with a constant temperature boundary at the inner wall

$$\begin{aligned}\frac{\partial\theta_{\mathrm{l},0}}{\partial\widetilde{\tau}}&=\frac{1}{\widetilde{\alpha}}\left(\frac{\partial^2\theta_{\mathrm{l},0}}{\partial\xi^2}+\frac{1}{\xi}\frac{\partial\theta_{\mathrm{l},0}}{\partial\xi}\right),\\ \theta_{\mathrm{l},0}(\beta,\widetilde{\tau})&=0,\\ \left.\frac{\partial\theta_{\mathrm{l},0}}{\partial\xi}\right|_{\xi=1}&=0,\\ \theta_{\mathrm{l},0}(\xi,\widetilde{\tau}=0)&=f(\xi),\end{aligned}\tag{5.23}$$

where $f(\xi)$ is given by the temperature profile at $\tau=\tau_0$. The exact solution for $\theta_{\mathrm{l},0}$ can be found by the method of separation of variables, and the detailed derivation is demonstrated in Appendix A. 2. The final solution is therefore expressed as

$$\begin{aligned}\theta_{\mathrm{l},0}&=\sum_{\mathrm{n}=1}^{\infty}\widetilde{c}_{\mathrm{n}}\widetilde{R}_{\mathrm{n}}(\widetilde{\lambda}_{\mathrm{n}},\xi)\exp(-\frac{1}{\widetilde{\alpha}}\lambda_{\mathrm{n}}^2\widetilde{\tau}),\\ \widetilde{R}_{\mathrm{n}}(\widetilde{\lambda}_{\mathrm{n}},\xi)&=J_0(\widetilde{\lambda}_{\mathrm{n}}\xi)Y_0(\widetilde{\lambda}_{\mathrm{n}}\beta)-J_0(\widetilde{\lambda}_{\mathrm{n}}\beta)Y_0(\widetilde{\lambda}_{\mathrm{n}}\xi),\\ J_1(\widetilde{\lambda}_{\mathrm{n}})Y_0(\widetilde{\lambda}_{\mathrm{n}}\beta)&-J_0(\widetilde{\lambda}_{\mathrm{n}}\beta)Y_1(\widetilde{\lambda}_{\mathrm{n}})=0,\\ \widetilde{c}_{\mathrm{n}}&=\left\{\int_{\widetilde{\xi}=\beta}^{1}\widetilde{\xi}f(\widetilde{\xi})\widetilde{R}_{\mathrm{n}}(\widetilde{\lambda}_{\mathrm{n}},\widetilde{\xi})\mathrm{d}\widetilde{\xi}\right\}\Big/\left\{\int_{\widetilde{\xi}=\beta}^{1}\widetilde{\xi}\widetilde{R}_{\mathrm{n}}^2(\widetilde{\lambda}_{\mathrm{n}},\widetilde{\xi})\mathrm{d}\widetilde{\xi}\right\}.\end{aligned}\tag{5.24}$$

Layer C

Another spatial scale in this regime is *Layer C* which is close to the moving boundary (also can be seen as an inner layer of *Regime II*). This layer, in contrast to *Layer B*, focuses on a smaller portion of the domain around the interface, considering both phases and the interface at a higher spatial resolution. Specifically, the radial coordinate and moving interface are re-scaled as

$$\tau=\widetilde{\tau}+\tau_0,\qquad \xi=\beta+\mathrm{Ste}^{\frac{1}{2}}\widetilde{\xi},\qquad \xi_{\mathrm{i}}=\beta+\mathrm{Ste}^{\frac{1}{2}}\widetilde{\xi}_{\mathrm{i}},\tag{5.25}$$

and we seek asymptotic solutions

$$\begin{aligned} \theta_{\mathrm{s}} &\sim \widetilde{\theta}_{\mathrm{s},0} + \mathrm{Ste}^{\frac{1}{2}}\widetilde{\theta}_{\mathrm{s},1} + \mathcal{O}(\mathrm{Ste}), \\ \theta_{\mathrm{l}} &\sim \widetilde{\theta}_{\mathrm{l},0} + \mathrm{Ste}^{\frac{1}{2}}\widetilde{\theta}_{\mathrm{l},1} + \mathcal{O}(\mathrm{Ste}), \\ \widetilde{\xi}_{\mathrm{i}} &\sim \widetilde{\xi}_{\mathrm{i},0} + \mathrm{Ste}^{\frac{1}{2}}\widetilde{\xi}_{\mathrm{i},1} + \mathcal{O}(\mathrm{Ste}). \end{aligned} \tag{5.26}$$

Then, the heat equations become

$$\begin{aligned} \beta\mathrm{Ste}\frac{\partial\theta_{\mathrm{s}}}{\partial\widetilde{\tau}} + \mathrm{Ste}^{\frac{3}{2}}\widetilde{\xi}\frac{\partial\theta_{\mathrm{s}}}{\partial\widetilde{\tau}} &= \beta\frac{\partial^2\theta_{\mathrm{s}}}{\partial\widetilde{\xi}^2} + \mathrm{Ste}^{\frac{1}{2}}\widetilde{\xi}\frac{\partial^2\theta_{\mathrm{s}}}{\partial\widetilde{\xi}^2} + \mathrm{Ste}^{\frac{1}{2}}\frac{\partial\theta_{\mathrm{s}}}{\partial\widetilde{\xi}}, \qquad 0 < \widetilde{\xi} < \widetilde{\xi}_{\mathrm{i}}, \\ \beta\mathrm{Ste}\frac{\partial\theta_{\mathrm{l}}}{\partial\widetilde{\tau}} + \mathrm{Ste}^{\frac{3}{2}}\widetilde{\xi}\frac{\partial\theta_{\mathrm{l}}}{\partial\widetilde{\tau}} &= \frac{1}{\widetilde{\alpha}}\beta\frac{\partial^2\theta_{\mathrm{l}}}{\partial\widetilde{\xi}^2} + \frac{1}{\widetilde{\alpha}}\mathrm{Ste}^{\frac{1}{2}}\widetilde{\xi}\frac{\partial^2\theta_{\mathrm{l}}}{\partial\widetilde{\xi}^2} + \frac{1}{\widetilde{\alpha}}\mathrm{Ste}^{\frac{1}{2}}\frac{\partial\theta_{\mathrm{l}}}{\partial\widetilde{\xi}}, \qquad \widetilde{\xi} > \widetilde{\xi}_{\mathrm{i}}, \end{aligned} \tag{5.27}$$

subject to the moving boundary condition

$$\left.\frac{\partial\theta_{\mathrm{s}}}{\partial\widetilde{\xi}}\right|_{\widetilde{\xi}=\widetilde{\xi}_{\mathrm{i}}} - \frac{1}{\widetilde{k}}\left.\frac{\partial\theta_{\mathrm{l}}}{\partial\widetilde{\xi}}\right|_{\widetilde{\xi}=\widetilde{\xi}_{\mathrm{i}}} = \frac{\mathrm{d}\widetilde{\xi}_{\mathrm{i}}}{\mathrm{d}\widetilde{\tau}}, \tag{5.28}$$

and fixed boundary conditions

$$\begin{aligned} -\left.\frac{\partial\theta_{\mathrm{s}}}{\partial\widetilde{\xi}}\right|_{\widetilde{\xi}=0} &= \mathrm{Ste}^{\frac{1}{2}}\mathrm{Bi}\Big[-1-\theta_{\mathrm{s}}(0,\widetilde{\tau})\Big], \\ \theta_{\mathrm{s}}(\widetilde{\xi}_{\mathrm{i}},\tau) &= 0, \\ \theta_{\mathrm{l}}(\widetilde{\xi}_{\mathrm{i}},\tau) &= 0, \\ \left.\frac{\partial\theta_{\mathrm{l}}}{\partial\widetilde{\xi}}\right|_{\widetilde{\xi}=\mathrm{Ste}^{-\frac{1}{2}}(1-\beta)} &= 0, \end{aligned} \tag{5.29}$$

as well as time conditions

$$\widetilde{\xi}_{\mathrm{i}}(0) = 0, \qquad \theta_{\mathrm{l}}(\widetilde{\xi},0) = f(\widetilde{\xi}). \tag{5.30}$$

At the leading order,

$$\frac{\partial^2\widetilde{\theta}_{\mathrm{s},0}}{\partial\widetilde{\xi}^2} = 0, \qquad 0 < \widetilde{\xi} < \widetilde{\xi}_{\mathrm{i},0}; \qquad \frac{\partial^2\widetilde{\theta}_{\mathrm{l},0}}{\partial\widetilde{\xi}^2} = 0, \qquad \widetilde{\xi} > \widetilde{\xi}_{\mathrm{i},0}, \tag{5.31}$$

subject to

$$\frac{\partial \widetilde{\theta}_{\mathrm{s},0}}{\partial \widetilde{\xi}}\bigg|_{\widetilde{\xi}=0}=0, \qquad \widetilde{\theta}_{\mathrm{s},0}(\widetilde{\xi}_{\mathrm{i},0})=0, \qquad \widetilde{\theta}_{\mathrm{l},0}(\widetilde{\xi}_{\mathrm{i},0})=0, \qquad \widetilde{\theta}_{\mathrm{l},0}(\infty)\sim \widetilde{a}_0(\widetilde{\tau})\widetilde{\xi}, \tag{5.32}$$

where $\widetilde{a}_0(\tau)$ will be defined by the matching part. Therefore, the solutions of $\widetilde{\theta}_{\mathrm{s},0}$ and $\widetilde{\theta}_{\mathrm{l},0}$ can be found as

$$\widetilde{\theta}_{\mathrm{s},0}=0, \qquad \widetilde{\theta}_{\mathrm{l},0}\sim \widetilde{a}_0(\widetilde{\tau})(\widetilde{\xi}-\widetilde{\xi}_{\mathrm{i},0}). \tag{5.33}$$

At the first order,

$$\beta\frac{\partial^2 \widetilde{\theta}_{\mathrm{s},1}}{\partial \widetilde{\xi}^2}+\frac{\partial \widetilde{\theta}_{\mathrm{s},0}}{\partial \widetilde{\xi}}=0, \qquad 0<\widetilde{\xi}<\widetilde{\xi}_{\mathrm{i},0}; \qquad \beta\frac{\partial^2 \widetilde{\theta}_{\mathrm{l},1}}{\partial \widetilde{\xi}^2}+\frac{\partial \widetilde{\theta}_{\mathrm{l},0}}{\partial \widetilde{\xi}}=0, \qquad \widetilde{\xi}>\widetilde{\xi}_{\mathrm{i},0}, \tag{5.34}$$

subject to

$$\begin{aligned} -\frac{\partial \widetilde{\theta}_{\mathrm{s},1}}{\partial \widetilde{\xi}}\bigg|_{\widetilde{\xi}=0} &= \mathrm{Bi}\Big[-1-\widetilde{\theta}_{\mathrm{s},0}(0,\widetilde{\tau})\Big], \\ \frac{\partial \widetilde{\theta}_{\mathrm{s},0}}{\partial \widetilde{\xi}}\bigg|_{\widetilde{\xi}=\widetilde{\xi}_{\mathrm{i},0}}&\widetilde{\xi}_{\mathrm{i},1}+\widetilde{\theta}_{\mathrm{s},1}(\widetilde{\xi}_{\mathrm{i},0},\widetilde{\tau})=0, \\ \frac{\partial \widetilde{\theta}_{\mathrm{l},0}}{\partial \widetilde{\xi}}\bigg|_{\widetilde{\xi}=\widetilde{\xi}_{\mathrm{i},0}}&\widetilde{\xi}_{\mathrm{i},1}+\widetilde{\theta}_{\mathrm{l},1}(\widetilde{\xi}_{\mathrm{i},0},\widetilde{\tau})=0, \\ \widetilde{\theta}_{\mathrm{l},1}(\infty,\tau)&\sim \widetilde{a}_0(\widetilde{\tau})\widetilde{\xi}^2+\widetilde{a}_1(\widetilde{\tau})\widetilde{\xi}, \end{aligned} \tag{5.35}$$

where $\widetilde{a}_1(\widetilde{\tau})$ will also be defined by the matching part. Similar to the leading order, we can find the solutions of $\widetilde{\theta}_{\mathrm{s},1}$ and $\widetilde{\theta}_{\mathrm{l},1}$

$$\widetilde{\theta}_{\mathrm{s},1}=\mathrm{Bi}(\widetilde{\xi}-\widetilde{\xi}_{\mathrm{i},0}), \qquad \widetilde{\theta}_{\mathrm{l},1}=\widetilde{a}_0(\tau)\bigg(-\frac{1}{2\beta}\widetilde{\xi}^2+\frac{1}{2\beta}\widetilde{\xi}_{\mathrm{i},0}^2-\widetilde{\xi}_{\mathrm{i},1}\bigg)+\widetilde{a}_1(\tau)\bigg(\widetilde{\xi}-\widetilde{\xi}_{\mathrm{i},0}\bigg). \tag{5.36}$$

Matching

The liquid phase solution from *Layer B* can be written into inner variables $(\widetilde{\xi}, \widetilde{\tau})$ to match with the inner region (*Layer C*)

$$\theta_{\mathrm{l}}(\widetilde{\xi}, \widetilde{\tau}) = \sum_{\mathrm{n}=1}^{\infty} \widetilde{c}_{\mathrm{n}} \left\{ J_0\left[\lambda_{\mathrm{n}}(\beta + \mathrm{Ste}^{\frac{1}{2}}\widetilde{\xi})\right] Y_0(\lambda_{\mathrm{n}}\beta) - J_0(\lambda_{\mathrm{n}}\beta) Y_0\left[\lambda_{\mathrm{n}}(\beta + \mathrm{Ste}^{\frac{1}{2}}\widetilde{\xi})\right]\right\} \exp(-\frac{\widetilde{\lambda}_{\mathrm{n}}^2}{\widetilde{\alpha}}\widetilde{\tau}). \tag{5.37}$$

Then, a limit as Ste → 0 can be taken to approach outer variables at the leading order

$$\begin{aligned} \overline{\theta}_{\mathrm{l},0}(\widetilde{\xi}, \widetilde{\tau}) &= \lim_{\mathrm{Ste}\to 0} \theta_{\mathrm{l}}(\widetilde{\xi}, \widetilde{\tau}) \\ &= \sum_{\mathrm{n}=1}^{\infty} \widetilde{c}_{\mathrm{n}} \left[J_0(\lambda_{\mathrm{n}}\beta) Y_0(\widetilde{\lambda}_{\mathrm{n}}\beta) - J_0(\widetilde{\lambda}_{\mathrm{n}}\beta) Y_0(\widetilde{\lambda}_{\mathrm{n}}\beta)\right] \exp(-\frac{\widetilde{\lambda}_{\mathrm{n}}^2}{\widetilde{\alpha}}\widetilde{\tau}) \\ &= 0, \end{aligned} \tag{5.38}$$

where the overhead bar $(-)$ is denoted as matching solutions after taking the limit. Similarly, the first-order liquid phase solution can be expressed as

$$\begin{aligned} \overline{\theta}_{\mathrm{l},0}(\widetilde{\xi}, \widetilde{\tau}) + \mathrm{Ste}^{\frac{1}{2}} \overline{\theta}_{\mathrm{l},1}(\widetilde{\xi}, \widetilde{\tau}) &= \lim_{\mathrm{Ste}\to 0} \theta_{\mathrm{l}}(\widetilde{\xi}, \widetilde{\tau}), \\ \overline{\theta}_{\mathrm{l},1}(\widetilde{\xi}, \widetilde{\tau}) &= \lim_{\mathrm{Ste}\to 0} \mathrm{Ste}^{-\frac{1}{2}} \sum_{\mathrm{n}=1}^{\infty} \widetilde{c}_{\mathrm{n}} \left\{ J_0\left[\widetilde{\lambda}_{\mathrm{n}}(\beta + \mathrm{Ste}^{\frac{1}{2}}\widetilde{\xi})\right] Y_0(\widetilde{\lambda}_{\mathrm{n}}\beta) \right. \\ &\qquad \left. - J_0(\widetilde{\lambda}_{\mathrm{n}}\beta) Y_0\left[\widetilde{\lambda}_{\mathrm{n}}(\beta + \mathrm{Ste}^{\frac{1}{2}}\widetilde{\xi})\right]\right\} \exp(-\frac{\widetilde{\lambda}_{\mathrm{n}}^2}{\widetilde{\alpha}}\widetilde{\tau}). \end{aligned} \tag{5.39}$$

Therefore, the limit can be evaluated by applying L'Hôpital's rule:

$$\overline{\theta}_{\mathrm{l},1}(\widetilde{\xi}, \widetilde{\tau}) = \sum_{\mathrm{n}=1}^{\infty} \widetilde{c}_{\mathrm{n}} \widetilde{\lambda}_{\mathrm{n}} \widetilde{\xi} \left[J_0(\widetilde{\lambda}_{\mathrm{n}}\beta) Y_1(\widetilde{\lambda}_{\mathrm{n}}\beta) - J_1(\widetilde{\lambda}_{\mathrm{n}}\beta) Y_0(\widetilde{\lambda}_{\mathrm{n}}\beta)\right] \exp(-\frac{\widetilde{\lambda}_{\mathrm{n}}^2}{\widetilde{\alpha}}\widetilde{\tau}). \tag{5.40}$$

Since the liquid-phase solution in the inner region (*Layer C*) was assumed to be in the form of

$$\widetilde{\theta}_{\mathrm{l},0} \sim \widetilde{a}_0(\widetilde{\tau})\widetilde{\xi}, \qquad \widetilde{\theta}_{\mathrm{l},1} \sim \widetilde{a}_0(\widetilde{\tau})\widetilde{\xi}^2 + \widetilde{a}_1(\widetilde{\tau})\widetilde{\xi}, \tag{5.41}$$

the undetermined variables $\widetilde{a}_0$ and $\widetilde{a}_1$ can be readily found by matching

$$\widetilde{a}_0(\widetilde{\tau}) = 0, \qquad \widetilde{a}_1(\widetilde{\tau}) = \sum_{\mathrm{n}=1}^{\infty} \widetilde{c}_{\mathrm{n}} \widetilde{\lambda}_{\mathrm{n}} \Big[J_0(\widetilde{\lambda}_{\mathrm{n}}\beta) Y_1(\widetilde{\lambda}_{\mathrm{n}}\beta) - J_1(\widetilde{\lambda}_{\mathrm{n}}\beta) Y_0(\widetilde{\lambda}_{\mathrm{n}}\beta) \Big] \exp(-\frac{\widetilde{\lambda}_{\mathrm{n}}^2}{\widetilde{\alpha}}\widetilde{\tau}). \tag{5.42}$$

Thus, the liquid-phase temperature in *Layer C* is expressed as:

$$\begin{aligned} &\widetilde{\theta}_{\mathrm{l},0}(\widetilde{\xi}, \widetilde{\tau}) = 0, \\ &\widetilde{\theta}_{\mathrm{l},1}(\widetilde{\xi}, \widetilde{\tau}) = \Big(\widetilde{\xi} - \widetilde{\xi}_{\mathrm{i},0} \Big) \sum_{\mathrm{n}=1}^{\infty} \widetilde{c}_{\mathrm{n}} \widetilde{\lambda}_{\mathrm{n}} \Big[J_0(\widetilde{\lambda}_{\mathrm{n}}\beta) Y_1(\widetilde{\lambda}_{\mathrm{n}}\beta) - J_1(\widetilde{\lambda}_{\mathrm{n}}\beta) Y_0(\widetilde{\lambda}_{\mathrm{n}}\beta) \Big] \exp(-\frac{\widetilde{\lambda}_{\mathrm{n}}^2}{\widetilde{\alpha}}\widetilde{\tau}). \end{aligned} \tag{5.43}$$

5.3.3 Regime III

The asymptotic solutions up until this point have primarily focused on the liquid temperature over a comparatively short time interval; however, as the interface moves, the solid will rapidly prevail over the liquid for a significantly more extended period with the release of latent heat. This, in turn, necessitates a re-scaling in the time scale that characterizes both the phase change and the existence of two phases. Therefore, a new temporal scale is introduced as

$$\widetilde{\tau} = \mathrm{Ste}(\tau - \tau_0), \tag{5.44}$$

and the two-phase Stefan problem can be reduced into a one-phase one as follows

$$\begin{aligned} \mathrm{Ste}\frac{\partial \theta_{\mathrm{s}}}{\partial \widetilde{\tau}} &= \frac{\partial^2 \theta_{\mathrm{s}}}{\partial \xi^2} + \frac{1}{\xi}\frac{\partial \theta_{\mathrm{s}}}{\partial \xi}, \\ -\frac{\partial \theta_{\mathrm{s}}}{\partial \xi}\bigg|_{\xi=\beta} &= \mathrm{Bi}\Big[-1 - \theta_{\mathrm{s}}(\beta, \widetilde{\tau}) \Big], \\ \frac{\partial \theta_{\mathrm{s}}}{\partial \xi}\bigg|_{\xi=\xi_{\mathrm{i}}} &= \frac{\mathrm{d}\xi_{\mathrm{i}}}{\mathrm{d}\widetilde{\tau}}, \\ \theta_{\mathrm{s}}(\xi_{\mathrm{i}}, \widetilde{\tau}) &= 0, \\ \xi_{\mathrm{i}}(0) &= \beta. \end{aligned} \tag{5.45}$$

It is noted that previous work done by McCue et al. [30] and Xu et al. [54] demonstrated the rationale for the abandonment of the thermal contribution of liquid phase using the method of composite asymptotic expansions, proving an exponential decay in the liquid temperature that leads to minimal effect on the Stefan condition. Despite the fact that one-phase reduction has been employed in many works [30, 40, 8, 34, 3, 54], its main shortcoming is that the interface motion is insensitive to the liquid phase. In other words, the sensible heat contribution from the liquid to the interface is ignored. To resolve this issue, the method of property averaging is employed to account for the existence of the liquid phase during freezing. The following scalings are introduced

$$\overline{\tau} = \overline{\mathrm{Ste}}\left(\frac{\overline{\alpha}t}{a^2} - \tau_0\right), \qquad \overline{\mathrm{Ste}} = \frac{\overline{c_p}\Delta T}{L}, \tag{5.46}$$

where $\overline{\alpha} = \frac{\alpha_{\mathrm{s}}+\alpha_{\mathrm{l}}}{2}$ and $\overline{c_p} = \frac{c_{p,\mathrm{s}}+c_{p,\mathrm{l}}}{2}$. Thereby, the reduced one-phase Stefan problem is converted into a property-averaged Stefan problem while rewriting it with respect to $\theta_{\mathrm{s}}(\xi, \xi_{\mathrm{i}})$ and $\overline{\tau}(\xi_{\mathrm{i}})$

$$\begin{aligned}
\overline{\mathrm{Ste}}\frac{\partial\theta_{\mathrm{s}}}{\partial\xi_{\mathrm{i}}}\left(\frac{\mathrm{d}\overline{\tau}}{\mathrm{d}\xi_{\mathrm{i}}}\right)^{-1} &= \frac{\partial^2\theta_{\mathrm{s}}}{\partial\xi^2} + \frac{1}{\xi}\frac{\partial\theta_{\mathrm{s}}}{\partial\xi}, \\
-\frac{\partial\theta_{\mathrm{s}}}{\partial\xi}\bigg|_{\xi=\beta} &= \mathrm{Bi}\Big[-1-\theta_{\mathrm{s}}(\beta,\overline{\tau})\Big], \\
\frac{\partial\theta_{\mathrm{s}}}{\partial\xi}\bigg|_{\xi=\xi_{\mathrm{i}}} &= \left(\frac{\mathrm{d}\overline{\tau}}{\mathrm{d}\xi_{\mathrm{i}}}\right)^{-1}, \\
\theta_{\mathrm{s}}(\xi_{\mathrm{i}},\xi_{\mathrm{i}}) &= 0, \\
\overline{\tau}(\beta) &= 0.
\end{aligned} \tag{5.47}$$

Then, we can approach the asymptotic solutions to θ_{s} and $\overline{\tau}$ as follows

$$\begin{aligned}
\theta_{\mathrm{s}} &\sim \theta_{\mathrm{s},0} + \overline{\mathrm{Ste}}\theta_{\mathrm{s},1} + \mathcal{O}(\overline{\mathrm{Ste}}^2), \\
\overline{\tau} &\sim \overline{\tau}_0 + \overline{\mathrm{Ste}}\overline{\tau}_1 + \mathcal{O}(\overline{\mathrm{Ste}}^2).
\end{aligned} \tag{5.48}$$

At the leading order $\mathcal{O}(\overline{\mathrm{Ste}}^0)$

$$\begin{aligned}
\frac{\mathrm{d}^2\theta_{\mathrm{s},0}}{\mathrm{d}\xi^2} + \frac{1}{\xi}\frac{\mathrm{d}\theta_{\mathrm{s},0}}{\mathrm{d}\xi} &= 0, \\
-\frac{\mathrm{d}\theta_{\mathrm{s},0}}{\mathrm{d}\xi}\bigg|_{\xi=\beta} &= \mathrm{Bi}\bigg[-1-\theta_{\mathrm{s},0}(\beta)\bigg], \\
\frac{\mathrm{d}\overline{\tau}_0}{\mathrm{d}\xi_\mathrm{i}}\left(\frac{\mathrm{d}\theta_{\mathrm{s},0}}{\mathrm{d}\xi}\bigg|_{\xi=\xi_\mathrm{i}}\right) &= 1, \\
\theta_{\mathrm{s},0}(\xi_\mathrm{i}) &= 0, \\
\overline{\tau}_0(\beta) &= 0.
\end{aligned} \tag{5.49}$$

The solutions for solid phase and moving boundary are

$$\begin{aligned}
\theta_{\mathrm{s},0} &= \frac{\mathrm{Bi}\beta(\ln\xi - \xi_\mathrm{i})}{1+\mathrm{Bi}\beta(\ln\xi_\mathrm{i} - \ln\beta)}, \\
\overline{\tau}_0 &= \frac{1}{4}\left\{\frac{(\beta\mathrm{Bi}-2)(\beta^2-\xi_\mathrm{i}^2)}{\beta\mathrm{Bi}} + 2\xi_\mathrm{i}^2(\ln\xi_\mathrm{i} - \ln\beta)\right\}.
\end{aligned} \tag{5.50}$$

At the first order $\mathcal{O}(\overline{\mathrm{Ste}}^1)$

$$\begin{aligned}
\frac{\mathrm{d}^2\theta_{\mathrm{s},1}}{\mathrm{d}\xi^2} + \frac{1}{\xi}\frac{\mathrm{d}\theta_{\mathrm{s},1}}{\mathrm{d}\xi} &= \frac{\mathrm{d}\theta_{\mathrm{s},0}}{\mathrm{d}\xi_\mathrm{i}}\left(\frac{\mathrm{d}\overline{\tau}_0}{\mathrm{d}\xi_\mathrm{i}}\right)^{-1}, \\
-\frac{\mathrm{d}\theta_{\mathrm{s},1}}{\mathrm{d}\xi}\bigg|_{\xi=\beta} &= -\mathrm{Bi}\theta_{\mathrm{s},1}(\beta), \\
\theta_{\mathrm{s},0}(\xi_\mathrm{i}) &= 0, \\
\frac{\mathrm{d}\overline{\tau}_1}{\mathrm{d}\xi_\mathrm{i}}\left(\frac{\mathrm{d}\theta_{\mathrm{s},0}}{\mathrm{d}\xi}\bigg|_{\xi=\xi_\mathrm{i}}\right) + \frac{\mathrm{d}\overline{\tau}_0}{\mathrm{d}\xi_\mathrm{i}}\left(\frac{\mathrm{d}\theta_{\mathrm{s},1}}{\mathrm{d}\xi}\bigg|_{\xi=\xi_\mathrm{i}}\right) &= 0, \\
\overline{\tau}_1(\beta) &= 0.
\end{aligned} \tag{5.51}$$

The solutions for solid phase and moving boundary are

$$\begin{aligned}\theta_{\mathrm{s},1} = {} & \frac{-\beta^3\mathrm{Bi}\Big\{\mathrm{Bi}\Big[\beta(\beta\mathrm{Bi}-2)-\mathrm{Bi}\xi_{\mathrm{i}}^2\Big]+2\Big\}\Big[\beta\mathrm{Bi}(\ln\beta-\ln\xi)-1\Big]}{4\xi_{\mathrm{i}}^2\Big[\beta\mathrm{Bi}(\ln\xi_{\mathrm{i}}-\ln\beta)+1\Big]^4} \\ & +\frac{\beta^2\mathrm{Bi}\Big\{-2\beta^2\mathrm{Bi}+\beta^3\mathrm{Bi}^2+\beta(2-\mathrm{Bi}^2\xi^2)+\mathrm{Bi}(\xi^2-\xi_{\mathrm{i}}^2)-\beta\mathrm{Bi}^2(\xi^2-\xi_{\mathrm{i}}^2)(\ln\beta-\ln\xi)\Big\}}{4\xi_{\mathrm{i}}^2\Big[\beta\mathrm{Bi}(\ln\beta-\ln\xi)-1\Big]^3},\end{aligned} \tag{5.52}$$

$$\overline{\tau}_1 = \frac{\beta(\beta\mathrm{Bi}-2)+\mathrm{Bi}\xi_{\mathrm{i}}^2}{4\mathrm{Bi}}+\frac{\beta\Big[\mathrm{Bi}(2\beta-\beta^2\mathrm{Bi}+\mathrm{Bi}\xi_{\mathrm{i}}^2)-2\Big]}{4\mathrm{Bi}\Big[\beta\mathrm{Bi}(\ln\beta-\ln\xi_{\mathrm{i}})-1\Big]}. \tag{5.53}$$

5.3.4 Regime IV

The domain is completely frozen and absent of any liquid when the moving interface reaches the outer surface. A new regime is established after this, namely *Regime IV*. The scaling of this regime describes the time after the total freezing time without any interface motion

$$\tau = \widetilde{\tau} + \tau_{\mathrm{c}}, \qquad \xi_{\mathrm{i}} = 1, \tag{5.54}$$

where τ_{c} is the dimensionless total freezing time. The problem is therefore reduced into a finite-extent heat conduction problem in the solid without any phase change

$$\begin{aligned}\frac{\partial\theta_{\mathrm{s}}}{\partial\widetilde{\tau}} &= \frac{\partial^2\theta_{\mathrm{s}}}{\partial\xi^2}+\frac{1}{\xi}\frac{\partial\theta_{\mathrm{s}}}{\partial\xi}, \\ -\frac{\partial\theta_{\mathrm{s}}}{\partial\xi}\bigg|_{\xi=\beta} &= \mathrm{Bi}\Big[-1-\theta_{\mathrm{s}}(\xi=\beta,\widetilde{\tau})\Big], \\ \frac{\partial\theta_{\mathrm{s}}}{\partial\xi}\bigg|_{\xi=1} &= 0, \\ \theta_{\mathrm{s}}(\xi,0) &= g(\xi).\end{aligned} \tag{5.55}$$

An exact solution exists by using the method of separation variables (same as *Regime I Layer A* with the full derivation in Appendix A. 1. The final solution is expressed as

$$
\begin{aligned}
\widetilde{\theta}_{\mathrm{s}}(\xi,\widetilde{\tau}) &= -1-\sum_{\mathrm{n}=1}^{\infty}\widetilde{c}_{\mathrm{n}}\widetilde{R}_{\mathrm{n}}(\widetilde{\lambda}_{\mathrm{n}},\xi)\exp(-\widetilde{\lambda}_{\mathrm{n}}^{2}\widetilde{\tau}),\\
\widetilde{R}_{\mathrm{n}}(\widetilde{\lambda}_{\mathrm{n}},\xi) &= -J_0(\widetilde{\lambda}_{\mathrm{n}}\xi)\Big[\mathrm{Bi}Y_0(\widetilde{\lambda}_{\mathrm{n}}\beta)+\widetilde{\lambda}_{\mathrm{n}}Y_1(\widetilde{\lambda}_{\mathrm{n}}\beta)\Big]+Y_0(\widetilde{\lambda}_{\mathrm{n}}\xi)\Big[\mathrm{Bi}J_0(\widetilde{\lambda}_{\mathrm{n}}\beta)+\widetilde{\lambda}_{\mathrm{n}}J_1(\widetilde{\lambda}_{\mathrm{n}}\beta)\Big]\\
-J_1(\widetilde{\lambda}_{\mathrm{n}})&\Big[\mathrm{Bi}Y_0(\widetilde{\lambda}_{\mathrm{n}}\beta)+\widetilde{\lambda}_{\mathrm{n}}Y_1(\widetilde{\lambda}_{\mathrm{n}}\beta)\Big]+Y_1(\widetilde{\lambda}_{\mathrm{n}})\Big[\mathrm{Bi}J_0(\widetilde{\lambda}_{\mathrm{n}}\beta)+\widetilde{\lambda}_{\mathrm{n}}J_1(\widetilde{\lambda}_{\mathrm{n}}\beta)\Big]=0,\\
\widetilde{c}_{\mathrm{n}} &= \Big\{\int_{\widetilde{\xi}=\beta}^{1}\widetilde{\xi}\Big[-1-g(\widetilde{\xi})\Big]\widetilde{R}_{\mathrm{n}}(\widetilde{\lambda}_{\mathrm{n}},\widetilde{\xi})\mathrm{d}\widetilde{\xi}\Big\}\Big/\Big\{\int_{\widetilde{\xi}=\beta}^{1}\widetilde{\xi}\widetilde{R}_{\mathrm{n}}^{2}(\widetilde{\lambda}_{\mathrm{n}},\widetilde{\xi})\mathrm{d}\widetilde{\xi}\Big\}.
\end{aligned}
\tag{5.56}
$$

5.3.5 Computation

Though the asymptotic analysis can produce a set of solutions at distinct temporal and spatial scales, it is also crucial to compute these solutions in a coherent and efficient way. In this sub-section, a succinct computation procedure of the asymptotic solutions is listed. An example is also made to illustrate every asymptotic scale and the unified solution about interface motion and temperature profile. The following is a breakdown of every step of the computation on the asymptotic solutions in terms of dimensionless variables and parameters.

1) Prescribe input parameters with respect to the geometry (β), thermophysical properties ($\widetilde{k},\widetilde{c}_p,\widetilde{\alpha}$), initial temperature ($\theta_{\mathrm{init}}$), dimensionless time ($\tau$), and dimensionless numbers (Bi,Ste);

2) Compute τ_0 and $\xi_{\mathrm{i}}(0<\tau\leq\tau_0)$ via *Regime I Layer A* by setting $\xi=\beta$. Specifically, if $\theta_{\mathrm{l}}(\beta,\tau)=0$ in Eq. (5.20), then $\tau=\tau_0$. Hence, $\xi_{\mathrm{i}}(0<\tau\leq\tau_0)=\beta$;

3) Compute $\theta_{\mathrm{l}}(\xi,0<\tau\leq\tau_0)$ via *Regime I Layer A* by setting ξ to be the value of interest;

4) Compute $\overline{\tau}$, ξ_{i}, and θ_{s} in the time domain $(\tau_0,\tau_{\mathrm{c}}]$ via *Regime III Layer D* using Eq. (5.48). Since ξ_{i} is the dependent variable for both $\overline{\tau}$ and θ_{s}, we input an array of ξ_{i} within $[\beta,1]$ in order to obtain the corresponding $\overline{\tau}$ and θ_{s}.

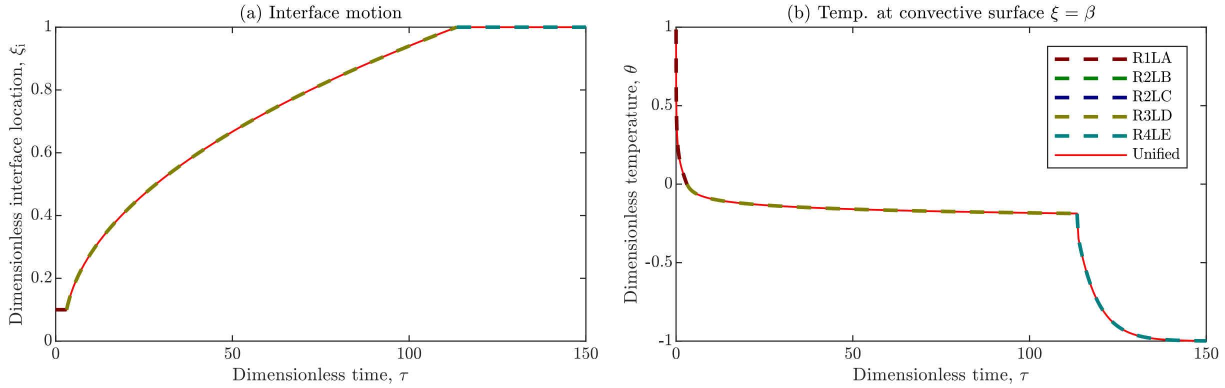

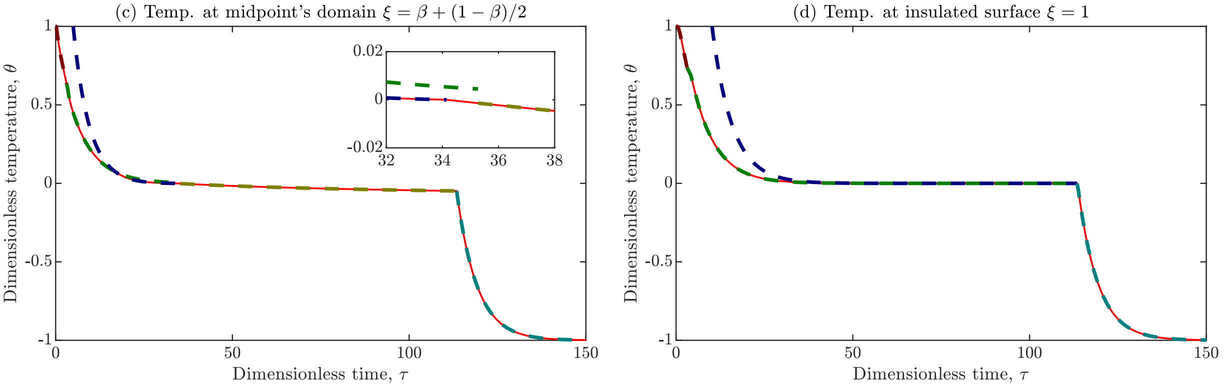

Figure 5.3: Solutions of separate regimes and layers, as well as a unified solution on dimensionless interface motion and temperature profiles at various locations, under the condition that $\theta_{\text{init}} = 1,\ \beta = 0.1,\ \text{Bi} = 1,\ \text{Ste} = 0.0629,\ \widetilde{k} = 4,\ \widetilde{c}_p = 0.5,\ \widetilde{\alpha} = 8$. Note that "R" and "L" are regime and layer, respectively. The dimensionless parameters are determined based on the ice-water thermosphyical properties listed in Table 5.4.

5) Compute the liquid temperature from τ_0 to the time when $\theta_{\text{l}}(\tau, \xi) = 0$. This requires the computation of both *Regime II Layer B* and *Regime II Layer C* in Eq. (5.24) and Eq. (5.43), respectively. If the point of interest ξ is at the convective (inner) boundary, then this regime will be substantially short; if ξ is at the insulated (outer) boundary, then it will be considerably long, and *Regime III* will be a single point at τ_{c}; and

6) Compute $\widetilde{\tau}$, ξ_{i}, and θ_{s} in the time domain $(\tau_{\text{c}}, \infty)$ via *Regime IV Layer E* using Eq. (5.56). The variable ξ_{i} will be equal to 1 at all times since the interface is stationary at the outer boundary.

Figure 5.3 shows an example of the dimensionless interface motion and temperature profile using different regimes and layers (abbreviated to "R" and "L," respectively) as well as the unified solution. The following dimensionless parameters are prescribed for this scenario: $\theta_{\text{init}} = 1,\ \beta = 0.1,\ \text{Bi} = 1,\ \text{Ste} = 0.0629,\ \widetilde{k} = 4,\ \widetilde{c}_p = 0.5,\ \widetilde{\alpha} = 8$. Note that the dimensionless values are calculated based on Table 5.4. The dimensionless interface is depicted in Fig. 5.3 (a), where R1LA, R3LD, and R4LE are combined into a unified asymptotic solution (in the solid red line). It is noted that *Regime II* does not have to contribute to the interface motion as there has also been a property-averaged consideration in *Regime III*. Figure 5.3 (b,c,d) demonstrates the dimensionless interface at the convective (inner) surface, middle of the domain, and insulated (outer) surface, i.e., $\xi = \beta, \beta + (1-\beta)/2, 1$. As can be seen, the presence of each scale could, to a great extent, vary based on the location of interest. At the inner surface, the liquid temperature is prevailed by R1LA till τ_0 because the interface will only start to move when the surface reaches its fusion. After τ_0, the dimensionless temperature will be below 0 at R3LD for the coexistence of both phases; it is then followed by pure heat conduction without phase change when $\tau > \tau_{\text{c}}$ at R4LE. However, when standing at the midpoint of the domain (as shown in Fig. 5.3 (c)), *Regime II* will be presented after τ_0. This is because liquid still passes at the midpoint after the interface moves from the convective surface. At the outer surface, *Regime III* will vanish in the temperature profile, and R3LD will solely serve to terminate R2LC using τ_{c}. Its solid temperature is, therefore, the consequence of pure heat conduction after phase change in *Regime IV*.

5.4 Numerical method

Outward solidification in an annulus can be solved numerically using the enthalpy method, in addition to the two-phase Stefan problem presented in Section 5.2.1. One of the pioneers employing the fixed-grid approach to solve the enthalpy formulation is Voller (and his coworkers) [46, 47], later referred to as *enthalpy method*. The method implements an arbitrary area in between the two phases (called *mushy zone*) to take account for the release of latent heat and adapt/smooth the abrupt transition during phase change, which in a way removes the non-linearity of the phase change problem. The mushy zone is also physically tangible, and its evolution during melting and freezing can be captured using a high-speed charged-coupled device (CCD) camera [57]. This study uses the enthalpy method to verify the developed asymptotic solution based on the two-phase Stefan problem.

The governing equation of the enthalpy method has the general form

$$\frac{\partial H}{\partial t} = \nabla \cdot (k \nabla T), \tag{5.57}$$

where H is the enthalpy that can be expressed as a function of temperature T

$$H = (1-\gamma) \int_{T_{\text{solidus}}}^{T} \rho c_{p,\text{s}} \mathrm{d}T + \gamma \int_{T_{\text{liquidus}}}^{T} \rho c_{p,\text{l}} \mathrm{d}T + \gamma \rho L, \tag{5.58}$$

and γ is the liquid fraction given by

$$\gamma = \begin{cases} 0 & , \quad T < T_{\text{solidus}} \\ \frac{T - T_{\text{solidus}}}{\Delta T_{\text{mushy}}} & , \quad T_{\text{solidus}} \leq T \leq T_{\text{liquidus}} \\ 1 & , \quad T > T_{\text{liquidus}} \end{cases}, \tag{5.59}$$

The variables T_{solidus}, T_{liquidus}, and ΔT_{mushy} are the solidus temperature, liquidus temperature, and temperature range for the mushy zone (i.e., $T_{\text{liquidus}} - T_{\text{solidus}}$), respectively. The discretization scheme is consistent with and documented in great detail in our previous work [54].

Two main aspects can support the accuracy of the numerical results by the enthalpy method: (i) the independency on the numbers of time steps N_{t} and mesh elements N_{r}; and (ii) the temperature range for the mushy zone ΔT_{mushy}. Comparisons for different numbers of time steps and mesh sizes with respect to temperature profiles and interface motion are made in Figure 5.4. Particularly, five variations of time-step and mesh counts are considered ($N_\mathrm{t} = N_\mathrm{r} = 100, 200, 400, 800, 1000$) while fixing the rest of the variables, such as $\Delta T_\mathrm{mushy}, \mathrm{Bi}, T_\mathrm{init}, T_\infty, b, a, r$, and thermophysical properties, as listed in Table 5.4. It is rather clear to see that the temperature curves in (a,b) converge for finer meshes and time steps; the cases of $N_\mathrm{t} = N_\mathrm{r} = 800, 1000$ provide acceptable outcomes with great consistency. Similarly, the interface motion for liquidus (c) and solidus (d) also draw the same conclusion. As can be observed in the zoomed-in interface location at $r_\mathrm{i} = 1$, the total freezing time can be varied by around 3.1% between the coarser and finest mesh counts and time-step sizes. Hence, $N_\mathrm{t} = N_\mathrm{r} = 800$ is selected to be the accurate and reliable number of time steps and mesh elements in this model. In addition, the effect of the mushy-zone temperature range ΔT_mushy is also an influential factor in the numerical results. Since the Stefan problem assumes a sharp interface between the two phases, the equivalent mushy-zone temperature range is zero, i.e., $\Delta T_\mathrm{mushy} = 0$. Previous study [54] has proven that the interface motion (specifically, the solidus and liquidus interfaces) could change drastically for different temperature ranges for the mushy zone, but the temperature curve remains the same; as $\Delta T_\mathrm{mushy} \to 0$, the deviation between the solidus and liquidus interfacial motion becomes minuscule. As a consequence, $\Delta T_\mathrm{mushy} = 0.001°\mathrm{C}$ is chosen to be the temperature range for the mushy zone to circumvent the effect of the mushy zone and make an equal comparison with the Stefan problem.

5.5 Results and discussion

5.5.1 Effect of Biot number

The Biot number (Bi) appears in the dimensionless problem due to the convective boundary. Traditionally, for conduction problems without phase change, the Biot number implies how significantly the temperature within the domain varies with the heat flux at its surface over time. When considering a phase-change problem governed by heat conduction, the significance of variation between the body temperature and surface heat flux will be subjected to the phases and stages being undergone. A few results generated by the developed asymptotic

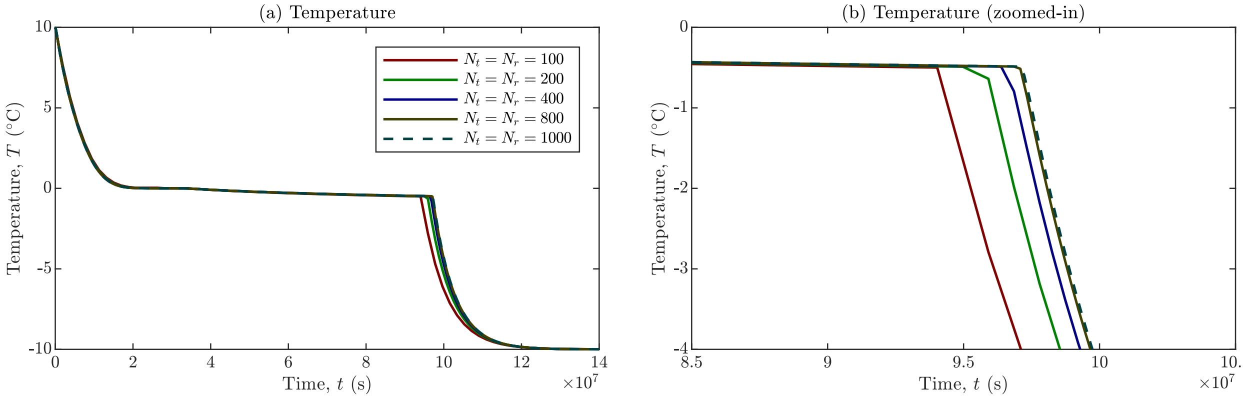

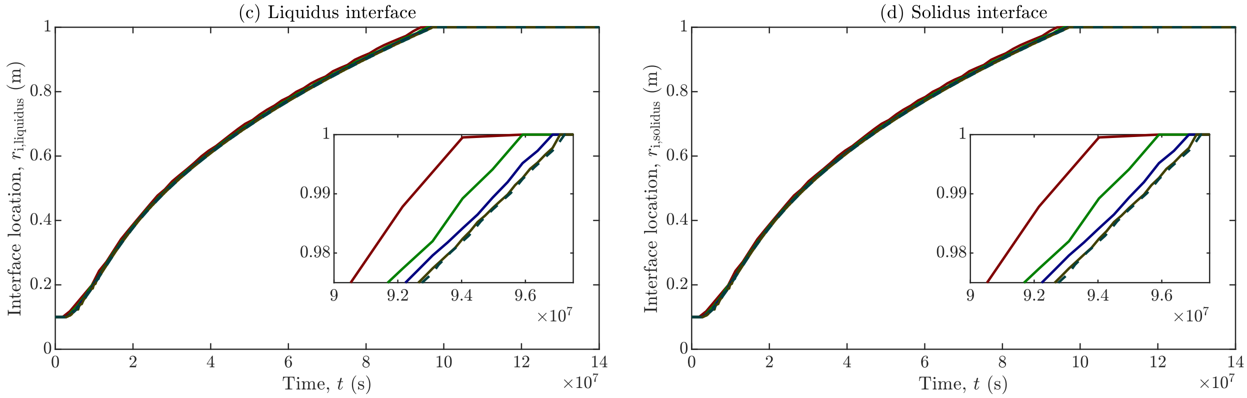

Figure 5.4: Comparisons of temperature profile (a,b) and interface motion (c,d) for various numbers of time steps N_{t} and mesh sizes N_{r}, under the condition that $\Delta T_{\mathrm{mushy}} = 0.001$°C, $\mathrm{Bi} = 1$, $T_{\mathrm{init}} = 10$°C, $T_\infty = -10$°C, $b = 0.1$ m, $a = 1.0$ m, $r = 5.5$ m, and ice-water thermophysical properties (See Table 5.4).

Table 5.4: List of thermophysical properties for ice-water PCM.

Property	Value	Unit
Ice		
Mass density, $\rho_{\mathrm{s}} = \rho$	1000	kg m^{-3}
Specific heat, $c_{p,\mathrm{s}}$	2100	J kg^{-1} K^{-1}
Thermal conductivity, k_{s}	2.22	W m^{-1} K^{-1}
Thermal diffusivity, α_{s}	1.06×10^{-6}	m^2 s^{-1}
Water		
Mass density, $\rho_{\mathrm{l}} = \rho$	1000	kg m^{-3}
Specific heat, $c_{p,\mathrm{l}}$	4200	J kg^{-1} K^{-1}
Thermal conductivity, k_{l}	0.555	W m^{-1} K^{-1}
Thermal diffusivity, α_{l}	1.32×10^{-7}	m^2 s^{-1}
Phase change		
Latent heat of fusion, L	3.34×10^5	J kg^{-1}

solution are presented and discussed to elaborate the effect of Biot numbers in the Stefan problems Numerical data using the enthalpy method is also used to verify the developed asymptotic solution.

Figure 5.5 shows the comparison of the dimensionless interface motion between the asymptotic solution and numerical results by the enthalpy method at various Biot numbers: $\mathrm{Bi} = 0.01, 0.1, 1, 10, 100, 1000$. As is evident from Fig. 5.5, the Biot number increases with the interface velocity, reducing the total freezing time τ_{c}. For large Biot numbers (i.e., when the Biot number exceeds 100), neither the interface velocity nor the freezing time change substantially. This happens because the large Biot number leads to an extremely high heat flux, which eventually turns into an isothermal boundary; that is, Eq. (5.4) becomes $T(r = b, t) = T_{\infty}$. The isothermal boundary with a two-phase Stefan problem in an annulus was previously studied in [54] using the asymptotic method, which was also verified with the numerical data using the same enthalpy method. Compared with the past work with an isothermal boundary [54], the solid-liquid interface does not move right away. This can be clearly observed in relatively small Biot numbers, e.g., $\mathrm{Bi} = 0.01, 0.1$. Meanwhile, the asymptotic solution with the convective boundary continues to have a rather slight overestimation on the interface than the numerical one. This is because the asymptotic expansion assumes Stefan number as its asymptotic limit to be extremely small (i.e., ignoring the contribution of the sensible heat, especially in the liquid phase), which to some extent omits the second term that slows down interface velocity in the Stefan condition as expressed in Eq. (5.6).

Figure 5.6 demonstrates the effect of Biot numbers with respect to dimensionless temperature profiles under the condition $\theta_{\mathrm{init}} = 1,\ \mathrm{Ste} = 0.0126,\ \xi = 1,\ \widetilde{k} = 4,\ \widetilde{c}_p = 0.5,\ \widetilde{\alpha} = 8$, in which the thermophysical properties are based on an ice-water PCM listed in Table 5.4. Both low and high Biot numbers are compared in Fig. 5.6(a) and (b), respectively. Increasing the Biot number is expected to enhance the heat conduction inside the PCM, contributing to a shorter freezing time. Some discrepancies are found in the liquid temperature, mainly

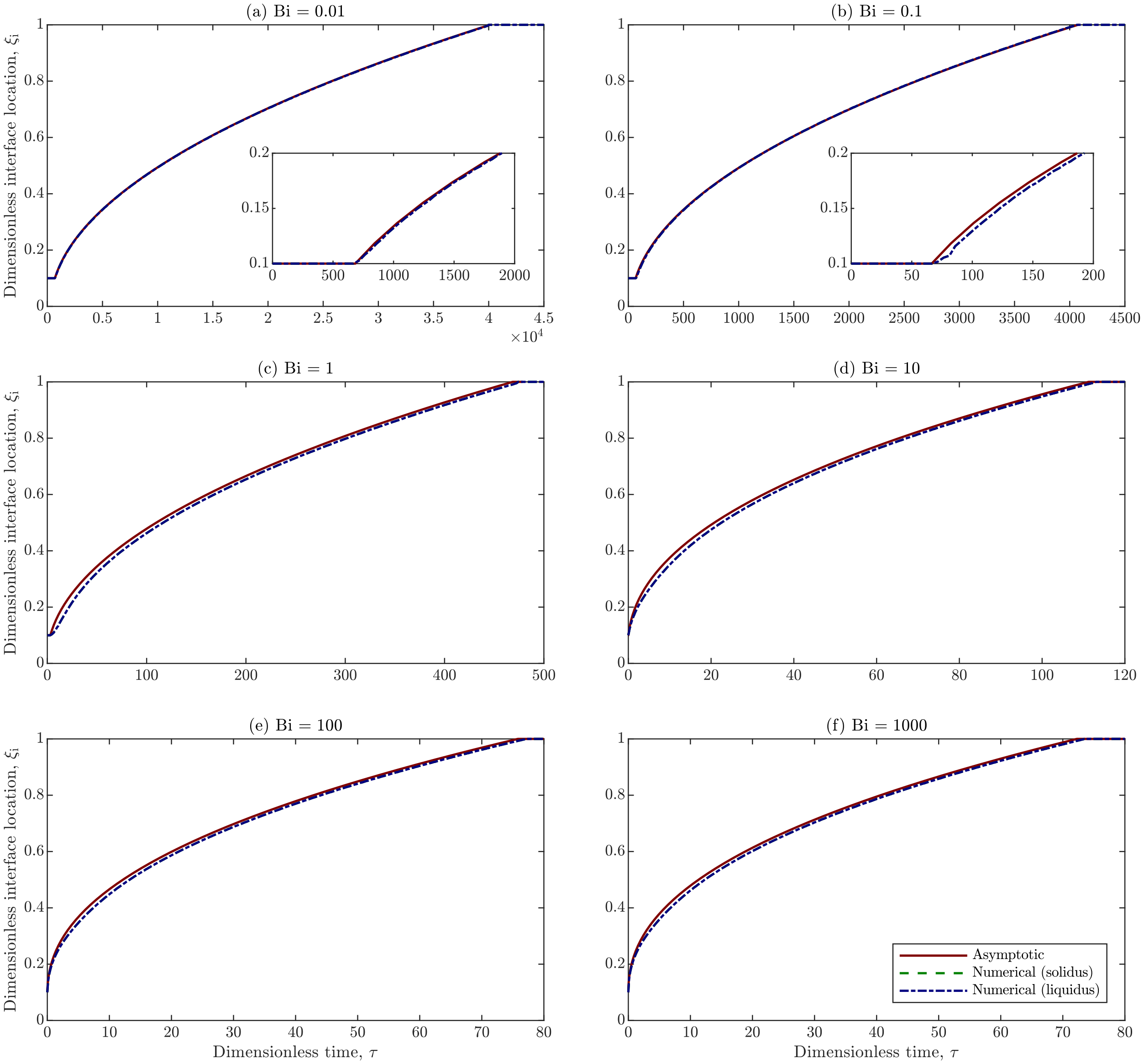

Figure 5.5: Comparisons of dimensionless interface motion between asymptotic and numerical (both solidus and liquidus) results for various Biot numbers under the condition that $\theta_{\text{init}} = 1,\ \beta = 0.1,\ \text{Ste} = 0.0126,\ \widetilde{k} = 4,\ \widetilde{c}_p = 0.5,\ \widetilde{\alpha} = 8.$

in high Biot numbers. Since the time interval of liquid temperature for the cooling stage is relatively short compared to the freezing stage, it plays a less significant role in the entire temperature profile. It also has no considerable difference among the Biot numbers. Another slight deviation is the total freezing time that leads to the difference in *Regime IV* due to the small Stefan number approximation in the analysis. From a physical standpoint, it is the disregard for sensible heat while undergoing the phase transition. However, such variation

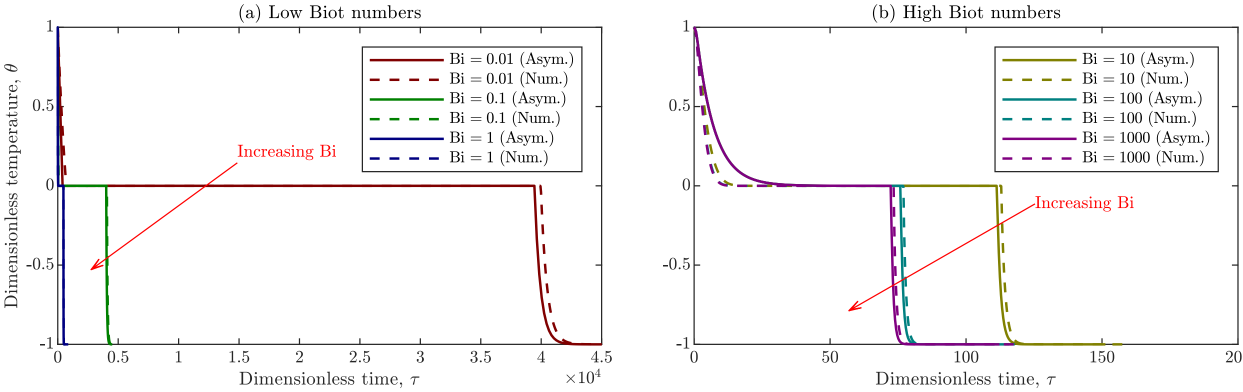

Figure 5.6: Effect of Biot number on the dimensionless temperature profile under the condition that $\theta_{\text{init}} = 1$, $\text{Ste} = 0.0126$, $\xi = 1$, $\widetilde{k} = 4$, $\widetilde{c}_p = 0.5$, $\widetilde{\alpha} = 8$.

shall become smaller as the Stefan number approaches zero, i.e., Ste → 0, shown in the following sub-section.

In addition, a particular study on the dimensionless pre-cooling and freezing times (τ_0 and τ_c) for Biot numbers is conducted in Fig. 5.7. Both asymptotic and numerical solutions are plotted. It is rather clear to observe that the pre-cooling and freezing times may seem insignificant at $\text{Bi} = 1$, but it is exponentially higher as $\text{Bi} \to 0$. When computing $\text{Bi} = 0.01$, τ_0 and τ_c are almost two orders of magnitude higher than the ones at $\text{Bi} = 1$. The results indicate the importance of abandoning the assumption that the solid-liquid interface will be moved right away at $\tau = 0$. Even though the assumption is valid in the Stefan problems with an isothermal boundary [30, 8, 34, 3, 54], it would limit the validity range of the asymptotic solutions to a convective boundary. The consistency between the asymptotic and numerical results also proves the accurate analysis in *Regime I*.

5.5.2 Effect of Stefan number

Another unique dimensionless parameter in the Stefan problems is the Stefan number (Ste), the ratio of sensible over latent heats, expressed as $c_p \Delta T / L$. The paramount presumption in the asymptotic analysis is the Stefan number approaches 0, which is valid in many engineering applications involving PCMs with respect to the specific heat c_p and latent heat L. The third

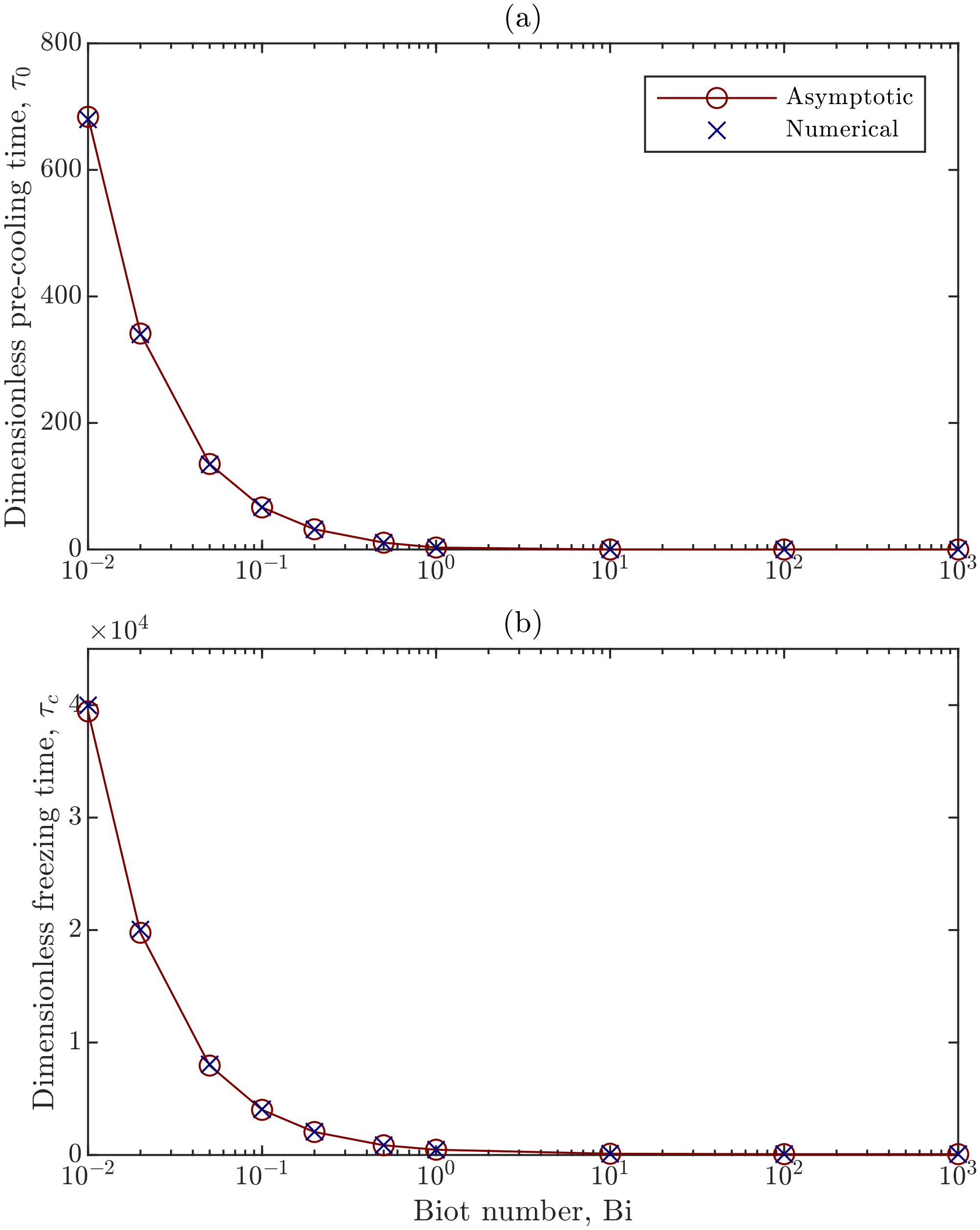

Figure 5.7: Effect of Biot number on dimensionless pre-cooling and freezing times under the condition that $\theta_{\text{init}} = 1,\ \text{Ste} = 0.0126,\ \widetilde{k} = 4,\ \widetilde{c}_p = 0.5,\ \widetilde{\alpha} = 8$.

part of Ste is the temperature interval in the sensible heat $\Delta T = T_{\text{f}} - T_{\infty}$; this term, however, depends on the operational environment. A high-temperature interval could result in Stefan numbers in the order of $\text{Ste} = \mathcal{O}(0.10)$, which would violate the asymptotic limit $\text{Ste} \to 0$ using the traditional asymptotic technique.

Figure 5.8 compares the asymptotic and numerical solutions concerning the dimensionless interface profile at various Stefan numbers. In this study, the Stefan numbers are varied based on the temperature difference ΔT in the sensible heat, as an example. Though the specific heat c_p and latent heat L in the Stefan number can also alter its magnitude, previous study has found minimal difference between the asymptotic and numerical results when changing ΔT, c_p or L for the same magnitude of Ste [54]. Four Stefan numbers of 0.0063, 0.0126, 0.0629, and 0.0943 are assumed that correspond to the ambient air temperatures of -1, -2, -10, and -15 °C, respectively, according to the data given in Table 5.4. As can be seen in Fig. 5.8, the significance of the overestimation of the interface location accelerates as the Stefan number increases. The asymptotic limit is often not greater than 0.01; that is, $\mathrm{Ste} \leq 0.01$. When $\mathrm{Ste} = 0.0629$ in Fig. 5.8(c), for instance, the asymptotic solution has a noticeable difference with the numerical data. There will inevitably be an overestimation of the conventional asymptotic expansion unless other techniques are introduced. In the analysis, the method of property averaging is utilized to compensate for the deviation for Stefan numbers greater than 0.01. The result shows that using the averaged thermophysical properties at the freezing stage can, to some extent, minimize the error in the asymptotic analysis for ignoring sensible heat in both phases. Hence, the validity range of the developed asymptotic solution can be enlarged to almost 0.10 as indicated in Fig. 5.8(c,d). Figure 5.9 demonstrates the corresponding dimensionless temperature profiles for the same Stefan numbers in Fig. 5.8, i.e., $\mathrm{Ste} = 0.0063,\ 0.0126,\ 0.0629,\ 0.0943$. The freezing time shortens with increasing Stefan numbers, giving the same tendency as the interface velocity. As a consequence, it can be concluded that the asymptotic solution with averaged thermophysical properties can enlarge the small Stefan number limit from 0.01 to 0.1, making it practical for more applications in thermal sciences.

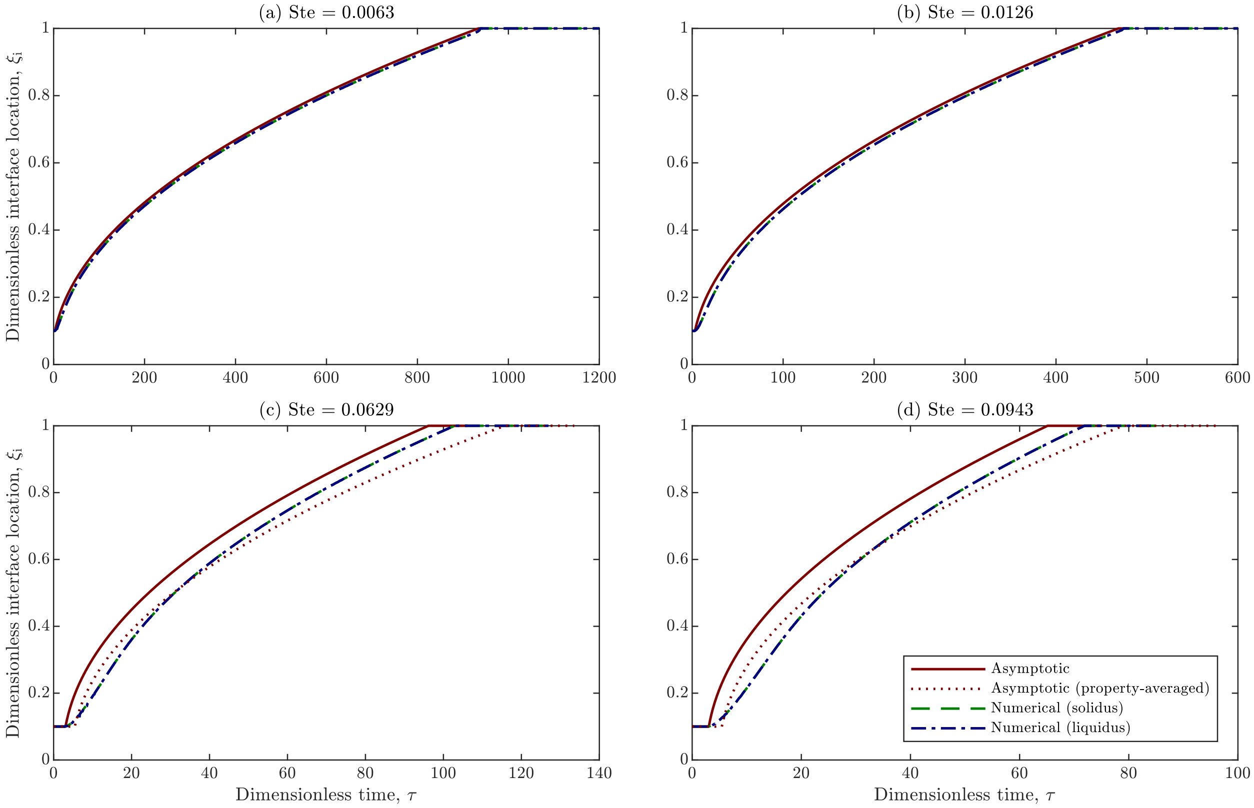

Figure 5.8: Comparisons of dimensionless interface motion between asymptotic and numerical (both solidus and liquidus) results for various Stefan numbers Ste, under the condition that $\theta_{\text{init}} = 1,\ \beta = 0.1,\ \text{Bi} = 1,\ \widetilde{k} = 4,\ \widetilde{c}_p = 0.5,\ \widetilde{\alpha} = 8$.

5.6 Conclusion

In this research, we formulated a two-phase Stefan problem in the annulus for outward solidification subjected to a convective or Robin boundary condition. Compared with the traditional formulation of Stefan problems, we did not make the assumption that the solid-liquid interface moves immediately with time, which provided a better representation of the phase change phenomenon initiated by a convective surface. A systematic asymptotic analysis was conducted based on four temporal and five spatial scales, and the property-averaging method was also employed. The following remarks can be concluded:

1) The asymptotic solution can predict the solid-liquid moving interface motion as well as the temperature profile at any point of the domain in a unified manner;

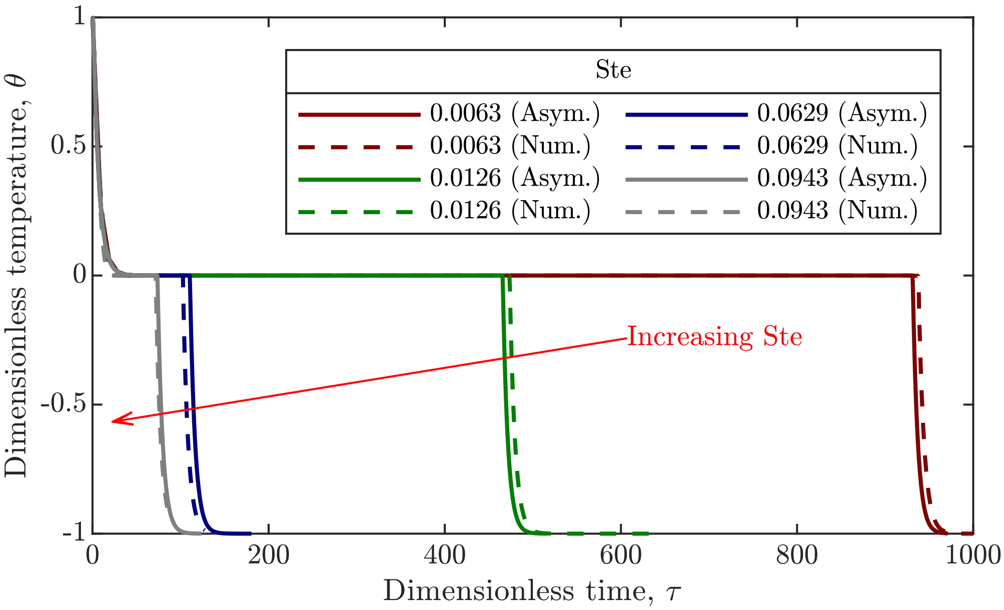

Figure 5.9: Effect of Stefan number on the dimensionless temperature profile under the condition that $\theta_{\text{init}} = 1$, $\text{Bi} = 1$, $\xi = 1$, $\widetilde{k} = 4$, $\widetilde{c}_p = 0.5$, $\widetilde{\alpha} = 8$. Note that $\text{Ste} = 0.0063,\ 0.0126,\ 0.0629,\ 0.0943$ are in the red, green, blue, and grey lines, respectively. The asymptotic solution is in the solid line, while the numerical result is in the dashed line.

2) The developed solution was verified with the enthalpy method that can simulate the same phase change problem through numerical discretization;

3) The Biot number is not influential to the accuracy of the asymptotic solution. For large Biot numbers, the pre-cooling time becomes exponentially apparent, which has been properly captured in the asymptotic analysis as a distinct scale;

4) Less accurate results could be found in large Stefan numbers due to the assumption of the asymptotic analysis; however, it was observed that the presented solution coupled with the method of property averaging was more accurate than the one using traditional asymptotic techniques.

It is recommended that future studies could investigate the extension to other Stefan problems with a convective boundary, such as Cartesian or spherical coordinates, different directions of the interfacial motion, incorporation of the convective term in the heat equations, and corresponding melting problems. Also, while the present study considers the motion of a sharp interface, the proposed method can be extended to model phase change problems where there exists a physical mushy region. Another potential research direction can be the correction of higher-order perturbation solutions, especially on the moving interface. Since it is inevitable to have diverged or extremely small higher-order terms when continuing to solve the asymptotic expansion, it would be more effective to have a correction term using advanced optimization methods or statistical analyses to minimize the difference between the asymptotic and true values.

Appendix A. Derivation of the exact solution to a cylindrical heat conduction problem using the separation of variables

A.1. Convective-insulated boundary conditions

Consider the following problem

$$\begin{aligned} \frac{1}{\alpha}\frac{\partial T}{\partial t} &= \frac{\partial^2 T}{\partial r^2} + \frac{1}{r}\frac{\partial T}{\partial r}, \qquad b < r < a, \qquad t > 0, \\ -k\frac{\partial T}{\partial r}\bigg|_{r=b} &= h\Big[T_\infty - T(b,t)\Big], \\ \frac{\partial T}{\partial r}\bigg|_{r=a} &= 0, \\ T(r,0) &= T_{\text{init}}. \end{aligned} \tag{5.60}$$

First, we linearly scale the temperature as $\widetilde{T} = T_\infty - T$ to remove the non-homogeneity in the convective boundary and the problem becomes

$$\begin{aligned} \frac{1}{\alpha}\frac{\partial \widetilde{T}}{\partial t} &= \frac{\partial^2 \widetilde{T}}{\partial r^2} + \frac{1}{r}\frac{\partial \widetilde{T}}{\partial r}, \\ k\frac{\partial \widetilde{T}}{\partial r}\bigg|_{r=b} &= h\widetilde{T}(b,t), \\ \frac{\partial \widetilde{T}}{\partial r}\bigg|_{r=a} &= 0, \\ \widetilde{T}(r,0) &= T_\infty - T_{\text{init}}. \end{aligned} \tag{5.61}$$

Second, the newly scaled temperature variable can be separated into $R(r)$ and $\Gamma(t)$ as follows

$$\widetilde{T}(r,t) = R(r) \times \Gamma(t). \tag{5.62}$$

Thus, the governing equation is now expressed as

$$\frac{R'' + \frac{1}{r}R'}{R} = \frac{\frac{1}{\alpha}\Gamma'}{\Gamma} = -\lambda^2, \tag{5.63}$$

and

$$
\begin{aligned}
&R'' + \frac{1}{r}R' = -\lambda^2 R, \qquad kR'(a) = hR(b), \qquad R'(a) = 0, \\
&\frac{1}{\alpha}\Gamma' = -\lambda^2\Gamma, \qquad \Gamma(0) = T_\infty - T_{\text{init}}.
\end{aligned}
\tag{5.64}
$$

For the spatial part $R(r)$, it becomes a Sturm-Liouville problem with the general solution

$$
R(r) = c_1 J_0(\lambda r) + c_2 Y_0(\lambda r). \tag{5.65}
$$

Substituting the first boundary condition, we find

$$
c_1 = \frac{-c_2[hY_0(\lambda b) + \lambda k Y_1(\lambda b)]}{hJ_0(\lambda b) + \lambda k J_1(\lambda b)}. \tag{5.66}
$$

Thus,

$$
\begin{aligned}
R(r) &= c_2\left\{ -\frac{hY_0(\lambda b) + \lambda k Y_1(\lambda b)}{hJ_0(\lambda b) + \lambda k J_1(\lambda b)} J_0(\lambda r) + Y_0(\lambda r)\right\} && (5.67)\\
&= c_3\left\{ J_0(\lambda r)\Big[hY_0(\lambda b) + \lambda k Y_1(\lambda b)\Big] - Y_0(\lambda r)\Big[hJ_0(\lambda b) + \lambda k J_1(\lambda b)\Big]\right\}. && (5.68)
\end{aligned}
$$

Substituting the second boundary condition, we find the eigenvalues can be found by [62]

$$
-J_1(\lambda a)\Big[hY_0(\lambda b) + \lambda k Y_1(\lambda b)\Big] + Y_1(\lambda a)\Big[hJ_0(\lambda b) + \lambda k J_1(\lambda b)\Big] = 0. \tag{5.69}
$$

For the temporal part $\Gamma(t)$, the general solution to $\Gamma(t)$ is

$$
\Gamma(t) = c_4 \exp(-\alpha\lambda^2 t). \tag{5.70}
$$

Lastly, the exact solution is forged by combining the two separated parts

$$\begin{aligned}\widetilde{T}(r,t) &= \sum_{\mathrm{n}=1}^{\infty} c_{\mathrm{n}} \left\{ J_0(\lambda_{\mathrm{n}} r)\Big[hY_0(\lambda_{\mathrm{n}} b) + \lambda_{\mathrm{n}} k Y_1(\lambda_{\mathrm{n}} b)\Big] - Y_0(\lambda_{\mathrm{n}} r)\Big[hJ_0(\lambda_{\mathrm{n}} b) + \lambda_{\mathrm{n}} k J_1(\lambda_{\mathrm{n}} b)\Big]\right\} \exp(-\alpha\lambda_{\mathrm{n}}^2 t)\\ &= \sum_{\mathrm{n}=1}^{\infty} c_{\mathrm{n}} R_{\mathrm{n}}(\lambda_{\mathrm{n}}, r)\exp(-\alpha\lambda_{\mathrm{n}}^2 t),\end{aligned} \tag{5.71}$$

where c_{n} can be found by the initial condition

$$\begin{aligned} c_{\mathrm{n}} &= \left\{ \int_b^a \widetilde{r}(T_\infty - T_{\mathrm{init}}) R_{\mathrm{n}}(\lambda_{\mathrm{n}}, \widetilde{r}) d\widetilde{r} \right\} \Big/ \left\{ \int_b^a \widetilde{r}[R_{\mathrm{n}}(\lambda_{\mathrm{n}}, \widetilde{r})]^2 d\widetilde{r} \right\}\\ &= \left\{ (T_\infty - T_{\mathrm{init}}) \int_b^a \widetilde{r} R_{\mathrm{n}}(\lambda_{\mathrm{n}}, \widetilde{r}) d\widetilde{r} \right\} \Big/ \left\{ \int_b^a \widetilde{r}[R_{\mathrm{n}}(\lambda_{\mathrm{n}}, \widetilde{r})]^2 d\widetilde{r} \right\}. \end{aligned} \tag{5.72}$$

A.2. Isothermal-insulated boundary conditions

Consider a similar problem yet with an isothermal boundary at the inner surface

$$\begin{aligned} \frac{1}{\alpha}\frac{\partial T}{\partial t} &= \frac{\partial^2 T}{\partial r^2} + \frac{1}{r}\frac{\partial T}{\partial r}, \qquad b < r < a, \qquad t > 0,\\ T(r=b,t) &= T_{\mathrm{b}},\\ \left.\frac{\partial T}{\partial r}\right|_{r=a} &= 0,\\ T(r,0) &= T_{\mathrm{init}}. \end{aligned} \tag{5.73}$$

First, a linear temperature shift is made using $\widetilde{T} = T - T_{\mathrm{b}}$ and the problem becomes

$$\begin{aligned} \frac{1}{\alpha}\frac{\partial \widetilde{T}}{\partial t} &= \frac{\partial^2 \widetilde{T}}{\partial r^2} + \frac{1}{r}\frac{\partial \widetilde{T}}{\partial r},\\ \widetilde{T}(r=b,t) &= 0,\\ \left.\frac{\partial \widetilde{T}}{\partial r}\right|_{r=a} &= 0,\\ \widetilde{T}(r,0) &= T_{\mathrm{init}} - T_{\mathrm{b}}. \end{aligned} \tag{5.74}$$

Second, the newly scaled temperature variable is separated into $R(r)$ and $\Gamma(t)$ in the same way as the previous problem and thus

$$\begin{aligned} &R'' + \frac{1}{r}R' = -\lambda^2 R, \qquad R(b) = 0, \qquad R'(a) = 0, \\ &\frac{1}{\alpha}\Gamma' = -\lambda^2\Gamma, \qquad \Gamma(0) = T_{\text{init}} - T_{\text{b}}. \end{aligned} \tag{5.75}$$

For the spatial part $R(r)$, the general solution is

$$R(r) = c_1 J_0(\lambda r) + c_2 Y_0(\lambda r). \tag{5.76}$$

Substituting the first boundary condition, we find

$$c_1 = \frac{-c_2 Y_0(\lambda b)}{J_0(\lambda b)}. \tag{5.77}$$

Thus,

$$\begin{aligned} R(r) &= c_2\left\{ -\frac{Y_0(\lambda b)}{J_0(\lambda b)}J_0(\lambda r) + Y_0(\lambda r)\right\} \\ &= c_3\left\{ J_0(\lambda r)Y_0(\lambda b) - Y_0(\lambda r)J_0(\lambda b)\right\}. \end{aligned} \tag{5.78}$$

Substituting the second boundary condition, we find the eigenvalues can be found by [54]

$$-J_1(\lambda a)Y_0(\lambda b) + Y_1(\lambda a)J_0(\lambda b) = 0. \tag{5.79}$$

For the temporal part $\Gamma(t)$, the general solution to $\Gamma(t)$ is

$$\Gamma(t) = c_4 \exp(-\alpha\lambda^2 t). \tag{5.80}$$

Lastly, we combined the two separated parts as a unified solution

$$\begin{aligned}\widetilde{T}(r,t) &= \sum_{\mathrm{n}=1}^{\infty} c_{\mathrm{n}} \Big\{ J_0(\lambda r) Y_0(\lambda b) - Y_0(\lambda r) J_0(\lambda b) \Big\} \exp(-\alpha \lambda_{\mathrm{n}}^2 t) \\ &= \sum_{\mathrm{n}=1}^{\infty} c_{\mathrm{n}} R_{\mathrm{n}}(\lambda_{\mathrm{n}}, r) \exp(-\alpha \lambda_{\mathrm{n}}^2 t),\end{aligned} \tag{5.81}$$

where c_{n} can be found by the initial condition

$$\begin{aligned}c_{\mathrm{n}} &= \Big\{ \int_b^a \widetilde{r}(T_{\mathrm{init}} - T_{\mathrm{b}}) R_{\mathrm{n}}(\lambda_{\mathrm{n}}, \widetilde{r}) d\widetilde{r} \Big\} \Big/ \Big\{ \int_b^a \widetilde{r} [R_{\mathrm{n}}(\lambda_{\mathrm{n}}, \widetilde{r})]^2 d\widetilde{r} \Big\} \\ &= \Big\{ (T_{\mathrm{init}} - T_{\mathrm{b}}) \int_b^a \widetilde{r} R_{\mathrm{n}}(\lambda_{\mathrm{n}}, \widetilde{r}) d\widetilde{r} \Big\} \Big/ \Big\{ \int_b^a \widetilde{r} [R_{\mathrm{n}}(\lambda_{\mathrm{n}}, \widetilde{r})]^2 d\widetilde{r} \Big\}.\end{aligned} \tag{5.82}$$

Bibliography

[1] S. Akhtar, M. Xu, and A. Sasmito. Verification and validation of droplet freezing for convective boundary condition using matched asymptotic perturbation method and computational fluid dynamics. In *ASME International Mechanical Engineering Congress and Exposition*, volume 59452, page V008T09A053. American Society of Mechanical Engineers, 2019.

[2] S. Akhtar, M. Xu, and A. P. Sasmito. Development and validation of a semi-analytical framework for droplet freezing with heterogeneous nucleation and non-linear interface kinetics. *International Journal of Heat and Mass Transfer*, 166:120734, 2021.

[3] S. Akhtar, M. Xu, and A. P. Sasmito. Development and validation of an asymptotic solution for a two-phase stefan problem in a droplet subjected to convective boundary condition. *International Journal of Thermal Sciences*, 164:106923, 2021.

[4] M. A. Alzoubi, M. Xu, F. P. Hassani, S. Poncet, and A. P. Sasmito. Artificial ground freezing: A review of thermal and hydraulic aspects. *Tunnelling and Underground Space Technology*, 104:103534, 2020.

[5] J. Bollati and D. A. Tarzia. Explicit solution for Stefan problem with latent heat depending on the position and a convective boundary condition at the fixed face using Kummer functions. *arXiv preprint arXiv:1610.09338*, 2016.

[6] J. Bollati and D. A. Tarzia. Exact solution for a two-phase Stefan problem with variable latent heat and a convective boundary condition at the fixed face. *Zeitschrift für Angewandte Mathematik und Physik*, 69(2):38, 2018.

[7] A. C. Briozzo and D. A. Tarzia. An explicit solution for an instantaneous two-phase Stefan problem with nonlinear thermal coefficients. *IMA Journal of Applied Mathematics*, 67(3):249–261, 2002.

[8] F. Brosa Planella, C. P. Please, and R. A. Van Gorder. Extended Stefan problem for solidification of binary alloys in a finite planar domain. *SIAM Journal on Applied Mathematics*, 79(3):876–913, 2019.

[9] J. Caldwell and Y. Kwan. On the perturbation method for the Stefan problem with time-dependent boundary conditions. *International Journal of Heat and Mass Transfer*, 46(8):1497–1501, 2003.

[10] A. N. Ceretani, N. N. Salva, and D. A. Tarzia. An exact solution to a Stefan problem with variable thermal conductivity and a Robin boundary condition. *Nonlinear Analysis: Real World Applications*, 40:243–259, 2018.

[11] V. Chaurasiya and J. Singh. An analytical study of coupled heat and mass transfer freeze-drying with convection in a porous half body: A moving boundary problem. *Journal of Energy Storage*, 55:105394, 2022.

[12] Z. Chen, C. Shu, Y. Liu, L. Zhang, Z. Zhang, and Z. Yuan. Isotherm-evolution-based interface tracking algorithm for modelling temperature-driven solid-liquid phase-change in multiphase flows. *International Journal of Thermal Sciences*, 177:107541, 2022.

[13] T. A. Dauzhenka and I. A. Gishkeluk. Quasilinear heat equation in three dimensions and Stefan problem in permafrost soils in the frame of alternating directions finite difference scheme. In *Proceedings of the World Congress on Engineering*, volume 1, pages 3–5, 2013.

[14] L.-T. Deck, D. R. Ochsenbein, and M. Mazzotti. Stochastic shelf-scale modeling framework for the freezing stage in freeze-drying processes. *International Journal of Pharmaceutics*, 613:121276, 2022.

[15] F. I. Dragomirescu, K. Eisenschmidt, C. Rohde, and B. Weigand. Perturbation solutions for the finite radially symmetric stefan problem. *International Journal of Thermal Sciences*, 104:386–395, 2016.

[16] D. A. Edwards and M. E. Mackay. Postextrusion heating in three-dimensional printing. *ASME Journal of Heat Transfer*, 142(5), 2020.

[17] F. Font, T. Myers, and S. Mitchell. A mathematical model for nanoparticle melting with density change. *Microfluidics and Nanofluidics*, 18(2):233–243, 2015.

[18] J. Gao, Y. Chan, T. Hou, and Y. Ren. Quasi-equilibrium approximation of the solidification process for micro phase change materials taking into account curvature and surface tension. *International Journal of Thermal Sciences*, 184:107916, 2023.

[19] S. C. Gupta. *The classical Stefan problem: Basic concepts, modelling and analysis with quasi-analytical solutions and methods*, volume 45. Elsevier, 2017.

[20] J. M. Hill. *One-dimensional Stefan problems: An introduction.* Longman Scientific & Technical, 1987.

[21] M. J. Hunt, F. Brosa Planella, F. Theil, and W. D. Widanage. Derivation of an effective thermal electrochemical model for porous electrode batteries using asymptotic homogenisation. *Journal of Engineering Mathematics*, 122:31–57, 2020.

[22] A. Ihsan, W. van Horssen, and J. Tuwankotta. On a multiple timescales perturbation approach for a Stefan problem with a time-dependent heat flux at the boundary. *Nonlinear Dynamics*, 110(3):2673–2683, 2022.

[23] L. M. Jiji and S. Weinbaum. Perturbation solutions for melting or freezing in annular regions initially not at the fusion temperature. *International Journal of Heat and Mass Transfer*, 21(5):581–592, 1978.

[24] S. Koga, M. Diagne, and M. Krstic. Control and state estimation of the one-phase Stefan problem via backstepping design. *IEEE Transactions on Automatic Control*, 64(2):510–525, 2018.

[25] S. Koga and M. Krstic. *Materials Phase Change PDE Control & Estimation: From Additive Manufacturing to Polar Ice.* Springer Nature, 2020.

[26] J. Kozak and T. Zakrzewski. Accuracy problems of additive manufacturing using SLS/SLM processes. In *AIP Conference Proceedings*, volume 2017, page 020010. AIP Publishing LLC, 2018.

[27] A. Kubica and K. Ryszewska. A self-similar solution to time-fractional Stefan problem. *Mathematical Methods in the Applied Sciences*, 44(6):4245–4275, 2021.

[28] G. Lamé and B. Clapeyron. Mémoire sur la solidification par refroidissement d'un globe liquide. In *Annales Chimie Physique*, volume 47, pages 250–256, 1831.

[29] D. Mazzeo and G. Oliveti. Thermal field and heat storage in a cyclic phase change process caused by several moving melting and solidification interfaces in the layer. *International Journal of Thermal Sciences*, 129:462–488, 2018.

[30] S. W. McCue, B. Wu, and J. M. Hill. Classical two-phase Stefan problem for spheres. *Proceedings of the Royal Society A: Mathematical, Physical and Engineering Sciences*, 464(2096):2055–2076, 2008.

[31] S. L. Mitchell and M. Vynnycky. On the numerical solution of two-phase Stefan problems with heat-flux boundary conditions. *Journal of Computational and Applied Mathematics*, 264:49–64, 2014.

[32] S. L. Mitchell and M. Vynnycky. On the accurate numerical solution of a two-phase Stefan problem with phase formation and depletion. *Journal of Computational and Applied Mathematics*, 300:259–274, 2016.

[33] M. Parhizi and A. Jain. Solution of the phase change stefan problem with time-dependent heat flux using perturbation method. *Journal of Heat Transfer*, 141(2):024503, 2019.

[34] F. B. Planella, C. P. Please, and R. A. Van Gorder. Extended Stefan problem for the solidification of binary alloys in a sphere. *European Journal of Applied Mathematics*, 32(2):242–279, 2021.

[35] D. Riseborough, N. Shiklomanov, B. Etzelmüller, S. Gruber, and S. Marchenko. Recent advances in permafrost modelling. *Permafrost and Periglacial Processes*, 19(2):137–156, 2008.

[36] S. D. Roscani, D. A. Tarzia, and L. D. Venturato. The similarity method and explicit solutions for the fractional space one-phase Stefan problems. *Fractional Calculus and Applied Analysis*, pages 1–27, 2022.

[37] R. D. Santiago, E. M. Hernández, and J. A. Otero. Constant mass model for the liquid-solid phase transition on a one-dimensional stefan problem: Transient and steady state regimes. *International Journal of Thermal Sciences*, 118:40–52, 2017.

[38] I. B. Sebastião, B. Bhatnagar, S. Tchessalov, S. Ohtake, M. Plitzko, B. Luy, and A. Alexeenko. Bulk dynamic spray freeze-drying part 1: modeling of droplet cooling and phase change. *Journal of Pharmaceutical Sciences*, 108(6):2063–2074, 2019.

[39] S. Stepanov, D. Nikiforov, and A. Grigorev. Multiscale multiphysics modeling of the infiltration process in the permafrost. *Mathematics*, 9(20):2545, 2021.

[40] S. Tabakova, F. Feuillebois, and S. Radev. Freezing of a supercooled spherical droplet with mixed boundary conditions. *Proceedings of the Royal Society A: Mathematical, Physical and Engineering Sciences*, 466(2116):1117–1134, 2010.

[41] D. A. Tarzia. Relationship between neumann solutions for two-phase lamé-clapeyron-stefan problems with convective and temperature boundary conditions. *arXiv preprint arXiv:1406.0552*, 2014.

[42] D. A. Tarzia and C. V. Turner. A note on the existence of a waiting time for a two-phase stefan problem. *Quarterly of applied mathematics*, 50(1):1–10, 1992.

[43] D. A. Tarzia and C. V. Turner. Estimation of the occurance of the phase-change process in spherical coordinates. *International communications in heat and mass transfer*, 26(4):559–568, 1999.

[44] V. Voller and F. Falcini. Two exact solutions of a Stefan problem with varying diffusivity. *International Journal of Heat and Mass Transfer*, 58(1-2):80–85, 2013.

[45] V. R. Voller. An exact solution of a limit case Stefan problem governed by a fractional diffusion equation. *International Journal of Heat and Mass Transfer*, 53(23-24):5622–5625, 2010.

[46] V. R. Voller and C. Prakash. A fixed grid numerical modelling methodology for convection-diffusion mushy region phase-change problems. *International Journal of Heat and Mass Transfer*, 30(8):1709–1719, 1987.

[47] V. R. Voller and C. Swaminathan. General source-based method for solidification phase change. *Numerical Heat Transfer, Part B Fundamentals*, 19(2):175–189, 1991.

[48] M. Vynnycky and S. Saleem. On the resolution of thermal gradients in a model for the continuous casting of binary alloys. *Applied Mathematics and Computation*, 2016.

[49] M. Vynnycky, S. Saleem, and H. Fredriksson. An asymptotic approach to solidification shrinkage-induced macrosegregation in the continuous casting of binary alloys. *Applied Mathematical Modelling*, 54:605–626, 2018.

[50] S. Wang, C. Wang, J. Wang, S. Jiang, T. Zhang, and Z. Ma. An analytical solution for a phase change nano-capsule cooled by forced convection. *International Journal of Heat and Mass Transfer*, 212:124267, 2023.

[51] S. Weinbaum and L. Jiji. Singular perturbation theory for melting or freezing in finite domains initially not at the fusion temperature. *Journal of Applied Mechanics*, 44(1):25–30, 1977.

[52] T. Wu, H.-C. Liaw, and Y.-Z. Chen. Thermal effect of surface tension on the inward solidification of spheres. *International journal of heat and mass transfer*, 45(10):2055–2065, 2002.

[53] M. Xu, S. Akhtar, M. A. Alzoubi, and A. P. Sasmito. Singular perturbation solution for a two-phase Stefan problem in outward solidification. In *ASME International Mechanical Engineering Congress and Exposition*, volume 59452, page V008T09A050. American Society of Mechanical Engineers, 2019.

[54] M. Xu, S. Akhtar, A. F. Zueter, M. A. Alzoubi, L. Sushama, and A. P. Sasmito. Asymptotic analysis of a two-phase Stefan problem in annulus: Application to outward solidification in phase change materials. *Applied Mathematics and Computation*, 408:126343, 2021.

[55] M. Xu, S. Akhtar, A. F. Zueter, V. Auger, M. A. Alzoubi, and A. P. Sasmito. Development of analytical solution for a two-phase Stefan problem in artificial ground freezing using singular perturbation theory. *Journal of Heat Transfer*, 142(12):122401, 2020.

[56] M. Xu, Y. Gao, F. Fang, S. Akhtar, B. A. Chaedir, and A. P. Sasmito. Experimental and unified mathematical frameworks of water-ice phase change for cold thermal energy storage. *International Journal of Heat and Mass Transfer*, 187:122536, 2022.

[57] B. Yang, A. Raza, F. Bai, T. Zhang, and Z. Wang. Microstructural evolution within mushy zone during paraffin's melting and solidification. *International Journal of Heat and Mass Transfer*, 141:769–778, 2019.

[58] Y. Zhou, X.-x. Hu, T. Li, D.-h. Zhang, and G.-q. Zhou. Similarity type of general solution for one-dimensional heat conduction in the cylindrical coordinate. *International Journal of Heat and Mass Transfer*, 119:542–550, 2018.

[59] Y. Zhou, X.-Y. Shi, and G.-Q. Zhou. Exact solution for a two-phase Stefan problem with power-type latent heat. *Journal of Engineering Mathematics*, 110(1):1–13, 2018.

[60] Y. Zhou and L.-j. Xia. Exact solution for Stefan problem with general power-type latent heat using Kummer function. *International Journal of Heat and Mass Transfer*, 84:114–118, 2015.

[61] A. Zueter, A. Nie-Rouquette, M. A. Alzoubi, and A. P. Sasmito. Thermal and hydraulic analysis of selective artificial ground freezing using air insulation: Experiment and modeling. *Computers and Geotechnics*, 120:103416, 2020.

[62] A. F. Zueter, M. Xu, M. A. Alzoubi, and A. P. Sasmito. Development of conjugate reduced-order models for selective artificial ground freezing: Thermal and computational analysis. *Applied Thermal Engineering*, 190:116782, 2021.

Part III

Multi-stage and Multi-scale Non-equilibrium Solidification

Chapter 6

Experimental and unified mathematical frameworks of the temperature transition of water-ice phase change cold thermal energy storage

Contents

Preface (Bridging Text)

Macro-scale equilibrium solidification was explored in depth through the framework of the two-phase Stefan problem from Chapters 3 to 5. Computationally efficient perturbation and asymptotic solutions were derived for various conditions, contributing to the rule-of-thumb thermal predictions of artificial ground freezing (AGF) for stabilizing mining infrastructure as well as phase change materials (PCMs) for cold thermal energy storage in mine remediation. The developed solutions not only filled research gaps in the literature of two-phase Stefan problems and analytical modeling of freezing processes, but also provided accurate, fast-to-compute, and easy-to-implement evaluations for mining applications involving solidification at a macro-scale level.

At meso- and micro-scale levels, the freezing phenomena lean towards a non-equilibrium, five-stage process, where supercooling, nucleation, and crystal growth must be considered in addition to the macro-scale behaviors. Moreover, when freezing mixtures, unique characteristics such as freeze-point depression and freeze concentration are also required for an accurate thermal prediction. In mining engineering, non-equilibrium processes can be particularly essential for the design of PCMs for cold thermal energy storage as well as spray freezing technology for mine heating, cooling, and decontamination.

In this chapter, the realm of non-equilibrium solidification was examined, with five distinct stages unfolding. A novel experimental system and a unified mathematical framework were established to capture the phase change process, effectively characterizing the multi-stage non-equilibrium solidification. A few key parameters were highlighted, including geometry, initial PCM temperature, heat transfer fluid temperature, and heat transfer coefficient (i.e., convective heat transfer at the PCM's surface), which in turn expedited the thermal design of PCMs for cold thermal energy storage in mines located in northern and remote areas. The insights and discussions presented in this chapter were published in the peer-reviewed journal article listed below.

M. Xu, Y. Gao, F. Fang, S. Akhtar, B. A. Chaedir, and A. P. Sasmito. Experimental and unified mathematical frameworks of water-ice phase change for cold thermal energy storage. *International Journal of Heat and Mass Transfer*, 187:122536, 2022.

Abstract

Cold thermal energy storage (CTES) is a process that supplies cold thermal energy to a medium for storage and extracts it whenever is needed. The storage medium is phase change material (PCM), which makes great use of the large quantity of latent heat released during solidification or melting. However, some key fundamental and applied issues have not yet been resolved: how do we overcome the thermal interference in PCMs from unstable microscopic crystallization and external mechanical forces? Are there any unified and robust models to predict the whole time evolution of phase change accurately and rapidly? To fulfill these research gaps, we firstly establish a novel, well-controlled experimental system for PCMs that mitigates the thermal disturbance over a medium to large volume during solidification, capable of measuring transient temperature data and characterizing freezing stages at both macro- and micro-scale. We also develop in detail a unified semi-analytical mathematical framework to model the solidification of PCMs, consisting of five subsequent stages: liquid supercooling, nucleation, recalescence, equilibrium freezing, and solid subcooling. The modeling results yield a good agreement with our experimental data in several scenarios, particularly the nucleation temperature and time as well as the total freezing time are accurately predicted. Lastly, we extend our study to investigate the thermal effects of various radial positions, geometries, initial temperatures, heat transfer fluid temperature, and heat transfer coefficients in the context of CTES system.

Keywords: Cold thermal energy storage, CTES, phase change material, PCM, solidification, freezing, nucleation, recalescence

6.1 Introduction

The increasing demand for cooling has led to significant energy consumption and emissions. According to the International Energy Agency (IEA), space cooling contributed almost 8.5% of total electricity consumption in 2019 and about 1 GtCO2 emissions. Cold energy storage technology is an effective means to relieve the gap between energy supply and demand, and reduce energy consumptions. Its effect on load shifting from on-peak hours (daytime) to off-peak hours (nighttime) is an important measure to improve energy savings.

Ice thermal energy storage (ITES) is one of the most commonly used types of cold energy storage not only for its excellent economic performance [14], but also for its ability to reduce fluctuations of energy flow occurred in renewable energy system such as solar and wind energy, or electric grid in general. Ice (or solid phase change material (PCM)) is stored at off-peak periods (during the night) when electricity tariff is low. During daytime, this stored ice PCM can be employed to meet the cooling demands or vice versa in the case of solar energy. The application of this technology for cooling has been proven to have economical and environmental benefits by lowering electricity consumption and CO_2 emissions. Rismanchi et al. [7] investigated the feasibility of employing ice thermal storage systems for office buildings cooling in Malaysia, showing that full storage strategy can reduce annual costs associated with air conditioning system by up to 35%. Sanaye and Shirazi [34] performed thermal modeling of an ice storage air-conditioning system to analyze the thermo-economic and environmental aspects of the system. Rahdar et al. [33] indicated that power consumption of ITES and PCM systems are 4.59% and 7.58% lower than the conventional system, respectively.

The literature is rife with experimental, analytical, and numerical studies on ice storage system and its performance. Abdelrahman [1] investigated experimentally the thermal performance of an ice storage system using twin concentric helical coil. Jannesari and Abdollahi [22] compared using numerical and experimental methods two heat transfer enhancement methods for ice formation in thermal storage system: usage of thin rings and annular fins around coils. El-Ghnam et al. [11] reported experimental results of study on the heat transfer during freezing and melting of water inside a spherical capsule. The heat transfer fluid used in the study is aqueous solution of 35 w.t.% ethylene glycol. The proposed device by Liu et al. [9] showed fast thermal response and efficient heat transfer performance during solidification and melting processes.

With regard to mathematical modeling, most studies used numerical algorithms and iterative processes to simulate phase change due to the complexity of an inherent moving interface between two phases. However, the expensive computational resources as well as the expertise in computational fluid dynamics (CFD) generated from numerical modeling become the main drawbacks. To overcome these, analytical and approximate analytical frameworks typically offer a closed-form solution that can be computed instantaneously. Xu et al. [47] developed an asymptotic solution to outward solidification in cylindrical PCMs, which was verified with numerical results, yet with much less computational cost In addition, asymptotic solutions for inward solidification of a spherical domain were also available in the literature subjected to a constant temperature [26] and convective [4] boundary conditions. Apart from the classical Stefan formulation, the Stefan problem has also been modified into other forms to incorporate the Gibbs-Thomson effect [10, 36], size-dependent thermophysical properties [13], and size/velocity-dependent phase change temperatures [29].

Erek and Dincer [12] developed a new heat transfer correlation by simulating a series of 120 numerical experiments to study the heat transfer behavior in an encapsulated ITES system and downstream. Shirazi et al. [38] developed a framework on an ice thermal energy storage system for gas turbine cycle inlet air cooling to perform energetic, exergetic, economic, and environmental analyses of the system. A novel dynamic model derived using population balance equation approach for the charging process of a cold energy thermal storage was proposed by Wu et al [44]. Xie and Yuan [45] evaluated numerically the impact of different parameters of thin layer ring on ice formation in a rectangular space. In addition, a numerical approach to analyze the phase changes of a full-scale vertical ice-on-coil latent thermal energy storage tank was proposed by Sang et al [35] based on the sample and interpolation (SI) method. The effects of tube arrangement and fins on improving ice formation in ice-on-coil thermal storage systems were studied numerically by Hamzeh and Miansari [17] using finite volume method. Pourakabar and Darzi [32] studied numerically the effects of different shell shapes and inner tubes arrangements on charging and discharging of PCMs inside cylindrical container. Mahdi and Nsofor [25] introduced a method to improve the PCM solidification rate in thermal storage systems by using nanoparticle-metal foam combination approach along with triplex-tube heat exchanger. A novel organic paraffin-based PCM mixture was employed as the energy storage material in the study conducted by Shao et al [37]. Zhang et al. [49] developed an unsteady model of the solidification process of water in a shell-tube ice storage (STIS) unit which was verified by a solidification experiment in a finned STIS unit. Yu et al. [48] focused their study on the role of metal foam in heat transfer enhancement of the cold thermal energy storage (CTES) system with a two-dimensional model. Vogel and Thess [42] developed a validated volume-of-fluid (VOF) CFD simulation and a simplified model based on the Boussinesq approximation to evaluate and visualize the influence of natural convection in a CTES system.

The fundamentals of icing nucleation dynamics and phenomena such as dendritic growth through desublimation, kinetic behaviors of droplets upon freezing, etc. were reviewed comprehensively by Zhao et al. [50]. Akhtar et al. [5] introduced a sensitivity analysis using the Monte-Carlo method to identify the influence of interface kinetics and curvature effects during the dendritic growth, and then optimized them by the minimization of the sum of the least-squares method. Further, a comprehensive review on cold energy storage technologies with PCMs and their applications in air conditioning was conducted in [24]. Despite the fact that there have been plentiful investigations on CTES system, few place emphases on microscopic behavior of the solidification (i.e., nucleation, recalescence/dendritic growth). These micro-scale behaviors can have significant influence on the supercooling degree and in turn affect total effective latent heat, and thus thermal storage capacity.

Recently, Akhtar et al. [3] developed a semi-analytical framework which accurately predicts the stages of droplet freezing and conducted a one-dimensional five-stage analysis. This droplet solidification framework was then extended to a spray configuration to examine the thermodynamics of spray freezing on a system level [2]. However, a great amount of exergy can still be found from this work: i) the one-dimensional five-stage analysis was sequential without a unified set of governing equations for multi-dimensional problems; and ii) the assumptions of linear temperature profile in recalescence and small Biot number limit in solid subcooling can be removed and resolved by a more versatile mathematical framework.

Another research gap in the literature lies on experimental control of PCM (particularly in large quantity of volume) during liquid supercooling and nucleation stages. Many factors can significantly influence the supercooling of PCM according to the physical mechanisms of crystallization, such as magnetic field, agitation, friction, electric field, shock waves or ultrasonic vibration [51]. These external perturbances affect the size and perfection of the crystal by increasing the nucleation density and adjusting the orientation and arrangement of the molecular chains in the melt [6]. In the cases of a very small volume quantity (e.g., a suspended water droplet [19, 27]), they were well controlled from the perturbances; however, to our best knowledge, there have not been any existing experimental setups to mitigate such external disturbance.

Inspired by these research gaps, the novelty of this study is in threefold:

i) Establish a novel, well-controlled experimental system for PCMs to attain the freezing curve, contact angle, and measured natural convection heat transfer coefficient;

ii) Formulate and analytically solve a rigorous two-dimensional unified mathematical model for PCMs, capable of capturing the five solidification stages at micro- and macro-scales with the effective latent heat storage; and

iii) Study a wide array of key operational parameters in CTES system after comprehensive model validations.

The outline of the paper is as follows. In Section 6.2, we present the experimental setup and methodology built in our laboratory. Measurements of temperature and contact angle as well as determination of heat transfer coefficient are explained in details. In Section 6.3, we establish a two-dimensional unified mathematical framework for inward cylindrical solidification of PCMs. A semi-analytical solution to this model is then developed by the employment of superposition, separation of variables, bisection, and perturbation methods. This newly established mathematical model is validated against our experimental results at various initial and heat transfer fluid temperatures in Section 6.4. In Section 6.5, we study the temperature profiles over radial coordinates, and the effects of initial temperature, heat transfer fluid temperature, and heat transfer coefficients based on CTES system. Lastly, we conclude our work by highlighting the usefulness of results in this study as well as the impact to the research community.

6.2 Experiments

Experiments were performed to measure the transient profile, determine contact angle and heat transfer coefficient of pure (deionized) water. This section begins with a summary of the experimental setup and measuring machines used in this work. Then, experimental methodology is documented in details from the measurements of temperature and heat transfer coefficient to contact angle.

6.2.1 Experimental setup

Figure 6.1(a) shows the experimental setup used in this study. The system consists of the test apparatus and data acquisition system. A long thin-walled cylinder test tube of radius a = 8.75 mm and height H = 193.60 mm filled with deionized water was immersed in a water bath. Three thermocouples were employed to monitor the stability of surrounding

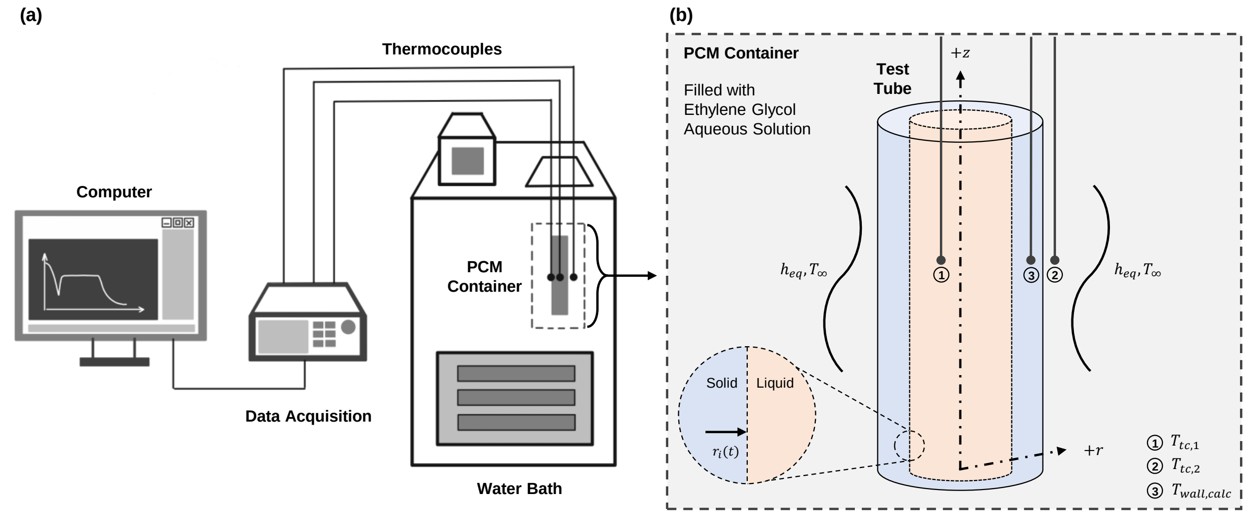

Figure 6.1: Schematic diagrams: (a) The experimental apparatus; and (b) The PCM container (the inset shows an inwardly moving boundary highlighting the solidification process during a time, $t_{nuc} < t < t_{crit}$).

temperature and determine the heat transfer coefficient. Data acquisition was performed by a data collector (THTZ Multiplex recorder) connected to a workstation computer. The water bath thermostat was also used with an agitator for cooling down the refrigerant to its desired temperature. Due to external shock and vibration caused by the agitator and potential turbulent flow, a PCM container was designed and placed in between the water bath and test tube. The PCM container also circumvented the strong impact of temperature fluctuations generated by the heat exchange with the outside environment.

As shown in Fig. 6.1(b), the thermocouples were placed in three different locations: first thermocouple was placed inside the test tube, second thermocouple was placed adjacent to the test tube wall in the PCM container, and the third thermocouple was placed far from the test tube in the PCM container. Their temperatures are denoted as $T_{tc,1}$, $T_{tc,2}$, and $T_{tc,3}$, respectively. Dimensions of test tube and thermocouple as well as the first thermocouple's location are listed in Table 6.1.

Table 6.1: Dimensions of the test tube and thermocouple along with locations.

Property	Value	Unit
Test tube		
Radius, a	8.75	mm
Length, H	193.60	mm
Thermocouple		
Radius, a_{tc}	2	mm
Length, H_{tc}	23	mm
Location of the 1st thermocouple		
Radial distance to the center, r_{tc}	7	mm
Depth from the bottom surface, z_{tc}	96.80	mm

6.2.2 Experimental methodology

Temperature profile in each solidification stage is of great interest to be examined experimentally despite challenges of thermal interference during crystallization and measurements of heat transfer coefficient. In this subsection, a novel experimental method for temperature measurement and determination of heat transfer coefficient. This method designs an extra layer between the PCM and coolant with an additional thermocouple, thus significantly minimizing thermal disturbance during phase change and increasing the accuracy of thermal measurements. The methodology to evaluate contact angle of deionized water is also established to facilitate the subsequent mathematical modeling.

Temperature measurement

A test tube was filled with liquid sample (i.e. deionized water) at its required initial temperature (T_{init}). The water bath thermostat was kept at constant temperature that is well below the nucleation temperature of liquid sample and expected surrounding temperature (T_∞). 40 vol.% ethylene glycol $(CH_2OH)_2$ aqueous solution was used as the refrigerant. A separate container, the PCM container, was filled with ethylene glycol aqueous solution and placed into the water bath. Volume fraction of the solution varies with expected T_∞. The agitator in the water both was activated for a period when a large amount of solid forms in the PCM container and $T_{tc,3}$ stays at expected T_∞. The prepared test tube filled with liquid sample was then placed into the PCM container and $T_{tc,1}$ and $T_{tc,2}$ were recorded until the desired time duration. Throughout the experiment, $T_{tc,3}$ was monitored to ensure that its temperature remains unchanged. Temperature transition over time was recorded every 1 second with accuracy within 0.1°C. The experiment was repeated five times for each testing scenario (i.e., a specific combination of T_{init} and T_∞) for reliability and reproducibility.

Determination of heat transfer coefficient

As liquid water solidifies in the test tube, heat transfer coefficient varies with time and solidification stages denoted as h^j. The superscript j represents the j-th time interval. In this study, the time-dependent heat transfer coefficient is determined by a heat balance model with the temperature measurements of three thermocouples.

At each stage, two energy balances are set based on the inner and outer surface of the steel wall. The inner surface equates the energy coming in from the first thermocouple to the inner wall with the energy coming out from the inner wall to the second thermocouple. On the other hand, the outer surface balances the heat conduction inside the steel wall with the convection subjected to the coolant temperature, as schematically shown in Fig. 6.1(b). Thus, two algebraic equations are formulated at every solidification stage. Specifically, during liquid supercooling stage, we find:

$$\begin{cases} k_\ell \frac{T^j_{tc,1} - T^j_{wall,calc}}{\Delta r} - k_{steel} \frac{T^j_{wall,calc} - T^j_{tc,2}}{\Delta r_{wall}} & = 0, \\ k_{steel} \frac{T^j_{wall,calc} - T^j_{tc,2}}{\Delta r_{wall}} + h^j (T^j_{tc,2} - T_\infty) & = 0. \end{cases} \tag{6.1}$$

In the equilibrium freezing stage, we have:

$$\begin{cases} k_\ell \frac{T^j_{tc,1} - T^j_{wall,calc}}{\Delta r} - k_{steel} \frac{T^j_{wall,calc} - T^j_{tc,2}}{\Delta r_{wall}} & = 0, \\ k_{steel} \frac{T^j_{wall,calc} - T^j_{tc,2}}{\Delta r_{wall}} + h^j (T^j_{tc,2} - T_\infty) & = 0. \end{cases} \tag{6.2}$$

Lastly, at the solid subcooling stage, we find:

$$\begin{cases} k_s \frac{T^j_{tc,1} - T^j_{wall,calc}}{\Delta r} - k_{steel} \frac{T^j_{wall,calc} - T^j_{tc,2}}{\Delta r_{wall}} & = 0, \\ k_{steel} \frac{T^j_{wall,calc} - T^j_{tc,2}}{\Delta r_{wall}} + h^j (T^j_{tc,2} - T_\infty) & = 0. \end{cases} \tag{6.3}$$

$k, c_p, \Delta r_{wall}$ are the thermal conductivity, specific heat, and wall thickness, respectively. The subscripts $\ell, s, steel$ represent liquid state, solid state, and stainless steel, respectively. In all stages, the two unknown variables are the calculated wall temperature $T^j_{wall,calc}$ and heat transfer coefficient h^j at the j-th time interval. As a result, the time-dependent heat transfer coefficient can be calculated based on the measurements of three thermocouples in our experimental setup.

Contact angle measurement

To measure the contact angle of deionized water, a droplet of liquid sample was placed on a flat surface made of 304 stainless steel, as shown in Fig. 6.2a. A contact angle tester ZJ-6900 (Shenzhen Zhi Jia Equipment Co., Ltd., China) was employed for measurements. Care was taken to remove any foreign agent on the surface of stainless steel. Prior to each testing, the stainless-steel surface was cleaned by ethyl alcohol and deionized water, and dried. As shown in Fig. 6.2b, contact angle of each end of the droplet was measured and an average value was calculated. This measurement was repeated six times. Images of the contact angle measurements were also collected.

6.3 Mathematical modeling

The domain is considered as a vertical cylinder of radius a and height H. The top and bottom ends of the cylinder are perfectly insulated, i.e., no flux conditions at $z = 0$ and $z = H$. The cylinder is initially at a spatially uniform temperature $T = T_{init}$; the outer surface $r = a$ is then subjected to convection with a heat transfer coefficient h and a surrounding temperature

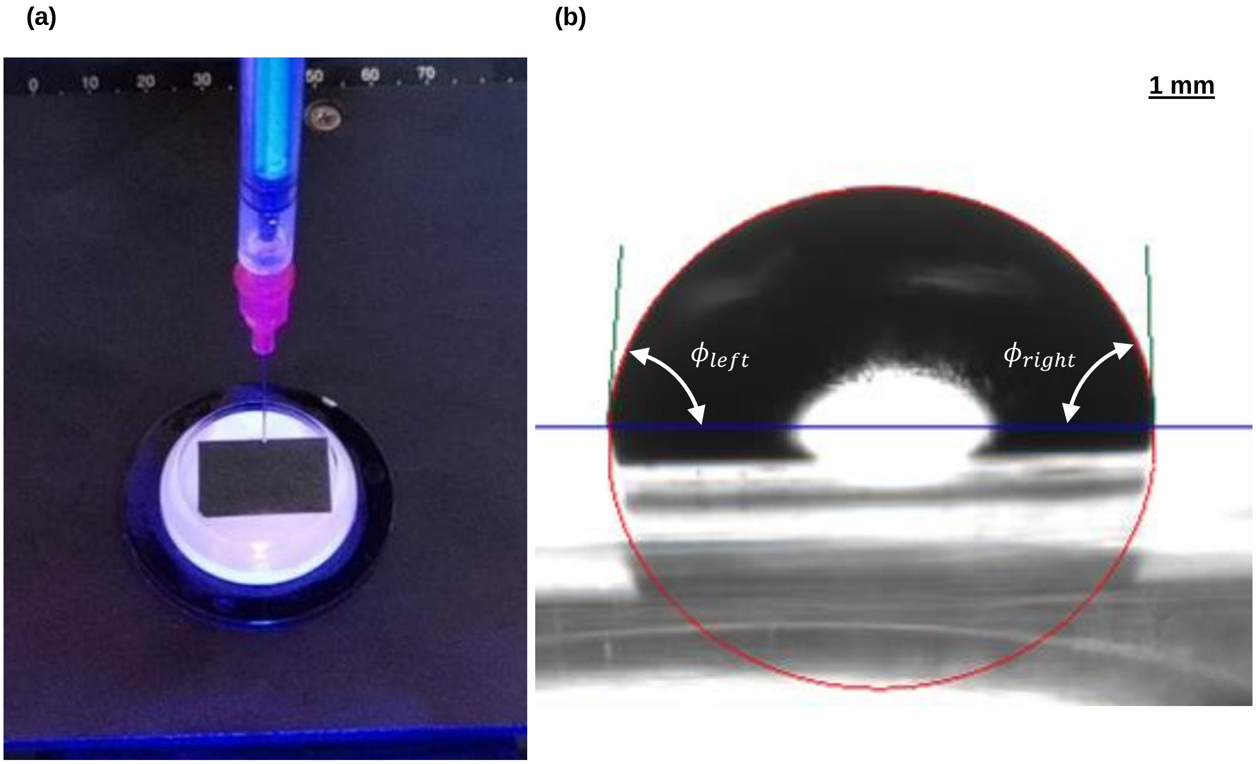

Figure 6.2: Measurement of the contact angle: (a) An image of the apparatus; and (b) A diagram of contact angle measured. The contact angle is obtained by the average value of the measurements from both sides, i.e., $\phi = (\phi_{left} + \phi_{right})/2$.

T_∞ for $t > 0$. This solidification problem contains five distinct stages at both macro- and micro-scale levels: liquid supercooling, nucleation, recalescence, equilibrium freezing, and solid subcooling. For mathematical simplification, the following assumptions are made:

i) Phase-dependent thermophysical properties are constant and uniform in each phase;

ii) Volumetric change in the liquid phase due to density is assumed to be negligible;

iii) Effect of natural convection in the liquid phase is neglected because the Richardson's number $Ri = Gr/Re^2 \gg 1$. Gr and Re are the Grashoff number and Reynolds number, respectively; and

iv) A semi-infinite problem is assumed in the axial direction, and thus the solid-liquid interface during phase change is considered to be sharp and varied in the radial coordinate only. That is, the two-dimensional (2-D) problem reduces to a one-dimensional (1-D) Stefan problem at the equilibrium freezing stage.

In this study, we present a unified solidification model, capable of capturing the five solidification stages at both macroscopic and microscopic scales. This unified model is governed by a 2-D heat conduction equation with an internal heat generation:

$$\frac{1}{\alpha}\frac{\partial T}{\partial t} = \frac{\partial^2 T}{\partial r^2} + \frac{1}{r}\frac{\partial T}{\partial r} + \frac{\partial^2 T}{\partial z^2} + \frac{g_0}{k},\ 0 < r < a,\ 0 < z < H,\ t > 0, \tag{6.4}$$

subject to the following fixed and moving boundary conditions:

$$\text{For } r = 0: \qquad T(r = 0, z, t) \Rightarrow \text{finite}, \tag{6.5}$$

$$\text{For } r = a: \qquad -k\frac{\partial T}{\partial r}\bigg|_{r=a} = h_{eq}\Big[T(r = a, z, t) - T_\infty\Big], \tag{6.6}$$

$$\text{For } r = r_i(t): \qquad k\frac{\partial T}{\partial r}\bigg|_{r=r_i(t)} = \rho L\frac{\mathrm{d}r_i}{\mathrm{d}t},\ T(r = r_i(t), z, t) = T_f, \tag{6.7}$$

$$\text{For } z = 0: \qquad \frac{\partial T}{\partial z}\bigg|_{z=0} = 0, \tag{6.8}$$

$$\text{For } z = H: \qquad \frac{\partial T}{\partial z}\bigg|_{z=H} = 0. \tag{6.9}$$

The time conditions are given by:

$$\begin{aligned} T(r, z, t = 0) &= T_{init}, \\ T(r, z, t = t_{nuc}) &= T_{nuc}, \\ T(r, z, t = t_{rec}) &= T_f, \\ T(r, z, t = t_{crit}) &= T_{crit}(r), \\ r_i(t = t_{rec}) &= 0, \\ r_i(t = t_{crit}) &= a. \end{aligned} \tag{6.10}$$

T, r, z, t are the temperature, radial coordinate axial coordinate and time, respectively.

$\alpha, k, \rho, L, h_{eq}, g_0$ are the thermal diffusivity, thermal conductivity, mass density, latent heat of fusion, equilibrium heat transfer coefficient and internal heat generation, respectively. The subscripts $i, f, init, nuc, rec, crit$ represent the solid-liquid interface, fusion state, initial state, nucleation, recalescence and critical state (a.k.a., total freezing state), respectively. In particular, t_{rec} is the time when recalescence stage is completed and the temperature jumps back to the fusion temperature; t_{crit} is the time when the entire domain becomes solid, which can also be seen as the end of equilibrium freezing. The internal heat generation, g_0, is expressed as a piece-wise function to capture the recalescence stage at a micro-scale level:

$$g_0 = \begin{cases} \frac{mc_p(T_f - T_{nuc})}{(t_{rec} - t_{nuc})V}, & \text{if } t_{nuc} < t < t_{rec}, \\ 0, & \text{elsewhere,} \end{cases} \tag{6.11}$$

where m and t_{nuc} the mass (kg) and nucleation time (s), respectively. V is the volume of the cylindrical domain (m^3), which can be obtained by $V = \pi a^2 H$. Further, the thermophysical properties are also given by a time-dependent piece-wise function:

$$[k, c_p, \rho, m] = \begin{cases} [k_\ell, c_{p,\ell}, \rho_\ell, m_\ell], & \text{if } 0 < t < t_{rec}, \\ [k_s, c_{p,s}, \rho_s, m_s], & \text{elsewhere.} \end{cases} \tag{6.12}$$

It is noted that Akhtar et al. [3] developed a semi-analytical framework on droplet solidification and conducted a similar five-stage analysis. Compared with Akhtar et al.'s work, this presented unified model has the following physical and mathematical differences and advancement: i) the current model studies a 2-D cylinder (except a 1-D assumption on the interface), while Akhtar et al. examined a 1-D sphere; ii) this framework unified the five stages by a single partial differential equation problem (including the internal heat generation) with a set of fixed and moving boundary conditions, but Akhtar et al. performed separate analyses for each stage; iii) The recalescence stage in this model is triggered by a heat equation with the internal heat generation that is not linear; however, Akhtar et al.

simplified this transient process by a linear line depending on the recalescence time; and iv) There is no small Biot number assumption throughout all the stages of this framework, while Akhtar et al. assumed a small Biot number in the solid subcooling stage.

6.3.1 Liquid supercooling stage

This stage solves a 2-D finite-extent transient heat conduction problem of the liquid phase subjected to a convective boundary without any heat generation:

$$\frac{1}{\alpha_\ell}\frac{\partial T_\ell}{\partial t} = \frac{\partial^2 T_\ell}{\partial r^2} + \frac{1}{r}\frac{\partial T_\ell}{\partial r} + \frac{\partial^2 T_\ell}{\partial z^2}, \tag{6.13}$$

subjected to the boundary conditions:

$$T_\ell(r=0,z,t) \Rightarrow \text{finite}, \tag{6.14}$$

$$-k_\ell \frac{\partial T_\ell}{\partial r}\bigg|_{r=a} = h_{eq}\Bigg[T_\ell(r=a,z,t) - T_\infty\Bigg], \tag{6.15}$$

$$\frac{\partial T_\ell}{\partial z}\bigg|_{z=0} = 0, \tag{6.16}$$

$$\frac{\partial T_\ell}{\partial z}\bigg|_{z=H} = 0. \tag{6.17}$$

and the initial condition:

$$T_\ell(r,z,t=0) = T_{init}. \tag{6.18}$$

An exact solution can be found by firstly applying the method of superposition and splitting into two sub-problems: transient and steady-state parts. The transient part is solved by separation of variables, while the steady-state part reduces to an ordinary differential equation without any axial dependency. Elaborate analytical treatments for this problem with an internal heat generation term are documented in the text [16]. The final analytical

Table 6.2: Thermophysical properties of water and ice.

Property	Value	Unit
Water		
Mass density, ρ_ℓ	999.84	kg m^{-3}
Specific heat, $c_{p,\ell}$	4219.40	J kg^{-1} K^{-1}
Thermal conductivity, k_ℓ	0.56109	W m^{-1} K^{-1}
Ice		
Mass density, ρ_s	916	kg m^{-3}
Specific heat, $c_{p,s}$	2050	J kg^{-1} K^{-1}
Thermal conductivity, k_s	2.22	W m^{-1} K^{-1}

solution is expressed as:

$$T_\ell(r,z,t) = \sum_{n=0}^{\infty}\sum_{m=1}^{\infty}\left[C_{nm}J_0(\beta_m r)\cos(\eta_n z)e^{-\alpha_\ell\lambda_{nm}^2 t}\right] + T_\infty,\ 0 < t < t_{nuc}, \tag{6.19}$$

where the eigenvalues, β_m, η_n, and λ_{nm}, are defined as:

$$\begin{aligned} &a\beta_m J_1(a\beta_m) = Bi_\ell J_0(a\beta_m),\ \text{for } m = 1,2,3,...\\ &\eta_n = \frac{n\pi}{H},\ \text{for } n = 0,1,2,...\\ &\lambda_{nm}^2 = \beta_m^2 + \eta_n^2. \end{aligned} \tag{6.20}$$

J_0 and J_1 are the Bessel functions of the first kind with orders zero and one, respectively. Bi_ℓ is the Biot number of the liquid phase given by $Bi_\ell = h_{eq}a/k_\ell$. This thermal conductivity k_ℓ is for the liquid phase here yet will be hinged on the domain of interest later. The thermophysical properties of pure water and ice are listed in Table 6.2. On the other hand, the corresponding eigencoefficients are determined by:

$$C_{nm} = \frac{\int_{z=0}^{H}\int_{r=0}^{a} r(T_{init} - T_\infty)J_0(\beta_m r)\cos(\eta_n z)\mathrm{d}r\mathrm{d}z}{\int_{r=0}^{a} rJ_0^2(\beta_m r)\mathrm{d}r\int_{z=0}^{H}\cos^2(\eta_n z)\mathrm{d}z}. \tag{6.21}$$

6.3.2 Nucleation stage

The nucleation rate for heterogeneous nucleation is defined as the product of pre- and exponential factors:

$$
\begin{aligned}
J(t) =&D\frac{A_w}{3}n_\ell^{\frac{7}{3}}\sqrt{\frac{A_w\sigma_{\ell s}}{\pi k_B T_\ell}}\sqrt{\frac{4}{2+\zeta_f}} \\
&\times \exp\left\{-\frac{[A_w\sigma_{\ell s}/(k_B T_\ell)]^3(2+\cos\phi)(1-\cos\phi)^2}{27[\ln(p_\ell/p_s)]^2}\right\},
\end{aligned} \tag{6.22}
$$

where the pre-factor includes: the self-diffusion coefficient of supercooled water D (m^2 s^{-1}), surface area of a water molecule A_w (m^2), number of density of molecules in the liquid particle n_ℓ (m^{-3}), interfacial surface tension $\sigma_{\ell s}$ (J m^{-2}), Boltzmann constant k_B (J K^{-1}), and a coefficient in the heterogeneous Zeldovich factor ζ_f (-). The coefficient ζ_f is defined as:

$$
\zeta_f = \frac{(1-X\cos\phi)[2-4X\cos\phi-(X^2\cos^2\phi-3)]}{(1-2X\cos\phi-X^2)^{\frac{3}{2}}}, \tag{6.23}
$$

where X is the ratio of radii between nucleating particle and critical embryo (-); ϕ is the contact angle (°). Furthermore, the exponential factor has: the contact angle ϕ (°), saturation pressure of water p_ℓ (Pa), and saturation pressure of ice p_s (Pa). These saturation pressures are temperature-dependent functions given in [28]. Definitions and formulations for each term are documented in the work [3] and listed in Table 6.3 based on this proposed model.

The parameter $\sigma_{\ell s}$ in Eqn. (6.22) is a critical factor in determining accuracy of the model as demonstrated in our previous study [3]. It is hypothesized in recent literature studies [41, 27] that $\sigma_{\ell s}$ is a strong function of droplet's water temperature and takes the form of the expression

$$
\sigma_{\ell s} = \sigma_0 + (T_\ell - 273.15)\times 10^{-4} \tag{6.24}
$$

where σ_0 is the baseline interfacial surface tension at the equilibrium freezing temperature

Table 6.3: Thermophysical and molecular parameters used at nucleation and recalescence stages.

Property	Value	Unit	Ref.
Self-diffusion coefficient of water, $D(T)$	$1.5 \times 10^{-6} \exp(-2045/T)$	$\mathrm{m^2\ s^{-1}}$	[27]
Surface area of water molecule, A_w	$4\pi r_0^2$	$\mathrm{m^2}$	[27]
Mean particle separation distance, r_0	$[3M_w/(4\pi N_A \rho_\ell)]^{1/3}$	m	[31]
Molar mass of water, M_w	18.05	$\mathrm{g\ mol^{-1}}$	[31]
Avogadro number, N_A	6.022×10^{23}	$\mathrm{mol^{-1}}$	[31]
Number density of molecules in liquid, n_ℓ	$N_A \rho_\ell / M_w$	$\mathrm{m^{-3}}$	[31]
Universal LM-K stability constant, σ^*	0.0253	-	[23]
Interfacial kinetics factor, σ_k	6.1×10^{-11}	m	[43]
Interfacial surface tension, $\sigma_{\ell s}(T)$	$\sigma_0 + (T - 273.15) \times 10^{-4}$	$\mathrm{J\ m^{-2}}$	[3, 8]
Radii ratio in the term ζ_f, X	R_p/r^*	-	[3]
Radius of nucleating particle, R_p	25.4×10^{-6}	m	[19]
Radius of critical embryo, $r^*(T)$	$2\sigma_{\ell s}/\{n_s[k_B T \ln(p_\ell/p_s)]\}$	m	[3]
Number density of molecules in liquid, n_s	$N_A \rho_s / M_w$	$\mathrm{m^{-3}}$	[31]
Boltzmann constant, k_B	1.38064×10^{-23}	$\mathrm{J\ K^{-1}}$	[31]
Volume of critical embryo, V^*	$4\pi(r^*)^3/3$	$\mathrm{m^3}$	[3]

(J m^{-2}). Considerable discrepancy is observed in the experimental measurements of σ_0 ranging from 0.025 - 0.044 (J m^{-2}) has been reported [15]. In our recent study [46] we hypothesize that this variation is a result of dependence of σ_0 on other factors such as surrounding temperature or purity of the liquid. To include this dependence in our model, we used a simple optimization search algorithm based on the gradient method to estimate the σ_0.

Following the determination of nucleation rate, the nucleation temperature can be examined by locating numbers of critical nuclei N_v, expressed as [40, 3]:

$$N_v = \int_{\widetilde{t}=0}^{t} (V_{init} - V^*) J(\widetilde{t}) \mathrm{d}\widetilde{t}, \tag{6.25}$$

where V_{init} and V^* are the volumes of initial state and crystal embryo (presumably spherical), respectively. $\widetilde{t}$ is an arbitrary time variable for integration purposes. If the number of critical nuclei reaches 1, then the liquid is deemed as its nucleation temperature. This nucleation criterion has been proved to be accurate for low and medium cooling rates (around $0.1 - 50°\text{C/s}$) [40], which represents this current study. Consequently, the time of nucleation is also known by settling the nucleation time during liquid supercooling. Such coupling of stages between the liquid supercooling and nucleation renders a solidification framework which accounts for both macroscopic and microscopic behaviors.

6.3.3 Recalescance stage

In the process of dendritic growth, there are three driving mechanisms for the total undercooling of the interface: steady-state thermal field, kinetic undercooling, and curvature effect, expressed as [5, 21]:

$$T_f - T_i = \Delta T_{th} + \Delta T_k + \Delta T_\sigma, \tag{6.26}$$

where $\Delta T_{th}, \Delta T_k, \Delta T_\sigma$ are thermal, kinetic and curvature undercoolings, respectively. This formulation can be further expressed in terms of interfacial temperature T_i and dendritic growth velocity v:

$$\frac{c_p(T_i - T_{nuc})}{L} = \mathrm{Iv}\left(\sqrt{\frac{d_0 v}{2\alpha_s \sigma^*}}\right) + \frac{c_p(T_f - T_i)}{L} + \frac{c_p \sigma_{\ell s} T_f}{L L_v}\sqrt{\frac{v\sigma^*}{2 d_0 \alpha_s}}, \tag{6.27}$$

where $\mathrm{Iv}(x)$ is the well-known Ivantsov's exact solution [20]. d_0, σ^*, L_v are the capillarity length (m), universal LM-K stability constant (-), and volumetric latent heat (J m^{-3}), respectively. The velocity of dendritic growth v, on the other hand, is defined based on the Wilson-Frenkel's work [43]:

$$v = \frac{6 d_0 D(T_i)}{2\alpha_s \sigma^* \sigma_k}\left[\exp\left(-\frac{L_m/N_A}{k_B T_f}\right) - \exp\left(-\frac{L_m/N_A}{k_B T_i}\right)\right], \tag{6.28}$$

where $D, \sigma_k, L_m, N_A, k_B$ are the self-diffusion coefficient of water (m^2 s^{-1}), interfacial kinetics factor (m), latent heat of fusion per unit mole (J mol^{-1}), Avogadro constant (mol^{-1}), and

Boltzmann constant (J K^{-1}), respectively. From the two algebraic equations (6.27) and (6.28), the two unknown variables (v, T_i) can be solved by a numerical scheme. Here, a bisection method was used.

Once the velocity of dendritic growth v is obtained from the algebraic equations (6.27) and (6.28), the time interval of recalescence stage (i.e., $t_{rec} - t_{nuc}$) can be calculated from the ratio of diameter over velocity: $t_{rec} - t_{nuc} = 2a/v$. As a consequence, the internal heat generation term g_0 representing the dendritic growth is known. To examine the temperature profile during recalescence, a 2-D transient heat conduction is solved in a similar manner to the liquid supercooling stage, yet with a non-zero internal heat generation g_0 in Eq. (6.11):

$$\frac{1}{\alpha_\ell}\frac{\partial T_\ell}{\partial t} = \frac{\partial^2 T_\ell}{\partial r^2} + \frac{1}{r}\frac{\partial T_\ell}{\partial r} + \frac{\partial^2 T_\ell}{\partial z^2} + \frac{g_0}{k_\ell}, \tag{6.29}$$

subjected to the boundary conditions:

$$T_\ell(r=0,z,t) \Rightarrow \text{finite}, \tag{6.30}$$

$$-k_\ell \frac{\partial T_\ell}{\partial r}\bigg|_{r=a} = h_{eq}\Big[T_\ell(r=a,z,t) - T_\infty\Big], \tag{6.31}$$

$$\frac{\partial T_\ell}{\partial z}\bigg|_{z=0} = 0, \tag{6.32}$$

$$\frac{\partial T_\ell}{\partial z}\bigg|_{z=H} = 0. \tag{6.33}$$

and the initial condition

$$T_\ell(r,z,t=t_{nuc}) = T_{nuc}. \tag{6.34}$$

The exact solution can also be obtained by the methods of superposition and separation of variables as follows:

$$\begin{aligned} T_\ell(r,z,t) = &\sum_{n=0}^{\infty}\sum_{m=1}^{\infty}\Big[D_{nm}J_0(\beta_m r)\cos(\eta_n z)e^{-\alpha_\ell \lambda_{nm}^2 t}\Big] \\ &+ \frac{a g_0}{2h_{eq}} + \frac{g_0}{2k_\ell}(a^2 - r^2) + T_\infty,\ t_{nuc} < t < t_{rec}, \end{aligned} \tag{6.35}$$

where the eigenvalues remain the same as determined in Eq. (6.20). The corresponding eigencoefficient is defined as:

$$D_{nm} = \frac{\int_{z=0}^{H} \int_{r=0}^{a} r(T_{nuc} - T_{\infty} - \frac{ag_0}{2h_{eq}} - \frac{g_0}{4k_\ell}(a^2 - r^2)) J_0(\beta_m r) \cos(\eta_n z) \mathrm{d}r \mathrm{d}z}{\int_{r=0}^{a} r J_0^2(\beta_m r) \mathrm{d}r \int_{z=0}^{H} \cos^2(\eta_n z) \mathrm{d}z}. \tag{6.36}$$

6.3.4 Equilibrium freezing stage

A 1-D classical one-phase Stefan problem in a finite cylindrical domain is formulated to govern this stage [18]. Since a portion of solid has been developed in the form of crystal during dendritic growth, the latent heat needs to be firstly re-scaled for equilibrium freezing, i.e., $L \Rightarrow L_{eff}$. This effective latent heat is derived from the energy balance and given by [39, 3]:

$$L_{eff} = \left(1 - \frac{c_{p,\ell}}{c_{p,s}} Ste_{nuc}\right) L, \tag{6.37}$$

where Ste_{nuc} is a local Stefan number for nucleation defined as $Ste_{nuc} = c_{p,s}(T_f - T_{nuc})/L$. It is worthwhile to mention that this effective latent heat has barely been introduced in the literature for modeling energy storage. The involvement of nucleation temperature in the local Stefan number Ste_{nuc} requires the consideration of nucleation theory at micro-scale level, in which most works are limited to macroscopic behaviors without taking into account nucleation and dendritic growth.

Exact solution to the Stefan problem does not exist because of its finite domain and convective boundary. An approximate analytical solution can be therefore forged by perturbation method [18, 30]. The merit of this approximation technique is that the perturbation series forces the complex problem to resort to solvable terms. Prior to the perturbation method, the problem is non-dimensionalized by the following variables:

$$\theta_s = \frac{T_s - T_f}{T_f - T_{\infty}},\ \xi = \frac{r}{a},\ \xi_i = \frac{r_i}{a}, \tag{6.38}$$

and dimensionless numbers:

$$Fo_s = \frac{\alpha_s(t - t_{rec})}{a^2},\ Bi_s = \frac{h_{eq}a}{k_s},\ Ste_s = \frac{c_{p,s}(T_f - T_\infty)}{L_{eff}}. \tag{6.39}$$

The dimensionless time is therefore defined as $\tau = Ste_s Fo_s$. To construct a perturbation series solution in an explicit form, the dimensionless problem is also reformulated with respect to $\theta_s(\xi, \xi_i)$ and $\tau(\xi_i)$ as follows:

$$\begin{aligned}
\frac{\partial^2\theta_s}{\partial\xi^2} + \frac{1}{\xi}\frac{\partial\theta_s}{\partial\xi} &= Ste_s\frac{\partial\theta_s}{\partial\tau}, \\
Bi_s\theta_s(\xi = 1, \xi_i) &= -\left.\frac{\partial\theta_s}{\partial\xi}\right|_{\xi=1}, \\
\left.\frac{\partial\theta_s}{\partial\xi}\right|_{\xi=\xi_i}\frac{\mathrm{d}\tau}{\mathrm{d}\xi_i} &= 1, \\
\theta_s(\xi = \xi_i, \xi_i) &= 1, \\
\tau(\xi_i = 1) &= 0.
\end{aligned} \tag{6.40}$$

One seeks to find the approximate analytical solutions valid for $Ste_s \ll 1$ in forms of regular perturbation expansions; that is,

$$\begin{aligned}
\theta_s(\xi, \xi_i; Ste_s) &\sim \theta_{s,0} + Ste_s\theta_{s,1} + Ste_s^2\theta_{s,2} + ..., \\
\tau(\xi_i; Ste_s) &\sim \tau_0 + Ste_s\tau_1 + Ste_s^2\tau_2 + ...,
\end{aligned} \tag{6.41}$$

where the subscripts $0, 1, 2$ represent the order of perturbation expansion. The zeroth-order solution can be found as follows:

$$\begin{aligned}
\theta_{s,0} &= \frac{-1 + Bi_s \ln\xi}{-1 + Bi_s \ln\xi_i}, \\
\tau_0 &= -\frac{(2 + Bi_s)(-1 + \xi_i^2)}{4Bi_s} + \frac{1}{2}\xi_i^2 \ln\xi_i.
\end{aligned} \tag{6.42}$$

6.3.5 Solid subcooling stage

As the phase change interface reaches the center, the whole cylinder is solidified. The frozen cylinder continues to cool down until equilibrium depending on the prescribed ambient temperature. This solid subcooling stage is modeled by a 2-D finite-extent pure conduction problem similar to the liquid supercooling process. Compared with the supercooling, this subcooling stage is in the solid phase instead of liquid. After the same analytical treatments, the exact solution is given by the text [16]:

$$T_s(r,z,t) = \sum_{n=0}^{\infty}\sum_{m=1}^{\infty}\left[E_{nm}J_0(\beta_m r)\cos(\eta_n z)e^{-\alpha_s\lambda_{nm}^2 t}\right] + T_\infty,\ t > t_{crit}. \tag{6.43}$$

While the eigenvalues remain identical to the ones in the liquid supercooling as expressed in Eq. (6.20), the eigencoefficients are determined as:

$$E_{nm} = \frac{\int_{z=0}^{H}\int_{r=0}^{a} r(T_{\text{crit}}(r) - T_\infty)J_0(\beta_m r)\cos(\eta_n z)\mathrm{d}r\mathrm{d}z}{\int_{r=0}^{a} rJ_0^2(\beta_m r)\mathrm{d}r\int_{z=0}^{H}\cos^2(\eta_n z)\mathrm{d}z}, \tag{6.44}$$

where $T_{\text{crit}}(r)$ is the temperature distribution at the critical time when the entire cylinder becomes solid in the previous stage.

6.3.6 Computational algorithm

The unified mathematical model is a sequential framework to solve the five solidification stages, where the terminal conditions (including both temperature and time conditions) of one stage will be the initial conditions of the following stage. The computational algorithm of this sequential model is outlined in a form of a flowchart, as shown in Fig. 6.3. The threshold temperature and time are also indicated at each solidification stage.

First of all, the liquid temperature T_ℓ at the liquid supercooling stage is calculated by Eq. (6.19) starting from the initial temperature T_{init} and time $t = 0$. Second, the nucleation temperature T_{nuc} and time t_{nuc} are found by the nucleation rate $J(t)$ in Eq. (6.22) and

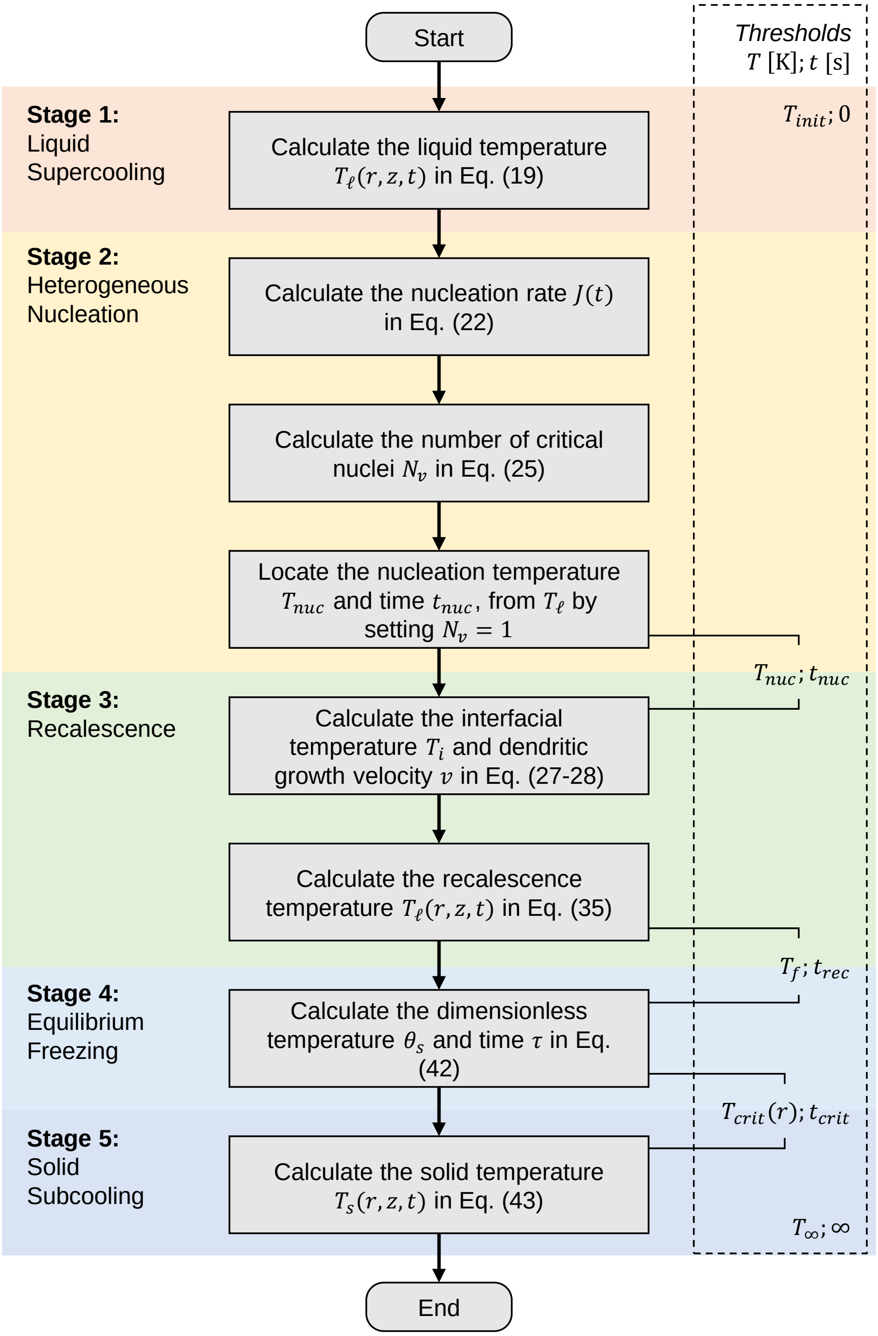

Figure 6.3: Flowchart to demonstrate the computational algorithm of the five-stage mathematical framework. The threshold column on the right shows the time t and temperature T bound for each solidification stage.

number of critical nuclei N_v in Eq. (6.25). When $N_v = 1$, T_{nuc} and t_{nuc} can be located from T_ℓ in the previous stage. Third, the recalescence temperature profile is calculated by Eq. (6.35) after numerically solving the interfacial temperature T_i and dendritic growth velocity v in Eq. (6.27-6.28). Recall that the recalescence finishes at the time t_{rec} (found by the relation $t_{rec} - t_{nuc} = 2a/v$) and at the fusion temperature T_f. Further, the temperature profile during equilibrium is calculated by the dimensionless form θ_s in Eq. (6.42), and this stage terminates at the total freezing time t_{crit} as the solid-liquid interface reaches the center of the cylinder. Last, the solid temperature T_s during solid subcooling is obtained from Eq. (6.43) until it reaches the surrounding temperature T_∞.

6.4 Model validation

To validate the numerical model, six different cases were carried out with various T_{init} and T_∞ values. Specific values of T_{init} and T_∞ in each case are listed in Table 6.4 along with calculated heat transfer coefficient at every time interval: h_1, h_2, h_3 in liquid supercooling, h_4 in equilibrium freezing, and h_5 in solid subcooling. In addition to the heat transfer coefficients, the effective latent heat are also tabulated for each case. The coefficient of interfacial surface tension σ_0 was calibrated to be 0.0175 (J/m^2) in all scenarios; the freezing behavior for each case was determined by measuring the temperature for a period of time (particularly, 2000 s). It should be emphasized that the effective latent heat varies as the initial or surrounding temperature changes, mainly because of the difference in T_{nuc} from Eq. (6.37) for each scenario. The thermal predictions from the semi-analytical model are qualitatively and quantitatively validated with the experimental measurement, as shown in Fig. 6.4.

Figure 6.4 shows that for all cases the numerical model was able to capture the different solidification stages throughout the experiment, i.e., liquid supercooling and nucleation, recalescence, equilibrium freezing, and solid subcooling stages. Overall, the model predictions agree well with the experimental measurements with an acceptable range of accuracy. The initial condition and the decay of the temperature profile during the liquid supercooling

Table 6.4: Parametric studies with calculated five heat transfer coefficients (W m^{-2} K^{-1}) and effective latent heat (J kg^{-1}) for different ambient and initial temperatures (°C).

Case	T_{init}	T_∞	h_1	h_2	h_3	h_4	h_5	L_{eff}
1	20	-17	212.97	112.56	75.66	95.32	20.67	295189.3
2	20	-14	313.85	124.23	87.37	77.25	46.58	295258.8
3	20	-11	301.71	159.42	79.35	65.07	42.57	295332.9
4	15	-14	276.20	109.47	77.51	73.26	41.22	295214.4
5	10	-14	399.17	203.04	94.55	87.25	16.41	295245.7
6	5	-14	151.03	199.57	86.82	62.76	24.88	295259.7

stage is well captured, and there is slight discrepancy in nucleation temperature between the model prediction and experimental values with an average accuracy of 16.33% for all six cases. Another thing to note here is that there is a discontinuity between the equilibrium freezing and subcooling curves as these stages are modeled separately. Nevertheless, the good agreement between numerical prediction and experimental results validates the use of the model in this study.

6.5 Results and discussions

6.5.1 Temperature distribution over radial coordinates

The spatial variation of temperature inside a cylinder is studied by plotting the dimensionless temperature against dimensionless radial coordinates, as shown in Fig. 6.5. Dimensionless radial coordinate of zero represents the center of the cylinder while -1 and 1 represent the convective boundary conditions. Dimensionless temperature value of above zero denotes liquid phase while below zero denotes solid phase.

Figure 6.5 shows the temperature plot as a function of radial coordinates at different time for four solidification stages: liquid supercooling, nucleation and recalescence, equilibrium freezing, and solid subcooling. In the liquid supercooling stage, heat conduction occurs from the sides of the cylinder to the center, demonstrated by the parabolic profile of temperature

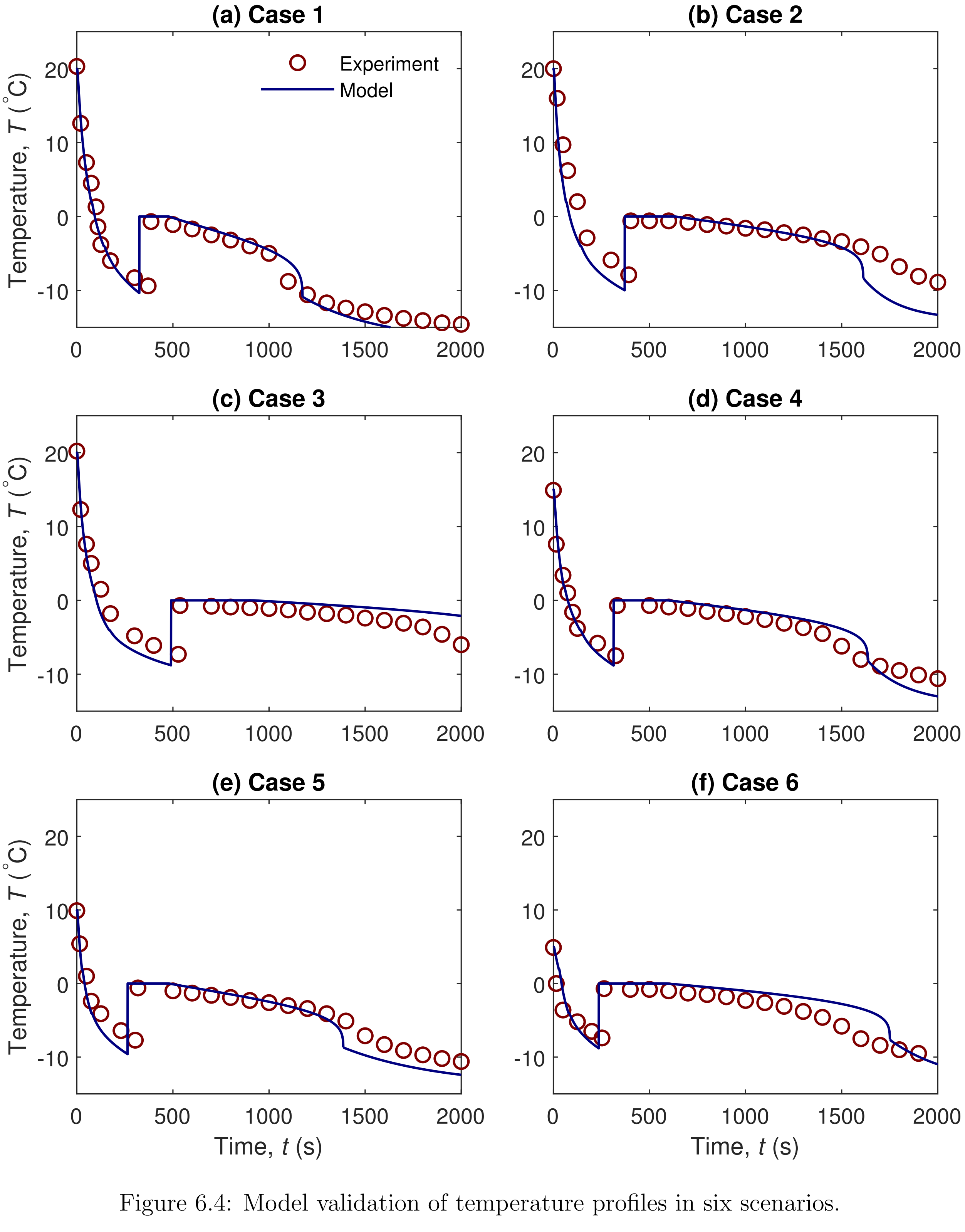

Figure 6.4: Model validation of temperature profiles in six scenarios.

curves (Fig. 6.5a). As time progresses, temperature goes down (cooling) at a faster rate on the sides than at the center. Next timescale is when nucleation and recalescence occurs

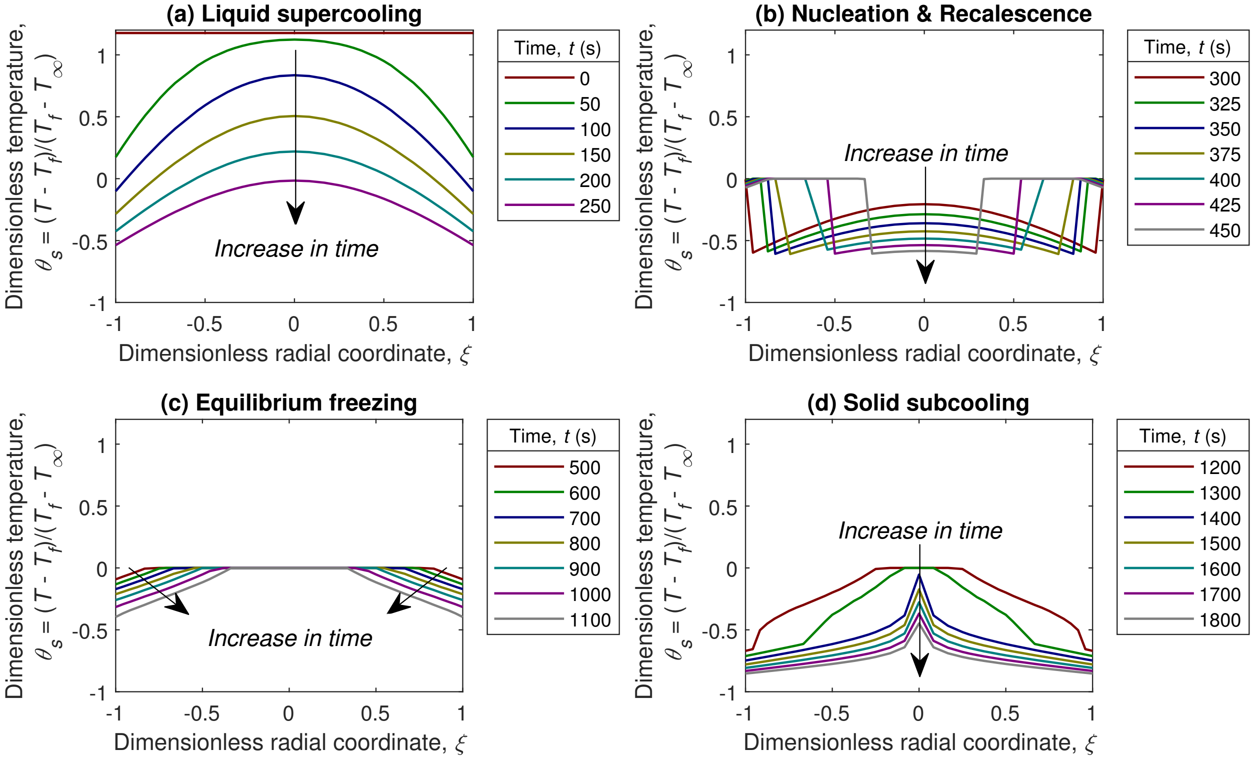

Figure 6.5: Temperature distribution over the radial coordinate in a) liquid supercooling, b) nucleation and recalescence, c) equilibrium freezing, and d) solid subcooling.

(Fig. 6.5b). The temperature cools down further as nucleation takes place and increases on the sides when recalescence starts to occur. The temperature at the center of the cylinder goes down as time goes by. It is also worth noting that during this stage and the next stage (equilibrium freezing), a mirrored temperature profile is observed on the two sides of the cylinder, which points to the symmetry of this setup. Once recalescence is completed, temperature increases to fusion temperature ($T_f = 0$) and stays at this T_f before water freezes completely. Again, the sides of the cylinder cool down faster than the center, as shown in Fig. 6.5c where the center is still at T_f while the sides start to demonstrate solid subcooling behavior. Finally, solid subcooling takes place from $t = 1200$ s (Fig. 6.5d). The phenomenon taking place at this stage is heat conduction. In this stage, temperature profile is not parabolic as in the liquid supercooling stage, due to nucleation and recalescence that took place. Nevertheless, the same behavior is observed: temperature on the sides of the cylinder is lower than that of the center.

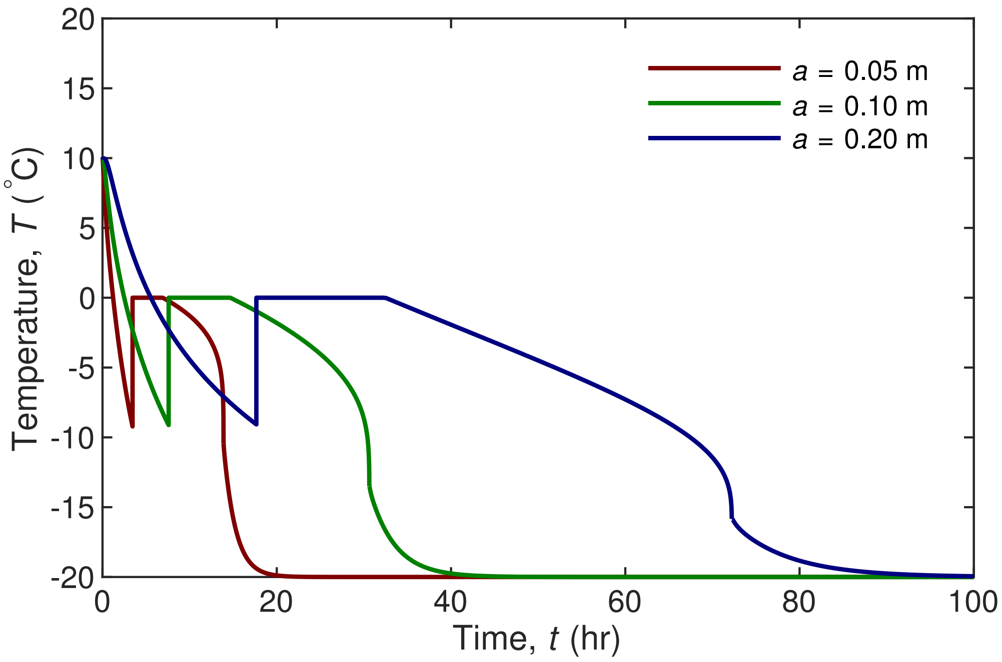

Figure 6.6: Temperature profile for various geometrical scenarios at a radius of a = 0.05, 0.10, 0.20 m.

6.5.2 Effects of geometry

The dimension of CTES system plays a crucial role in the total freezing time of PCM, which in turn affects thermal performance and efficiency of CTES system. It is therefore an important design consideration for CTES system. To study the effect of geometry on solidification, radius (a) of the cylindrical pipe is varied. Three values are chosen: $a = 0.05$ m, 0.1 m, and 0.2 m. It can be inferred from Figure 6.6 that smaller domain, as reflected by smaller radius, results in faster nucleation and freezing time. Nucleation time are 3.45 hr, 7.59 hr, and 17.66 hr, for radius of 0.05 m, 0.1 m, and 0.2 m, respectively, while nucleation temperature stays approximately the same. In other words, nucleation takes longer by 4.14 hr and 10.07 hr when the radius is increased from 0.05 m to 0.1 to 0.2 m. Total freezing time also increases significantly as the domain is increased; at 0.05 m radius, total freezing time is 13.89 hr, at 0.1 m radius the total freezing time is increased to 30.62 hr, and jumps to 72.22 hr for radius of 0.2 m.

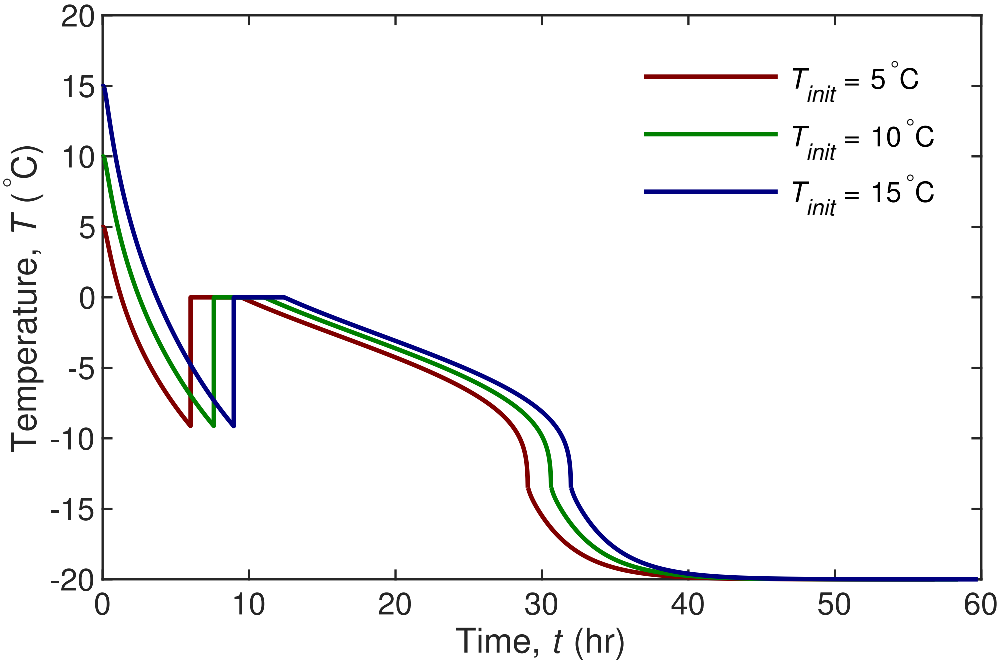

Figure 6.7: Temperature profile for various initial temperatures: $T_{init} = 5$, 10, 15°C.

6.5.3 Effects of initial temperature

Another essential design consideration is the temperature of PCM at its initial state. According to the geological location of CTES system, it is possible to have a wide range of initial temperatures. In this study, the effect of initial water temperature on the freezing behavior is analyzed by varying three different values 5°C, 10°C, and 15°C while all other parameters are kept constant. As shown in Fig. 6.7, all three cases display the same behavior with slightly delayed timescale as the initial temperature is increased.

Nucleation time, i.e., time to reach the nucleation temperature is longer for higher initial temperature owing to higher sensible heat. However, the increase in time to reach nucleation temperature is not significant; 6.01 hr to 7.59 hr to 8.95 hr when the initial fluid temperature is increased from 5°C to 10°C to 15°C. This represents an average of 22.17% per 5°C increase. Total freezing time, defined as the sum of time of each stages up until equilibrium freezing stage ends, i.e., when the entire domain is frozen, is longer due to the additional sensible heat resulted from increased initial temperature. The delay in total freezing time is approximately 5%. An important thing to note here is that while its effect on nucleation time is more apparent, initial temperature has minuscule effect on nucleation temperature, with only about 0.16% difference under the investigated range. This is because in this case the surrounding (heat transfer fluid) temperature is fixed at -20°C. Related to application of cold storage, it can be observed that more total energy can be stored with higher initial temperature. This is reflected by the larger area under the curve for higher temperature.

6.5.4 Effects of heat transfer fluid temperature

HTF temperature is also critical to the phase change process in CTES system, in which the HTF temperature represents the surrounding temperature (T_∞). To examine the effect of HTF temperature, T_∞ is varied from -10°C to -20°C to -30°C. Figure 6.8 shows that T_∞ significantly influences the freezing curve behavior and time. In general, colder temperature results in faster cooling. Liquid supercooling/nucleation time decreases by 245.79% and 70.62% as T_∞ is decreased from -10°C to -20°C and from -20°C to -30°C, respectively. Total freezing time is delayed by 57.65% between -10°C and -20°C and 35.34% between -20°C and -30°C. This is owing to the fact that the heat flux with the surrounding is higher as T_∞ is lowered. The nucleation temperature is $-9.134, -9.120, -9.0126$°C for $T_\infty = -10, -20, -30$°C, respectively. Insights to the effect of heat transfer fluid temperature is useful in real world application for temperature adjustment based on the desired charging time. For faster charging, lower (colder) heat transfer fluid temperature is recommended.

6.5.5 Effects of heat transfer coefficient

Most importantly, the heat transfer coefficient of any CTES system influences the rate of solidification and the overall thermal efficiency. In this study, three values of heat transfer coefficients (W m^{-2} K^{-1}) were studied to determine the effect of heat transfer coefficients h on solidification behavior: 10, 50, and 100 (W m^{-2} K^{-1}). The heat transfer coefficient was previously denoted as h_{eq} in the model development which varied from one stage to another,

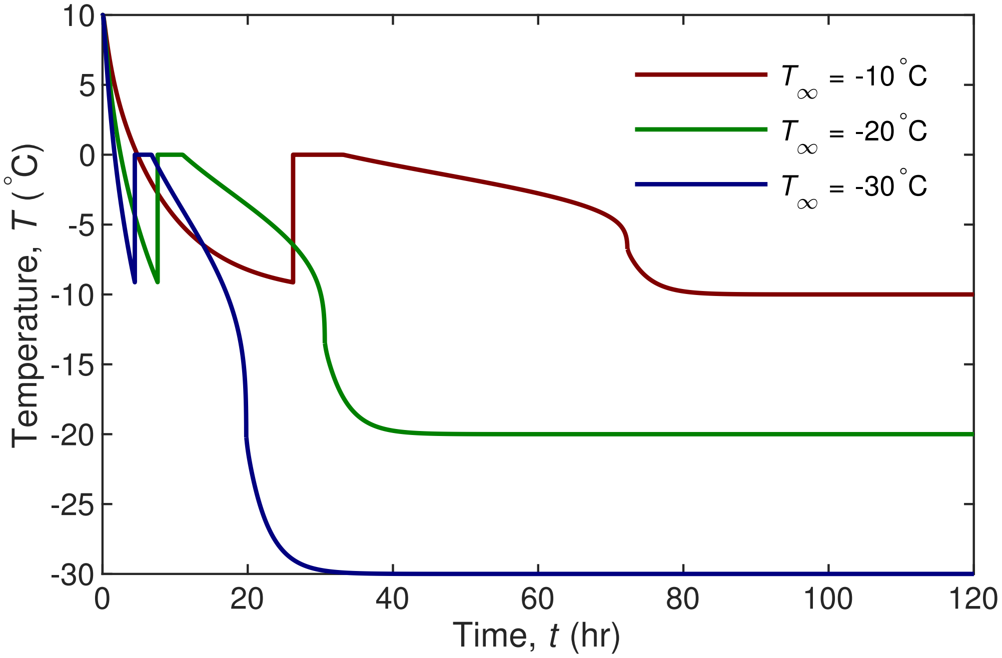

Figure 6.8: Temperature profile for various heat transfer fluid temperatures: $T_\infty = -10$, -20, -30°C.

but for simplicity a constant value was used here to better demonstrate the influence on the entire evolution. Higher heat transfer coefficient (for e.g., 500 or 1000 (W $\mathrm{m^{-2}\ K^{-1}}$)) were also considered. However, no significant changes from the 100 (W $\mathrm{m^{-2}\ K^{-1}}$) case were observed from employing high coefficients. Hence, the highest coefficient plotted in Fig. 6.9 is the case for 100 (W $\mathrm{m^{-2}\ K^{-1}}$). From Fig. 6.9, it can be observed that high heat transfer coefficients correlates to faster solidification. This is expected as high coefficients induces high heat transfer rate which in return leads to stronger cooling rate. Nevertheless, the significance of the difference in total freezing time varies. It seems that enhancement in cooling rate is more significant at lower heat transfer coefficient. Increasing the heat transfer coefficient from 10 to 50 (W $\mathrm{m^{-2}\ K^{-1}}$) reduces the nucleation time by 67.03% and total freezing time by 65.72%, while increasing the coefficient from 50 to 100 (W $\mathrm{m^{-2}\ K^{-1}}$) reduces the nucleation time by 25.56% and total freezing time by 23.99%.

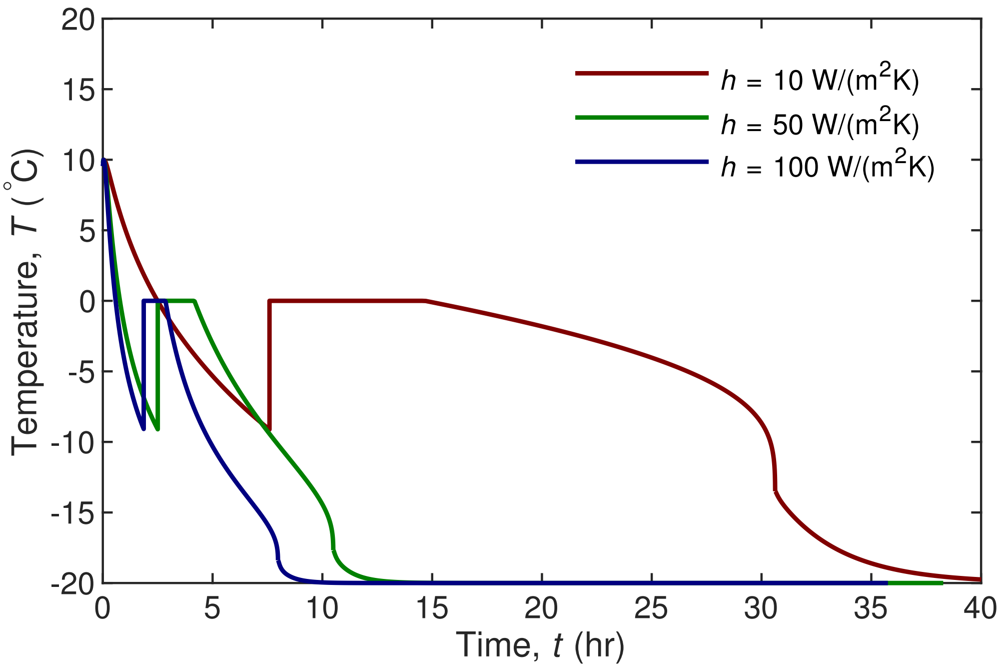

Figure 6.9: Temperature profile for various heat transfer coefficients: $h = 10, 50, 100$ W/(m^{2}K).

6.6 Conclusion

This paper firstly built up a novel experimental apparatus for the thermal analysis of PCMs, particularly evaluating transient temperature profile during inward solidification of a cylinder along with contact angle measurement. This apparatus employed additional care between the water bath and test tube to mitigate any internal influence from crystallization and external disturbance caused by machine vibration and coolant fluid flow. Since the heat transfer coefficient varies significantly among solidification stages, a comprehensive procedure to determine the heat transfer coefficient based on energy balance at each time interval was introduced. This experimental system should readily extend to other geometrical domains of interest, thus providing guidelines to further experimental research on phase change heat transfer.

A rigorous two-dimensional mathematical framework was also established to unify all the solidification stages from micro- to macro-scale. Specifically, this framework consisted of one set of governing partial differential equations subjected to a number of fixed and moving boundaries with time conditions. An accurate and fast-to-compute semi-analytical solution to this problem was developed and validated against experimental results. Future modeling works could center around the other boundary conditions, geometries, and considerations of volume shrinkage or expansion during phase change.

Lastly, we studied a number of important design and operational considerations in CTES system, including temperature distribution over radial coordinates, operational domain, initial temperature, heat transfer fluid temperature, and heat transfer coefficient. These investigations not only proved the reliability and robustness of our modeling framework in CTES system, but also shed light on the thermal design and operation of CTES system.

Nomenclature

Letters

a	Cylinder radius
H	Cylinder height
V	Cylinder volume
V^*	Critical embryo volume
A	Surface area
T	Temperature
t	Time
r	Radial coordinate
z	Axial coordinate
r_i	Interface location
L	Latent heat of fusion
L_{eff}	Effective latent heat of fusion
L_m	Latent heat of fusion per unit mole
L_v	Volumetric latent heat of fusion
k	Thermal conductivity
k_B	Boltzmann constant
h	Heat transfer coefficient
c_p	Specific heat
p	Saturation pressure
J	Nucleation rate
D	Self-diffusion coefficient
d_0	Capillarity length
n	Number density of a molecule
N_A	Avogadro constant
N_v	Number of critical nuclei
X	Radii ratio between nucleating particle and critical embryo
g_0	Internal heat generation
M_w	Molar mass of water
m	Mass
v	Dendritic growth velocity
r_0	Mean particle separation distance
r^*	Critical embryo radius
Ste	Stefan number
Bi	Biot number
Fo	Fourier number
Gr	Grashoff number
Re	Reynolds number
Ri	Richardson number
J_0	Bessel function of the first kind with order zero
J_1	Bessel function of the first kind with order one
C, D, E	Eigencoefficients

Greek symbols

α	Thermal diffusivity
ρ	Mass density
ϕ	Contact angle
$\sigma_{\ell s}$	Interfacial surface tension
σ_0	Baseline interfacial surface tension
σ^*	Universal LM-K stability constant
σ_k	Interfacial kinetics factor
ζ_f	Heterogeneous Zeldovich factor
β, λ, η	Eigenvalues
θ	Dimensionless temperature
ξ	Dimensionless radial coordinate
ξ_i	Dimensionless interface location
τ	Dimensionless time

Superscripts and subscripts

tc	Thermocouple
ℓ	Liquid or water
s	Solid or ice
f	Fusion
$init$	Initial
i	Interfacial
∞	Surrounding
j	j-th time interval
$wall$	Tube wall
$calc$	Calculated
$steel$	Steel material
nuc	Nucleation
rec	Recalescence
$crit$	Critical or total freezing
eq	Equilibrium
w	Water molecule
th	Thermal
k	Kinetic
σ	Curvature

Bibliography

[1] H. Abdelrahman, H. Refaey, A. Alotaibi, A. A. Abdel-Aziz, and M. Abd Rabbo. Experimental investigations on the thermal performance of an ice storage system using twin concentric helical coil. *Applied Thermal Engineering*, 179:115737, 2020.

[2] S. Akhtar, M. Xu, and A. Sasmito. Spray freezing for mine heating a statistical perspective. In *Mine Ventilation*, pages 357–365. CRC Press, 2021.

[3] S. Akhtar, M. Xu, and A. P. Sasmito. Development and validation of a semi-analytical framework for droplet freezing with heterogeneous nucleation and non-linear interface kinetics. *International Journal of Heat and Mass Transfer*, 166:120734, 2021.

[4] S. Akhtar, M. Xu, and A. P. Sasmito. Development and validation of an asymptotic solution for a two-phase stefan problem in a droplet subjected to convective boundary condition. *International Journal of Thermal Sciences*, 164:106923, 2021.

[5] S. Akhtar, M. Xu, and A. P. Sasmito. A novel crystal growth model with nonlinear interface kinetics and curvature effects: Sensitivity analysis and optimization. *Crystal Growth & Design*, 21(6):3251–3265, 2021.

[6] Z. Cai, Y. Zhang, J. Li, Y. Shang, H. Huo, J. Feng, S. S. Funari, and S. Jiang. Temperature-dependent selective crystallization behavior of isotactic polypropylene with a β-nucleating agent. *Journal of Applied Polymer Science*, 128(1):628–635, 2013.

[7] D. Calì, T. Osterhage, R. Streblow, and D. Müller. Energy performance gap in refurbished german dwellings: Lesson learned from a field test. *Energy and buildings*, 127:1146–1158, 2016.

[8] S. Coriell, S. Hardy, and R. Sekerka. A non-linear analysis of experiments on the morphological stability of ice cylinders freezing from aqueous solutions. *Journal of Crystal Growth*, 11(1):53–67, 1971.

[9] H. Ding, Y. Tian, C. Wen, C. Wang, and C. Sun. Polydispersed droplet spectrum and exergy analysis in wet steam flows using method of moments. *Applied Thermal Engineering*, 182:116148, 2021.

[10] F. I. Dragomirescu, K. Eisenschmidt, C. Rohde, and B. Weigand. Perturbation solutions for the finite radially symmetric stefan problem. *International Journal of Thermal Sciences*, 104:386–395, 2016.

[11] R. I. ElGhnam, R. A. Abdelaziz, M. H. Sakr, and H. E. Abdelrhman. An experimental study of freezing and melting of water inside spherical capsules used in thermal energy storage systems. *Ain Shams Engineering Journal*, 3(1):33–48, 2012.

[12] A. Erek and I. Dincer. Numerical heat transfer analysis of encapsulated ice thermal energy storage system with variable heat transfer coefficient in downstream. *International Journal of Heat and Mass Transfer*, 52(3-4):851–859, 2009.

[13] F. Font. A one-phase Stefan problem with size-dependent thermal conductivity. *Applied Mathematical Modelling*, 63:172–178, 2018.

[14] S. A. Ghoreishi-Madiseh, A. F. Kuyuk, H. Kalantari, and A. P. Sasmito. Ice versus battery storage; a case for integration of renewable energy in refrigeration systems of remote sites. *Energy Procedia*, 159:60–65, 2019.

[15] L. Gránásy, T. Pusztai, and P. F. James. Interfacial properties deduced from nucleation experiments: A Cahn–Hilliard analysis. *The Journal of Chemical Physics*, 117(13):6157–6168, 2002.

[16] D. W. Hahn and M. N. Özisik. *Heat conduction.* John Wiley & Sons, 2012.

[17] H. A. Hamzeh and M. Miansari. Numerical study of tube arrangement and fin effects on improving the ice formation in ice-on-coil thermal storage systems. *International Communications in Heat and Mass Transfer*, 113:104520, 2020.

[18] J. M. Hill. *One-dimensional Stefan problems: An introduction.* Longman Scientific & Technical, 1987.

[19] J. P. Hindmarsh, A. B. Russell, and X. D. Chen. Experimental and numerical analysis of the temperature transition of a suspended freezing water droplet. *International Journal of Heat and Mass Transfer*, 46(7):1199–1213, 2003.

[20] G. Ivantsov. Temperature field around a spherical, cylindrical, and needle-shaped crystal, growing in a pre-cooled melt. *Temperature Field Around a Spherical*, 58:567–569, 1985.

[21] K. A. Jackson. *Kinetic Processes: Crystal growth, diffusion, and phase transformations in materials.* John Wiley & Sons, 2006.

[22] H. Jannesari and N. Abdollahi. Experimental and numerical study of thin ring and annular fin effects on improving the ice formation in ice-on-coil thermal storage systems. *Applied Energy*, 189:369–384, 2017.

[23] J. Langer and J. Müller-Krumbhaar. Stability effects in dendritic crystal growth. *Journal of Crystal Growth*, 42:11–14, 1977.

[24] S. Li, Z. Liu, and X. Wang. A comprehensive review on positive cold energy storage technologies and applications in air conditioning with phase change materials. *Applied Energy*, 255:113667, 2019.

[25] J. M. Mahdi and E. C. Nsofor. Melting enhancement in triplex-tube latent heat energy storage system using nanoparticles-metal foam combination. *Applied Energy*, 191:22–34, 2017.

[26] S. W. McCue, B. Wu, and J. M. Hill. Classical two-phase Stefan problem for spheres. *Proceedings of the Royal Society A: Mathematical, Physical and Engineering Sciences*, 464(2096):2055–2076, 2008.

[27] Z. Meng and P. Zhang. Dynamic propagation of ice-water phase front in a supercooled water droplet. *International Journal of Heat and Mass Transfer*, 152:119468, 2020.

[28] D. M. Murphy and T. Koop. Review of the vapour pressures of ice and supercooled water for atmospheric applications. *Quarterly Journal of the Royal Meteorological Society: A Journal of the Atmospheric Sciences, Applied Meteorology and Physical Oceanography*, 131(608):1539–1565, 2005.

[29] T. G. Myers, M. G. Hennessy, and M. Calvo-Schwarzwälder. The Stefan problem with variable thermophysical properties and phase change temperature. *International Journal of Heat and Mass Transfer*, 149:118975, 2020.

[30] A. H. Nayfeh. *Introduction to perturbation techniques*. John Wiley & Sons, 2011.

[31] R. Perry and G. DW. *Perry's chemical engineers' handbook*. New York: McGraw-Hill, 2007.

[32] A. Pourakabar and A. A. R. Darzi. Enhancement of phase change rate of PCM in cylindrical thermal energy storage. *Applied Thermal Engineering*, 150:132–142, 2019.

[33] M. H. Rahdar, A. Emamzadeh, and A. Ataei. A comparative study on pcm and ice thermal energy storage tank for air-conditioning systems in office buildings. *Applied Thermal Engineering*, 96:391–399, 2016.

[34] S. Sanaye and A. Shirazi. Thermo-economic optimization of an ice thermal energy storage system for air-conditioning applications. *Energy and Buildings*, 60:100–109, 2013.

[35] W. H. Sang, Y. T. Lee, J. D. Chung, S. T. Kim, T. Kim, C.-H. Oh, and K.-H. Lee. Efficient numerical approach for simulating a full scale vertical ice-on-coil type latent thermal storage tank. *International Communications in Heat and Mass Transfer*, 78:29–38, 2016.

[36] K. Schulte and B. Weigand. On the analytical modelling of the initial ice growth in a supercooled liquid droplet. *International Journal of Heat and Mass Transfer*, 127:1070–1081, 2018.

[37] Y. Shao, K. Soh, Y. Wan, M. Kumja, Z. Khin, M. Islam, and K. Chua. Simulation and experimental study of thermal storage systems for district cooling system under commercial operating conditions. *Energy*, page 117781, 2020.

[38] A. Shirazi, M. Aminyavari, B. Najafi, F. Rinaldi, and M. Razaghi. Thermal–economic–environmental analysis and multi-objective optimization of an internal-reforming solid oxide fuel cell–gas turbine hybrid system. *International Journal of Hydrogen Energy*, 37(24):19111–19124, 2012.

[39] S. Tabakova, F. Feuillebois, and S. Radev. Freezing of a supercooled spherical droplet with mixed boundary conditions. *Proceedings of the Royal Society A: Mathematical, Physical and Engineering Sciences*, 466(2116):1117–1134, 2010.

[40] K. Tanaka, T. Yamamoto, K. Nagashima, and K. Tsukamoto. A new method of evaluation of melt/crystal interfacial energy and activation energy of diffusion. *Journal of Crystal Growth*, 310(6):1281–1286, 2008.

[41] K. K. Tanaka and Y. Kimura. Theoretical analysis of crystallization by homogeneous nucleation of water droplets. *Physical Chemistry Chemical Physics*, 21(5):2410–2418, 2019.

[42] J. Vogel and A. Thess. Validation of a numerical model with a benchmark experiment for melting governed by natural convection in latent thermal energy storage. *Applied Thermal Engineering*, 148:147–159, 2019.

[43] T. Wang, Y. Lu, L. Ai, Y. Zhou, and M. Chen. Dendritic growth model involving interface kinetics for supercooled water. *Langmuir*, 35(15):5162–5167, 2019.

[44] J. Wu, E. Gagnière, F. Jay, and C. Jallut. Population balance modeling for the charging process of a PCM cold energy storage tank. *International Journal of Heat and Mass Transfer*, 85:647–655, 2015.

[45] J. Xie and C. Yuan. Parametric study of ice thermal storage system with thin layer ring by taguchi method. *Applied Thermal Engineering*, 98:246–255, 2016.

[46] M. Xu, S. Akhtar, and A. P. Sasmito. A heterogeneous nucleation model for supercooled water and sucrose solution droplets under ultra-cold environments. In *ASME International Mechanical Engineering Congress and Exposition (*Accepted*)*, 2021.

[47] M. Xu, S. Akhtar, A. F. Zueter, M. A. Alzoubi, L. Sushama, and A. P. Sasmito. Asymptotic analysis of a two-phase Stefan problem in annulus: Application to outward solidification in phase change materials. *Applied Mathematics and Computation*, 408:126343, 2021.

[48] C. Yu, Q. Peng, X. Liu, P. Cao, and F. Yao. Role of metal foam on ice storage performance for a cold thermal energy storage (CTES) system. *Journal of Energy Storage*, 28:101201, 2020.

[49] C. Zhang, Q. Sun, and Y. Chen. Solidification behaviors and parametric optimization of finned shell-tube ice storage units. *International Journal of Heat and Mass Transfer*, 146:118836, 2020.

[50] Y. Zhao, Q. Guo, T. Lin, and P. Cheng. A review of recent literature on icing phenomena: Transport mechanisms, their modulations and controls. *International Journal of Heat and Mass Transfer*, 159:120074, 2020.

[51] Y. Zhao, X. Zhang, X. Xu, and S. Zhang. Research progress in nucleation and supercooling induced by phase change materials. *Journal of Energy Storage*, 27:101156, 2020.

Chapter 7

Development of a multi-stage model for freezing of a suspended binary solution droplet

Contents

Preface (Bridging Text)

Spray freezing (SF) is a renewable energy-based and cost-effective technology for mine heating and cooling (e.g., in the Frood-Stobie Mine, Ontario) as well as decontamination of mine wastewater (e.g., in the Colomac Mine, Northwest Territories). Similar to phase change materials (PCMs), SF also exploits cold energy and the solid-liquid phase change. For example, in decontamination, SF can reject contaminated particles from the ice during freezing, thereby separating purified water in the ice from contaminants as a wastewater pre-treatment method.

In Chapter 6, experimental and unified mathematical frameworks were developed for multi-stage non-equilibrium solidification in pure substances, such as ice/water phase change. A thorough investigation was conducted on the five-stage solidification process and its application to PCMs for cold thermal energy storage. However, non-pure substances such as mixtures have a wide range of applications, including the decontamination of wastewater using SF. Freezing mixtures undergo a similar five-stage solidification process but with more complex phenomena such as freeze concentration, freeze-point depression (FPD), as well as unique nucleation and recalescence stages.

In this chapter, multi-stage non-equilibrium solidification in mixtures was explored, which encompasses coupled heat and mass transport along with FPD. Such phenomena are not exhibited by pure substances. Specifically, a novel five-stage solidification model for binary mixtures was established using a hybrid analytical-numerical method. Stochastic nucleation behavior with mass concentration is characterized through gradient-based optimization. Sucrose aqueous solution droplets were studied and examined in this chapter because sufficient experimental data were available in the literature to quantify the stochastic nature through optimization. Nevertheless, the framework and results can be applied to contaminated chemicals such as arsenic and zinc, which are commonly found in mine wastewater. The insights and discussions presented in this chapter were published in the peer-reviewed journal article listed below.

M. Xu, S. Akhtar, M. Mohit, and A. P. Sasmito. Development of a multi-stage model for freezing of a suspended binary solution droplet. *International Journal of Heat and Mass Transfer*, 221:125115, 2024

Abstract

The importance of developing spray freeze-drying technology for extending the shelf life of biological and pharmaceutical materials has never been greater, given the increasing food shortage and the strong demand for pharma processes. In particular, the best thermal design and application of spray freeze-drying technologies now depend on the estimation of nucleation behavior for droplet solidification (especially the droplets of binary mixtures). Although earlier nucleation models could estimate the nucleation rate and temperature of solidifying droplets, few considered extreme environmental factors, such as extremely low ambient temperatures below -60°C. To ensure the preservation and storage of biological and pharmaceutical products, such as vaccines and protein drugs, these conditions are extremely important. Hence, developing an accurate and trustworthy mathematical framework for simulating nucleation is paramount. In this study, a multi-stage, hybrid analytical-numerical model for droplet solidification is developed while coupled with a gradient-based optimization algorithm. Specifically, the five-stage solidification of binary mixtures is simulated (including supercooling of liquid, nucleation, recalescence, equilibrium freezing, and subcooling of solid), which captures the dynamic behaviors of temperature and composition or solute concentration during phase change. The heterogeneous nucleation of a binary-mixture droplet in a frigid environment is predicted and validated against a series of experiments on single suspended droplets at a wide range of ambient temperatures between -20 and -160°C. The freezing curves of different solute concentrations are also validated against experimental data. It is found that significant variations in interfacial tension lead to abrupt changes in nucleation temperature for extremely cold environments. Further, the effects of the concentration, contact angle, droplet size, and heat transfer coefficient are also investigated.

Keywords: Nucleation, optimization, droplet freezing, solidification, phase change

7.1 Introduction

The study of droplet freezing or solidification is of fundamental importance in understanding the physics of phase change heat transfer, which has a variety of practical applications in both nature and industry. Specifically, droplet freezing can be exploited in lyophilization (or freeze-drying) for food [14, 12] and pharmaceutical products [56, 27], production of ice slurry using spray freezing technology [18, 19], frosting and defrosting (or anti-icing) applications [28, 41, 49], and spray freezing for underground mine heating [1, 50] to mention but a few. The solidification process, not limited to a droplet, is a multi-scale, multi-stage, and multi-physics phenomenon. It generally undergoes supercooling, freezing, and subcooling at the macroscale, crystal growth at the mesoscale, and nucleation at the microscale. Though heat transfer dominates the phase change process due to the release of latent heat, the mass diffusion of solute, change in volume (mechanically), and effect of pressure (hydraulically) could also influence solidification.

In accordance with the material, there are two distinct kinds of droplet freezing: one is the solidification of a droplet with pure substance, while another involves freezing a binary solution droplet. Extensive time in the literature has been spent on droplet solidification filled with pure substances, especially water. Traditional frameworks, such as the Stefan problem [35, 3], can be implemented to model droplet solidification. However, most of them failed to capture the transport phenomena at the meso- and micro-scales, i.e., nucleation and crystal growth. Hindmarsh et al. [26] captured the temperature transition of freezing a suspended water droplet through experiments and validated the experimental data against a heat balance model solved numerically. The results were accurately measured and predicted, demonstrating four distinct solidification stages (i.e., supercooling, recalescence or crystal growth, freezing, and cooling). Meng and Zhang [36] performed a similar laboratory experiment of suspending a water droplet. However, compared with Hindmarsh et al.'s setup a copper ring was included around the droplet's top surface for a more straightforward activation of heterogeneous nucleation. Meanwhile, a three-dimensional numerical model was built using the enthalpy method to simulate each solidification stage. Akhtar et al. [2] developed a semi-analytical, five-stage solidification model that incorporated the heterogeneous nucleation between the supercooling and recalescence stages as well as the effects of interface kinetics and surface curvature during crystal growth. The sensitivity of the Arrhenius-type equation and modified Wilson–Frenkel model (for the heterogeneous nucleation and crystal growth, respectively) were then statistically studied and optimized using the Monte-Carlo method [4].

A significantly less time has been spent on freezing a droplet filled with impure substance, e.g., a binary mixture. Compared with pure solution, the addition of solute in the binary solution has a direct impact on the freezing curve. Specifically, the mass transfer happens concurrently with the solidification, resulting in variations of the nucleation temperature, fusion point, and solid-liquid interface motion [17, 13]. The freeze point depression (the decrease in the fusion point) and freeze concentration (the downward temperature curve during the freezing stage) were systematically studied experimentally and numerically in [22] for freezing a suspended sucrose droplet. The nucleation phenomena (categorized as surface- and volume-based) for these sucrose droplets with different concentrations were explored in [24]. Sebastião et al. [45, 46] developed theoretical models (using the energy balance and computational fluid dynamics) to investigate the dynamics of the spray freeze-drying technology from the solidification of a sucrose droplet. Their modeling results were validated against several experimental data in the literature. The sucrose aqueous solution has risen particular attention in food and pharmaceutical; this is because it is commonly used as a cryoprotectant in protein formulations, and the stability of proteins can be affected by the freeze concentration of sucrose [54, 15]. In addition to sucrose droplets, the solidification of a droplet filled with salts [11, 29], a spherical binary melt [42, 16], and mannitol solution [7] are also of practical interest in frosting/anti-icing, metal/alloy, and vacuum freeze-drying applications.

When looking into the nucleation stage of solidification, the formation of an ice embryo by overcoming the Gibbs free energy is a stochastic process that occurs at a microscopic level. The nucleation temperature (also referred to as the supercooling degree), along with the instantaneous time, plays a significant role in the temperature transition of droplet freezing. Theoretically, incorrect nucleation temperature and time will bring forward or postpone the subsequential solidification stages, thus leading to a wrong freezing time that miscalculates the thermal performance. The Cryo Scanning Electron Microscope (Cryo-SEM) images results of freezing a sucrose droplet have demonstrated a significant correlation between the nucleation temperature and the crystal size distribution and microstructure [23]. In-depth investigations on the nucleation temperature have also been made by conducting extensive experimental tests on suspended [44] and sessile droplets [61, 60].

Thus far, there are still a few research gaps that need to be filled in the context of freezing a binary droplet solution:

i) The mathematical model based on the classical nucleation theory (CNT) has been developed for pure water droplets [36, 2], but not for binary solutions. The alternation of corresponding microscopic properties (e.g., interfacial tension, contact angle, self diffusivity) and thermophysical properties has not yet been clarified.

ii) Considerable studies have been carried out with an ambient temperature higher than −40°C, thus limiting the range of applications. Ultra-low environmental conditions have been proven to be useful in the storage of food and pharmaceutical products [44].

iii) There is also a lack of accurate modeling of heterogeneous nucleation that captures its spontaneous nature. Most studies have either neglected the randomness or calibrated it into the uncertainty of the prefactor or exponential factor in the CNT.

In light of these research gaps, this study proposes a gradient-based optimization framework coupling with a multi-stage model for droplet solidification. Remarkably, the interfacial tension in a heterogeneous model is optimized at various air temperatures (from $-20°\mathrm{C}$ to $-160°\mathrm{C}$). The randomness during nucleation is considered based on the analysis of experimental data and incorporated in the optimized framework, while all solidification stages are well captured in the multi-stage model for freezing a binary droplet. Moreover, the effects of solute concentration, contact angle, heat transfer coefficient, and droplet size are also studied.

7.2 Methodology

7.2.1 Multi-stage modeling

In this subsection, a hybrid multi-stage droplet solidification model for binary solutions is developed, capable of predicting the nucleation dynamics and freeze concentration. The assumptions are summarized as follows:

- Volume change during solidification (also referred to as the effect of density change) is considered negligible to the temperature transition of droplet freezing.
- Effect of natural convection inside the droplet is not included, assuming a Richardson number less than unity $Ri \ll 1$.
- The concentration gradient during equilibrium freezing only occurs in the solid phase but not in the liquid (the assumption of Scheil equation).

- The crystal growth velocity (also referred to as tip velocity) is assumed to be constant in the recalescence stage.

The computational domain is schematically shown in Fig. 7.1, where a sucrose solution droplet is suspended by a thermocouple under a cold environment. The solidification process undergoes five stages: liquid supercooling, heterogeneous nucleation, recalescence, freezing, and solid subcooling. Though the solidification stages are similar to the water droplet, the mass transfer of sucrose plays a crucial effect in each and every stage. Figure 7.2 demonstrates the temperature-composition phase diagram of amorphous sucrose and sucrose solutions based on experimental data [43]. The diagram categorizes four phases: solution, supersaturated solution, ice & freeze-concentrated solution/glass, and glass. In the scope of this study, solution and ice & freeze-concentrated solution are of particular interest representing the liquid and solid phases, respectively. The boundary between these phases is the so-called freeze point depression (FPD) which can not exceed the maximum freeze-concentrated composition $C_{g,max}$. In the context of sucrose aqueous solution, it is approximately 80% depending on the specific correlation used.

Liquid supercooling

The heat transfer inside the liquid droplet during supercooling is governed by

$$\frac{\partial^2 T_\ell}{\partial r^2} + \frac{2}{r}\frac{\partial T_\ell}{\partial r} = \frac{1}{\alpha_\ell}\frac{\partial T_\ell}{\partial t} \tag{7.1}$$

where T, r, t, α are the temperature (K), radial coordinate (m), time (s), and thermal diffusivity (m^2 s), respectively. The subscript ℓ represents the homogenized liquid phase. The liquid droplet is subjected to a convective boundary at the outer surface without any heat

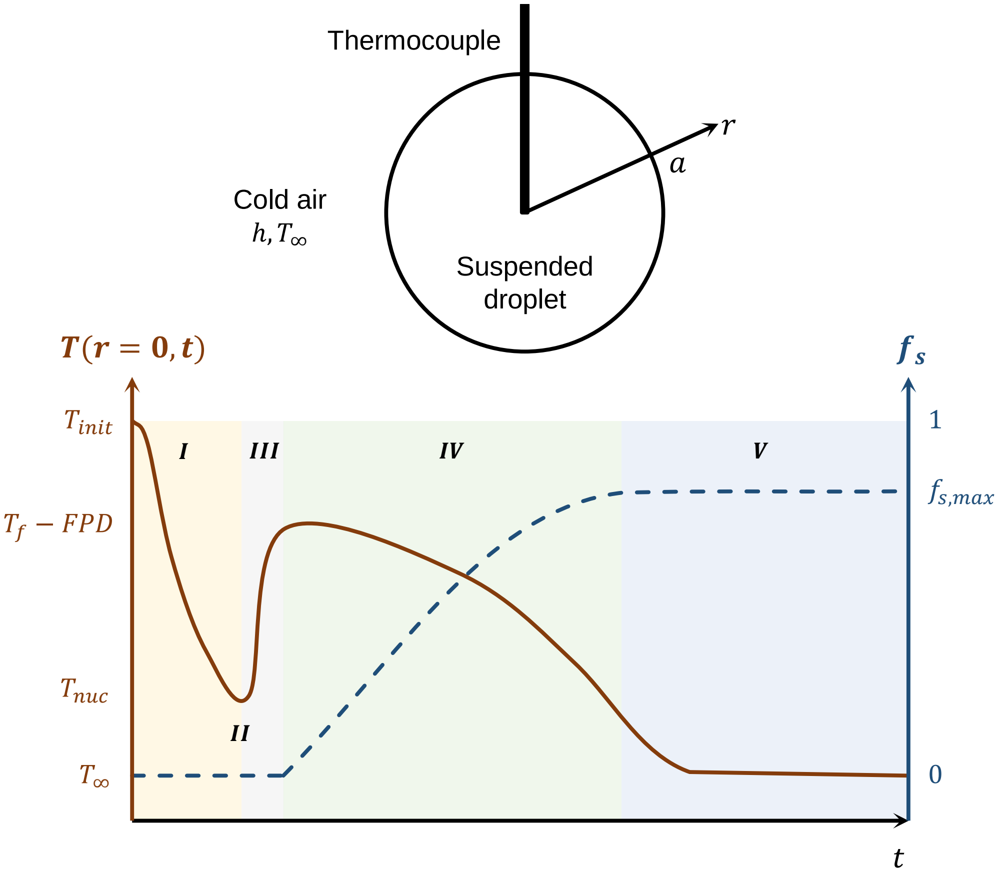

Figure 7.1: Schematic diagram of a suspended droplet subjected to a cold environment and corresponding temperature T and solid volume fraction f_s.

flux in the center (also referred to as a symmetry condition)

$$-k_\ell \frac{\partial T_\ell}{\partial r}\bigg|_{r=a} = h_{eq}\Big[T_\ell(a,t) - T_\infty\Big] \tag{7.2}$$

$$\frac{\partial T_\ell}{\partial r}\bigg|_{r=0} = 0 \tag{7.3}$$

and the initial condition is prescribed as

$$T_\ell(r, t=0) = T_{init} \tag{7.4}$$

where $k, h_{eq}, T_\infty(t), T_{init}$ are the thermal conductivity (W m^{-1} K^{-1}), equivalent heat transfer coefficient (W m^{-2} K^{-1}), surrounding temperature (K), and initial temperature (K), respec-

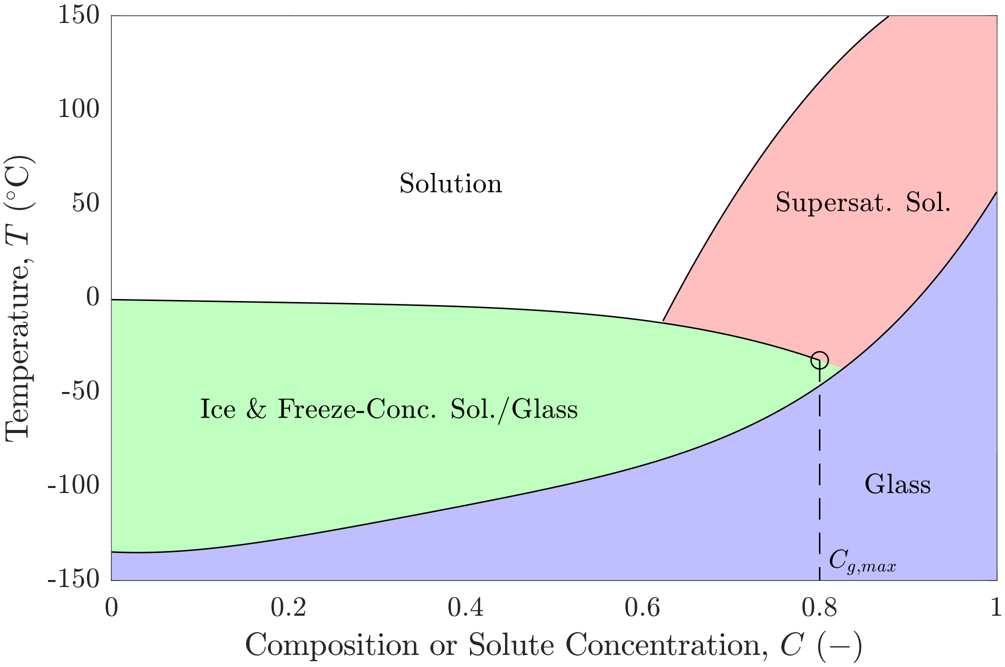

Figure 7.2: Temperature-composition phase diagram of sucrose (adopted from [43, 45]).

tively. The equivalent heat transfer coefficient calculated by multiple influential mechanisms will be discussed at the end of this sub-section.

The partial differential equation (PDE) with the boundary conditions is separable and an exact solution can be obtained by using the method of separation of variables. Due to the lengthy derivation, the analytical treatment used is demonstrated in Appendix A. Here, we can directly write down the final solution

$$\begin{aligned} T(r,t) &= T_\infty + \frac{1}{r}\sum_{n=1}^{\infty} C_n \sin(\lambda_n r)\exp(-\alpha_\ell \lambda_n^2 t) \\ \lambda_n \cot(\lambda_n a) &= \frac{1}{a} - \frac{h_{eq}}{k_\ell} \\ C_n &= \frac{4(T_{init} - T_\infty)[\lambda_n a \cos(\lambda_n a) - \sin(\lambda_n a)]}{\lambda_n[\sin(2\lambda_n a) - 2\lambda_n a]} \end{aligned} \tag{7.5}$$

Despite the fact that the temperature at the droplet's center $T(r = 0, t)$ cannot be found directly using Eq. (7.5), the limit at $r \to 0$ exists. Employing the L'Hôpital's rule at

Table 7.1: A list of thermophysical properties for water, ice, sucrose, and sucrose aqueous solutions.

Property	Material	Value	Note/Ref.
Thermal conductivity, k ($\mathrm{W \cdot m^{-1} \cdot K^{-1}}$)	k_{water}	0.555	[2]
	k_{ice}	2.22	[2]
	$k_{sucrose}$	0.164	[33]
	k_ℓ	$(1 - C_\ell)k_{water} + C_\ell k_{sucrose}$	weighted average
	k_s	$(1 - C_s)k_{ice} + C_s k_{sucrose}$	weighted average
Mass density, ρ ($\mathrm{kg \cdot m^{-3}}$)	ρ_{water}	999.8	[2]
	ρ_{ice}	916.2	[2]
	$\rho_{sucrose}$	1588	[20]
	ρ_ℓ	$(1 - C_\ell)\rho_{water} + C_\ell \rho_{sucrose}$	weighted average
	ρ_s	$(1 - C_s)\rho_{ice} + C_s \rho_{sucrose}$	weighted average
Specific heat, c_p ($\mathrm{J \cdot kg^{-1} \cdot K^{-1}}$)	$c_{p,water}$	4200	[2]
	$c_{p,ice}$	2100	[2]
	$c_{p,sucrose}$	1252	[20]
	$c_{p,\ell}$	$[(1 - C_\ell)(\rho c_p)_{water} + C_\ell(\rho c_p)_{sucrose}]/\rho_\ell$	weighted average
	$c_{p,s}$	$[(1 - C_s)(\rho c_p)_{ice} + C_s(\rho c_p)_{sucrose}]/\rho_s$	weighted average

$\lim_{r\to 0} T(r,t)$, the exact solution at the center is expressed as

$$T(r = 0, t) = T_\infty + \sum_{n=1}^{\infty} C_n \lambda_n \exp(-\alpha_\ell \lambda_n^2 t) \tag{7.6}$$

The temperature transition at the droplet's center is of particular interest, because a great number of experiments used a suspended droplet approach for measurements. In addition, the thermophysical properties of the pure water, ice, sucrose, and sucrose aqueous solution are listed in Table 8.4. It is noted that the method of weighted averaging is applied for the aqueous solution based on the weighted concentration of sucrose, C (w.t.%).

Heterogeneous nucleation

The solid phase in a liquid droplet starts with an ice embryo seen as a cluster of ice molecules. The process of forming a new phase is broadly defined as "nucleation", regardless of the type of phase transformation. Theoretical analysis of nucleation dates back to the 1920s, when Max Volmer (a German physical chemist) studied the reason behind the undercooling behavior of liquids [57]. Volmer identified an energy barrier that the new phase has to overcome for its formation in the bulk phase. The new phase (here, the ice embryo) is less stable than the bulk phase due to the surface tension. As a result, the change in free energy

ΔG is expressed as

$$\Delta G = \underbrace{-\frac{4\pi r^3}{3}\Delta G_V}_{\text{formation of the new phase}} + \underbrace{2\pi r^2\sigma}_{\text{surface tension}} \tag{7.7}$$

where the first term is the decreasing free energy due to the formation of the new phase. The second term is to quantify the free energy caused by the surface tension, and σ is the (interfacial) surface tension per unit length. The subscript V is denoted as the volumetric or bulk phase. A critical radius r^* exists based on Eq. (7.7), providing the maximum change in the free energy (denoted as ΔG^*). This is the free-energy barrier that the new phase has to overcome. Moreover, the new phase is assumed to be spherical with a radius r, and the isolated-sphere assumption is known as the "*Volmer-Weber model*" that originates the classical nucleation theory [10].

The classical nucleation theory (CNT) considers a sharp interface between the new (solid) phase consisting of a cluster of ice molecules and the bulk liquid, and the kinetic process of the nucleating particles is governed by the macroscopic principles [9]. Owing to the CNT, the nucleation rate is quantified by an Arrhenius equation

$$J = J_0 \exp\left(- \frac{\Delta G^* \varphi_{het}}{k_B T_\ell}\right) \tag{7.8}$$

where the prefactor J_0 is proportional to the number of ice molecules (i.e., monomers) per unit volume of the liquid phase from which the nucleating cluster is form. The exponential factor, on the other hand, measures the chance of reaching the (homogeneous) free-energy barrier ΔG^* with the critical radius of R^*. k_B is the Boltzmann constant; φ_{het} is the heterogeneous factor that corrects the homogeneous energy barrier ΔG^* using the contact angle. Specifically, the prefactor J_0 is calculated by

$$J_0 = n_\ell Z f \tag{7.9}$$

where n_ℓ is the number density of molecules in the bulk liquid. Z is the Zeldovich factor expressed as [55]

$$Z = \underbrace{\frac{\sqrt{A\sigma/(\pi k_B T_\ell)}}{3i^{*2/3}}}_{\text{homogeneous part}} \times \underbrace{\sqrt{\frac{4}{2+\zeta_{het}}}}_{\text{heterogeneous correction}} \tag{7.10}$$

where the heterogeneous factor ζ_{het} is given by

$$\zeta_{het} = \frac{(1 - Xm)[2 - 4Xm - (X^2m^2 - 3)]}{(1 - 2Xm + X^2)^{3/2}} \tag{7.11}$$

X is the radius ratio of the nucleating particle (or the droplet) R over critical nucleus R^*; $m = \cos\theta$ based on Young's equation, where θ is the contact angle between the nucleating cluster and the surface of the pre-existing (liquid) phase. The attachment rate of liquid molecules to a critical nucleus with the size i^* is denoted as f; that is,

$$f = Ai^{*2/3} n_\ell^{4/3} D_\ell \tag{7.12}$$

where A and D_ℓ are the surface area and self-diffusivity of the liquid phase. In addition, the energy barrier for nucleating an ice embryo from the bulk liquid in Eq. (7.7) at the critical radius R^* can be rearranged into [39]

$$\Delta G^* = \frac{16\pi\sigma^3 {v_{m,s}}^2}{3(k_B T_\ell \ln S)^2} \tag{7.13}$$

where S is the saturation ratio with respect to the ice (solid phase); that is, $S = P_\ell/P_s$, where P is the saturation vapor pressure [40]. Moreover, the heterogeneous factor that considers the reduction of ΔG^* due to the foreign surface is written as [39]

$$\varphi_{het} = \frac{(2+m)(1-m)^2}{4} \tag{7.14}$$

The chemical and physical properties mentioned above are listed in Table 7.2 for predicting the solidification of a sucrose aqueous droplet. It is worth mentioning that the saturation ra-

Table 7.2: A list of physical and microscopic properties during nucleation.

Property	Value	Note/Ref.
Molar mass of water, M_{water} ($\mathrm{kg \cdot mol^{-1}}$)	18.02×10^{-3}	[37]
Avogadro's number, N_A ($\mathrm{mol^{-1}}$)	6.022×10^{23}	[37]
Boltzmann's constant, k_B ($\mathrm{J \cdot K^{-1}}$)	1.3806×10^{-23}	[37]
Saturation vapor pressure of water, P_{water} (Pa)	$610.94 \times \exp\{[17.625(T-273.15)]/(T-30.11)\}$	[5]
Saturation vapor pressure of ice, P_{ice} (Pa)	$611.21 \times \exp\{[22.587(T-273.15)]/(T+0.71)\}$	[5]
Self diffusivity of sucrose, $D_{sucrose}$ ($\mathrm{m^2 \cdot s^{-1}}$)	$3.367 \times 10^{-13}T^2 - 1.544 \times 10^{-10}T + 1.781 \times 10^{-8}$	fitted from [62]

tio S remains the same for the phase change of ice-water and sucrose aqueous solution. Generally, the saturation pressure of the mixture can be calculated by $P_{mixture} = \chi_{solvent} P_{solvent}$ by Raoult's law [37], where χ is the mole fraction. Since the mole fractions of water and ice are approximately the same, the saturation ratios of pure ice-water and aqueous solution stay unchanged.

After calculating the rate of heterogeneous nucleation J, it is essential to determine when the nucleation will occur, namely the nucleation criterion. Thus far, two forms of the nucleation criterion have been commonly used in the literature: one is to quantify the number of critical nuclei, and another is to evaluate the cumulative probability of nucleation. First, the number of critical nuclei N_v is expressed as [53, 2, 59]

$$N_v = \int_{\widetilde{t}=0}^{t} \left[V_0 - V^*(\widetilde{t}) \right] J(\widetilde{t}) \mathrm{d}\widetilde{t} \tag{7.15}$$

where V_0, V^* are the initial droplet's volume and the volume of the critical nucleus with the radius r^*, respectively. At certain combinations of the cooling rate and the droplet size, the nucleation occurs when N_v reaches 1. On the other hand, a more general criterion is to determine the cumulative probability P_n [47, 48, 44]; that is,

$$P_n = 1 - \exp\left(-\frac{1}{\beta} \int_{\widetilde{T}=T_f}^{T} J(\widetilde{T}) \mathrm{d}\widetilde{T} \right) \tag{7.16}$$

where β is the cooling rate. It is noted that this form of P_n assumes a statistically inhomogeneous Poisson process; other statistical assumptions could also be applied, such as homogeneous Poisson, homogeneous non-Poisson, and pair-correlation [47]. In this study, the nucleation criterion using the cumulative probability given in Eq. (7.16) is utilized since the cooling rate can be incorporated without any limitation.

Recalescence

The recalescence stage is referred to as the time when the ice crystal or dendrite propagates from its nucleus form to the entire domain. From the thermal aspect, the temperature rises from the nucleation temperature T_{nuc} to the freezing point T_f. Since the freezing point changes with the solute concentration in a binary mixture, it implies the point at its initial concentration, i.e., C_0. To capture the recalescence stage, a direct approach is first to calculate the crystal growth velocity v and then find the recalescence time by $\Delta t_{rec} = R/v$. It is noted that this growth velocity (also known as the tip velocity) is assumed to be constant for simplicity.

While the tip velocity has been proven to be a power-type function of supercooling or undercooling degree for pure substances (such as in ice-water phase change [2, 44]), the velocity for binary mixtures also requires the consideration of solute concentration. In this study, the dendritic growth velocity is expressed as

$$v = p_1 \times \left(\frac{\Delta T_{supercool}}{\mu_s} \right)^{p_2} \tag{7.17}$$

where p_1, p_2 are constants listed in Table 7.3, and μ_s is the dynamic viscosity of the crystal or solid phase. The dynamic viscosity has dependencies on both the temperature and concentration; in the case of sucrose aqueous droplets, it can be found by Génotelle's equation [31, 34]

$$\log \left(\frac{\mu_s}{\mu^*} \right) = a_1 + a_2 \chi_{sucrose} \Phi (b_1 + b_2 \chi_{sucrose}^n) \tag{7.18}$$

where a_1, a_2, b_1, b_2, n are constants and Φ is the reduced temperature summarized in Table 7.3. μ^* is the reference viscosity with the value of 10^{-3} $(\mathrm{Pa} \cdot \mathrm{s})$. $\chi_{sucrose}$ is the mole fraction

Table 7.3: A list of properties and constants during recalescence.

Property/Constant	Value	Note/Ref.
p_1; p_2	1.468×10^{-10}; 2.186	Fitted in Fig. 7.3
a_1; a_2; b_1; b_2; n	-0.1245; 22.452; 1.095; 46.39; 1.303	[31]
Reference kinetic viscosity, μ^* (Pa $\cdot$ s)	10^{-3}	[31]
Reduced temperature, Φ $(-)$	$(303.15 - T)/(T - 182.15)$	[31]
Molar mass of sucrose, $M_{sucrose}$ (kg $\cdot$ mol^{-1})	342.3×10^{-3}	[34]

calculated by the ratio of the amount of sucrose in moles ($n_{sucrose}$) over the total amount of sucrose and water in moles (n_{total})

$$\chi_{sucrose} = \frac{n_{sucrose}}{n_{total}} = \frac{C_0/M_{sucrose}}{C_0/M_{sucrose} + (1 - C_0)/M_{water}} \tag{7.19}$$

where M is the molar mass and the initial solute concentration C_0 is assumed to be in the crystal during recalescence.

In this study, several experimental datasets on the tip velocity of sucrose aqueous solution are selected and then correlated using the power-type expression shown in Eq. (7.17). The selection of experimental data is restricted to the studies which indicated the quantities of the crystal growth velocity, solute concentration, and supercooling degree, albeit many more experiments are available in the literature. This is because $v, C_0, \Delta T_{supercool}$ are of the utmost importance for the crystal growth model. Figure 7.3 demonstrates the influence of the growth rate over $\Delta T_{supercool}/\mu_s$ for the sucrose aqueous solutions. Four experimental studies [52, 32, 38, 25] are chosen at various solute concentrations ($5.6 - 80.3\%$) and supercooling degrees ($5 - 13.5$K), which in turn indicates the validity range of the developed model. It is found that the crystal growth velocity can be predicted using Eq. (7.17), where the constants are calibrated as $p_1 = 1.468 \times 10^{-10}$ and $p_2 = 2.186$ with an R-squared (or the coefficient of determination) of 0.9828.

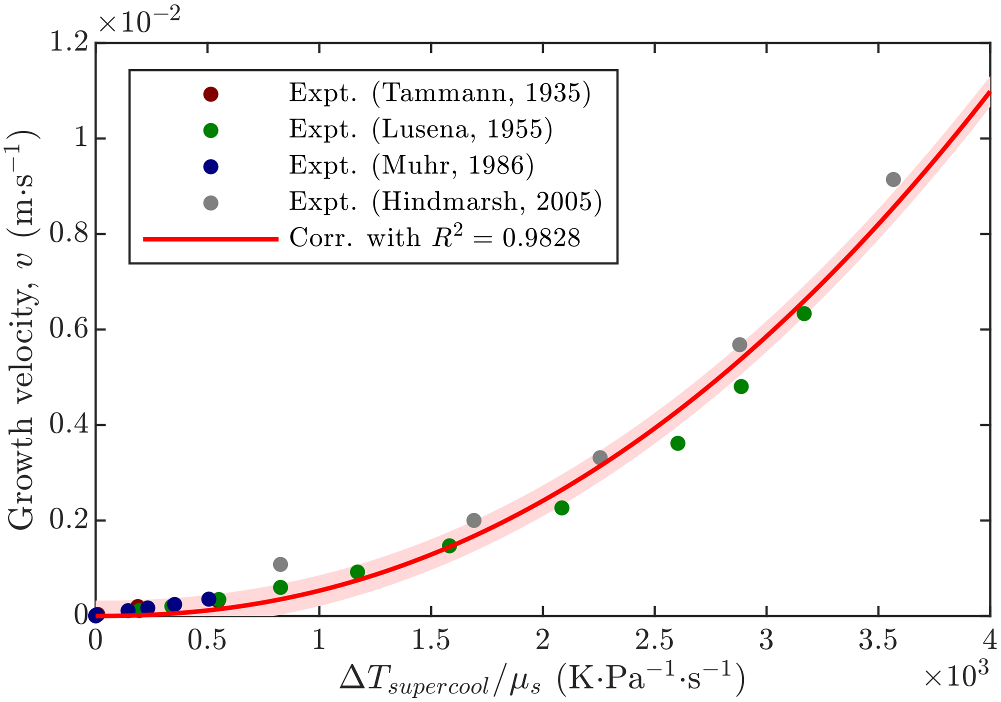

Figure 7.3: A graph of the crystal growth velocity v over $\Delta T_{supercool}/\mu_s$ for sucrose aqueous droplets. Both experimental data (in dots) and the correlation (in the line) are plotted.

Equilibrium freezing

The overall heat balance for the freezing and subcooling stages considers the latent heat in the solid phase and the total heat transfer rate

$$L_{eff}\frac{\mathrm{d}m_s}{\mathrm{d}t} = q_{total} \tag{7.20}$$

where L_{eff} is the effective latent heat that takes into account the supercooling degree [51, 3]

$$L_{eff} = \left(1 - \frac{c_{p,\ell}}{c_{p,s}}\mathrm{Ste}_{nuc}\right)L \tag{7.21}$$

Ste_{nuc} is the local Stefan number based on the supercooling degree; that is, $\mathrm{Ste}_{nuc} = c_{p,s}(T_f - T_{nuc})/L$. m_s is the mass of the solid phase that can be calculated as $m_s = m_{total}f_s$, where m_{total}, f_s are the total mass of the droplet and solid volume fraction, respectively. Since the mass is conserved (i.e., $\mathrm{d}m/\mathrm{d}t = 0$), the droplet's mass can be found by its initial state with

$m_{total} = 4/3\pi R^3 \rho_\ell$. For the right-hand side of the heat balance, the total heat transfer rate q_{total} sums up the heat transfers due to convection, mass transfer, radiation, and heat loss from the thermocouple during measurements

$$q_{total} = q_c + q_m + q_r + q_{tc} = h_{eq} A (T - T_\infty) \tag{7.22}$$

The subscripts c, m, r, tc represent convection from the surrounding air, mass transfer, radiation, and heat loss from the thermocouple, respectively. h_{eq} is the equivalent heat transfer rate that unified all the heat transfer rates. Each local heat transfer rate per unit area is calculated as

$$\begin{aligned} \dot{q}_c &= \frac{q_c}{A} = h_c (T - T_\infty) \\ \dot{q}_m &= \frac{q_m}{A} = L_{eff} h_m (a_w \rho_{v/d,s} - \rho_{v/a}) \\ \dot{q}_r &= \frac{q_r}{A} = \varepsilon \sigma_{sb} (T^4 - {T_\infty}^4) \end{aligned} \tag{7.23}$$

where $a_w, \rho_{v/d,s}, \rho_{v/a}, \varepsilon, \sigma_{sb}$ are the water activity, mass density for the vapor-droplet in the solid state, emissivity, and Stefan–Boltzmann constant, respectively. The local heat transfer coefficients h_c and h_m are given by the empirical correlations from the Nussult and Sherwood numbers [6]

$$\begin{aligned} \mathrm{Nu} &= \frac{2Rh_c}{k_a} = 2 + 0.6\mathrm{Re}^{\frac{1}{2}}\mathrm{Pr}^{\frac{1}{3}} \\ \mathrm{Sh} &= \frac{2Rh_m}{D_{v/a}} = 2 + 0.6\mathrm{Re}^{\frac{1}{2}}\mathrm{Sc}^{\frac{1}{3}} \end{aligned} \tag{7.24}$$

where $\mathrm{Re}, \mathrm{Pr}, \mathrm{Sc}$ are the Reynolds, Prandtl, and Schmidt numbers expressed as

$$\mathrm{Re} = \frac{2R\rho_a v_a}{\mu_a}, \ \mathrm{Pr} = \frac{\mu_a}{\rho_a \alpha_a}, \ \mathrm{Sc} = \frac{\mu_a}{\rho_a D_{v/a}} \tag{7.25}$$

$\mu_a, \alpha_a, D_{v/a}$ are the air viscosity, thermal diffusivity of the air, and vapor-air diffusivity, respectively.

To couple the solid volume fraction f_s with the mass diffusion (i.e., sucrose concentration C), Scheil equation is employed

$$\frac{C_\ell}{C_0} = \frac{1}{(1 - f_s)^{(1-k_e^*)}} \tag{7.26}$$

where C_ℓ, C_0 are the sucrose concentration at the liquid phase and initial state. k_e^* is the equilibrium partition coefficient calculated by the sucrose concentration's ratio of solid over liquid phases at equilibrium, i.e., C_s^*/C_ℓ^*. Since sucrose is nearly insoluble in ice, $C_s^* \approx 0$ leads to $k_e^* = 0$ for sucrose aqueous solution. It is noted that the Scheil equation assumes no concentration gradient in the liquid phase, and the solidification is at its equilibrium condition. Moreover, since the coupling method requires the relationship between the freezing point and concentration, it is essential to introduce the freezing point depression (FPD); that is, the difference in temperature between the mixture's freezing point T_f and water's freezing point 273.15 (K). In the case of sucrose aqueous solution, the following correlation is employed based on the experimental data [30]

$$FPD = 33.744{C_\ell}^3 - 0.8979{C_\ell}^2 + 6.0822C_\ell \tag{7.27}$$

which is valid for 0.5w.t.% $\leq C_\ell \leq$ 40w.t.% [22].

Solid subcooling

For solidifying pure substances (e.g., a pure water droplet), the solid subcooling stage starts when the entire material is frozen [26, 2]. However, it is different when freezing binary mixtures. The solute's presence results in some solutes being trapped in the liquid phase due to the insolubility with the ice, which makes it impossible for the material to fully transform into a solid. In other words, the solid volume fraction f_s can never reach 1. Therefore, the subcooling criterion for freezing a water droplet cannot be used for freezing an aqueous sucrose droplet. An alternative method is to evaluate the criterion based on the temperature; that is, if the droplet's temperature reaches the surrounding air temperature T_∞, then the equilibrium freezing ends, and the solid subcooling stage begins. This allows the calculation of the previous equilibrium freezing stage continues because the droplet's temperature will no longer be changed after T_∞. So do the solute concentration in the liquid phase C_ℓ and solid volume fraction f_s. The maximum values for C_ℓ and f_s are obtained in the solid subcooling, namely $C_{\ell,max}$ and $f_{s,max}$, respectively. It is noted that $C_{\ell,max}$ in this case is equivalent to the maximal freeze-concentrated solution $C_{g,max}$ mentioned in the phase diagram (Fig. 7.2).

Computation

The multi-stage solidification model for freezing a droplet filled with a binary mixture has different formulations and methods at each stage. It is therefore vital to compute them logically and effectively. In this sub-section, a concise computation process of the multi-stage model is listed as follows.

i) The *liquid supercooling* stage is computed based on the analytical solution (that is exact), as expressed in Eq. (7.5) for a general location r or Eq. (7.6) at the droplet's center $r = 0$.

ii) The *heterogeneous nucleation* stage first calculates the nucleation rate J in Eq. (7.9) and then find the cumulative probability P_n in Eq. (7.16) using the the trapezoidal rule. The numerical approximation of the integral is given by

$$\int_{\widetilde{T}=T_f}^{T} J(\widetilde{T})\mathrm{d}\widetilde{T} \approx \frac{\Delta\widetilde{T}}{2}\sum_{n=1}^{N}\left[J(\widetilde{T}_{n-1}) + J(\widetilde{T}_n)\right] \tag{7.28}$$

where N is the total number of discretized element and $\Delta\widetilde{T} = (T - T_f)/N$. At $P_n = 1$, the time and temperature are at their nucleation, i.e., t_{nuc} and T_{nuc}.

iii) The *equilibrium freezing* stage is solved in an iterative fashion, where the solid volume

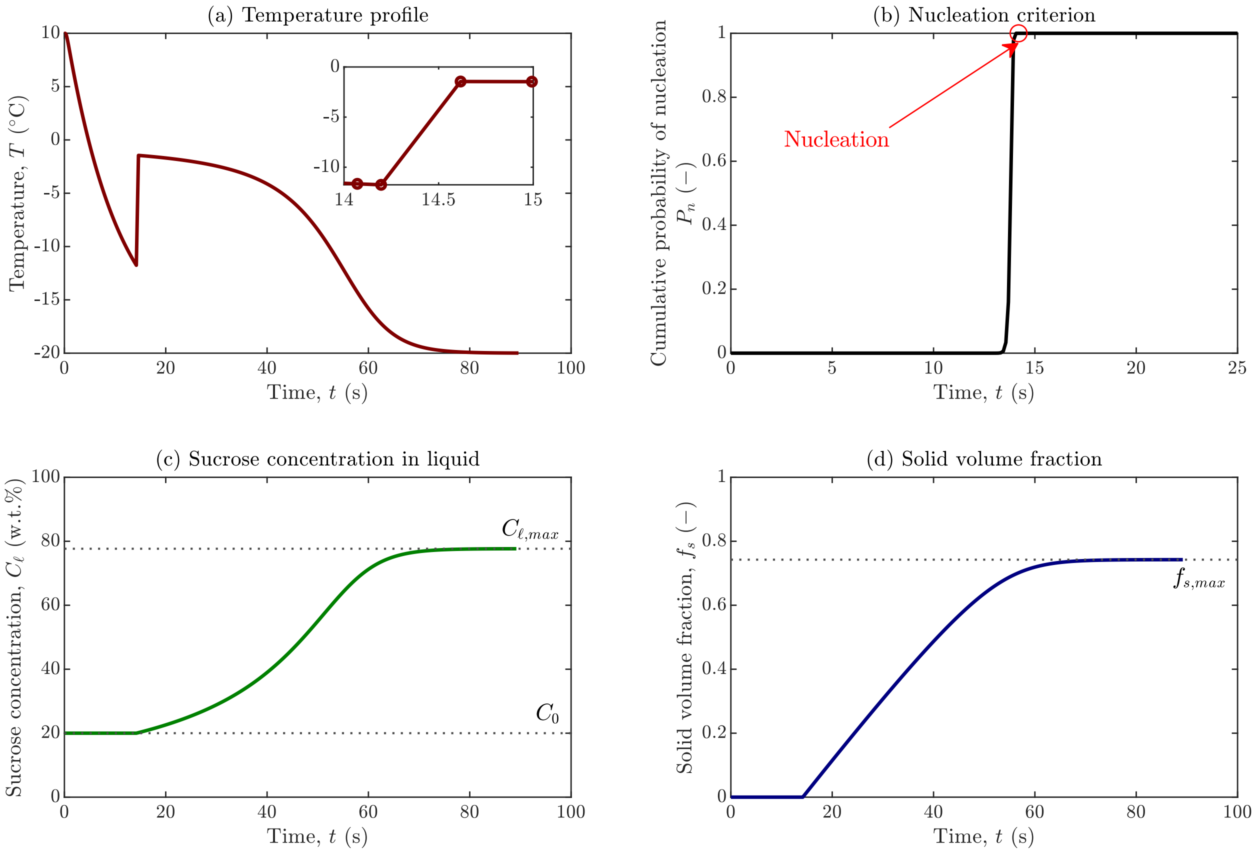

Figure 7.4: A hypothetical example of solidifying a sucrose aqueous droplet under the following condition $R = 0.75$ (mm), $C_0 = 20$ w.t.%, $T_{init} = 10$ (°C), $T_\infty = -20$ (°C), $h_{eq} = 100$ (W m^{-2} K^{-1}), $\beta = 20$ (°C s^{-1}), $\sigma_0 = 0.025$ (J m^{-2}), $\theta = 70$ (°).

fraction at the i-th time step is given by

$$f_s^i = f_s^{i-1} + {q_{total}}^{i-1} \frac{t^i - t^{i-1}}{L_{eff} m_{total}} \tag{7.29}$$

Here, the superscript $i-1$ stands for the quantity at the previous time iteration.

iv) The *solid subcooling* stage continues the iteration of *equilibrium freezing*. It starts when the droplet's temperature reaches the surrounding air temperature, i.e., $T = T_\infty$.

7.2.2 Gradient-based optimization

The presented mathematical model for solidifying binary mixtures can capture the physics of phase change. However, this physics-based model is insufficient for the nucleation stage due to the spontaneous and random nature of nucleation. Recent experimental data have shown that the nucleation temperature of a water droplet can vary widely from −5°C to −20°C under the same cooling rate; it also continues to change as the droplet is surrounded by ultra-cold environments, e.g., $T_\infty = -140$°C [44]. Hence, the stochastic process of nucleation brings the motivation to incorporate a statistical model into the physics-based framework. Among all the microscopic variables in the heterogeneous nucleation model, most properties depend on the material itself (such as self-diffusivity, the number density of molecules, droplet size, and saturation pressure), which shall exclude from the statistical analysis. Nevertheless, the contact angle θ and interfacial tension σ could physically be different in each solidification process. Both of them contribute to the prefactor and exponential factor in the Arrenhenius equation (7.9) that defines the nucleation rate. Since a consistent experimental setup is usually applied when measuring the droplet's temperature (i.e., a thermocouple placed in the droplet's center), the contact angle between the nucleation site and pre-existing liquid phase remains constant. For this reason, an optimization method is established for the interfacial tension or energy σ in the nucleation model.

When considering ice-water phase change, the interfacial tension, σ (J m^{-2}), is given by [53, 36]

$$\sigma(T_\ell) = \sigma_0 + (T_\ell - 273.15) \times 10^{-4}, \tag{7.30}$$

where σ_0 is 0.025 (J m^{-2}) [8], and T_ℓ is the droplet's temperature governed by the liquid supercooling stage before nucleation in Kelvin. It is found that Eq. (7.30) does not change the nucleation temperature as significantly as the experimental data indicated in [44], especially when the air temperature is below −40 °C. To incorporate the effects of the surrounding temperature and solute concentration into the surface tension, a modified equation for solidifying binary mixtures is proposed as

$$\sigma(T_\ell, T_\infty, C_0) = \sigma_0(T_\infty, C_0) + (T_\ell - 273.15) \times 10^{-4} \tag{7.31}$$

where $\sigma_0(T_\infty, C_0)$ is a function with respect to the surrounding temperature T_∞ and intial solute concentration C_0.

The gradient-based optimization algorithm is structured as follows. First, let the $f_{nuc}(\sigma_0)$ be a function to find the nucleation temperature based on the aforementioned physics-based model; it includes both the calculation of the heterogenous nucleation rate (Eq. (7.9)) and the nucleation criterion to determine T_{nuc} and t_{nuc} using the cumulative probability

$$T_{nuc} := f_{nuc}(\sigma_0) \tag{7.32}$$

It is noted that σ bundles with the surrounding temperature and initial solute concentration. Other thermophysical properties and the droplet's temperature are also changed accordingly. Second, single-variable minimization has the form

$$\underset{\sigma_0}{\text{minimize}} \quad \left| f_{nuc}(\sigma_0) - {T_{nuc}}^{expt} \right| \quad \text{subject to} \quad T_\infty,\ C_0$$

where ${T_{nuc}}^{expt}$ is the nucleation temperature based on the experimental data. In this way, a set of optimized σ_0 is obtained by the optimization, and polynomial-based correlations can be found for each initial solute concentration C_0. In this study, the benchmark experimental data for ${T_{nuc}}^{expt}$ are taken from Sebastião et al. [44].

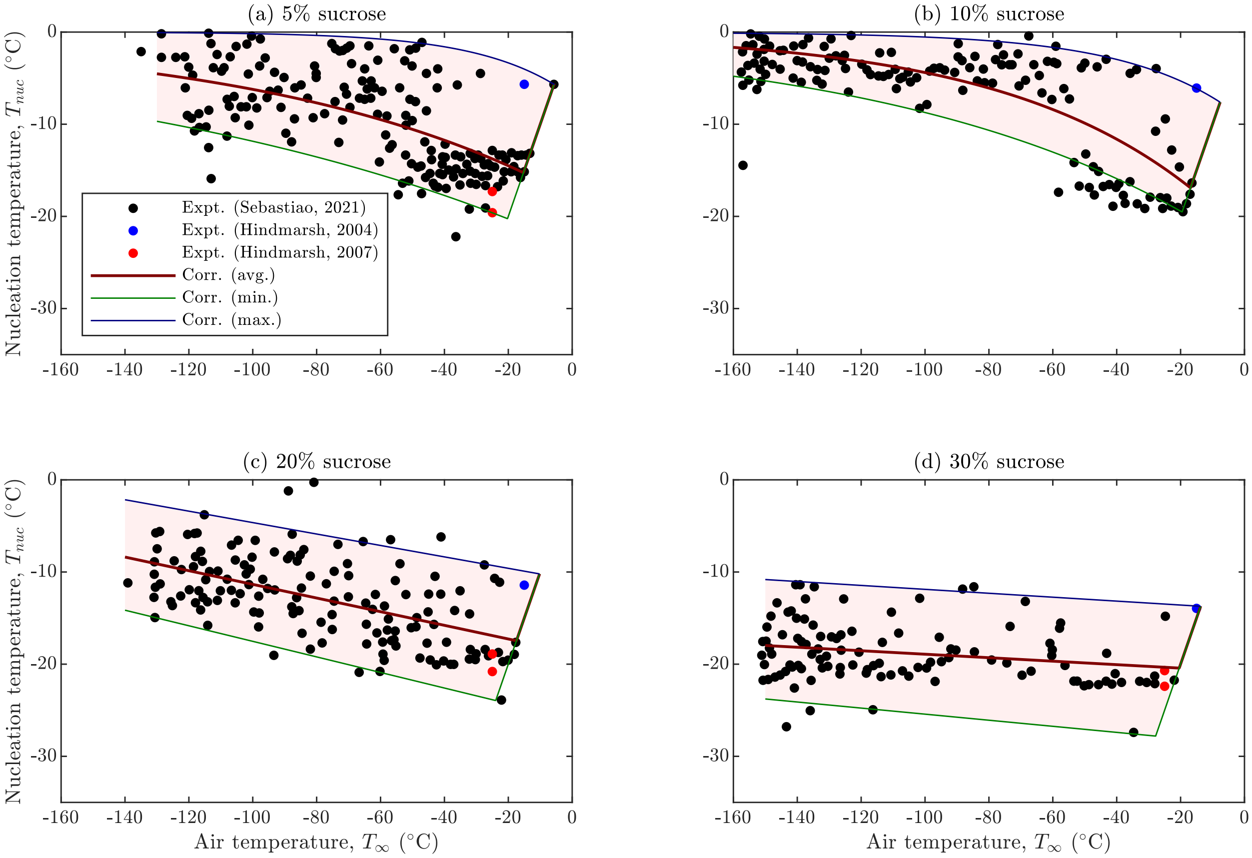

Figure 7.5: Influence of the air temperature T_∞ on the nucleation temperature T_{nuc} for various initial sucrose concentrations C_0: (a) 5%, (b) 10%, (c) 20%, and (d) 30%. Both experimental data (in dots) and correlations (in solid lines) are plotted.

7.3 Model validation

Figure 7.5 shows the influence of the air temperature over the nucleation temperature for various initial sucrose concentrations C_0, including (a) 5%, (b) 10%, (c) 20%, and (d) 30% sucrose droplets. In particular, three primary experimental data on these sucrose droplets are plotted [44, 22, 24]. Xu et al. [58] attempted to correlate Sebastião et al.'s data set [44] with an averaged polynomial fit. Since the nucleation temperatures are scattered over different air temperatures for all the sucrose droplets (reflecting the random nature of nucleation), a single correlation could not represent or predict nucleation. As a result, three correlations that cover the whole range of nucleation temperatures (i.e., maximum, minimum, and averaged) are proposed in Fig. 7.5. Generally, as the air temperature decreases, the nucleation tends to increase for all the sucrose concentrations. A colder environment implies a higher thermal gradient between the droplet's surface and the ambient air, thus triggering the ice embryo to form faster than usual. This is the primary reason why the nucleation temperature approaches 0°C in ultra-cold environments. In a warmer environment, on the other hand, the nucleation temperature also gets higher. This tendency is associated with the energy conservation that the nucleation temperature cannot be lower than the surroundings. Hence, this constraint is applied to the correlations is $T_{nuc} \not< T_\infty$. In addition, the initial concentration of sucrose is found to impact the relationship between T_{nuc} and T_∞. That is, the 30% sucrose aqueous droplets seem to have a more linear tendency when compared with the 5% droplets. The trend of pure water droplets is also noted to be more non-linear than any sucrose aqueous droplets [44, 58].

Figure 7.6 demonstrates the relationship of the air temperature on the surface tension coefficient σ_0 for the above-mentioned four initial concentrations of sucrose aqueous droplets. The surface tension coefficient is firstly optimized based on the three correlations of T_{nuc} over T_∞ through Eq. (7.2.2) as shown in dots in Fig. 7.6, and then the optimized values of σ_0 are correlated based on T_∞. Recall that the surface tension coefficient of ice-water phase change is 0.025 ($\mathrm{J \cdot m^{-2}}$) [8]; however, σ_0 varies from 0 to 0.025 ($\mathrm{J \cdot m^{-2}}$) in sucrose aqueous droplets over the range of $-160^\circ\mathrm{C} \leq T_\infty \leq -15^\circ\mathrm{C}$. It is interesting to observe that the linearity of the σ_0 correlation is consistent with the one for the nucleation temperature, which indicates a relatively linear relationship between the T_{nuc} and σ_0 on different T_∞. Meanwhile, the surface tension coefficient decreases with the decrease in the ambient air temperature. Though the decline in the surface energy at the solid-liquid interface results in a weaker nucleation rate, the significant temperature drop T_ℓ is more dominant for the probability nucleation, thereby leading to relatively immediate nucleation.

With an accurate range of the surface tension coefficient for various sucrose concentrations, the heterogeneous nucleation can be predicted systematically and reliably. It is

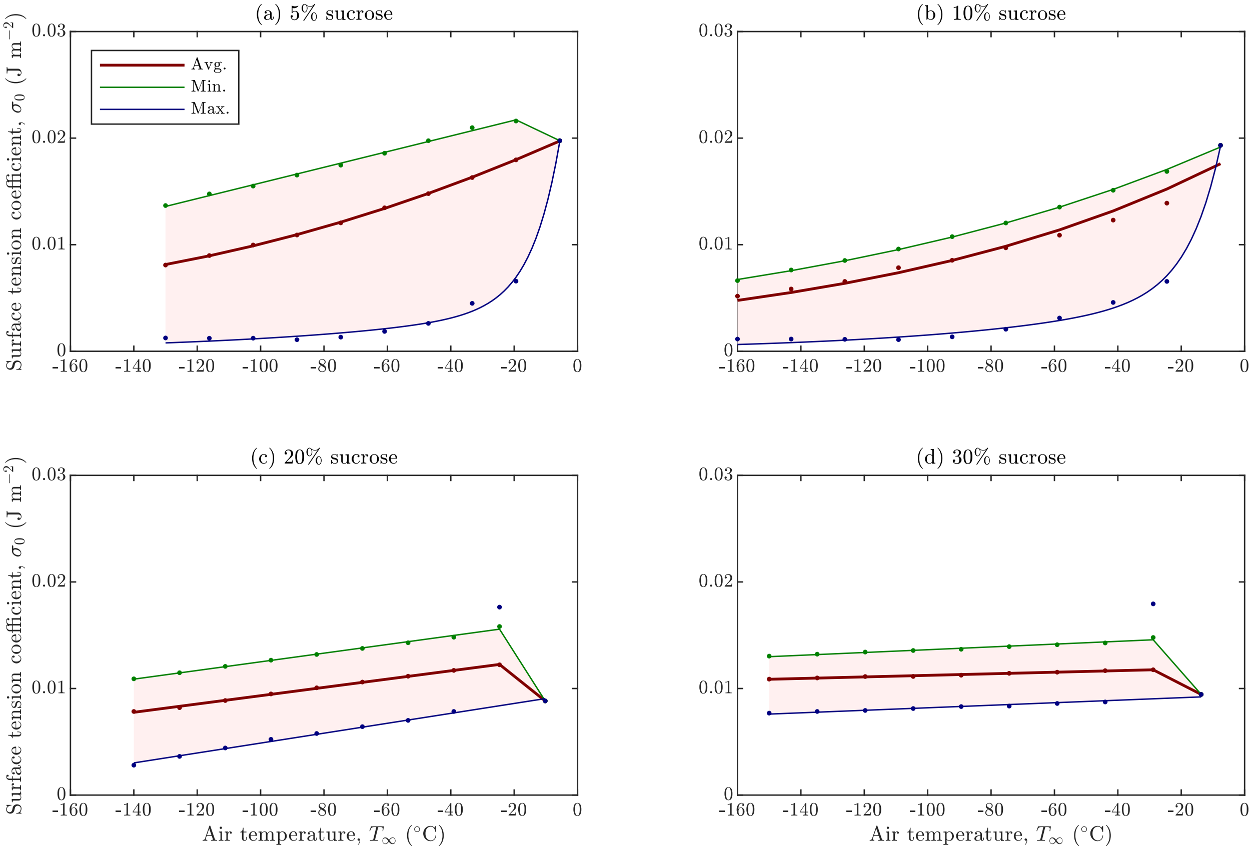

Figure 7.6: Influence of the air temperature T_∞ on the surface tension coefficient σ_0 for various initial sucrose concentrations C_0: (a) 5%, (b) 10%, (c) 20%, and (d) 30%. Both optimized results (in dots) and correlations (in solid lines) are plotted.

therefore important to apply the multi-stage solidification model coupled with optimization and validate against the experimental data. Hindmarsh et al. [22] measured the temperature transition of a suspended sucrose aqueous droplet for various initial concentrations. Figure 7.7 shows the comparison between the experimental (in red circles) and simulated results (in blue lines) at the above-mentioned four sucrose concentrations, particularly $C_0 = 5\%, 10\%, 20\%, 30\%$. It is noticed that these initial concentrations were not exact in the experiments because uncertainty exists during the preparation of the sucrose droplets [22]. Another indicator is the measured freezing point right after the recalescence stage, in which they are not matched with the universal correlation (expressed in Eq. (7.27)) when $C_\ell = C_0$. For this reason, a correction is firstly made based on the freezing point to find the actual C_0 using Eq. (7.27) at each scenario. After that, the temperature profile at the

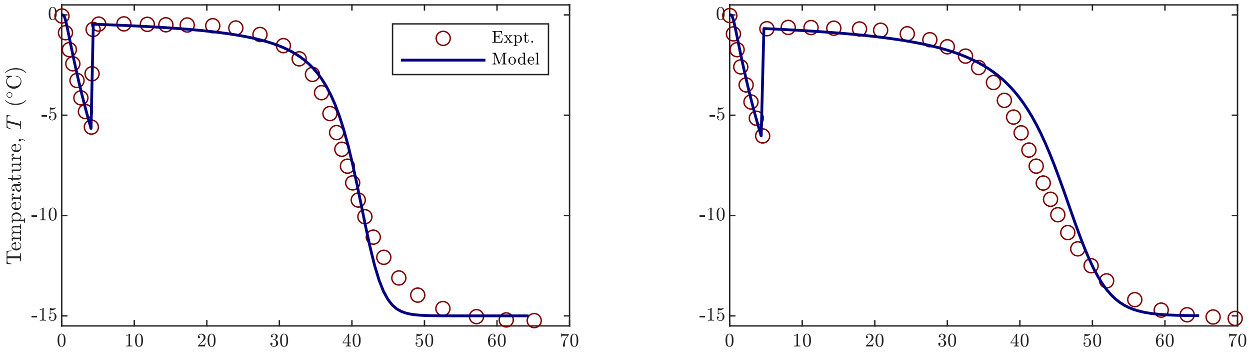

(a) 5% sucrose

(b) 10% sucrose

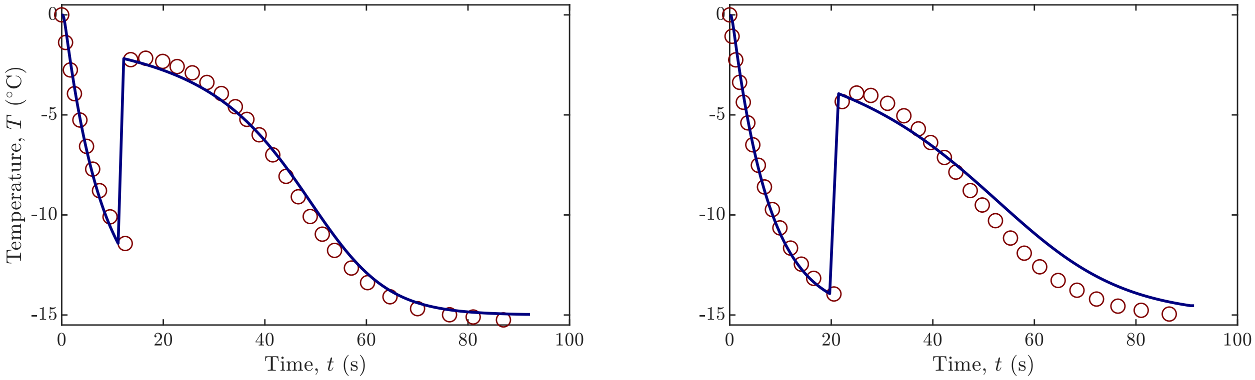

(c) 20% sucrose

(d) 30% sucrose

Figure 7.7: Comparisons of temperature profiles between the experimental (in circles) and modeling data (in the solid lines) for various initial sucrose concentrations C_0: (a) 5%, (b) 10%, (c) 20%, and (d) 30%.

droplet's center is predicated on the newly developed correlation on σ_0. As shown in Fig. 7.7, the simulated temperature at every solidification stage is well-validated against the experimental data. Specifically, the nucleation temperature was not taken as an a priori in the solidification framework, making it more versatile to be applied in predicting the thermal behavior of droplet solidification filled with binary mixtures. It is noted that the effect of initial concentrations will be discussed in the subsequent section.

7.4 Parametric studies

In this section, a few key parameters in the presented multi-stage solidification model are studied. First and foremost, the effect of initial concentration is investigated by continuing

(a) Temperature profile

(b) Probability of nucleation

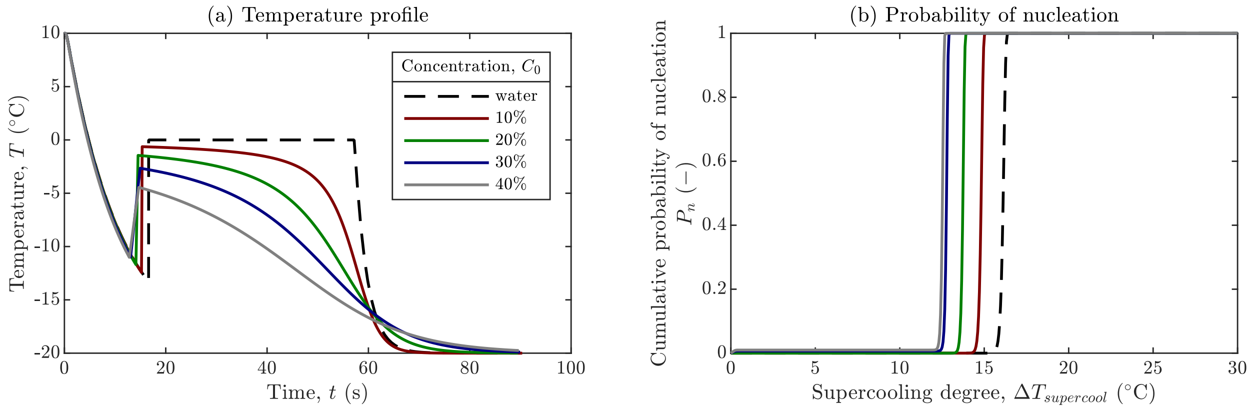

(c) Concentration in liquid

(d) Solid volume fraction

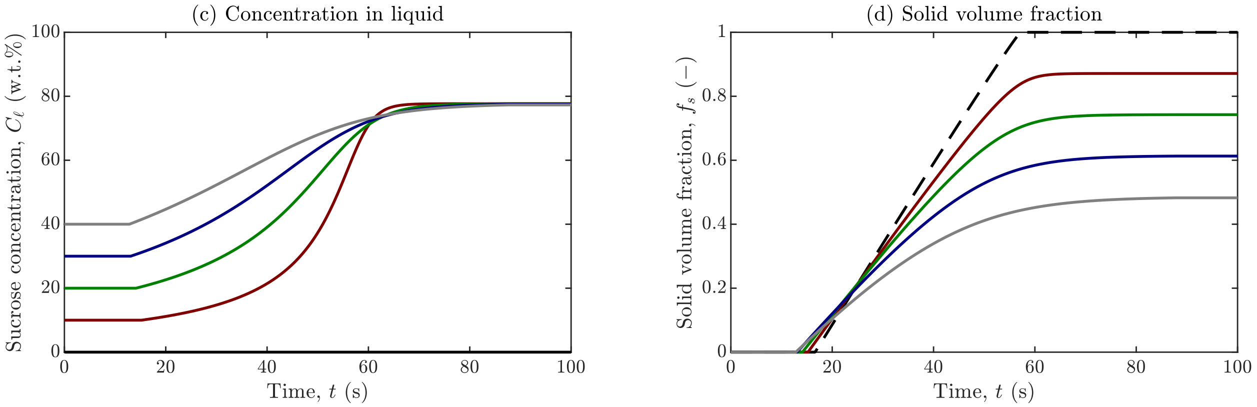

Figure 7.8: Effect of the sucrose aqueous droplet's initial concentration with respect to: (a) temperature profile, (b) cumulative probability over supercooling degree, (c) concentration in the liquid phase, and (d) solid volume fraction, under the condition of $R = 0.75$ mm and $\theta = 70°$. The solidification of water droplet (i.e., $C_0 = 0$ w.t.%) is also plotted in the dotted line as a reference using the model from [2].

the validated scenarios from Section 7.3. The sensitivity of the contact angle to the heterogeneous nucleation and the overall temperature transition is then analyzed. Lastly, various heat transfer coefficients and droplet sizes are evaluated, underlying their significance in spray freezing-related technologies.

7.4.1 Effect of solute concentration

Four different sucrose aqueous concentrations are displayed in Fig. 7.8, including 10%, 20%, 30%, and 40%. The case of freezing a pure water droplet is also graphed as a benchmark using the multi-stage solidification framework established by Akhtar et al. [2]. As shown in

Fig. 7.8(a), the temperature transitions of the liquid supercooling are consistent in all concentrations. However, each concentration indicates a different nucleation temperature/time (or supercooling degree) and recalescence time, making it further in the subsequent stages. Compared with the pure water droplet, the sucrose aqueous droplets (regardless of the concentration) have a smoother transition between the freezing and subcooling stages due to the freeze concentration and FPD. In other words, the temperature or freezing point declines as the concentration increases in the liquid during solidification. Since there is no change in concentration for the water droplet, the temperature remains at its fusion temperature. However, once the freezing is completed and the entire droplet is frozen, the sensible heat dominates the heat transfer at the subcooling stage. In addition, the nucleation is found to be different among the droplets, as can be observed in Fig. 7.8(b). The cumulative probability reaches one at various supercooling degrees $\Delta T_{supercool}$, resulting in different nucleation times under similar cooling environments. Specifically, a higher concentration gives rise to a lower supercooling degree. In the scenario of the water droplet, the supercooling degree is the highest, leading to the lowest nucleation temperature.

Figure 7.8(c) shows the sucrose concentration in the liquid phase C_ℓ over time t. It is clear to see that the concentration stays the same at its initial state before nucleation and begins to increase during phase change. This implies that the sucrose (as a solute) starts to diffuse after the nucleation occurs. The increase in the solute concentration stops at the end of phase change; that is, the droplet's temperature reaches the ambient air temperature. It is noted that the solute concentration will not exceed 100 w.t.% in the sucrose aqueous droplets, because there will always be a certain amount of sucrose traps in the solid phase, making it impossible to be transferred into the liquid. The maximum solute concentration $C_{\ell,max}$ is found to be the same (almost 80 w.t.%) for all the sucrose droplets. The value of the maximum point is also reflected by the temperature-composition phase diagram of sucrose given by Fig. 7.2. Moreover, the solid volume fraction f_s over time t is plotted in Fig. 7.8(d). The solid volume fraction has a similar tendency compared with the solute concentration.

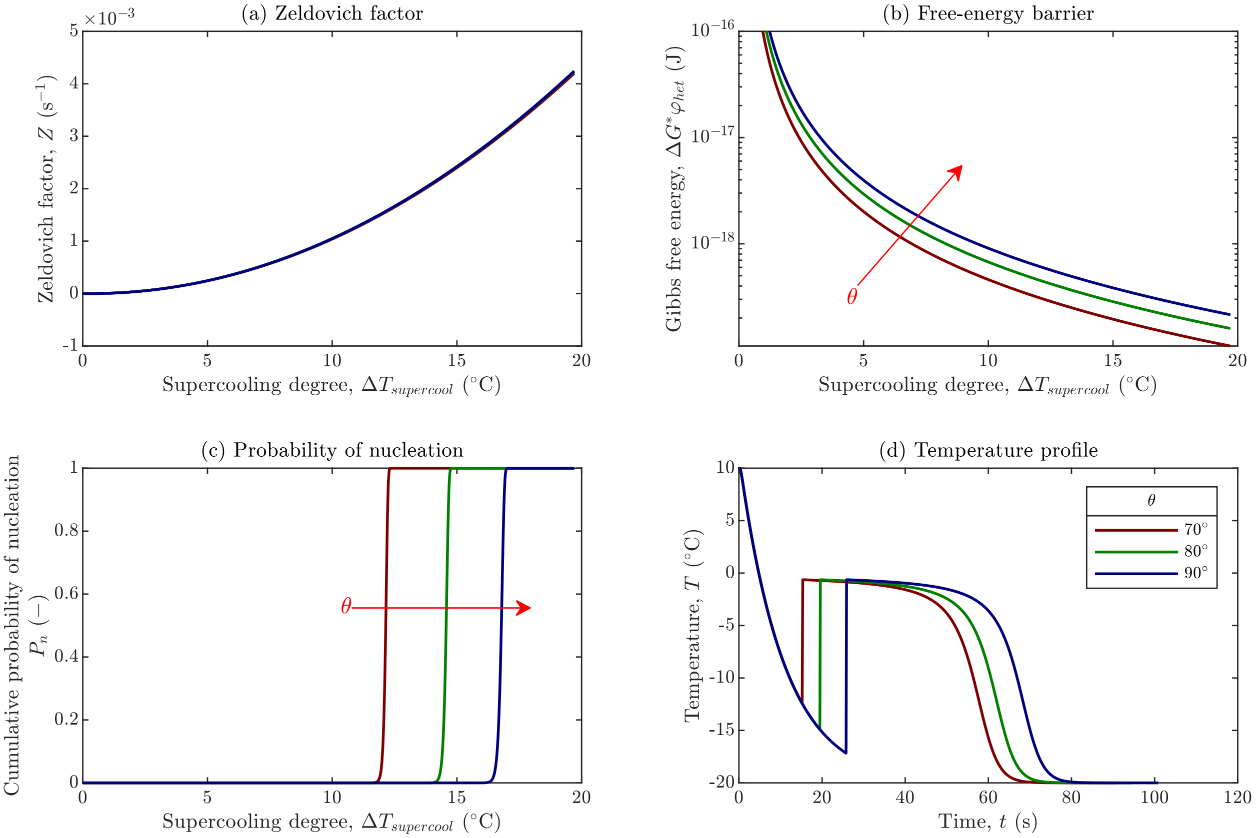

Figure 7.9: Effect of the contact angle during nucleation with respect to: (a) Zeldovich factor, (b) free-energy barrier, (c) cumulative probability over supercooling degree, and (d) temperature profile, under the condition of $R = 0.75$ mm and $C_0 = 20$ w.t.%.

It first remains unchanged before nucleation and then increases during the phase transition. Nevertheless, the solid volume fractions for different concentrations begin at 0, and their maximum values vary with the initial concentrations. This is because sucrose is insoluble in ice (i.e., $k_e^* = 0$) and it will be trapped in the liquid phase regardless the heat transfer between the droplet and the air. The initial amount of sucrose in the droplet, therefore, has a direct influence on the maximum ice content (also can be seen as $f_{s,max}$).

7.4.2 Effect of contact angle

When revisiting the influential factors in the heterogeneous nucleation (particularly, the nucleation rate $J(t)$ and probability of nucleation P_n), the interfacial tension σ and contact angle θ are the parameters that are independent of the thermophysical and/or chemical properties of the droplet. The quantitative study on the interfacial tension has been conducted through the gradient-based optimization in Sections 7.2.2 and 7.3, while respecting a consistent angle due to the experimental setup. In this sub-section, the effect of contact angle is investigated by fixing the other parameters, including the interfacial tension.

The nucleation rate $J(t)$ (as expressed in Eq. (7.8)) consists of the pre-factor and exponential factor, in which the contact angle appears in both parts. Specifically, the Zeldovich factor inside pre-factor (in Eq. 7.10) depends on the contact angle. Figure 7.9(a) shows the Zeldovich factor over supercooling degree for three contact angles: $\theta = 70°, 80°, 90°$. No significant difference among the contact angles is found in the Zeldovich factor. However, when evaluating the free-energy barrier $\Delta G^* \varphi_{het}$ in Fig. 7.9(b), the change is more intensive than the one for the Zeldovich factor. The Gibbs free energy is much higher as the contact angle increases. This implies that it requires more energy to surpass the barrier for larger contact angles, which in turn delays the time of nucleation. Moreover, Figure 7.9(c) graphs the cumulative probability of nucleation over supercooling degree. The probability is calculated from both the nucleation rate $J(t)$ and the cooling rate β, as expressed in Eq. (7.16). Under the same cooling rate, the probability of nucleation reaching 1 (i.e., the moment the nucleation occurs) happens at a higher $\Delta T_{supercool}$ for a larger contact angle. Hence, the nucleation temperature decreases with the increase of the contact angle. Lastly, the temperature profiles of the three contact angles are shown in Fig. 7.9(d). The rise of the contact angle postpones the nucleation time and reduces the nucleation temperature, which shifts the freezing curve during phase change. The total freezing time, therefore, becomes longer for a larger contact angle.

7.4.3 Effect of heat transfer coefficient

The heat transfer coefficient indicates the strength of the heat transfer toward the droplet's surface. This is particularly important for spray freezing-related applications because it cultivates the effect from the ambient air to the droplet. In this study, the equivalent heat

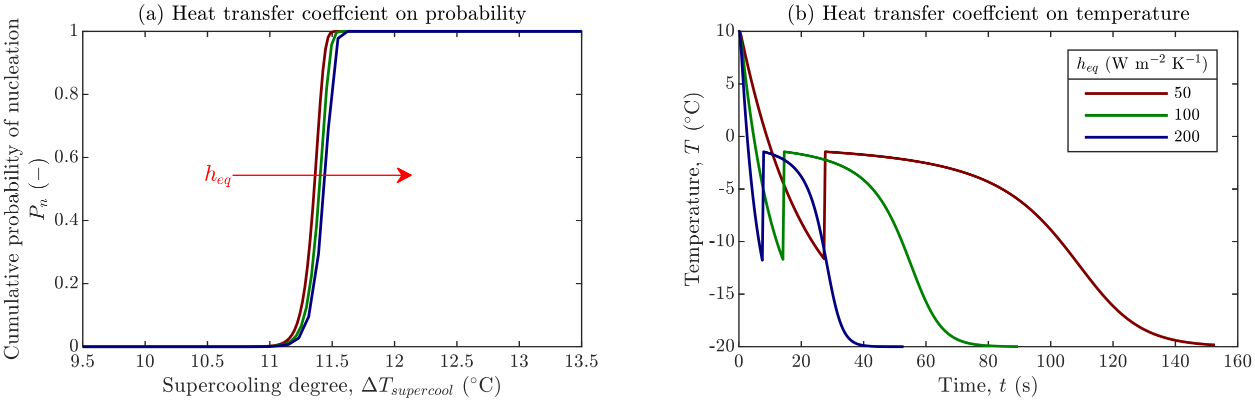

(a) Heat transfer coeffcient on probability

(b) Heat transfer coeffcient on temperature

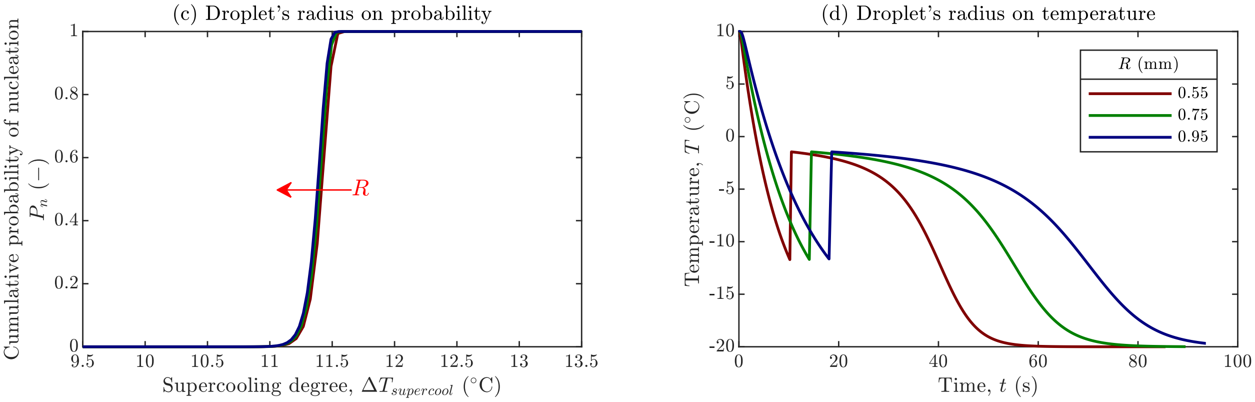

(c) Droplet's radius on probability

(d) Droplet's radius on temperature

Figure 7.10: Effect of the heat transfer coefficient (a,b) and droplet's radius (c,d) on the probability of nucleation and temperature, under the condition of $C_0 = 20$ w.t.% and $\theta = 70°$.

transfer coefficient h_{eq} considers the convection from the ambient air, mass transfer, radiation, and heat loss due to the thermocouple. Figure 7.10(a) demonstrates the probability of nucleation for three heat transfer coefficients: $h_{eq} = 50, 100, 200$ $(\mathrm{W} \cdot \mathrm{m}^{-2} \cdot \mathrm{K}^{-1})$. It can be seen that h_{eq} does not have a significant effect on the supercooling degree (and thus the nucleation temperature). This can be explained by the fact that the heat transfer coefficient, Though the heat transfer coefficient has a direct influence on the liquid temperature, it affects the nucleation rate (for both the pre-factor and exponential factor) to a minimal extent. However, the temperature gradient of the liquid varies greatly as can be observed in Fig. 7.10. The higher the heat transfer coefficient is, the faster the liquid cools down to its nucleation. Since the nucleation temperature does not change much, shorter nucleation times can be seen. In addition to the liquid temperature, the solid temperature will also drop faster for a higher h_{eq}, which implies a more rapid freezing point depression during the phase transition. This finding can be beneficial when requiring more ice production, such as ice slurry production using spray freezing [18]. Increasing the heat transfer coefficient (e.g., rising air velocity) can improve production without compensating energy for nucleation dynamics.

7.4.4 Effect of droplet size

Apart from the heat transfer coefficient, the droplet's volume is also a sensitive parameter, especially in a spray. In the spray, a wide range of droplet size distribution can be found depending on the spray's level; larger droplets are seen near the nozzle, while smaller ones are away from the nozzle. Figure 7.10(c,d) shows the probability of nucleation and temperature profiles for three droplet radii: $R = 0.55, 0.75, 0.95$ (mm). It is found that the supercooling degree does not change much within the three droplet sizes, but the freezing curves shift linearly. Particularly, a smaller droplet size has a shorter nucleation time but with a similar nucleation temperature. This finding can be applied in the same way as the heat transfer coefficient in order to satisfy specific freezing demands. For instance, if a system aims to produce more ice, then a smaller particle size distribution should be more preferable, which can be achieved by modifying the flow rate or spray nozzle. It is also noted that the conclusion here may not be drawn when the difference of droplet size is in orders of magnitude or in different spatial scales.

7.5 Conclusion

In conclusion, we presented a novel multi-stage mathematical framework coupled with the gradient-based optimization algorithm to predict the droplet solidification filled with the binary mixture, capable of considering the randomness of heterogeneous nucleation. Due to the spontaneous and random nature of nucleation, it is inevitable to experimentally observe multiple values of nucleation temperature under the same surrounding environment. Hence, it is necessary to model the range of nucleation temperatures rather than a single value. Our modeling results were first validated against experimental data in the literature and then performed parametric studies on various parameters in the model, including the solute concentration, contact angle, heat transfer coefficient, and droplet size. The main findings of this paper are summarized as follows.

i) The universal interfacial tension coefficient ($\sigma_0 = 0.025$ $(\mathrm{J} \cdot \mathrm{m}^{-2})$) cannot accurately predict nucleation for ultra-cold environments (esp., $< -60°\mathrm{C}$). Based on the gradient-based optimization method, σ_0 in sucrose aqueous droplets could vary from 0 to 0.025 $(\mathrm{J} \cdot \mathrm{m}^{-2})$ over the range of $-160°\mathrm{C} \leq T_\infty \leq -15°\mathrm{C}$.

ii) The solute concentration was seen to have a direct impact on the nucleation. The higher the solute concentration is, the lower the nucleation temperature will be.

iii) The contact angle was found to be rather sensitive to the nucleation temperature and time, especially the Gibbs free energy barrier in the nucleation rate. A higher contact angle leads to a higher energy barrier and thus less chance to activate nucleation (which implies a lower nucleation temperature).

iv) The heat transfer coefficient and droplet size did not affect the nucleation as significantly as the solute concentration and contact angle. Nevertheless, major differences were captured in terms of the temperature profile, particularly the rates of supercooling and freezing curves (that is, the transient temperature transitions for the liquid and solid phases).

It was recommended that future work could investigate the effect of the crystal growth rate in the binary solution droplets using empirical correlations or physics-based modeling, explore the formulations and methodologies to track the solid-liquid interface under both heat and mass transfer, and perform droplet solidification experiments on different solutes to understand the nucleation, freezing point depression, and freeze concentration on these droplets.

Appendix A. Derivation of the exact solution to a spherical heat conduction problem using the separation of variables

The PDE problem is given by

$$\begin{aligned}
\frac{\partial^2 T_\ell}{\partial r^2} + \frac{2}{r}\frac{\partial T_\ell}{\partial r} &= \frac{1}{\alpha_\ell}\frac{\partial T_\ell}{\partial t} \\
-k_\ell \frac{\partial T_\ell}{\partial r}\bigg|_{r=a} &= h_{eq}\Big[T_\ell(a,t) - T_\infty\Big] \\
\frac{\partial T_\ell}{\partial r}\bigg|_{r=0} &= 0 \\
T(r,0) &= T_{init}
\end{aligned} \tag{7.33}$$

First of all, a new temperature variable is introduced as $\widetilde{T}_\ell = r(T_\ell - T_\infty)$ to make the Robin boundary homogeneous and simplify the governing equation. Thus, the problem becomes

$$\begin{aligned}
\frac{\partial^2 \widetilde{T}_\ell}{\partial r^2} &= \frac{1}{\alpha_\ell}\frac{\partial \widetilde{T}_\ell}{\partial t} \\
\frac{\partial \widetilde{T}_\ell}{\partial r}\bigg|_{r=a} + \left(\frac{h_{eq}}{k_\ell} - \frac{1}{a}\right)\widetilde{T}_\ell(r=a,t) &= 0 \\
\widetilde{T}_\ell(r=0,t) &= 0 \\
\widetilde{T}_\ell(r,t=0) &= r(T_{init} - T_\infty)
\end{aligned} \tag{7.34}$$

It is then transformed into the problem in the text [21] on pages 194–197 and derived therein. Note that the insulated boundary at the droplet's center can be changed into a finite temperature condition when the singularity appears as $r = 0$; that is, $T(r \to 0, t) \Rightarrow$ finite.

After separating the new temperature variable into $R(r)$ and $\Gamma(t)$ as

$$\widetilde{T}(r,t) = R(r) \times \Gamma(t) \tag{7.35}$$

and substituting the boundary/initial conditions into it, the exact solution is given by

$$\widetilde{T}(r,t) = \sum_{n=1}^{\infty} C_n \sin(\lambda_n r) \exp(-\alpha_\ell \lambda_n^2 t) \tag{7.36}$$

The eigenvalues λ_n are determined by the following transcendental equation

$$\lambda_n \cot(\lambda_n a) = \frac{1}{a} - \frac{h_{eq}}{k_\ell} \tag{7.37}$$

while the corresponding eigencoefficients C_n are found by

$$C_n = \frac{\int_{r=0}^{a} r(T_{init} - T_\infty)\sin(\lambda_n r)dr}{\int_{r=0}^{a} \sin^2(\lambda_n r)dr} = (T_{init} - T_\infty) \times \frac{4[\lambda_n a \cos(\lambda_n a) - \sin(\lambda_n a)]}{\lambda_n[\sin(2\lambda_n a) - 2\lambda_n a]} \tag{7.38}$$

Nomenclature

Letters

T	Temperature (K)
t	Time (s)
P	Saturation pressure (Pa)
J	Nucleation rate ($\mathrm{m}^{-3}\ \mathrm{s}^{-1}$)
G	Gibbs free energy (J)
m	$\cos\theta$ ($-$)
D	Self-diffusion coefficient ($\mathrm{m}^2\ \mathrm{s}^{-1}$)
V	Volume (m^3)
R	Radius (m)
X	Ratio of radii with respect to the critical nucleus, R/R^* ($-$)
i	Dimensionless size ($-$)
Z	Zeldovich factor (s^{-1})
k_B	Boltzmann constant ($\mathrm{J\ K}^{-1}$)
n	Number density of molecules (m^{-3})

Greek symbols

σ	Interfacial tension ($\mathrm{J\ m}^{-2}$)
φ, ζ	Factors in nucleation ($-$)
θ	Contact angle (°)
μ_s	Dynamic viscosity of sucrose aqueous solution ($\mathrm{Pa \cdot s}$)
μ^*	Reference dynamic viscosity of water ($\mathrm{Pa \cdot s}$)

Superscripts and subscripts

$*$	Critical
s	Solid
ℓ	Liquid
het	Heterogeneous
m	Molecular or molar
V	Volumetric or bulk

Bibliography

[1] S. Akhtar, M. Xu, and A. Sasmito. Spray freezing for mine heating a statistical perspective. In *Mine Ventilation*, pages 357–365. CRC Press, 2021.

[2] S. Akhtar, M. Xu, and A. P. Sasmito. Development and validation of a semi-analytical framework for droplet freezing with heterogeneous nucleation and non-linear interface kinetics. *International Journal of Heat and Mass Transfer*, 166:120734, 2021.

[3] S. Akhtar, M. Xu, and A. P. Sasmito. Development and validation of an asymptotic solution for a two-phase stefan problem in a droplet subjected to convective boundary condition. *International Journal of Thermal Sciences*, 164:106923, 2021.

[4] S. Akhtar, M. Xu, and A. P. Sasmito. A novel crystal growth model with nonlinear interface kinetics and curvature effects: Sensitivity analysis and optimization. *Crystal Growth & Design*, 21(6):3251–3265, 2021.

[5] O. A. Alduchov and R. E. Eskridge. Improved magnus form approximation of saturation vapor pressure. *Journal of Applied Meteorology and Climatology*, 35(4):601–609, 1996.

[6] T. L. Bergman, T. L. Bergman, F. P. Incropera, D. P. Dewitt, and A. S. Lavine. *Fundamentals of heat and mass transfer.* John Wiley & Sons, 2011.

[7] L. Chun, M. Sha, Z. Naijun, L. Zhiqiang, and S. Wenjun. Real-time observation of the freezing stage of the mannitol solution using high-resolution optical microscopy. *International Journal of Thermal Sciences*, 188:108225, 2023.

[8] S. Coriell, S. Hardy, and R. Sekerka. A non-linear analysis of experiments on the morphological stability of ice cylinders freezing from aqueous solutions. *Journal of Crystal Growth*, 11(1):53–67, 1971.

[9] S. P. Das. *Statistical physics of liquids at freezing and beyond.* Cambridge University Press, 2011.

[10] P. Debenedetti. Metastable liquids princeton university press, 1997.

[11] A. Dehghani-Sanij, S. MacLachlan, G. Naterer, Y. Muzychka, R. Haynes, and V. Enjilela. Multistage cooling and freezing of a saline spherical water droplet. *International Journal of Thermal Sciences*, 147:106095, 2020.

[12] Y. Du, M. Zhang, A. S. Mujumdar, W. Liu, and C. Yang. Innovative applications of freeze-drying to produce compound formula instant foods: A review. *Drying Technology*, 40(13):2583–2597, 2022.

[13] M. C. Erickson and Y.-C. Hung. *Quality in frozen food.* Springer Science & Business Media, 2012.

[14] K. Fan, M. Zhang, and A. S. Mujumdar. Recent developments in high efficient freeze-drying of fruits and vegetables assisted by microwave: A review. *Critical Reviews in Food Science and Nutrition*, 59(8):1357–1366, 2019.

[15] T.-H. Fan, J.-Q. Li, B. Minatovicz, E. Soha, L. Sun, S. Patel, B. Chaudhuri, and R. Bogner. Phase-field modeling of freeze concentration of protein solutions. *Polymers*, 11(1):10, 2018.

[16] D. L. Feltham and J. Garside. Analytical and numerical solutions describing the inward solidification of a binary melt. *Chemical Engineering Science*, 56(7):2357–2370, 2001.

[17] D. Fisher and W. Kurz. Fundamentals of solidification. *Fundamentals of Solidification*, pages 1–316, 1998.

[18] Y. Gao, Y. Ning, C. Wu, M. Xu, S. Akhtar, A. S. Mujumdar, and A. P. Sasmito. Experimental investigation of producing ice slurry with water using opposed-nozzle impinging jet method. *Applied Thermal Engineering*, 219:119568, 2023.

[19] Y. Gao, Y. Ren, M. Xu, J. Liu, A. S. Mujumdar, and A. P. Sasmito. Influence of thermal cycling on stability and thermal conductivity of nanofluid ice slurry. *International Journal of Thermal Sciences*, 185:108113, 2023.

[20] D. W. Green and M. Z. Southard. *Perry's Chemical Engineers' Handbook.* McGraw-Hill Education, 2019.

[21] D. W. Hahn and M. N. Özisik. *Heat conduction.* John Wiley & Sons, 2012.

[22] J. Hindmarsh, A. Russell, and X. Chen. Experimental and numerical analysis of the temperature transition of a freezing food solution droplet. *Chemical Engineering Science*, 59(12):2503–2515, 2004.

[23] J. Hindmarsh, A. Russell, and X. Chen. Fundamentals of the spray freezing of foods—microstructure of frozen droplets. *Journal of Food Engineering*, 78(1):136–150, 2007.

[24] J. Hindmarsh, A. Russell, and X. Chen. Observation of the surface and volume nucleation phenomena in undercooled sucrose solution droplets. *The Journal of Physical Chemistry C*, 111(16):5977–5981, 2007.

[25] J. Hindmarsh, A. Russell, and X. D. Chen. Measuring dendritic growth in undercooled sucrose solution droplets. *Journal of Crystal Growth*, 285(1-2):236–248, 2005.

[26] J. P. Hindmarsh, A. B. Russell, and X. D. Chen. Experimental and numerical analysis of the temperature transition of a suspended freezing water droplet. *International Journal of Heat and Mass Transfer*, 46(7):1199–1213, 2003.

[27] E. Jakubowska and J. Lulek. The application of freeze-drying as a production method of drug nanocrystals and solid dispersions–a review. *Journal of Drug Delivery Science and Technology*, 62:102357, 2021.

[28] M.-H. Kim, H. Kim, K.-S. Lee, and D. R. Kim. Frosting characteristics on hydrophobic and superhydrophobic surfaces: A review. *Energy Conversion and Management*, 138:1–11, 2017.

[29] L. S. Lam, K. R. Sultana, K. Pope, and Y. Muzychka. Effect of thermal transport on solidification of salt and freshwater water droplets on marine surfaces. *International Journal of Heat and Mass Transfer*, 153:119452, 2020.

[30] D. R. Lide. Handbook of chemistry and physics, 1999.

[31] M. P. Longinotti and H. R. Corti. Viscosity of concentrated sucrose and trehalose aqueous solutions including the supercooled regime. *Journal of Physical and Chemical Reference Data*, 37(3):1503–1515, 2008.

[32] C. Lusena. Ice propagation in systems of biological interest. III. effect of solutes on nucleation and growth of ice crystals. *Archives of Biochemistry and Biophysics*, 57(2):277–284, 1955.

[33] D. A. Maccarthy and N. Fabre. Thermal conductivity of sucrose. *Food properties and computer-aided engineering of food processing systems*, pages 105–111, 1989.

[34] M. Mathlouthi and P. Reiser. *Sucrose: properties and applications*. Springer Science & Business Media, 1995.

[35] S. W. McCue, B. Wu, and J. M. Hill. Classical two-phase Stefan problem for spheres. *Proceedings of the Royal Society A: Mathematical, Physical and Engineering Sciences*, 464(2096):2055–2076, 2008.

[36] Z. Meng and P. Zhang. Dynamic propagation of ice-water phase front in a supercooled water droplet. *International Journal of Heat and Mass Transfer*, 152:119468, 2020.

[37] M. J. Moran, H. N. Shapiro, D. D. Boettner, and M. B. Bailey. *Fundamentals of Engineering Thermodynamics*. John Wiley & Sons, 2010.

[38] A. Muhr and J. Blanshard. Effect of polysaccharide stabilizers on the rate of growth of ice. *International Journal of Food Science & Technology*, 21(6):683–710, 1986.

[39] B. J. Murray, S. Broadley, T. Wilson, J. Atkinson, and R. Wills. Heterogeneous freezing of water droplets containing kaolinite particles. *Atmospheric Chemistry and Physics*, 11(9):4191–4207, 2011.

[40] B. J. Murray and E. J. Jensen. Homogeneous nucleation of amorphous solid water particles in the upper mesosphere. *Journal of atmospheric and solar-terrestrial physics*, 72(1):51–61, 2010.

[41] L. Oberli, D. Caruso, C. Hall, M. Fabretto, P. J. Murphy, and D. Evans. Condensation and freezing of droplets on superhydrophobic surfaces. *Advances in Colloid and Interface Science*, 210:47–57, 2014.

[42] F. B. Planella, C. P. Please, and R. A. Van Gorder. Extended Stefan problem for the solidification of binary alloys in a sphere. *European Journal of Applied Mathematics*, 32(2):242–279, 2021.

[43] Y. Roos and M. Karel. Amorphous state and delayed ice formation in sucrose solutions. *International Journal of Food Science & Technology*, 26(6):553–566, 1991.

[44] I. B. Sebastião, B. Bhatnagar, and S. Tchessalov. A kinetic model for spray-freezing of pharmaceuticals. *Journal of Pharmaceutical Sciences*, 110(5):2047–2062, 2021.

[45] I. B. Sebastião, B. Bhatnagar, S. Tchessalov, S. Ohtake, M. Plitzko, B. Luy, and A. Alexeenko. Bulk dynamic spray freeze-drying part 1: modeling of droplet cooling and phase change. *Journal of Pharmaceutical Sciences*, 108(6):2063–2074, 2019.

[46] I. B. Sebastião, B. Bhatnagar, S. Tchessalov, S. Ohtake, M. Plitzko, B. Luy, and A. Alexeenko. Bulk dynamic spray freeze-drying part 2: model-based parametric study for spray-freezing process characterization. *Journal of Pharmaceutical Sciences*, 108(6):2075–2085, 2019.

[47] R. Shaw, A. Kostinski, and M. L. Larsen. Towards quantifying droplet clustering in clouds. *Quarterly Journal of the Royal Meteorological Society: A journal of the atmospheric sciences, applied meteorology and physical oceanography*, 128(582):1043–1057, 2002.

[48] R. A. Shaw, A. J. Durant, and Y. Mi. Heterogeneous surface crystallization observed in undercooled water. *The Journal of Physical Chemistry B*, 109(20):9865–9868, 2005.

[49] K. Shi and X. Duan. Freezing delay of water droplets on metallic hydrophobic surfaces in a cold environment. *Applied Thermal Engineering*, 216:119131, 2022.

[50] J. Stachulak. Ventilation strategy and unique air conditioning at inco limited. *CIM Bulletin (Canadian Institute of Mining and Metallurgy);(Canada)*, 84(950), 1991.

[51] S. Tabakova, F. Feuillebois, and S. Radev. Freezing of a supercooled spherical droplet with mixed boundary conditions. *Proceedings of the Royal Society A: Mathematical, Physical and Engineering Sciences*, 466(2116):1117–1134, 2010.

[52] G. Tammann and A. Büchner. Die unterkühlungsfähigkeit des wassers und die lineare kristallisationsgeschwindigkeit des eises in wäßrigen lösungen. *Zeitschrift für anorganische und allgemeine Chemie*, 222(4):371–381, 1935.

[53] K. K. Tanaka and Y. Kimura. Theoretical analysis of crystallization by homogeneous nucleation of water droplets. *Physical Chemistry Chemical Physics*, 21(5):2410–2418, 2019.

[54] R. Van der Sman. Phase field simulations of ice crystal growth in sugar solutions. *International Journal of Heat and Mass Transfer*, 95:153–161, 2016.

[55] H. Vehkamäki, A. Määttänen, A. Lauri, I. Napari, and M. Kulmala. The heterogeneous zeldovich factor. *Atmospheric Chemistry and Physics*, 7(2):309–313, 2007.

[56] S. Vessot and J. Andrieu. A review on freeze drying of drugs with tert-butanol (tba)+ water systems: characteristics, advantages, drawbacks. *Drying Technology*, 30(4):377–385, 2012.

[57] M. Volmer and A. Weber. Keimbildung in übersättigten gebilden. *Zeitschrift für physikalische Chemie*, 119(1):277–301, 1926.

[58] M. Xu, S. Akhtar, and A. P. Sasmito. A heterogenous nucleation model for supercooled water and sucrose solution droplets under ultra-cold environments. In *ASME*

International Mechanical Engineering Congress and Exposition, volume 85673, page V011T11A068. American Society of Mechanical Engineers, 2021.

[59] M. Xu, Y. Gao, F. Fang, S. Akhtar, B. A. Chaedir, and A. P. Sasmito. Experimental and unified mathematical frameworks of water-ice phase change for cold thermal energy storage. *International Journal of Heat and Mass Transfer*, 187:122536, 2022.

[60] H. Zhang, Z. Jin, M. Jiao, and Z. Yang. Experimental investigation of the impact and freezing processes of a water droplet on different cold concave surfaces. *International Journal of Thermal Sciences*, 132:498–508, 2018.

[61] X. Zhang, X. Wu, and J. Min. Freezing and melting of a sessile water droplet on a horizontal cold plate. *Experimental Thermal and Fluid Science*, 88:1–7, 2017.

[62] B. Zobrist, V. Soonsin, B. P. Luo, U. K. Krieger, C. Marcolli, T. Peter, and T. Koop. Ultra-slow water diffusion in aqueous sucrose glasses. *Physical Chemistry Chemical Physics*, 13(8):3514–3526, 2011.

Chapter 8

Multi-scale analysis for solidification of phase change materials (PCMs): Experiments and modeling

Contents

Preface (Bridging Text)

Chapters 6 and 7 presented multi-stage frameworks for solidifying pure substances and mixtures during the non-equilibrium process. The multi-stage approach was based on a time-sequential method, which did not include spatial resolution. The effect of spatial scales could be particularly vital for understanding crystal morphology and nucleation sites, thus benefiting the design and optimization of applications involving non-equilibrium solidification. For mining applications, crystal characterization with spatiotemporal considerations could impact energy storage via phase change materials (PCMs) and the quality of ice production using spray freezing (SF).

In this chapter, non-equilibrium solidification was investigated from a multi-scale perspective, departing from the sequential multi-stage approach used in the previous two chapters. This multi-scale analysis facilitated a temporally and spatially coupled framework at macro-, meso-, and micro-scale levels while still capturing the five stages of solidification. Novel laboratory experiments and mathematical modeling were developed, with a particular focus on the characterization of crystal growth and morphology using state-of-the-art image analysis and phase field method. The phase field model was validated against the experimental observations via image analysis. The results clearly indicated a non-linear crystal growth rate with complex morphology in non-equilibrium solidification.

The outcome of this multi-scale analysis provided a useful guideline for designing PCMs for cold thermal energy storage, particularly coupling the PCM size and charging conditions. The spatial effect of crystal growth can influence the thermal performance of PCMs during meso-scale solidification. In addition, the crystal growth also affected the ice quality of SF, which is a key component of the ice stope production of mine heating and cooling. This framework offered a multi-scale physical prediction of the non-equilibrium freezing process, capable of estimating multiple temporal and spatial scales in the phase change process. The insights and discussions presented in this chapter were published in the peer-reviewed journal article listed below.

M. Xu, Y. Hanawa, S. Akhtar, A. Sakuma, J. Zhang, J. Yoshida, M. Sanada, Y. Sasaki, and A. P. Sasmito. Multi-scale analysis for solidification of phase change materials (PCMs): Experiments and modeling. *International Journal of Heat and Mass Transfer*, 212:124182, 2023.

Abstract

We present a multi-scale solidification framework for pure substances using laboratory experiments and mathematical modeling. The multi-scale phenomena of solidification are experimentally captured by the state-of-the-art thermal control chamber and optical devices. In particular, the transient temperature over five solidification stages is observed under various cooling rates, while the nucleation site and crystal evolution are captured and further processed via image analysis. A unified mathematical model is also formulated to examine the solidification process at three scales quantitatively: (i) the supercooling, freezing, and subcooling stages with a time-dependent boundary at the macroscale are analytically solved by Duhamel's theorem and perturbation method; (ii) the two-dimensional (2D) dendritic growth at the mesoscale is computed by the Allen-Cahn equation through phase field modeling; and (iii) the heterogeneous nucleation at the microscale is numerically simulated. The results demonstrated that the experimental data and modeling were in close agreement for the freezing curve, nucleation temperature, nucleation time, 2D crystal evolution, and freezing time.

Keywords: Solidification, multi-scale, phase change heat transfer, crystal growth, phase field, experiment, mathematical model

8.1 Introduction

The word “solidification” or “freezing” means a phase-change process when a liquid turns into a solid due to its relatively lower temperature below the fusion point. Fundamental research on solidification to understand and predict the complex phase-change process can facilitate diverse applications – spray freeze-drying for biological materials (both pharmaceutical [51, 52, 50] and food [22, 13] products), sublimation drying of semiconductors to prevent the collapse of nanostructure [44, 49, 20], solidification of metallic alloys to improve the effectiveness of continuous casting [60, 10, 45], artificial ground freezing as a geotechnical-support method in civil and mining projects [6, 7, 65], phase change materials (PCMs) for cold energy thermal storage [43, 58, 41], and utilization of ice slurry as a secondary refrigerant in cooling systems [42, 16, 15], and spray-freezing technology for sustainable mine heating [1, 2] to name a few.

Though transport phenomena of solidification vary with materials, solidifying pure liquids to crystalline solids has been found to undergo five distinct stages in many experimental studies regardless of the geometry or ambient conditions [38, 24, 36, 64]. The five solidification stages are briefly described as follows.

1) *Supercooling of liquid*: The pure liquid is cooled from its initial temperature to one even below the fusion temperature. Forming crystalline solids requires atoms to move into a solid lattice structure, thus reducing the temperature below fusion [5]. The supercooled liquid is at a thermodynamically stable state [11, 57].

2) *Nucleation*: The initial formation of a new phase (here, the solid) usually demands an energy barrier (i.e., Gibbs energy). Nucleation happens spontaneously and assists the supercooled liquid to overcome the barrier, thus creating the first ice embryo, a solid cluster of hexagonal molecules for ice-water phase change [27].

3) *Recalescence (also known as crystal growth)*: Followed by the formation of the first

ice nucleus, ice crystal propagates in the melt, and the supercooled temperature rises rapidly back to its equilibrium freezing point (i.e., fusion temperature) due to the release of latent heat. The kinetics of crystalline interface along with its morphology is non-linear and non-equilibrium [33, 32, 26, 55, 34]. The growth rate of the interface can be influenced by thermal (or diffusive), kinetic, and curvature (or Gibbs-Thompson effect) [27, 3].

4) *Freezing*: The phase-change process when solid and liquid phases coexist in the domain is commonly referred to as "freezing" at a macroscopic level. Both sensible and latent heats drive the solid-liquid interface between the two phases (mathematically formulated by the well-known "Stefan condition" [59, 48]).

5) *Subcooling of solid*: Once no more liquid exists in the melt and no latent heat remains, the solid phase subcools or cools down to a steady-state temperature through the sensitive heat only.

In the case of non-pure liquids (for instance, binary mixtures), the phase-change process and solidification stages would alter due to freezing point depression and freeze concentration [22]. Mass diffusion is therefore needed to be considered, while the phase-change process takes place. Nevertheless, the scope of this study is the fundamental research on solidifying PCMs of pure substances through experiments and mathematical modeling.

A variety of mathematical models have been established to examine the phase-change process at a macroscopic level with three distinct stages, where the nucleation and recalescence stages are absent and the liquid PCM only cools down to its fusion temperature (i.e., without supercooling). The three-stage macro-scale solidification can be modeled using the formulation of Stefan problems. Due to the nonlinearity in the Stefan condition (a moving boundary condition), exact solutions are restricted to 1D semi-infinite domains and simple boundaries [19]. When the self-similar solutions are no longer tangible, approximate analytical methods are employed with certain assumptions (e.g., a small Stefan number, $Ste \ll 1$).

Table 8.1: Summary of some approximate analytical methods used in Stefan problems.

Method	Reference
Heat balance integral	Goodman [17], Mitchell and Myers [37]
Regular perturbation	Hill [21]
Singular perturbation	Riley et al. [47], Weinbaum and Jiji [62, 29], Tabakova et al. [56]
Asymptotic analysis	McCue et al. [35], Planella et al. [10, 45], Xu et al. [63]

These methods, including the heat balance integral, regular perturbation, singular perturbation, and asymptotic analysis, are briefly summarized in Table 8.1; detailed descriptions of the methods can be found in the referred works and references therein. In addition, iterative techniques, sometimes known as hybrid numerical-analytical solutions, have also received much attention in recent years [39, 12, 28, 13].

Very few of the existing frameworks attempted to capture all the five stages of solidification. Hindmarsh et al. [24] developed a numerical model for freezing a suspended water droplet to predict the temperature transition for all the five stages. Their numerical model included a one-dimensional (1D) heat conduction equation and heat balances with a moving boundary. Akhtar et al. [3] formulated and solved a semi-analytical five-stage framework for droplet solidification, while incorporating heterogeneous nucleation and non-linear interface kinetics at the nucleation and recalescence stages. 1D finite-extent transient heat equations and a one-phase Stefan problem were solved using the method of separation of variables and perturbation series, respectively; on the other hand, the crystal growth velocity (including the Wilson-Frenkel model) was approximated numerically. Further, two-dimensional (2D) solidification model with five stages in a hollow cylinder was also established for cold thermal energy storage system in a similar approach, yet with a 2D space and an improvement of implementing recalescence as an internal heat generation in the heat equation [64].

In the present paper, we establish a multi-scale solidification framework through experiments and mathematical modeling, capable of predicting the thermal behavior of PCM at macro-, meso-, and micro-scales. Compared with above-mentioned works in the literature, the following research gaps are addressed herein: (i) temperature distribution and crystal growth evolution are measured experimentally through state-of-art equipment (e.g., high-precision thermocouples and high-speed cameras) as well as thorough image analysis; (ii) the mathematical model is formulated and solved based on space and time scales, i.e., multi-scale analysis (rather than solidification stages), even though all the stages are also captured via the multi-scale framework; and (iii) 2D evolution of crystal growth along with the temperature profile of PCM is simulated and validated against experiments. It is also noted that since the presented multi-scale framework characterizes and couples various spatial and temporal scales during solidification, it offers a more versatile and rigorous study for experimentation and modeling compared to the existing multi-stage approaches analyzed in temporal/chronological order.

This paper is comprised of five sections. We begin in Section 8.1 (as discussed here) with a brief introduction to the transport phenomena during solidification and the research gaps to be filled in this work. In Section 8.2, we present the experimental setup used as well as measurements of temperature and crystal evolution. The instrumentation precision and image analysis are also explained in detail. In Section 8.3, we formulate the multi-scale solidification frameworks and then solve the problem at each scale using both analytical and numerical methods. In Section 8.4, we compare and validate the predicted temperature distribution, nucleation, and crystal growth of PCM with experimental data. Some cooling rates are also studied to explore a variety of cooling environments for PCMs. Lastly, our study is summarized, and the key contributions are concluded with recommendations for future work.

8.2 Experiments

8.2.1 Experimental setup

Experiments were conducted at the research laboratory in SCREEN Holdings Co., Ltd., (Japan) in collaboration with Kyoto Institute of Technology (Japan) and McGill University (Canada). The objectives of the experiments are twofold: (1) measure the temperature profile over time of the PCM sample at various cooling rates using thermocouples; and (2) capture the 2D structure of rapid crystal growth on the top layer of the sample using a high-speed camera.

The experimental setup is schematically demonstrated in Fig. 8.1. Two samples (i.e., both deionized water (N_2 saturated: $15 \sim 16$ ppm, dissolved O_2: 20 ppb, specific resistance: 18 MΩcm)) were placed in a thermally controlled chamber: one was used for observation, and another one was for temperature measurement. The observation and temperature measurement samples were placed on their respective sides and cooled down, and then solidified by the cooling plate located at the bottom. The temperature of the cooling plate was controlled by Peltier (Sensor Controls CHP-77HI Revision). Thermocouples are put down in temperature measurement samples and used to measure temperature over time.

At the same time, a ring-shaped light-emitting diode (LED) light (CCS LDR2-170SW2-LA) and a high-resolution, high-speed camera (GoPro10) were installed at the top of the chamber for optical measurements. The time precision of the camera is 0.0042 s; that is, the imaging data can be updated every 0.0042 s. Moreover, two thermocouples are placed on the top layer of the temperature measurement samples, and a third one is connected to the cooling plate. It is noted that the height of the PCM samples is 500 μm, so it is difficult to place the thermocouples at an exact location with such a thin depth. However, temperature discrepancies were not found as long as the thermocouple's tip was on the top surface of the PCM. The precision of the thermocouples is ±2.5°C. The time precision of the temperature

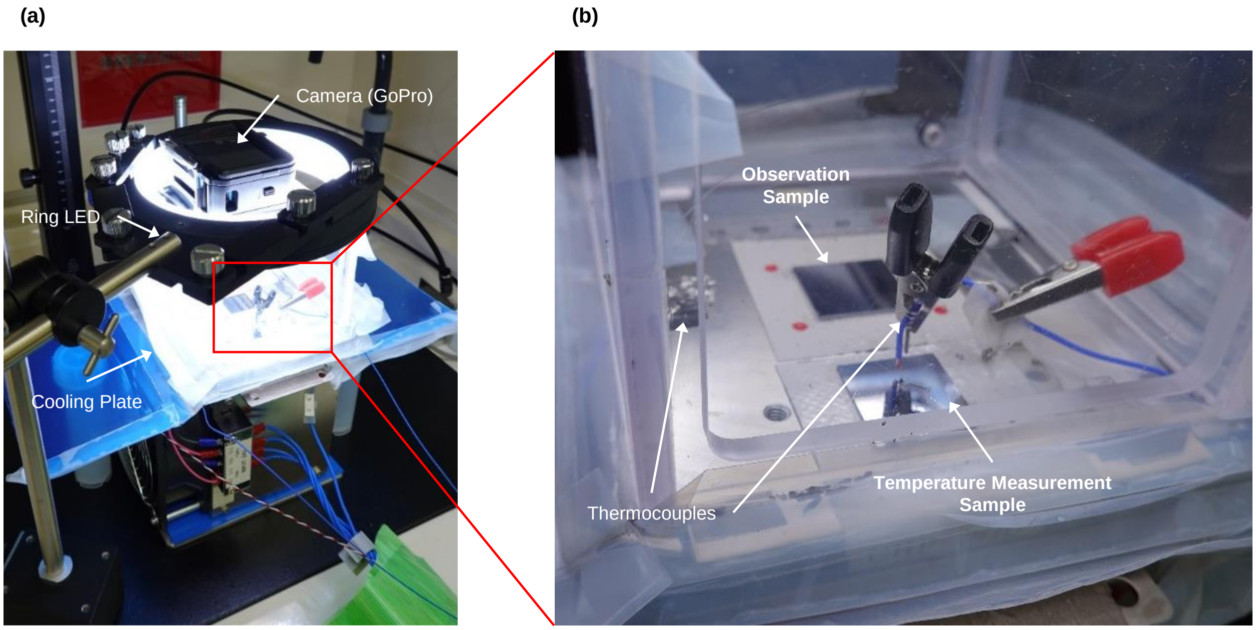

Figure 8.1: Experimental facilities are used to measure temperature and crystal growth.

measurement is 0.1 s. During observation, N_2 (dew point -50°C or less) flowed into the chamber at 1 (L min^{-1}) or less to prevent condensation. All experiments were performed in the class 30 (0.3 μm) FED-STD 209D clean room (temperature: 23 ± 1°C, humidity: $50 \pm 1\%$, differential pressure from outside: 30 to 50 Pa).

8.2.2 Temperature measurements

Prior to the freezing process, the sample solution (i.e., distilled water) and the substrate were prepared through a cautious procedure. The substrate is firstly cut from a new clean bare Si-water (Si(100) surface, P-type (B-doped, 1-100ωcm)) of 300 mm in diameter by approximately 2 cm^2 (t0.775 mm). Then, after debris on the substrate is removed by an air blow gun, organic matter on the substrate surface is removed by UV (ultraviolet) cleaning, allowing minimal thermal contact resistance between the substrate and water. At the UV cleaning, a Si oxide film (approximately 2 nm thick) is formed on the substrate surface. The distilled water (about 250 μL) is placed on the top of the substrate in the control chamber; it then waits until a steady temperature is reached, which is seen as the initial temperature of the PCM, T_{init}.

Once the sample is ready, the cooling plate is set to be a desired cooling rate β by Peltier, and the temperature of the PCM begins to be recorded by a data logger (Keyence NR-600). The temperature measurement terminates when the entire PCM is frozen and reaches its steady state temperature. Moreover, the temperature of the cooling plate is also monitored in the same time frame, which facilitates the determination of a time-dependent boundary condition in the following mathematical model.

This study carried out four cooling rates: $100, 30, 10, 3°\mathrm{C}\ \mathrm{min}^{-1}$. For these cooling rates, the time duration of experiments varied from 5 to 12.5 minutes, and the initial temperature has a range between 5.65 and 7°C. It was found that the ambient air in the control chamber had a negligible effect on either the PCM or cooling plate because of the well-insulated space and minimal airflow.

8.2.3 Image analysis for crystal growth

Apart from the temperature measurements of PCM, the evolution of crystal growth is also examined as a novelty of this experimental study. Videos with a constant sampling rate are photographed during the crystallization for each cooling rate. The following steps are taken to obtain the transient interfacial location and crystal velocity:

1) Place a standard ruler in the luma image so that the locations can be defined with an objective pixel-length to millimeter conversion by summarizing and analyzing its Discrete Cosine Transformation (DCT) data. This procedure defines the x- and y-coordinates that capture the interfacial location at each time frame;

2) The video data $\mathbf{L_x}(t)$ is then normalized by

$$\mathbf{Y_x}(t) = \frac{\mathbf{L_x}(t) - \min \mathbf{L_x}(t)}{\max[\mathbf{L_x}(t) - \min \mathbf{L_x}(t)]} \tag{8.1}$$

From this relatively normalized information $\mathbf{Y_x}(t)$, the contour image of time-anchor

$\mathbf{t_x}$ is defined by removing data out of the measurement limit, as demonstrated in Figure 8.2(a,c);

3) Since the sample boundary may be disturbed during the experiments, the crystal front can be approximated by fitting all the distribution of time-anchor into a conic surface as shown in Figure 8.2(b,d);
4) The distribution of time-anchor of each two frames can also be fitted using the approximated conic surface. This indicates the change in crystal velocity (approximated by the gradient of conic surface), as illustrated in Figure 8.3.

8.3 Mathematical modeling

8.3.1 Multi-scale framework

Solidification of a PCM made of a pure substance undergoes five distinct stages, as explained in Section 8.1: (1) supercooling (of liquid), (2) nucleation, (3) recalescence, (4) (equilibrium) freezing, and (5) subcooling (of solid). These stages are viewed as physically occuring at all macro-, meso-, and micro-scales. A conceptual diagram is illustrated in Fig. 8.4 to characterize and differentiate each solidification scale. More specifically, the macro-scale solidification includes the liquid supercooling, equilibrium freezing, and solid subcooling; a liquid PCM cools down to its fusion temperature, encounters the coexistence of solid and liquid phases (i.e., freezing), and further subcools till the steady-state temperature is reached. The meso-scale solidification deals with the recalescence stage when ice crystals propagate in the PCM before the solid phase appears and initiates the freezing process. Lastly, nucleation stages are captured at the microscale, where the liquid PCM undercools below the fusion temperature to the nucleation temperature; that is, the relatively small ice embryos appear within the PCM in a stochastic way by overcoming the Gibbs-free energy.

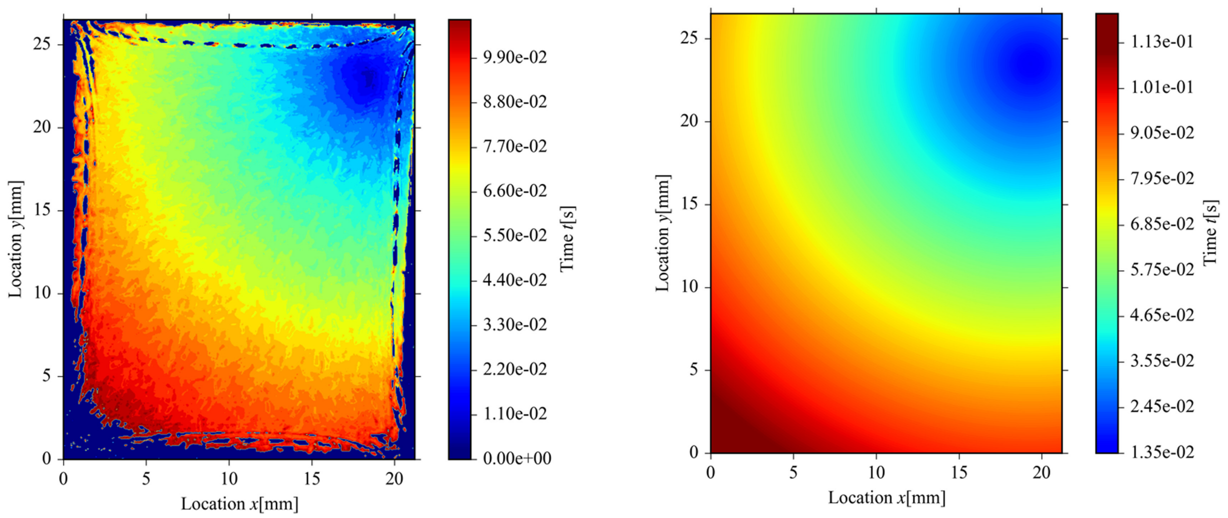
(a) Observed crystal evolution at 30°C/min

(b) Approximated crystal evolution at 30°C/min

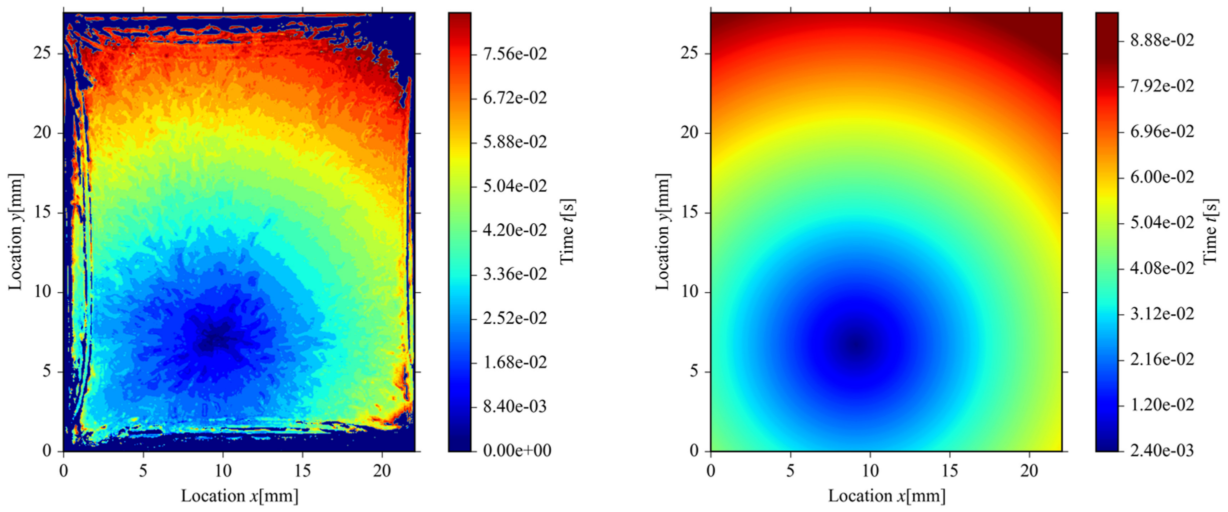
(c) Observed crystal evolution at 100°C/min

(d) Approximated crystal evolution at 100°C/min

Figure 8.2: Image analysis of crystal growth on the transient interfacial location at (a,b) $\beta = 30$ (°C min^{-1}) and (c,d) $\beta = 100$ (°C min^{-1}). (a,c) are the observed crystal evolution using a self-adaptive limit of measurement; (b,d) are the approximated crystal evolution with the conic fitting.

In the following subsections, mathematical formulations of this multi-scale framework are presented scale by scale based on the geometry and boundaries of the PCM in the experiments. A schematic diagram of the PCM in both 3D and 2D plane views along with the boundary conditions are illustrated in Fig. 8.5. Assumptions are also made at each solidification scale; however, some general assumptions for this framework are given as

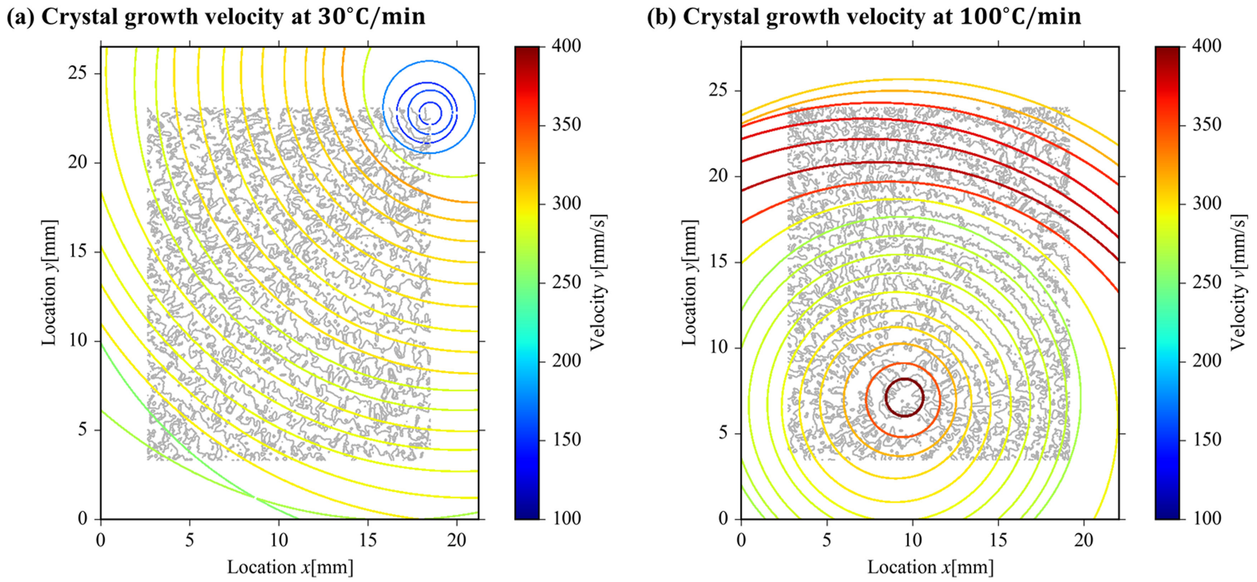

Figure 8.3: Image analysis of crystal growth on the interfacial velocity at (a) $\beta = 30$ (°C min^{-1}) and (b) $\beta = 100$ (°C min^{-1}).

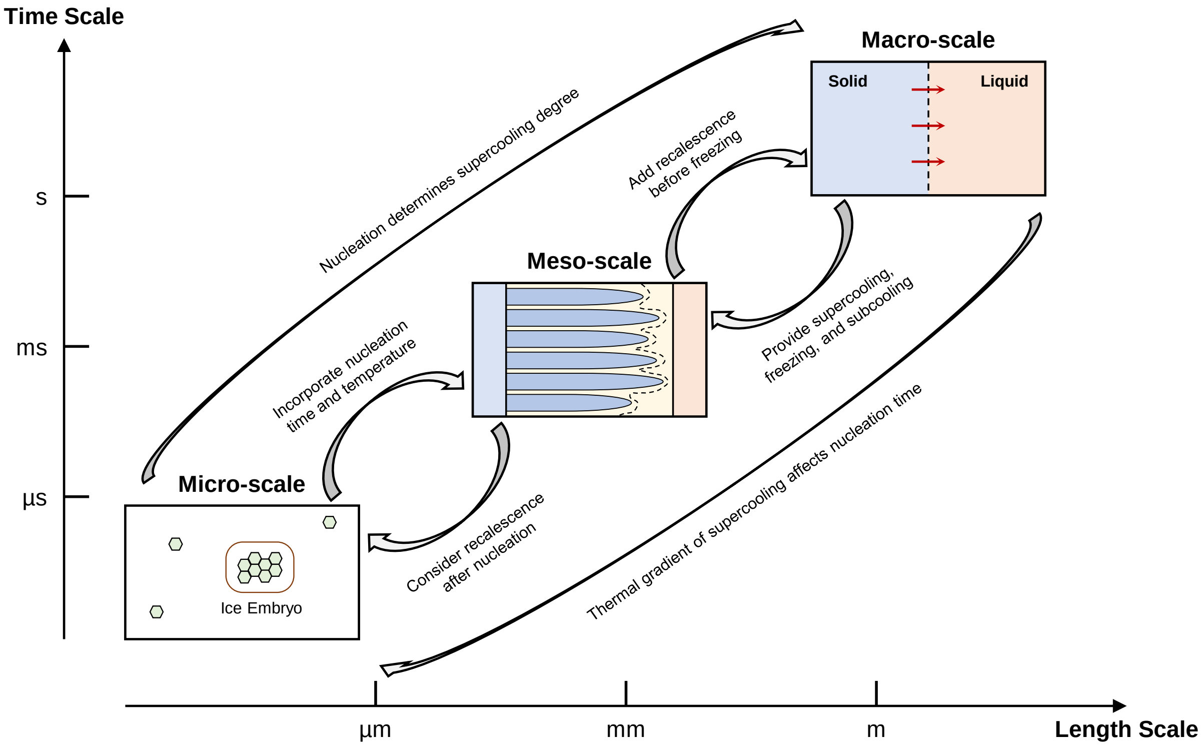

Figure 8.4: Conceptual diagram of the multi-scale solidification framework based on length and time scales.

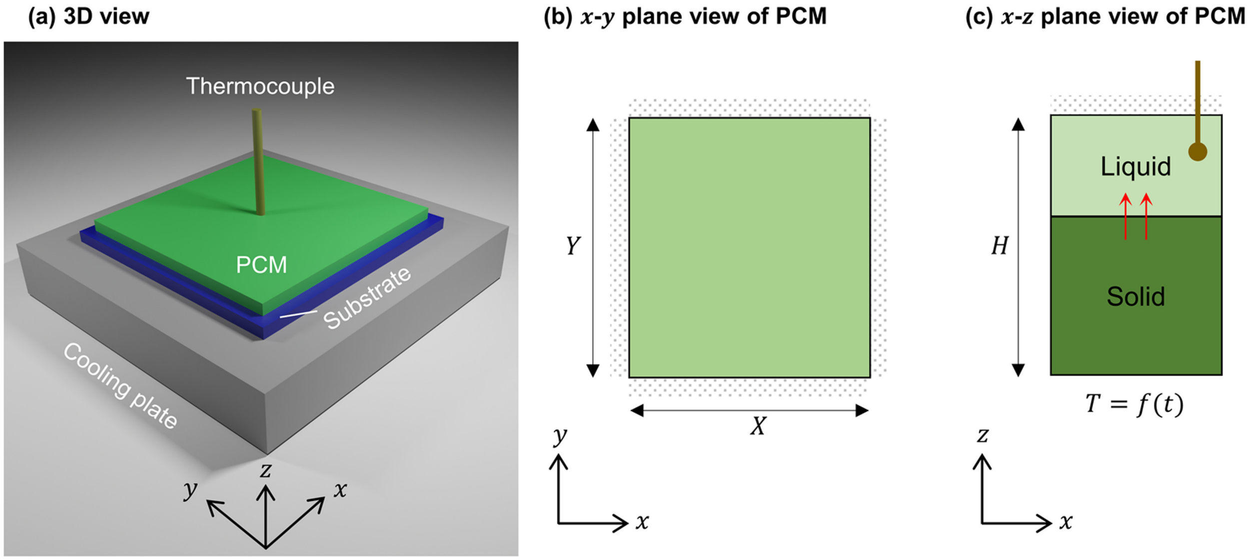

Figure 8.5: Schematic diagram of the 3D and 2D plane views of the PCM.

follows:

1) The PCM is assumed to be a pure substance (here, initially water) without any impurity;

2) The computational domain of PCM is a rectangular cuboid. The bottom side is connected to a programmed cooling plate (which is assumed to be a time-dependent boundary condition), while the other sides are exposed to thermally controlled ambient air (which are assumed to be no-flux boundary conditions);

3) The effect of volume change due to density during the solidification process is considered to be negligible; and

4) The phase-dependent thermophysical properties of PCM are considered.

Macro-scale model

The macro-scale model assumes the solidification of a homogeneous material for the 2D PCM, which reduces the model dimension to 1D; the freezing front also moves towards only one coordinate (here, z-coordinate). Liquid supercooling, equilibrium freezing and solid subcooling stages are captured at the macroscale.

The 1D heat conduction problem that governs this macro-scale model is expressed as:

$$\frac{\partial}{\partial z}\left(k\frac{\partial T}{\partial z}\right) = \rho c_p \frac{\partial T}{\partial t},\ 0 < z < H,\ t > 0 \tag{8.2}$$

where z, k, T, ρ, c_p, t, H are the z-coordinate (m), thermal conductivity (W m^{-1} K^{-1}), temperature (K), mass density (kg m^{-3}), specific heat (J kg^{-1} K^{-1}), time (s), and height of the sample (m), respectively. k, ρ, c_p can also be bundled into thermal diffusivity α (m^2 s^{-1}), assuming these thermal diffusivities are independent of space and temperature (yet dependent of phase), where $\alpha = k/(\rho c_p)$. It is noted that the dependent variable is a function of the z-coordinate and time without the x- and y-coordinates, i.e., $T(z, t)$. The PCM is in contact with the substrate (seen as a perfect conductor) next to a cooling plate. The cooling plate is then a boundary condition for the PCM as follows:

$$T(z = 0, t) = T_{plate}(t),\ t > 0 \tag{8.3}$$

where $T_{plate}(t)$ is the time-dependent temperature of the cooling plate (K). On the other hand, the initial condition of the PCM is assumed to be uniform as follows:

$$T(z, t = 0) = T_{init} \tag{8.4}$$

where T_{init} is the initial temperature of the PCM (K).

After the liquid PCM is supercooled, nucleation and recalescence rapidly occur at the meso- and micro-scale, which prompts a crystallized PCM at its fusion temperature T_f. The crystallized PCM (still considered as the liquid phase) then undergoes equilibrium freezing, where both solid and liquid phases coexist in the domain. As a result, a mathematical expression is required to describe the dynamically changing phases, and a moving boundary condition is implemented to track the solid-liquid interface:

$$k_s \frac{\partial T_s}{\partial z}\bigg|_{z=z_i(t)} = \rho_s L \frac{\mathrm{d}z_i}{\mathrm{d}t},\ 0 < z < H,\ t_1 < t < t_2 \tag{8.5}$$

where $z_i(t)$ and L are the interface location in the z-coordinate (m) and latent heat of fusion (J kg^{-1}), respectively. The subscript s is denoted as the solid phase. t_1 and t_2 are the times to start and complete the (equilibrium) freezing process (s), respectively. It is also noted that two governing equations (i.e., Eq. (8.2)) are presented for each phase during the equilibrium freezing stage.

Meso-scale model

The meso-scale model aims at simulating the 2D crystal growth in the recalescence stage. In this study, a 2D heat conduction problem with a time-dependent source term based on the crystal's solid fraction, ϕ, is first considered in the thermal field. The solid fraction's motion in the source term (i.e., $\partial\phi/\partial t$) is then described from the free energy function using the so-called Allen-Cahn equation (a.k.a., the phase-field model) to predict the anisotropic crystal growth in the continuum field.

First of all, the thermal equation (assuming the heat conduction is dominant) is written as:

$$\alpha\frac{\partial^2 T}{\partial x^2} + \alpha\frac{\partial^2 T}{\partial y^2} + \frac{L}{c_p}\frac{\partial\phi}{\partial t} = \frac{\partial T}{\partial t} \tag{8.6}$$

where x, ϕ are the x-coordinate (m) and solid fraction or order parameter $(-)$, respectively. Apart from the diffusion and transient terms for sensible heat based on Fourier's law, the second term on the left-hand side is a source term which takes the latent heat during solidification into account. Previously, Xu et al. [64] also incorporated a source term $\Delta T_{supercool}/\Delta t_{rec}$ by assuming a constant crystal growth velocity, where $\Delta T_{supercool}$ is the supercooling degree calculated by the difference between the fusion and nucleation temperatures (see the detailed derivation in Appendix A. The main improvement in this study is that the velocity of crystal growth varies with time, in which acceleration will occur.

Prior to the introduction of the phase-field equation, it is essential to non-dimenionalize the 2D heat equation (Eq. (8.6)) using the following dimensionless variables:

$$\widetilde{T} = \frac{T - T_{nuc}}{T_f - T_{nuc}}, \qquad \widetilde{t} = \frac{\alpha t}{\bar{\varepsilon}^2}, \qquad \widetilde{x} = \frac{x}{\bar{\varepsilon}}, \qquad \widetilde{y} = \frac{y}{\bar{\varepsilon}}, \qquad \mathrm{Ste} = \frac{c_p(T_f - T_{nuc})}{L} \tag{8.7}$$

where T_{nuc} is the nucleation temperature that will be coupled with the micro-scale model, and $\bar{\varepsilon}$ is the (isotropic) interfacial width. Here, T_{nuc} and $\bar{\varepsilon}$ can be overlooked as arbitrary constants for the scaling purpose, but they will be scaled back when the dimensionless solution is dimensionalized. It is noted that the dimensionless time $\widetilde{t}$ is also known as the Fourier number characterizing the transient heat conduction [25]. As a consequence, the dimensionless heat equation is expressed as:

$$\frac{\partial^2 \widetilde{T}}{\partial \widetilde{x}^2} + \frac{\partial^2 \widetilde{T}}{\partial \widetilde{y}^2} + \frac{1}{\mathrm{Ste}} \frac{\partial \phi}{\partial \widetilde{t}} = \frac{\partial \widetilde{T}}{\partial \widetilde{t}} \tag{8.8}$$

The non-dimensional heat equation has the same form with the literature [30, 61]. The inverse Stefan number is often referred to as a dimensionless parameter that is proportional to latent heat while inversely proportional to sensible heat. All the thermophysical properties used here are based on the solid, since it prevails over the liquid during recalescence.

Employing the Allen-Cahn equation, the time derivative of solid fraction in Eq. (8.6) can also be expressed as [46]

$$\tau \frac{\partial \phi}{\partial \widetilde{t}} = -\frac{\delta F}{\delta \phi} \tag{8.9}$$

This is known as the time-dependent Ginzburg–Landau equation, where τ is the characteristic (or relaxation) timescale and F is the Ginzburg–Landau type free energy. The relaxation timescale plays an important role in the interfacial kinetics which is proportional to the inverse Stefan number, but one shall quantify τ and $1/\mathrm{Ste}$ separately due to their difference in the fields. Here, the free energy is considered to be dependent of the order parameter ϕ

and dimensionless temperature $\widetilde{T}$:

$$F = \int_{\cancel{V}} \left[\frac{1}{2} |\varepsilon \nabla \phi|^2 + f(\phi, \widetilde{T}) \right] \mathrm{d}\cancel{V} \tag{8.10}$$

where ε is the gradient energy coefficient (equivalent to interfacial thickness) and $f(\phi, \widetilde{T})$ is the bulk free energy or free energy density which can be then described as the combination of a free energy in each phase and an energy hump [9]. For instance, in Kobayashi's works [30, 31] the bulk free energy is calculated by:

$$f(\phi, \widetilde{T}) = \phi(1-\phi)(\phi - \frac{1}{2} + m) \tag{8.11}$$

Here, m is the thermodynamic driving force parameter that is defined as $m = \frac{N}{\pi} \tan^{-1}[\gamma(1-\widetilde{T})], m \in (-\frac{1}{2}, \frac{1}{2})$, where N, γ are the positive constant satisfying $N < 1$ and dimensionless parameter corresponding to the supercooling temperature, respectively. It is rather clear to observe the three solutions: $\phi = 0, 1, \frac{1}{2}$, where the two former solutions are stable yet the latter is not [31].

As a consequence, the functional derivative in a 2D Cartesian coordinate can be written as [30]:

$$\tau \frac{\partial \phi}{\partial \widetilde{t}} = \frac{\partial}{\partial \widetilde{y}} \left(\varepsilon \frac{\partial \varepsilon}{\partial \theta} \frac{\partial \phi}{\partial \widetilde{x}} \right) - \frac{\partial}{\partial \widetilde{x}} \left(\varepsilon \frac{\partial \varepsilon}{\partial \theta} \frac{\partial \phi}{\partial \widetilde{y}} \right) + \nabla \cdot (\varepsilon^2 \nabla \phi) + \phi(1-\phi)(\phi - \frac{1}{2} + m) \tag{8.12}$$

where θ is the angle between the tip velocity and positive x-direction. It is worth mentioning that the first two terms on the right-hand side of the equation are owing to the introduction of anisotropy, in which ϕ is a non-constant and depends on θ. These parameters are defined as follows:

$$\varepsilon = \bar{\varepsilon}\Big\{1 + \delta \cos\Big[j(\theta - \theta_0)\Big]\Big\} \tag{8.13}$$

$$\theta = \tan^{-1}\left(\frac{\partial\phi/\partial\widetilde{y}}{\partial\phi/\partial\widetilde{x}}\right) \tag{8.14}$$

where δ, j, θ_0 are the strength of anisotropy, mode number of anisotropy, and initial offset angle, respectively. It is noted that $\varepsilon = \bar{\varepsilon}$ represents an isotropic case, in which the first two terms in Eq. (8.12) will become zero. In this study, the 2D domain is perpendicular to the solidification direction and exposed to the ambient air. Since the air is static, the convective heat transfer coefficient with the PCM is considered to be extremely small, which results in no-flux boundaries. Hence, the no-flux or insulated conditions are prescribed around the boundaries of the 2D domain; that is,

$$\left.\frac{\partial\widetilde{T}}{\partial\widetilde{x}}\right|_{\widetilde{x}=0} = \left.\frac{\partial\widetilde{T}}{\partial\widetilde{x}}\right|_{\widetilde{x}=1} = \left.\frac{\partial\widetilde{T}}{\partial\widetilde{y}}\right|_{\widetilde{y}=0} = \left.\frac{\partial\widetilde{T}}{\partial\widetilde{y}}\right|_{\widetilde{y}=1} = 0 \tag{8.15}$$

Micro-scale model

Nucleation occurs at the micro-scale, where a critical nucleus overcomes the Gibbs free energy and turns into an ice embryo. Nucleation can be categorized based on its cause, either homogeneous or heterogenous; however, it is mostly heterogeneous in reality, in which a foreign substance initiates the nucleus site. The nucleation rate $J(t)$ for the heterogeneous nucleation is written as [3, 64]

$$J(t) = D\frac{A_w}{3}n_\ell^{\frac{7}{3}}\sqrt{\frac{A_w\sigma_{\ell s}}{\pi k_B T_\ell}}\sqrt{\frac{4}{2+\zeta_f}} \times \exp\left\{-\frac{[A_w\sigma_{\ell s}/(k_B T_\ell)]^3(2+\cos\Phi)(1-\cos\Phi)^2}{27[\ln(p_\ell/p_s)]^2}\right\}, \tag{8.16}$$

where the pre-factor includes: the self-diffusion coefficient of supercooled water D (m^2 s^{-1}), surface area of a water molecule A_w (m^2), number density of molecules in the liquid particle n_ℓ (m^{-3}), interfacial surface tension $\sigma_{\ell s}$ (J m^{-2}), Boltzmann constant k_B (J K^{-1}), and a

Table 8.2: A list of physical and microscopic properties during nucleation.

Property	Value	Ref.
Self diffusivity of water, D ($\mathrm{m}^2 \cdot \mathrm{s}^{-1}$)	$1.5 \times 10^{-6} \exp(-2045/T)$	[36]
Surface area of water molecule, A_w (m^2)	$4\pi r_0^2 = 4\pi[3M_w/(4\pi N_A \rho_\ell)]^{2/3}$	[36]
Molar mass of water, M_w ($\mathrm{kg} \cdot \mathrm{mol}^{-1}$)	18.02×10^{-3}	[40]
Avogadro's number, N_A (mol^{-1})	6.022×10^{23}	[40]
Number density of molecules in liquid, n_ℓ (m^{-3})	$N_A \rho_\ell / M_w$	[18]
Interfacial surface tension, $\sigma_{\ell s}$ ($\mathrm{J} \cdot \mathrm{m}^{-2}$)	$0.025 + (T - 273.15) \times 10^{-4}$	[3, 14]
Boltzmann's constant, k_B ($\mathrm{J} \cdot \mathrm{K}^{-1}$)	1.3806×10^{-23}	[40]
Ratio of nucleating over critical particles in ζ_f, R ($-$)	$H/r^* = H/(2\sigma_{\ell s}/\{n_s[k_B T \ln(p_\ell/p_s)]\})$	[3]
Number density of molecules in liquid, n_s (m^{-3})	$N_A \rho_s / M_w$	[18]
Contact angle, Φ ($^\circ$)	$72 - 76$	[3]
Saturation vapor pressure of water, p_ℓ (Pa)	$610.94 \times \exp\{[17.625(T - 273.15)]/(T - 30.11)\}$	[4]
Saturation vapor pressure of ice, p_s (Pa)	$611.21 \times \exp\{[22.587(T - 273.15)]/(T + 0.71)\}$	[4]

coefficient in the heterogeneous Zeldovich factor ζ_f ($-$). The coefficient ζ_f is defined as:

$$\zeta_f = \frac{(1 - R\cos\Phi)[2 - 4R\cos\Phi - (R^2\cos^2\Phi - 3)]}{(1 - 2R\cos\Phi - R^2)^{\frac{3}{2}}}, \tag{8.17}$$

where R is the ratio of radii between nucleating particle and critical embryo ($-$); Φ is the contact angle ($^\circ$). Furthermore, the exponential factor has the contact angle Φ ($^\circ$) and saturation pressure p (Pa), respectively. These saturation pressures are temperature-dependent functions given in [4]. Definitions and formulations for the above-mentioned terms also are documented in the works [3] and [64]. For the completeness of this work, the physical and microscopic properties used in the heterogeneous nucleation are listed in Table 8.2.

To quantitatively measure the nucleation criterion is defined by the cumulative probability factor P_n [54, 50], rather than the number of nuclei in [3, 64] to incorporate the effect of cooling rate. The cumulative probability of nucleation P_n depends on the instantaneous cooling rate $\beta = dT/dt$ and temperature T; this dependency is taken the assumption that the random nucleation events are governed by statistically inhomogeneous Poisson processes (i.e., the nucleus positions are statistically independent from each other yet characterized by the Poisson distribution on any scale [53]). The cumulative probability $P_n(\beta, T)$ is therefore expressed as:

$$P_n(\beta, T) = 1 - \exp\left(-\frac{1}{\beta}\int_{T'=T_{init}}^{T} J(T')\mathrm{d}T' \right) \tag{8.18}$$

where T' is the temperature integration variable.

8.3.2 Solution methods

Analytical solution

Exact solutions exist during the macroscale solidification, where the liquid PCM cools down from T_{init} before freezing and the solid PCM subcools after freezing, namely the liquid supercooling and solid subcooling stages. In these stages, a partial differential equation based on transient heat conduction without any phase change can be formulated in the 1-D domain:

$$\frac{\partial^2 T}{\partial z^2} = \frac{1}{\alpha}\frac{\partial T}{\partial t} \tag{8.19}$$

$$T(z=0,t) = T_{plate}(t) \tag{8.20}$$

$$T(z \to \infty, t) \to \text{finite} \tag{8.21}$$

It is noted the temperature and thermophysical properties will be based on either liquid or solid PCM. For the liquid PCM, the exact solution to T_ℓ, subjected to an initial condition (Eq. (8.4)), can be solved analytically by the Duhamel's theorem [19]; the final solution is written as:

$$T_\ell(z,t) = T_{init} + \frac{z}{\sqrt{4\pi\alpha_\ell}}\int_{t'=0}^{t} \frac{f(t')}{(t-t')^{3/2}} \exp\left[-\frac{z^2}{4\alpha_\ell(t-t')} \right] dt' \tag{8.22}$$

where $f(t) = T_{plate}(t) - T_{init}$ and t' is the time integration variable. At a macro-scale, T_ℓ will end at t_1 after reaching the fusion temperature T_f. However, when combined with the micro-scale solidification for nucleation, the temperature of the liquid PCM will terminate at $t = t_{nuc}$, indicating that the PCM has supercooled below T_f to its nucleation temperature T_{nuc} and the first ice embryo has been formed within the domain.

During phase change at the macro-scale, a non-linear moving boundary is prescribed at the solid-liquid interface as expressed in Eq. (8.5), also known as the Stefan condition. Therefore, the problem becomes a classical one-phase Stefan problem over a semi-infinite Cartesian domain:

$$\frac{\partial^2 T_s}{\partial z^2} = \frac{1}{\alpha_s}\frac{\partial T_s}{\partial t},\ z > 0,\ t_1 < t < t_2 \tag{8.23}$$

$$T_s(z = 0, t) = T_{plate}(t) \approx \bar{T}_{plate} \tag{8.24}$$

$$T_s(z \to \infty, t) \to \text{finite} \tag{8.25}$$

$$T_s(z, t = t_1) = T_f \tag{8.26}$$

$$k_s \frac{\partial T_s}{\partial r}\bigg|_{z=z_i(t)} = \rho_s L \frac{\mathrm{d}z_i}{\mathrm{d}t} \tag{8.27}$$

Here, we use an average of the time-dependent plate temperature as $\bar{T}_{plate}$ because of the assumption that the temperature deviation for $t_1 \le t \le t_2$ is much smaller than the ones for $t < t_1$ and $t > t_2$. The exact solution can be obtained by introducing the similarity variable [21]. Thus, the moving interface is

$$z_i(t) = 2\lambda\sqrt{\alpha_s t} \tag{8.28}$$

where λ is found by the transcendental equation

$$\lambda \exp(\lambda^2)\mathrm{erfc}(\lambda) = \frac{1}{\sqrt{\pi}}\mathrm{Ste}_s = \frac{1}{\sqrt{\pi}}\frac{c_{p,s}(T_f - \bar{T}_{plate})}{L} \tag{8.29}$$

where Ste_s is the Stefan number based on the solid phase given by $\mathrm{Ste}_s = c_{p,s}(T_f - \bar{T}_{plate})/L$.

After the entire PCM is frozen, the solid PCM subcools with pure conduction in a similar fashion as the above-mentioned liquid supercooling. However, the initial condition is taken as $T_s(z, t = t_2) = T_f$ rather than T_{init}. The exact solution is then derived using the same methodology as Eq. (8.22):

$$T_s(z,t) = T_f + \frac{z}{\sqrt{4\pi\alpha_s}} \int_{t'=0}^{t} \frac{g(t')}{(t-t')^{3/2}} \exp\left[-\frac{z^2}{4\alpha_s(t-t')}\right] dt' \tag{8.30}$$

where $g(t) = T_{plate}(t) - T_f$.

Numerical solution

Numerical algorithms are implemented in the meso-scale and micro-scale models, since it is difficult to seek for analytical solutions while coupling two differential equations. The finite difference method and numerical integration are used in the meso-scale and micro-scale models, respectively. The dimensionless 2D heat equation (8.8) and Allen-Cahn equation (8.9) are coupled and solved using the finite difference algorithm. The 2D space is meshed using uniform square grids and the spacial derivatives are approximated through five-point stencil; for instance

$$(\nabla\phi)_{i,j} \approx \frac{\phi_{i+1,j} - 2\phi_{i,j} + u_{i-1,j}}{(\Delta\widetilde{x})^2} + \frac{\phi_{i,j+1} - 2\phi_{i,j} + u_{i,j-1}}{(\Delta\widetilde{y})^2} \tag{8.31}$$

where the subscripts i, j are the node number in the dimensionless x- and y-directions, respectively. Δx and Δy are the uniform mesh size in the dimensionless x- and y-directions, respectively. On the other hand, the temporal terms are explicitly discretized by the Euler method; for example,

$$\frac{\partial\phi}{\partial t} \approx \frac{\phi_{i,j}^{n+1} - \phi_{i,j}^{n}}{\Delta\widetilde{t}} \tag{8.32}$$

where the superscript n represents the n-th time step and $\Delta\widetilde{t}$ is the dimensionless time step size. The numerical implementation for the phase field model can also be found in the text [8]. It is noted that the seed (or nucleus) location is random within the 2D domain due to the stochastic nature of nucleation. However, the location would not affect the crystal growth rate or the time interval of recalescence, which will be elaborated in detail in Section 8.4.2.

As regards the micro-scale model, the objective is to calculate the nucleation temperature and time (T_{nuc} and t_{nuc}) based on heterogeneous nucleation from the Arrhenius-type equation as written in Eq. (8.16) and inhomogeneous Poisson process given in Eq. (8.18). A numerical algorithm is programmed here without much computational time and power. The nucleation rate $J(t)$ is computed from time t which corresponds to liquid temperature solved by Eq. (8.22), mainly focusing on the supercooled temperature (i.e., $T_\ell < T_f$). The criterion to terminate the supercooling is prescribed when the cumulative probability P_n reaches 1 in Eq. (8.18). The right-hand side of the equation involves a temperature integral which can be numerically integrated by a straightforward trapezoidal rule. It is noted that a finer time step Δt is carried out to obtain a finer temperature ΔT, thus providing a more accurate approximation of the numerical integration.

8.4 Results and discussion

In this section, the temperature profile (also referred as "freezing curve"), freezing time, crystal growth evolution, and cumulatively probability of nucleation are examined by the above-mentioned experimental and modeling frameworks. Four cooling rates are studied to explore the effect of ambient environments on the PCM; corresponding mathematical functions to each cooling rate in terms of the time-dependent plate temperature T_{plate} is listed in Table 8.3. Both experimental and simulated results are compared and validated for each cooling rate.

8.4.1 Macro-scale: Freezing curve and freezing time

The four cooling rates, β, examined in the experiments are recorded and measured in terms of the plate temperature, T_{plate}. Table 8.3 lists the interpolated temperature distribution of T_{plate} for each β using a sum of (two) sine functions; that is, $T_{plate}(t) \approx \sum_{i=1}^{2} A_i \sin(B_i t + C_i)$.

Table 8.3: Temperature distribution of the four cooling rates examined.

Cooling rate β (°C min^{-1})	Temperature of the cooling plate T_{plate} (°C)
3	$19.22\sin(0.002862t + 2.848) + 0.5511\sin(0.01618t - 2.356)$
10	$22.33\sin(0.006459t + 2.771) + 4.638\sin(0.01454t - 2.584)$
30	$-13.72\exp(0.0007817t) + 19.09\exp(-0.01765t)$
100	$-16.23\exp(0.0007384t) + 21.26\exp(-0.01978t)$

Table 8.4: A list of geometrical and macro-scale thermophysical properties of PCM used in the multi-scale model.

Property	Value	Unit
Geometry		
Length, X	2.0×10^{-2}	m
Width, Y	2.5×10^{-2}	m
Height, H	5.0×10^{-6}	m
Ice		
Mass density, ρ_s	916	kg m^{-3}
Specific heat, $c_{p,s}$	2050	J kg^{-1} K^{-1}
Thermal conductivity, k_s	2.22	W m^{-1} K^{-1}
Thermal diffusivity, α_s	1.18×10^{-6}	m^2 s^{-1}
Water		
Mass density, ρ_ℓ	1000	kg m^{-3}
Specific heat, $c_{p,\ell}$	4219	J kg^{-1} K^{-1}
Thermal conductivity, k_ℓ	0.56	W m^{-1} K^{-1}
Thermal diffusivity, α_ℓ	1.33×10^{-7}	m^2 s^{-1}

The freezing curves of the PCM are also measured using the thermocouple at the top surface of the PCM, $z = H$, to test the effect of cooling rate and subsequently be used for the purpose of model validation. Meanwhile, the multi-scale model is developed based on the geometrical and macro-scale thermophysical properties of the PCM, as listed in Table 8.4, at an initial temperature 7°C. As for the micro-scale thermophysical properties in Eq. (8.16) and Eq. (8.17), the values are consistent with Akhtar et al.'s work [3] and the references therein.

Figure 8.6 demonstrates freezing curves of the PCM at different cooling rates, $\beta = 3, 10, 30, 100$ (°C min^{-1}). It is rather clear to see that the cooling rate has direct influences on

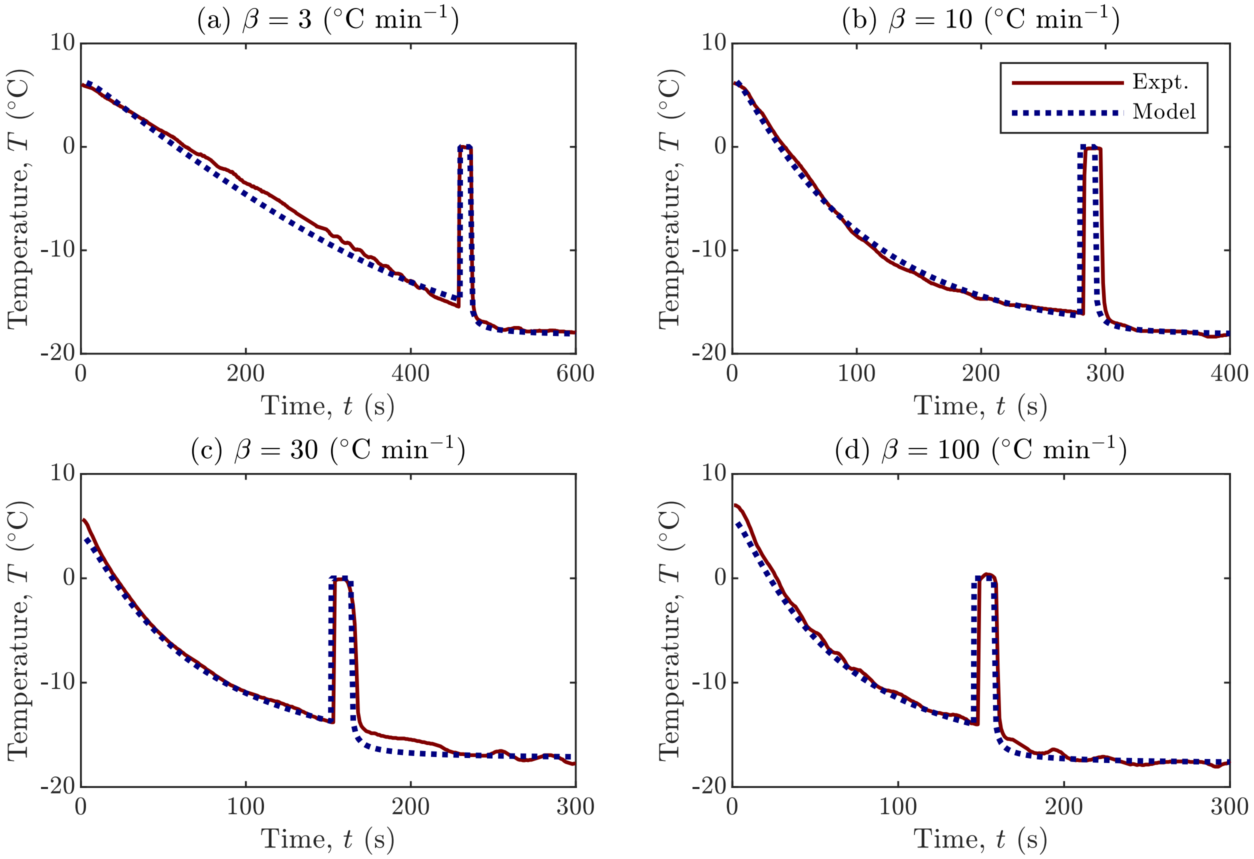

Figure 8.6: Model validation of temperature profile of the PCM at four different cooling rates: (a) $\beta = 3$ (°C min^{-1}); (b) $\beta = 10$ (°C min^{-1}); (c) $\beta = 30$ (°C min^{-1}); and (d) $\beta = 100$ (°C min^{-1}). The experiment is in the red solid line, while the model is in the blue dotted line.

the freezing curve concerning the macro-scale solidification, i.e., the supercooling, freezing and subcooling stages. First of all, the diffusive behavior due to heat conduction during supercooling becomes much more linear for lower cooling rates, especially at $\beta = 3$°C min^{-1}, thus rendering a longer time period for supercooling. This is because lower cooling rates gives a smaller thermal gradient from the cooling plate, which requires more time for the PCM to cool down till nucleation. It is also noted that the nucleation temperatures are approximately -14°C in all the cooling rates; more physical insights for the heterogeneous nucleation will be discussed in the sub-section 8.4.3, as it is a micro-scale phenomenon.

Second, the freezing time (i.e., $\Delta t_{freezing} = t_2 - t_1$) has a moderate influence on the examined cooling rates from both experimental and modeling perspectives. Since the thermocouple was placed on the top surface of PCM, the freezing time is considered for the duration when the temperature remains at the fusion temperature. It is found that the freezing time varies within the range of $7 \sim 13$ seconds, and as β is increased by order of magnitude (e.g., from 3 to 30°C min^{-1}), the freezing time is roughly shortened by a half. It is worth mentioning the anisotropic solidification during the freezing stage mostly likely occurred in the experiment for all cooling rates. The anisotropy begins in the recalescence stage (which will later be presented in the sub-section 8.4.2 for meso-scale results), thereby making the PCM freeze in a non-uniform and anisotropic manner. Owing to the analytical solution developed for the moving boundary expressed in Eq. (8.28), the dimensionless freezing time $Fo_{s,freezing} = \alpha_s \Delta t_{freezing}/H^2$ can be calculated by

$$Fo_{s,freezing} \sim \frac{1}{4\lambda^2} = \frac{1}{4} \times \left[f(Ste_s)\right]^{-2} \tag{8.33}$$

after scaling the z-coordinate as $\widetilde{z} = z/H$. Recall that the Stefan number depends on the specific heat, latent heat, and temperature difference between its fusion and cooling plate. As a consequence, the change in cooling plate temperature (in the order of 10^0 or 10^1) is much less efficacious compared with the massive amount of latent heat released during phase change (in the order of 10^6), which elucidates the reason why the cooling rate has a relatively minimal effect on the freezing time. Lastly, the subcooling portion of the freezing curves has a steep temperature gradient after the entire PCM is frozen. This stage is independent of others (due to the absence of phase change) and the temperature rapidly cools down to be consistent with the cooling plate.

8.4.2 Meso-scale: Crystal growth

As can be seen in Fig. 8.4, the meso-scale solidification separates from the aforementioned macro-scale freezing, concentrating on the propagation of crystal growth. The meso-scale behavior decouples from the macro-scale freezing stages because of the temporal and spatial scale, so the freezing curve shown in Fig. 8.6 can no longer analyse the transport phenomenon for crystal growth. As a result, 2D experiment images and 2D phase field model are used to capture the meso-scale solidification.

Figure 8.2 demonstrates the ice crystal propagation at $\beta = 30, 100$ (°C min^{-1}) via the image analysis explained in the sub-section 8.2.3. It is clear to observe that the ice crystal instantaneously formed around the boundaries of the domain, because the ice embryo or the first nucleus (that triggers crystal growth) is most favourably appeared when a great amount of ambient air as a foreign agent is in contact. The ice crystal inside the PCM domain is immediately formed and propagated; its location as seen in the figure, however, depends on the nucleation happening at the microscale. In order to quantify the crystal propagation without the influence from the boundaries, the image size is reduced by $2 \sim 3$ mm from each end, which evaluates the front of ice crystal.Contour plots for ice crystal interface and velocity are then approximated in Fig. 8.3 by assuming the crystal is isotropic. It is found that the total time of crystal propagation drops by about 21% from $\beta = 30$ to 100 (°C min^{-1}), while the velocity is surged, nearly four times and to be seeming with respect to the cooling rate. Though the duration of recalescence and the velocity of crystal growth take place in meso-scale, they are essential to be considered in many practical applications, as faster crystal growth leads to higher mechanical force and quicker heat release, and vice versa. For example, the sublimation of semi-conductors may be beneficial for low cooling rates to preserve the micro- or nano-structure from collapsing during freezing, similar to the freezing of foods and biological products to protect essential nutrients. On the other hand, cold thermal energy storage systems would prefer a higher cooling rate so that the charging and discharging cycles could be shortened.

Model validation

Figure 8.7 shows the validation of the 2D phase field model against the experiments at two cooling rates: $\beta = 30, 100$ (°C min^{-1}) in the subplots (a,b,c) and (d,e,f), respectively. Three different time frames are selected for each cooling rate; both measured (in the black dots) and approximated (in the red dots) experimental data are presented, in which the approximated results are given by the image analysis explained in the sub-section 8.2.3. On the other hand, the modeling outputs are demonstrated in terms of the order parameter ϕ, physically implying the interfacial width during recalescence. Prior to the comparisons between the modeling and experimental data, the following dimensionless parameters are implemented in the phase field model: $T_0 = -15°\text{C}$, $T_f = 0°\text{C}$, $\bar{\varepsilon} = 0.01$ (mm), $\text{Ste}^{-1} = 10.86$, $j = \delta = \theta_0 = 0$, $N = 0.9$, $\gamma = 10$. It is noted that the thermophysical properties to calculate the dimensionless time $\widetilde{t}$ and Stefan number Ste are consistent with the values listed in Table 8.4 with a latent heat of $L = 334,000$ (J kg^{-1}) for ice-water phase change. Though the above-mentioned parameters remain the same in both cooling rates, the relaxation timescale τ alters and corresponding calibrations are also applied, specifically $\tau = (3.4 \pm 0.6) \times 10^{-4}$ for the lower cooling rate and $\tau = 2.5 \times 10^{-4}$ for the higher one. It is expected that higher cooling rates can shorten the phase change process, thus leading to a smaller relaxation timescale.

For the lower cooling rate, the ice nucleus initiates at the top right corner of the PCM, and the coordinates are assumed to be at ($x = 19$ mm, $y = 23.75$ mm) based on the experimental observation. As can be seen in Fig. 8.7 (a), the crystal develops rapidly from its seed location in an isotropic fashion; the crystal propagation finishes at slightly over 0.1 s as most of the PCM domain covers by the ice crystal indicated in Fig. 8.7 (c). On the other hand, the case with a higher cooling rate grows the ice crystal at a different location, at the left bottom of the domain ($x = 9.11$ mm, $y = 6.75$ mm) owing to the experiment. Compared with the lower cooling rate at the same time frame $t = 0.021$ s (i.e., compare Fig. 8.7 (d) with (a)), the ice crystal is approximately doubled to tripled in size with a similar isotropic behavior. The time period to complete recalescence for the higher cooling rate is about 0.08 s, which is more than 20% faster than the lower cooling rate. It can be concluded that the 2D meso-scale model using phase field can well simulate the ice crystal observed experimentally at different cooling rates and seed locations. Incorporating 2D phase field into the multi-scale framework

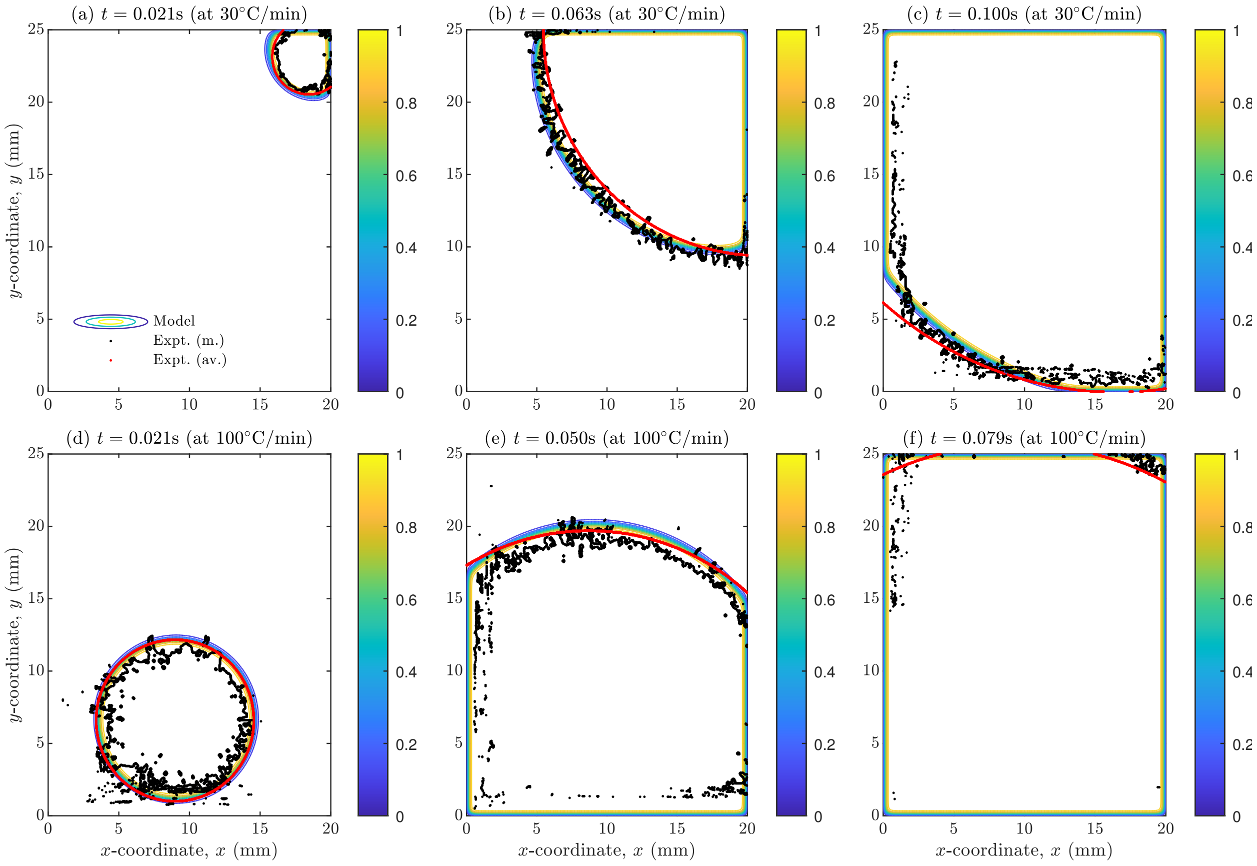

Figure 8.7: Model validation of crystal evolution of the PCM over time at two cooling rates: (a,b,c) $\beta = 30$ (°C min^{-1}); and (d,e,f) $\beta = 100$ (°C min^{-1}). The color bar indicates the phase-field (or order) parameter ϕ. The measuring data is in the black dots, and the approximated or averaged one is in the red dots.

facilitates the observations on crystal morphology and investigations on the effect of seed location, in which the commonly-used Langer and Muller-Krumbhaar (LM-K) [33, 32] is unable to do. In addition, the location of the ice nucleus (or seed) is taken as a priori for the validation purpose, but a separate analysis on the effect of seed locations is conducted in Appendix B. The results show that the seed location does not change the velocity and time period of the crystal growth, albeit the stochastic nature on the origin of the nucleus.

Effect of anisotropy

Figures 8.8 and 8.9 display the modeling results using the phase field model for $\beta = 30$ and 100 (°C min^{-1}), respectively; both order parameter ϕ and temperature $\widetilde{T}$ are plotted for every time frame (with four in total). Moreover, the effect of directional solidification (i.e., isotropic v.s. anisotropic) is also explored for each cooling rate. Table 8.5 lists the properties related to the phase field model consistent with [30]; two mode numbers of anisotropy, $j = 0, 6$ are studied to compare the effect of anisotropy. It is interesting to note that the location of the ice nucleus along with the boundaries has a considerable influence on the crystal evolution regardless anisotropy. This impact is particularly obvious in Fig 8.8, since the nucleus appears at the right corner of the PCM and very close to the top and right boundaries. When the crystal has not been propagated much near the boundaries in the first time frame (a,e,i,m), the front of ϕ and $\widetilde{T}$ remain at its prescribed morphology. However, as the ice crystal grows nearly half of the boundaries in the later times, the morphology alters and the crystal accumulates at the boundaries. In the end, the front of ice crystal is dominated by the boundaries, rather than the mode number of anisotropy defined in the first place. This observation, nevertheless, is not lucid in Fig. 8.9 because the nucleus location is relatively further from the boundaries than the one in Fig. 8.8. It is inevitable that the boundaries will eventually affect the crystal propagation as can be seen in Fig. 8.9 (c,d), but the pre-defined anisotropy remains its characteristics for most of the time, which is independent of the cooling rate. As regards anisotropy, the phase-field results indicate that the mode number only affects the morphology along with some minor thermal gradient near the crystal front, but the crystal velocity and the recalescence time are approximately the same.

8.4.3 Micro-scale: Nucleation and probability

Nucleation is a spontaneous event in which the first nucleus (an ice embryo) can be formed anywhere in the PCM, as can be observed experimentally in Figs. 8.2 and 8.3 The most favorable site for the nucleus is near the PCM boundaries adjacent to the ambient air. This is because a relatively massive amount of foreign material (here, air) is in contact with the PCM and prompts the heterogeneous nucleation. This circumstance is also referred as

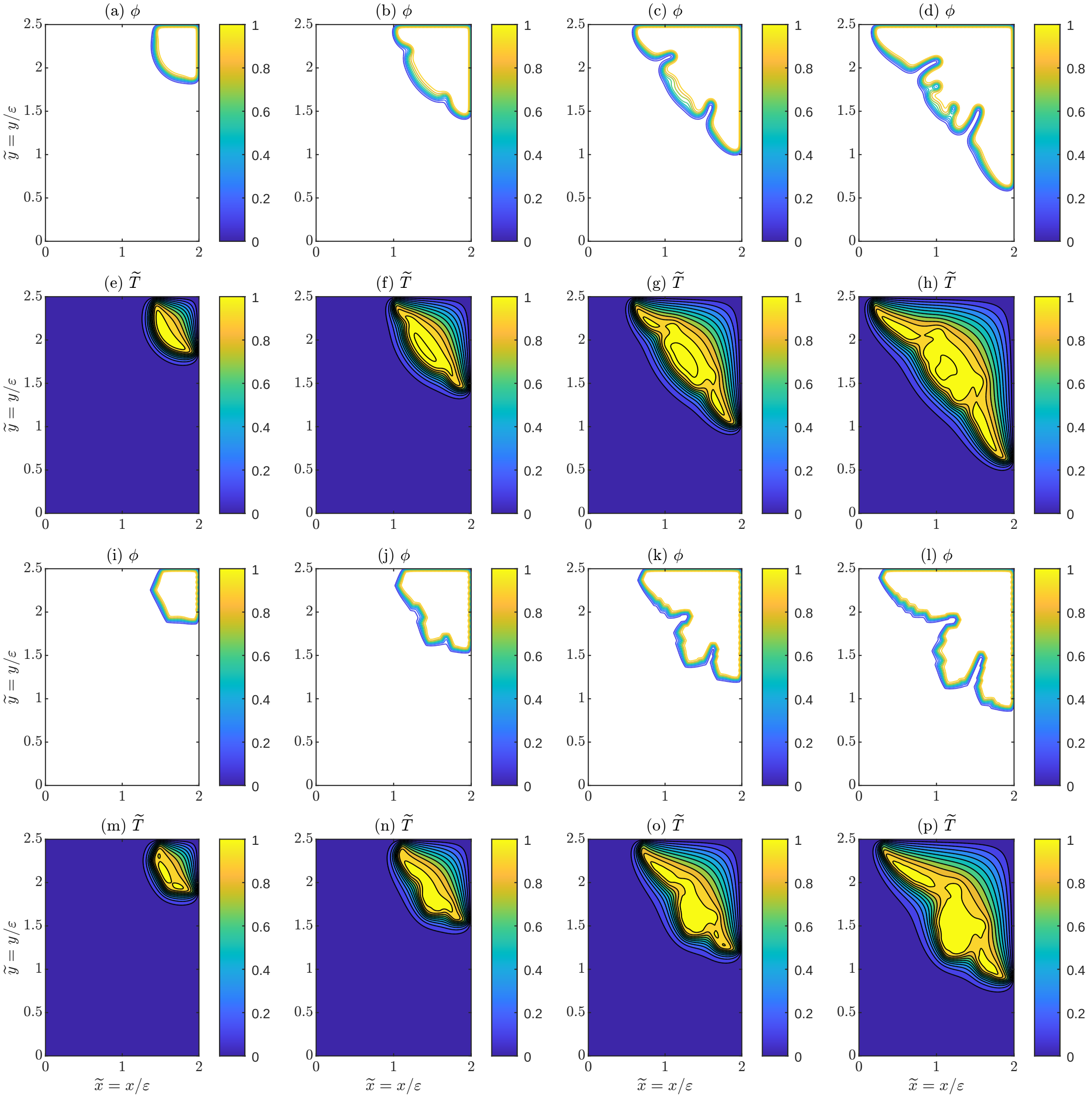

Figure 8.8: 2D contour of crystal growth at meso-scale for $\beta = 30$ (°C min^{-1}) in terms of order parameter ϕ and temperature $\widetilde{T}$. Each column represents a time frame, with a total of four time frames; the first two rows are for the isotropic case, while the last two are anisotropic with $j = 6$. The numerical simulation is at an equally spaced time from $\widetilde{t} = \widetilde{t}_{nuc}$ to $\widetilde{t} = \widetilde{t}_{nuc} + N_{\widetilde{t}} \times \Delta\widetilde{t}$, where $N_{\widetilde{t}} = 800$ and $\Delta\widetilde{t} = 5 \times 10^{-4}$.

"surface nucleation" [23]. In contrast, "volume nucleation" is defined due to the nucleation event that happened within the volume of PCM, in which the nucleation site can hardly be predicted, but the nucleation time and temperature can, e.g., via the Arrhenius-type

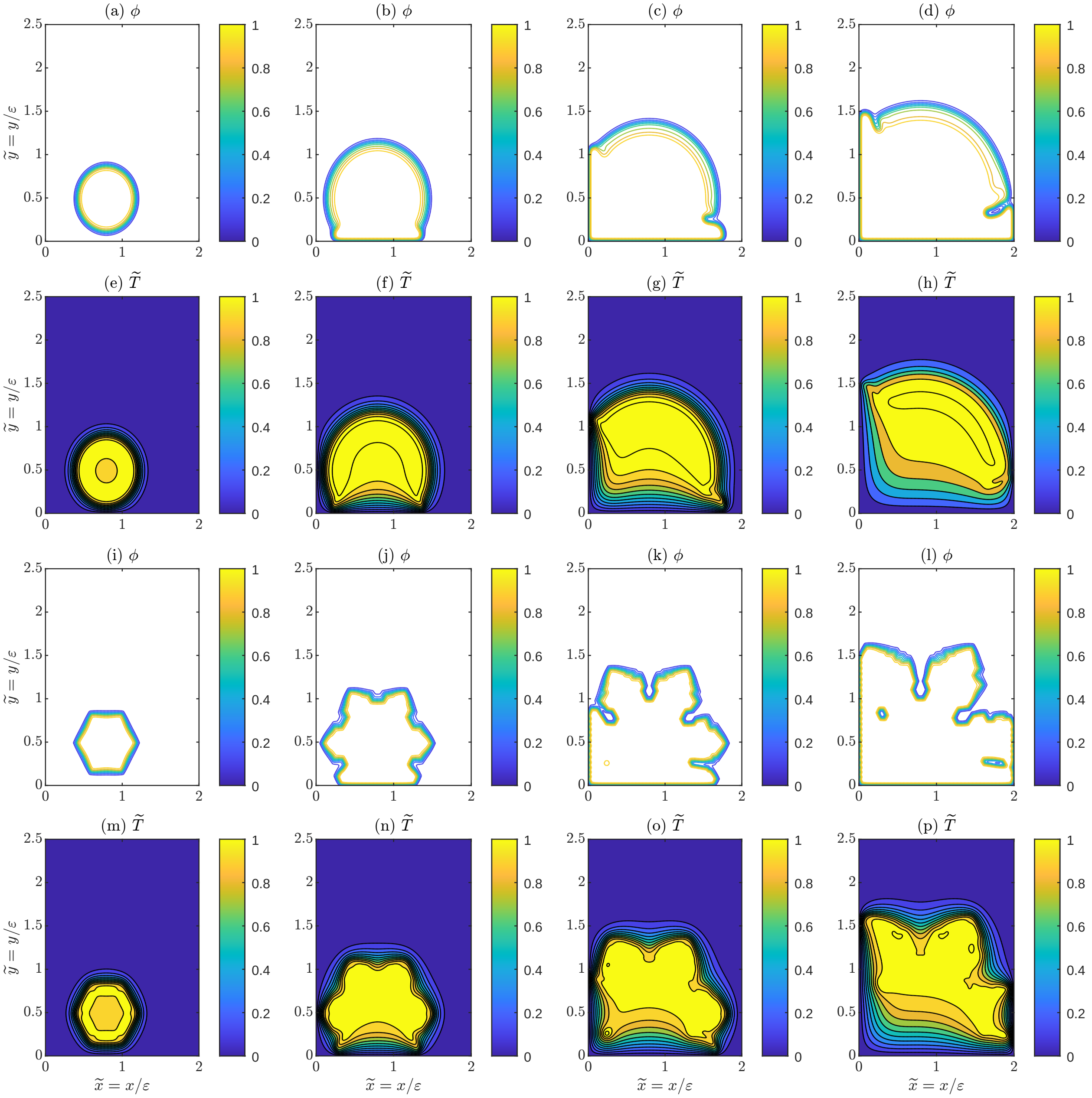

Figure 8.9: 2D contour of crystal growth at meso-scale for $\beta = 100$ (°C min^{-1}) in terms of order parameter ϕ and temperature $\widetilde{T}$. Each column represents a time frame, with a total of four time frames; the first two rows are for the isotropic case, while the last two are anisotropic with $j = 6$. The numerical simulation is at an equally spaced time from $\widetilde{t} = \widetilde{t}_{nuc}$ to $\widetilde{t} = \widetilde{t}_{nuc} + N_{\widetilde{t}} \times \Delta\widetilde{t}$, where $N_{\widetilde{t}} = 800$ and $\Delta\widetilde{t} = 5 \times 10^{-4}$.

Eq. (8.16). Table 8.6 summarizes the nucleation time t_{nuc} and temperature T_{nuc} obtained from experiments and mathematical modeling at different cooling rates β.

The nucleation time varies with cooling rate in a significant manner, yet the nucleation

Table 8.5: A list of properties used in the phase field model at the mesoscale.

Property	Value	Unit	Note/Ref.
Relaxation timescale, τ	3.0×10^{-4}	-	Calibrated by cooling rates
Interfacial width, $\bar{\epsilon}$	0.01	mm	Arbitrary but greater than the mesh size
Mode number of anisotropy, j	$0, 6$	-	Change with crystal morphology
Initial offset angle, θ_0	0	$^\circ$	Change with crystal morphology
Strength of anisotropy, δ	0.1	-	[30]
Positive constant in m, N	0.9	-	[30]
Parameter for supercooling in m, γ	50	-	[30]

Table 8.6: Comparison between experimental and modeling results on nucleation events for different cooling rates at micro-scale.

Cooling rates β (°C min^{-1})	Nucleation time t_{nuc} (s)			Nucleation temp. T_{nuc} (°C)		
	expt.	model	% dev.	expt.	model	% dev.
3	458	459.6	0.35	-15.45	-14.76	4.47
10	282	279.3	0.96	-16.15	-16.34	1.18
30	153	151.5	0.98	-13.80	-13.69	0.80
100	148	145.5	1.69	-14.00	-13.99	0.07

temperature does not. From a theoretical point of view, the nucleation temperature depends on the micro-scale properties of the PCM that remain the same for different cooling rates. Another influential factor for T_{nuc} was revealed to be the surrounding temperature in a recent work [50]; however, in this study, the ambient air temperature is well controlled and equal for all cooling rates. As β increases to an order of magnitude higher, from 3 to 30 and from 10 to 100 (°C min^{-1}), t_{nuc} is found to be reduced by approximately 64% and 48% in the experiments. Moreover, the deviation between the experimental and theoretical results on t_{nuc} is well within 1.7% for all circumstances. As discussed in the macro-scale results, the cooling rate is directly associated with the temperature gradient of the cooling plate, which is the gradient of the PCM during supercooling. Adjusting and toning the cooling rate can either accelerate or delay the nucleation event, therefore fitting the specific need for each thermal application. With regards to the nucleation temperature, an average value can be found to be -14.85°C based on all the cooling rates studied, with less than ± 1.3°C deviation. Compared with the modeling results, the average error is roughly 1.63% in terms of the nucleation temperature. It can be therefore concluded that the developed multi-scale solidification model can predict the micro-scale phenomenon of pure PCM using the heterogeneous nucleation analysis.

8.5 Conclusion

In this research, multi-scale solidification of pure PCM was studied experimentally and theoretically, capable of capturing transport phenomena during phase change at the macro-, meso-, and micro-scale. Owing to the spatial and temporal differences in these scales, separate laboratory tools (e.g., thermocouples, high-speed camera) and techniques (e.g., data logger, image analysis) were utilized in the experiments so that all the solidification scales were measured. On the other hand, the multi-scale framework was firstly forged at individual scales and then coupled with each other; both analytical numerical approaches were implemented depending on the complexity of the problem.

In the experiments, freezing curves were recorded for different cooling rates; both macro-scale stages and micro-scale nucleation were observed. It was found that the cooling rates had a significant effect on the supercooling and nucleation time, whereas a minimal influence on the freezing time and nucleation temperature was seen. Moreover, 2D image analysis allowed us to disclose the evolution of crystal growth with complex morphology during recalescence. Though the initial crystal site was shown as a random event, the interfacial font and velocity were approximately through imaging techniques.

As regards the multi-scale solidification model, it was validated against the experimental results at each scale. The macro-scale model with the Stefan condition solved analytically (e.g., the Duhamel's theorem and similarity solution) was proved to be an accurate and computationally friendly approach, particularly for the prediction of diffusive stages like supercooling and subcooling as the tracking of the moving boundary. The meso-scale model using the phase field method could simulate the morphology of ice crystals with the consideration of anisotropy during recalescence, while the micro-scale framework was based on the nucleation rate through heterogeneous nucleation. It was concluded that the influence on anisotropy was much weaker than the nucleus site; when the site is near the boundaries, the crystal growth would be governed by the boundary effect.

It is recommended that future work on multi-scale solidification should explore in the following directions: solidification of non-pure PCMs, such as binary mixtures and porous media; moving towards multi-physics and multi-scale analysis by incorporating other physical fields, e.g., mechanical, hydraulic, and chemical fields; and study on three-dimensional solidification models at the macro- and meso-scale to seek for higher resolution results.

Appendix A. Comparison between the previous work from Chapter 6 and this study concerning the source term

The unified formulation during the recalescence stage in [64] was given by

$$\frac{1}{\alpha}\frac{\partial T}{\partial t} = \nabla^2 T + \frac{g_0}{k} \tag{8.34}$$

where $g_0 = (mc_p\Delta T_{supercool})/(\forall \Delta t_{rec})$ and $\Delta T_{supercool} = T_f - T_{nuc}$. Compared with the formulation in Eq. (8.6), the equivalent source term is

$$\frac{g_0}{k}\alpha = \frac{mc_p\Delta T_{supercool}}{\forall \Delta t_{rec}}\frac{\alpha}{k} = \frac{mc_p\Delta T_{supercool}}{\forall \Delta t_{rec} c_p \rho} = \frac{\Delta T_{supercool}}{\Delta t_{rec}} \tag{8.35}$$

Hence,

$$\frac{L}{c_p}\frac{\partial \phi}{\partial t} \equiv \frac{\Delta T_{supercool}}{\Delta t_{rec}} \tag{8.36}$$

if assuming that the velocity of crystal growth is constant throughout the recalescence stage.

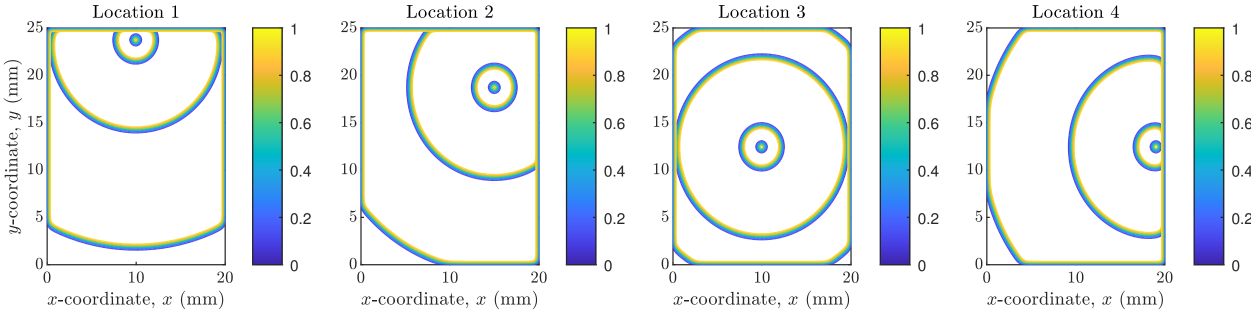

Figure 8.10: Comparison of various seed locations at $\beta = 3$ (°C min^{-1}) at four time frames. The color bar indicates the phase-field (or order) parameter ϕ.

Appendix B. Effect of seed location

As discussed in Section 8.4.2, the seed locations for the validation cases are taken as a priori due to the randomness of nucleation. Here, we demonstrate other possible locations of the nucleus. It is noted that at the cooling rate $\beta = 3$ (°C min^{-1}) the seed appears at the top right corner of PCM, and leading to a recalescence time of $\Delta t_{rec} \approx 0.1$ s. Owing to the symmetry of the no-flux boundaries, the nucleus could also grow from other four possible sites: (1) the top middle, (2) a diagonally quarter away from the top right corner, (3) the middle of the domain, and (4) the right of the center. Hence, Figure 8.10 simulates the above-mentioned four seed sites to capture the potential evolution of crystal growth with the same cooling conditions and properties used in the phase field model. When evaluating the time period for recalescence for the four locations along with the one shown in Fig. 8.7(a,b,c), the difference is minor with an order of 0.01 s. This reveals that the random nucleus site can affect the evolution of the crystal growth, but it does not have a significant influence on the recalescence time. As a consequence, in the case when the seed site location is unknown, then the model would still offer a relatively accurate and reliable prediction with some certainty that can be pre-defined, e.g., 0.1 s.

Nomenclature

Letters

Ste	Stefan number $(-)$
t	Time (s)
x	x-coordinate (m)
y	y-coordinate (m)
z	z-coordinate (m)
X	Length of PCM (m)
Y	Width of PCM (m)
H	Height of PCM (m)
v	Velocity $(\mathrm{m} \cdot \mathrm{s}^{-1})$
T	Temperature (K)
k	Thermal conductivity $(\mathrm{W} \cdot \mathrm{m}^{-1} \cdot \mathrm{K}^{-1})$
c_p	Specific heat $(\mathrm{J} \cdot \mathrm{kg}^{-1} \cdot \mathrm{K}^{-1})$
L	Latent heat of fusion $(\mathrm{J} \cdot \mathrm{kg}^{-1})$
F	Ginzburg–Landau type free energy $(-)$
f	Bulk free energy $(-)$
$\not{V}$	Volume (m^3)
m	Thermodynamic driving force parameter $(-)$
N	Positive constant in m $(-)$
j	Mode number of anisotropy $(-)$
J	Nucleation rate $(\mathrm{m}^{-3} \cdot \mathrm{s}^{-1})$
D	Self-diffusion coefficient $(\mathrm{m}^2 \cdot \mathrm{s}^{-1})$
n	Number density of molecules (m^{-3})
A_w	Surface area of a water molecule (m^2)
k_B	Boltzmann constant $(\mathrm{J} \cdot \mathrm{K}^{-1})$
R	Ratio of radii between nucleating and critical particles $(-)$
p	Saturation pressure (Pa)
M_w	Molar mass of water $(\mathrm{kg} \cdot \mathrm{mol}^{-1})$
N_A	Avogadro's number (mol^{-1})
r_0	Mean inter-particle distance (m)
P_n	Cumulative probability of nucleation $(-)$
Fo	Fourier number $(-)$

Greek symbols

β	Cooling rate $(\mathrm{K} \cdot \mathrm{s}^{-1})$
ρ	Mass density $(\mathrm{kg} \cdot \mathrm{m}^{-3})$
α	Thermal diffusivity $(\mathrm{m}^2 \cdot \mathrm{s}^{-1})$
ϕ	Crystal's solid fraction $(-)$
ε	Gradient energy coefficient $(-)$
γ	Dimensionless parameter for supercooling $(-)$
τ	Characteristic timescale $(-)$

δ	Strength of anisotropy $(-)$
θ_0	Initial offset angle $(^\circ)$
θ	Angle between tip velocity and x-coordinate $(^\circ)$
$\sigma_{\ell s}$	Interfacial surface tension $(\mathrm{J \cdot m^{-2}})$
ζ_f	Coefficient in the heterogeneous Zeldovich factor $(-)$
Φ	Contact angle $(^\circ)$
λ	Eigenvalues $(-)$

Superscripts and subscripts

$plate$	Cooling plate
$init$	Initial
f	Fusion
i	Interfacial
s	Solid phase
ℓ	Liquid phase
$supercool$	Supercooling
rec	Recalescence
nuc	Nucleation
$freezing$	Freezing
$\bar{\ }$	Isotropic or averaged
$\tilde{\ }$	Dimensionless

Bibliography

[1] S. Akhtar, A. Madiseh, and A. Sasmito. Numerical investigation of a novel phase-change renewable energy system for underground mine heating and cooling. *Refrigeration Science and Technology*, 2018, 2018.

[2] S. Akhtar, M. Xu, and A. Sasmito. Spray freezing for mine heating a statistical perspective. In *Mine Ventilation*, pages 357–365. CRC Press, 2021.

[3] S. Akhtar, M. Xu, and A. P. Sasmito. Development and validation of a semi-analytical framework for droplet freezing with heterogeneous nucleation and non-linear interface kinetics. *International Journal of Heat and Mass Transfer*, 166:120734, 2021.

[4] O. A. Alduchov and R. E. Eskridge. Improved magnus form approximation of saturation vapor pressure. *Journal of Applied Meteorology and Climatology*, 35(4):601–609, 1996.

[5] V. Alexiades. *Mathematical modeling of melting and freezing processes.* Routledge, 2018.

[6] M. A. Alzoubi, M. Xu, F. P. Hassani, S. Poncet, and A. P. Sasmito. Artificial ground freezing: A review of thermal and hydraulic aspects. *Tunnelling and Underground Space Technology*, 104:103534, 2020.

[7] M. A. Alzoubi, A. Zueter, A. Nie-Rouquette, and A. P. Sasmito. Freezing on demand: A new concept for mine safety and energy savings in wet underground mines. *International Journal of Mining Science and Technology*, 29(4):621–627, 2019.

[8] S. B. Biner et al. *Programming phase-field modeling.* Springer, 2017.

[9] W. J. Boettinger, J. A. Warren, C. Beckermann, and A. Karma. Phase-field simulation of solidification. *Annual Review of Materials Research*, 32(1):163–194, 2002.

[10] F. Brosa Planella, C. P. Please, and R. A. Van Gorder. Extended Stefan problem for solidification of binary alloys in a finite planar domain. *SIAM Journal on Applied Mathematics*, 79(3):876–913, 2019.

[11] H. B. Callen. Thermodynamics and an introduction to thermostatistics. *John Wiley & Sons, New York*, 1960.

[12] I. S. Carvalho, R. M. Cotta, C. P. Naveira-Cotta, and M. K. Tiwari. Hybrid integral transform analysis of supercooled droplets solidification. *Proceedings of the Royal Society A*, 477(2248):20200874, 2021.

[13] V. Chaurasiya and J. Singh. An analytical study of coupled heat and mass transfer freeze-drying with convection in a porous half body: A moving boundary problem. *Journal of Energy Storage*, 55:105394, 2022.

[14] S. Coriell, S. Hardy, and R. Sekerka. A non-linear analysis of experiments on the morphological stability of ice cylinders freezing from aqueous solutions. *Journal of Crystal Growth*, 11(1):53–67, 1971.

[15] Y. Gao, Y. Ning, C. Wu, M. Xu, S. Akhtar, A. S. Mujumdar, and A. P. Sasmito. Experimental investigation of producing ice slurry with water using opposed-nozzle impinging jet method. *Applied Thermal Engineering*, 219:119568, 2023.

[16] Y. Gao, Y. Ning, M. Xu, C. Wu, A. S. Mujumdar, and A. P. Sasmito. Numerical investigation of aqueous graphene nanofluid ice slurry passing through a horizontal circular pipe: Heat transfer and fluid flow characteristics. *International Communications in Heat and Mass Transfer*, 134:106022, 2022.

[17] T. R. Goodman. The heat balance integral and its application to problems involving change of phase. *ASME Journal of Heat Transfer*, 80:335, 1958.

[18] D. W. Green and M. Z. Southard. *Perry's Chemical Engineers' Handbook*. McGraw-Hill Education, 2019.

[19] D. W. Hahn and M. N. Özisik. *Heat conduction*. John Wiley & Sons, 2012.

[20] Y. Hanawa, Y. Sasaki, S. Uchida, T. Funayoshi, M. Otsuji, H. Takahashi, and A. Sakuma. Thermomechanical formulation of freezing point depression behavior of liquid on solid surface with nanostructure. In *ASME International Mechanical Engineering Congress and Exposition*, volume 84591, page V011T11A014. American Society of Mechanical Engineers, 2020.

[21] J. M. Hill. *One-dimensional Stefan problems: An introduction*. Longman Scientific & Technical, 1987.

[22] J. Hindmarsh, A. Russell, and X. Chen. Experimental and numerical analysis of the temperature transition of a freezing food solution droplet. *Chemical Engineering Science*, 59(12):2503–2515, 2004.

[23] J. Hindmarsh, A. Russell, and X. Chen. Observation of the surface and volume nucleation phenomena in undercooled sucrose solution droplets. *The Journal of Physical Chemistry C*, 111(16):5977–5981, 2007.

[24] J. P. Hindmarsh, A. B. Russell, and X. D. Chen. Experimental and numerical analysis of the temperature transition of a suspended freezing water droplet. *International Journal of Heat and Mass Transfer*, 46(7):1199–1213, 2003.

[25] F. P. Incropera, D. P. DeWitt, T. L. Bergman, A. S. Lavine, et al. *Fundamentals of heat and mass transfer*, volume 6. Wiley New York, 1996.

[26] K. A. Jackson. The interface kinetics of crystal growth processes. *Interface Science*, 10(2):159–169, 2002.

[27] K. A. Jackson. *Kinetic Processes: Crystal growth, diffusion, and phase transformations in materials*. John Wiley & Sons, 2006.

[28] A. Jain and M. Parhizi. Conditionally exact closed-form solution for moving boundary problems in heat and mass transfer in the presence of advection. *International Journal of Heat and Mass Transfer*, 180:121802, 2021.

[29] L. M. Jiji and S. Weinbaum. Perturbation solutions for melting or freezing in annular regions initially not at the fusion temperature. *International Journal of Heat and Mass Transfer*, 21(5):581–592, 1978.

[30] R. Kobayashi. Modeling and numerical simulations of dendritic crystal growth. *Physica D: Nonlinear Phenomena*, 63(3-4):410–423, 1993.

[31] R. Kobayashi. A numerical approach to three-dimensional dendritic solidification. *Experimental Mathematics*, 3(1):59–81, 1994.

[32] J. Langer. Dendritic sidebranching in the three-dimensional symmetric model in the presence of noise. *Physical Review A*, 36(7):3350, 1987.

[33] J. Langer, R. Sekerka, and T. Fujioka. Evidence for a universal law of dendritic growth rates. *Journal of Crystal Growth*, 44(4):414–418, 1978.

[34] K. G. Libbrecht. Physical dynamics of ice crystal growth. *Annual Review of Materials Research*, 47:271–295, 2017.

[35] S. W. McCue, B. Wu, and J. M. Hill. Classical two-phase Stefan problem for spheres. *Proceedings of the Royal Society A: Mathematical, Physical and Engineering Sciences*, 464(2096):2055–2076, 2008.

[36] Z. Meng and P. Zhang. Dynamic propagation of ice-water phase front in a supercooled water droplet. *International Journal of Heat and Mass Transfer*, 152:119468, 2020.

[37] S. L. Mitchell and T. G. Myers. Application of standard and refined heat balance integral methods to one-dimensional Stefan problems. *SIAM Review*, 52(1):57–86, 2010.

[38] O. Miyawaki, T. Abe, and T. Yano. A numerical model to describe freezing of foods when supercooling occurs. *Journal of Food Engineering*, 9(2):143–151, 1989.

[39] A. D. Monde and P. R. Chakraborty. Prediction of cooling curves for controlled unidirectional solidification under the influence of shrinkage: A semi-analytical approach. *Metallurgical and Materials Transactions B*, 49:3306–3316, 2018.

[40] M. J. Moran, H. N. Shapiro, D. D. Boettner, and M. B. Bailey. *Fundamentals of Engineering Thermodynamics*. John Wiley & Sons, 2010.

[41] B. Nie, A. Palacios, B. Zou, J. Liu, T. Zhang, and Y. Li. Review on phase change materials for cold thermal energy storage applications. *Renewable and Sustainable Energy Reviews*, 134:110340, 2020.

[42] L. Onokoko, M. Poirier, N. Galanis, and S. Poncet. Experimental and numerical investigation of isothermal ice slurry flow. *International Journal of Thermal Sciences*, 126:82–95, 2018.

[43] E. Oró, A. De Gracia, A. Castell, M. M. Farid, and L. F. Cabeza. Review on phase change materials (PCMs) for cold thermal energy storage applications. *Applied Energy*, 99:513–533, 2012.

[44] M. N. Patel, S. Sirard, R. Limary, and D. Hymes. Freeze drying of high aspect ratio structures. In *Solid State Phenomena*, volume 219, pages 119–122. Trans Tech Publ, 2015.

[45] F. B. Planella, C. P. Please, and R. A. Van Gorder. Extended Stefan problem for the solidification of binary alloys in a sphere. *European Journal of Applied Mathematics*, 32(2):242–279, 2021.

[46] N. Provatas and K. Elder. *Phase-field methods in materials science and engineering.* John Wiley & Sons, 2011.

[47] D. Riley, F. Smith, and G. Poots. The inward solidification of spheres and circular cylinders. *International Journal of Heat and Mass Transfer*, 17(12):1507–1516, 1974.

[48] L. Rubinstein. *The Stefan problem*, volume 8. American Mathematical Soc., 2000.

[49] Y. Sasaki, Y. Hanawa, M. Otsuji, N. Fujiwara, M. Kato, Y. Yamaguchi, and H. Takahashi. Breakthrough of sublimation drying by liquid phase deposition. In *Solid State Phenomena*, volume 314, pages 172–177. Trans Tech Publ, 2021.

[50] I. B. Sebastião, B. Bhatnagar, and S. Tchessalov. A kinetic model for spray-freezing of pharmaceuticals. *Journal of Pharmaceutical Sciences*, 110(5):2047–2062, 2021.

[51] I. B. Sebastião, B. Bhatnagar, S. Tchessalov, S. Ohtake, M. Plitzko, B. Luy, and A. Alexeenko. Bulk dynamic spray freeze-drying part 1: modeling of droplet cooling and phase change. *Journal of Pharmaceutical Sciences*, 108(6):2063–2074, 2019.

[52] I. B. Sebastião, B. Bhatnagar, S. Tchessalov, S. Ohtake, M. Plitzko, B. Luy, and A. Alexeenko. Bulk dynamic spray freeze-drying part 2: model-based parametric study for spray-freezing process characterization. *Journal of Pharmaceutical Sciences*, 108(6):2075–2085, 2019.

[53] R. Shaw, A. Kostinski, and M. L. Larsen. Towards quantifying droplet clustering in clouds. *Quarterly Journal of the Royal Meteorological Society: A journal of the atmospheric sciences, applied meteorology and physical oceanography*, 128(582):1043–1057, 2002.

[54] R. A. Shaw, A. J. Durant, and Y. Mi. Heterogeneous surface crystallization observed in undercooled water. *The Journal of Physical Chemistry B*, 109(20):9865–9868, 2005.

[55] A. Shibkov, Y. I. Golovin, M. Zheltov, A. Korolev, and A. Leonov. Morphology diagram of nonequilibrium patterns of ice crystals growing in supercooled water. *Physica A: Statistical Mechanics and its Applications*, 319:65–79, 2003.

[56] S. Tabakova, F. Feuillebois, and S. Radev. Freezing of a supercooled spherical droplet with mixed boundary conditions. *Proceedings of the Royal Society A: Mathematical, Physical and Engineering Sciences*, 466(2116):1117–1134, 2010.

[57] D. Turnbull. Phase changes. In *Solid state physics*, volume 3, pages 225–306. Elsevier, 1956.

[58] C. Veerakumar and A. Sreekumar. Phase change material based cold thermal energy storage: Materials, techniques and applications – A review. *International Journal of Refrigeration*, 67:271–289, 2016.

[59] C. Vuik. Some historical notes about the Stefan problem. 1993.

[60] M. Vynnycky, S. Saleem, and H. Fredriksson. An asymptotic approach to solidification shrinkage-induced macrosegregation in the continuous casting of binary alloys. *Applied Mathematical Modelling*, 54:605–626, 2018.

[61] J. A. Warren, R. Kobayashi, A. E. Lobkovsky, and W. C. Carter. Extending phase field models of solidification to polycrystalline materials. *Acta Materialia*, 51(20):6035–6058, 2003.

[62] S. Weinbaum and L. Jiji. Singular perturbation theory for melting or freezing in finite domains initially not at the fusion temperature. *Journal of Applied Mechanics*, 44(1):25–30, 1977.

[63] M. Xu, S. Akhtar, A. F. Zueter, M. A. Alzoubi, L. Sushama, and A. P. Sasmito. Asymptotic analysis of a two-phase Stefan problem in annulus: Application to outward solidification in phase change materials. *Applied Mathematics and Computation*, 408:126343, 2021.

[64] M. Xu, Y. Gao, F. Fang, S. Akhtar, B. A. Chaedir, and A. P. Sasmito. Experimental and unified mathematical frameworks of water-ice phase change for cold thermal energy storage. *International Journal of Heat and Mass Transfer*, 187:122536, 2022.

[65] A. F. Zueter, M. Xu, M. A. Alzoubi, and A. P. Sasmito. Development of conjugate reduced-order models for selective artificial ground freezing: Thermal and computational analysis. *Applied Thermal Engineering*, 190:116782, 2021.

Part IV

Final Remarks

Chapter 9

Scholarly discussion of all the findings

9.1 Overview

This dissertation advances our fundamental understanding of solidification processes, including both equilibrium and non-equilibrium phenomena across various temporal and spatial scales. The original frameworks and investigations presented herein contribute significantly to state-of-the-art technological development and optimization in mining engineering. These contributions include advancements in phase change materials (PCMs) for energy storage, artificial ground freezing (AGF) for protecting and stabilizing ore deposits, and spray freezing (SF) for mine heating, cooling, and decontamination purposes. The applications are not limited to mining; they also extend to the storage and processing of biological materials (e.g., foods and vaccines), manufacturing semiconductors using sublimation drying, and latent heat thermal energy storage via PCMs for buildings and greenhouses across multidisciplinary domains.

The development of frameworks also provides original knowledge and findings from fundamental aspects. In the equilibrium process, the perturbation and asymptotic solutions to the two-phase Stefan problems have not been fully explored prior to this thesis, particularly in an annulus that could be applied in a variety of engineering designs. The established systematic asymptotic analysis for the classical two-phase Stefan problem is the first work conducted in cylindrical coordinates subject to both Dirichlet and Robin boundaries. In the non-equilibrium process, experimental and unified mathematical frameworks have not been explored for inward solidification, while stochastic nucleation and crystal growth were also unclear at multiple spatiotemporal scales. The 2D unified mathematical framework, multistage solidification of binary solutions, and 2D crystal characterization via experiments and modeling are at the forefront of the literature. More detailed discussions are provided in the following subsections.

9.2 Equilibrium process

Extensive research in the literature has predicted the equilibrium process of solidification through numerical approaches. These approaches often prescribe a diffusive solid-liquid interface with an implicit tracking scheme, such as enthalpy formulation and the volume-of-fluid method, as reviewed in Part I. However, these numerical models are usually associated with high computational costs and software expertise, making them difficult to apply in practice. Taking AGF as an example, it is inefficient to numerically examine days of operation with porous ground tens or hundreds of meters in radius.

In the second part of this dissertation, approximate analytical solutions were developed for two-phase Stefan problems within a hollow cylinder through rigorous mathematical analyses. These solutions were verified against numerical algorithms such as the enthalpy method, demonstrating accuracy, reliability, and computational efficiency. The cylindrical geometry ensures applicability to various engineering technologies, including PCMs, AGF, heat exchangers, and thermosiphons. With the assumption of a small Stefan number, these analytical solutions accurately predict nonlinear phase change phenomena, including transient temperature changes in both phases, solid-liquid interfacial motions, and total freezing time, within seconds on a standard two-core workstation. Additionally, expertise in numerical simulations or independent studies on mesh elements and time steps was not required for these analytical solutions. One can directly apply the solutions for total freezing/charging time, interface movement, and temperature profiles in any desired computational tools (e.g., Excel, Matlab, Python).

9.2.1 Discussion of Chapter 3

The prevailing physical phenomenon of AGF is the freezing process. Transient temperature, freezing front, and total freezing time are the key parameters for the design and operation of AGF [3]. The developed singular perturbation solution can analytically approximate the Stefan problem with a highly nonlinear moving boundary, even at its leading order. The analytical solution has a significant computational advantage over conventional numerical simulations. Conventional numerical simulations are usually associated with long computational times and high computational power. This is because the ground size can be in the orders of 10^1 to 10^2 meters while the freezing time is in weeks or months operating for years in underground tunnels [4]. When considering the complex structure of soils with nonlinear phase change as demonstrated in Fig. 2.10, it would be quite time-consuming to predict the thermal performance.

Employing the method of volume averaging, it was found that the sophisticated porous soil structure could be simplified into a homogenized material with effective thermophysical properties. Utilizing the Stefan number (i.e., the ratio of sensible to latent heats) that is intrinsically small in the freezing process, perturbation series solutions to a cylindrical Stefan problem can be found in both long- and short-time scales at the leading order. As a result, the numerically verified analytical solution could produce a rapid and rule-of-thumb approximation of the AGF process, in terms of the total freezing time, freezing front, and transient temperature. It is noted, however, that the Stefan number, as a perturbation parameter in a perturbation series, cannot exceed 0.01, which is the major limitation of this method.

The developed analytical solution to AGF has the potential to be implemented as a fundamental computing algorithm in software for industrial use. Since the computational cost is rather minimal, it can be compiled into an application for existing programming software, e.g., MATLAB Apps, Python Library Application Programming Interface (API), and commercial mine design software, or new and stand-alone software that can be quickly installed in any operational systems.

In AGF, the ground porosity and operational conditions could affect the effective specific heat, latent heat, initial temperature, and coolant temperature, resulting in a relatively large Stefan number. In such scenarios, the developed asymptotic solutions that assume a small (less than unity) Stefan number may not be accurate for engineering purposes. It could be interesting to develop a correction term after the leading and first-order terms, thus providing a more versatile solution for all ground types. Similar approaches can be applied to PCMs, as the material types and storage conditions may also vary.

9.2.2 Discussion of Chapter 4

AGF has been widely employed in permafrost-rich areas for the safety of underground mines, as mine operations are vulnerable to permafrost degradation [2]. In extreme scenarios, catastrophic consequences would be experienced leading to the collapse of underground tunnels and failure of waste management systems. Conventional AGF systems require high energy input associated with a large number of carbon footprints, and thus renewable energy-based solutions are in great demand in their efforts to adapt to today's changing climate. A common approach of the renewable energy-based AGF is the use of thermosiphons which are passive heat exchangers to transfer heat between the cold air and the ground. Case studies have been conducted in the Giant Mine Remediation Project; however, storage systems were needed to store cold energy during winters and supply it in summers [13], as shown in Fig. 9.1. Chapter 4 addressed the quantification of cold thermal energy storage using PCM via asymptotic methods.

When comparing singular perturbation with asymptotic analysis, both methods construct perturbation series solutions or asymptotic expansions through an intrinsically small

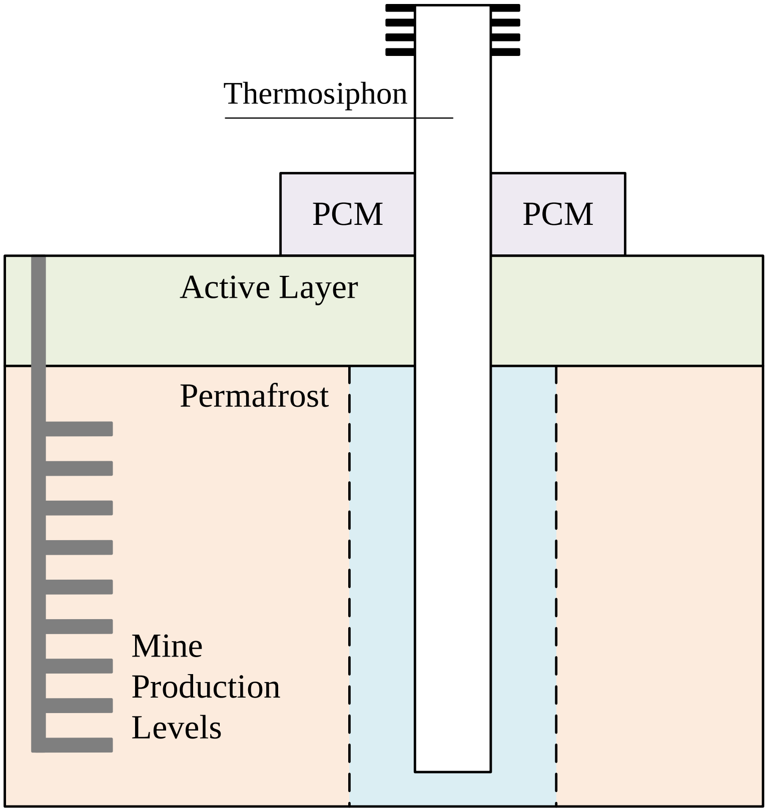

Figure 9.1: Conceptual diagram of renewable energy-based artificial ground freezing with PCMs as cold thermal energy storage.

parameter, e.g., the Stefan number in classical Stefan problems. It was found that the latter approach can be more systematic in reducing orders at both temporal and spatial scales. The former one, however, is often limited to order reduction for time scales. Overall, the asymptotic methods were shown to be quite effective in generating approximate analytical solutions to Stefan problems, and spatiotemporal scales can be directly related to freezing physics. In macro-scale solidification, it will be a three-stage equilibrium process, including pre-cooling of liquid, equilibrium freezing, and subcooling of solid.

An alternative approach to solving the Stefan problems is the use of heat balance integral that is conducted based on a polynomial approximation of the temperature profile [10].

Higher-order polynomials are seemingly more accurate than the lower-order ones; however, higher-order approximations can also be oscillatory, making them difficult to evaluate the accuracy. Unlike the heat balance integral methods, the main advantage of the asymptotic methods is that accuracy only depends on the small perturbation parameter. While studying the effect of the Stefan number on the solution's accuracy in Chapter 4, a rather linear behavior was observed; however, more comprehensive evaluations should be conducted with a wider range of Stefan numbers to draw a more convincing conclusion on such an effect. It is also noted that the error analysis could also facilitate the development of a correction term for relatively high Stefan numbers as mentioned in the previous sub-section.

In the asymptotic analysis, the leading (or zeroth-) and first-order solutions have been found. One may consider continuing to solve higher-order solutions since the sub-problems in each order are often ordinary differential equations and analytical solutions can be quickly found. Despite the lengthy derivation and analysis at the higher orders, one would not be able to guarantee the convergence. This is because the perturbation series are power series that may converge slowly and in some cases might diverge. As a result, it is more efficient and practical to only consider the solutions in the first one or two orders and evaluate their accuracy in specific applications.

In the field of PCMs, three major categories, namely organic, inorganic salt hydrates, and eutectic compounds, were compared and analyzed, particularly in terms of the geometry, phase-dependent thermophysical properties, such as thermal conductivity and specific heat, and Stefan number. From this fundamental comparison, the PCM storage or charging time was found significantly related to the thermal conductivity. While the inherent thermal conductivity of the PCM is crucial during the selection of energy storage, adding a small amount of highly conductive additives like nanoparticles [7] and metals (in the form of foams [5]) can be quite effective.

9.2.3 Discussion of Chapter 5

As climatic conditions such as wind speed and air temperature affect PCM storage, especially when coupled with thermosiphons to extract and store cold energy, the original Dirichlet (or isothermal) boundary [12] was replaced with a more realistic Robin (or convective) boundary, enhancing versatility for practical applications. The convective boundary abandons the assumption that the interface moves instantaneously with time, which was common in solving two-phase Stefan problems. With a systematic asymptotic analysis, new spatial and temporal scales were introduced to capture the pre-cooling or pre-charging time when the solid-liquid interface has not moved.

The climatic effect was fundamentally characterized through the Biot number, a dimensionless parameter characterizing convective heat transfer from the surface to PCM's interior. From the applied aspect, a higher wind speed gives a higher Biot number and vice versa. When using PCM as a cold thermal energy storage unit for thermosiphons, the wind speed could vary drastically over time, particularly under today's changing climate. In addition, the motion of heat transfer fluid inside the thermosiphon which is often characterized by mass flow rate also influences the heat transfer coefficient in the convective boundary, thus altering the Biot number. It was found that the total energy storage time decreased with the rise of the Biot number, while both the pre-cooling time and storage time increased exponentially at small Biot numbers.

Regarding the methodology, since the asymptotic solutions to Stefan problems may include infinite series for heat equations (e.g., exact solution to Sturm–Liouville problems), it is essential to have a sufficient number of terms with eigenvalues and corresponding eigencoefficients to ensure convergence. This is perhaps the most important component when computing asymptotic solutions. It is rather difficult to provide a universal number for eigenvalue terms, so the sensitivity analysis on the number of eigenvalues is required. Nonetheless, the independence of eigenvalues is far more effortless than that of mesh elements and time steps in numerical models.

9.3 Non-equilibrium process

The equilibrium process of freezing at the macro-scale level has been studied in Part II through the development of analytical solutions (using singular perturbation and asymptotic analysis), which in turn facilitates the rule-of-thumb, fast-to-compute, and easy-to-implement thermal prediction to AGF for stabilizing uranium ore deposits, PCM for cold thermal energy storage, and thermosiphons for mine remediation. In the third part of this dissertation, the non-equilibrium freezing process was explored by considering multiple temporal and spatial scales for pure substances and binary mixtures. Specifically, both multi-stage and multi-scale frameworks using mathematical modeling and laboratory experiments have been conducted for cold thermal energy storage with PCM as well as mine heating, cooling, and wastewater treatment via SF.

In the multi-stage frameworks, there are five distinct stages: liquid supercooling, heterogeneous nucleation, recalescence, equilibrium freezing, and solid subcooling. Well-controlled thermal systems were established by adding a PCM casing outside the testing material to minimize flow disturbances. Unified and computationally efficient mathematical models were developed and solved using semi-analytical methods. Furthermore, mass/solute diffusion was included in phase change heat transfer through the Scheil equation, and stochastic nucleation phenomena were characterized over various ambient temperatures. In the multi-scale frameworks, crystal growth and morphology were carefully examined through laboratory experiments and predicted by the phase field model under multi-scale analysis, covering solidification in Cartesian, spherical, and cylindrical coordinates.

9.3.1 Discussion of Chapter 6

When utilizing PCMs for cold thermal energy storage, annular PCMs can be used as thermal enhancements for many cylindrical heat exchangers or pipes. Analyzing non-equilibrium freezing in PCMs is particularly crucial at the micro- and meso-scale levels related to nucleation and recalescence. Nucleation supercools the liquid PCM below its freezing point and affects the latent heat of fusion. Recall that the effective latent heat is expressed as [11, 1]:

$$L_{\mathrm{eff}} = \left(1 - \frac{c_{p,\mathrm{l}}}{c_{p,\mathrm{s}}}\mathrm{Ste}_{\mathrm{nuc}}\right)L \tag{9.1}$$

where $\mathrm{Ste}_{\mathrm{nuc}} = c_{p,\mathrm{s}}(T_{\mathrm{f}} - T_{\mathrm{nuc}})/L$. Taking the ice-water phase change as an example, the effective latent heat can be reduced by 19% compared with its original value. This will significantly influence the capacity of energy storage using PCM, not to mention that the spatial effects may result in possible mechanical changes that will be discussed further in Chapter 8.

In the sixth chapter of this thesis, the 2D unified multi-stage analysis provided an accurate and useful guideline for examining the charging time, temperature, and solid/liquid fraction during non-equilibrium processes. The literature includes many frameworks on 1D non-equilibrium analysis via experiments and modeling, particularly on droplets. The present 2D analysis enabled non-equilibrium freezing in both radial and axial coordinates, capable of predicting five-stage solidification.

From the experimental aspect, the design of ethylene glycol solution between the water bath and test sample allowed an accurate characterization of the supercooling, nucleation, and crystal growth during solidification while minimizing disturbances from machinery vibration. It is noted that the experimental disturbances from the machinery may not necessarily occur when freezing a small volume of PCM, e.g., freezing a droplet and forming a snowflake. As the volume increases, the control of crystallization becomes significantly more challenging at the meso-scale level. Nevertheless, the addition of ethylene glycol around the test sample was found particularly effective in preserving the crystalline structure. The five-stage freezing process was successfully captured with the thermocouple inside the test sample, while the convective heat transfer coefficient was calculated through the thermocouples in the ethylene glycol and water bath. Other encapsules with different geometries and material types could also be implemented in a similar experimental design.

From the modeling aspect, the semi-analytical modeling approach was computationally efficient and easy to implement with non-equilibrium phenomena (e.g., supercooling, heterogeneous nucleation, and crystal growth) that could not be simulated in conventional software using computational fluid dynamics (CFD). The conventional CFD approach requires the energy balance between neighboring nodes. Taking the heat flux as an example, the heat flux coming out of the left node should be equal to the one coming inside the right node. However, this is not the case for nucleation events when an ice nucleus spontaneously occurs at a random location in the computational domain, leading to a fast release of latent heat. Even if one could manage to incorporate such phenomena, the time step and mesh element must be reconstructed at a much higher resolution, thus increasing the computational cost. As a result, the multi-stage, semi-analytical method offered in-depth physical insights into the thermal design, operation, and optimization of PCMs for cold thermal energy storage with minimal computational cost.

One may wonder about the discharge process of PCMs after energy storage, which is related to the melting phenomenon. The melting process can also be predicted by the developed asymptotic solutions with rescaled temperature. However, the influence of natural convection in the liquid phase may need to be considered. This effect can be quantified by Richardson's number, the ratio of buoyancy to flow shear. When natural convection prevails, from the modeling point of view, a convective or advective term must be incorporated into the governing heat equations. The experimental investigation into natural convection may take into account the effect of gravity on the PCM configuration.

9.3.2 Discussion of Chapter 7

For SF, non-equilibrium freezing can reject contaminated particles into the liquid water, leaving purified water in its ice form. This is also referred to as cryopurification. The mining industry produces a significant amount of wastewater with contaminants such as arsenic and zinc, which are often discharged into the environment. SF utilizes the unique environmental conditions in Canada to freeze mine wastewater for decontamination.

In Chapter 7, the developed multi-stage droplet solidification framework for binary solutions can directly contribute to the prediction of freezing wastewater via SF at the droplet level. Particularly, the transient movement of solute or freeze concentration was predicted by coupling the energy balance with the Scheil equation. The quantities of the solid fraction, liquid concentration, and temperature can be rapidly estimated with the multi-stage framework. Unfortunately, the literature lacks experimental data on the solidification of contaminated droplets; sucrose solution is one of the few examples available. Even though the analysis was not specifically conducted for mine-impacted water, the principles, phenomena, and results of sucrose droplets remain the same.

Figure 9.2 demonstrates the solute concentration over the radial coordinate using the same data shown in Fig. 7.4. As can be seen, the initial concentration of solute is at 20%; after the ice (or solid phase) forms, the solute is being concentrated or rejected towards the droplet's center. Purified water with 0% solute concentration can be observed in the solid phase. The maximum solute concentration is reached when the liquid is at its saturation. As a consequence, freezing aqueous solution can significantly concentrate the solutes in the liquid phase while keeping the solid phase as pure ice, without any chemical or greenhouse gas emissions.

With the above-mentioned findings on droplet solidification, one may investigate a wide range of contaminants in mines (e.g., arsenic, sodium, chloride, magnesium) with various concentrations and operational points (e.g., air temperature, droplet diameter). Owing to

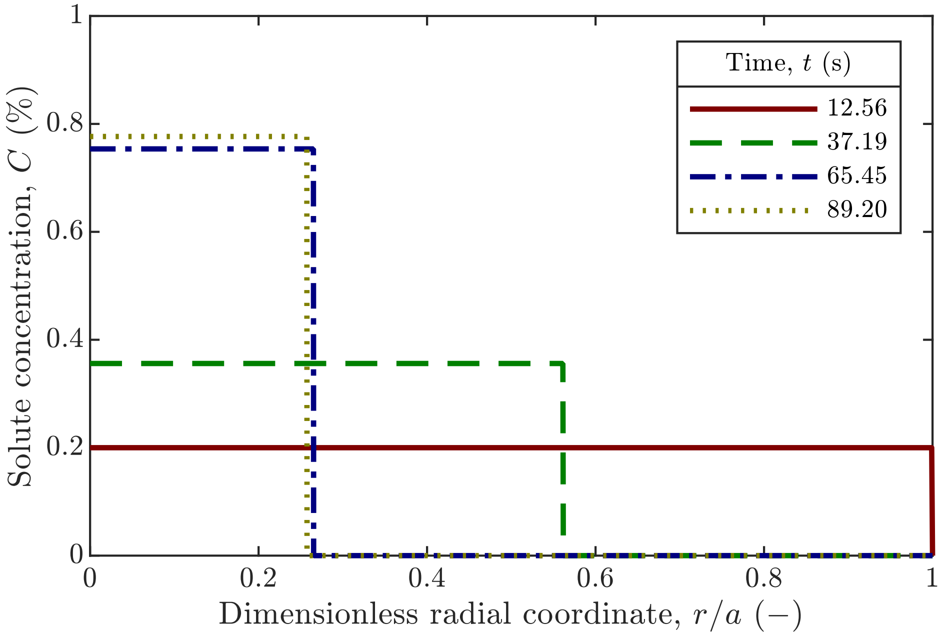

Figure 9.2: A graph of solute concentration over the radial coordinate of a droplet with the same dataset in Figure 7.4.

the location and origin of the mine water, the optimal strategy will be developed at specific mine sites. In Canada, with long winter seasons and cold temperatures, SF is a cost-effective and efficient approach to pre-treat mine wastewater instead of adding chemicals. There is no need for a refrigeration system to lower the air temperature as cold air is abundant in northern regions. The only two main energy inputs for the SF process are to pump water or wastewater into the air and to separate the contaminants from purified via drying or crushing methods.

Although droplet dynamics and spray atomization may largely influence the performance of SF for mine heating and cooling, spraying contaminated mine water in an open space might have minimal impact on fluid dynamics. However, it is also crucial to investigate the pumping power and particle sizes in the field for optimizing the SF performance. One may also look into the separation of purified ice and contaminated liquid after spraying wastewater into cold air. In cases where drinking water is needed, further purification can also be applied.

9.3.3 Discussion of Chapter 8

The most significant contribution to the development of multi-scale analysis in Chapter 8 over the multi-stage frameworks was the spatiotemporal influence on the non-equilibrium freezing process, particularly in heterogeneous nucleation and recalescence. With the assumption of a uniform, parabolic crystal growth rate, one would not be able to characterize the impact of crystal and nucleus (the origin of the crystal) on PCM energy storage and the ice quality produced by SF.

It was found that the crystal growth velocity can be highly nonlinear with complex morphology depending on the cooling rate. The cooling rate also influenced the supercooling degree. This is particularly important because the amount of energy stored in PCM and the heating capacity in SF are based on the latent heat and the effective value during the non-equilibrium process requires the nucleation temperature or supercooling degree. Without considering the non-equilibrium process, one would not be able to accurately evaluate the performance of PCM and SF.

From experimental results, the exact nucleation site could not be found consistently since heterogeneous nucleation is a stochastic and spontaneous event. The nucleation site was therefore taken as a priori in the multi-scale modeling. When studying the effect of nucleation sites under the same cooling rate using the validated multi-scale model, it was clear that the period of recalescence was minimally affected. However, the location of nucleation and its corresponding crystal growth may affect the structure of PCM devices and the ice quality of SF at the meso- or smaller scales.

For the PCM devices, structural design may be included to ensure mechanical support and/or thermal enhancement (e.g., metal foams mentioned in the discussion of Chapter 4). As heterogeneous nucleation usually occurs in practice originating from a foreign agent, the crystal propagation may exert additional force on the structure. Research on micro- or nano-structure devices like semiconductors has shown a significant impact on their structures

[8, 9]. The effect of density change in solidifying droplets with nanoparticles was found to be around 15% at macro-scale [6]. The interaction between the thermal and mechanical fields during non-equilibrium solidification centers around the crystal growth velocity and morphology that have been captured in the multi-scale framework.

Regarding the ice quality in SF, the produced ice could be either in a block or slurry form, depending on crystal propagation. Though block ice demonstrates complete utilization of solidification and release of latent heat, concerns may arise about the removal of the ice in the SF system. Ice slurry, on the other hand, may not undergo a full solidification process; however, it is much easier to remove and utilize for the cooling process. The multi-scale analysis systematically evaluates solidification at different spatiotemporal scales with both equilibrium and non-equilibrium processes, which in turn accurately quantifies the ice quality for the practical use of SF technology.

Bibliography

[1] S. Akhtar, M. Xu, and A. P. Sasmito. Development and validation of a semi-analytical framework for droplet freezing with heterogeneous nucleation and non-linear interface kinetics. *International Journal of Heat and Mass Transfer*, 166:120734, 2021.

[2] M. Alzoubi, S. A. Ghoreishi-Madiseh, A. P. Sasmito, N. Kunz, and A. Guimaraes. Renewable energy-based artificial ground freezing as an adaptation solution for sustainability of permafrost in post-climate change conditions. In *IOP Conference Series: Earth and Environmental Science*, volume 268, page 012128. IOP Publishing, 2019.

[3] M. A. Alzoubi, M. Xu, F. P. Hassani, S. Poncet, and A. P. Sasmito. Artificial ground freezing: A review of thermal and hydraulic aspects. *Tunnelling and Underground Space Technology*, 104:103534, 2020.

[4] M. A. Alzoubi, A. Zueter, A. Nie-Rouquette, and A. P. Sasmito. Freezing on demand: A new concept for mine safety and energy savings in wet underground mines. *International Journal of Mining Science and Technology*, 29(4):621–627, 2019.

[5] K. Boomsma and D. Poulikakos. On the effective thermal conductivity of a three-dimensionally structured fluid-saturated metal foam. *International journal of heat and mass transfer*, 44(4):827–836, 2001.

[6] F. Font, T. Myers, and S. Mitchell. A mathematical model for nanoparticle melting with density change. *Microfluidics and Nanofluidics*, 18(2):233–243, 2015.

[7] Y. Gao, Y. Ning, C. Wu, M. Xu, S. Akhtar, A. S. Mujumdar, and A. P. Sasmito. Experimental investigation of producing ice slurry with water using opposed-nozzle impinging jet method. *Applied Thermal Engineering*, 219:119568, 2023.

[8] Y. Hanawa, J. Zhang, A. P. Sasmito, M. Xu, S. Akhtar, M. Mohit, J. Yoshida, K. Sawada, Y. Sasaki, and A. Sakuma. Kinetics formulation for two-dimensional growth behavior of water/ice interface on si substrate. *Langmuir*, 2024.

[9] Y. Hanawa, J. Zhang, A. P. Sasmito, M. Xu, S. Akhtar, M. Mohit, J. Yoshida, K. Sawada, Y. Sasaki, and A. Sakuma. New formulas for evaluation of cyclohexanol solidification on substrates with surface nanostructures. *ACS Omega*, 2024.

[10] S. L. Mitchell and T. G. Myers. Application of standard and refined heat balance integral methods to one-dimensional Stefan problems. *SIAM Review*, 52(1):57–86, 2010.

[11] S. Tabakova, F. Feuillebois, and S. Radev. Freezing of a supercooled spherical droplet with mixed boundary conditions. *Proceedings of the Royal Society A: Mathematical, Physical and Engineering Sciences*, 466(2116):1117–1134, 2010.

[12] M. Xu, S. Akhtar, A. F. Zueter, M. A. Alzoubi, L. Sushama, and A. P. Sasmito. Asymptotic analysis of a two-phase Stefan problem in annulus: Application to outward solidification in phase change materials. *Applied Mathematics and Computation*, 408:126343, 2021.

[13] A. F. Zueter and A. P. Sasmito. Cold energy storage as a solution for year-round renewable artificial ground freezing: Case study of the giant mine remediation project. *Renewable Energy*, 203:664–676, 2023.

Chapter 10

Original contributions and future work

10.1 Contributions to the original knowledge

This dissertation makes significant contributions to our understanding of macro-scale equilibrium and multi-stage/multi-scale non-equilibrium solidification processes. These contributions are summarized from both fundamental and applied perspectives.

In macro-scale equilibrium solidification, key fundamental contributions include:

- Systematic singular perturbation and asymptotic analysis to reduce the orders of classical two-phase Stefan problems using a small Stefan number.
- Development of singular perturbation and asymptotic solutions for cylindrical two-phase Stefan problems with Dirichlet (isothermal) and Robin (convective) boundaries.
- Comparisons between analytical solutions from Stefan problems and numerical simulations using the enthalpy method in terms of computational time and the impact of the mushy-zone temperature range.

From the applied perspective, the macro-scale equilibrium process contributed to our understanding through:

- Development of easy-to-compute, quick-to-compute, and mesh-free solutions for the thermal assessment of macro-scale freezing processes in pure substances and porous media.

- Rule-of-thumb estimations of AGF with various soil types, including total freezing time, interface motion, and transient temperature, thus offering fast thermal analysis, design, and optimization of AGF systems for ground integrity.
- Computationally efficient thermal predictions of PCMs for cold thermal energy storage, including charging time, temperature profiles, and interface movement.

For multi-stage and multi-scale non-equilibrium solidification, the main fundamental contributions are:

- Development of a novel unified multi-stage solidification model in 2D with heterogeneous nucleation and non-equilibrium interfacial kinetics, validated by laboratory experiments.
- Creation of a fully coupled multi-stage framework for freezing binary solutions through energy balance and Scheil's equation, as well as a gradient-based optimization method for heterogeneous nucleation.
- Multi-scale analysis of solidification with 2D non-linear crystal characterization at meso-scale through laboratory experiments and mathematical modeling.

Key applied contributions on the non-equilibrium process include:

- Accurate thermal estimation of PCMs for cold thermal energy storage at non-equilibrium using semi-analytical schemes to ensure computational efficiency.
- Physics-based analysis of solute concentration, nucleation, crystal growth, and FPD in binary solutions for decontamination of wastewater through SF by concentrating contaminants in the liquid phase and leaving purified water in the ice form.
- Incorporation of spatial scales in multi-scale frameworks, capturing intricate phenomena such as non-linear crystal growth and morphology for PCM energy storage and ice quality in SF.

10.2 Recommendations for future work

It is recommended that future studies in the field of solidification could include the following. First, the effect of density change in the macro-scale equilibrium process was assumed to be negligible in this dissertation. In some cases, the density difference in the solid and liquid phases may lead to a visible change in volume, resulting in a dual-moving boundary problem. One moving boundary is between the solid and liquid phases, while another is at the outer boundary, which will move due to the volume change. Although the volume change could be roughly estimated by the mass density, the dynamic interactions between the solid-liquid interface and the moving boundary during the phase change process would not be captured.

In addition to the volume change, another improvement in the equilibrium process could be the addition of mass diffusion, which is then mathematically categorized as the extended Stefan problem. Both thermal and concentration fields will be included, leading to four governing partial differential equations (PDEs) and two moving boundaries in a two-phase problem. The dual-moving boundary and extended Stefan problems will result in a more complex asymptotic analysis due to the non-linearity in more moving boundaries and the additional PDEs. However, numerical simulations would lead to even higher computational costs because of the convergence of more conservation equations and moving meshes. The successful development of asymptotic solutions would greatly improve the understanding of new physical phenomena, including volume and concentration changes, with a relatively low computational cost.

Regarding non-equilibrium solidification, the spontaneous heterogeneous nucleation phenomenon was captured using the classical nucleation theory, and the effect of ambient temperature was also studied extensively. However, future work could consider the stochastic process of nucleation through other approaches, such as the phase field method, stochastic modeling, and physics-informed neural networks. It may not be possible to predict the exact site of heterogeneous nucleation, but one could analyze the impact of heterogeneous nucleation originating in certain areas of the domain. When designing PCMs with complex structures, such as composite PCMs with metal foams for thermal enhancement, the consideration of nucleation and its subsequent phenomenon on crystal growth can prevent structures or patterns from deforming. In fact, such thermomechanical effects have already been observed in semiconductor manufacturing during sublimation drying.

Meanwhile, the material type for crystal characterization in the multi-scale analysis was limited to ice and water. Other substances and mixtures applicable to certain applications should also be explored. For example, investigating non-equilibrium solidification of binary mixtures with contaminants such as arsenic, zinc, and brine can be an interesting research topic in the future while advancing our applied knowledge of the performance of mine wastewater treatment via SF. It is expected that different material types will demonstrate unique solute concentrations and freeze-point depressions, indicating varying levels of contaminant removal. One may also be interested in optimizing contaminant removal by carefully controlling the cooling condition and droplet/particle size.

Lastly, the advancement of equilibrium and non-equilibrium solidification at multiple temporal and spatial scales has proven the concept's applicability in mining, including PCMs for energy storage, geotechnical support, and mine heating and cooling. Nevertheless, for each specific application, there is still industry-oriented research to be conducted. This includes optimizing the material type and size of PCMs for cold thermal energy storage, studying hydraulic and mechanical aspects of AGF, and analyzing atomization dynamics of SF for mine heating and cooling. For instance, the temperature variations in AGF will influence the permeability and groundwater flow, which require hydraulic considerations. The temperature and flow pressure from the thermal and hydraulic aspects will also affect the mechanical behavior of the ground, such as stress and strain, which could be particularly intensive for porous ground.

Publications

Note: Publications included in this thesis are highlighted; * denotes equal authorship; ___ denotes presenting author.

Peer-reviewed journal articles

Research Theme I - Energy systems: Thermal energy storage, artificial ground freezing, geothermal

1) M. Zolfagharroshan, A. F. Zueter, M. S. Tareen, **M. Xu**, and A. P. Sasmito. Two-phase closed thermosyphons (TPCT) for geothermal energy extraction: A computationally efficient framework. *Applied Thermal Engineering*, 248:123205, 2024.

2) M. S. Tareen, A. F. Zueter, M. Zolfagharroshan, **M. Xu**, and A. P. Sasmito. Seasonal ground cold energy storage potential for data center cooling using thermosyphon: A comparative study of five cities in Canada for carbon footprint reduction. *Journal of Energy Storage*, 84:111486, 2024.

3) Y. Hanawa, J. Zhang, A. P. Sasmito, **M. Xu**, S. Akhtar, M. Mohit, J. Yoshida, K. Sawada, Y. Sasaki, and A. Sakuma. Kinetics formulation for two-dimensional growth behavior of water/ice interface on Si substrate. *Langmuir*, 40(8):4033–4043, 2024.

4) **M. Xu**, S. Akhtar, M. Mohit, A. F. Zueter, and A. P. Sasmito. Asymptotic analysis of a two-phase Stefan problem in an annulus with the convective boundary. *International Journal of Thermal Sciences*, 196:108744, 2024.

5) **M. Xu**, Y. Hanawa, S. Akhtar, A. Sakuma, J. Zhang, J. Yoshida, M. Sanada, Y. Sasaki, and A. P. Sasmito. Multi-scale analysis for solidification of phase change materials (PCMs): Experiments and modeling. *International Journal of Heat and Mass Transfer*, 212:124182, 2023.

6) M. A. Hefni*, **M. Xu***, A. F. Zueter, F. Hassani, M. A. Eltaher, H. M. Ahmed, H. A. Saleem, H. A. Ahmed, G. S. Hassan, K. I. Ahmed, and A. P. Sasmito. A 3D space-marching analytical model for geothermal borehole systems with multiple heat exchangers. *Applied Thermal Engineering*, 216:119027, 2022.

7) **M. Xu**, Y. Gao, F. Fang, S. Akhtar, B. A. Chaedir, and A. P. Sasmito. Experimental and unified mathematical frameworks of water-ice phase change for cold thermal energy storage. *International Journal of Heat and Mass Transfer*, 187:122536, 2022.

8) P. H. Agson-Gani, A. F. Zueter, **M. Xu**, S. A. Ghoreishi-Madiseh, J. C. Kurnia, and A. P. Sasmito. Thermal and hydraulic analysis of a novel double-pipe geothermal heat exchanger with a controlled fractured zone at the well bottom. *Applied Energy*, 310:118407, 2022.

9) M. A. Hefni*, **M. Xu***, F. Hassani, S. A. Ghoreishi-Madiseh, H. M. Ahmed, H. A. Saleem, H. A. Ahmed, G. S. Hassan, K. I. Ahmed, and A. P. Sasmito. An analytical model for transient heat transfer with a time-dependent boundary in solar-and waste-heat-assisted geothermal borehole systems: From single to multiple boreholes. *Applied Sciences*, 11(21):10338, 2021.

10) **M. Xu**, S. Akhtar, A. F. Zueter, M. A. Alzoubi, L. Sushama, and A. P. Sasmito. Asymptotic analysis of a two-phase Stefan problem in annulus: Application to outward solidification in phase change materials. *Applied Mathematics and Computation*, 408:126343, 2021.

11) A. F. Zueter, **M. Xu**, M. A. Alzoubi, and A. P. Sasmito. Development of conjugate reducedorder models for selective artificial ground freezing: Thermal and computational analysis. *Applied Thermal Engineering*, 190:116782, 2021.

12) **M. Xu**, S. Akhtar, A. F. Zueter, V. Auger, M. A. Alzoubi, and A. P. Sasmito. Development of analytical solution for a two-phase Stefan problem in artificial ground freezing using singular perturbation theory. *Journal of Heat Transfer*, 142(12):122401, 2020.

13) M. A. Alzoubi, **M. Xu**, F. P. Hassani, S. Poncet, and A. P. Sasmito. Artificial ground freezing: A review of thermal and hydraulic aspects. *Tunnelling and Underground Space Technology*, 104:103534, 2020.

Research Theme II - Renewable heating and cooling with spray freezing

14) Y. Gao*, M. Mohit*, J. Luo, **M. Xu**, F. Fang, A. S. Mujumdar, and A. P. Sasmito. Development of a novel continuous nanofluid ice slurry generator: Experimental and theoretical studies. *Applied Thermal Engineering*, 244:122667, 2024.

15) **M. Xu**, S. Akhtar, M. Mohit, and A. P. Sasmito. Development of a multi-stage model for freezing of a suspended binary solution droplet. *International Journal of Heat and Mass Transfer*, 221:125115, 2024.

16) Y. Gao, J. Luo, F. Fang, **M. Xu**, M. Mohit, T. Shamim, and A. P. Sasmito. On the stability of nanofluid ice slurry produced via impinging stream method under thermal and phase-change cycles. *Case Studies in Thermal Engineering*, 52:103725, 2023.

17) S. Akhtar, **M. Xu**, M. Mohit, and A. P. Sasmito. A comprehensive review of modeling water solidification for droplet freezing applications. *Renewable and Sustainable Energy Reviews*, 188:113768, 2023.

18) Y. Gao, Y. Ren, **M. Xu**, J. Liu, A. S. Mujumdar, and A. P. Sasmito. Influence of thermal cycling on stability and thermal conductivity of nanofluid ice slurry. *International Journal of Thermal Sciences*, 185:108113, 2023.

19) Y. Gao, Y. Ning, C. Wu, **M. Xu**, S. Akhtar, A. S. Mujumdar, and A. P. Sasmito. Experimental investigation of producing ice slurry with water using opposed-nozzle impinging jet method. *Applied Thermal Engineering*, 216:119568, 2023.

20) Y. Gao, Y. Ning, **M. Xu**, C. Wu, A. S. Mujumdar, and A. P. Sasmito. Numerical investigation of aqueous graphene nanofluid ice slurry passing through a horizontal circular pipe: Heat transfer and fluid flow characteristics. *International Communications in Heat and Mass Transfer*, 134:106022, 2022.

21) S. Akhtar, **M. Xu**, and A. P. Sasmito. A novel crystal growth model with nonlinear interface kinetics and curvature effects: Sensitivity analysis and optimization. *Crystal Growth & Design*, 21(6):3251–3265, 2021.

22) S. Akhtar, **M. Xu**, and A. P. Sasmito. Development and validation of a semi-analytical framework for droplet freezing with heterogeneous nucleation and non-linear interface kinetics. *International Journal of Heat and Mass Transfer*, 166:120734, 2021.

23) S. Akhtar, **M. Xu**, and A. P. Sasmito. Development and validation of an asymptotic solution for a two-phase Stefan problem in a droplet subjected to convective boundary condition. *International Journal of Thermal Sciences*, 164:106923, 2021.

Research Theme III - Sustainability and safety in mines

24) J. Zhao, W. Liu, J. Shen, **M. Xu**, and A. P. Sasmito. A real-time monitoring temperature-dependent risk index for predicting mine water inrush from collapse columns through a coupled thermal–hydraulic-mechanical model. *Journal of Hydrology*, 607:127565, 2022.

25) J. Zhao, W. Liu, J. Shen, **M. Xu**, and A. P. Sasmito. Fractal treelike fracture network model for hydraulically and mechanically induced dynamic changes in the non-Darcy coefficient during the process of mine water inrush from collapsed columns. *Fractals*, 29(07):2150218, 2021.

26) E. Su, Y. Liang, Q. Zou, **M. Xu**, and A. P. Sasmito. Numerical analysis of permeability rebound and recovery during coalbed methane extraction: Implications for CO_2 injection methods. *Process Safety and Environmental Protection*, 149:93–104, 2021.

27) E. Su, Y. Liang, X. Chang, Q. Zou, **M. Xu**, and A. P. Sasmito. Effects of cyclic saturation of supercritical CO_2 on the pore structures and mechanical properties of bituminous coal: An experimental study. *Journal of CO2 Utilization*, 40:101208, 2020.

Peer-reviewed conference proceedings

Research Theme I - Energy systems: Thermal energy storage, artificial ground freezing, geothermal

1) **M. Xu**, S. Akhtar, A. F. Zueter, M. Mohit, and A. P. Sasmito. Analytical modeling of metal foam composite phase change materials (PCM) in thermal energy storage using asymptotic analysis. In *ASME International Mechanical Engineering Congress and Exposition*, volume 87677, page V010T11A024. American Society of Mechanical Engineers, 2023.

2) M. Mohit*, **M. Xu***, S. Akhtar, and A. P. Sasmito. Development of modified perturbation solutions to the one-phase Stefan problems with a convective boundary. In *ASME International Mechanical Engineering Congress and Exposition*, volume 87677, page V010T11A061. American Society of Mechanical Engineers, 2023.

3) M. Zolfagharroshan, **M. Xu**, A. Zueter, and A. Sasmito. Theoretical study of counter-current liquid-vapor flow under condensation conditions over non-isothermal vertical

wall of two-phase closed thermosyphon. In *ASME International Mechanical Engineering Congress and Exposition*, volume 87677, page V010T11A043. American Society of Mechanical Engineers, 2023.

4) A. F. Zueter, **M. Xu**, P. Agson-Gani, M. Zolfagharroshan, N. Bahrani, and A. P. Sasmito. Thermal analysis of U-type geothermal heat exchangers of complex configurations using novel reduced-order models. In *Proceedings of the 15th International Conference on Applied Energy (ICAE)*. 2023.

5) M. Zolfagharroshan, **M. Xu**, M. S. K. Tareen, A. F. Zueter, A. P. Sasmito, and M. Kang. Geothermal Energy Potential from Abandoned Oil and Gas Wells in Appalachian Basin of New York and Pennsylvania. In *Proceedings of the 15th International Conference on Applied Energy (ICAE)*. 2023. [**Selected for Special Issue**]

6) M. Zolfagharroshan, A. F. Zueter, **M. Xu**, and A. P. Sasmito. A novel reduced-order model for transient heat transfer in thermosyphon for geothermal systems. In *Proceedings of the 16th International Conference on Heat Transfer, Fluid Mechanics and Thermodynamics (HEFAT)*. 2022.

7) P. H. Agson-Gani, A. F. Zueter, **M. Xu**, and A. P. Sasmito. Development of a 1+1D reduced-order model in double-pipe geothermal heat exchanger systems: From single to multiple boreholes. In *Proceedings of the 13th International Conference on Applied Energy (ICAE)*. 2021. [**Selected for Special Issue**]

8) **M. Xu**, S. A. Ghoreishi-Madiseh and A. P. Sasmito. Analytical solution for computationally efficient closed-loop geothermal system using multiple boreholes equipped with coaxial heat exchangers. In *Proceedings of the 15th International Conference on Heat Transfer, Fluid Mechanics and Thermodynamics (HEFAT)*. 2021. [**Best Paper Award**]

9) **M. Xu**, S. Akhtar, A. F. Zueter, M. A. Alzoubi, and A. P. Sasmito. Analytical modeling of out- ward solidification with convective boundary in cylindrical coordinates. In *ASME International Mechanical Engineering Congress and Exposition*, volume 84591, page V011T11A012. American Society of Mechanical Engineers, 2020.

10) A. F. Zueter, **M. Xu**, M. A. Alzoubi, and A. P. Sasmito. Effect of freeze pipe eccentricity in artificial ground freezing applications. In *ASME International Mechanical Engineering Congress and Exposition*, volume 84591, page V011T11A036. American Society of Mechanical Engineers, 2020.

11) **M. Xu**, S. Akhtar, M. A. Alzoubi, and A. P. Sasmito. Singular perturbation solution for a two-phase Stefan problem in outward solidification. In *ASME 2019 International Mechanical Engineering Congress and Exposition*. American Society of Mechanical Engineers Digital Collection, 2019.

12) **M. Xu**, S. Akhtar, M. A. Alzoubi, and A. P. Sasmito. Development and verification of two-phase Stefan problem using perturbation method for artificial ground freezing. In *Proceedings of the 27th Canadian Congress of Applied Mechanics (CANCAM)*. 2019.

Research Theme II - Renewable heating and cooling with spray freezing

13) M. Mohit, **M. Xu**, and A. Sasmito. Parametric studies of spray characteristics on the performance of spray freezing for sub-artic mine air heating. In *Proceedings of the 28th International Mining Congress and Exhibition (IMCET)*. 2023.

14) M. Mohit, S. Akhtar, **M. Xu**, and A. Sasmito. Incorporating droplet dynamics to improve the reduced-order model of spray freezing for mine heating applications. In *Underground Ventilation*, pages 569–577. CRC Press, 2023.

15) **M. Xu**, S. Akhtar, and A. Sasmito. A multiscale modeling framework for droplet solidification using phase field method. In *Proceedings of the 16th International Conference on Heat Transfer, Fluid Mechanics and Thermodynamics (HEFAT)*. 2022.

16) Y. Gao, **M. Xu**, C. Wu, F. Fang, S. Akhtar, A. S. Mujumdar, and A. Sasmito. Experimental and analytical investigations of ice slurry production using spray freezing. In *Proceedings of the 14th International Conference on Applied Energy (ICAE)*. 2022.

17) **M. Xu**, S. Akhtar, and A. P. Sasmito. A heterogeneous nucleation model for supercooled water and sucrose solution droplets under ultra-cold environments. In *ASME International Mechanical Engineering Congress and Exposition*, volume 85673, page V011T11A068. American Society of Mechanical Engineers, 2021.

18) S. Akhtar, **M. Xu**, and A. Sasmito. Spray freezing for mine heating a statistical perspective. In *Mine Ventilation*, pages 357–365. CRC Press, 2021. **[Best Student Paper Award]**

19) S. Akhtar, **M. Xu**, and A. Sasmito. Verification and validation of droplet freezing for convective boundary condition using matched asymptotic perturbation method and computational fluid dynamics. In *ASME 2019 International Mechanical Engineering Congress and Exposition*. American Society of Mechanical Engineers Digital Collection, 2019.

Oral and poster communications

1) **M. Xu**, M. Mohit, L. Chen, L. Jiang, A. P. Sasmito. Development of a modified perturbation solution to the Stefan problem for artificial ground freezing. In *The 6th International Symposium on Mine Safety Science and Engineering (ISMSSE).* August 18-20, 2023, Harbin, China.

2) **M. Xu**. Experimental evaluation of the optimum discharge pressure control of a carbon dioxide direct expansion ground source heat pump (CO2-DX-GSHP) for space heating application. In *CanmetENERGY in Varennes, Natural Resources Canada.* January 30, 2023, Varennes, QC, CA.

3) **M. Xu**, A. F. Zueter, A. P. Sasmito. Development and validation of a space-marching analytical model for selective artificial ground freezing in underground mines. In *Canadian Institute of Mining, Metallurgy and Petroleum (CIM) Convention & EXPO 2022.* May 1-4, 2022, Vancouver, BC, CA.

4) B. Teufel, S. Oh, C. Poitras, C. Ruman, A. Pasco, **M. Xu**, L. Sushama, M. Kumral, A. Sasmito. Sustainable northern landscapes and engineering systems. In *Annual McGill Sustainability Systems Initiative (MSSI) Research Symposium.* October 16, 2019, Montréal, QC, CA.

Bibliography

[1] H. Abdelrahman, H. Refaey, A. Alotaibi, A. A. Abdel-Aziz, and M. Abd Rabbo. Experimental investigations on the thermal performance of an ice storage system using twin concentric helical coil. *Applied Thermal Engineering*, 179:115737, 2020.

[2] S. Akhtar, A. Madiseh, and A. Sasmito. Numerical investigation of a novel phase-change renewable energy system for underground mine heating and cooling. *Refrigeration Science and Technology*, 2018, 2018.

[3] S. Akhtar, M. Xu, M. Mohit, and A. P. Sasmito. A comprehensive review of modeling water solidification for droplet freezing applications. *Renewable and Sustainable Energy Reviews*, 188:113768, 2023.

[4] S. Akhtar, M. Xu, and A. Sasmito. Verification and validation of droplet freezing for convective boundary condition using matched asymptotic perturbation method and computational fluid dynamics. In *ASME International Mechanical Engineering Congress and Exposition*, volume 59452, page V008T09A053. American Society of Mechanical Engineers, 2019.

[5] S. Akhtar, M. Xu, and A. Sasmito. Spray freezing for mine heating a statistical perspective. In *Mine Ventilation*, pages 357–365. CRC Press, 2021.

[6] S. Akhtar, M. Xu, and A. P. Sasmito. Development and validation of a semi-analytical framework for droplet freezing with heterogeneous nucleation and non-linear interface kinetics. *International Journal of Heat and Mass Transfer*, 166:120734, 2021.

[7] S. Akhtar, M. Xu, and A. P. Sasmito. Development and validation of an asymptotic solution for a two-phase stefan problem in a droplet subjected to convective boundary condition. *International Journal of Thermal Sciences*, 164:106923, 2021.

[8] S. Akhtar, M. Xu, and A. P. Sasmito. A novel crystal growth model with nonlinear interface kinetics and curvature effects: Sensitivity analysis and optimization. *Crystal Growth & Design*, 21(6):3251–3265, 2021.

[9] O. A. Alduchov and R. E. Eskridge. Improved magnus form approximation of saturation vapor pressure. *Journal of Applied Meteorology and Climatology*, 35(4):601–609, 1996.

[10] V. Alexiades. *Mathematical modeling of melting and freezing processes.* CRC Press, 1992.

[11] V. Alexiades. *Mathematical modeling of melting and freezing processes.* Routledge, 2018.

[12] H. M. Ali, M. M. Janjua, U. Sajjad, W.-M. Yan, et al. A critical review on heat transfer augmentation of phase change materials embedded with porous materials/foams. *International Journal of Heat and Mass Transfer*, 135:649–673, 2019.

[13] M. Alzoubi, S. A. Ghoreishi-Madiseh, A. P. Sasmito, N. Kunz, and A. Guimaraes. Renewable energy-based artificial ground freezing as an adaptation solution for sustainability of permafrost in post-climate change conditions. In *IOP Conference Series: Earth and Environmental Science*, volume 268, page 012128. IOP Publishing, 2019.

[14] M. A. Alzoubi, A. Madiseh, F. P. Hassani, and A. P. Sasmito. Heat transfer analysis in artificial ground freezing under high seepage: Validation and heatlines visualization. *International Journal of Thermal Sciences*, 139:232–245, 2019.

[15] M. A. Alzoubi, A. Nie-Rouquette, S. A. Ghoreishi-Madiseh, F. P. Hassani, and A. P. Sasmito. On the concept of the freezing-on-demand (FoD) in artificial ground freezing for long-term applications. *International Journal of Heat and Mass Transfer*, 143:118557, 2019.

[16] M. A. Alzoubi, A. Nie-Rouquette, and A. P. Sasmito. Conjugate heat transfer in artificial ground freezing using enthalpy-porosity method: Experiments and model validation. *International Journal of Heat and Mass Transfer*, 126:740–752, 2018.

[17] M. A. Alzoubi, S. Poncet, and A. P. Sasmito. Hybrid artificial ground freezing as a sustainable solution for containing hazardous-waste in critical environmental projects. *Cold Regions Science and Technology*, 192:103401, 2021.

[18] M. A. Alzoubi, M. Xu, F. P. Hassani, S. Poncet, and A. P. Sasmito. Artificial ground freezing: A review of thermal and hydraulic aspects. *Tunnelling and Underground Space Technology*, 104:103534, 2020.

[19] M. A. Alzoubi, A. Zueter, A. Nie-Rouquette, and A. P. Sasmito. Freezing on demand: A new concept for mine safety and energy savings in wet underground mines. *International Journal of Mining Science and Technology*, 29(4):621–627, 2019.

[20] O. B. Andersland and B. Ladanyi. *Frozen ground engineering.* John Wiley & Sons, 2003.

[21] S. Arena, E. Casti, J. Gasia, L. F. Cabeza, and G. Cau. Numerical simulation of a finned-tube lhtes system: influence of the mushy zone constant on the phase change behaviour. *Energy Procedia*, 126:517–524, 2017.

[22] T. Battle. Mathematical modelling of solute segregation in solidifying materials. *International Materials Reviews*, 37(1):249–270, 1992.

[23] N. Beaupere, U. Soupremanien, and L. Zalewski. Experimental measurements of the residual solidification duration of a supercooled sodium acetate trihydrate. *International Journal of Thermal Sciences*, 158:106544, 2020.

[24] T. L. Bergman, T. L. Bergman, F. P. Incropera, D. P. Dewitt, and A. S. Lavine. *Fundamentals of heat and mass transfer*. John Wiley & Sons, 2011.

[25] B. C. Bernstein, T. P. Ratvasky, D. R. Miller, and F. McDonough. Freezing rain as an in-flight icing hazard. Technical report, 2000.

[26] K. W. Biggar, R. Donahue, D. Sego, M. Johnson, and S. Birch. Spray freezing decontamination of tailings water at the colomac mine. *Cold Regions Science and Technology*, 42(2):106–119, 2005.

[27] S. B. Biner et al. *Programming phase-field modeling*. Springer, 2017.

[28] B. K. Biskaborn, S. L. Smith, J. Noetzli, H. Matthes, G. Vieira, D. A. Streletskiy, P. Schoeneich, V. E. Romanovsky, A. G. Lewkowicz, A. Abramov, et al. Permafrost is warming at a global scale. *Nature Communications*, 10(1):264, 2019.

[29] W. J. Boettinger, J. A. Warren, C. Beckermann, and A. Karma. Phase-field simulation of solidification. *Annual Review of Materials Research*, 32(1):163–194, 2002.

[30] J. Bollati, J. Semitiel, and D. A. Tarzia. Heat balance integral methods applied to the one-phase Stefan problem with a convective boundary condition at the fixed face. *Applied Mathematics and Computation*, 331:1–19, 2018.

[31] J. Bollati and D. A. Tarzia. Explicit solution for Stefan problem with latent heat depending on the position and a convective boundary condition at the fixed face using Kummer functions. *arXiv preprint arXiv:1610.09338*, 2016.

[32] J. Bollati and D. A. Tarzia. Exact solution for a two-phase Stefan problem with variable latent heat and a convective boundary condition at the fixed face. *Zeitschrift für Angewandte Mathematik und Physik*, 69(2):38, 2018.

[33] J. Bollati and D. A. Tarzia. Approximate solutions to one-phase stefan-like problems with space-dependent latent heat. *European Journal of Applied Mathematics*, 32(2):337–369, 2021.

[34] K. Boomsma and D. Poulikakos. On the effective thermal conductivity of a three-dimensionally structured fluid-saturated metal foam. *International journal of heat and mass transfer*, 44(4):827–836, 2001.

[35] R. Boussaa, L. Hachani, O. Budenkova, V. Botton, D. Henry, K. Zaidat, H. B. Hadid, and Y. Fautrelle. Macrosegregations in sn-3 wt% pb alloy solidification: Experimental and 3d numerical simulation investigations. *International Journal of Heat and Mass Transfer*, 100:680–690, 2016.

[36] A. C. Briozzo and D. A. Tarzia. An explicit solution for an instantaneous two-phase Stefan problem with nonlinear thermal coefficients. *IMA Journal of Applied Mathematics*, 67(3):249–261, 2002.

[37] F. Brosa Planella, C. P. Please, and R. A. Van Gorder. Instability in the self-similar motion of a planar solidification front. *IMA Journal of Applied Mathematics*, 83(1):106–130, 2018.

[38] F. Brosa Planella, C. P. Please, and R. A. Van Gorder. Extended Stefan problem for solidification of binary alloys in a finite planar domain. *SIAM Journal on Applied Mathematics*, 79(3):876–913, 2019.

[39] F. Brosa Planella, C. P. Please, and R. A. Van Gorder. Extended Stefan problem for the solidification of binary alloys in a sphere. *European Journal of Applied Mathematics*, page 1–38, 2020.

[40] J. Broughton, G. Gilmer, and K. A. Jackson. Crystallization rates of a lennard-jones liquid. *Physical Review Letters*, 49(20):1496, 1982.

[41] L. F. Cabeza, A. Castell, C. Barreneche, A. De Gracia, and A. I. Fernández. Materials used as PCM in thermal energy storage in buildings: A review. *Renewable and Sustainable Energy Reviews*, 15(3):1675–1695, 2011.

[42] Z. Cai, Y. Zhang, J. Li, Y. Shang, H. Huo, J. Feng, S. S. Funari, and S. Jiang. Temperature-dependent selective crystallization behavior of isotactic polypropylene with a β-nucleating agent. *Journal of Applied Polymer Science*, 128(1):628–635, 2013.

[43] J. Caldwell and Y. Kwan. On the perturbation method for the Stefan problem with time-dependent boundary conditions. *International Journal of Heat and Mass Transfer*, 46(8):1497–1501, 2003.

[44] J. Caldwell and Y.-Y. Kwan. A brief review of several numerical methods for one-dimensional Stefan problems. *Thermal Science*, 13(2):61–72, 2009.

[45] D. Calì, T. Osterhage, R. Streblow, and D. Müller. Energy performance gap in refurbished german dwellings: Lesson learned from a field test. *Energy and buildings*, 127:1146–1158, 2016.

[46] H. B. Callen. Thermodynamics and an introduction to thermostatistics. *John Wiley & Sons, New York*, 1960.

[47] M. Calvo-Schwarzwälder. Non-local effects and size-dependent properties in Stefan problems with Newton cooling. *Applied Mathematical Modelling*, 76:513–525, 2019.

[48] M. Calvo-Schwarzwälder, T. G. Myers, and M. G. Hennessy. The one-dimensional Stefan problem with non-Fourier heat conduction. *International Journal of Thermal Sciences*, 150:106210, 2020.

[49] E. Canzian, F. Santiago, A. B. Lopes, and A. Barañano. Spherical solidification: An application of the integral methods. *International Journal of Thermal Sciences*, 177:107575, 2022.

[50] E. Canzian, F. Santiago, A. B. Lopes, M. Barbosa, and A. Barañano. On the application of the double integral method with quadratic temperature profile for spherical solidification of lead and tin metals. *Applied Thermal Engineering*, 219:119528, 2023.

[51] Y. Cao, W. Tan, and Z. Wu. Aircraft icing: An ongoing threat to aviation safety. *Aerospace Science and Technology*, 75:353–385, 2018.

[52] T. Carozzani, C.-A. Gandin, H. Digonnet, M. Bellet, K. Zaidat, and Y. Fautrelle. Direct simulation of a solidification benchmark experiment. *Metallurgical and Materials Transactions A*, 44:873–887, 2013.

[53] H. S. Carslaw and J. C. Jaeger. Conduction of heat in solids. *Oxford: Clarendon Press, 1959, 2nd ed.*, 1959.

[54] H. S. Carslaw and J. C. Jaeger. *Conduction of heat in solids.* Clarendon press, 1992.

[55] I. S. Carvalho, R. M. Cotta, C. P. Naveira-Cotta, and M. K. Tiwari. Hybrid integral transform analysis of supercooled droplets solidification. *Proceedings of the Royal Society A*, 477(2248):20200874, 2021.

[56] A. S. Casparian and G. Sirokman. *Applied Chemistry for Environmental Engineering.* Momentum Press, 2016.

[57] A. N. Ceretani, N. N. Salva, and D. A. Tarzia. Approximation of the modified error function. *Applied Mathematics and Computation*, 337:607–617, 2018.

[58] A. N. Ceretani, N. N. Salva, and D. A. Tarzia. An exact solution to a Stefan problem with variable thermal conductivity and a Robin boundary condition. *Nonlinear Analysis: Real World Applications*, 40:243–259, 2018.

[59] C. Chan and F. Tan. Solidification inside a sphere—an experimental study. *International Communications in Heat and Mass Transfer*, 33(3):335–341, 2006.

[60] P. Chandrasekaran, M. Cheralathan, and R. Velraj. Effect of fill volume on solidification characteristics of di (deionized) water in a spherical capsule–an experimental study. *Energy*, 90:508–515, 2015.

[61] P. Chandrasekaran, M. Cheralathan, and R. Velraj. Influence of the size of spherical capsule on solidification characteristics of DI (deionized water) water for a cool thermal energy storage system–an experimental study. *Energy*, 90:807–813, 2015.

[62] S. Chang, H. Qi, S. Zhou, and Y. Yang. Experimental study on freezing characteristics of water droplets on cold surfaces. *International Journal of Heat and Mass Transfer*, 194:123108, 2022.

[63] S. Chang, H. Qi, S. Zhou, and Y. Yang. Experimental and numerical study on freezing process of water droplets under surfaces with different wettability. *Applied Thermal Engineering*, 219:119516, 2023.

[64] G. Chaudhary and R. Li. Freezing of water droplets on solid surfaces: An experimental and numerical study. *Experimental Thermal and Fluid Science*, 57:86–93, 2014.

[65] V. Chaurasiya, R. Kumar Chaudhary, A. Wakif, and J. Singh. A one-phase stefan problem with size-dependent thermal conductivity and moving phase change material under the most generalized boundary condition. *Waves in Random and Complex Media*, pages 1–29, 2022.

[66] V. Chaurasiya and J. Singh. An analytical study of coupled heat and mass transfer freeze-drying with convection in a porous half body: A moving boundary problem. *Journal of Energy Storage*, 55:105394, 2022.

[67] V. Chaurasiya, S. Upadhyay, K. N. Rai, and J. Singh. A new look in heat balance integral method to a two-dimensional stefan problem with convection. *Numerical Heat Transfer, Part A: Applications*, 82(9):529–542, 2022.

[68] V. Chaurasiya, A. Wakif, N. A. Shah, and J. Singh. A study on cylindrical moving boundary problem with variable thermal conductivity and convection under the most realistic boundary conditions. *International Communications in Heat and Mass Transfer*, 138:106312, 2022.

[69] S. Chen, B. Merriman, S. Osher, and P. Smereka. A simple level set method for solving stefan problems. *Journal of Computational Physics*, 135(1):8–29, 1997.

[70] X. D. Chen and P. Chen. Freezing of aqueous solution in a simple apparatus designed for measuring freezing point. *Food Research International*, 29(8):723–729, 1996.

[71] Z. Chen, C. Shu, Y. Liu, L. Zhang, Z. Zhang, and Z. Yuan. Isotherm-evolution-based interface tracking algorithm for modelling temperature-driven solid-liquid phase-change in multiphase flows. *International Journal of Thermal Sciences*, 177:107541, 2022.

[72] L. Chun, M. Sha, Z. Naijun, L. Zhiqiang, and S. Wenjun. Real-time observation of the freezing stage of the mannitol solution using high-resolution optical microscopy. *International Journal of Thermal Sciences*, 188:108225, 2023.

[73] E. Clouet. Modeling of nucleation processes. *arXiv preprint arXiv:1001.4131*, 2010.

[74] S. Coriell, S. Hardy, and R. Sekerka. A non-linear analysis of experiments on the morphological stability of ice cylinders freezing from aqueous solutions. *Journal of Crystal Growth*, 11(1):53–67, 1971.

[75] Q. Dang, M. Song, C. Dang, T. Zhan, and L. Zhang. Experimental study on solidification characteristics of sessile urine droplets on a horizontal cold plate surface under natural convection. *Langmuir*, 38(25):7846–7857, 2022.

[76] Q. Dang, M. Song, X. Zhang, L. Zhang, K. Shao, and J. Shen. Experimental study about solidification processes of sessile deformed water droplets on the biaxial inclined

cold plate surface under natural convection. *Applied Thermal Engineering*, 236:121883, 2024.

[77] S. P. Das. *Statistical physics of liquids at freezing and beyond*. Cambridge University Press, 2011.

[78] T. A. Dauzhenka and I. A. Gishkeluk. Quasilinear heat equation in three dimensions and Stefan problem in permafrost soils in the frame of alternating directions finite difference scheme. In *Proceedings of the World Congress on Engineering*, volume 1, pages 3–5, 2013.

[79] D. S. de Oliveira and F. B. Ribeiro. Heat conduction equation solution in the presence of a change of state in a bounded axisymmetric cylindrical domain. *ASME Journal of Heat Transfer*, 133(6), 2011.

[80] P. Debenedetti. Metastable liquids princeton university press, 1997.

[81] L.-T. Deck, D. R. Ochsenbein, and M. Mazzotti. Stochastic shelf-scale modeling framework for the freezing stage in freeze-drying processes. *International Journal of Pharmaceutics*, 613:121276, 2022.

[82] A. Dehghani-Sanij, S. MacLachlan, G. Naterer, Y. Muzychka, R. Haynes, and V. Enjilela. Multistage cooling and freezing of a saline spherical water droplet. *International Journal of Thermal Sciences*, 147:106095, 2020.

[83] A. Delgado and D.-W. Sun. Heat and mass transfer models for predicting freezing processes–a review. *Journal of Food Engineering*, 47(3):157–174, 2001.

[84] X. Deng, S. Pan, Z. Wang, K. Ke, and J. Zhang. Application of the Darcy-Stefan model to investigate the thawing subsidence around the wellbore in the permafrost region. *Applied Thermal Engineering*, 156:392–401, 2019.

[85] H. Ding, Y. Tian, C. Wen, C. Wang, and C. Sun. Polydispersed droplet spectrum and exergy analysis in wet steam flows using method of moments. *Applied Thermal Engineering*, 182:116148, 2021.

[86] P. Ding and Z. Liu. Accelerating phase-field modeling of solidification with a parallel adaptive computational domain approach. *International Communications in Heat and Mass Transfer*, 111:104452, 2020.

[87] A. Ditkowski and Y. Harness. High-order embedded finite difference schemes for initial boundary value problems on time dependent irregular domains. *Journal of Scientific Computing*, 39:394–440, 2009.

[88] W. Dobinski. Permafrost. *Earth-Science Reviews*, 108(3-4):158–169, 2011.

[89] F. I. Dragomirescu, K. Eisenschmidt, C. Rohde, and B. Weigand. Perturbation solutions for the finite radially symmetric stefan problem. *International Journal of Thermal Sciences*, 104:386–395, 2016.

[90] Y. Du, M. Zhang, A. S. Mujumdar, W. Liu, and C. Yang. Innovative applications of freeze-drying to produce compound formula instant foods: A review. *Drying Technology*, 40(13):2583–2597, 2022.

[91] D. A. Edwards and M. E. Mackay. Postextrusion heating in three-dimensional printing. *ASME Journal of Heat Transfer*, 142(5), 2020.

[92] R. I. ElGhnam, R. A. Abdelaziz, M. H. Sakr, and H. E. Abdelrhman. An experimental study of freezing and melting of water inside spherical capsules used in thermal energy storage systems. *Ain Shams Engineering Journal*, 3(1):33–48, 2012.

[93] A. Erek and I. Dincer. Numerical heat transfer analysis of encapsulated ice thermal energy storage system with variable heat transfer coefficient in downstream. *International Journal of Heat and Mass Transfer*, 52(3-4):851–859, 2009.

[94] M. C. Erickson and Y.-C. Hung. *Quality in frozen food.* Springer Science & Business Media, 2012.

[95] M. Faden, A. König-Haagen, and D. Brüggemann. An optimum enthalpy approach for melting and solidification with volume change. *Energies*, 12(5):868, 2019.

[96] K. Fan, M. Zhang, and A. S. Mujumdar. Recent developments in high efficient freeze-drying of fruits and vegetables assisted by microwave: A review. *Critical Reviews in Food Science and Nutrition*, 59(8):1357–1366, 2019.

[97] L. Fan and J. Khodadadi. A theoretical and experimental investigation of unidirectional freezing of nanoparticle-enhanced phase change materials. *ASME Journal of Heat Transfer*, 134(9), 2012.

[98] T.-H. Fan, J.-Q. Li, B. Minatovicz, E. Soha, L. Sun, S. Patel, B. Chaudhuri, and R. Bogner. Phase-field modeling of freeze concentration of protein solutions. *Polymers*, 11(1):10, 2018.

[99] M. M. Farid, A. M. Khudhair, S. A. K. Razack, and S. Al-Hallaj. A review on phase change energy storage: materials and applications. *Energy Conversion and Management*, 45(9-10):1597–1615, 2004.

[100] M. Farzaneh. *Atmospheric icing of power networks.* Springer Science & Business Media, 2008.

[101] D. L. Feltham and J. Garside. Analytical and numerical solutions describing the inward solidification of a binary melt. *Chemical Engineering Science*, 56(7):2357–2370, 2001.

[102] D. Fisher and W. Kurz. Fundamentals of solidification. *Fundamentals of Solidification*, pages 1–316, 1998.

[103] D. Fisher, M. Rappaz, and W. Kurz. Fundamentals of solidification. *Fundamentals of Solidification*, pages 1–353, 2023.

[104] A. S. Fleischer. *Thermal energy storage using phase change materials: fundamentals and applications*. Springer, 2015.

[105] B. Florio and T. Myers. The melting and solidification of nanowires. *Journal of Nanoparticle Research*, 18(6):168, 2016.

[106] F. Font. A one-phase Stefan problem with size-dependent thermal conductivity. *Applied Mathematical Modelling*, 63:172–178, 2018.

[107] F. Font, T. Myers, and S. Mitchell. A mathematical model for nanoparticle melting with density change. *Microfluidics and Nanofluidics*, 18(2):233–243, 2015.

[108] J. D. Ford, N. Couture, T. Bell, and D. G. Clark. Climate change and Canada's north coast: Research trends, progress, and future directions. *Environmental Reviews*, 26(1):82–92, 2018.

[109] A. Galfré, X. Huang, F. Couenne, and C. Cogné. The phase field method—from fundamentals to practical applications in crystal growth. *Journal of Crystal Growth*, page 127334, 2023.

[110] J. Gao, Y. Chan, T. Hou, and Y. Ren. Quasi-equilibrium approximation of the solidification process for micro phase change materials taking into account curvature and surface tension. *International Journal of Thermal Sciences*, 184:107916, 2023.

[111] Y. Gao, J. Luo, F. Fang, M. Xu, M. Mohit, T. Shamim, and A. P. Sasmito. On the stability of nanofluid ice slurry produced via impinging stream method under thermal and phase-change cycles. *Case Studies in Thermal Engineering*, 52:103725, 2023.

[112] Y. Gao, Y. Ning, C. Wu, M. Xu, S. Akhtar, A. S. Mujumdar, and A. P. Sasmito. Experimental investigation of producing ice slurry with water using opposed-nozzle impinging jet method. *Applied Thermal Engineering*, 219:119568, 2023.

[113] Y. Gao, Y. Ning, C. Wu, M. Xu, S. Akhtar, A. S. Mujumdar, and A. P. Sasmito. Experimental investigation of producing ice slurry with water using opposed-nozzle impinging jet method. *Applied Thermal Engineering*, 219:119568, 2023.

[114] Y. Gao, Y. Ning, M. Xu, C. Wu, A. S. Mujumdar, and A. P. Sasmito. Numerical investigation of aqueous graphene nanofluid ice slurry passing through a horizontal circular pipe: Heat transfer and fluid flow characteristics. *International Communications in Heat and Mass Transfer*, 134:106022, 2022.

[115] Y. Gao, Y. Ren, M. Xu, J. Liu, A. S. Mujumdar, and A. P. Sasmito. Influence of thermal cycling on stability and thermal conductivity of nanofluid ice slurry. *International Journal of Thermal Sciences*, 185:108113, 2023.

[116] S. A. Ghoreishi-Madiseh, A. F. Kuyuk, H. Kalantari, and A. P. Sasmito. Ice versus battery storage; a case for integration of renewable energy in refrigeration systems of remote sites. *Energy Procedia*, 159:60–65, 2019.

[117] T. S. Glickman. *Glossary of meteorology.* American Meteorological Soc., 2000.

[118] T. Gong, Y. Chen, S. Li, Y. Cao, D. Li, X.-Q. Chen, G. Reinhart, and H. Nguyen-Thi. Revisiting dynamics and models of microsegregation during polycrystalline solidification of binary alloy. *Journal of Materials Science & Technology*, 74:155–167, 2021.

[119] T. R. Goodman. The heat balance integral and its application to problems involving change of phase. *ASME Journal of Heat Transfer*, 80:335, 1958.

[120] M. Gortych, Z. Lipnicki, and B. Weigand. An experimental and theoretical study of the solidification process of phase change materials in a horizontal annular enclosure. *Applied Thermal Engineering*, 161:114140, 2019.

[121] M. H. Grabow, G. H. Gilmer, and A. F. Bakker. Molecular dynamics studies of silicon solidification and melting. *MRS Online Proceedings Library*, 141:349–354, 1988.

[122] L. Gránásy, T. Pusztai, and P. F. James. Interfacial properties deduced from nucleation experiments: A Cahn–Hilliard analysis. *The Journal of Chemical Physics*, 117(13):6157–6168, 2002.

[123] D. W. Green and M. Z. Southard. *Perry's Chemical Engineers' Handbook*. McGraw-Hill Education, 2019.

[124] L. Guo, Z. Zhang, X. Wang, Q. Yu, Y. You, C. Yuan, Y. Xie, and T. Gou. Stability analysis of transmission tower foundations in permafrost equipped with thermosiphons and vegetation cover on the Qinghai-Tibet Plateau. *International Journal of Heat and Mass Transfer*, 121:367–376, 2018.

[125] S. C. Gupta. *The classical Stefan problem: Basic concepts, modelling and analysis with quasi-analytical solutions and methods*, volume 45. Elsevier, 2017.

[126] L. Hachani, B. Saadi, X. D. Wang, A. Nouri, K. Zaidat, A. Belgacem-Bouzida, L. Ayouni-Derouiche, G. Raimondi, and Y. Fautrelle. Experimental analysis of the solidification of Sn–3 wt.% Pb alloy under natural convection. *International Journal of Heat and Mass Transfer*, 55(7-8):1986–1996, 2012.

[127] L. Hachani, K. Zaidat, and Y. Fautrelle. Experimental study of the solidification of Sn–10 wt.% Pb alloy under different forced convection in benchmark experiment. *International Journal of Heat and Mass Transfer*, 85:438–454, 2015.

[128] D. W. Hahn and M. N. Özisik. *Heat conduction*. John Wiley & Sons, 2012.

[129] H. A. Hamzeh and M. Miansari. Numerical study of tube arrangement and fin effects on improving the ice formation in ice-on-coil thermal storage systems. *International Communications in Heat and Mass Transfer*, 113:104520, 2020.

[130] Y. Hanawa, Y. Sasaki, S. Uchida, T. Funayoshi, M. Otsuji, H. Takahashi, and A. Sakuma. Thermomechanical formulation of freezing point depression behavior of liquid on solid surface with nanostructure. In *ASME International Mechanical Engineering Congress and Exposition*, volume 84591, page V011T11A014. American Society of Mechanical Engineers, 2020.

[131] Y. Hanawa, J. Zhang, A. P. Sasmito, M. Xu, S. Akhtar, M. Mohit, J. Yoshida, K. Sawada, Y. Sasaki, and A. Sakuma. Kinetics formulation for two-dimensional growth behavior of water/ice interface on si substrate. *Langmuir*, 2024.

[132] Y. Hanawa, J. Zhang, A. P. Sasmito, M. Xu, S. Akhtar, M. Mohit, J. Yoshida, K. Sawada, Y. Sasaki, and A. Sakuma. New formulas for evaluation of cyclohexanol solidification on substrates with surface nanostructures. *ACS Omega*, 2024.

[133] J. Hao, P. Jia, T. Wu, W. Li, J. Chen, X. Yang, X. Wu, G. Hu, K. Cui, and M. Zhang. Numerical analysis of the impacts of rainfall on permafrost-related slope stability on the qinghai–tibet plateau. *Journal of Hydrology: Regional Studies*, 47:101439, 2023.

[134] M. G. Hennessy, M. Calvo-Schwarzwälder, and T. G. Myers. Modelling ultra-fast nanoparticle melting with the Maxwell-Cattaneo equation. *Applied Mathematical Modelling*, 69:201–222, 2019.

[135] M. G. Hennessy, M. C. Schwarzwälder, and T. G. Myers. Asymptotic analysis of the guyer–krumhansl–stefan model for nanoscale solidification. *Applied Mathematical Modelling*, 61:1–17, 2018.

[136] L. A. Herraiz, M. A. Herrero, and J. J. Velázquez. A note on the dissolution of spherical crystals. *Proceedings of the Royal Society of Edinburgh Section A: Mathematics*, 131(2):371–389, 2001.

[137] J. M. Hill. *One-dimensional Stefan problems: An introduction.* Longman Scientific & Technical, 1987.

[138] J. Hindmarsh, A. Russell, and X. Chen. Experimental and numerical analysis of the temperature transition of a freezing food solution droplet. *Chemical Engineering Science*, 59(12):2503–2515, 2004.

[139] J. Hindmarsh, A. Russell, and X. Chen. Fundamentals of the spray freezing of foods—microstructure of frozen droplets. *Journal of Food Engineering*, 78(1):136–150, 2007.

[140] J. Hindmarsh, A. Russell, and X. Chen. Observation of the surface and volume nucleation phenomena in undercooled sucrose solution droplets. *The Journal of Physical Chemistry C*, 111(16):5977–5981, 2007.

[141] J. Hindmarsh, A. Russell, and X. D. Chen. Measuring dendritic growth in undercooled sucrose solution droplets. *Journal of Crystal Growth*, 285(1-2):236–248, 2005.

[142] J. P. Hindmarsh, A. B. Russell, and X. D. Chen. Experimental and numerical analysis of the temperature transition of a suspended freezing water droplet. *International Journal of Heat and Mass Transfer*, 46(7):1199–1213, 2003.

[143] P. V. Hobbs. *Ice physics*. OUP Oxford, 2010.

[144] F. Hong and H.-H. Qiu. Experimental study on rapid solidification process using a novel ultrasound technique. *Experimental Thermal and Fluid Science*, 30(1):17–26, 2005.

[145] J. Hunt and K. Jackson. Binary eutectic solidification. *Transactions of the Metallurgical Society of AIME*, 236(6):843, 1966.

[146] M. J. Hunt, F. Brosa Planella, F. Theil, and W. D. Widanage. Derivation of an effective thermal electrochemical model for porous electrode batteries using asymptotic homogenisation. *Journal of Engineering Mathematics*, 122:31–57, 2020.

[147] A. Ihsan, W. van Horssen, and J. Tuwankotta. On a multiple timescales perturbation approach for a Stefan problem with a time-dependent heat flux at the boundary. *Nonlinear Dynamics*, 110(3):2673–2683, 2022.

[148] F. P. Incropera, D. P. DeWitt, T. L. Bergman, A. S. Lavine, et al. *Fundamentals of heat and mass transfer*, volume 6. Wiley New York, 1996.

[149] S. P. Ishwarya, C. Anandharamakrishnan, and A. G. Stapley. Spray-freeze-drying: A novel process for the drying of foods and bioproducts. *Trends in Food Science & Technology*, 41(2):161–181, 2015.

[150] K. Ismail, C. Alves, and M. Modesto. Numerical and experimental study on the solidification of pcm around a vertical axially finned isothermal cylinder. *Applied Thermal Engineering*, 21(1):53–77, 2001.

[151] G. Ivantsov. Temperature field around a spherical, cylindrical, and needle-shaped crystal, growing in a pre-cooled melt. *Temperature Field Around a Spherical*, 58:567–569, 1985.

[152] M. A. Jaafar, D. R. Rousse, S. Gibout, and J.-P. Bédécarrats. A review of dendritic growth during solidification: Mathematical modeling and numerical simulations. *Renewable and Sustainable Energy Reviews*, 74:1064–1079, 2017.

[153] K. A. Jackson. The interface kinetics of crystal growth processes. *Interface Science*, 10(2):159–169, 2002.

[154] K. A. Jackson. *Kinetic Processes: Crystal growth, diffusion, and phase transformations in materials*. John Wiley & Sons, 2006.

[155] K. A. Jackson. *Kinetic processes: Crystal growth, diffusion, and phase transitions in materials.* John Wiley & Sons, 2010.

[156] A. Jain and M. Parhizi. Conditionally exact closed-form solution for moving boundary problems in heat and mass transfer in the presence of advection. *International Journal of Heat and Mass Transfer*, 180:121802, 2021.

[157] E. Jakubowska and J. Lulek. The application of freeze-drying as a production method of drug nanocrystals and solid dispersions–a review. *Journal of Drug Delivery Science and Technology*, 62:102357, 2021.

[158] H. Jannesari and N. Abdollahi. Experimental and numerical study of thin ring and annular fin effects on improving the ice formation in ice-on-coil thermal storage systems. *Applied Energy*, 189:369–384, 2017.

[159] L. M. Jiji and S. Weinbaum. Perturbation solutions for melting or freezing in annular regions initially not at the fusion temperature. *International Journal of Heat and Mass Transfer*, 21(5):581–592, 1978.

[160] Z. Jin, H. Zhang, and Z. Yang. Experimental investigation of the impact and freezing processes of a water droplet on an ice surface. *International Journal of Heat and Mass Transfer*, 109:716–724, 2017.

[161] L. Karlsson, H. Lycksam, A.-L. Ljung, P. Gren, and T. S. Lundström. Experimental study of the internal flow in freezing water droplets on a cold surface. *Experiments in Fluids*, 60:1–10, 2019.

[162] M. Kaviany. *Principles of heat transfer in porous media.* Springer Science & Business Media, 2012.

[163] M. Z. Khalid, M. Zubair, and M. Ali. An analytical method for the solution of two phase Stefan problem in cylindrical geometry. *Applied Mathematics and Computation*, 342:295–308, 2019.

[164] A. Khalifa, L. Tan, A. Date, and A. Akbarzadeh. A numerical and experimental study of solidification around axially finned heat pipes for high temperature latent heat thermal energy storage units. *Applied Thermal Engineering*, 70(1):609–619, 2014.

[165] L. Khatra and H. El Qarnia. Semianalytical solution for pcm solidification during the discharging of a planar thermal energy accumulator. *International Journal of Energy Research*, 43(13):7573–7582, 2019.

[166] H. Kiani, Z. Zhang, and D.-W. Sun. Experimental analysis and modeling of ultrasound assisted freezing of potato spheres. *Ultrasonics Sonochemistry*, 26:321–331, 2015.

[167] M.-H. Kim, H. Kim, K.-S. Lee, and D. R. Kim. Frosting characteristics on hydrophobic and superhydrophobic surfaces: A review. *Energy Conversion and Management*, 138:1–11, 2017.

[168] J. King and D. Riley. Asymptotic solutions to the stefan problem with a constant heat source at the moving boundary. *Proceedings of the Royal Society of London. Series A: Mathematical, Physical and Engineering Sciences*, 456(1997):1163–1174, 2000.

[169] R. Kobayashi. Modeling and numerical simulations of dendritic crystal growth. *Physica D: Nonlinear Phenomena*, 63(3-4):410–423, 1993.

[170] R. Kobayashi. A numerical approach to three-dimensional dendritic solidification. *Experimental Mathematics*, 3(1):59–81, 1994.

[171] S. Koga, M. Diagne, and M. Krstic. Control and state estimation of the one-phase Stefan problem via backstepping design. *IEEE Transactions on Automatic Control*, 64(2):510–525, 2018.

[172] S. Koga and M. Krstic. *Materials Phase Change PDE Control & Estimation: From Additive Manufacturing to Polar Ice.* Springer Nature, 2020.

[173] J. Kozak and T. Zakrzewski. Accuracy problems of additive manufacturing using SLS/SLM processes. In *AIP Conference Proceedings*, volume 2017, page 020010. AIP Publishing LLC, 2018.

[174] A. Kubica and K. Ryszewska. A self-similar solution to time-fractional Stefan problem. *Mathematical Methods in the Applied Sciences*, 44(6):4245–4275, 2021.

[175] A. Kucera and J. M. Hill. On inward solidifying cylinders and spheres initially not at their fusion temperature. *International Journal of Non-linear Mechanics*, 21(1):73–82, 1986.

[176] A. Kumar. A Stefan problem with moving phase change material, variable thermal conductivity and periodic boundary condition. *Applied Mathematics and Computation*, 386:125490, 2020.

[177] A. Kumar, Rajeev, and J. Gómez-Aguilar. A numerical solution of a non-classical stefan problem with space-dependent thermal conductivity, variable latent heat and robin

boundary condition. *Journal of Thermal Analysis and Calorimetry*, 147(24):14649–14657, 2022.

[178] A. Kumar, M. J. Walker, S. Sundarraj, and P. Dutta. Grain floatation during equiaxed solidification of an al-cu alloy in a side-cooled cavity: Part i—experimental studies. *Metallurgical and Materials Transactions B*, 42:825–836, 2011.

[179] B. L. Kurylyk. Discussion of 'a simple thaw-freeze algorithm for a multi-layered soil using the Stefan equation' by Xie and Gough (2013). *Permafrost and Periglacial Processes*, 26(2):200–206, 2015.

[180] J. Kyselica, P. Guba, and M. Chudjak. Recalescence dynamics and solidification of a supercooled melt in a finite domain. *International Journal of Heat and Mass Transfer*, 159:120048, 2020.

[181] L. S. Lam, K. R. Sultana, K. Pope, and Y. Muzychka. Effect of thermal transport on solidification of salt and freshwater water droplets on marine surfaces. *International Journal of Heat and Mass Transfer*, 153:119452, 2020.

[182] G. Lamé and B. Clapeyron. Mémoire sur la solidification par refroidissement d'un globe liquide. In *Annales Chimie Physique*, volume 47, pages 250–256, 1831.

[183] F. Lamraoui, G. Fortin, R. Benoit, J. Perron, and C. Masson. Atmospheric icing impact on wind turbine production. *Cold Regions Science and Technology*, 100:36–49, 2014.

[184] J. Langer. Dendritic sidebranching in the three-dimensional symmetric model in the presence of noise. *Physical Review A*, 36(7):3350, 1987.

[185] J. Langer and H. Müller-Krumbhaar. Theory of dendritic growth—i. elements of a stability analysis. *Acta Metallurgica*, 26(11):1681–1687, 1978.

[186] J. Langer and J. Müller-Krumbhaar. Stability effects in dendritic crystal growth. *Journal of Crystal Growth*, 42:11–14, 1977.

[187] J. Langer, R. Sekerka, and T. Fujioka. Evidence for a universal law of dendritic growth rates. *Journal of Crystal Growth*, 44(4):414–418, 1978.

[188] M. Le Maguer. Mechanics and influence of water binding on water activity. In *Water Activity*, pages 1–25. Routledge, 2017.

[189] J. Lee and G. Son. A sharp-interface level-set method for compressible bubble growth with phase change. *International Communications in Heat and Mass Transfer*, 86:1–11, 2017.

[190] A. Léoni, M. Mondot, F. Durier, R. Revellin, and P. Haberschill. State-of-the-art review of frost deposition on flat surfaces. *International Journal of Refrigeration*, 68:198–217, 2016.

[191] A. G. Lewkowicz and R. G. Way. Extremes of summer climate trigger thousands of thermokarst landslides in a high arctic environment. *Nature communications*, 10(1):1329, 2019.

[192] G.-y. Li, J. Zhang, Z.-w. Zhou, F. Wang, D. Chen, Y.-p. Cao, and G. Wu. A novel freezing point determination method for oil–contaminated soils based on electrical resistance measurement and its influencing factors. *Science of the Total Environment*, 721:137821, 2020.

[193] S. Li, Z. Liu, and X. Wang. A comprehensive review on positive cold energy storage technologies and applications in air conditioning with phase change materials. *Applied Energy*, 255:113667, 2019.

[194] K. G. Libbrecht. The physics of snow crystals. *Reports on Progress in Physics*, 68(4):855, 2005.

[195] K. G. Libbrecht. Physical dynamics of ice crystal growth. *Annual Review of Materials Research*, 47:271–295, 2017.

[196] D. R. Lide. Handbook of chemistry and physics, 1999.

[197] D. R. Lide. *CRC handbook of chemistry and physics*, volume 85. CRC press, 2004.

[198] Z. Lipnicki, D. Sasse, and B. Weigand. Experimental and analytical investigation of the solidification around cooled cylinders subjected to free convection. *International Journal of Heat and Mass Transfer*, 78:321–329, 2014.

[199] Z. Lipnicki and B. Weigand. An experimental and theoretical study of solidification in a free-convection flow inside a vertical annular enclosure. *International Journal of Heat and Mass Transfer*, 55(4):655–664, 2012.

[200] Z. Lipnicki, B. Weigand, T. Małolepszy, and P. Grabas. An experimental and analytical study of solidification around an array of horizontal cylinders subjected to free convection flow. *International Journal of Thermal Sciences*, 173:107378, 2022.

[201] Y. Liu, T. Ming, Y. Wu, R. de Richter, Y. Fang, and N. Zhou. Desalination of seawater by spray freezing in a natural draft tower. *Desalination*, 496:114700, 2020.

[202] Z. Liu, F. Lou, X. Qi, Q. Wang, B. Zhao, J. Yan, and Y. Shen. Experimental study on cold storage phase-change materials and quick-freezing plate in household refrigerators. *Journal of Food Process Engineering*, 42(7):e13279, 2019.

[203] Z. Liu, X. Sun, and C. Ma. Experimental study of the characteristics of solidification of stearic acid in an annulus and its thermal conductivity enhancement. *Energy Conversion and Management*, 46(6):971–984, 2005.

[204] G. S. H. Lock. *Latent heat transfer: an introduction to fundamentals.* Oxford University Press, 1994.

[205] M. P. Longinotti and H. R. Corti. Viscosity of concentrated sucrose and trehalose aqueous solutions including the supercooled regime. *Journal of Physical and Chemical Reference Data*, 37(3):1503–1515, 2008.

[206] J. López, P. Gómez, and J. Hernández. A volume of fluid approach for crystal growth simulation. *Journal of Computational Physics*, 229(19):6663–6672, 2010.

[207] V. J. Lunardini. *Heat transfer in cold climates.* Van Nostrand Reinhold Co, 1981.

[208] C. Lusena. Ice propagation in systems of biological interest. III. effect of solutes on nucleation and growth of ice crystals. *Archives of Biochemistry and Biophysics*, 57(2):277–284, 1955.

[209] D. A. Maccarthy and N. Fabre. Thermal conductivity of sucrose. *Food properties and computer-aided engineering of food processing systems*, pages 105–111, 1989.

[210] M. M. MacDevette and T. G. Myers. Contact melting of a three-dimensional phase change material on a flat substrate. *International Journal of Heat and Mass Transfer*, 55(23-24):6798–6807, 2012.

[211] J. M. Mahdi and E. C. Nsofor. Melting enhancement in triplex-tube latent heat energy storage system using nanoparticles-metal foam combination. *Applied Energy*, 191:22–34, 2017.

[212] M. Mathlouthi and P. Reiser. *Sucrose: properties and applications.* Springer Science & Business Media, 1995.

[213] D. Mazzeo and G. Oliveti. Thermal field and heat storage in a cyclic phase change process caused by several moving melting and solidification interfaces in the layer. *International Journal of Thermal Sciences*, 129:462–488, 2018.

[214] S. W. McCue, J. R. King, and D. S. Riley. Extinction behaviour for two–dimensional inward-solidification problems. *Proceedings of the Royal Society of London. Series A: Mathematical, Physical and Engineering Sciences*, 459(2032):977–999, 2003.

[215] S. W. Mccue, J. R. King, and D. S. Riley. The extinction problem for three-dimensional inward solidification. *Journal of Engineering Mathematics*, 52:389–409, 2005.

[216] S. W. McCue, B. Wu, and J. M. Hill. Classical two-phase Stefan problem for spheres. *Proceedings of the Royal Society A: Mathematical, Physical and Engineering Sciences*, 464(2096):2055–2076, 2008.

[217] S. W. McCue, B. Wu, and J. M. Hill. Micro/nanoparticle melting with spherical symmetry and surface tension. *IMA Journal of Applied Mathematics*, 74(3):439–457, 2009.

[218] B. McDonald, P. Patel, and B. Zhao. Droplet freezing and ice adhesion strength measurement on super-cooled hydrophobic surfaces. *The Journal of Adhesion*, 93(5):375–388, 2017.

[219] Z. Meng and P. Zhang. Dynamic propagation of ice-water phase front in a supercooled water droplet. *International Journal of Heat and Mass Transfer*, 152:119468, 2020.

[220] Z. Meng and P. Zhang. Freezing dynamics of supercooled micro-sized water droplets. *International Journal of Heat and Mass Transfer*, 193:122955, 2022.

[221] Mining Association of Canada. The Canadian mining story: Economic impacts and drivers for the global energy transition. `https://mining.ca/flippingbooks/mac-report-2023`, 2023.

[222] S. Mitchell and M. Vynnycky. Verified reduction of a model for a continuous casting process. *Applied Mathematical Modelling*, 48:476–490, 2017.

[223] S. L. Mitchell. Applying the combined integral method to two-phase stefan problems with delayed onset of phase change. *Journal of Computational and Applied Mathematics*, 281:58–73, 2015.

[224] S. L. Mitchell and T. Myers. Improving the accuracy of heat balance integral methods applied to thermal problems with time dependent boundary conditions. *International Journal of Heat and Mass Transfer*, 53(17-18):3540–3551, 2010.

[225] S. L. Mitchell and T. G. Myers. Approximate solution methods for one-dimensional solidification from an incoming fluid. *Applied Mathematics and Computation*, 202(1):311–326, 2008.

[226] S. L. Mitchell and T. G. Myers. Application of standard and refined heat balance integral methods to one-dimensional Stefan problems. *SIAM Review*, 52(1):57–86, 2010.

[227] S. L. Mitchell and M. Vynnycky. On the numerical solution of two-phase Stefan problems with heat-flux boundary conditions. *Journal of Computational and Applied Mathematics*, 264:49–64, 2014.

[228] S. L. Mitchell and M. Vynnycky. On the accurate numerical solution of a two-phase Stefan problem with phase formation and depletion. *Journal of Computational and Applied Mathematics*, 300:259–274, 2016.

[229] O. Miyawaki, T. Abe, and T. Yano. A numerical model to describe freezing of foods when supercooling occurs. *Journal of Food Engineering*, 9(2):143–151, 1989.

[230] M. Mohit, S. Akhtar, M. Xu, and A. Sasmito. Incorporating droplet dynamics to improve the reduced-order model of spray freezing for mine heating applications. In *Underground Ventilation*, pages 569–577. CRC Press, 2023.

[231] A. D. Monde and P. R. Chakraborty. Prediction of cooling curves for controlled unidirectional solidification under the influence of shrinkage: A semi-analytical approach. *Metallurgical and Materials Transactions B*, 49:3306–3316, 2018.

[232] N. O. Moraga and C. H. Salinas. Numerical model for heat and fluid flow in food freezing. *Numerical Heat Transfer: Part A: Applications*, 35(5):495–517, 1999.

[233] M. J. Moran, H. N. Shapiro, D. D. Boettner, and M. B. Bailey. *Fundamentals of Engineering Thermodynamics.* John Wiley & Sons, 2010.

[234] F. Mosally, A. S. Wood, and A. Al-Fhaid. An exponential heat balance integral method. *Applied Mathematics and Computation*, 130(1):87–100, 2002.

[235] A. Mostafavi, M. Parhizi, and A. Jain. Theoretical modeling and optimization of fin-based enhancement of heat transfer into a phase change material. *International Journal of Heat and Mass Transfer*, 145:118698, 2019.

[236] S. Motahar, A. A. Alemrajabi, and R. Khodabandeh. Experimental study on solidification process of a phase change material containing tio2 nanoparticles for thermal energy storage. *Energy Conversion and Management*, 138:162–170, 2017.

[237] A. Muhr and J. Blanshard. Effect of polysaccharide stabilizers on the rate of growth of ice. *International Journal of Food Science & Technology*, 21(6):683–710, 1986.

[238] A. M. Mullis. A free boundary model for shape preserving dendritic growth at high undercooling. *Journal of Applied Physics*, 80(7):4129–4136, 1996.

[239] D. M. Murphy and T. Koop. Review of the vapour pressures of ice and supercooled water for atmospheric applications. *Quarterly Journal of the Royal Meteorological Society: A Journal of the Atmospheric Sciences, Applied Meteorology and Physical Oceanography*, 131(608):1539–1565, 2005.

[240] B. J. Murray, S. Broadley, T. Wilson, J. Atkinson, and R. Wills. Heterogeneous freezing of water droplets containing kaolinite particles. *Atmospheric Chemistry and Physics*, 11(9):4191–4207, 2011.

[241] B. J. Murray and E. J. Jensen. Homogeneous nucleation of amorphous solid water particles in the upper mesosphere. *Journal of atmospheric and solar-terrestrial physics*, 72(1):51–61, 2010.

[242] J. D. Murray. *Asymptotic analysis*, volume 48. Springer Science & Business Media, 2012.

[243] T. Myers. Optimal exponent heat balance and refined integral methods applied to Stefan problems. *International Journal of Heat and Mass Transfer*, 53(5-6):1119–1127, 2010.

[244] T. Myers and S. L. Mitchell. Application of the combined integral method to stefan problems. *Applied Mathematical Modelling*, 35(9):4281–4294, 2011.

[245] T. G. Myers, M. G. Hennessy, and M. Calvo-Schwarzwälder. The Stefan problem with variable thermophysical properties and phase change temperature. *International Journal of Heat and Mass Transfer*, 149:118975, 2020.

[246] C. Naaktgeboren. The zero-phase stefan problem. *International Journal of Heat and Mass Transfer*, 50(23-24):4614–4622, 2007.

[247] A. Najim and S. Krishnan. Experimental study on progressive freeze-concentration based desalination employing a rectangular channel crystallizer. *Environmental Science: Water Research & Technology*, 9(3):850–860, 2023.

[248] A. H. Nayfeh. *Perturbation methods*. John Wiley & Sons, 2008.

[249] A. H. Nayfeh. *Introduction to perturbation techniques*. John Wiley & Sons, 2011.

[250] H. Nazir, M. Batool, F. J. B. Osorio, M. Isaza-Ruiz, X. Xu, K. Vignarooban, P. Phelan, A. M. Kannan, et al. Recent developments in phase change materials for energy storage applications: A review. *International Journal of Heat and Mass Transfer*, 129:491–523, 2019.

[251] B. Nie, A. Palacios, B. Zou, J. Liu, T. Zhang, and Y. Li. Review on phase change materials for cold thermal energy storage applications. *Renewable and Sustainable Energy Reviews*, 134:110340, 2020.

[252] R. Nigo, Y. M. J. Chew, N. Houghton, W. Paterson, and D. Wilson. Experimental studies of freezing fouling of model food fat solutions using a novel spinning disc apparatus. *Energy & fuels*, 23(12):6131–6145, 2009.

[253] C. Nikolopoulos. A model for melting of a pure material during modulated temperature differential scanning calorimetry. *SIAM Journal on Applied Mathematics*, 62(4):1176–1196, 2002.

[254] T. Nishinaga. *Handbook of crystal growth: Fundamentals*. Elsevier, 2014.

[255] B. E. K. Nygaard, J. E. Kristjánsson, and L. Makkonen. Prediction of in-cloud icing conditions at ground level using the wrf model. *Journal of Applied Meteorology and Climatology*, 50(12):2445–2459, 2011.

[256] L. Oberli, D. Caruso, C. Hall, M. Fabretto, P. J. Murphy, and D. Evans. Condensation and freezing of droplets on superhydrophobic surfaces. *Advances in Colloid and Interface Science*, 210:47–57, 2014.

[257] M. Olguin, M. Medina, M. C. Sanziel, and D. A. Tarzia. Behavior of the solution of a stefan problem by changing thermal coefficients of the substance. *Applied Mathematics and Computation*, 190(1):765–780, 2007.

[258] E. Olsson and G. Kreiss. A conservative level set method for two phase flow. *Journal of Computational Physics*, 210(1):225–246, 2005.

[259] E. Olsson, G. Kreiss, and S. Zahedi. A conservative level set method for two phase flow ii. *Journal of Computational Physics*, 225(1):785–807, 2007.

[260] L. Onokoko, M. Poirier, N. Galanis, and S. Poncet. Experimental and numerical investigation of isothermal ice slurry flow. *International Journal of Thermal Sciences*, 126:82–95, 2018.

[261] E. Oró, A. De Gracia, A. Castell, M. M. Farid, and L. F. Cabeza. Review on phase change materials (PCMs) for cold thermal energy storage applications. *Applied Energy*, 99:513–533, 2012.

[262] S. Osher and J. A. Sethian. Fronts propagating with curvature-dependent speed: Algorithms based on Hamilton-Jacobi formulations. *Journal of Computational Physics*, 79(1):12–49, 1988.

[263] Y. Pan, K. Shi, X. Duan, and G. F. Naterer. Experimental investigation of water droplet impact and freezing on micropatterned stainless steel surfaces with varying wettabilities. *International Journal of Heat and Mass Transfer*, 129:953–964, 2019.

[264] P. Papon, J. Leblond, and P. H. Meijer. The physics of phase transitions: Concepts and applications. 2006.

[265] M. Parang, D. Crocker, and B. Haynes. Perturbation solution for spherical and cylindrical solidification by combined convective and radiative cooling. *International Journal of Heat and Fluid Flow*, 11(2):142–148, 1990.

[266] O. Parent and A. Ilinca. Anti-icing and de-icing techniques for wind turbines: Critical review. *Cold Regions Science and Technology*, 65(1):88–96, 2011.

[267] M. Parhizi and A. Jain. Analytical modeling and optimization of phase change thermal management of a Li-ion battery pack. *Applied Thermal Engineering*, 148:229–237, 2019.

[268] M. Parhizi and A. Jain. Solution of the phase change stefan problem with time-dependent heat flux using perturbation method. *Journal of Heat Transfer*, 141(2):024503, 2019.

[269] M. Parhizi and A. Jain. Theoretical modeling of a phase change heat transfer problem with a pre-melted or pre-solidified region. *International Journal of Heat and Mass Transfer*, 136:635–643, 2019.

[270] M. N. Patel, S. Sirard, R. Limary, and D. Hymes. Freeze drying of high aspect ratio structures. In *Solid State Phenomena*, volume 219, pages 119–122. Trans Tech Publ, 2015.

[271] R. Pedroso and G. Domoto. Perturbation solutions for spherical solidification of saturated liquids. *ASME Journal of Heat Transfer*, 95(1):42–46, 02 1973.

[272] J. Pereira da Cunha and P. Eames. Thermal energy storage for low and medium temperature applications using phase change materials - A review. *Applied Energy*, 177:227–238, 2016.

[273] R. Perry and G. DW. *Perry's chemical engineers' handbook*. New York: McGraw-Hill, 2007.

[274] E. Pimentel, S. Papakonstantinou, and G. Anagnostou. Numerical interpretation of temperature distributions from three ground freezing applications in urban tunnelling. *Tunnelling and Underground Space Technology*, 28:57–69, 2012.

[275] E. Pimentel, A. Sres, and G. Anagnostou. Large-scale laboratory tests on artificial ground freezing under seepage-flow conditions. *Geotechnique*, 62(3):227, 2012.

[276] F. B. Planella, C. P. Please, and R. A. Van Gorder. Extended Stefan problem for the solidification of binary alloys in a sphere. *European Journal of Applied Mathematics*, 32(2):242–279, 2021.

[277] T. J. Porter, S. W. Schoenemann, L. J. Davies, E. J. Steig, S. Bandara, and D. G. Froese. Recent summer warming in northwestern Canada exceeds the holocene thermal maximum. *Nature communications*, 10(1):1631, 2019.

[278] A. Pourakabar and A. A. R. Darzi. Enhancement of phase change rate of PCM in cylindrical thermal energy storage. *Applied Thermal Engineering*, 150:132–142, 2019.

[279] N. Provatas and K. Elder. *Phase-field methods in materials science and engineering*. John Wiley & Sons, 2011.

[280] M. Prud'Homme, T. H. Nguyen, and D. L. Nguyen. A heat transfer analysis for solidification of slabs, cylinders, and spheres. *ASME Journal of Heat Transfer*, 111(3):699–705, 1989.

[281] M. H. Rahdar, A. Emamzadeh, and A. Ataei. A comparative study on pcm and ice thermal energy storage tank for air-conditioning systems in office buildings. *Applied Thermal Engineering*, 96:391–399, 2016.

[282] K. Raj, P. Vellaichamy, V. Ramalingam, et al. Development of novel correlations towards the freezing time estimation of phase change material inside a cylindrical capsule involving thickness and its thermal conductivity for thermal storage applications–an experimental and parametric studies. *Journal of Energy Storage*, 72:108629, 2023.

[283] M. K. Rathod and J. Banerjee. Thermal stability of phase change materials used in latent heat energy storage systems: A review. *Renewable and Sustainable Energy Reviews*, 18:246–258, 2013.

[284] S. Ray, A. K. Suthar, and S. Saha. An exponentially accurate spectral reconstruction technique for the single-phase one-dimensional stefan problem with constant coefficients. *International Journal of Heat and Mass Transfer*, 158:119841, 2020.

[285] H.-S. Ren. Application of the heat-balance integral to an inverse stefan problem. *International Journal of Thermal Sciences*, 46(2):118–127, 2007.

[286] H. Ribera, T. G. Myers, and M. M. MacDevette. Optimising the heat balance integral method in spherical and cylindrical Stefan problems. *Applied Mathematics and Computation*, 354:216–231, 2019.

[287] D. Riley, F. Smith, and G. Poots. The inward solidification of spheres and circular cylinders. *International Journal of Heat and Mass Transfer*, 17(12):1507–1516, 1974.

[288] D. Riseborough, N. Shiklomanov, B. Etzelmüller, S. Gruber, and S. Marchenko. Recent advances in permafrost modelling. *Permafrost and Periglacial Processes*, 19(2):137–156, 2008.

[289] Y. Roos and M. Karel. Amorphous state and delayed ice formation in sucrose solutions. *International Journal of Food Science & Technology*, 26(6):553–566, 1991.

[290] S. D. Roscani, D. A. Tarzia, and L. D. Venturato. The similarity method and explicit solutions for the fractional space one-phase Stefan problems. *Fractional Calculus and Applied Analysis*, pages 1–27, 2022.

[291] D. Rozmanov and P. G. Kusalik. Temperature dependence of crystal growth of hexagonal ice (i h). *Physical Chemistry Chemical Physics*, 13(34):15501–15511, 2011.

[292] B. Rubinsky and A. Shitzer. Analysis of a Stefan-like problem in a biological tissue around a cryosurgical probe. *ASME Journal of Heat Transfer*, 98(3):514–519, 1976.

[293] L. Rubinstein. *The Stefan problem*, volume 8. American Mathematical Soc., 2000.

[294] N. Sadoun, E.-K. Si-Ahmed, and P. Colinet. On the refined integral method for the one-phase stefan problem with time-dependent boundary conditions. *Applied Mathematical Modelling*, 30(6):531–544, 2006.

[295] S. Sanaye and A. Shirazi. Thermo-economic optimization of an ice thermal energy storage system for air-conditioning applications. *Energy and Buildings*, 60:100–109, 2013.

[296] W. H. Sang, Y. T. Lee, J. D. Chung, S. T. Kim, T. Kim, C.-H. Oh, and K.-H. Lee. Efficient numerical approach for simulating a full scale vertical ice-on-coil type latent thermal storage tank. *International Communications in Heat and Mass Transfer*, 78:29–38, 2016.

[297] R. D. Santiago, E. M. Hernández, and J. A. Otero. Constant mass model for the liquid-solid phase transition on a one-dimensional stefan problem: Transient and steady state regimes. *International Journal of Thermal Sciences*, 118:40–52, 2017.

[298] I. Sari, L. Hachani, A. Kharicha, Y. Fautrelle, B. Pichat, and K. Zaidat. 3d numerical simulation and experimental investigation of pure tin solidification under natural and forced convection. *International Journal of Thermal Sciences*, 164:106900, 2021.

[299] Y. Sasaki, Y. Hanawa, M. Otsuji, N. Fujiwara, M. Kato, Y. Yamaguchi, and H. Takahashi. Breakthrough of sublimation drying by liquid phase deposition. In *Solid State Phenomena*, volume 314, pages 172–177. Trans Tech Publ, 2021.

[300] R. Scardovelli and S. Zaleski. Direct numerical simulation of free-surface and interfacial flow. *Annual Review of Fluid Mechanics*, 31(1):567–603, 1999.

[301] M. Schremb, J. M. Campbell, H. K. Christenson, and C. Tropea. Ice layer spreading along a solid substrate during solidification of supercooled water: Experiments and modeling. *Langmuir*, 33(19):4870–4877, 2017.

[302] K. Schulte and B. Weigand. On the analytical modelling of the initial ice growth in a supercooled liquid droplet. *International Journal of Heat and Mass Transfer*, 127:1070–1081, 2018.

[303] E. A. Schuur, A. D. McGuire, C. Schädel, G. Grosse, J. W. Harden, D. J. Hayes, G. Hugelius, C. D. Koven, P. Kuhry, D. M. Lawrence, et al. Climate change and the permafrost carbon feedback. *Nature*, 520(7546):171–179, 2015.

[304] R. P. Sear. Nucleation: Theory and applications to protein solutions and colloidal suspensions. *Journal of Physics: Condensed Matter*, 19(3):033101, 2007.

[305] I. B. Sebastião, B. Bhatnagar, and S. Tchessalov. A kinetic model for spray-freezing of pharmaceuticals. *Journal of Pharmaceutical Sciences*, 110(5):2047–2062, 2021.

[306] I. B. Sebastião, B. Bhatnagar, S. Tchessalov, S. Ohtake, M. Plitzko, B. Luy, and A. Alexeenko. Bulk dynamic spray freeze-drying part 1: modeling of droplet cooling and phase change. *Journal of Pharmaceutical Sciences*, 108(6):2063–2074, 2019.

[307] I. B. Sebastião, B. Bhatnagar, S. Tchessalov, S. Ohtake, M. Plitzko, B. Luy, and A. Alexeenko. Bulk dynamic spray freeze-drying part 1: modeling of droplet cooling and phase change. *Journal of Pharmaceutical Sciences*, 108(6):2063–2074, 2019.

[308] I. B. Sebastião, B. Bhatnagar, S. Tchessalov, S. Ohtake, M. Plitzko, B. Luy, and A. Alexeenko. Bulk dynamic spray freeze-drying part 2: model-based parametric study for spray-freezing process characterization. *Journal of Pharmaceutical Sciences*, 108(6):2075–2085, 2019.

[309] H. Shabgard, W. Zhu, and A. Faghri. Integral solution of two-region solid–liquid phase change in annular geometries and application to phase change materials–air heat exchangers. *Energies*, 12(23):4474, 2019.

[310] Y. Shao, K. Soh, Y. Wan, M. Kumja, Z. Khin, M. Islam, and K. Chua. Simulation and experimental study of thermal storage systems for district cooling system under commercial operating conditions. *Energy*, page 117781, 2020.

[311] R. Shaw, A. Kostinski, and M. L. Larsen. Towards quantifying droplet clustering in clouds. *Quarterly Journal of the Royal Meteorological Society: A journal of the atmospheric sciences, applied meteorology and physical oceanography*, 128(582):1043–1057, 2002.

[312] R. A. Shaw, A. J. Durant, and Y. Mi. Heterogeneous surface crystallization observed in undercooled water. *The Journal of Physical Chemistry B*, 109(20):9865–9868, 2005.

[313] M. Sheikholeslami and O. Mahian. Enhancement of PCM solidification using inorganic nanoparticles and an external magnetic field with application in energy storage systems. *Journal of Cleaner Production*, 215:963–977, 2019.

[314] C. Shen, J. Simmons, and Y. Wang. Effect of elastic interaction on nucleation: Ii. implementation of strain energy of nucleus formation in the phase field method. *Acta Materialia*, 55(4):1457–1466, 2007.

[315] K. Shi and X. Duan. Freezing delay of water droplets on metallic hydrophobic surfaces in a cold environment. *Applied Thermal Engineering*, 216:119131, 2022.

[316] A. Shibkov, Y. I. Golovin, M. Zheltov, A. Korolev, and A. Leonov. Morphology diagram of nonequilibrium patterns of ice crystals growing in supercooled water. *Physica A: Statistical Mechanics and its Applications*, 319:65–79, 2003.

[317] A. Shirazi, M. Aminyavari, B. Najafi, F. Rinaldi, and M. Razaghi. Thermal–economic–environmental analysis and multi-objective optimization of an internal-reforming solid oxide fuel cell–gas turbine hybrid system. *International Journal of Hydrogen Energy*, 37(24):19111–19124, 2012.

[318] A. Shitzer. Cryosurgery: Analysis and experimentation of cryoprobes in phase changing media. *ASME Journal of Heat Transfer*, 133(1):011005, 2011.

[319] J. Simmons, C. Shen, and Y. Wang. Phase field modeling of simultaneous nucleation and growth by explicitly incorporating nucleation events. *Scripta Materialia*, 43(10):935–942, 2000.

[320] T. Singla, B. Kumar, and S. Sharma. Numerical study of the melting process of spherical phase change material with variable thermal conductivity. *Indian Journal of Physics*, pages 1–9, 2023.

[321] J. W. Sitison and D. A. Edwards. The heat balance integral method for cylindrical extruders. *Journal of Engineering Mathematics*, 122:1–16, 2020.

[322] D. R. Smith. *Singular-perturbation theory: An introduction with applications.* Cambridge University Press, 1985.

[323] W. R. Smith. Models for solidification and splashing in laser percussion drilling. *SIAM Journal on Applied Mathematics*, 62(6):1899–1923, 2002.

[324] M. Song and C. Dang. Review on the measurement and calculation of frost characteristics. *International Journal of Heat and Mass Transfer*, 124:586–614, 2018.

[325] A. Soward. A unified approach to Stefan's problem for spheres and cylinders. *Proceedings of the Royal Society of London. A. Mathematical and Physical Sciences*, 373(1752):131–147, 1980.

[326] J. Stachulak. Ventilation strategy and unique air conditioning at inco limited. *CIM Bulletin (Canadian Institute of Mining and Metallurgy);(Canada)*, 84(950), 1991.

[327] D. M. Stefanescu. *Science and engineering of casting solidification*. Springer, 2015.

[328] S. Stepanov, D. Nikiforov, and A. Grigorev. Multiscale multiphysics modeling of the infiltration process in the permafrost. *Mathematics*, 9(20):2545, 2021.

[329] C. Swaminathan and V. R. Voller. A general enthalpy method for modeling solidification processes. *Metallurgical Transactions B*, 23(5):651–664, 1992.

[330] K. Szilder. Theoretical and experimental study of ice accretion due to freezing rain on an inclined cylinder. *Cold Regions Science and Technology*, 150:25–34, 2018.

[331] S. Tabakova, F. Feuillebois, and S. Radev. Freezing of a supercooled spherical droplet with mixed boundary conditions. *Proceedings of the Royal Society A: Mathematical, Physical and Engineering Sciences*, 466(2116):1117–1134, 2010.

[332] G. Tammann and A. Büchner. Die unterkühlungsfähigkeit des wassers und die lineare kristallisationsgeschwindigkeit des eises in wäßrigen lösungen. *Zeitschrift für anorganische und allgemeine Chemie*, 222(4):371–381, 1935.

[333] F. Tan. An experimental study on channels formation during solidification of aqueous ammonium chloride. *Applied Thermal Engineering*, 25(14-15):2169–2192, 2005.

[334] K. Tanaka, T. Yamamoto, K. Nagashima, and K. Tsukamoto. A new method of evaluation of melt/crystal interfacial energy and activation energy of diffusion. *Journal of Crystal Growth*, 310(6):1281–1286, 2008.

[335] K. K. Tanaka and Y. Kimura. Theoretical analysis of crystallization by homogeneous nucleation of water droplets. *Physical Chemistry Chemical Physics*, 21(5):2410–2418, 2019.

[336] D. A. Tarzia. Relationship between neumann solutions for two-phase lamé-clapeyron-stefan problems with convective and temperature boundary conditions. *arXiv preprint arXiv:1406.0552*, 2014.

[337] D. A. Tarzia and C. V. Turner. A note on the existence of a waiting time for a two-phase stefan problem. *Quarterly of applied mathematics*, 50(1):1–10, 1992.

[338] D. A. Tarzia and C. V. Turner. Estimation of the occurance of the phase-change process in spherical coordinates. *International communications in heat and mass transfer*, 26(4):559–568, 1999.

[339] H. Tounsi, A. Rouabhi, and E. Jahangir. Thermo-hydro-mechanical modeling of artificial ground freezing taking into account the salinity of the saturating fluid. *Computers and Geotechnics*, 119:103382, 2020.

[340] H. Tounsi, A. Rouabhi, M. Tijani, and F. Guérin. Thermo-hydro-mechanical modeling of artificial ground freezing: application in mining engineering. *Rock Mechanics and Rock Engineering*, 52(10):3889–3907, 2019.

[341] R. Trivedi and W. Kurz. Dendritic growth. *International Materials Reviews*, 39(2):49–74, 1994.

[342] D. Turnbull. Phase changes. In *Solid state physics*, volume 3, pages 225–306. Elsevier, 1956.

[343] J. J. Vadasz, J. P. Meyer, S. Govender, and G. Ziskind. Experimental study of vibration effects on heat transfer during solidification of paraffin in a spherical shell. *Experimental Heat Transfer*, 29(3):285–298, 2016.

[344] R. Van der Sman. Phase field simulations of ice crystal growth in sugar solutions. *International Journal of Heat and Mass Transfer*, 95:153–161, 2016.

[345] R. van der Sman. Multiscale simulations of directional ice crystal growth in sugar solutions. *Food Structure*, 30:100214, 2021.

[346] J. Van Huissteden. *Thawing Permafrost*, volume 1143. Springer, 2020.

[347] C. Veerakumar and A. Sreekumar. Phase change material based cold thermal energy storage: Materials, techniques and applications – A review. *International Journal of Refrigeration*, 67:271–289, 2016.

[348] H. Vehkamäki, A. Määttänen, A. Lauri, I. Napari, and M. Kulmala. The heterogeneous zeldovich factor. *Atmospheric Chemistry and Physics*, 7(2):309–313, 2007.

[349] S. Vessot and J. Andrieu. A review on freeze drying of drugs with tert-butanol (tba)+ water systems: characteristics, advantages, drawbacks. *Drying Technology*, 30(4):377–385, 2012.

[350] M. P. Vikram, V. Kumaresan, S. Christopher, and R. Velraj. Experimental studies on solidification and subcooling characteristics of water-based phase change material (pcm) in a spherical encapsulation for cool thermal energy storage applications. *International Journal of Refrigeration*, 100:454–462, 2019.

[351] M. Vitel, A. Rouabhi, M. Tijani, and F. Guérin. Modeling heat transfer between a freeze pipe and the surrounding ground during artificial ground freezing activities. *Computers and Geotechnics*, 63:99–111, 2015.

[352] M. Vitel, A. Rouabhi, M. Tijani, and F. Guérin. Thermo-hydraulic modeling of artificial ground freezing: Application to an underground mine in fractured sandstone. *Computers and Geotechnics*, 75:80–92, 2016.

[353] J. Vogel and A. Thess. Validation of a numerical model with a benchmark experiment for melting governed by natural convection in latent thermal energy storage. *Applied Thermal Engineering*, 148:147–159, 2019.

[354] V. Voller and M. Cross. Accurate solutions of moving boundary problems using the enthalpy method. *International Journal of Heat and Mass Transfer*, 24(3):545–556, 1981.

[355] V. Voller and M. Cross. An explicit numerical method to track a moving phase change front. *International Journal of Heat and Mass Transfer*, 26(1):147–150, 1983.

[356] V. Voller and F. Falcini. Two exact solutions of a Stefan problem with varying diffusivity. *International Journal of Heat and Mass Transfer*, 58(1-2):80–85, 2013.

[357] V. R. Voller. An exact solution of a limit case Stefan problem governed by a fractional diffusion equation. *International Journal of Heat and Mass Transfer*, 53(23-24):5622–5625, 2010.

[358] V. R. Voller, M. Cross, and N. Markatos. An enthalpy method for convection/diffusion phase change. *International Journal for Numerical Methods in Engineering*, 24(1):271–284, 1987.

[359] V. R. Voller and C. Prakash. A fixed grid numerical modelling methodology for convection-diffusion mushy region phase-change problems. *International Journal of Heat and Mass Transfer*, 30(8):1709–1719, 1987.

[360] V. R. Voller and C. Swaminathan. General source-based method for solidification phase change. *Numerical Heat Transfer, Part B Fundamentals*, 19(2):175–189, 1991.

[361] V. R. Voller, J. B. Swenson, and C. Paola. An analytical solution for a Stefan problem with variable latent heat. *International Journal of Heat and Mass Transfer*, 47(24):5387–5390, 2004.

[362] M. Volmer and A. Weber. Keimbildung in übersättigten gebilden. *Zeitschrift für physikalische Chemie*, 119(1):277–301, 1926.

[363] V. Voulgaropoulos, N. Le Brun, A. Charogiannis, and C. N. Markides. Transient freezing of water between two parallel plates: A combined experimental and modelling study. *International Journal of Heat and Mass Transfer*, 153:119596, 2020.

[364] C. Vuik. Some historical notes about the Stefan problem. 1993.

[365] M. Vynnycky and S. Saleem. On the resolution of thermal gradients in a model for the continuous casting of binary alloys. *Applied Mathematics and Computation*, 2016.

[366] M. Vynnycky, S. Saleem, and H. Fredriksson. An asymptotic approach to solidification shrinkage-induced macrosegregation in the continuous casting of binary alloys. *Applied Mathematical Modelling*, 54:605–626, 2018.

[367] A. Wallman, J. King, and D. Riley. Asymptotic and numerical solutions for the two-dimensional solidification of a liquid half-space. *Proceedings of the Royal Society of London. Series A: Mathematical, Physical and Engineering Sciences*, 453(1962):1397–1410, 1997.

[368] G.-X. Wang and E. Matthys. Experimental determination of the interfacial heat transfer during cooling and solidification of molten metal droplets impacting on a metallic substrate: effect of roughness and superheat. *International Journal of Heat and Mass Transfer*, 45(25):4967–4981, 2002.

[369] S. Wang, C. Wang, J. Wang, S. Jiang, T. Zhang, and Z. Ma. An analytical solution for a phase change nano-capsule cooled by forced convection. *International Journal of Heat and Mass Transfer*, 212:124267, 2023.

[370] T. Wang, Y. Lu, L. Ai, Y. Zhou, and M. Chen. Dendritic growth model involving interface kinetics for supercooled water. *Langmuir*, 35(15):5162–5167, 2019.

[371] X. Wang and Y. Fautrelle. An investigation of the influence of natural convection on tin solidification using a quasi two-dimensional experimental benchmark. *International Journal of Heat and Mass Transfer*, 52(23-24):5624–5633, 2009.

[372] J. A. Warren, R. Kobayashi, A. E. Lobkovsky, and W. C. Carter. Extending phase field models of solidification to polycrystalline materials. *Acta Materialia*, 51(20):6035–6058, 2003.

[373] S. Weinbaum and L. Jiji. Singular perturbation theory for melting or freezing in finite domains initially not at the fusion temperature. *Journal of Applied Mechanics*, 44(1):25–30, 1977.

[374] S. Weinbaum and L. M. Jiji. Singular perturbation theory for melting or freezing in finite domains initially not at the fusion temperature. *Journal of Applied Mechanics, Transactions ASME*, 44(1):25–30, 1977.

[375] Y. Wen, J. Simmons, C. Shen, C. Woodward, and Y. Wang. Phase-field modeling of bimodal particle size distributions during continuous cooling. *Acta Materialia*, 51(4):1123–1132, 2003.

[376] S. Whitaker. Flow in porous media I: A theoretical derivation of Darcy's law. *Transport in Porous Media*, 1(1):3–25, 1986.

[377] J. A. Wilson, M. Haghshenas, and R. Kumar. Phase-change mechanism for evaporation in porous media using volume of fluid: Implicit formulation of interfacial temperature. *International Communications in Heat and Mass Transfer*, 103:90–99, 2019.

[378] A. S. Wood. A new look at the heat balance integral method. *Applied Mathematical Modelling*, 25(10):815–824, 2001.

[379] B. Wu, S. W. McCue, P. Tillman, and J. M. Hill. Single phase limit for melting nanoparticles. *Applied Mathematical Modelling*, 33(5):2349–2367, 2009.

[380] J. Wu, E. Gagnière, F. Jay, and C. Jallut. Population balance modeling for the charging process of a PCM cold energy storage tank. *International Journal of Heat and Mass Transfer*, 85:647–655, 2015.

[381] T. Wu, H.-C. Liaw, and Y.-Z. Chen. Thermal effect of surface tension on the inward solidification of spheres. *International journal of heat and mass transfer*, 45(10):2055–2065, 2002.

[382] T. Wu, X. Zhou, L. Zhang, X. Zhang, X. He, and Y. Xu. Theory and technology of real-time temperature field monitoring of vertical shaft frozen wall under high-velocity groundwater conditions. *Cold Regions Science and Technology*, 189:103337, 2021.

[383] J. Xie and C. Yuan. Parametric study of ice thermal storage system with thin layer ring by taguchi method. *Applied Thermal Engineering*, 98:246–255, 2016.

[384] M. Xu, S. Akhtar, M. A. Alzoubi, and A. P. Sasmito. Singular perturbation solution for a two-phase Stefan problem in outward solidification. In *ASME International Mechanical Engineering Congress and Exposition*, volume 59452, page V008T09A050. American Society of Mechanical Engineers, 2019.

[385] M. Xu, S. Akhtar, M. Mohit, and A. P. Sasmito. Development of a multi-stage model for freezing of a suspended binary solution droplet. *International Journal of Heat and Mass Transfer*, 221:125115, 2024.

[386] M. Xu, S. Akhtar, and A. P. Sasmito. A heterogeneous nucleation model for supercooled water and sucrose solution droplets under ultra-cold environments. In *ASME International Mechanical Engineering Congress and Exposition (*Accepted*)*, 2021.

[387] M. Xu, S. Akhtar, and A. P. Sasmito. A heterogenous nucleation model for supercooled water and sucrose solution droplets under ultra-cold environments. In *ASME International Mechanical Engineering Congress and Exposition*, volume 85673, page V011T11A068. American Society of Mechanical Engineers, 2021.

[388] M. Xu, S. Akhtar, A. F. Zueter, M. A. Alzoubi, L. Sushama, and A. P. Sasmito. Asymptotic analysis of a two-phase Stefan problem in annulus: Application to outward solidification in phase change materials. *Applied Mathematics and Computation*, 408:126343, 2021.

[389] M. Xu, S. Akhtar, A. F. Zueter, V. Auger, M. A. Alzoubi, and A. P. Sasmito. Development of analytical solution for a two-phase Stefan problem in artificial ground freezing using singular perturbation theory. *Journal of Heat Transfer*, 142(12):122401, 2020.

[390] M. Xu, Y. Gao, F. Fang, S. Akhtar, B. A. Chaedir, and A. P. Sasmito. Experimental and unified mathematical frameworks of water-ice phase change for cold thermal energy storage. *International Journal of Heat and Mass Transfer*, 187:122536, 2022.

[391] M. Xu, Y. Hanawa, S. Akhtar, A. Sakuma, J. Zhang, J. Yoshida, M. Sanada, Y. Sasaki, and A. P. Sasmito. Multi-scale analysis for solidification of phase change materials (PCMs): Experiments and modeling. *International Journal of Heat and Mass Transfer*, 212:124182, 2023.

[392] Z. Yan, M. Zhang, Y. Lai, W. Pei, T. Luo, F. Yu, and S. Yang. Countermeasures combined with thermosyphons against the thermal instability of high-grade highways

in permafrost regions. *International Journal of Heat and Mass Transfer*, 153:119047, 2020.

[393] B. Yang, X. Fu, W. Yang, N. Sun, S. Hu, Y. Lu, and M.-B. Yang. Prediction of heat conduction with phase-change effects during cooling stage of injection molding of high-density polyethylene: approximate integral approach. *Journal of Macromolecular Science, Part B*, 49(4):734–749, 2010.

[394] B. Yang, A. Raza, F. Bai, T. Zhang, and Z. Wang. Microstructural evolution within mushy zone during paraffin's melting and solidification. *International Journal of Heat and Mass Transfer*, 141:769–778, 2019.

[395] Y. Yao, C. Li, Z. Tao, R. Yang, and H. Zhang. Experimental and numerical study on the impact and freezing process of a water droplet on a cold surface. *Applied Thermal Engineering*, 137:83–92, 2018.

[396] M. Ye, G. Hu, F. Guo, W. Huang, Z. Wang, X. Zhao, and Y. Li. A novel semi-analytical solution for calculating the temperature distribution of the lithium-ion batteries during nail penetration based on Green's function method. *Applied Thermal Engineering*, page 115129, 2020.

[397] F. Yigit. Approximate analytical and numerical solutions for a two-dimensional stefan problem. *Applied Mathematics and Computation*, 202(2):857–869, 2008.

[398] C. Yu, Q. Peng, X. Liu, P. Cao, and F. Yao. Role of metal foam on ice storage performance for a cold thermal energy storage (CTES) system. *Journal of Energy Storage*, 28:101201, 2020.

[399] Z.-T. Yu, L.-W. Fan, Y.-C. Hu, and K.-F. Cen. Perturbation solution to heat conduction in melting or solidification with heat generation. *Heat and Mass Transfer*, 46:479–483, 2010.

[400] C. Zhang, Q. Sun, and Y. Chen. Solidification behaviors and parametric optimization of finned shell-tube ice storage units. *International Journal of Heat and Mass Transfer*, 146:118836, 2020.

[401] H. Zhang, K. El Kadi, M. I. H. Ali, and I. Janajreh. Cryo-powered desalination: Experimental investigations on brine droplets freezing in a natural convection environment. *Desalination*, 567:116974, 2023.

[402] H. Zhang, Z. Jin, M. Jiao, and Z. Yang. Experimental investigation of the impact and freezing processes of a water droplet on different cold concave surfaces. *International Journal of Thermal Sciences*, 132:498–508, 2018.

[403] H. Zhang, S. Savvopoulos, H. Hatzikirou, and I. Janajreh. Experimental and mathematically validated studies of pure water droplet freezing under natural free convection. *Desalination*, 555:116512, 2023.

[404] M. Zhang, W. Pei, Y. Lai, F. Niu, and S. Li. Numerical study of the thermal characteristics of a shallow tunnel section with a two-phase closed thermosyphon group in a permafrost region under climate warming. *International Journal of Heat and Mass Transfer*, 104:952–963, 2017.

[405] X. Zhang, X. Liu, X. Wu, and J. Min. Simulation and experiment on supercooled sessile water droplet freezing with special attention to supercooling and volume expansion effects. *International Journal of Heat and Mass Transfer*, 127:975–985, 2018.

[406] X. Zhang, X. Wu, and J. Min. Freezing and melting of a sessile water droplet on a horizontal cold plate. *Experimental Thermal and Fluid Science*, 88:1–7, 2017.

[407] Y. Zhao, Q. Guo, T. Lin, and P. Cheng. A review of recent literature on icing phenomena: Transport mechanisms, their modulations and controls. *International Journal of Heat and Mass Transfer*, 159:120074, 2020.

[408] Y. Zhao, X. Zhang, X. Xu, and S. Zhang. Research progress in nucleation and supercooling induced by phase change materials. *Journal of Energy Storage*, 27:101156, 2020.

[409] M. Zhelnin, A. Kostina, A. Prokhorov, O. Plekhov, M. Semin, and L. Levin. Coupled thermo-hydro-mechanical modeling of frost heave and water migration during artificial freezing of soils for mineshaft sinking. *Journal of Rock Mechanics and Geotechnical Engineering*, 14(2):537–559, 2022.

[410] J. Zhou, W. Zhao, and Y. Tang. Practical prediction method on frost heave of soft clay in artificial ground freezing with field experiment. *Tunnelling and Underground Space Technology*, 107:103647, 2021.

[411] Y. Zhou, X.-x. Hu, T. Li, D.-h. Zhang, and G.-q. Zhou. Similarity type of general solution for one-dimensional heat conduction in the cylindrical coordinate. *International Journal of Heat and Mass Transfer*, 119:542–550, 2018.

[412] Y. Zhou, X.-Y. Shi, and G.-Q. Zhou. Exact solution for a two-phase Stefan problem with power-type latent heat. *Journal of Engineering Mathematics*, 110(1):1–13, 2018.

[413] Y. Zhou, Y.-J. Wang, and W.-K. Bu. Exact solution for a Stefan problem with latent heat a power function of position. *International Journal of Heat and Mass Transfer*, 69:451–454, 2014.

[414] Y. Zhou and L.-j. Xia. Exact solution for Stefan problem with general power-type latent heat using Kummer function. *International Journal of Heat and Mass Transfer*, 84:114–118, 2015.

[415] Z.-Q. Zhu, M.-J. Liu, N. Hu, Y.-K. Huang, L.-W. Fan, Z.-T. Yu, and J. Ge. Inward solidification heat transfer of nano-enhanced phase change materials in a spherical capsule: an experimental study. *Journal of Heat Transfer*, 140(2):022301, 2018.

[416] B. Zobrist, V. Soonsin, B. P. Luo, U. K. Krieger, C. Marcolli, T. Peter, and T. Koop. Ultra-slow water diffusion in aqueous sucrose glasses. *Physical Chemistry Chemical Physics*, 13(8):3514–3526, 2011.

[417] A. Zueter, A. Nie-Rouquette, M. A. Alzoubi, and A. P. Sasmito. Thermal and hydraulic analysis of selective artificial ground freezing using air insulation: Experiment and modeling. *Computers and Geotechnics*, 120:103416, 2020.

[418] A. F. Zueter and A. P. Sasmito. Cold energy storage as a solution for year-round renewable artificial ground freezing: Case study of the giant mine remediation project. *Renewable Energy*, 203:664–676, 2023.

[419] A. F. Zueter, M. Xu, M. A. Alzoubi, and A. P. Sasmito. Development of conjugate reduced-order models for selective artificial ground freezing: Thermal and computational analysis. *Applied Thermal Engineering*, 190:116782, 2021.